NBS SPECIAL PUBLICATION 568

U.S. DEPARTMENT OF COMMERCE / National Bureau of Standards

Laser Induced Damage in Optical Materials: 1979

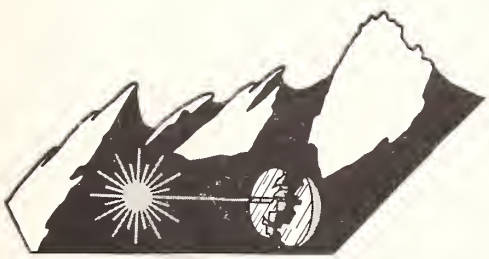

BOULDER DAMAGE SYMPOSIUM

ASTM

STP 726

NATIONAL BUREAU OF STANDARDS

The National Bureau of Standards[1] was established by an act of Congress on March 3, 1901. The Bureau's overall goal is to strengthen and advance the Nation's science and technology and facilitate their effective application for public benefit. To this end, the Bureau conducts research and provides: (1) a basis for the Nation's physical measurement system, (2) scientific and technological services for industry and government, (3) a technical basis for equity in trade, and (4) technical services to promote public safety. The Bureau's technical work is performed by the National Measurement Laboratory, the National Engineering Laboratory, and the Institute for Computer Sciences and Technology.

THE NATIONAL MEASUREMENT LABORATORY provides the national system of physical and chemical and materials measurement; coordinates the system with measurement systems of other nations and furnishes essential services leading to accurate and uniform physical and chemical measurement throughout the Nation's scientific community, industry, and commerce; conducts materials research leading to improved methods of measurement, standards, and data on the properties of materials needed by industry, commerce, educational institutions, and Government; provides advisory and research services to other Government agencies; develops, produces, and distributes Standard Reference Materials; and provides calibration services. The Laboratory consists of the following centers:

Absolute Physical Quantities[2] — Radiation Research — Thermodynamics and Molecular Science — Analytical Chemistry — Materials Science.

THE NATIONAL ENGINEERING LABORATORY provides technology and technical services to the public and private sectors to address national needs and to solve national problems; conducts research in engineering and applied science in support of these efforts; builds and maintains competence in the necessary disciplines required to carry out this research and technical service; develops engineering data and measurement capabilities; provides engineering measurement traceability services; develops test methods and proposes engineering standards and code changes; develops and proposes new engineering practices; and develops and improves mechanisms to transfer results of its research to the ultimate user. The Laboratory consists of the following centers:

Applied Mathematics — Electronics and Electrical Engineering[2] — Mechanical Engineering and Process Technology[2] — Building Technology — Fire Research — Consumer Product Technology — Field Methods.

THE INSTITUTE FOR COMPUTER SCIENCES AND TECHNOLOGY conducts research and provides scientific and technical services to aid Federal agencies in the selection, acquisition, application, and use of computer technology to improve effectiveness and economy in Government operations in accordance with Public Law 89-306 (40 U.S.C. 759), relevant Executive Orders, and other directives; carries out this mission by managing the Federal Information Processing Standards Program, developing Federal ADP standards guidelines, and managing Federal participation in ADP voluntary standardization activities; provides scientific and technological advisory services and assistance to Federal agencies; and provides the technical foundation for computer-related policies of the Federal Government. The Institute consists of the following centers:

Programming Science and Technology — Computer Systems Engineering.

[1]Headquarters and Laboratories at Gaithersburg, MD, unless otherwise noted; mailing address Washington, DC 20234.
[2]Some divisions within the center are located at Boulder, CO 80303.

Laser Induced Damage In Optical Materials: 1979

Proceedings of a Symposium Sponsored by:
National Bureau of Standards
American Society for Testing and Materials
Office of Naval Research
Department of Energy
Defense Advanced Research Project Agency

October 30-31, 1979
NBS, Boulder, Colorado 80303

Edited by:

Harold E. Bennett
Naval Weapons Center
China Lake, California 93555

Alexander J. Glass
Lawrence Livermore Laboratories
Livermore, California 94550

Arthur H. Guenther
Air Force Weapons Laboratory
Kirtland Air Force Base, New Mexico 97117

Brian E. Newnam
Los Alamos Scientific Laboratory
Los Alamos, New Mexico 87545

BOULDER DAMAGE SYMPOSIUM

U.S. DEPARTMENT OF COMMERCE, Philip M. Klutznick, Secretary
Luther H. Hodges, Jr., Deputy Secretary
Jordan J. Baruch, Assistant Secretary for Productivity, Technology and Innovation

NATIONAL BUREAU OF STANDARDS, Ernest Ambler, Director

Issued July 1980

Library of Congress Catalog Card Number: 80-600100

National Bureau of Standards Special Publication 568
Nat. Bur. Stand. (U.S.), Spec. Publ. 568, 530 pages (July 1980)
CODEN: XNBSAV

U.S. GOVERNMENT PRINTING OFFICE
WASHINGTON: 1980

For sale by the Superintendent of Documents, U.S. Government Printing Office, Washington, D.C. 20402
Price $9.50
(Add 25 percent for other than U.S. mailing).

Foreword

The Proceedings contain the papers presented at the Tenth Anniversary Symposium on Optical Materials for High Power Lasers held at the National Bureau of Standards in Boulder, Colorado, on October 30-31, 1979. The Symposium was jointly sponsored by the National Bureau of Standards, the American Society for Testing and Materials, the Office of Naval Research, the Defense Advanced Research Projects Agency, and the Department of Energy. The Symposium was attended by about 150 scientists from the United States, the United Kingdom, France, Canada, West Germany and Denmark. It was divided into sessions devoted to the following topics: Transparent Optical Materials and the Measurement of Their Properties, Mirrors and Surfaces, Thin Film Characteristics, Thin Film Damage, Considerations for High Power Systems, and finally Theory and Breakdown. The Symposium Co-Chairmen were Dr. Harold E. Bennett of the Naval Weapons Center, Dr. Alexander J. Glass of the Lawrence Livermore Laboratory, Dr. Arthur H. Guenther of the Air Force Weapons Laboratory, and Dr. Brian E. Newnam of the Los Alamos Scientific Laboratory. They also served as editors of this report.

The editors assume full responsibility for the summary, conclusions, and recommendations contained in the report, and for the summaries of discussion found at the end of each paper. The manuscripts of the papers presented at the Symposium have been prepared by the designated authors, and questions pertaining to their content should be addressed to those authors. The interested reader is referred to the bibliography at the end of the summary article for general references to the literature of laser damage studies. The Twelfth Annual Symposium on this topic will be held in Boulder, Colorado, from September 30 to October 1, 1980. A concerted effort will be made to ensure closer liaison between the practitioners of high peak power and the high average power community.

The principal topics to be considered as contributed papers in 1980 do not differ drastically from those enumerated above. We expect to hear more about improved scaling relations as a function of pulse duration, area, and wavelength, and to see a continuing transfer of information from research activities to industrial practice. New sources at shorter wavelengths continue to be developed, and a corresponding shift in emphasis to short wavelength and repetitively pulsed damage problems is anticipated. Fabrication and test procedures will continue to advance, particularly in the diamond-turned optics and thin film areas.

The purpose of these symposia is to exchange information about optical materials for high power lasers. The editors will welcome comment and criticism from all interested readers relevant to this purpose, and particularly relative to our plans for the Twelfth Annual Symposium.

H.E. Bennett, A.J. Glass,
A.H. Guenther and B.E. Newnam
Co-Chairmen

DISCLAIMER

Certain papers contributed to this publication have been prepared by other than NBS authors. These papers have not been reviewed or edited by NBS; therefore, the National Bureau of Standards accepts no responsibility for comments or recommendations contained therein.

Certain commercial equipment, instruments, and materials are identified in this publication in order to explain the experimental procedure adequately. Such identification in no way implies approval, recommendation, or endorsement by the National Bureau of Standards, nor does it imply that the equipment, instruments, or materials identified are necessarily the best available for the purpose.

CONTENTS

Surface and Mirrors

Thin Film Characterization

Thin Film Damage

Systems

Theory and Breakdown

SYMPOSIUM WELCOME

Arthur H. Guenther
Air Force Weapons Laboratory
Kirtland AFB, New Mexico 87117

Last year at the Tenth Annual Boulder Damage Symposium, Alex Glass expressed his hope that it might be the last. We made a vain attempt to call a close to these annual gatherings because of two reasons. First, we thought that after ten years we should have been able to solve the problem of laser damage and move on to new challenges, but as we enter our second decade the continued attendance and interest accorded these annual sojourns to Boulder indicate that laser damage is still a subject of import to a large, varied and growing community. The second and perhaps subconsciously greater reason for our predisposition to suggest a cessation was a result of the pressures of other commitments for both Alex and myself. However, since you the participants would have no talk of concluding this series we did the next best thing, which some of you may have noticed from the published program, that is, enlisting the services and aid of two additional individuals well known for their many contributions in the laser damage area. They are from the two largest concerned organization in this technology, namely DOD and DOE, whose interests span the field from high average power, generally CW, to high peak power, presently single pulse interaction regimes. Undoubtedly somewhere in the future these diverse extremes will meet in the shorter wavelength, high power, rep rate laser arena. These individuals, two gluttons for punishment, I mean pillars of perseverance, are old timer Hal Bennett from the Michelson Laboratory at the Naval Weapons Center and Brian Newnam, one of a more recent vintage, young enough to have accomplished his doctoral research in laser damage, from the Los Alamos Scientific Laboratory. Hopefully, this selection suggests a certain objectivity on Alex's and my part, since we asked individuals from the enemy's camp--I mean sister laboratories. Both being government organizations, we hope to be able to rely upon a certain donation of necessary resources, primarily in the secretarial and communication areas which are essential in the operation of any meeting such as this one.

This now enlarged steering committee would like to formally welcome you to the Tenth Anniversary Damage Symposium. We are pleased to see many familiar faces, and again would like to specifically welcome those of you who are new to these deliberations. We would especially like to welcome our foreign participants who have through their attendance added a truly international flavor to this meeting. However, we are disappointed that other anticipated contributors from abroad could not come and present their latest work. However, it is anticipated that in some cases their manuscripts will be included in the conference proceedings.

I would be remiss if I did not mention that due to a reorganization here at the National Bureau of Standards we have a new team responsible for the sponsorship and operation of the meeting proper as well as publication of the proceedings. Bob Kamper, Chief, Electromagnetic Technology Division, has graciously offered the services of Aaron Sanders, Group Leader, Optical Electronic Metrology Group, and his able assistant, Mrs. Norma Lear, two individuals of long standing interest and association with this meeting, to coordinate the Bureau's involvement. We welcome the opportunity to work with two such cooperative and capable individuals, as we say farewell and many thanks to Hal Boyne and his staff who so admirably aided us in the past.

Concerning this year's meeting, you will note from the program that an acceptable basis for observed scaling relations of laser damage thresholds with a variety of parameters may be just around the corner. I believe this results from several factors. In the first place, this year there are many more than the usual number of papers which can be characterized as theoretical, and, in the main, they are supported by carefully obtained experimental data. In the second place, these more analytical reports with their adjunct data are taken on real world samples, and thus are of immediate interest to anyone interested in the response of optical elements in practical high

power laser environments. Finally, the samples utilized in these tests (with the aid and input of material scientists) have been characterized better and more completely. In the future, we expect that the real world response will be unraveled even further as use of sophisticated and sensitive characterization methods become more generally available. However, any quantum jumps in damage resistance I feel will come from improvements in materials purity and more importantly in fabrication and deposition procedures, such as in the areas of polishing, the introduction of chemical vapor deposited materials and proper background gases in the deposition of thin films or through continued progress in the area of forging of large size optical elements. Certainly any improvements in damage threshold arising from developments in these areas can only be realized in real applications through concurrent advancements in avoiding environmental degradations introduced in the utilization of these elements in the comparatively adverse environments associated with operating systems. On the other hand, quantum jumps in our understanding of the damage mechanism will undoubtedly come in part from work presently being performed at shorter wavelengths, with the impact of rep-rated studies still largely in the future.

Thus we see the narrowing of our more fundamental interests to the arena of material response and scaling primarily in those domains where the elements will be used and not necessarily as keys to delineating the intrinsic response of pure dielectric or metallic elements to high power coherent optical radiation. The intrinsic behavior of the interaction scenario will have to wait, if it ever comes, as one may never be able to convince everyone that they have intrinisc breakdown data upon which to benchmark their theory, and thus I tend to agree with Prof. Manenkov that there may never have been intrinsic material breakdown and that all threshold data is impurity or imperfection dominated. However, there is still plenty of good physics and chemistry in the laser damage field, as we will see during this symposium.

We would like to second John Detrio's invitation to the participants of this meeting to aid in the establishment of a separate ASTM Committee on Lasers and Optics. After all, this meeting and the reason for our being here was initiated and supplied by the ASTM over a decade ago.

Recalling those early stages of the ASTM Committee's activities in this symposium, it is with much sorrow and regret that we note the passing of one of the early mainstays of the ASTM's activities and this conference. He was a man dedicated to the highest professional and individual qualities, and as such has set a high standard for us to emulate, Allan Carlson, President of Cleveland Crystal, passed from the scene this August. Allan was one of the earliest members of the ASTM Subcommittee on Laser Standards and chaired the group on crystals. He participated in this meeting many times and contributed significantly to the development of crystalline materials for large aperture, high power lasers. Both his personal qualities and his technical contributions will be sorely missed.

In closing, I would like to acknowledge the continuing financial support of the Defense Advanced Research Projects Agency, the Office of Naval Research, the National Bureau of Standards, and the Department of Energy, and particularly to John Detrio and the American Society of Test and Materials for professional sponsorship. I am sure I speak for Drs. Bennett, Glass and Newnam in wishing you a warm welcome to this our Tenth Anniversary Damage Symposium.

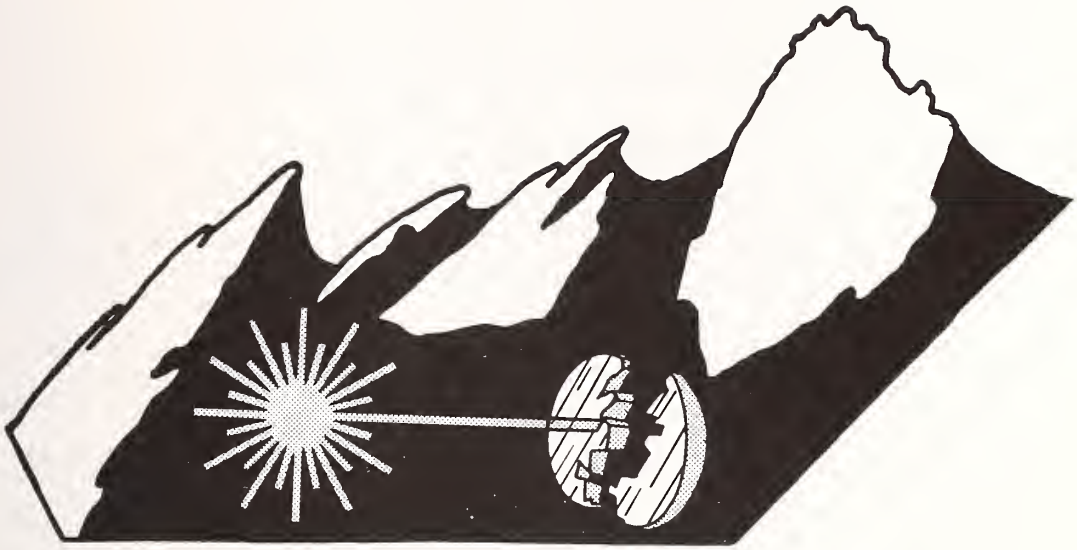

BOULDER DAMAGE SYMPOSIUM

In commemoration of our tenth anniversary meeting and in expectation of its continuance, the organizers of this meeting decided that it would be appropriate to establish a logo which could be used to highlight the symposium and its future correspondence and publications. Thus a contest was held during this meeting, with the ground rules that the logo must be simple, and easily recognizable as representing the subject of the symposium. After a difficult time of evaluating over 30 entries, the organizers of the conference selected the logo you see decorating this our tenth anniversary proceedings. It was submitted by Major J. R. Bettis (USAF) of the US Naval Academy. Jerry is well known to the participants of this conference for his many technical presentations and stimulating demeanor. He now has made a contribution of another sort, one we are sure is as important and lasting.

REMARKS TO ELEVENTH ANNUAL SYMPOSIUM
OPTICAL MATERIALS FOR HIGH POWER LASERS (SOMHPL)

Major Harry V. Winsor, USAF
Defense Advanced Research Projects Agency, Materials Sciences office
1400 Wilson Boulevard
Arlington, Virginia 22209

Welcome to this year's "Boulder Damage Symposium" (BDS). Our topic of laser damage to mirrors and window materials has expanded until it now encompasses the making and using of all sorts of optical components for high power (mostly pulsed) laser systems. Somehow, however, SOMHPL is much harder to say than BDS!

DARPA remains interested in the progress shown at this meeting as well as at closed topical meetings and it is my pleasure to give a summary of the reasons for our continued interest.

Laser systems for space defense and various other military applications have been one of DARPA's primary thrusts for more than 10 years. The success of these programs depends on having suitable components to handle and direct the laser beam so that it performs its intended function. Most high power laser components require thin film coatings for reflection control, so a large amount of our research has been devoted to achieving improved thin film behavior. Several specific thin film efforts are worthy of note here:

Hydrogen Fluoride lasers emit light at around 2.8 um, which lies in the center of the hydrogen band for most materials containing hydrogen. Removing all hydrogen from a thin film requires exacting care and specific measures during film deposition. This is because the tolerable amount of hydrogen may go below the equivalent of two monolayers of water! This must be achieved with components which can be handled in a real world containing humidity, fuel vapors, and other hydrocarbon vapors. If we go into space, we must add molecular and atomic hydrogen bombardment. Recent thin film research reported at this meeting and elsewhere promises to make substantial improvements in space tolerant films for HF lasers.

Films are important to UV lasers as well. Here, since no CW UV laser of high power has been built, the research problems center about how one develops the ability to withstand repetitive pulses of laser energy as high as 10 Joules/cm^2/pulse. While the pheonomena of single pulse damage have been investigated for many years, almost no work has been done on the durability of repetitive pulsed coatings. I suspect there are many surprises in store for thin film designers when this work is performed - in fact several phenomena have been observed at the present state of our researches:

One appears to be thermal fatigue of the mirror's metal substrate under a loading less than 10% of the single shot damage threshold. Nominally identical sample, with somewhat higher absorption, did not exhibit this effect. It would appear that absorption measurements must be refined to measure either transient (bleachable) absorption, or the location of absorption within the film to give us diagnostics suitable for making orderly progress in overcoming these effects.

The other is that films on metal substrates may exhibit two thresholds: one at initiation of damage and another for propagation of the damage. With large components, it is possible that isolated sites may exhibit initiation at fluxes well below a more uniform propagation threshold, allowing the component to be used with isolated damage sites without further concern. Under other conditions, the propagation threshold may be well below the desired operational loading, necessitating perfect control of the initiation threshold. The field of high power thin films is now mature enough that these distinctions must be taken into account in most further research and development.

With these problems, and the desire to exploit IR, UV and Visible lasers for military and civilian applications, a new era of more basic research appears to be upon us. DARPA will be steering its research toward these more fundamental topics as soon as the rather more applied tasks have been accomplished.

Passing on to the topic of mirrors, it is apparent that the problem of selecting the correct substrate material has not yet been reduced to a simple procedure, and it may never be. The heat exchange function must not set requirements that affect the optical requirements the mirror must meet. This is ever harder to accomplish as the system designers seek to raise the power density in their beam trains. New methods of removing heat rapidly and requiring lower coolant pump power are needed. Lower pumping pressures are especially sought, since the current generation of mirrors must be polished under pressure - not an easy operation. The next generation may have to be polished under flow conditions - an even harder proposition - unless better cooling methods are devised.

Another example of the incompatibilities encountered in mirrors is the choice of thermal conductivity for the substrate. Higher thermal conductivity is a virtue, as long as the thermal expansion and elastic modulus are not compensatingly worse. The substrate however will experience no thermal distortion if its thermal expansion coefficient is zero. This is obtainable - but it requires a much lower thermal conductivity, which lowers the pulse damage threshold of the thin film, and consequently the fatigue limit power threshold.

Still another example of conflicting requirements that do not appear until the component is assembled and characterized is due to the metallurgical condition of the substrate. Molybdenum suitable for high performance heat exchangers does not appear to be polishable to UV tolerances. The problems of making mirrors is becoming a multidisciplinary problem of first order - a fact that was remarked upon last year, but is now a far more immediate concern.

Windows have not received much attention at DARPA over the last year, but may still be required for many proposed laser systems. Developments that may help when windows are addressed again include the successful forging of IR lenses to figure from KBr blanks. This technology appears exciting for its promise of reducing polishing lead time significantly. Current trials show that every lens produced meets IR specs, and it appears that control to visible tolerances can be obtained with several years more research.

Fiber optics and integrated optics may well need to borrow from the many technologies, tricks and theories developed under laser damage and power handling component research, since power densities in optical fibers are approaching component damage levels. Specific near term problems will concern the insertion of maximum power at 1.45 um into silicon waveguides. These problems arise when trying to use the fibers for great distances without introducing repeaters.

In all the above efforts, and in general, it is apparent that the cost of the optics must be reduced, and that the reliability and ability to design to desired performance must increase. This is the task ahead of us over the next several years as this field matures. I know that this conference will continue to play an important role in improving optical components technology and I hope you enjoy it as much as I will!

Laser Induced Damage in Optical Materials

Tenth Anniversay ASTM Symposium

October 30-31, 1979

Abstract

The Tenth Anniversary Symposium on Optical Materials for High Power Lasers (Boulder Damage Symposium) was held at the National Bureau of Standards in Boulder, Colorado, 30-31 October 1979. The Symposium was held under the auspices of ASTM Committee F-1, Subcommittee on Laser Standards, with the joint sponsorship of NBS, the Defense Advanced Research Project Agency, the Department of Energy, and the Office of Naval Research. About 150 scientists attended the Symposium, including representatives of the United Kingdom, France, Canada, Japan, West Germany and Denmark. The Symposium was divided into sessions concerning Transparent Optical Materials and the Measurement of Their Properties, Mirrors and Surfaces, Thin Film Characteristics, Thin Film Damage, Considerations for High Power Systems, and finally Theory and Breakdown. As in previous years, the emphasis of the papers presented at the Symposium was directed toward new frontiers and new developments. Particular emphasis was given to materials for high power apparatus. The wavelength range of prime interest was from 10.6 μm to the uv region. Highlights included surface characterization, thin film substrate boundaries, and advances in fundamental laser-matter threshold interactions and mechanisms. The scaling of damage thresholds with pulse duration, focal area, and wavelength was discussed in detail. Harold E. Bennett of the Naval Weapons Center, Alexander J. Glass of the Lawrence Livermore Laboratory, Arthur H. Guenther of the Air Force Weapons Laboratory, and Brian E. Newnam of the Los Alamos Scientific Laboratory were co-chairmen of the Symposium. The Twelfth Annual Symposium is scheduled for 30 September - 1 October 1980 at the National Bureau of Standards, Boulder, Colorado.

Key Words: Laser damage; laser interaction; optical components; optical fabrication; optical materials and properties; thin film coatings.

1. Introduction

The Tenth Anniversary Symposium on Optical Materials for High Power Lasers (Boulder Damage Symposium) was held, as in previous years, at the National Bureau of Standards in Boulder, Colorado, 30-31 October 1979. The Symposium was held under the auspices of the ASTM Committee F-1, Subcommittee on Laser Standards, with the joint sponsorship of NBS, the Defense Advanced Research Projects Agency, the Department of Energy, and the Office of Naval Research. Working sessions of the Committee F-1 Subcommittee on Lasers were held on Monday, 29 October. About 150 scientists attended the Symposium, including representatives of the United Kingdom, France, Canada, Japan, West Germany and Denmark. The Symposium was divided into sessions concerning Transparent Optical Materials and the Measurement of Their Properties, Mirrors and Surfaces, Thin Film Characteristics, Thin Film Damage, Considerations for High Power Systems, and finally Theory and Breakdown. As in previous years, several poster sessions were held. The general consensus of those presenting poster papers and those viewing them was highly favorable. In all, over forty technical presentations

were made. Harold E. Bennett of the Naval Weapons Center, Alexander J. Glass of the Lawrence Livermore Laboratory, Arthur H. Guenther of the Air Force Weapons Laboratory, and Brian E. Newnam of the Los Alamos Scientific Laboratory, were co-chairmen of the Symposium. At this, our Tenth Anniversary Symposium, a logo was selected to highlight this series of meetings as we embark on our second decade of damage studies. The purpose of these symposia is to exchange information about optical materials for high power lasers. The authors will welcome comments and criticism from all interested readers relevant to this purpose and particularly relative to our plans for the Twelfth Annual Symposium, scheduled for 30 September - 1 October 1980, at the National Bureau of Standards, Boulder, Colorado.

2. Principal Conclusions

The field of laser-induced damage in optical material continues to attract considerable interest. The specific focus of the field, however, changes as problems are solved and new applications emerge. It is obvious after a decade of research in the response of optical materials to high power laser radiation and the impact it has had on laser system design that a reassessment needs to be made. In simpler terms, somewhat simple problems have been overcome primarily through the applications of obvious solutions such as high-purity starting materials, high-precision fabrication and the identification of damage initiators through the use of existing instrumental methods. However, now that the cream has been skimmed, we are left with the requirement to go back to first principles and make long-range plans to allow one to optimize optical material and system performance. As an indication of this philosophy, Major Harry Windsor, Defense Advanced Research Projects Agency, indicated that that agency was encouraging more fundamental work on material and material/optical interactions than formerly was the case. Studies will undoubtedly become more experimental in attempting to identify salient properties and features of the fundamental laser material interaction scenario and thus less applied. This is not to mean that applied technology will not continue but the emphasis will most certainly change. It is anticipated that the directly applied work will concentrate on real world components as opposed to studying intrinsic damage mechanisms in an attempt to reduce costs and improve component reliability. As far as the U.S. Government is concerned, increased emphasis will be given to shorter wavelength systems, particularly those which can be repetitively pulsed, an area in which there is scant data to date. There is no question that as one approaches the uv, novel polishing procedures, more stringent coating tolerances, etc., will be required.

At the Symposium, the presented papers concentrated on materials and measurement of their properties, mirrors and optical surfaces, thin films and damage sensitivity, systems considerations and, as usual, theory and breakdown phenomena. As expected, the majority of papers again concerned the Achilles heel of thin films. It was there, together with new revealing theoretical descriptions of the interaction process, that the greatest advances were reported.

2.1 Materials and Measurements

In the area of materials and measurements, continuing attention is being given to the area of press forging as a technique for the low cost manufacture of large, low-cost transparent elements. The use of hot isostatic pressing (HIP) techniques is proving successful in removing veils within the material. The optical performance of forged calcium fluoride for infrared windows was not markedly improved by the HIP process, but elimination of veils led to potential improvement in the short-pulse damage threshold over windows which contain veils. Press forging of lithium fluoride and calcium fluoride has shown increased resistance to humidity and, in the case of lithium fluoride, the highest surface damage threshold of any ultraviolet crystal studied to date. In an additional study, two-stage forging of lithium fluoride was found necessary to avoid veiling in that material. This process increased the micro yield strength by a factor of 10 while producing little, if any, increase in scattering.

Several new candidate laser materials were discussed including yttrium orthophosphate (YPO_4) proposed as a substitute for calcite. Beryllium fluoride (BeF_2) glasses as a low index but hygroscopic material was proposed as a host for laser glasses. Indications from reflectivity measurements were that its band gap is similar to that of lithium fluoride. The lowest energy reflectance peak was located at 12.8 eV. This material should be usable to 150 nm. Other materials discussed included YLF and KYF which have shown potential to be grown to large-diameter crystals. Continued interest in chalcogenide glasses was also evident. In an interesting study it was noticed there was an increase in absorption measured by a reflectivity change just prior to catastrophic damage which could serve as a nondestructive prethreshold test for these materials.

Two papers concerned themselves with the performance of windows at 10.6 μm. In one case, absorbed CO_2 laser radiation in a ZnSe window produced the expected thermal lensing; however, the minimum focal spot size was not changed over that manifest under low-power conditions. The other work of note concerned damage in alkali halides. It was revealed that the electric field at which damage occurred on the surfaces of state-of-the-art crystals of NaCl and KCl was only one-half of the bulk damage value. There was considerable agreement with previously reported Russian work that adsorbed water is the main initiator in the surface damage process at 10.6 μm. Freshly cleaved NaCl samples exhibited an initial damage threshold more than double that of polished surfaces. However, after less than one week, only a 50 percent advantage was measured, presumably due to readsorption of moisture.

Improvements in materials require the development of more sensitive techniques to measure properties of import and thus be able to assess progress. Two novel spectroscopic applications were discussed which will play a major role in the development of optical materials as well as become an adjunct to damage threshold experiments. The first method concerns the use of photo-acoustic spectroscopy to identify damage-sensitive areas from increased localized absorption both within the bulk of materials and for thin films, as well. In this latter case one is required to determine both surface (film) and volume (substrate) terms. The Bennett-Forman and modified two layer Rosencwaig-Gersho theories had nearly identical results and were in good agreement with experimental data. The other

method concerned wavelength modulation spectroscopy. This technique was also shown to be a very sensitive method to identify impurities on the surface or within a sample. Reproducibility can be as high as a part in 10^{-6}. One is able to identify particular constituents and the type of chemical bonding. It also appears to be a powerful technique to study the effect of adsorbed materials on surfaces; however, it has not yet been determined how quantitative this technique will be.

In a somewhat related paper the total nonlinear indices, including electronic and nuclear contributions, for 25 liquids useful as index matching fluids, were calculated. Values ranged from 10^{-13} esu for acetic acid to 10^{-11} for CS_2. The nonlinear index was seen to decrease as the Abbe value (γ_d) increased.

2.2 Mirrors and Surfaces

In the area of mirrors and surfaces, diamond turning has lead to great improvement in the fabrication of precise metallic optics. Its extension to dielectrics such as SrFe and CaF_2, however, appears to offer no real advantage in damage resistance (at the HF and DF laser wavelengths) over normal polishing. The advantage comes in the speed of fabrication and is thus a positive economic factor. However, a totally different surface finishing technique, laser annealing of glasses, has resulted in improved damage thresholds. This is a very exciting observation but not totally unexpected since flame polishing, acid etching or any other process which tends to remove impurities as a method to improve surface damage resistance is well-known. More work needs to be done in this area, such as the demonstration of an ability to maintain a surface figure of high tolerance. It could well be a useful adjunct to diamond machining.

As an indication that we have progressed in the understanding of laser interaction with materials, particularly in the case of metals, several papers dealt with both the theory of repetitive interaction of laser pulses with copper and experimental verification of the theoretical predictions. The onset of laser-induced slip of copper was shown to occur at fluence levels of a few joules to tens of joules per square centimeter depending on the pulse length. Damage was shown to be cumulative and could result in coating degradation and increased scattering for mirrors under continued laser irradiation. Theoretical predictions were shown to be in essential agreement with experimental results obtained over very small areas. If one continued to pulse until melt damage, the experimentally measured threshold agreed with a first principles calculation to better than one percent. It was observed that slip threshold was inversely proportional to the melt threshold. Micromachining is a technique that can produce nearly undistorted surfaces exhibiting low slip and high melt thresholds. In related work on copper mirrors, the ion implantation of aluminum followed by oxidation in air produced a stable oxide layer which was believed to be a double layer of CuO on the outside and probably $CuAlO_2$ between the substrate and outer layer. This surface was very resistant to further oxidation and maintained a very high reflectivity in excess of 98 percent at 1.06 μm.

2.3 Systems

Papers discussing engineering details relating to system design and performance were heard. One interesting presentation concerned the selection of components in high average power laser systems. These systems normally employ cooled mirrors and uncooled windows. Using an exponential Strehl relation as an indicator of the figure of system performance, expressions were developed to describe distortion in high power systems. It was concluded that the windows frequently compensate for the distortions normally introduced by cooled mirrors. Perhaps of more utility is the proposed application of Weibull statistics, which is a distribution based upon critical flaws, to characterize the brittle fracture of IR windows. The Weibull distribution is appropriate to these low ductility components and allows scaling from small to large samples. This should be an important engineering tool in systems design. Its application is an indicator of the growing maturity of the field.

2.4 Thin Film Characterization and Design

As is the usual case, the greatest number of presentations at the Symposium concerned thin films, both their characterization and damage threshold. This is not surprising considering that the damage threshold of thin films is routinely lower than surface damage thresholds and lower still than bulk breakdown limits. However, from this year's Symposium it is obvious to note the increased sophistication with which this area is being attacked, and real improvement both in performance and understanding of films that has been made. Of considerable importance is the careful correlation of optical and physical properties with process variables. In this regard, a correlation of these process variables with grain size in TiO_2 films was heard. It was shown that there was a ratio of 8 to 1 in damage threshold when the grain size changed from 20 to 600 Å. The smaller size grain film corresponds to a glassy coating exhibiting a lower refractive index film. Similar careful work was performed on two other promising new coating materials, tantalum oxide and niobium tantalium pentoxide. Another new material discussed at the conference was alpha-silicon hydride, an amorphous silicon hydride which has a refractive index of about 3. These films were all produced by rf sputtering.

In some cases, improvement in damage threshold can be achieved through design. One design trick is the use of overcoats. Although the particular mechanism which leads to an improvement is not definitely established, the use of SiO_2 overcoats on high reflectivity coatings leads, on the average, to a 50 percent improvement in the pulsed laser damage threshold. Reproducibility of improvement is reported to be about 30 percent.

Even before we have arrived at a satisfactory understanding and development of thin film technology, very stringent coating requirements are being established. Not the least of these are stringent tolerances and uniformities in phase sensitive optical coating for use in cylindrical unstable resonators. These types of annular resonators are very sensitive to polarization and one must design phase-shifting coatings to maintain proper polarization such that one can operate in low-order models. The very idea that people are considering these stringent coating specifications is an indication of our progress in the field. However, it is still a very tough problem area.

Central to progress in thin films is the development of techniques to characterize films not only from an optical standpoint but from a chemical and structural standpoint as well. This year several papers dealt with various aspects of this concern. The high temperature properties of molybdenum reflectors was correlated with the substrate structure. Chemical vapor disposition of molybdenum was used to produce very high reflectivity, better than super polished or sputtered molybdenum, achieving almost 99 percent reflectivity at 10 μm. By annealing at temperatures between 700 and 1000° C, the molybdenum film was converted to a body centered cubic form, resulting in the very high reflectivity with relatively large grain sizes.

Reflection spectroscopy was also used as a tool to identify contaminants in evaporated films of ThF_4, ZnS, ZnSe, and SiO. The presence of the contaminant could be assigned to either the bulk or the surface of the material with a sensitivity as good or better than calorimetric procedures. The obvious advantage of this technique is that measurements can be made over a broad wavelength range. Two other techniques were useful in the mapping of damage sensitive areas. These were spatially resolved photoacoustic spectroscopy and a new microscopic technique called TIRM which stands for total internal reflection microscopy. The latter may be used in conjunction with a Nomarsky microscope. Greatly improved sensitivity in locating sites potentially susceptible to damage have been demonstrated by both techniques.

The identification of water within materials at certain wavelengths continues to be an area of considerable interest. We can not only determine the presence of water but determine its location, whether within a film layer, at an interface between layers or between the film and substrate. This has proven to be very important when dealing with coatings at the HF wavelengths. The presence of water in components used in the HF lasers is without question the prime factor leading to a decreased damage resistance at that wavelength compared to operation at the DF wavelength. Anytime a new material is proposed, such as NaF, one of the first procedures will be to assess its affinity for water when used at specific wavelengths.

We continue to see an increase in the growth of the use of advanced instrumental techniques such as SEMS, SIMS, AES, ESCA (XPS) to analyze impurities and defects in thin films. Most recently these techniques have been employed to study ThF_4 films and locate the usual impurities of $ThOF_2$ and ThO_2.

2.5 Thin Film Damage

This years Symposium was highlighted by the reporting of large quantities of damage thresholds for thin films. The data was of high quality and directly applicable not only to revealing the mysteries of thin film damage but also as useful indicators in the selection of thin film materials for high power laser applications. The data spanned pulse lengths from picoseconds to milliseconds from the ultraviolet to the infrared. Several efforts were pointed towards the frequency dependence of damage in a variety of thin film materials. The data reported at the meeting was used in several instances to support the selection of a particular damage mechanism, most notably the impurity dominated model as

opposed to avalanche or multi-photon processes. This does not mean that these later processes are ruled out as playing a role in the resultant morphology of catastrophic damage. Oxide and fluorides were highlighted in the results and important differences in the responses of these classes of materials were identified.

Concerning pulse length scaling, none was observed in one report for pulses ranging between 100 and 700 ps at 266 nm. However, the same authors and others at the meeting often have found the normal $t^{1/2}$ scaling at longer nanosecond pulse lengths. Damage threshold scaling with film thickness was used to support the impurity model. Attempts to scale damage with film absorption met with mixed results; however, when the absorption was high, there was correlation between damage sensitivity and film absorption. But, on high quality films where absorption was low, variations of the damage threshold with film absorption were not readily evident. Some interesting results on the damage sensitivity of films subjected to 800 ns, 1 μm laser pulses were reported. At these relatively long pulse lengths correlation between film absorption and damage threshold was also reported. The ratio of the temperature at damage to the melting temperature of the substrate material was nearly a constant. There was not much variation in the damage threshold at these relatively long pulse lengths since most of the materials tested were refractory oxides.

To the trick of using overcoats to improve damage thresholds must now be added the use of chemically graded index surfaces. In this process, material is leached from a glass to reduce the index in a controlled manner. This obviates, in many applications, the need for the application of damage-prone antireflection coatings. Damage thresholds have been reported as high as 30-50 J/cm^2 for 1 ns pulses at 1.06 μm. Achieved reflectivities ranged from 1/10 to 2/10 of a percent. These high damage values are obtained only after the material is subjected to initial damage pulses at the 8-12 J/cm^2 range. Normally, AR coatings under the same conditions fail at about 4 J/cm^2. These graded index surfaces are porous; thus we will have to await full impact of the potentially larger scattering and handling sensitivity which should be characteristic of this type of surface.

Historically, the session devoted to theory and breakdown phenomena has been among the most agitated. In comparison, this year the participants were more attentive, primarily for two reasons. First, some of the presentations were not very controversial and secondly, theories were supported by careful experimental data as opposed to the conjecture previously heard when there was inadequate data available.

In the first category, the individual theories due to Keldysh, Braunstein, and Basov were compared based on their ability to accurately predict multi-photon absorption coefficients. Keldysh appeared to be the preferred description in cases of import to this meeting. An ancillary paper dealt with a comparison of multiphoton and avalanche processes in damage. In that report, it was concluded that much more work needs to be done before one can adequately describe the breakdown processes. Furthermore, one needs to understand the interdependence of the two breakdown theories. An improvement in the description of avalanche breakdown was also heard. This year the inclusion of the Holstein theory for phonon-assisted absorption was included. The key feature of that theory, as opposed to the intermediate collision model, is that the electron can absorb essentially all the photon

energy in a single event rather than in many small increments as for example in a series of scattering processes. This approach is probably appropriate between 1 and 10 μm, but at shorter wavelengths a further evaluation is necessary.

Another interesting paper dealt with the subject of stimulated Brillouin scattering (SBS) and its use as a limiter of nonlinear processes such as self-focusing within materials. Methods of preventing feedback from SBS were also discussed.

The two most important analytical revelations at this meeting concerned the frequency dependence of thin film damage based on an impurity model and a quantitative assessment of focal volume effects in relation to recently reported Soviet work. Concerning the thin film issue, early work on the role that metallic impurities play in damage of bulk dielectrics has been extended to dielectric impurities in optical thin films. Impurities were assumed to be no larger than the thickness of the films. Based upon this restriction, Mie scattering was involved to describe the absorption of the impurities invoked. From studies of damage to a variety of materials, general agreement was obtained with the predictions of the theory. Interestingly, the theory predicts that as one progresses to thinner films the damage resistance increases. This may offer great benefit for ultraviolet coatings. In the other prime theoretical work, a resolution of the difference between small focal spot size and large focal spot size data for bulk damage was presented. Generally there is very little spot-size dependence for large beams while there is a spot size effect for small beams. This difference manifests itself in a different frequency scaling as well. This data now adequately describes some heretofore confusing results reported by Soviet workers.

3. Summary of Papers

The subject matter of the Tenth Anniversary (Eleventh) Symposium covered six broad areas of interest to the high power laser community. These are (1) Transparent Optical Materials and the Measurement of Their Properties, (2) Mirrors and Surfaces, (3) Thin Film Characteristics, (4) Thin Film Damage, (5) Considerations for High Power Systems, and finally (6) Theory and Breakdown. These Conference Proceedings are organized accordingly. In this Section, a concise summary of each paper is provided. Closely related papers are discussed together, whenever possible. The interested reader is referred to the complete manuscript of any paper for further details. Our intention here is to provide the reader with an overview of the Symposium and to identify the topics of current interest, and the authors and sponsoring organization of the papers. Each topical area is introduced with a brief statement of the underlying problems and the status of understanding within the area of interest as well as to highlight this year's presented papers.

3.1 Transparent Optical Materials and the Measurement of Their Properties

As is the usual case, this year's Symposium led off with papers dealing with transparent optical materials, the measurement of their properties, and the correlation of these properties with failure. The materials discussed were those most useful at the extremes of the high power frequency regimes, namely the near ultraviolet and the infrared at 10.6 μm.

The first set of papers reported the continuing advances being made in the press-forging of optical materials, namely LiF, CaF_2, and NaCl. Another paper concerned itself with the accurate prediction of the physical response of ZnSe windows subjected to high power CO_2 lasers.

Until this year, LiF has not been seriously considered as a practical window material for uv lasers because of its low yield strength and low fracture energy. To overcome these objections, J.F. Ready and H. Vora of the Honeywell Corporate Material Sciences Center have produced polycrystalline LiF windows using a two-stage forging process. Use of the two-step process was found necessary to avoid veiling in the bulk material at total thickness reductions of up to 75 percent. Depending on the percent reduction and forging temperature, the optical inhomogeneity of the forged windows was greater than the single-crystal starting material by a factor of between 30 to 750 percent, but the absolute values remained in the 10^{-6} range.

Although the visible absorption of one forged window did increase by a factor of two between 458 and 514 nm, the laser damage resistance for short pulses was not affected. Measurements (at the Lawrence Livermore Laboratory) at 1064 with FWHM 1-ns pulses yielded rear surface and bulk thresholds of 8 and $\sim$ 20 J/cm^2, respectively, which were the same as for single-crystalline windows. Likewise, at 266 nm with 700-ps pulses, front-surface thresholds of both forged and single-crystal samples were 14 J/cm^2.

Their studies of the microyield behavior, i.e., plastic deformation at a small fraction of the conventional yield strength, showed that the threshold for LiF single crystals can be increased by an order of magnitude by press forging. Finally, no increase in either grain size or optical scattering was observed when forged specimens were exposed to ambient conditions for one year or to elevated humidity (94% at 39° C) for a period of five days.

One of the problems resulting from forging of crystalline windows to increase their mechanical strength is the production of optical scattering sites in the bulk material, commonly referred to as veils. Elimination of these veils from CaF_2 was the object of a study conducted by A.K. Hopkins of the Air Force Materials Laboratory, R.H. Anderson and J.F. Ready of Honeywell and J.M. Bennett, P.C. Archibald and D.K. Burge of the Naval Weapons Center. First, they determined that the veils did not contain entrapped gases. This is consistent with the conclusions of previous electron micrograph examinations at Honeywell where it was shown that veils are microvoids caused by the coalescence of vacancies. With the object of collapsing these postulated voids, they heated previously forged samples of CaF_2 to 750° C (below the 800° C recrystallization temperature) in argon within an autoclave for a period of ten hours, a process known as hot isostatic pressing (HIP). This HIP process did significantly reduce the veil content without any increase in the grain size (10 μm). Interestingly, pits were observed on previously smooth surfaces as if the veils migrated to the surface from the bulk.

HIP-processing appeared to slightly increase the optical absorption at 2.7 and 3.8 μm. Optical inhomogeneity also increased but remained in the range of 1 to 3 parts in 10^6. The scattering in the visible was reduced by a factor of eight and it became more spatially uniform. However, at 3.39 μm, reduction of scattering was not generally observed.

Furthermore, the spatial variation of the scattering was not appreciably affected. No obvious correlation was found between the high-scattering areas in the visible and infrared either before or after HIP-processing. They concluded that the optical performance of forged CaF_2, as an infrared window, was not obviously improved by the HIP process, but further, systematic parameter variations need to be explored before a final judgment can be rendered.

For use in short-pulse laser applications, elimination of veils within the bulk can only increase the damage threshold since microvoids are sites of enhanced electric field. Such evidence was observed in alkali halides at 10.6 μm, as reported by Newnam and co-workers at Los Alamos in a later paper.

Polycrystalline forged NaCl is being increasingly specified as the window material of choice for high-power infrared lasers. The results of an experimental investigation on the homogeneity of the mechanical, thermal and optical properties throughout a given forging were described by G.A. Graves, J.A. Detrio, D. McCullum and D.A. Dempsey of the University of Dayton Research Institute. The test object of their study was a 32-cm diameter Polytran (Harshaw) hot-forged disc from which more than 100 specimens were cut from prescribed locations in three planes. Overall, the properties were found to be uniform throughout the forging within the experimental limits of the measurement techniques employed.

Values of the average yield and ultimate mechanical strengths of 70 uniaxial flexural test bars were 15 ± 3 MPa and 23 ± 6 MPa, respectively. The only significant variation observed was between samples from different azimuthal locations. For the biaxial mechanical strength, measured in a concentric ring structure, the average yield and ultimate strengths were 18 ± 2 and 26 ± 4 MPa, respectively.

The total absorption (bulk + surfaces) was measured calorimetrically at 10.6, 9.27, 5.3, 3.8, 2.7 and 1.3 μm on samples with surfaces polished by Harshaw and some of which were subsequently treated by an HCl-etch. At each wavelength, the variation in the absorption coefficients β had a standard deviation of ± 10 percent among the samples with an exception at 3.8 μm, where β was homogeneous to only ± 40 percent. The magnitudes of β for "polished only" samples at these wavelengths were approximately 3, 2, 0.3, 0.5, 2 and 1×10^{-3} cm^{-1}. The etch-treated samples had a moderately reduced absorption, but at 3.8 μm a large (nearly 50%) reduction was observed.

The average coefficient of thermal expansion for several samples was $42.8 \pm 0.9 \times 10^{-6}/°C$ and the average value of the specific heat was 0.2 cal/gm/°C over the temperature range of -65 to 200° C. Finally, the microstructure was determined to be uniform with an average grain size of 34 μm, and the average Knoop hardness for four samples was 20 kgm/mm^2 for a 50 gm load.

The object of a study, conducted by J.A. Detrio, J.A. Fox and J.M. O'Hare of the University of Dayton Research Institute, was to assess the accuracy of prediction of the optical, thermal and mechanical responses of ZnSe windows subjected to high power CO_2 laser radiation. In particular, the temperature distribution, optical distortion and strain were measured for three ZnSe specimens with absorption coefficients between 0.006 and 0.020 cm^{-1}. When the transmitted beam was focused, the focal plane was observed to shift toward the

focusing mirror but without any significant change in the minimum beam diameter. The largest shift was associated with the largest window absorption. However, the value of the spot size was not accurately predicted by the thermal model. For laser powers of 230 and 705 W and beam diameters of 2.1 and 4.2 mm, the predicted and measured temperature rises at the edge of the windows were in good agreement. The measured radial distribution of temperature rise was lower than that predicted (60 to 70% at the center) however. The least agreement of the thermal model was in predicting the strain in the window. This was a result of the considerable uncertainty (30 to 100%) in the measured values due to the gauges themselves.

Another diverse group of papers dealt more with the measurement of optical properties for materials important in high power laser systems. These included the determination of non-linear indices of refraction for several candidate index matching fluids, and the use of wavelength modulation spectroscopy to measure very small ($\sim 10^{-5}$ cm^{-1}) absorption coefficients in the infrared. This latter technique offers potentially greater detectability for adsorbed as well as included impurities. Finally, the use of synchrotron radiation to measure the photo-electron spectra in the valence band region of low index materials such as BeF_2 glasses was reported.

Nonlinear phase distortion leading to self-focusing is an especially critical issue whenever liquids are used for either cooling or index-matching the optical components of high-power lasers. For 25 liquids, D.C. Brown, J.M. Rinefierd, S.D. Jacobs and J.A. Abate, of the University of Rochester, computed the electronic, nuclear and total nonlinear refractive indices. For the electronic portion, they used the equation of Boling, Glass and Owyoung which requires measurements of only the linear index at the sodium "d" lines and the Abbe value γ_d. For nine of the liquids, they computed the nuclear portion and the total nonlinear index n_2^T using the values of the Born-Oppenheimer coefficient B_o as previously reported by Hellwarth. Values n_2^T ranged from 10^{-13} esu for acetic acid to 10^{-11} esu for carbon disulphide. For these nine liquids a good correlation of decreasing n_T with increasing γ_d was observed.

The capability of wavelength modulation spectroscopy (WMS) to measure absorption coefficients α at levels of 10^{-5} cm^{-1} for a 1-cm sample length in the infrared from 2.5 to 12.0 μm was described by R. Braunstein and R.K. Kim of the University of California at Los Angeles and M. Braunstein of Hughes Research Laboratories. Previously, they had developed this technique for use in the ultraviolet and visible regions. WMS is a measure of the energy derivative of the absorption coefficient from which the absolute value of α is obtained by integrating the observed derivative spectra. The constant of integration can be determined by a supplementary laser calorimetric measurement at a fixed single wavelength.

The power of this technique was illustrated by absorption measurements of KBr and KCl crystals in laboratory air and in dry N_2 with a calorimetric measurement at 3.8 μm (DF laser) as the reference. From the details of the observed structure, identification of volume and surface impurities was possible. The spectral distribution of the various KBr and KCl samples all had the same dominant features with slight differences attributed to various surface contaminants and differences in crystallinity and growth procedures.

Continuing the search and evaluation of new materials for high-power laser systems, R.T. Williams, D.J. Nagel and P.H. Klein of the Naval Research Laboratory and M.J. Weber of Lawrence Livermore Laboratory reported on their recent synchrotron radiation studies of pure beryllium fluoride (BeF_2) glass. BeF_2 glasses are of special interest because of their very low nonlinear refractive indices. Due to its low linear index (e.g., n = 1.275 at 587.6 nm), BeF_2 may also be a useful multilayer coating material if its highly hygroscopic properties can be shielded.

Measurements in ultra-high vacuum included the reflectance in the range 9 eV to 120 eV and the photoelectron spectra in the valence-band region. A lowest-energy reflectance peak was found at 12.8 eV, implying an exciton resonance at 13.1 eV, similar to LiF. The photoelectron spectra for the bulk revealed a valence band which is roughly symmetrical and about 5.8-eV wide (FWHM), with a tail of states extending out to 7 eV. These features are consistent with previous measurements that the practical transmission limit is 150 nm (8.3 eV).

The final group of papers in this topical area dealt primarily with crystalline and glassy materials ranging from the role iron impurities play in damage of infrared materials to stress failure analysis in sapphire, and a variety of ir materials. Between the papers, other reports detailed characteristics for $LiYF_4$, KYF and YPO_4 crystals. The first two materials can act as hosts for rare-earths, while the phosphate was assessed for its potential use as a polarizer.

To reach the intrinsic damage threshold limit, a material must be free of deleterious defects such as impurities and dislocations. D.F. Edwards and B.E. Newnam of Los Alamos Scientific Laboratory, and W.J. Fredericks of Oregon State University (OSU) reported on their efforts to isolate the significant impurities in KBr crystals that limit the laser damage threshold. Seven high purity samples of KBr were grown at OSU from starting material purified by selective ion filters. The concentrations of OH, O_2, halogen ions and heavy-metal ions were restricted to less than 100 ppb and there were very few dislocations because of carefully controlled growth and annealing conditions. The two major impurities, Rb^+ and Fe^+, were in concentrations ranging from 5 to 9 ppm and 0.030 to 0.150 ppm, respectively. From light scattering measurements with an Argon laser of the unshifted Rayleigh peak (intrinsic + extrinsic contributions) relative to the shifted Brillouin peaks (intrinsic contributions, only), correlation was found with the Fe^{2+} concentration, but none was found for the Rb^+ concentration. Laser damage measurements at 1.06 μm (27 ns pulsewidth, 90 μm spot-size radius) obtained bulk thresholds ranging from 0.4 to 1.1 MV/cm. Consistently higher thresholds were obtained for the crystals exposed to an oxygen atmosphere (during growth) below the melting point. Correlation of the scattering measurements and the damage thresholds must await repeat of the scattering measurements in which surface scattering contributions are eliminated by index matching in a liquid.

T.M. Pollak, R.C. Folweiler, E.P. Chicklis and J.W. Baer of Sanders Associates and A. Linz and D. Gabbe of Massachusetts Institute of Technology reviewed the optical properties and crystal-growth procedures for two fluoride-crystal families which exhibit a natural rare-earth site, in particular $LiYF_4$, (YLF) and KYF. These materials are characterized by

a low nonlinear refractive index (0.6 X 10^{-13} esu) and short wavelength cutoffs of 120 nm and less than 200 nm, respectively. Over twenty laser transitions have been demonstrated from 300 nm to 3.9 μm for doped YLF, and Tm:YLF is currently being assessed for use as a storage laser at 453 nm for laser fusion applications. In addition, Tb-doped YLF and KYF have a large Verdet constant, e.g., ∿ 0.4 min/Oe-cm at 633 nm, making them useful as Faraday rotator materials.

A top-seeded solution growth technique, related to that of Czochralski, was described which has been optimized to allow growth of 10 cm diameter YLF with a low density of scattering sites. Technical problems were also addressed in scaling to a 40-cm diameter.

Yttrium orthophosphate YPO_4 (also referred to as xenotime) was evaluated as a potential substitute for calcite polarizers in a paper presented by R. Allen, L. Esterowitz and P.H. Klein of the Naval Research Laboratory, V.O. Nicolai of the Office of Naval Research and W.K. Zwicker of Philips Laboratories. YPO_4 is mechanically harder than calcite and insoluble in water. However, it's birefringence of + 0.107 at 589 nm is only 62 percent of that of $CaCO_3$. The fact that YPO_4 can be grown synthetically in the laboratory and its relatively high damage resistance are compensating factors in its favor. Crystals, measuring about 15 X 3 X 0.7 mm, were grown at Philips Laboratories by solution of yttrium oxide in excess lead pyrophosphate which was slowly cooled. The region of transparency (80% or higher transmittance) was determined to extend from 0.5 to 4.5 μm with major absorption bands at 2000 and 3000 cm^{-1}.

The largest faces, being optically smooth, were suitable for measuring the surface damage resistance. When irradiated with 17-ns (FWHM) pulses at 1.06 μm focused to a 0.25 mm (FWHM) spot, no damage was observed unless accompanied by luminous discharge at the surface. A threshold of 2.2 - 2.4 GW/cm^2 was obtained for both single-shot (1 - on - 1) and multiple-shot (N - on - 1) irradiation. Identical measurements on calcite obtained a slightly lower value of 2.0 - 2.4 GW/cm^2. Further work will be directed toward growing larger crystals for practical application.

In predicting the likelihood of mechanical failure of optical components exposed to high-power laser irradiation, attention has usually been directed to the limits set by fracture under thermally-induced tensile stresses at the cold edges of centrally-heated windows. Compressive stress, however, may cause earlier failure via plastic flow if sufficiently high temperatures are reached. As reported by P. Miles, J. Gallagher and R. Gentilman of Raytheon Missile Systems Division, such conditions occurred in their experiments with CO_2-laser irradiated sapphire crystals. Directing a 1.3-cm diameter beam of relatively uniform intensity on a 5-cm diameter sapphire window, they obtained heat deposition rates of between 10^2 to 10^4 W/cm^2 for exposure times between 0.5 and 10 seconds. Due to the high absorption coefficient of sapphire at 10.6 μm, the laser heating was confined to the first few micrometers at the front surface. Two distinct effects, light scattering and then a bright incandescence, preceded the surface fracture that occurred on further heating or cool-down. The initiation time τ of both effects was describable by the equation $H^2\tau$ = constant, where H is the average laser intensity and the constant is proportional to the square of the temperature rise. These observations indicated the occurrence

of plastic deformation of the heated region under the action of compressive and shear stresses followed by tensile failure on cool-down.

To explain these phenomena, a detailed thermo-mechanical analysis was carried out (using a temperature-dependent thermal conductivity) to predict the temperature and stress conditions throughout the disc samples as a function of time, flux level and flux distribution. Compressive stresses in excess of 200,000 psi were calculated as having caused the observed fracture. The overall conclusion was that compressive failure is likely to precede tensile fracture in most experiments where partially heated discs are used.

Infrared laser window materials of current interest, such as ZnSe, CaF_2 and the alkali halides, exhibit brittle fracture when heated by intense laser radiation. The mechanical failure criteria and statistical techniques applicable in brittle materials were discussed by J.A. Detrio and G.A. Graves of the University of Dayton Research Institute, and J.M. Wimmer of the AiResearch Mfg. Co. The authors centered their discussion on the three salient characteristics describing failure of brittle materials: (1) lack of appreciable ductility prior to fracture, (2) initiation by flaws, and (3) statistical occurrence of failure. Fracture by tensile stress was cited as dominant, and the Weibull mathematical function was shown to be useful to describe the distribution of critical flaws. The Weibull distribution also explicitly allows scaling from small test specimens to larger window sizes.

Flaws may be introduced in the manufacture, handling and in use of laser windows. An interesting example of flaws generated during use is the heating of absorbing inclusions which are not relevant to the mechanical strength until irradiated by the laser. Likewise, absorption by dust particles on the surface can be the fatal flaw, causing localized stress. Other factors which can cause early failure of brittle windows are slow crack growth caused by a corrosive agent such as water, residual stresses introduced during the fabrication process, cyclic loading and vibratory loads and mounting stresses. To improve the reliability of a window in actual performance, it was suggested that an array of windows be proof-tested to screen those parts containing critical flaws.

3.2 Mirrors and Surfaces

The papers dealing with mirrors and surfaces were divided between failure to metal mirrors and dielectric surfaces. The first paper dealing with metal mirrors was concerned with the response of each element when subjected to repetitive laser pulses. Papers along these lines have been eagerly awaited by the Symposium participants. Other papers on metal mirrors were centered on a first principal calculation of an ultimate melt failure criteria and experimental verification, while the last paper dealt with the treatment of Cu surfaces by Al implantation as a means of stabilizing high reflectivity by avoiding environmental degradation.

Intergranular and intragranular slip in metal surfaces exposed to high-intensity, pulsed laser radiation has been reported experimentally and explained qualitatively by Porteus, et. al, at a previous symposium. Now H.M. Musal, Jr., of Lockheed Palo Alto Research Laboratory has developed a quantitative theory predicting the flux level at which

slip will be observed with optical absorptance, thermal conductivity, density, specific heat, modulus of elasticity, Poisson ratio, yield stress, coefficient of thermal expansion and laser pulse fluence and duration as parameters. Numerical values for slip threshold calculated for copper using this theory are in reasonably good agreement with previously reported experimental results. One result of this new work is that the temperature rise at which plastic yield will occur is very low, being approximately 20° K for pure copper under short-pulse, large spot size laser irradiation. Repetitive-pulse irradiation, where each pulse raises the temperature by more than 40° K , is expected to cause progressive surface degradation via slip bands, intergranular slip and fatigue cracking. A mechanism for increased optical scattering and coating degradation caused by localized delamination or cracking of the film under continued laser irradiation is suggested by this mechanism and should be investigated further.

Laser damage thresholds observed experimentally are usually significantly lower than those predicted theoretically from the material properties of the irradiated samples. Some of this disagreement can be attributed to experimental uncertainty, but much of it arises because the surface conditions of the samples differs from that assumed in the calculations. A paper by J.O. Porteus, D.L. Decker, D.J. Grandjean, S.C. Seitel and W.N. Faith of Michelson Laboratory, Naval Weapons Center, reported the results of a study of the effect of surface conditions on damage threshold in copper. They obtained excellent agreement with theory when using samples with the highest quality surface conditions. They reported that the measured peak damage threshold for laser-induced melting of pure single-crystal copper prepared in ultrahigh vacuum was 76.6 ± 8.6 J/cm^2 for a nominally 100 ns pulse length. This value agrees almost exactly with a first-principles calculation of the melt threshold of copper for this pulse shape. The quoted uncertainty in the measurement was 10 percent. This agreement between theory and experiment is very reassuring since in typical damage experiments agreement between theory and experiment to within a factor of 2 is generally considered good.

Porteus, et al., further considered the effect of diamond turning and mechanical polishing on the damage threshold of copper. They found, as expected, that the surface distortion introduced by finishing reduced the melt threshold by as much as 20 percent even for these carefully finished surfaces. However, the threshold for laser-induced slip, which was only 16 J/cm^2 for the single-crystal sample, increased to 44 J/cm^2 for the sample with the 20 percent decrease in melt threshold and was nearly inversely proportional to melt threshold. This behavior is expected on theoretical grounds as a result of the crystalline disorder at the surface produced by optical finishing. Center-turned diamond-machined samples exhibited the least surface disorder, approaching the single-crystal sample in both melt and slip thresholds. Laser-induced pitting also exhibited a low damage threshold in commercially available copper, although it was several times that for laser-induced slip. Under optimum conditions polishing can increase the threshold for pitting, probably by "healing over" small defects with disordered material. A more reliable method for raising the slip and pitting threshold, however, is vapor deposition of the copper. No slip was observed for these samples and the pitting and melting thresholds coincided.

Silicon carbide substrates were used for the particular samples tested and the reduced melt threshold observed (50 J/cm^2) was attributed to their poor conductivity. The melt threshold increased with increasing thickness of copper, and calculations indicate that if higher conductance substrates were used, a significant improvement in damage threshold would have been observed. Even with silicon carbide substrates, these vapor-deposited copper samples showed the highest threshold for initial damage of any tested.

The development of environmentally stable copper mirrors for pulsed-laser applications was reported by M. Oron, L.G. Svendsen and G. Sorensen of the Institute for Physics, University of Aarhus, Denmark. Fresh copper mirrors have good reflectivity and high damage thresholds but oxidation lowers their damage resistance. By ion implanting electropolished copper surfaces with aluminum at energies of 60-80 keV at dosages of 1-2 x 10^{17} $ions/cm^2$ and then annealing in air for several hours at 200° C for several days at 100° C, they produced double layers, the outer one consisting of CuO, the inner one probably $CuAlO_2$ as determined by secondary-ion mass spectroscopy and Rutherford backscattering. The reflectance of these ion-implanted surfaces at a wavelength of 1.06 μm remained at about 0.98, whereas the reflectivity of copper surfaces which were not implanted dropped to 0.50-0.60 after a heavy tarnish layer was formed by oxidation in air at 200° C for 100-200 minutes. The ion-implanted samples, although initially grey in color, regained their red copper color after annealing, whereas the area which was not implanted was tarnished. Significant protection against oxidation was thus furnished by the ion implantation process followed by surface oxidation. Laser annealing offers another avenue for modifying metal-surface properties of ion-implanted samples and should be explored further.

On the dielectric surface front (and rear), a report on extending diamond turning to materials such as CaF_2, MgF_2 and SrF_2 was heard. However, as might be expected, adsorbed water played a role in controlling their utility at HF frequencies. A following paper dealt with the assessment of diamond-turned dielectric surface topography and scattering behavior. The last two papers also were concerned with surface preparation procedures, one with cleaning, etching, etc., of NaCl and KCl surfaces and the last with the use of a high power CO_2 laser to "treat" fused silica surfaces. These last two papers quantified the damage resistance of these new surface treatments. Undoubtedly more will be heard of these innovations.

Inasmuch as diamond turning of metal optics has led to an improvement in the damage resistance over polished elements, M.J. Soileau, J.O. Porteus and D.L. Decker, of the Naval Weapons Center, reported on a detailed study of the efficacy of diamond turning dielectrics such as CaF_2, MgF_2 and SrF_2 for use as windows at 2.7 and 3.8 μm. Damage testing was done at these wavelengths using ∿ 55-μm spot diameters at the e^{-2} points employing a single-mode pulsed laser of ∿ 100 ns FWHM. Unlike earlier studies on diamond-turned KCl, a relatively soft material where an improvement over polished surfaces was manifest, diamond turned surfaces of SrF_2, CaF_2 and polycrystalline MgF_2 exhibited damage thresholds of the same order as polished surfaces of these materials at HF/DF wavelengths. Failure for CaF_2 and SrF_2 appeared to be an electron avalanche initiated by defects and impurities for both classes of surface finishing. MgF_2, on the other hand, apparently fails through the

absorption by defects present throughout the material. Lower thresholds at HF frequencies and a larger n-on-1 effect at this wavelength indicated that absorbed water has a significant effect on surface damage thresholds. The best damage thresholds were usually obtained for CaF_2 with polycrystalline MgF_2 very, very poor by comparison.

In a continuation of their efforts to assess the suitability of diamond-turning for the generation of optical-tolerance surfaces of dielectrics and semiconductors, D.L. Decker, D.J. Grandjean and J.M. Bennett studied the optical and surface characteristics of diamond-turned Ge, CaF_2, MgF_2, SrF_2, KCl and GaAs. The surfaces were generated on a new machine at their organization, the Naval Weapons Center, and were characterized by an analysis of scattered and absorbed light, profilometry and various microscopic techniques. As an indicator of surface quality, the TIS (total integrated scatter) at two different wavelengths (0.647 and 3.39 μm) were determined and compared to high-quality, conventionally polished material. For MgF_2, CaF_2 and SrF_2 at 3.39 μm the TIS of polished and and diamond-turned surfaces was 0.006 and 0.01, 0.00004 and 0.00003 - 0.004, 0.0001 and 0.0001 - 0.0006, respectively, indicative of quite good surfaces. It was noted that much of the residual scattering in the diamond-turned samples arose from turning debris and that improved cleaning procedures are needed. The damage resistance of these samples was assessed in another work at the Symposium.

In a very careful study, B.E. Newnam, A.V. Nowak and D.H. Gill of the Los Alamos Scientific Laboratory evaluated the short-pulse (1.7 ns), 10.6 μm damage to the surfaces and bulk of NaCl and KCl window materials. As the Soviets have previously reported in longer pulse width experiments, the limiting factor in surface thresholds is adsorbed water. In particular, Kovalev and Faizullov had determined that a freshly HCl-etched NaCl surface, while initially exhibiting a marked improvement in damage resistance, readsorbed a water layer in under 20 minutes with a concurrent loss in damage resistance. This behavior was also extended to cleaved surfaces in this study. The damage threshold of NaCl and KCl is of considerable import to LASL since 8.5-cm thick windows up to 48 cm in diameter are used in their CO_2 laser-fusion program and represent not only a design constraint to their systems but are as well a considerable capital investment.

The laser used for damage testing operated at 10.59 μm (P20) in the TEM_{00} mode. Pulse widths could be varied from 1 to 65 ns (FWHM). Experiments were conducted over 0.15 to 1.5-mm radius spot sizes in air at 600 Torr. Usually 40-60 sites were interrogated in a 1-on-1 irradiation sequence. Criteria for damage were permanent disruption or increased light scatter. The rear surface damage threshold for NaCl was 7 J/cm^2 compared to 4 J/cm^2 for KCl.

Some other noteworthy conclusions from this work were (1) no spot-size dependence was evident for beam radii from 0.14 to 1.5 mm; (2) a freshly cleaved NaCl surface exhibited a front-surface damage threshold of 17.6 ± 0.6 J/cm^2 and after 10 days the resistance dropped to 13.1 ± 1.5 J/cm^2; (3) for recently grown high-quality samples the ratio of bulk-to-exit surface thresholds (MV/cm) was almost two, while for the bulk-to-front surface the ratio was somewhat less; and (4) the scaling of electric field breakdown proposed by Bettis, House, Guenther and Austin of atomic density/(n^2-1) was fit exactly, while the pulse width

dependence for the exit-surface damage from 1.7 to 65 ns followed $t^{1/3}$ rather than the proposed $t^{1/2}$ scaling.

Any polishing or finishing procedure which cleans up surfaces, i.e., removes contaminates or heals geometrical defects, leads to improved damage resistance. Such techniques as acid-etching, flame-polishing or low energy ion-planing at angles near grazing incidence have all demonstrated this feature. Unfortunately, these techniques are difficult to control for the maintenance of surface figure and are expensive and time consuming. Now another polishing technique has been added. Taking a lead from the laser annealing of semiconductors, P.A. Temple, of the Naval Weapons Center and D. Milam and W.H. Lowdermilk, of the Lawrence Livermore Laboratories, have made a preliminary investigation of the efficacy of CO_2-laser polishing of fused silica surfaces for improving the damage resistance of such elements to pulsed 1.06 μm laser radiation. Preliminary results are most encouraging. Their analysis shows that under controlled conditions of appropriate scanning rates the absorbed 10.6 μm CO_2 radiation causes the removal of a uniform layer of fused silica and a probable refusing of surface and subsurface regions, leading to a very low scatter, smooth surface. Whereas normally polished SiO_2 surfaces damage at levels from 10 to 20 J/cm^2 using a 1 ns, 1.06 μm laser, corresponding CO_2 laser polished Suprasil II fused quartz surfaces damaged anywhere from 1 1/2 to 2 1/2 times that level with many less initiating sites evident.

A physical inspection indicated that the laser polished surfaces were depressed below the mean surface level and that these regions were under a tensile stress. These observations lead to the obvious question -- can one retain optical figure when employing CO_2 laser polishing?

3.3 Thin Film Characteristics

As might be expected, the majority of papers presented at the Symposium were concerned with thin films, the most damage-sensitive class of optical materials frequently employed in high power laser systems. Because of the number of papers devoted to optical coatings, we have separated them into sections on thin film characterization and thin film damage studies. The properties of coatings continues to be of crucial interest to the high power laser community. Coating absorption is typically orders of magnitude larger than would be predicted from the absorption coefficients of the coating materials in bulk form, and this year's Symposium contained several papers shedding new light on this puzzling situation. Water in the film volume or at interfaces has been quantitatively identified as the source of most of the absorption at HF wavelengths and several powerful experimental techniques are reported for analyzing its presence. Happily, they all give results which are essentially in agreement and provide a satisfying experimental redundancy.

There is relatively little data in the literature concerning the behavior of films at elevated temperatures, and two papers addressed that question. The deposition of superior films of molybdenum, a high temperature substrate material, was also reported. The application of Photoacoustic Spectroscopy (PAS) to thin-film absorption, its spatial variation and the possible relation to laser damage was discussed in three papers. In the final

paper in this section, a novel experimental technique for detecting surface defects and laser-induced surface damage with greatly increased sensitivity was reported.

A theoretical analysis by Sparks at a previous Symposium concluded that contaminants such as water were the principal cause of absorption in multilayer films. Experimental verification of this conclusion and a technique for experimentally separating surface and bulk absorption in single layer films has been presented at previous symposia. Now T.M. Donovan and P.A. Temple of Michelson Laboratory, Naval Weapons Center, and S.C. Wu and T.A. Tombrello of the California Institute of Technology have reported similar results for two-layer films and have applied a novel nuclear resonant technique to the problem which may be applicable to multilayers. They have shown that the hydrogen concentrations determined using this technique correlate very well with both bulk and surface absorption as determined using the calorimetric technique on single line HF measurements at six wavelengths between 2.7 and 2.9 μm and with the spectral absorption of water at these wavelengths. The nuclear reaction $^{19}F + {}^{1}H \rightarrow {}^{16}O + {}^{4}He + \gamma$, which is very sensitive to the accelerating voltage of ^{19}F, was used to profile through the films and detect both the position and concentration of H present. Comparing these results with the calorimetric results and with the calculated absorption of water gives a redundant experiment leading conclusively to the identification of most of the H being found as H_2O. Measurements on various kinds of films led them to conclude that, in NaF and ThF_4 films, the water is uniformly distributed through the film, whereas in As_2Se_3 and ZnS, it occurs primarily at interfaces. They succeeded in reducing the water content of ThF_4 films by a factor of 50 by encapsulating with ZnS. SiO_x and Al_2O_3 films showed both significant volume and interface absorption. As in the other cases tested, the absorption values obtained using the nuclear resonance and calorimetric techniques were in good agreement.

Key to reducing absorption by contaminants in multilayer dielectric films is an understanding of what the contaminant is and where it is located in the coating. Internal and external reflectance spectroscopy provides a powerful tool for characterizing contaminants. Its application to optical thin films was discussed by W.N. Hansen, L. Pearson and G. Hansen of Utah State University and W.J. Anderson of the United States Air Force Academy. To illustrate the technique, evaporated films of ThF_4 (some capped with 2 μm thick layers of ZnS and ZnSe) and single layers of ZnS, ZnSe and SiO_x were analyzed. The coatings were deposited on both silver-coated microscope slides and on ZnSe and Ge internal reflection plates. In some cases a thin 100 Å SiO_x layer was deposited between the silver and the ZnS and ZnSe coatings to demonstrate the sensitivity of the technique in detecting or ignoring surface layers.

By changing the angle of incidence and polarization ratio of the incident light for both external and internal reflection, the high field intensity in the standing wave could be positioned at an interface or within the bulk of the film. Multiple reflections also enhanced the signal-to-background ratio. The films, bulk or interface absorption could thus be enhanced thousands or millions of times as compared to transmission or reflection measurements at normal incidence, and a position in the film could be selected. Hansen has written a comprehensive paper in the Journal of the Optical Society describing this procedure, and the present paper applies these results to optical films of current interest.

A principal result was that all ThF_4 films contained large amounts of water in the bulk of the film. Even encapsulated films exhibited this behavior, and great care must be taken to prevent its occurrence. In a paper by Donovan, et al., in which an entirely different technique for monitoring water content in films was used, the same conclusion was reached. Donovan, however, reported some encapsulated ThF_4 films with relatively low water content, so encapsulation may be effective. It is clearly difficult. Hansen, et al., make the point that reflection spectroscopy is a very convenient method for easily monitoring the success or failure of encapsulation. In the case of ZnS and ZnSe films, water was not found in significant quantities in the films themselves, but existed primarily at the film/substrate interface. These results are again in agreement with Donovan's result and also with those of Temple, et al., reported at last year's Conference. The films also contained a small amount of hydrocarbon contaminant at the film/substrate interface. The silicon monoxide films contained some water, much less than ThF_4 and much more than ZnS or ZnSe, and the stoichiometry of the SiO_x films could be determined conveniently by this method. Finally, the 100 Å thick SiO_x film could be either readily observed or not unobserved depending on the experimental conditions used, illustrating a versatile selectivity and sensitivity for this analytical procedure.

An analysis of some typical multilayer coatings containg ZnS and ThF_4 using Scanning Auger Microscopy (often called Auger Electron Spectroscopy or AES), X-ray Photoelectron Spectroscopy (XPS), (often called Electron Spectroscopy of Chemical Analysis (ESCA)), and Secondary-Ion Mass Spectroscopy (SIMS) was presented by T.W. Humpherys, R.L. Lusk and K.C. Jungling of the Air Force Weapons Laboratory. Each film in this study was approximately 2000 Å thick. SIMS data was taken during Ar^+ sputtering with XPS and AES data taken between sputtering sequences to afford coating profiles. Vacuum was in the low 10^{-10} Torr range. Several prominent dust particles were found on the otherwise featureless surface and were sputter-profiled. Sputtering into the ZnS film revealed additional defect sites, each enclosed by a halo. The point defect and halo region remained intact as the ThF_4 film was penetrated. A substantial amount of oxygen was found in the ThF_4 film outside the halo area, suggesting the presence of water. Studies using other techniques support this conclusion. In the halo area, AES indicated a fluorine deficiency and oxygen enhancement. Also, Zn and Na signatures were found as well as S. It was proposed that point defects in the ThF_4 film were composed of, or are a trap for, ZnS. A SIMS comparison on Balzers ThF_4 and RAP grown ThF_4 revealed more of the impurities Na, Al, Li and K in the RAP-grown film than in the commercial evaporant material. Similar analyses were made on the starting materials with similar results.

Films in storage were also analysed and found to deteriorate as a function of time. Defect centers in this case appeared to be pores with a halo pattern similar to that of a snowflake. Water may enter through such pores. Not all films studied exhibited numerous impurity sites and halos. None of the films studied, however, were completely free from point defects or impurity sites. Surface analysis techniques, such as AES, XFS and SIMS, are thus extremely useful and are fast becoming an integral characterization technique during the development and analysis of thin-film coatings. Continued use of such analysis

techniques should provide a significant insight into the performance exhibited by many thin-film coatings.

Most measurements of absorption in multilayer dielectric films are made at room temperature. However, laser-induced heating may occur prior to damage, and the high temperature absorption of the films as well as that at room temperature is of importance in high average power applications. H. Küster and J. Ebert, of the Institut für Angewandte Physik, Universität Hannover, have devised a technique for measuring, to a first approximation, this high-temperature absorption at 1.06 μm by measuring the temperature of the coating for known laser fluences using an optical pyrometer. The emittance of the samples as a function of temperature was measured independently using an electric oven. They found that film behavior can be fit to an exponential increase in absorption with temperature. Using this model, they have determined the absorption coefficients of Al_2O_3, BeO, MgO, HfO_2, ZrO_2, Nd_2O_3, CeO_2, TiO_2 and SiO_2 films about 5000 Å thick, deposited on Suprasil I substrates. They also compared the damage threshold for a long-pulse Nd^{3+} glass laser having a pulse width of 800 ns, with the observed high temperature absorption coefficients. Several interesting results emerged. The damage threshold, to a good approximation, was inversely proportional to the absorption coefficient at 600° C for all materials tested. By contrast, the same plot made using ambient temperature absorption coefficients, the agreement between theory and experiment was very poor. As an additional test, ZrO_2 layers having different absorption coefficients at 600° C were damage tested. Again the inverse relationship between damage threshold and absorption coefficient held. Damage occurred to all coatings at surface temperatures of 625° C ± 55°, regardless of the melting temperatures of the coating materials, which varied from 1840° C to 2700° C. The authors concluded that the surface temperature at which damage occurred was probably determined more by the relatively low melting point of the substrate material than by the melting point of these coating materials.

Similar behavior has been observed for electrically pulsed, coated filaments, where the coating material is ejected at a temperature corresponding to the filament rather than to any thermal property of the coating material itself. There was some correlation between the damage threshold of the oxide coatings tested and band edge for ultraviolet absorption, although SiO_2 and BeO had anomalously high damage thresholds and Al_2O_3 had an anomalously low threshold. Nevertheless, the probability is that the shorter the wavelength of the ultraviolet absorption edge the higher the damage threshold will be at a wavelength of 1.06 μm. This is not too surprising since shorter cut-off wavelengths generally correspond to lower refractive indices.

Most reflectance and transmittance measurements are made at room temperature. An instrument development reported by M.R. Jacobson and R.D. Lamoreaux of the Optical Sciences Center, University of Arizona, makes it possible to measure reflectance on mirrors at temperatures up to 700° C and the transmittance of windows heated to 500° C. The sample chamber is evacuated to about 5×10^{-6} Torr to prevent sample degradation during testing. This double-beam instrument affords relative reflectance or absolute transmittance and can be used for measurement between 0.38 and 15 μm. An unheated aluminum standard is employed in the relative reflectance mode of operation. Heaters are used on the edges of the

transmittance samples and on the back of the reflectance samples. Temperature is monitored using thermocouples cemented to the heating blocks. A Leiss sodium chloride double-pass double-prism monochromator equipped with a stepper motor disperses the light, which is detected using a thermocouple or a combination lead sulfide-silicon photodiode detector. The output of the instrument is computerized for rapid data analysis. Scanning from 0.38 to 15 μm takes about 20 minutes, and contains 340 data points. No estimate of accuracy was given.

The most common mirror material used for high-power laser applications is molybdenum. Frequently, in infrared applications molybdenum mirrors are used uncoated, so a high infrared reflectance is desirable and may lead to an increased damage threshold. G.E. Carver and B.O. Seraphin of the Optical Sciences Center, University of Arizona, have demonstrated that molybdenum deposited by one of two chemical vapor-deposition processes on fused silica substrates and subsequently annealed at 750 - 1000 °C can have a reflectance at a wavelength of 10 μm of 0.987, which is 0.005 higher than the highest value reported for mechanically polished molybdenum. The reflectance is stable under ambient conditions to within 1 percent over the measurement period of 45 days. Total integrated scatter for the best of these films was 1.2×10^{-3} at a wavelength of 0.63 μm, which corresponds to an rms roughness of 18 Å before and after annealing. The two CVD processes are the pyrolysis of $Mo(CO)_6$ and the reduction of $MoCl_5$. Grain sizes obtained by the two processes were similar and ranged from 0.03 to 0.5 μm in diameter.

Photoacoustic spectroscopy (PAS) offers considerable promise as an alternate evaluation technique for thin-film coated optical samples. The sensitivity of PAS is comparable to that of calorimetry. However, interpretation of the experimental results in terms of a theoretical model is not nearly as well understood for PAS as for calorimetry. In a pair of papers, Nils C. Fernelius of the University of Dayton Research Insitute, compared the experimental results for both amplitude and phase measurements using PAS on an anti-reflection coated ZnSe laser window with calorimetric results and with the theoretical predictions of the Bennett-Forman (BF) theory and a modified Rosencwaig-Gersho (RG) theory. Unlike the BF theory, the unmodified RG theory does not allow for surface absorption. Even though analysis suggested that 93 percent of the absorption in this particular sample arose from bulk absorption and only 7 percent from surface absorption, the unmodified RG theory predicts only a 0.04° change in phase angle for frequency changes over a large frequency range, 1 Hz to 10 kHz, as compared to an observed 7° change over a smaller frequency range, 100 Hz to 1 kHz. Furthermore, the frequency dependence, which was experimentally varied as $f^{-1.04}$, is predicted by the simple RG theory to vary as $f^{-1.5}$.

The BF theory can be reduced to the product of a term containing the dimensions of the cell, type of gas, etc., and a term containing the sum of contributions from surface and bulk absorption. The experimental phase-angle variation of 7° between 100 Hz and 1 kHz was obtained for a ratio between surface and bulk absorption of only 0.03. Utilizing the calorimetric results of an effective absorption coefficient $\beta_{eff} = 7.07 \times 10^{-3}$ cm^{-1}, one predicts the bulk absorption coefficient to be 6.6×10^{-3} cm^{-1} and the surface absorption to be 2×10^{-4} cm^{-1}. The frequency dependence observed for this choice of values was approximately $f^{-1.0}$.

The RG theory was extended by Fernelius to cover a double layer structure. The results using this modified theory were in good agreement with the BF theory and with the experimental results both in amplitude and in phase angle. Additional experimental studies applying these theoretical results would be most desirable.

R.P. Freeze and K.J. Teegarden of the Institute of Optics, University of Rochester reported its use as a scanning technique for identifying potential laser damage sites on substrate surfaces and films exposed to high-intensity laser irradiation. Scan rates of less than 400 ns per resolution point were demonstrated on germanium films deposited on germanium substrates. However, since the surface to be examined had to be encapsulated in a cell which fit tightly to the surface, the technique at present is restricted to an analysis of laboratory-sized specimens. Good agreement is reported between average absorptance results obtained using PAS and those using calorimetry for absorptance values of $\sim$ 1 percent. Signal-to-noise ratios of $\sim$ 50:1 were demonstrated for PAS. Thus samples having absorptance values 10 times smaller could presumably be accurately measured as well. Damage from pulsed CO_2 laser irradiation all correlated with PAS structure. However, there was little relationship between the size of the damage site and the height of the PAS peak and many more PAS peaks were recorded than resulting damage sites. A clearer understanding of the relationship between absorption as determined by PAS and damage is clearly dictated.

There is a history in the Damage Symposium of the development of increasingly sensitive techniques for detecting laser damage. Now P.A. Temple of Michelson Laboratory, Naval Weapons Center has reported a new technique which is significantly more sensitive than Nomarski microscopy, the interferometric technique now nearly universally used for determining the presence of laser damage. Temple has called the new technique total internal reflection microscopy (TIRM). If the substrate is transparent, an intense visible laser having as much as 2 W of power is coupled into the substrate through a prism and matching index fluid such that the beam is incident internally on the surface to be inspected at slightly more than the critical angle, i.e., total internal reflection. If the surface is perfect, no light escapes. If there are imperfections, however, they scatter and light escapes and can be viewed with an external microscope. This microscope can be a Nomarski microscope, so that the two techniques are complementary. If a polarized light is used, the standing wave field near the surface is nearly an order of magnitude higher for internal reflection than it is for the external reflection case used in dark-field microscopy. Temple developed two instruments utilizing TIRM, one for in situ measurements of laser damage and another utilizing Nomarski and TIRM together. Using these instruments he was able to show that details of the damage process invisible using Nomarski were readily observable using TIRM. However, there was little correlation between scattering sites seen before laser damage occurred and the location of subsequent damage pits; and thus unfortunately, it cannot be used as a screening instrument.

3.4 Thin Film Damage

Equal in importance to film characterization is resistance to laser damage. The Symposium has fortunately been a gathering place for the reporting and collecting of damage susceptibilities. In many cases, the documentation of this data ensures that the testing limits are specified. The Symposium organizers have tried to ensure that efforts to identify, develop and assess the utility of new materials is reported whether or not the effort was successful. Along these lines, papers on both the continual development of thin film materials such as TℓI and novel materials, such as chalcogenide glasses were heard. In addition, reports of numerous damage surveys and parametric studies were presented. They will undoubtedly serve as a benchmark for future progress and for any proposed analytical description of laser induced damage to thin film.

For many years, Honeywell has been perfecting the use of TℓI as a coating material for the infrared. At this year's Symposium T.W. Boord, P.P. Chow, W.B. Harrison and J.E. Starling, all of Honeywell, reported on improvements in the clarity and environmental stability of anti-reflective coatings containing TℓI, achieved through the use of a thin SrF_2 film to mask the texture of polycrystalline substrates. The best masking layer thickness was determined to be $\sim$ 200 Å. On the other concern, the environmental stability of 3-layer AR coatings was improved by substituting either NaF or PbF_2 for the usually employed hygroscopic KCℓ layer. However, the deposited films containing the fluorides exhibited much higher absorption. It is hoped that improvements in deposition procedures will alleviate this latter problem.

Chalcogenide glasses are being considered as thin-film optical switches in the infrared. Obviously their ability to withstand intense laser irradiation will determine their ultimate suitability for use in high power lasers. To this end W.E. Kienzle of Science Applications, Inc., and N.I. Marzwell of Rockwell International performed a comprehensive study of deposition parameters affecting the damage threshold of the chalcogenide glass material $Tl_2SeAs_2Te_3$ in film thicknesses from 0.6 to 9.9 μm. Changes in the refractive index and absorption coefficient were deduced from measured reflectance- and transmittance-spectrophotometer curves. The deposition parameters varied were sputtering pressure, sputtering voltage, azimuthal target/source geometry and substrate-target separation. Damage testing was accomplished by using a 2 to 4 ms pulsed CO_2 laser emitting up to 0.16 J/pulse focused to a spot diameter of 0.4 mm.

The chalcogenide studied in this research effort was an amorphous semiconductor which when irradiated by infrared light had a rate of energy absorption that increased markedly with an increase in temperature. This effect led to a drastic change in light transmission resulting from free-carrier absorption. Its onset corresponds to the switching rate of the device which can vary from nanoseconds to microseconds depending on the incident flux and film thickness.

The largest group of papers in this section deals with the very important areas of (1) the correlation of deposition conditions with resultant characteristics such as grain size and damage susceptibility, (2) the utility of overcoatings to improve damage resistance in multilayer stacks designed for use as high reflectors, and (3) three papers which together

represent a major reliable and very useful contribution to this thin film damage data base. These latter papers not only shed light on the role of defects, the limits of correlation of damage sensitivity with film absorption, but most importantly, frequency dependence of damage and its interrelation with both the mechanical and optical properties such as film thickness and refractive index. In many cases, data were also recorded as a function of pulse length, albeit only over a limited range.

It is well known that processing variables and deposition techniques are prime factors governing thin-film character and performance. Furthermore, some materials can only be deposited with high quality by a specific method. To this end, W.T. Pawlewicz, R. Busch, D.D. Hays, P.M. Martin and N. Laegreid of the Battelle-Pacific Northwest Laboratory, assessed the potential of reactively sputtered optical coatings for use at 1.064 μm. Specific materials studied were TiO_2, $In_{1.9}Sn_{0.1}O_3$(ITO), Ta_2O_5, Nb_2O_5, amorphous aSi:H and SiO_2, with the latter several emphasizing the need for high-index coatings. A principal feature of the research on TiO_2, the material on which most of the work was done, was the demonstration that precise control of the crystalline phase and grain size are important factors governing both the optical properties and damage sensitivity. Glassy coatings of this material were determined to be the most damage resistant.

All coatings were rf-sputtered in an Ar/O_2 atmosphere with the exception of the amorphous alloy a-Si:H which was deposited in Ar/H_2. Principal deposition parameters affecting the resulting material properties were substrate temperature (20° to 700° C), oxygen or hydrogen partial pressure (0 to 10 Pa) and rf-induced dc bias voltage applied to the substrate (0 to 500 V dc). Films were characterized as to crystalline structure, phase composition and grain size. Optical properties were assessed spectrophotometrically and the optical constants were deduced over the wavelength range 0.2 to 2.5 μm. Damage thresholds were reported at this meeting in another paper by the group at Lawrence Livermore Laboratory.

This work is both comprehensive and of a nature necessary to improve our understanding of the film preparation -- film properties -- damage sensitivity sequence. More such work is necessary. Some of the principal results of this research are the controlled variation of TiO_2 coating properties, with microstructure which can be varied from the glassy state to 60-nm grain size, and the demonstrated ability to control phase composition from 60 percent anatase/40 percent rutile to 100 percent rutile. The relationship between grain size and refractive index has been established for rutile coatings. Finally, the relatively high damage resistance and low attenuation have been demonstrated for reactively sputtered, transparent coatings of ITO.

Recent damage results on silica/titania reflectors were revealed by C.K. Carniglia, J.H. Apfel, T.H. Allen and T.A. Tuttle of the Optical Coating Laboratory, and W.H. Lowdermilk, D. Milam and R. Rainer of the Lawrence Livermore Laboratory. As is the interest of these authors, tests were accomplished using 1 ns laser pulses at 1.06 μm. Samples tested were limited to variations of 15-layer silica/titania high-reflectance coatings. They determined that a halfwave silica overcoat increases the average damage threshold by about 50 percent, with the standard deviation of damage threshold for a series of coatings of about 30 percent of the average value. These deviations were determined to be due to point-to-point and coating run-to-run variations. By shifting film boundaries relative to the

field, they found (like others at the Symposium) that neither the average field nor the peak field in the outer silica or titania layers correlated with damage, but as might be expected it was the field at the first or outermost silica/titania boundary that showed a correlation. It is well known that absorption and impurities frequently are concentrated at interfaces. In addition, for these high reflectors damage did correlate inversely with absorption levels, when absorptance was > 100 ppm. Absorption in the films was controlled by varying the oxygen pressure during deposition of the titania layers. Extensive morphological examination clearly indicated the uniform or "bulk" absorption damage characteristic of high absorptance films vis-a-vis the point damage associated with low absorptance films with isolated impurities. The absorption is expected to play an even greater role for coated components under rep-rated conditions.

One group vitally interested in pulsed laser-induced damage to optical components is the Lawrence Livermore Laboratory. This year W.H. Lowdermilk, D. Milam and F. Rainer, of that organization, reported on a comprehensive set of damage tests performed on both optical coatings and surfaces to aid in establishing damage thresholds for different substrate materials, surface preparations, coating materials and designs. This study was performed as an aid in investigating the causes of damage and identifying promising materials and processes. Not surprisingly, they found that defects (not yet identified) dominated all surface and film thresholds. They are responsible for the relatively large absorption coefficient characteristic of films ($1\text{-}10^{3}$ cm^{-1}) and surfaces (10^{-3} to 10 cm^{-1}) compared to bulk values (10^{-4} to 10^{-3} cm^{-1}). Polishing compounds are an apparent source of absorbing surface layer impurities. Along these lines, concerning absorption and its effect on damage sensitivity, a series of high reflectivity coatings where absorption varied from 10^{-5} to 10^{-2} were fabricated. Generally, coatings with absorption greater than 10^{-4} had damage thresholds which decreased with increasing absorption, while coatings whose absorption was less than 10^{-4} were uncorrelated with absorption. Of course, what is important is where the absorption is and if it coincides with a high field in the standing wave, i.e., probably not the absolute value of absorption. Many conclusions which were drawn from this comprehensive study will have to await the test of time and attention of others in the field for corroboration. Some of the conclusions are not in complete accord with other observations presented at this series of meetings.

Hard data on the damage resistance of optical thin films is always of interest, particularly when the tests cover a wide range of parameters and are performed on carefully characterized samples. This year T.W. Walker, A.H. Guenther and C.G. Fry of the Air Force Weapons Laboratory and P. Nielsen of the Air Force Institute of Technology subjected CaF_2, MgF_2, ThF_4, MgO, Al_2O_3, T_iO_2, SiO_2, HfO_2 and ZrO_2 films of various thickness (1 λ, 1/2 λ, 1/4 λ, 1/6 λ and 1/8 λ at 1.06 μm) to 5- and 15-ns duration laser pulses (t_p) of 1.06 μm, 0.53 μm, 0.35 μm, and 0.27 μm to assess their damage resistance. It was found that the pulse length dependence of breakdown fit a square root of t_p curve for most all materials. The only exceptions were some oxides at 1.06 μm. Interestingly, fluoride and oxide films were more damage resistant in thinner coatings which did not correlate with changes in the E field inside the films. Breakdown thresholds decreased with decreasing wavelength and

increasing absorption coefficient although the correlation was not linear.

Morphological investigation indicated a gradual but marked change from large isolated pits at 1.06 μm to a more uniformly disturbed region at 0.27 μm. This trend, together with the pulse length and film thickness dependence, were discussed in detail later by the same principal author, where impurity, avalanche and multiphoton approaches to the damage process were considered. The wealth of data reported in this paper should be very useful as benchmarks against which parametric trends predicted by various theories can be compared. All films were prepared under similar conditions, on commonly polished substrates and finally, tested in the same laboratory on the same laser under essentially identical conditions.

In yet another paper, indicative of the growing interest in short wavelength lasers, T.F. Deaton and W.L. Smith of the Lawrence Livermore Laboratory discussed a comprehensive series of laser-induced damage tests at 266 nm using pulses of ∿ 150 ps and 1.0 ns. In this survey, 30 different samples were tested which included dielectric and metallic reflectors, anti-reflection films, an extensive series of fluoride and oxide films and twelve bare surfaces of common substrate and crystalline materials. Some interesting damage values reported in J/cm^2 were, for bare surfaces at ∿ 100 ps: fused silica, 3.0 ± 1.0; BK-7, 2.9 ± 0.8 and KDP, > 1.7 ± 0.3, while at ∿ 700 ps the damage levels were 10.0 ± 3.0, 1.9 ± 0.7, 6.5 ± 1.4 for the same materials respectively. At 700 ps, the damage level for LiF was 14.4 ± 2.5. All results however, were indicative (to a large extent) of surface properties rather than bulk behavior. At the short pulse lengths used in this study there was very little discernable difference in the damage threshold of the eight halfwave fluorides and oxides tested, save the very poor performance of Y_2O_3 films. As a result of this clustering no attempt was made at correlating thresholds and bulk material properties. An average pulse length dependence of $\sqrt{t}$ was observed for the bare surfaces and some dielectric reflectors.

3.5 Considerations for High Power Systems

Of course the end product of this Conference is to lead to improved systems as opposed to an individual element, as in performance or altruistic research pursuits. Thus the interrelation, correlation and infusion of the more fundamental and somewhat esoteric studies into the real world of improving large, often complex high power lasers is the benchmark upon which the Conference must be measured. Two very interesting papers were presented this year relating ultimate system performance to fundamental characteristics of optical elements. One dealt primarily with thermal distortion, while the other was concerned with the polarization sensitivity of thin films and its influence on resonator performance.

C.A. Klein of Raytheon presented a summary of the argument relating the wavefront distortion produced by various components in an optical train to the resulting fluence which can be deposited on a target in the far field. He adopted the exponential expression for the generalized Strehl relation which, for reductions in focused intensity of more than 0.6, gives a better approximation to the exact degradation of target intensity than the more commonly used parabolic expression. Using the exponential relation, he developed compact

expressions for contributions from both cooled mirrors and an exit window to the wavefront distortion and concurrent decrease in peak focused intensity on target. The analysis was conveniently expressed for use by the systems designer. In calculating mirror distortion he assumed that the mirror is cooled and comes to equilibrium in a time short compared to the length of the laser pulse. Thus there is no time-dependent term in the expression for mirror distortion, and uncooled mirrors are not considered. In the case of window distortion, cooling and lateral heat conduction during irradiation were neglected, a good approximation in most applications, and the single-pulse distortion was calculated in terms of pulse duration. Time dependence is thereby included in the window distortion. If window materials are taken singly, the figure of merit for CaF_2 is nearly four orders of magnitude higher than ZnSe for comparable window thicknesses, and KCl is over one order of magnitude higher than ZnSe. However, Klein emphasized that ZnSe has a positive distortion coefficient and hence will cancel some of the distortion introduced by the mirror train. On the other hand, the distortion coefficient of KCl is negative. Thus, for pulse lengths of a critical length, a ZnSe window will compensate to first order for thermally-induced mirror aberrations. For longer pulse lengths window distortion dominates, ultimately rendering the beam unfocusable. The author concludes that "the presence of a positively lensing window, however, always results in a substantial enhancement of the energy-delivery capability of HEL systems." It is not clear that this conclusion is justified except in special cases.

Unstable resonators are frequently used in high power laser systems. Their mode structure can be calculated using scalar field theory provided the polarization state is unchanged during a round trip through the resonator. However, if the resonator contains an odd number of conical elements, a 90° phase shift is introduced during the round trip and compensation must be made to stabilize the optimum resonator mode structure. In the case of the half-symmetric unstable resonator with a coated rear cone, W.P. Latham, Jr., of the Air Force Weapons Laboratory, pointed out that this polarization effect can be removed by using a coating on the conical element which introduces a 90° phase shift upon reflection.

If the coating is imperfect, the $\ell = 2$ mode will be present as well as the desired $\ell = 0$ mode. If there is substantial power in the $\ell = 2$ mode, the power-method calculation technique does not converge, but if only a small percentage of power is in this mode it can be employed to establish tolerances on the coating design. The resulting coating tolerances are extremely tight. To maintain most of the power in the $\ell = 0$ mode the phase shift of the coating should be $90° \pm 5°$. A narrow band, 90° phase-shifting coating design has been reported using quarterwave multilayer dielectric stacks, but Latham indicated that if it is designed for a wavelength of 3.8 μm, the ± 5° phase shift will be exceeded at wavelengths more than 0.2 μm on either side of 3.8 μm. DF lasers may have significant power levels over a broader wavelength range. A broader band, 20-layer coating employing ZnS and ThF_4 was designed to meet this restraint. However, appropriate deposition conditions and damage resistance with these close-tolerance coating designs are still to be demonstrated.

3.6 Theory and Breakdown

The utility of much that has gone before not only applies in the near term to improved system performance, but more importantly for longer range application, forms the basis for an understanding of the interaction of intense coherent optical radiation with matter. The session dealing with Theory and Breakdown always leads to the greatest and often most heated participation of the attendees. This year's was no exception. Very basic papers on a detailed formalism describing multiphoton absorption and avalanche breakdown were heard, as well as an extended and more comprehensive model for wavelength-sensitive, impurity-initialed breakdown on optical thin films. That paper was followed by reporting of very carefully performed experimental measurements to elucidate the focal volume and frequency dependence of bulk breakdown, which led to an unraveling of data presented at previous symposiums in this series. Finally, a paper dealing with the influence of stimulated Brillouin scattering on the damage process in solid state lasers was presented, followed by the last paper dealing with an attempt to computer-model the resulting morphology of laser-induced damage in the bulk of optical materials. An inspection of the growing number of analytical papers presented at the Symposium will attest to the maturity of the field of laser-induced damage. These theoretical expositions generally attempt to correlate with the expanding data base of carefully performed experiments in which there is not only wide acceptance, but high confidence. In addition, we now see the theorists suggesting determinative validation experiments. This synergestic interaction is most rewarding.

As time progresses, interest increases in short-wavelength high- power lasers whether pulsed, rep-rated or continuous wave. While one generally feels that thermal distortion in windows due to absorption can be handled semi-quantitatively, calculation of the absorption itself is another matter. This latter subject was addressed in a pair of papers dealing with nonlinear absorption in direct gap crystals and the competition between avalanche (impact) and multiphoton ionization by A. Vaidyanathan, T.W. Walker and A.H. Guenther of the Air Force Weapons Laboratory, together with S.S. Mitra of the University of Rhode Island and L.M. Narducci of Drexel University. In the first paper, they performed a critical analysis of available theoretical descriptions for nonlinear absorption processes. They specifically treated the Keldysh, Braunstein and Basov formulations. It was shown that the Keldysh treatment is very closely related to Braunstein's formula for allowed-allowed transitions, while the Basov formula corresponds to Braunstein's allowed-forbidden case. Concerning this latter case, there are several errors in the original Basov treatment which have been identified and corrected. The inclusion of non-parabolic energy bonds and excitonic intermediate state in the Braunstein treatment leads to much improved agreement with reported measurements. In general, the allowed-forbidden formulas lead to gross underestimates of the two-photon absorption coefficients, while both the Keldysh and Braunstein allowed-allowed treatements afford better agreement.

A point of further interest is that the Keldysh formula offers a sufficiently accurate description of the multiphoton absorption process even when the photon multiplicity is small. These just stated conclusions are drawn from a comparison of available experimental results and calculations based upon the improved theoretical descriptions. Materials

considered were several direct gap crystals and semiconductors including NaCl, KCl, RbCl, KBr and RbI, plus CdS, ZnSe, GaAs, InP, CdTe and InSb.

In the companion paper on competing mechanisms in pulsed laser-induced damage, the workers at the Air Force Weapons Laboratory computed the damage thresholds for several alkali halides by means of separate avalanche and improved multiphoton models as well as by a combination of the two. The damage criterion was the production of 10^{18} e/cm^3 in the conduction band. Calculations were performed for both picosecond and nanosecond pulse durations for wavelengths ranging from 0.355 μm to 1.064 μm. Neither mechanism studied can adquately explain all the observed features such as the reported scaling relations in laser-induced damage. However, the avalanche mechanism treatment offers better agreement with measured values. The multiphoton treatment gives opto-electric field strengths substantially higher when it is used alone. However, when photon multiplicity is ≤ 4, the damage fields predicted by the latter model can be smaller than those calculated for avalanche multiplication, and are in better agreement with experimental results. The authors concluded that since neither treatment adequately explains all the appropriate features of damage, such as frequency and pulse length dependence, it is better to combine them. This was done in a simple manner with improved results. They were careful to point out that a more careful meshing of these two approaches is necessary with appropriate attention given to their interdependency, such as including the effect of multiphoton transitions on the avalanche growth-rate constant.

There has not been an adequately comprehensive model of electron avalanche breakdown in dielectric solids, capable of explaining all the observed features of pulsed laser-induced breakdown. However, until recently there has not been an adequate data base to discriminate among competing theories. A.A. Manenkov and his co-workers at the Lebedev Physical Institute reported such a set of data at the 1978 Symposium giving breakdown thresholds for a variety of alkali halides as a function of band gap, laser wavelength, and most important, temperature. In a paper presented at the 1979 Symposium, Marshall Sparks, T. Holstein, R. Warren, D.L. Mills, A.A. Maradudin, L.J. Shem, E. Loh, Jr., and F. King, all of the Pacific Sierra Research Corporation, presented a theoretical model of avalanche breakdown which predicts results in good agreement with Manenkov's experimental results.

The model of Sparks, et al., represents a significant advance over the theory of the Lebedev group in that it models electron-phonon collision processes more realistically. In particular, the dependence of the rates at which electrons lose energy to the lattice, and at which the electron current relaxes, are taken to be energy-dependent. The energy dependence of these rates were calculated on a detailed basis which took explicit account of Umklapp processes. Fairly uncomplicated results for theoretical expressions were obtained from a simplified model of the growth of the electron energy distribution in the presence of the optical field. A clear difference was found between the temperature dependence at low frequencies, and at high frequencies, where the distinction lies in the comparison of the optical frequency to the electron current relaxation rate. These predictions generally agree with Manenkov's observations. The relative values of the breakdown thresholds for LiF, NaF, NaCl, KCl, and KBr are in excellent agreement with Manenkov's measurements, and

additionally the absolute damage threshold values for these materials at 293° K and 1.06 μm are in general agreement with the observations.

Using Hopper and Uhlmann's classical paper describing metallic impurity initiated breakdown in glass hosts as a jumping-off point, T.W. Walker, A. Vaidynathan and A.H. Guenther of the Air Force Weapons Laboratory, and P. Nielsen of the Air Force Institute of Technology, extended the early model to dielectric impurities as optical thin films with great success. The success of the improved model was judged by its ability to predict the parametric-variation of thin film damage as a function of film thickness, pulse length and frequency, extracted from a comprehensive set of experimental damage assessments reported earlier at the Symposium.

In studying this problem, the authors happened upon an exact solution of the thermal equations by Goldenberg and Tranter. There, it is not assumed that the radial distribution within the impurity particle is constant, an important feature when dealing with dielectric impurities, since the thermal conductivity of the impurity is small.

A new feature in this proposed model is the inclusion of a Mie absorption coefficient for the impurity particle. For non-metallic impurities, the model predicts a damage threshold dependent upon film thickness, pulse length and frequency all in essential agreement with experimental results on fluoride films of calcium, thorium and magnesium. This arises from the fact that the model predicts that different sized impurities are the most damage sensitive at different pulse lengths and frequencies, the pulse length variation of damage goes almost $t^{1/2}$. However, the exact description better fits the data of Milam, et al., (presented at an earlier conference in this series) for the pulse-length dependence of damage to fused silica surfaces.

There has been a continuing controversy arising from conflicting reports on the subject of the scaling relationships governing the variation of damage thresholds with spot size and frequency. Nowhere has there been more disagreement than when dealing with wide band gap materials in the infrared. In a major effort to resolve this issue, M.J. Soileau of the Naval Weapons Center, M. Bass of the University of Southern California and P.H. Klein of the Naval Research Laboratory, studied the frequency and volume dependence of laser-induced damage in the alkali halides NaCl and KCl prepared by several procedures. The experimental parameters were varied throughout the investigation in pulse widths (31 - 140 ns), wavelength (10.6, 3.8, 2.7 and 1.06 μm) and spot size or focal volume. Failure was assumed to be multiphoton assisted (impurity) electron avalanche. A scaling distinction was made when describing focal volumes -- small being volumes < $1/Ne$ ($\sim 3 - 5 \times 10^{-9}$ cm^{-3}), where N_e is the free electron density. Under this condition frequency dependance of breakdown is determined by multiphoton ionization of impurities. On the other hand, for large focal volumes, ($>.10^{-4}$ cm^{-3}) it was postulated that the free electrons initially present in the crystal initiate breakdown and the frequency dependence is determined in this case by the electron-phonon relaxation time. This leads to the conclusion that for large focal volumes breakdown fields increase with increasing laser frequency, and the opposite behavior for small focal volumes. It is noteworthy to point out that the authors did not find a pulse-width dependence for the relatively long pulsewidths employed in this study. Furthermore,

as a result of their effort one should not attempt to infer n_2 (the nonlinear index) from laser-induced breakdown intensities as has been attempted and reported several times in the past.

An area not discussed at these Symposiums for many years was the subject of a paper by P. Balkevcius, E. Kosenko, J. Lukosius and E. Maldutis, of the Institute of Physics of the Academy of Science of Lithuania. They experimentally investigated the influence of stimulated Brillouin scattering (SBS) on the threshold and morphological character of bulk laser-induced damage. Uusing a 0.53 μm laser of either 10 or 20 ns pulse duration, they varied the spectral purity of the incident laser from < 0.2 to 2 cm^{-1} employing both single and multifrequency operation. Samples tested were K-8 optical glass and fused silica. From their studies it was concluded that sufficient upstream SBS conversion can prevent damage by limiting power in the focal volume and furthermore, that SBS can also modify greatly the damage threshold of optical surfaces. Careful measurements of the redistribution of incident laser light into SBS allowed them to understand the difference between narrow-spectrum (large SBS) and wide-spectrum (low SBS) damage morphologically. For example, wide-spectrum laser radiation having the same power as narrow spectrum interactions always produced long, thin tracks due to self-focusing, evidently a result of the narrow-spectrum irradiation being converted to SBS. Therefore, the exact relation between self-focusing and SBS can be different depending on the coherence length. When it is small, self-focusing suppresses SBS; when it is large, self-compression causes SBS which then scatters out the radiant energy, limiting the tendency of the beam to self focus.

Last year at the Tenth Boulder Damage Symposium, P. Kelly and D. Ritchie of the National Research Council of Canada and A. Schmid and P. Braunlich of Washington State University presented a preliminary account of the use of a "particle in cell" (PIC) computer code to simulate laser induced damage morphology. This year they reported on an improved version (PULSE) which now incorporates the flexibility to accomodate variations in flux, wavelength, material or temperature dependance of the dielectric function and electronic excitation of the solid (avalanche, multiphoton, etc.). An important addition treats the conversion of energy in the phonon field to excited electron and phonon distributions which can increase the lattice temperature. However, many additional features of the real-world laser damage scenario await inclusion, such as impurities and defects as well as adequate treatment of additional nonlinearities beyond multiphoton generation. A computer simulation of the spatial-temporal behavior of a fast, just-damaging pulse focused into an optical material was illustrated in the form of a 16-mm movie. If anyone is interested in further details of this work, contact the authors directly.

4. Recommendations

A survey of the papers given at this year's Symposium reveals that the question of laser damage and related material properties has become a much more mature technology in the eleven years since the Symposia were initiated. The number of questions yet unanswered is at least as large as those under discussion earlier, but now they tend to be more quantitative, often subtler and frequently more closely related to laser performance in actual

devices than in earlier years. The theories are less global and qualitative and tend to be susceptible to quantitative verification. Interaction between theorists and experimentalists tends to be closer and a high standard of experimental work is now demanded. Many of the sources of systematic error in earlier measurements are now well documented and those careless enough to repeat them do so at their peril.

New experimental techniques are still being developed and their use is welcomed. This year saw the introduction of two novel techniques. One was total internal reflection microscopy (TIRM) which has a sensitivity to surface defects or imperfections well over an order of magnitude better than differential interference contrast (Nomarski) microscopy, previously regarded as the most sensitive practical technique employing optical microscopy. The second is quantitative wavelength modulation spectroscopy, which is believed to have a sensitivity comparable to calorimetery for detecting absorption. Both these techniques deserve to be exploited commercially and TIRM now is. Photoacoustic spectroscopy is a third relatively new experimental technique and its use in identifying potential laser damage sites as well as in making sensitive and quantitative absorption measurements, which was discussed in this Symposium, will surely receive further attention. The importance of and paucity of information on damage properties at temperatures above or below ambient was emphasized and will be pursued. Finally, the use of electron spectroscopic techniques such as AES, ESCA and SIMS for evaluating the absorption and damage characteristics of thin films and surfaces was re-emphasized and is expected to become a necessary tool in all well-equipped laboratories investigating such effects.

Extension of laser damage and component measurements into the ultraviolet region was a feature of this Symposium. Clearly much more work needs to be done in this area. The physics of the damage process changes as the interband edge is approached and as the scale of defects, which may be important, decreases. Clearly, optical scattering and the possible relation between scattering level and laser damage threshold becomes even more important. Veils in window materials, which are reported to have little effect on the infrared damage threshold of alkaline earths, may become important in the visible and ultraviolet. The degradation (e.g., via color center formation) of some materials exposed to ultraviolet radiation and implications on damage threshold is a fertile field for further work. Considerable uncertainty exists concerning the optical properties of films at ultraviolet wavelengths and better data needs to be generated. Their nonlinear absorption coefficients, in particular, need to be explored. The possibility that BeF_2 films might be made less hygroscopic could, if demonstrated, have far-reaching results in ultraviolet coating design and should be explored. Also the polishing of surfaces for ultraviolet use is a challenging question and may significantly limit the usefulness of ultraviolet systems if presently ongoing investigations are not successful. Laser polishing and its apparent beneficial effect on laser damage thresholds needs to be pursued aggressively.

An increased emphasis on scale-up processes and an understanding of how to develop components for use in actual systems was evident in this Symposium. The use of the Weibull distribution and proof testing of large components susceptible to brittle fracture was clearly outlined and will be increasingly used by systems engineers in the future. Scale-

up of materials such as CaF_2, YPO_4, YLF and KYF for use in actual devices will be pursued as will the use of strengthened LiF. Stress calculations, the spatial distribution of temperature and the resulting tensile or compressive stress on large brittle window samples will hopefully be used by laser engineers to prevent catastrophic failure due to system design errors. The system requirements for multilayer films used in novel laser cavity designs such as the half-symmetric unstable resonator provide further evidence of the demand for continued development of multilayer film technology. On the other hand, simple laser systems may benefit by the possibility of oxidation-resistant, bare copper mirrors raised by the technique of ion implantation of aluminum and subsequent annealing. This technique merits further study.

The problem of the sensitivity of thin films to laser damage is of continuing importance. Several redundant techniques for separating and measuring the magnitude of surface and bulk absorption in thin films were reported at this Symposium. They include a resonant nuclear technique for determining the presence of H, and thus H_2O or OH^- or a hydrocarbon, measurement of H using SIMS, measurement of localized absorption using internal and external reflection spectroscopy and adiabatic calorimetry. The location and magnitude of surface and bulk absorption in multilayer as well as single-layer films can now be investigated using a combination of these techniques. How to reduce the level of water and other contaminants is the next problem. In theoretical treatments of thin film damage threshold it is important to use values derived from these thin film measurements rather than intrinsic material measurements when predicting film performance.

Our quantitative understanding of laser damage continues to grow satisfyingly. The demonstration that the laser damage threshold predicted for copper using a sophisticated temperature-dependent theory agrees to within experimental uncertainty (10%) with that determined experimentally on samples whose surface structure is nearly undistorted is most satisfying. The damage threshold decreased as the surface disorder increased, again in agreement with theoretical expectations. It would be most desirable to qualify this decrease, however, in terms of measurable surface parameters so that a predictive capability can exist. Also such measurements should be carried out on other metals to understand the generality and limitations of this nascent theory.

Another theoretical triumph was the demonstration that laser-induced slip, which occurs at much lower levels than melting, can be predicted quantitatively by theory. Such slip may increase scattered light, degrade coating performance and reduce damage threshold. Its continued development may in fact precipitate catastrophic damage in laser components. These possibilities have not, however, been demonstrated and more experimental and theoretical work employing large spot sizes should be done to determine the implications of this theory.

Since real devices, particularly those operating in the ultraviolet, are frequently repetitively pulsed, there is a growing need for damage thresholds under repetitive pulse conditions. Also, very long quasi-cw pulse lengths (10-20 μs) need to be investigated. Damage in low-absorption films or surfaces frequently occurs at localized defect sites and the identification of these sites is thus a crucial problem. Precatastrophic damage

measurements and the full use of the analytical techniques now at our disposal are thus essential. Mie absorption in films and the consequent sharp resonances possible as a function of wavelength or defect size and shape needs to be evaluated analytically using adequate experimental data, most of which at present is unavailable. The possibility of non-uniformities in impurity, distribution, grain boundary effects, and results of micro-scans of the sample for localized impurities should also be investigated.

Over the many years of this Symposium, numerous and often conflicting reports of spot-size effects have been heard. On several occasions, scaling laws have been proposed, justified primarily using selected data from the proceedings of this meeting and the Soviet literature. However, in many instances no effect has been seen. This is an area which demands attention since individuals are, in some instances, unwarrantingly relying on unverified scaling relations. A careful assessment of spot-size effects should be undertaken to determine and bound any range of application. Of course, other experimental parameters such as pulse length, sample properties, etc., should be held constant while varying the spot size over a sufficiently large range of diameters. Then other experimental conditions can be altered to bound the parameter space and identify any interdependency. To this area of concern, we should add the need for hard experimental data on repetitively irradiated samples. One must not rely on single exposure failure thresholds as absolute indicators of component failure thresholds when they are intended for use in repetitively pulsed systems. Thus, the scaling of damage thresholds from single event levels to a range of repetitively pulsed conditions is needed as well.

A very satisfying theoretical explanation of size and wavelength in damage thresholds based on an avalanche model and self-defocusing was reported at this Symposium. It should be pursued and the experimental results on which it is based should be extended to shorter wavelengths. Multiphoton effects will become increasingly important as the wavelength decreases, and a complete theory must include them. Although to a first approximation the two effects may be additive, they are doubtless synergistic. The additive approximation may be a poor one and should be investigated. In developing the formalism required for treating the interdependency of multiphoton and avalanche mechanisms, the Soviet literature should be consulted. Too little acquaintance with it is found in nearly all aspects of laser damage phenomena reported in the West. The same may be said of the potential contribution which could be made by other scientific disciplines to the laser damage field. For example, more chemists should be involved, not only for the insight which they can furnish in surface-related matters such as adsorption, but to help explain why, for example, fluorides behave so much differently from refractory oxides when used in thin films.

Laser damage is a fertile area for a multidisciplinarian approach and furnishes a continuing number of challenges for both scientific and engineering efforts of the highest order. It is to be anticipated that continued progress in this area during the next year will make next year's Symposium as productive as this year's has been.

5. Acknowledgment

The editors would like to acknowledge the invaluable assistance of Mr. Aaron A. Sanders, Ms. Norma Lear, Ms. Shir Lee Brubaker, and the other involved staff members of the National Bureau of Standards in Boulder, Colorado, for their interest, support, and untiring efforts in the professional operation of the Symposium and in the preparation and publication of the Proceedings. The continued success of the Damage Symposia would not have been possible without the enthusiastic support of those named above.

6. Bibliography

1. A.J. Glass and A.H. Guenther, Editors, "Damage in Laser Glass," ASTM Special Technical Publication 469, ASTM, Philadelphia, PA (1969).
2. A.J. Glass and A.H. Guenther, Editors, "Damage in Laser Materials," NBS Special Publication 341 (1970).
3. N. Bloembergen, "Fundamentals of Damage in Laser Glass," National Materials Advisory Board Publication NMAB-271, National Academy of Sciences (1970).
4. N. Bloembergen, "High Power Infrared Laser Windows," National Materials Advisory Board Publication NMAB-292, National Academy of Sciences (1972).
5. A.J. Glass and A.H. Guenther, Editors, "Damage in Laser Materials: 1971," NBS Special Publication 356 (1971).
6. A.J. Glass and A.H. Guenther, Editors, "Laser Induced Damage of Optical Materials: 1972," NBS Special Publication 372 (1972).
7. A.J. Glass and A.H. Guenther, "Laser Induced Damage of Optical Elements, A Status Report," Applied Optics 12, 637-649 (1973).
8. A.J. Glass and A.H. Guenther, Editors, "Laser Induced Damage in Optical Materials: 1973," NBS Special Publication 387 (1973).
9. A.J. Glass and A.H. Guenther, "Laser Induced Damage in Optical Materials, 1973: A Conference Report," Applied Optics 14, 74-88 (1974).
10. A.J. Glass and A.H. Guenther, Editors, "Laser Induced Damage in Optical Material: 1974," NBS Special Publication 414 (1974).
11. A.J. Glass and A.H. Guenther, "Laser Induced Damage in Optical Materials: 6th ASTM Symposium," Applied Optics 14, 698-715 (1975).
12. A.J. Glass and A.H. Guenther, Editors, "Laser Induced Damage in Optical Materials: 1975," NBS Special Publication 435 (1975).
13. A.J. Glass and A.H. Guenther, "Laser Induced Damage in Optical Materials: 7th ASTM Symposium," Applied Optics 15, No. 6, 1510-1529 (1976).
14. A.J. Glass and A.H. Guenther, Editors, "Laser Induced Damage in Optical Materials: 1976," NBS Special Publication 462 (1976).
15. A.J. Glass and A.H. Guenther, "Laser Induced Damage in Optical Materials: 8th ASTM Symposium," Applied Optics 16, No. 5, 1214-1231 (1977).
16. A.J. Glass and A.H. Guenther, Editors, "Laser Induced Damage in Optical Materials: 1977," NBS Special Publication 509 (1977).
17. A.J. Glass and A.H. Guenther, "Laser Induced Damage in Optical Materials: 9th ASTM Symposium," Applied Optics 17, No. 15, 2386-2411 (1978).
18. A.J. Glass and A.H. Guenther, Editors, "Laser Induced Damage in Optical Materials: 1978," NBS Special Publication 541 (1978).
19. A.J. Glass and A.H. Guenther, "Laser Induced Damage in Optical Materials; 10th ASTM Symposium," Applied Optics 18, No. 13, 2212-2129 (1979).

PRESS FORGING AND OPTICAL PROPERTIES OF LITHIUM FLUORIDE*

J. F. Ready and H. Vora
Honeywell Corporate Material Sciences Center
10701 Lyndale Avenue South
Bloomington, Minnesota 55420

Lithium fluoride is an important candidate material for windows on high-power, short-pulse ultraviolet and visible lasers. Lithium fluoride crystals have been press forged in one step over the temperature range 300-600°C to obtain fine-grained polycrystalline material with improved mechanical properties. The deformation that can be given to a lithium fluoride crystal during forging is limited by the formation of internal cloudiness (veiling) with the deformation limit increasing with increasing forging temperature from about 40% at 400°C to 65% at 600°C. To suppress veiling, lithium fluoride crystals were forged in two steps over the temperature range 300-600°C, to total deformations of 69-76%, with intermediate annealing at 700°C. This technique yields a material which has lower scattering with more homogeneous microstructure than that obtained in one-step forging. The paper will describe the results of characterization of various optical and mechanical properties of single-crystal and forged lithium fluoride, including scattering, optical homogeneity, residual absorption, damage thresholds, environmental stability, and thresholds for microyield.

Key words: Fluorides; forging; laser windows; lithium fluoride; mechanical properties; optical properties; ultraviolet transmission.

1. Introduction

Improved materials for the laser-assisted, thermonuclear-fusion program are needed for optical components to be used in the beam, including windows, lenses and isolators. The materials will be exposed to high-power, short-duration laser pulses, possibly at short wavelengths in the blue or ultraviolet portions of the spectrum. These materials have a number of stringent requirements, including high transmission at ultraviolet wavelengths, resistance to damage by the high-power laser beam, low scattering losses, a low value of the nonlinear index of refraction, and high mechanical strength, at least for some applications such as windows for gaseous systems operating at pressures of many atmospheres. Lithium fluoride (LiF) possesses a combination of optical properties which is of interest for window application on such lasers. These properties include a large band gap for transmission in the visible and ultraviolet, low refractive index for high damage threshold, and low nonlinear refractive index which minimizes beam break up and self focussing.

Pure LiF single crystals, while they show excellent transmission in the visible and ultraviolet, are characterized by low yield strength and low fracture energy. Also, the diameter of the largest commercially available LiF crystals is limited. The objective of our program is to overcome these shortcomings of LiF crystals without degrading their good optical properties. For this purpose, we have investigated the response of LiF single crystals to press forging, an approach that has been used successfully in the past to improve mechanical properties and increase the diameter of single crystals of various alkali halides and alkaline earth fluorides [1,2].[1] We have characterized the effects of press forging on the optical and mechanical properties of LiF. In an earlier paper, it was shown that press forging increases the fracture energy and the compressive yield strength of LiF single crystals by more than an order of magnitude [3].

---

* Work supported by the U.S. Department of Energy under Contract #ED-78-C-08-1555.

[1] Figures in brackets indicate the literature references at the end of this paper.

2. Press Forging and Veiling

All LiF crystals were forged isostatically in the presence of a helium atmosphere at 13.8 MN/m^2 in a system that has been described elsewhere [3]. The crystals were forged using a displacement rate of 0.013 cm/min for the top ram. Most of the crystals used for forging were of <100> orientation and of dimensions 2.54 cm in height and 3.8 cm in diameter, although crystals of different aspect ratios and orientations were occasionally employed, as described below.

Several LiF crystals were forged initially over a temperature range 300-600°C to deformations of up to 80%. Deformation is defined as the percentage reduction of the original height of the starting material. These forged samples were polished and examined visually using an optical microscope in transmission for the presence of internal defects that might have been introduced by press forging. These examinations indicated that excessive deformation at any temperature introduces veils (or internal cloudiness) which act as scattering centers and look like voids or partially-healed cracks in an optical microscope. The observed limit for deformation without veiling was about 40 percent at 300°C. This limit increased with increasing forging temperature to about 65 percent at 600°C (Figure 1). Metallographic examinations indicated that the employment of forging temperature of 600°C or higher for large-scale deformation would be undesirable because it produces a coarse-grained material possessing non-uniform grain size.

A few crystals of <110> and <111> orientations were forged to determine the effect of initial orientation on veiling in press-forged LiF. After these samples were forged to 50% deformation at 500°C, veils were observed in the billet of <111> orientation, but not in that of <110> orientation. A sample of <110> orientation forged at 600°C to 69% reduction in height was observed to be nearly free of veils. All press-forged LiF samples of <110> orientation were elliptical in cross section with the length of the minor diagonal equal to the length of the diameter of the starting single crystal.

In order to suppress veiling in samples forged to large reductions and to produce a material possessing more uniform microstructure, several LiF crystals were forged in two steps. The forging billet is first given X% reduction at some temperature T_1 (step 1) and later given an additional Y% reduction at some temperature T_2 (step 2). Between steps, the forging billet is annealed at some temperature $T_3 > T_1$ and T_2 to induce recovery. The billets for various two-step forgings were obtained by cutting Harshaw crystals (3.8 cm dia. x 2.54 cm ht.) of <100> orientation either along the (100) plane into two sections of equal heights or along the (010) and (001) planes into identical quarters. In one case, sample H-32, the forging billet was an uncut Harshaw crystal.

All two-step forgings were examined visually for the presence of veils and were classified as veiled or unveiled. The results of this examination and the forging parameters of various two-step forgings are summarized in table 1. The data in table 1 indicate that the two-step forging approach permits a large scale deformation (amounting to 69-75% reduction in height) of LiF without introducing veils. Samples classified in table 1 as unveiled may contain a very few internal defects which are difficult to detect either visually or microscopically. Metallographic examinations of two-step forgings have revealed the presence of fine, and fairly uniform, grains of size in the range 15-30μm.

3. Optical Properties

3.1. Scattering Profiles

We have measured scattering profiles of several single-crystal and press-forged LiF samples with a laser flying-spot scanner, which uses a helium-neon laser as a light source and galvanometer deflectors, and a photo diode positioned such that it detects scattered light at 90° from the forward direction. Figure 2 illustrates the scattering profile obtained by scanning over a 5 mm x 5 mm area of a sample of forged LiF which contained veils because of excessive deformation.

Scattering profiles of two-step forgings which appeared unveiled in a visual examination indicate the presence of a few scattering centers, which are not seen in the scattering

profiles of single crystals or single crystals forged to low reductions. Since such scattering centers are fine and their density low, it is felt that a fine adjustment of the two-step forging parameters would enable us to prevent veils in LiF crystals press forged to a total reduction of $\sim$ 75%.

3.2. Optical Homogeneity

Measurements of the optical inhomogeneity of several LiF crystals at 633 nm have been made, both before and after forging, using the technique described by Bennett et al. [4]. The optical inhomogeneity is defined by $\Delta\eta/\eta$, where $\Delta\eta$ is the variation in the index of refraction η of the sample averaged over its thickness. A description of the experimental procedures employed in the present work has appeared elsewhere [3]. Table 2 summarizes the measured optical inhomogeneities of various LiF samples, along with their forging parameters. The data indicate that the Harshaw LiF single crystals possess very good optical homogeneity ($\Delta\eta/\eta$ in the range 7×10^{-7} - 3×10^{-6}), and that the LiF single crystals can be press forged without seriously degrading their optical homogeneities. In the worst case, sample H - <110> - 2, the observed increase in $\Delta\eta/\eta$ is by about a factor of eight, but in four out of the remaining six samples, H - <111> - 4, H-28 Q-2, H-32 and H-36 Q-4, the observed increase in $\Delta\eta/\eta$ is less than a factor of two. Samples press forged in two steps can retain an optical inhomogeneity in the range of a few parts in 10^6.

3.3. Optical Absorption

We are currently investigating the residual ultraviolet and visible absorption in LiF using absorption calorimetry with a line-tunable argon ion laser. The laser is a Spectra-Physics Model 171-19 which operates single line at nine wavelengths in the visible (454.5-528 nm) at power levels in the range 0.7-6.5 watts, and multiline in the ultraviolet at a power level of 2 watts which is distributed $\sim$ 45%, 45% and 10% among three lines of wavelengths 364, 351 and 339 nm, respectively. Most of our measurements were made at three wavelengths in the visible, 514.5, 488 and 457.9 nm, and using multiline operation in the ultraviolet. Some single-line data were obtained in the ultraviolet using an external prism. The laser calorimetric data that have been obtained are summarized in Figure 3. The data indicate that the forging of sample H-31 at 525°C to 61% reduction raises its absorption by approximately a factor of two. Note that the residual absorption in the ultraviolet and visible in sample H-41, and in the ultraviolet in sample H-42, is a factor of four or more lower than the absorption of an Optovac LiF crystal reported by Harrington et. al. [5].

3.4. Damage Thresholds

Dr. D. Milam of the Lawrence Livermore Laboratory has measured bulk and rear-surface damage thresholds of both single-crystal and press-forged LiF for 1-ns, 1064-nm laser pulses. The samples used in this work were forged at Honeywell and polished at either Lawrence Livermore Laboratory or at Honeywell Ceramics Center. Table 3 summarizes the data obtained by Dr. Milam. Within the limits of the errors, the rear-surface damage threshold is not significantly changed by the forging process. Also the polishing procedure used does not seem to change the surface threshold significantly. The bulk damage thresholds remain high after forging, in fact higher than the values for the single crystals. The bulk damage threshold for one single-crystal sample does seem anomolously low.

Front-surface damage thresholds of single-crystal and press-forged LiF for 700-ps, 266-nm laser pulses have been measured by Drs. T. F. Deaton and W. L. Smith, Lawrence Livermore Laboratory. Their data are given in table 4. Both samples used in this study were polished at Honeywell. Under these irradiation conditions the relatively high value of damage threshold does not appear to be reduced by the forging operation.

4. Environmental Stability

Press-forged crystals of many pure alkali halides may undergo grain growth or secondary recrystallization when aged at room temperature for a long period of time [6]. These processes are accelerated if the relative humidity of the surrounding atmosphere is high. Such samples often show internal cloudiness, which is not present in the as-forged crystals. Studies of the microstructures and scattering profiles of press-forged LiF crystals before and after exposure to a relative humidity of 94% at 39°C for periods up to five days show

no increase in either grain size or optical scattering due to the exposure. Similarly, periodic examinations of the microstructures of several press-forged LiF crystals exposed to ambient conditions of room temperature and relative humidity for periods up to one year have not shown a significant increase in grain size. Thus press forged LiF is stable under reasonable environmental conditions.

5. Threshold for Microyield

Strengths of alkali halides are usually measured in compression at offset strains of 0.1 or 0.2%, or in 3- or 4-point bending. In bending experiments, one measures the proportional limit which corresponds to the stress at which the stress-strain curve deviates from linearity. Our measurements of the conventional yield strengths indicate that the press forging increases the strength of LiF crystals to values in the range 20.7-55.2 MN/m^2 (3000-8000 psi). For comparison the starting single crystals have values around 2.4 MN/m^2 (350 psi).

The fact that many materials can undergo plastic deformation at a small fraction of their conventional yield strengths is of concern in precision design. We have studied the microyield behavior of LiF. The samples for these studies were mechanically polished bars $\sim$ 2.5 mm x 6.5 mm in cross section and 2.5 cm or more in length. These samples were subjected to a series of load-unload cycles in 4-point bending with a distance of 1.91 cm between the supporting pins and 0.79 cm between the loading pins. The load on the sample was increased incrementally in successive cycles. After each cycle the permanent strain was measured by a bonded wire resistance strain gage which was attached to the sample face subjected to maximum tensile stresses. Figure 4 illustrates the microyield behavior of one single-crystal (H-31) and two press-forged (H-31 and H-42) LiF samples. The measured thresholds for microyield were 1.37 MN/m^2 (200 psi) for the single-crystal sample and 10.3 MN/m^2 (1500 psi) and 13.8 MN/m^2 (2000 psi) for the forged samples H-31 and H-42, respectively. A conventional proportional limit of 55.1 MN/m^2 was measured for a sample prepared from forging H-42. These results indicate that press forging also significantly increases the microyield strength of LiF.

6. Summary

Studies of the response of LiF crystals to press forging indicate that they are susceptible to veiling at large deformation. Using a two-step forging approach, a significant reduction in the degree of veiling has been achieved in crystals forged to reductions of 70-75%. Forged LiF crystals have been shown to possess stable microstructure which is not changed by aging in ordinary ambient environments or after exposure to an atmosphere of high relative humidity. Studies of the microyield behavior indicate that the threshold for microyield of LiF single crystals can be increased by an order of magnitude by press forging. Results of optical characterization indicate that the LiF single crystals can be press forged without seriously degrading their optical homogeneity, transmission in the ultraviolet and visible, and thresholds for damage by short laser pulses of 266 nm and 1004 nm wavelength.

Table 1. Forging parameters for various two-step forgings.

Forging		% Reduction (Forging Temp., ^oC) Step 1	Step 2	Overall Reduction	Comment
H-27	(S* II)	45 (500)	45 (500)	70	Unveiled
H-28	(q* I)	55 (600)	45 (500)	76	Veiled
H-28	(q II)	43 (400)	56 (500)	75	Unveiled
H-32		42 (400)	52 (525)	73	Veiled
H-34	(q I)	28 (300)	58 (500)	69	Unveiled
H-34	(q II)	28 (300)	62 (525)	72	Unveiled
H-34	(q III)	72 (525)			Veiled (One-Step Forging)

* S - Section
q - Quarter

All two-step forgings were annealed at 700^{o}C for 1-4 hrs. between steps.

Table 2. Optical inhomogeneity, before and after forging, of various LiF samples.

Sample	Forging Parameters (% Reduction - Forging Temperature)	Inhomogeneity ($\Delta n/n$) Before Forging	After Forging
H-<110>-2	50%-500°C	7.1×10^{-7}	5.4×10^{-6}
H-<110>-3	69%-600°C	1.5×10^{-6}	8.1×10^{-6}
H-<110>-4	50%-500°C	1.3×10^{-6}	1.7×10^{-6}
H-28 Q-1	55%-600°C + 45% - 600°C	1.7×10^{-6}	7.0×10^{-6}
H-28 Q-2	43%-400°C + 56% - 500°C	1.7×10^{-6}	2.6×10^{-6}
H-32	42%-400°C + 52% - 525°C	1.2×10^{-6}	2.3×10^{-6}
H-36 Q-4	37%-350°C + 30% - 360°C + 50% - 500°C	3.0×10^{-6}	5.5×10^{-6}

Table 3. Damage thresholds for 1-ns, 1064 nm laser pulses for single-crystal and press-forged LiF.

Sample	Polish	Damage Threshold (J/cm^2) Rear Surface	Bulk
Single Crystal	Lawrence Livermore Laboratory	10 ± 1.0	24 ± 4
Press Forged	Lawrence Livermore Laboratory	8 ± 1.5	> 24
Single Crystal	Honeywell	7.3 ± 0.7	9 ± 1.3
Press Forged	Honeywell	8.5 ± 1.4	∿ 20

Table 4. Damage thresholds for 700-ps, 266-nm laser pulses for single-crystal and press-forged LiF.

Sample	Polish	Front Surface Damage Threshold (J/cm^2)
Single-Crystal	Honeywell	14.3 ± 2.5
Press-Forged	Honeywell	14.4 ± 2.5

Acknowledgments

We would like to thank Drs. D. Milam, T. F. Deaton and W. L. Smith of Lawrence Livermore Laboratory for performing the measurements of laser damage threshold. We also acknowledge the capable technical assistance of Clark Olson, Dick Brinda, Mark Paquette and Don Parkin in performing the press forging and experimental measurements. We also thank Joe Starling of the Honeywell Ceramics Center who polished some of the samples for laser damage testing.

References

[1] Bernal G., E., Koepke, B. G., Stokes, R. J., and Anderson, R. H., in Proc. Conf. High Power Infrared Laser Window Materials (October 30-November 1, 1972), Bedford, Mass., Carl A. Pitha, Ed., p. 413 (1973). Air Force Cambridge Research Laboratories, AFCRL-TR-73-0372.

[2] Anderson, R. H., Skogman, R. A., and Vora, H., Opt. Eng. 18, #6 (1979).

[3] Ready, J. F., Vora, H., Skogman, R. A., Leung, K. M., and Bernal G., E., in Laser Induced Damage in Optical Materials: 1978 (NBS Special Publication 541), Glass, A. J. and Guenther, A. H., Eds., p. 59 (1978).

[4] Bennett, H. E., Bethke, J. W., and Norris, W. P., in Proceedings of the High Power Laser Optical Components and Component Materials Meeting, 3-4 October 1977, Boulder, Colorado, Harris, J. S. and Strecker, C. L., eds., p. 328.

[5] Harrington, J. A., Bobbs, B. L., Braunstein, M., Braunstein, R., Kim, R. Y., and Stearns, R., in Laser Induced Damage in Optical Materials: 1977 (NBS Special Publication 509), Glass, A. J., and Guenther, A. H., eds. p. 127 (1977).

[6] Koepke, B. G., Anderson, R. H., Bernal G., E., and Stokes, R. J., J. Appl. Phys. 45, 969 (1974).

Figures

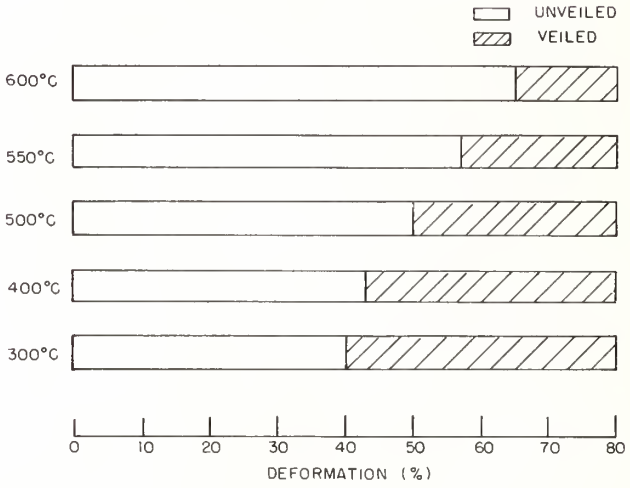

Figure 1. Excessive deformation at any temperature introduces veils in LiF. This figures shows the approximate deformation limits at various forging temperatures.

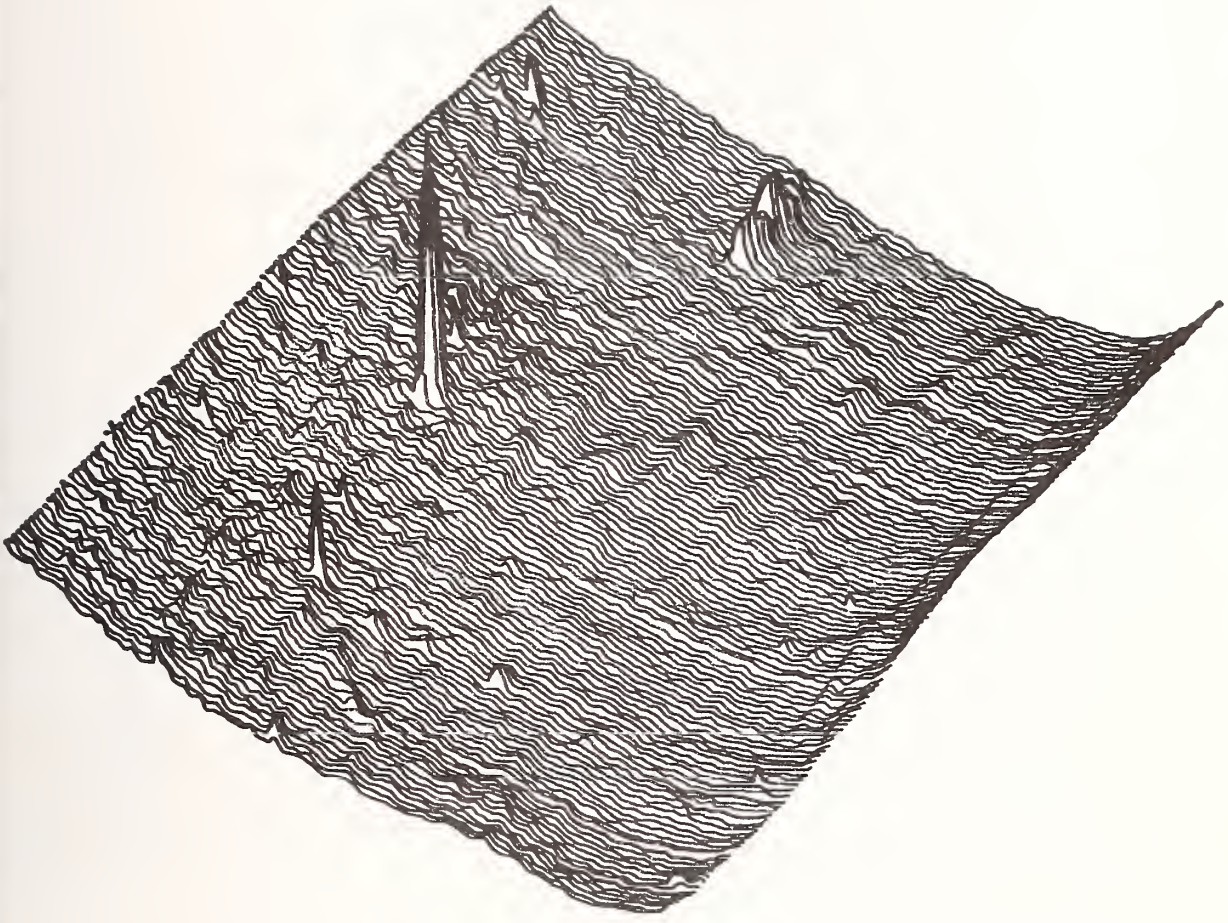

Figure 2. Scattering profile of a 5 mm x 5 mm area of a veiled LiF sample.

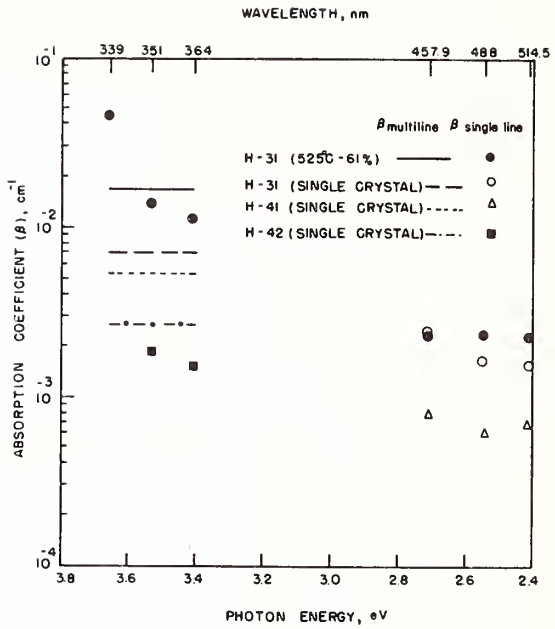

Figure 3. Residual ultraviolet and visible absorption in various LiF samples.

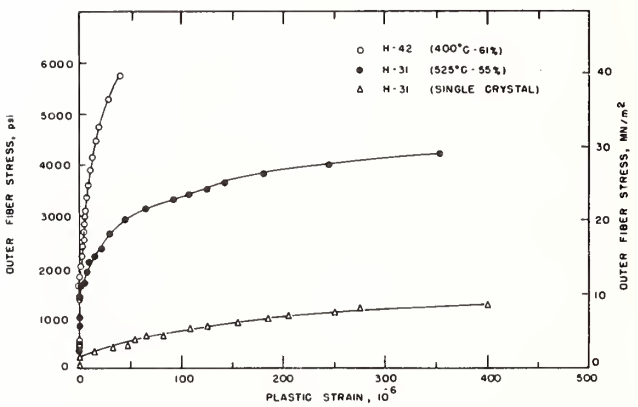

Figure 4. Microyield behavior of single-crystal and press-forged LiF.

OPTICAL PROPERTIES OF FORGED CaF_2

A. K. Hopkins
Air Force Materials Laboratory
Wright-Patterson AFB, Ohio 45433

and

R. H. Anderson, J. F. Ready
Honeywell Corporate Material Sciences Center
Bloomington, Minnesota 55420

and

J. M. Bennett, P. C. Archibald and D. K. Burge
Michelson Laboratory, Physics Division
Naval Weapons Center, China Lake, California 93555

To satisfy the dimensional requirements for large CaF_2 optical components while reducing the sensitivity of this material to thermal and mechanical damage, some form of deformation processing is likely. Strengthened, fine grain polycrystalline CaF_2 can be routinely obtained by isostatic forging. When the deformation of the single crystal exceeds 50%, "veiling" appears within the bulk of the forging and increases with increasing deformation.

To assess the effects of forging and the resultant "veiling" on the optical properties of CaF_2, forgings of ⟨111⟩, ⟨100⟩ and ⟨113⟩ orientations were prepared. Scattering measurements were made in the visible and at 3.39 μm. Then these forgings were isostatically hot pressed (HIP) in an effort to eliminate the veiling. The scattering levels in the visible and at 3.39 μm were remeasured. Homogeneity measurements were obtained using two different methods for single crystal, forged and forged plus HIP CaF_2. Photographs of the stress birefringence in the same three conditions were also taken. These optical data are presented and discussed.

Key words: Calcium fluoride; hot isostatic forging; hot isostatic pressing; laser windows; optical absorption; optical homogeneity; optical scattering; stress birefringence.

1. Introduction

Calcium fluoride is a leading candidate for application as a laser window because it exhibits low infrared absorption, high mechanical strength, respectable thermal conductivity, low thermal expansion and small dn/dT. The major limitation to its use, however, is the susceptibility to surface flaws in the form of scratches, digs and chips. Because of this flaw sensitivity, CaF_2 does not obey a Petch relationship of fracture strength inversely proportional to the square root of the grain size. Previous studies have demonstrated an improvement of fracture surface energy of about an order of magnitude as the grain size is reduced from that of a single crystal to values of 10 μm [1][1]. Data from various sources indicate a surface energy dependence inversely proportional to grain size to the one-fifth power. Qualitatively, single crystals of CaF_2 that have undergone press forging are observed to be less sensitive to thermal and mechanical shock.

In order to satisfy the dimensional requirements of large laser optical components, there are two leading methods of manufacture: large single-crystal growth and fusion casting. The former, by definition, yields enormous grain sizes, and the latter produces equiaxed grains averaging 1 to 2 cm. Thus, the material produced by the fusion casting process has a flaw sensitivity, if related to the grain size, not much different than that of single-crystal material. Thermo-mechanical processing of this large grain material —

[1] Figures in brackets indicate the literature references at the end of this paper.

either single crystal or fusion cast – is required to minimize the grain size and maximize the fracture surface energy. Hot press forging of the CaF_2 at temperatures below that at which recrystallization occurs is an ideal method of grain refinement. Mechanical constraint on the free periphery of the workpiece during forging is desired to reduce tensile stresses below the level at which cracking would occur. The constraint mechanism chosen for this study is pressurized inert gas (helium) in the forging chamber [2].

When the deformation exceeds 50% true strain, optical scattering sites occur in the bulk of the forged sample. In some starting crystal orientations (e.g., ⟨100⟩, ⟨113⟩), these sites, called "veils," occur in a random fashion and cause a uniform clouding in the forging. Other orientations (e.g., ⟨111⟩) produce a striated veiling as if the phenomenon were occurring on slip planes within the bulk. Electron micrograph examinations suggest that veiling is caused by microvoids or void sheets formed by the coalescence of vacancies, which were produced by dislocation intersections and annihilations as a consequence of plastic deformation [2]. Since these veils cause scattering of light in the visible spectrum, studies have been pursued to determine the effect of the veils at the wavelengths of intended use, 2.7 and 3.8 μm, and to establish methods to solve this problem.

2. Experimental Program/Results

Since the veils were postulated to be microvoids caused by the coalescence of vacancies, a method was sought which would collapse or compact the voids and render the bulk material transparent at all wavelengths of interest. In the metal-working industry, voids within forged or cast products have been successfully eliminated through the process of isostatically pressing the workpiece at elevated temperatures, otherwise known as hot isostatic pressing (HIP). The workpiece is placed in an autoclave and raised to a temperature approximating the recrystallization temperature, simultaneously imposing inert gas at high pressure on the piece; these conditions are maintained until the voids are collapsed, perhaps several hours in duration. After this autoclave processing, the piece is cooled, removed from the autoclave and examined by any of several techniques to determine its residual porosity. A series of these experiments was conducted on several samples of single-crystal CaF_2 that had been hot isotatic forged and in which a large number of veils were present. The following describes the experimental program and the results.

2.1 Hot Isostatic Forging

A number of single crystals were purchased from Optovac Corp. in a variety of crystallographic orientations: ⟨100⟩, ⟨111⟩, ⟨112⟩ and ⟨113⟩. For this study, Honeywell thermomechanically processed crystals of selected orientation for grain refinement according to the following schedules:

⟨100⟩, ⟨111⟩, ⟨113⟩: At 750°C with a helium gas pressure of 13.8 MPa, forge at 250 μm/min for 30% true strain; anneal at pressure and temperature for 6 hrs (annealing at each step under identical conditions); forge an additional 15% at 190 μm/min; anneal for 6 hrs; forge an additional 10% at 63 μm/min; anneal for 6 hrs; forge an additional 5% at 25 μm/min; anneal for 6 hrs; slow cool to room temperature at 25°C/hr.

⟨113⟩: At 750°C with a helium gas pressure of 13.8 MPa, forge at 250 μm/min for 60% true strain with no annealing and rapid cool-down to room temperature.

The two forging schedules were pursued to determine the effect of strain rate, annealing and cooling on the production of veils. For all practical purposes, the high strain rate, single-step forging with no anneal and rapid cool-down did not magnify the veil production nor content.

2.2 Hot Isostatic Pressing

In order to determine if veils contained entrapped gases, a small chordal slice was taken from the ⟨113⟩ sample in figure 1, wrapped in Ta foil, inserted in a furnace and heated at atmospheric pressure to 750°C. The test philosophy was that if the sample contained entrapped gas, the veils would greatly expand upon heating at atmospheric pressure

and either fracture the specimen or remain as enlarged optical scattering sites. Post-heat treatment examination revealed no substantial change in veil content, size or fractures of the specimen.

A second piece of the same ⟨113⟩ sample (the segment to the right in figure 1) was wrapped in Ta foil, placed in an autoclave and heated to 750°C in an argon atmosphere at a pressure of 138 MPa for a period of three hours. Upon rapid cooling to ambient conditions, the piece was found to have significantly reduced veiling, but the veils were not totally eliminated.

A third set of experiments was run in which a sample of ⟨111⟩ orientation (the piece to the left in figure 2) was wrapped in Ta foil, placed in an autoclave and heated to 750°C in an argon atmosphere at 276 MPa for a period of three hours. Virtually total elimination of the veils resulted.

Encouraged by these results, a set of experiments was designed in which quantitative reductions of the veil content could be evaluated. Samples of three orientations of CaF_2 ⟨100⟩, ⟨111⟩ and ⟨113⟩ were forged by Honeywell. The ⟨100⟩ and the ⟨111⟩ samples were forged at the sequential strain rates with intermediate anneals, as discussed in section 2.1. The ⟨113⟩ sample was forged at the higher strain rate with no annealing or slow cool-down, as discussed in section 2.1. Pre-HIP-processed optical absorption measurements were made at the Air Force Materials Laboratory and scattering measurements made at the Naval Weapons Center. A HIP-processing run was conducted at Battelle Memorial Institute using their autoclave capable of accepting workpieces up to 30.5 cm in diameter, a typical laser window size. This autoclave is limited in pressure to 207 MPa. The samples were wrapped in Ta foil and heated to 750°C in an argon atmosphere at 207 MPa for a period of 10 hours. Again veiling was virtually eliminated. Post-HIP-processed optical absorption, scattering, homogeneity and stress birefringence measurements were made. The results of these measurements are discussed below.

Two other results of the HIP-process experiments are noteworthy. The first is with regard to the appearance of pits on the specimen surface after HIP-processing. Before being placed in the autoclave, the samples were optically polished. After HIP-processing, examination of the samples revealed many pits, a number of which were replicas of the striated veils, as noted in figure 3. This pitting led to the postulation that veils migrated to the surface from the bulk. Thus, the bulk material is seen to collapse upon itself.

The other result of the HIP-processing is that the grain size did not change, remaining approximately 10 μm. This is not surprising in that the HIP temperature is below the recrystallization temperature (800°C for highly mechanically strained CaF_2).

2.3 Optical Absorption Measurements

Three samples of CaF_2 (⟨100⟩, ⟨111⟩ and ⟨113⟩) were examined for their optical absorption before and after HIP-processing. A 10-watt HF/DF chemical laser was used to provide the requisite energy at 2.7 and 3.8 μm with the absorption determined in an adiabatic calorimeter. The results are shown in table 1.

Table 1. Absorption measurements in forged/HIP-processed CaF_2.

Sample orientation	Before HIP β (cm^{-1})		After HIP_A β (cm^{-1})		After HIP_B β (cm^{-1})	
	2.7 μm	3.8 μm	2.7 μm	3.8 μm	2.7 μm	3.8 μm
⟨100⟩	2.97×10^{-4}	1.91×10^{-4}	7.80×10^{-4}	4.40×10^{-4}	6.67×10^{-4}	2.62×10^{-4}
⟨111⟩	1.74×10^{-4}	0.827×10^{-4}	4.07×10^{-4}	1.44×10^{-4}	---*	---*
⟨113⟩	3.95×10^{-4}	2.42×10^{-4}	8.65×10^{-4}	6.57×10^{-4}	5.99×10^{-4}	2.38×10^{-4}

*Specimen fractured, data inconclusive.

The last two sets of columns, labeled "After HIP_A" and "After HIP_B", represent two different methods of specimen polishing. Honeywell polished the samples before HIP-processing using

various grit sizes of diamond powder (down to 0.3 μm) in a kerosene solvent. After HIP-processing, the University of Dayton Research Institute repolished the samples before making the second set of absorption measurements. They used alumina grit (down to 0.3 μm) in a water solvent. The data after this polish are represented by After HIP_A. To eliminate this variable, Honeywell again polished the samples using diamond/kerosene. The third set of data representing this final polish is shown as After HIP_B.

2.4 Homogeneity

In order to determine the effects of the forging and HIP-processing on the homogeneity of the CaF_2, the optical homogeneity was measured using two different methods. The first method was an interferometric technique developed by Bennett and co-workers [4] in which a sample with flat, parallel sides is inserted between two optical flats having high reflectance coatings. An index matching fluid is used to eliminate the effect of the sample surfaces. Fizeau fringes are formed between the coated surfaces, and the fringe pattern is detected with a TV camera and displayed on a TV monitor screen. Photographs of the interference fringes are then digitized and the digitized interferograms converted to contours of optical path difference through the use of the computer program FRINGE developed at the Optical Sciences Center, University of Arizona.

Figure 4 shows a typical fringe pattern obtained in the interferometer. The circular fringes are ghosts caused by reflection of the laser light from the faceplate of the vidicon. The straight fringes near the edges are the Fizeau fringes outside the sample. The slightly curved fringes near the center are the fringes obtained through the thickness of the sample. The curvature represents the inhomogeneity of the sample.

The inhomogeneity, expressed as the variation Δn in the index of refraction from its average value, is given by the equation [4]:

$$\Delta n = \frac{\lambda}{2T} \frac{a}{b} \quad , \tag{1}$$

where λ, the wavelength of the helium-neon laser used as a light source in the interferometer, is 633 nanometers, a is the peak-to-valley irregularity in the fringes, b is the separation between the fringes, and T is the sample thickness. Results are shown in table 2, which gives the inhomogeneity in terms of the root-mean-square value of the variation of the index of refraction. Results are presented for three different crystallographic orientations for the starting material.

Table 2. Inhomogeneity of CaF_2.
(All values are Δn in units of 10^{-6}.)

Sample	Inter-ferometric (rms value)	Stress birefringence ("typical")
⟨100⟩ Orientation		
Single crystal	0.5	0.2
Forged	0.6	1.1
Forged and HIP-processed	2.3	1.0
⟨111⟩ Orientation		
Single crystal	0.3	0.2
Forged	0.5	2.0
Forged and HIP-processed	1.8	1.0
⟨113⟩ Orientation		
Single crystal	0.2	0.2
Forged	0.3	2.0
Forged and HIP-processed	0.6	3.0

The lowest values of the inhomogeneity are the values for the single-crystal material. Forging increases the inhomogeneity, and forging and HIP-processing increase the inhomogeneity still further. However, the inhomogeneity for forged and HIP-processed material is still in the range of a few parts in 10^6.

The second method of determining inhomogeneity involved measurements of stress birefringence. These measurements were carried out using a circular polariscope. The circular polariscope allows quantitative measurement of the inhomogeneity to be made by determining the angle of rotation of a final polarizer used to extinguish the transmission [5]. This is essentially a point-by-point measurement made manually at a number of different positions on the sample.

Figures 5-7 show transmission patterns in the circular polariscope caused by stress birefringence in the CaF_2 samples. These samples are oriented in the ⟨100⟩ direction. The photographs were taken with the polarizers crossed so that the light transmitted is a rough measure of the amount of stress-induced birefringence. Figure 5 shows a single crystal sample, figure 6 a forged sample, and figure 7 a sample which was forged and HIP-processed. The pattern of stress becomes progressively more complex in this series of three photographs.

Results are presented in table 2 for typical values of inhomogeneity caused by stress birefringence. These values are a subjective interpretation of what represents a "typical value" for a sample, rather than representing a rigorous mathematical characterization such as a root mean square value. The values do, however, compare reasonably well with the values of inhomogeneity obtained from the interferometric measurement. The inhomogeneity caused by stress birefringence tends to be lowest for the single-crystal material and highest for the forged and HIP-processed material. The order of magnitude is also comparable to that obtained in the interferometric measurement. The implication, therefore, is that the inhomogeneity is due mainly to the presence of stress-induced birefringence in the samples, and that the stress-induced birefringence increases as the material is forged and HIP-processed. Although forging and HIP-processing increase the inhomogeneity, it still remains in the low 10^{-6} range.

2.5 Optical Scattering Measurements

Bulk forward scattering measurements were made on the Optical Evaluation Facility [6] by placing the CaF_2 sample in a cell containing a liquid whose refractive index matched that of the sample and measuring the total light scattered out of the transmitted beam, as a function of position on the sample. This method of measurement eliminated the effect of scattering from the surfaces of the sample, which otherwise might mask the bulk scattering. Scattering from the outer surfaces of the CaF_2 windows on the cell was determined by measuring the forward scattering with the sample removed and the cell filled with the index matching fluid. The orientation of the sample in the cell was recorded, and maps were made of the total bulk forward scattering as a function of position on the sample. It was hoped to be able to correlate areas having high scattering levels with the veils in the as-forged material. Secondly, by measuring the scattering as a function of position on the sample before and after the HIP-processing, it was hoped to determine whether the high scatter points changed by the processing. Unfortunately, neither of these objectives was achieved. It was not possible to correlate either the bulk forward scattering in the visible spectral region (6471 Å) or in the infrared (3.39 μm) with observable veils in the samples. Secondly, since the identifying index marks on the samples were removed during the repolishing after HIP-processing, it was not possible to compare the spatial location of the scattering in the two cases. However, by rotating the contour plots for both the visible and infrared scattering, it appears that the high scattering areas do not correlate. More will be said about this result later.

The results of the bulk forward scattering measurements are given in table 3 and are shown in figures 8-15. Table 3 lists the average values of the scattering in the visible and infrared spectral regions for the as-forged samples with veils and for the same samples after HIP-processing. Sample ⟨111⟩ developed a crack during the repolishing, and hence only a few measurements were made after HIP-processing. Enough data were taken on the other two samples to enable contour maps and three-dimensional scattering plots to be made. In the maps and plots the contribution of the scattering from the cell was not subtracted from the

scattering measurements because it was quite uniform and did not vary from point to point. For the as-forged samples the scattering contribution from the cell is less than one-fourth of the total scattering (cell + sample) at 6471 Å and about one-third of the total scattering at 3.39 μm. After HIP-processing the contribution from the cell is about one-third of the total scattering at 6471 Å. In the infrared it is about one-third of the total scattering for samples ⟨100⟩ and ⟨111⟩ but almost equal to the total scattering for sample ⟨113⟩. This latter sample had by far the lowest average infrared scattering but had scattering comparable to that of the other samples in the visible.

Table 3. Bulk forward scattering in CaF_2.

Sample orientation	Forged, with veils		After HIP-processing	
	6471 Å	3.39 μm	6471 Å	3.39 μm
⟨100⟩	$2.11\pm0.54\times10^{-2}$	$4.07\pm1.77\times10^{-4}$ [a]	$3.60\pm0.86\times10^{-3}$	$5.35\pm2.12\times10^{-4}$ [b]
⟨111⟩	$1.23\pm0.56\times10^{-2}$	$4.74\pm1.79\times10^{-4}$ [a]	$2.78\pm0.69\times10^{-3}$	$6.73\pm2.80\times10^{-4}$ [c]
⟨113⟩	$2.34\pm0.53\times10^{-2}$	$6.75\pm1.64\times10^{-4}$ [b]	$3.16\pm0.49\times10^{-3}$	$2.94\pm2.19\times10^{-4}$ [d]
Cell only	$3.04\pm0.84\times10^{-3}$	$1.53\pm0.40\times10^{-4}$	1.29×10^{-3}	2.18×10^{-4}
	Data corrected for scattering from cell			
⟨100⟩	1.81×10^{-2}	2.54×10^{-4}	2.31×10^{-3}	3.17×10^{-4}
⟨111⟩	0.93×10^{-2}	3.21×10^{-4}	1.49×10^{-3}	4.55×10^{-4}
⟨113⟩	2.04×10^{-2}	5.22×10^{-4}	1.87×10^{-3}	0.76×10^{-4}

[a] Averages of 817 points in concentric circles; radial increment 0.050 inch, maximum radius 0.800 inch.
[b] Averages of 631 points in concentric circles; radial increment 0.050 inch, maximum radius 0.700 inch.
[c] Averages of 35 points on an 0.500 inch radius circle.
[d] Averages of 469 points in concentric circles; radial increment 0.050 inch, maximum radius 0.600 inch.

By comparing the as-forged and HIP-processed scattering values in table 3, it is seen that the HIP-process reduced the visible scattering by about a factor of eight on the average, but did very little to the infrared scattering. The average infrared scattering level actually increased for samples ⟨100⟩ and ⟨111⟩.

The contour plots in figures 8-11 show primarily the variation of the scattering level at different places on the sample. (The orientation of the sample was the same for the pair of plots in each figure.) The following features are evident in the plots: (1) For sample ⟨100⟩ there is a large spatial variation in the visible scattering, while in the infrared the scattering level is more uniform, although isolated high spots are present; there is very little correlation between the high scattering points in the visible and in the infrared. (2) After HIP-processing the visible scattering is much more uniform over the sample, but the spatial variation in the infrared scattering is essentially unchanged; the high scatter regions in the visible and infrared again show very little correlation. (3) The spatial variation in the visible scattering for sample ⟨113⟩ before HIP-processing is less than for sample ⟨100⟩; the gradations seem to be more like undulations over the surface rather than like point defects; there appears to be no correlation between the spatial patterns in the visible and infrared scattering. (4) After HIP-processing sample ⟨113⟩ has extremely small spatial variation in the scattering both in the visible and infrared spectral regions. This effect is especially pronounced in the visible where the contour interval in figure 11 is half that in figure 10. The few isolated high scattering areas in the infrared scattering do not correlate with high areas of visible scatter or with high areas in the infrared scatter before HIP-processing. This latter conclusion can be drawn by rotating one contour plot relative to the other since the orientation of the second plot is not known relative to the first.

Figures 12-15 give a three-dimensional representation of the same scattering values that were shown in the contour plots. In this representation the position on the sample surface is shown in the x-y plane, while the magnitude of the scattering is shown in the z direction. (The orientation of the sample is the same for the pair of plots in each figure.) In the after-HIP-processing plots, the scales for the visible and infrared differ by a factor of 10, while for the as-forged plots the scales differ by a factor of 40. The feature most clearly shown in the three-dimensional plots is the spiky nature of the infrared scattering as compared to the visible scattering.

3.0 Conclusions

Qualitatively, higher pressures and longer times for the HIP-process progressively reduce the veil content. Only one set of optical measurements was made on the HIP-processed material and that at 207 MPa and 10 hours. Regarding the optical absorption, HIP-processing appears to slightly increase the absorption at 2.7 and 3.8 μm. The optical inhomogeneity increases after HIP-processing but remains in the range of 1 to 3 parts in 10^6. The main contribution to optical inhomogeneity is stress-induced birefringence.

The general conclusions which can be drawn from the scattering measurements are as follows: (1) There is no obvious correlation between the veils in the as-forged material and either the visible or infrared scattering. (2) In the visible the HIP-processing reduces the scattering by about a factor of eight on the average and reduces the spatial variation of the scattering. (3) In the infrared the HIP-processing does not affect the scattering (except for sample ⟨113⟩) and does not affect the spatial variation of the scattering. (4) There is no obvious correlation between high-scattering areas in the visible and infrared either before or after HIP-processing.

For applications such as infrared windows, it is not clear that HIP-processing improves the performance of the material. Further work is needed to understand the interrelations between visible and infrared scattering, absorption, and homogeneity. Systematic variation of HIP-processing parameters and their effects on these optical properties is required. This should better define the importance of HIP-processing for improving the performance of infrared window materials.

References

[1] Anderson, R., Skogman, R., Ready, J., and Bennett, J., "Bulk Optical Properties of Fine Grained Forged Calcium Fluoride," in Laser Induced Damage in Optical Materials: 1978, A. J. Glass and A. H. Guenther, eds., National Bureau of Standards, Washington, DC, 1978 (NBS Spec. Publ. 541), pp. 70-77.

[2] Anderson, R., Koepke, B., and Bernal G., E., "Intermediate Temperature (0.5 to 0.7 T_{mp} °K) Forging of Calcium Fluoride Crystals," in Laser Induced Damage in Optical Materials: 1976, A. J. Glass and A. H. Guenther, eds., National Bureau of Standards, Washington, DC, 1976 (NBS Spec. Publ. 462), pp. 87-94.

[3] Bernal G., E. et al, A Study of Polycrystalline Halides for High Power Laser Applications, Final Technical Report on Contract DAHC-15-73-C-0464, Honeywell Inc. Corporate Material Sciences Center (May 1978).

[4] Bennett, H. E., Bethke, J. W., and Norris, W. P., "Optical Homogeneity Measurement Technique for Laser Windows," in Proceedings of the High Power Laser Optical Components and Component Materials Meeting, J. S. Harris and C. L. Strecker, eds., DARPA, 1977, pp. 327-338.

[5] Dally, J. W., and Riley, W. F., Experimental Stress Analysis, McGraw-Hill Book Co., New York (1965).

[6] Bennett, H. E., and Stanford, J. L., "Structure-Related Optical Characteristics of Thin Metallic Films in the Visible and Ultraviolet," J. Res. Natl. Bur. Stands. 80A, 643 (1976).

Figure 1. ⟨113⟩ Forged/HIP.

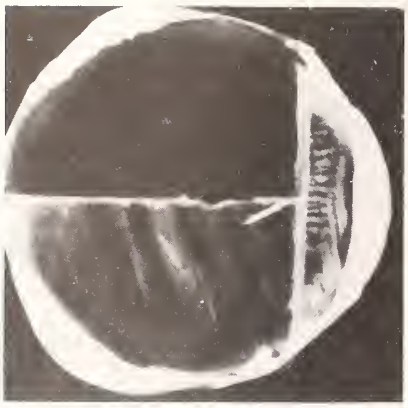

Figure 2. ⟨111⟩ Forged/HIP.

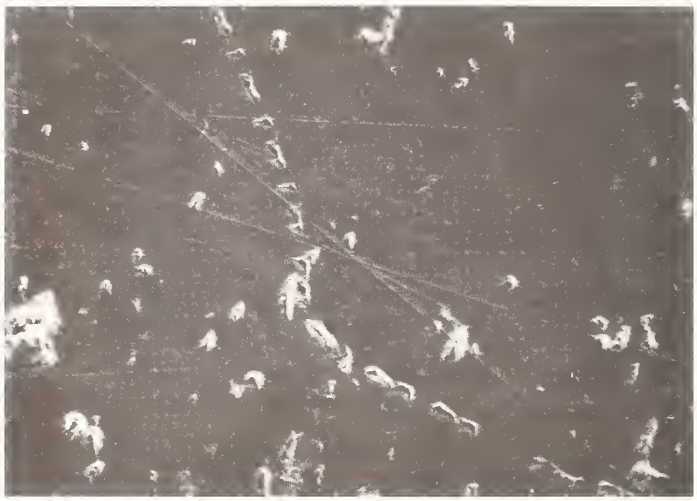

Figure 3. Surface pit replication of veils. 500X magnification. The scratches remain from the initial polishing.

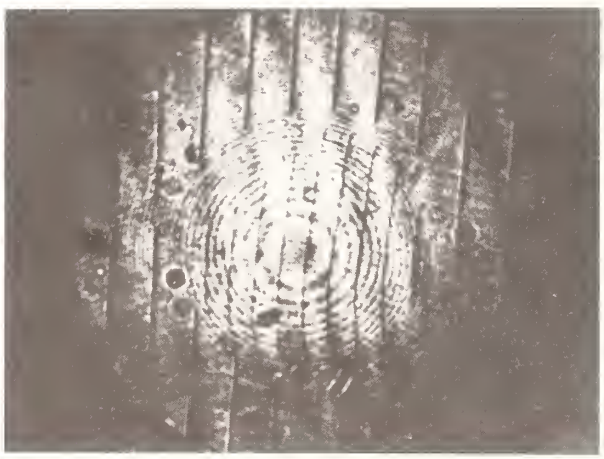

Figure 4. Fizeau fringes in single-crystal CaF_2.

Figure 5. Stress birefringence in single-crystal CaF_2.

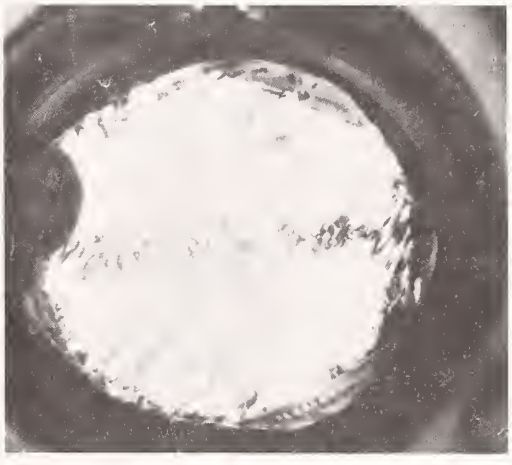

Figure 6. Stress birefringence in forged CaF_2.

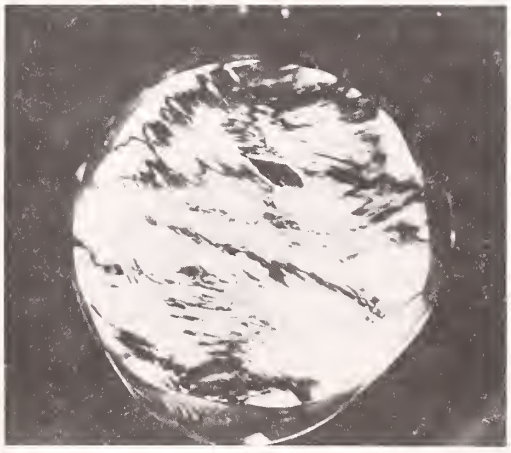

Figure 7. Stress birefringence in forged and HIP-processed CaF_2.

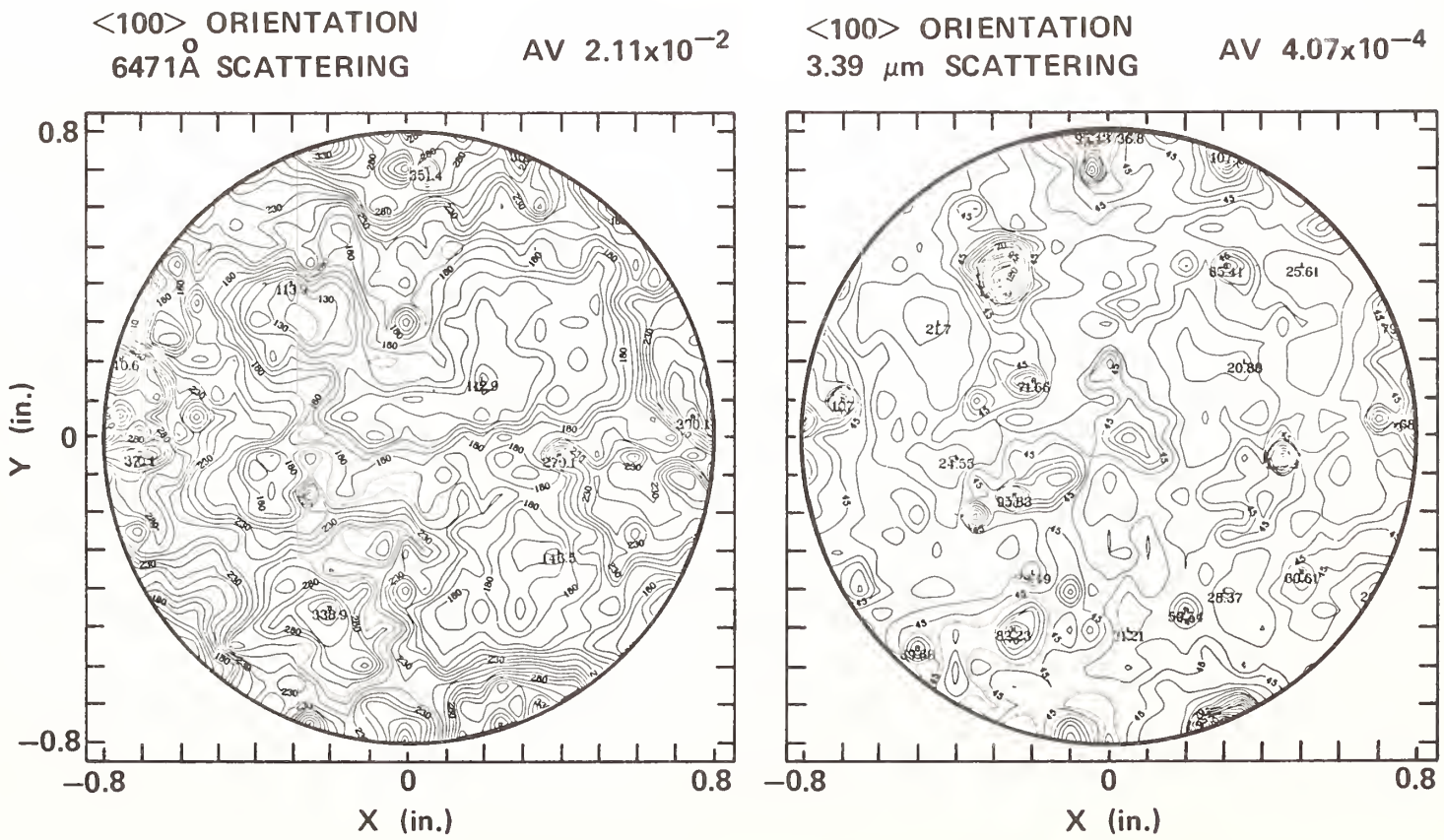

Figure 8. Bulk forward scattering in ⟨100⟩ CaF_2 with veils.

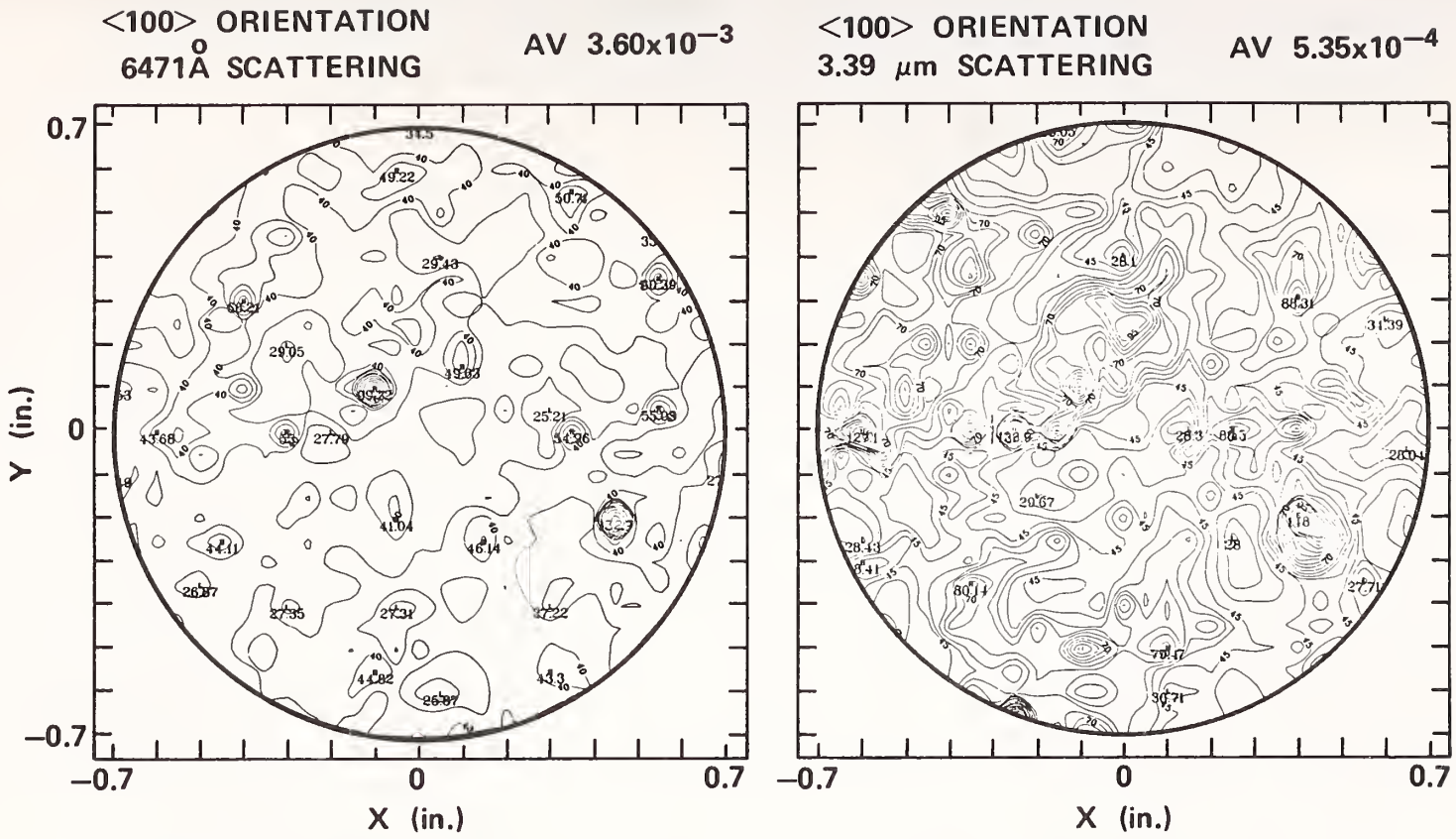

Figure 9. Bulk forward scattering in ⟨100⟩ CaF_2 after HIP-processing.

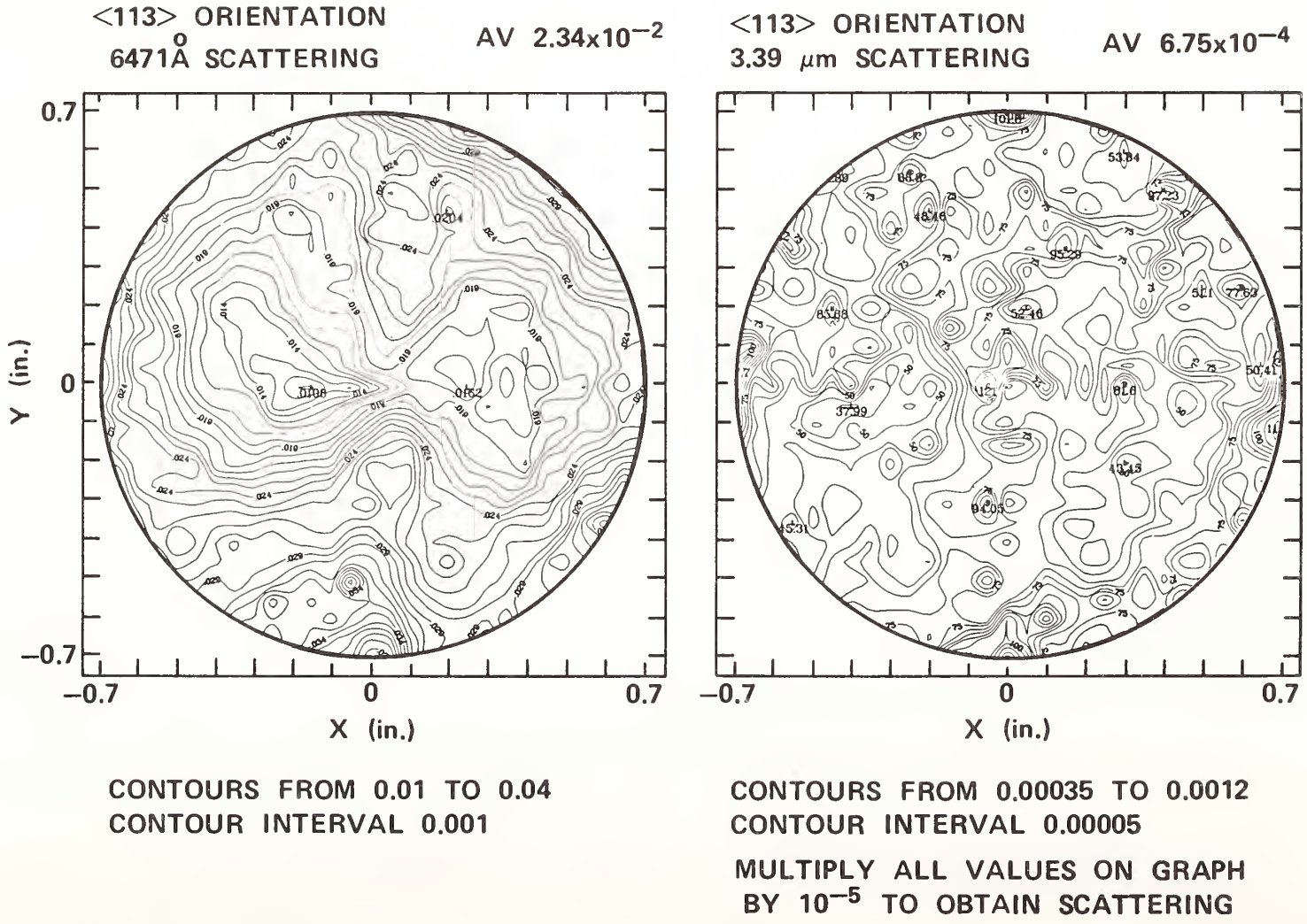

Figure 10. Bulk forward scattering in ⟨113⟩ CaF_2 with veils.

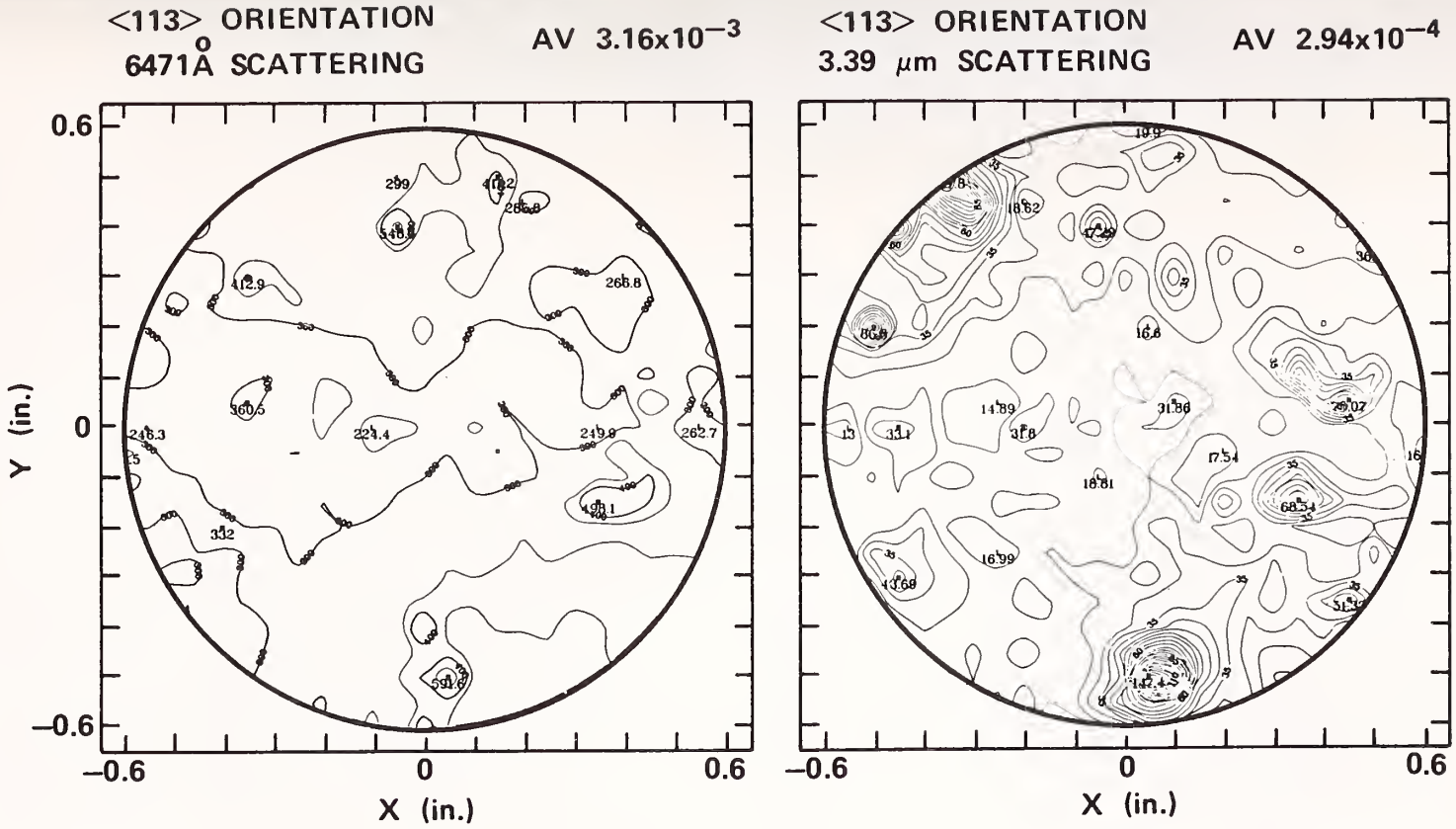

Figure 11. Bulk forward scattering in ⟨113⟩ CaF_2 after HIP-processing.

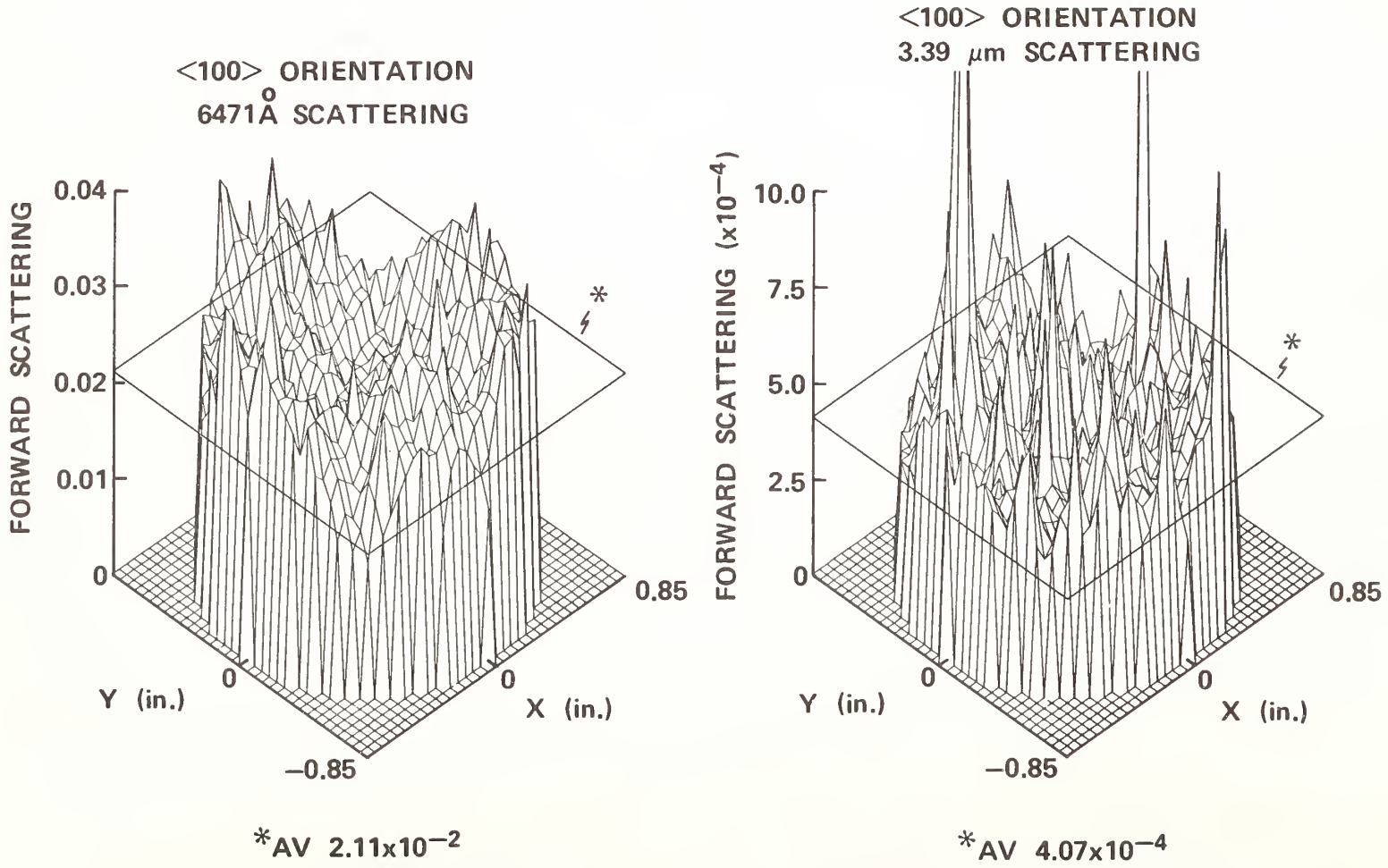

Figure 12. Three-dimensional plot of bulk forward scattering in ⟨100⟩ CaF_2 with veils.

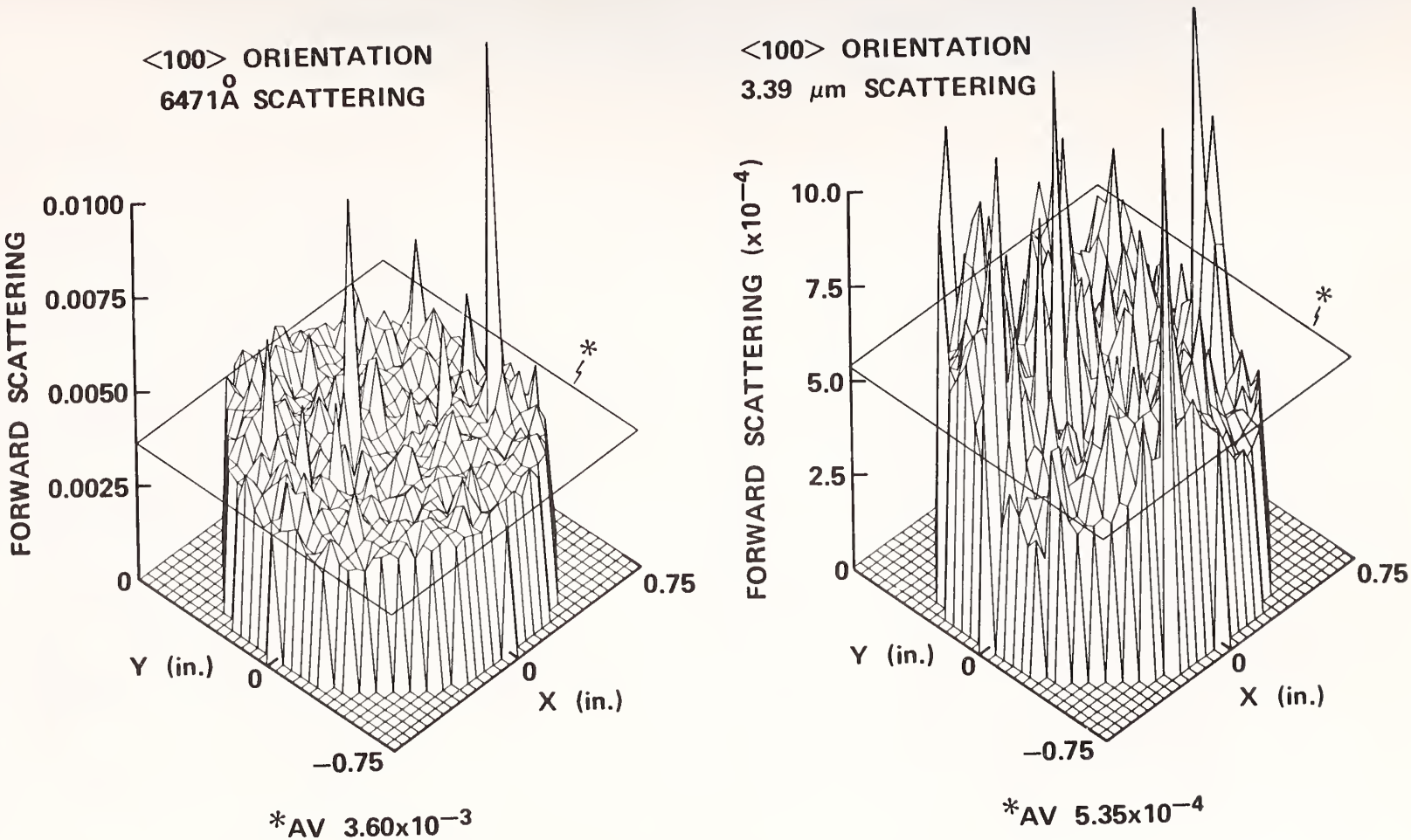

Figure 13. Three-dimensional plot of bulk forward scattering in ⟨100⟩ CaF_2 after HIP-processing.

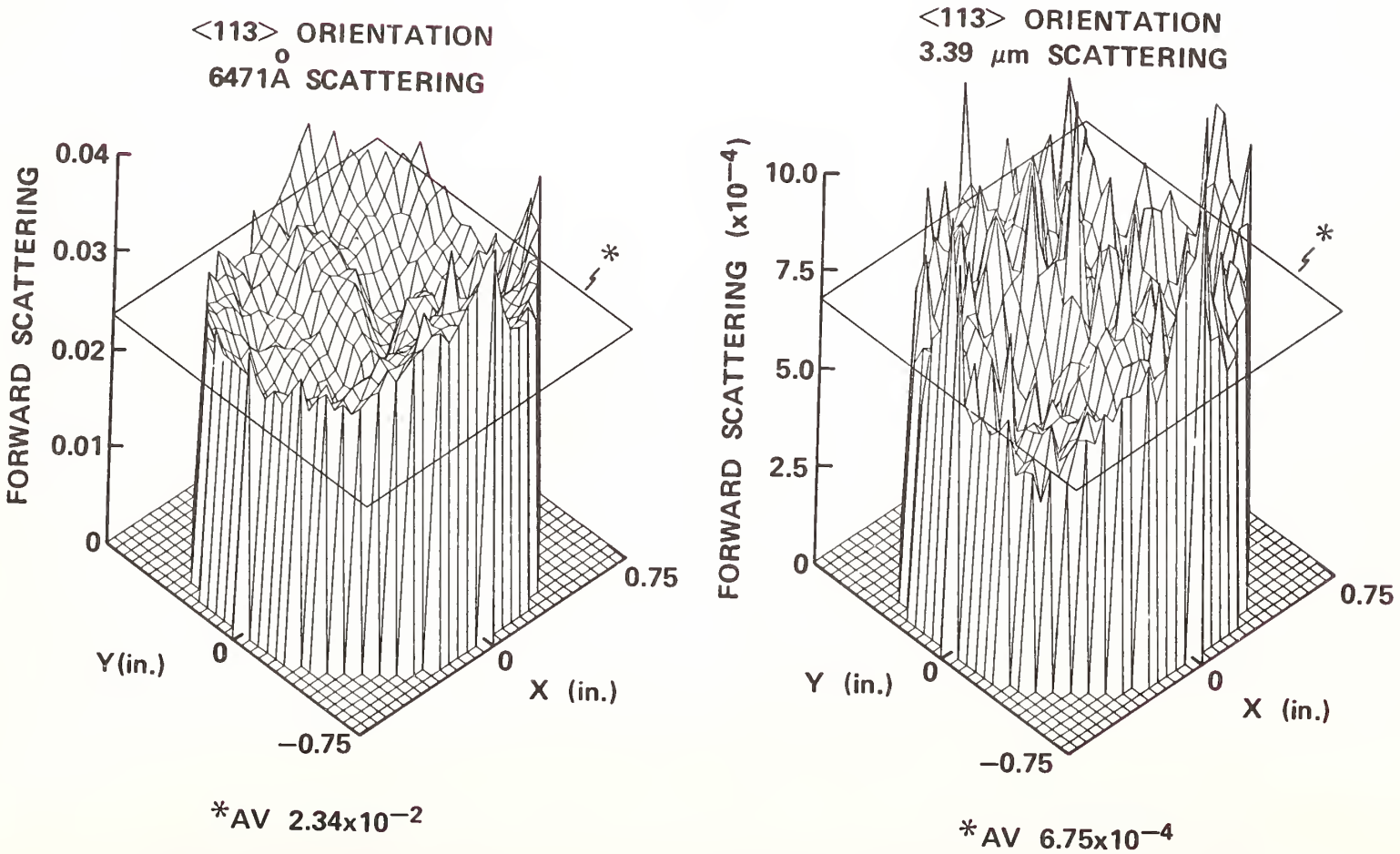

Figure 14. Three-dimensional plot of bulk forward scattering in ⟨113⟩ CaF_2 with veils.

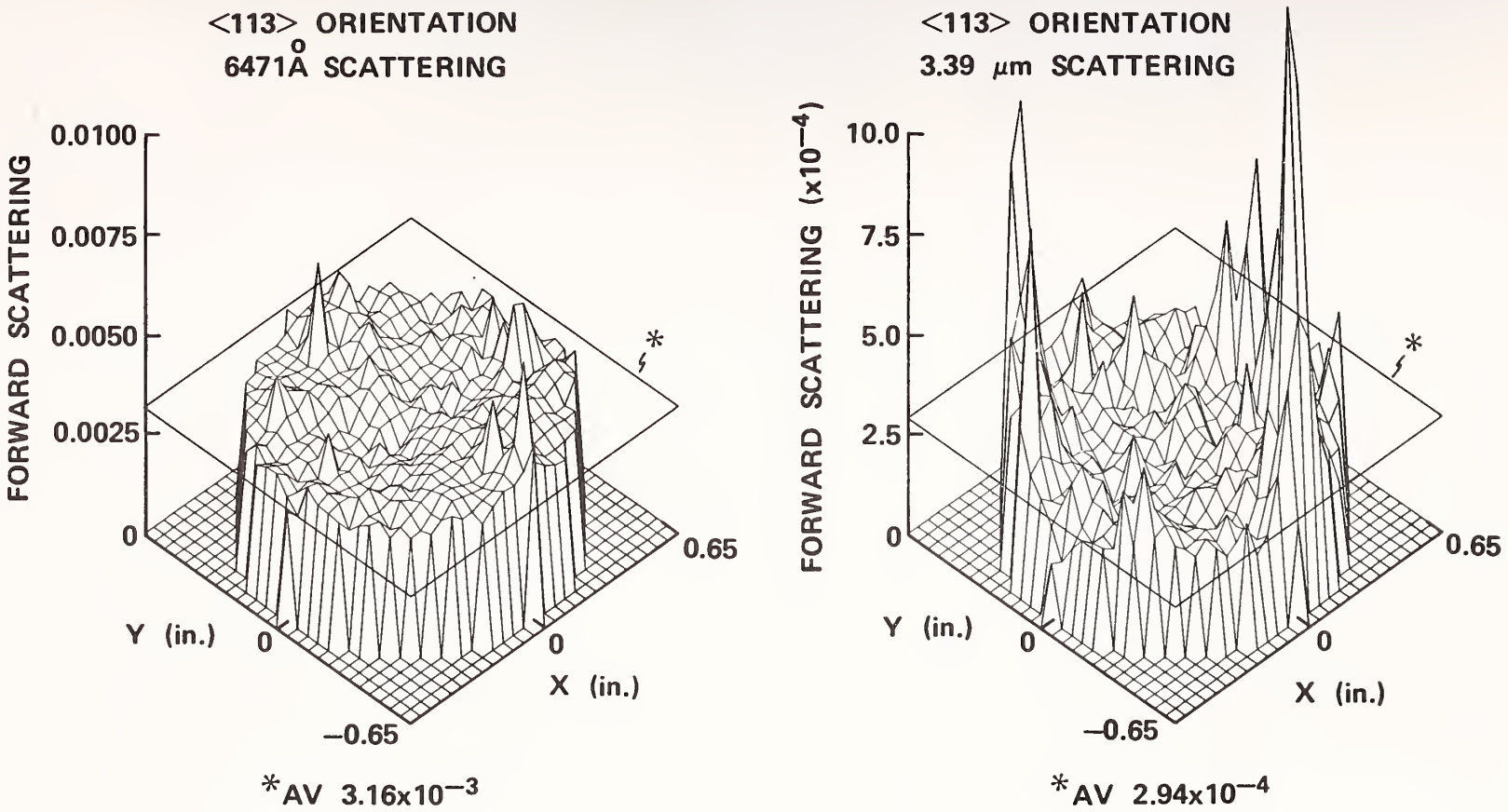

Figure 15. Three-dimensional plot of bulk forward scattering in ⟨113⟩ CaF_2 after HIP-processing.

MECHANICAL AND OPTICAL PROPERTIES OF FORGED NaCl*

George A. Graves, John A. Detrio,
Dale McCullum, and David A. Dempsey
University of Dayton Research Institute
Dayton, Ohio 45469

The mechanical and infrared laser absorption properties were determined on test specimens cut from a 32-cm diameter forging of Polytran Nacl produced by Harshaw. The homogeneity of the mechanical and optical properties statistically showed a significant dependence of the ultimate strength on azimuthal position in the forging. The absorption of the specimens at CO_2, CO, HF/DF, and Nd:YAG laser wavelengths were measured and no significant dependence on specimen location was observed. The absorption variations were less than 10 percent for all of the laser wavelengths studied except at 3.8 μm (40 percent). Other properties examined include specific heat, thermal expansion, and hardness. Strength measurements were made with both uniaxial flexural bars and biaxial disc test specimens.

Key words: Hardness; homogeneity; infrared laser absorption properties; mechanical properties; specific heat; thermal expansion

1. Introduction

Increasing interest in polycrystalline NaCl material for use as high energy laser windows provided the initiative for this investigation. Although a number of studies have been performed on the mechanical and optical properties of polycrystalline NaCl, no comprehensive investigation has been accomplished on a single forging that included information on both sets of properties. Therefore, a designed experiment was initiated that would provide sufficient information to determine the homogeneity of mechanical and optical properties within a single forging of NaCl material.

Specimens to conduct the investigation were obtained from a 32-cm diameter Polytran® NaCl hot forged disk, prepared by Harshaw Chemical Company, Solon, Ohio. Ten optical (O), two long optical (LO), 72 uniaxial flexural test (FT), and 20 biaxial flexural test (BF) specimens were cut from the forged disk in accordance with the sectioning diagram shown in Figure 1. The specimens were prepared by Harshaw. The specifications for specimens preparation are given in Table 1. The cutting diagram only shows the layout for the top of the forging, whereas the disk was actually sectioned into three slabs of material. In order to make the most economical use of the hot forged material the O specimens, due to their greater thickness, were all cut from the top layer and the BF disks were taken from the middle and bottom layers. The LO specimens' thickness was that of the original forging. The FT specimens were divided equally between the top, middle, and bottom layers (24 each).

2. Test Procedures

Specimen Handling

The specimens were received in sealed plastic bags containing dessicant. They were immediately inspected and placed in vacuum dessicators until just prior to testing.

---

* This work is supported by the Air Force Materials Laboratory, Wright-Patterson Air Force Base, Ohio 45433.

Table 1. Specifications for specimens from 32-cm diameter Polytran® NaCl.

1. "O" specimens: 10 each; diameter 38.1 ± 0.5 mm; thickness - 8.9 mm (+1.3, -0.00 inch) with size to be maximized as total material thickness permits; polish - "absorption coefficient sample" polish with flatness λ/10 at 10.6μm parallelism of less than 30 arc seconds, and scratch/dig better than 60/40.

2. "BF" specimens: 20 each; diameter - 38.1 ± 0.5 mm; thickness - 2.5 mm (+0.5, -0.0 mm); polish - same as "O" specimens.

3. "LO"specimens: 2 each; length - 102 ± 1 mm; width - 25.4 ± 1.3 mm: thickness - 25.4 mm (+0.0, -6.4 mm) with size to be maximized as total material thickness permits; polish, long surfaces - best defect-free surface possible so as to minimize mechanical damage site, parallelism of 0.1 mm or better, 0.8 mm approximate radius on all edges; polish, end faces - "absorption coefficient sample"; polish as "O" specimens above.

4. "FT" specimens: 72 each; length - 57.2 ± 1.3 mm. width - 10.2 ± 0.5 mm; thickness 5.1 ± 0.5 mm; polish - same as "LO" specimens, long surfaces.

Uniaxial Flexural Tests

Flexural strengths were obtained by testing prismatic beam specimens in four-point bending using kinematically designed fixtures. A universal testing machine was used to load the specimens at a rate of 8.3×10^{-6} m/s at 23°C. An LVDT deflectometer was used to obtain center-point specimen deflection as a function of applied load.

Biaxial Flexure

A concentric ring configuration was used to obtain biaxial flexural strengths. The outer load ring had a diameter of 32 mm and the inner load ring a diameter of 16 mm. The specimens were loaded at a rate of 8.3×10^{-6} m/s at 23°C.

Hardness

Room temperature hardness measurements were performed at 50 and 100 gm loads using a Knoop diamond indentor.

Coefficient of Thermal Expansion

A quartz tube dilatometer was employed for thermal expansion measurements over a temperature range of -65 to 200°C. The thermal expansion detected by an LVDT unit and recorded simultaneously with temperature on an X-Y recorder.

Specific Heat

A differential scanning calorimeter was used to determine specific heat. The reference sample was aluminum oxide.

Thermal Diffusivity

The thermal diffusivity was measured by a flash technique developed by Parker, et al.[1][1]. A Xenon flash lamp was used as the heat source. A 13 by 13 by 3 mm specimen, coated on one side with graphite powder, was used.

[1]Figures in brackets indicate the literature references at the end of this paper.

The temperature rise on the back surface of the specimen is sensed by an E-type thermocouple and the temperature rise recorded on an X-Y recorder.

Optical Measurements

The as-received surface finish was provided by Harshaw as specified.

The specimens were prepared for absorption measurements according to the following procedures:

1. A beaker was filled with 300 ml of concentrated HCl.

2. Two beakers were filled with 300 ml of 2-propanol. One beaker was placed directly beneath a heat gun.

3. The specimens were etched in the HCl solution for two minutes at approximately 22°C with gentle agitation.

4. The specimens were rinsed for twenty (20) seconds in the first 2-propanol rinse.

5. Rinse for five (5) seconds in the second 2-propanol rinse and removed slowly so that they dried as it is withdrawn.

6. The chemicals were changed after every three (3) specimens. The heat gun was on only during the final rinse cycle. Extended operation might raise the temperature of the chemicals and change the etching process.

The laser parameters used throughout the study were held as constant as practical for each laser used. The laser parameters were: power (nominal) - 10W, spot size - 4 mm, irradiation time - 250s, and cooling time - 1000s.

The effective absorption coefficient, β_e, was defined by:

$$\beta_e = \beta + 2a_s/\ell \qquad (1)$$

where β is the bulk absorption coefficient (cm^{-1}), a_s is the single surface absorption coefficient (fractional power absorbed), and ℓ is the specimen thickness (cm). The effective absorption was measured, for low loss materials, by the interpretation of the laser-induced heating and subsequent cooling of the irradiated specimen. The equation used was:

$$\beta_e = (mC_p/\ell) \cdot 2n/(n^2+1) \cdot (\Delta T/\Delta t)_{Net} \cdot (1/P_T) \qquad (2)$$

The parameters are defined in Table 2.

Table 2. Parameters used to obtain the absorption coefficient from calorimetric absorption data for NaCl specimens.

Parameter		Value	Mass
m specimen mass		---	g
C_p specific heat capacity		0.847	$J\ g^{-1}°C^{-1}$
ℓ thickness		0.89	cm
P_T laser power		~10	W
$(\Delta T/\Delta t)_{Net}$ net heating rate		---	$°C\ sec^{-1}$
n refraction index		1.490	10.6 μm
	CO_2	1.499	9.27 μm
	CO	1.518	5.3 μm
	HF/DF	1.522	3.8 μm
		1.525	2.7 μm
	Nd:YAG	1.510	1.3 μm

3. Discussion of Results

Mechanical Tests

The yield and ultimate strengths were determined for 70 uniaxial flexural test (FT) bars. Two of the specimens were too short to allow for proper testing. The average yield and average ultimate strength for the three layers are shown in Table 3.

Table 3. Mechanical strength results for Polytran® hot forged NaCl.

	Layer					
	Top		Middle		Bottom	
	MPa	(ksi)	MPa	(ksi)	MPa	(ksi)
Yield Strength	14.3	(2.1)	15.0	(2.2)	15.5	(2.3)
Standard Dev.	3.6	(0.5)	2.9	(0.4)	2.8	(0.4)
Ultimate Strength	23.3	(3.4)	23.8	(3.5)	22.9	(3.3)
Standard Dev.	6.0	(0.9)	5.5	(0.8)	5.3	(0.8)

Four groups of flexural test specimens were selected to permit statistical analysis of the ultimate and yield strength measurements for effects due to azimuthal position at 90°, 180°, 225°, and 315° (Figure 1), layer (top, middle, and bottom), and radial position (inside and outside).

An analysis of variance for this factorial experiment showed that the only factor which produced a significant effect at the 95 percent level of confidence was that of azimuthal position. The results were identical for both ultimate and yield strength. The average strength was significantly greater for specimens along the 90° and 180° positions than along the 225° and 315° positions. There was no significant difference between the 90° and 180° positions nor was there any difference between the 225° and 315° positions. No significant differences were found due to layers, radial position, or joint effects.

The results of the biaxial tests are shown in Table 4. The biaxial strength measurements were analyzed to test for differences between the middle and bottom layers. Since the biaxial were obtained from the two layers at identical locations, the measurements were treated as paired comparisons and the average differences between the strengths at each location were tested to determine if it was significantly different from zero. No significant differences were found at the 95 percent level of confidence for either the ultimate or yield strengths.

Optical Tests

For convenience the results are discussed in order of decreasing wavelength. The overall results are summarized in Figure 2 which shows the absorption at the laser wavelengths. Both the as-received and freshly etched data are illustrated; the error bars are the standard deviation of the measurements.

The objective of the optical evaluation portion of this study was to assess the absorption homogeneity of the NaCl forging. This assessment was made by measuring the calorimetric absorption at various laser wavelengths and at different locations on the forging. The variations in absorption within one specimen were measured by sampling the center and three points on a 0.95 cm diameter circle; the variation within the forging was measured by taking samples from various locations across the forging. The data are then analyzed to provide the homogeneity--defined as the standard deviation of the absorption measurements.

Table 4. Biaxial mechanical strength results for Polytran® hot forged NaCl.

Standard Deviation	Yield Strength MPa	(ksi)	Ultimate Strength MPa	(ksi)
Middle	18.1	(2.6)	28.0	(4.1)
Standard Deviation	1.55	(0.23)	2.2	(0.32)
Bottom	18.1	(2.6)	25.4	(3.7)
Standard Deviation	2.2	(0.32)	3.9	(0.57)

The influence of surface treatment on the measured absorption was studied by comparing the effect of results for specimens in the as-received condition, immediately after etching, and after etching and storage.

CO_2 Absorption:

The absorption was significantly higher at 10.6 μm than at 9.27 μm, and the etched specimens are significantly lower in absorption than the as-received specimens at both wavelengths. There appeared to be a significant "interaction" or correlation between the surface treatment and the absorption at 9.27 μm. The conclusion was that there is significant surface absorption at 9.27 μm. The 10.6 μm absorption was predominantly bulk absorption or the surface absorption was not influenced by etching in HCl.

The variation of absorption within a given specimen was within ±10 percent. The variations within the entire forging were also ±10 percent. A slight systematic difference was observed in the absorption measured at the center of a specimen and that measured on the 0.95 cm radius. This bias was a result of the experimental conditions and not variations in the specimen. One specimen showed an anomalously high absorption at both wavelengths. The cause of the increased absorption was not determined.

The CO laser absorption at 5.3 μm was approximately a tenth of that measured at CO_2 wavelengths. The measured values were approximately 0.003 to 0.004 cm^{-1} with a standard deviation of ±10 percent. The as-received specimens were only slightly higher in absorption than the etched specimens.

HF/DF Absorption:

The DF (3.8 μm) absorption was significantly lower than the HF (2.7 μm) values in all cases. The variations over the forging were not statistically significant. The 2.7 μm data gave a homogeneity of ±10 percent, but the 3.8 μm data were homogeneous to only ±40 percent.

Etching significantly improved the absorption of the specimens with a greater (nearly 50 percent) reduction observed at 3.8 μm. The 2.7 μm (HF) averages were not significantly reduced by the etching procedure. The implication was that either the bulk absorption was dominant at 2.7 μm or that the etching procedure was ineffectual at 2.7 μm. The dominant role of atmospheric water vapor contaminants in producing HF absorption was frequently cited as producing surface absorption. Therefore, the aqueous solutions used to etch the specimens may not remove the water.

I Absorption:

The absorption measured at 1.3 μm (iodine laser operation, 1.319 μm approximated by 1.315 μm Nd:YAG (laser) was between 0.0006 cm^{-1} and 0.0009 cm^{-1} and was not strongly dependent upon the surface treatment. Two specimens had a very high absorption that could not be readily explained. The homogeneity of the forging was between 8 and 14 percent (excluding the high absorbers).

Thermal Properties

Thermal Expansion:

The coefficient of thermal expansion was determined using specimens taken from several different areas of the forging. The average coefficient of thermal expansion obtained for the forging was 42.8 x $10^{-6}°C^{-1}$ (S.D. = 0.86 x 10^{-6}) over the temperature range of -65°C to 200°C.

Specific Heat:

Specific heat measurements were conducted on two specimens for the forging from 62°C (335°K) to 207°C (485°K). C_p values were calculated at 5°C temperature intervals resulting in an average specific heat value of 0.2 cal/gm/°C over the temperature range for both specimens.

Microstructure and Microhardness

The microstructure of the forged material was uniform throughout the forging. A typical microstructure is shown in Figure 3. The average grain size was 34 μm. The average Knoop hardness value obtained from four randomly selected specimens using a 50 gram load was 20.1 kg/mm^2.

4. Conclusions

With the exception of ultimate and yield flexural strength variations relative to azimuthal position the mechanical, optical, and thermal properties were uniform throughout the bulk of the Harshaw Polytran® NaCl hot forged material, within the limits of the experimental design.

5. Acknowledgements

The support of the Air Force Materials Laboratory, Wright-Patterson Air Force Base, Ohio is gratefully acknowledged. The contractual effort concerning the mechanical characterization of infrared window materials is monitored by Mr. Charles Strecker. The optical characterization of laser window materials has been monitored by Dr. G. Edward Kuhl and Dr. Walter Knecht.

6. References

[1] Parker, W. J., et al., "Flash Method of Determining Thermal Diffusivity, Heat Capacity, and Thermal Conductivity," J. Appl. Phys., 32(9), pp. 1679-1687 (1961).

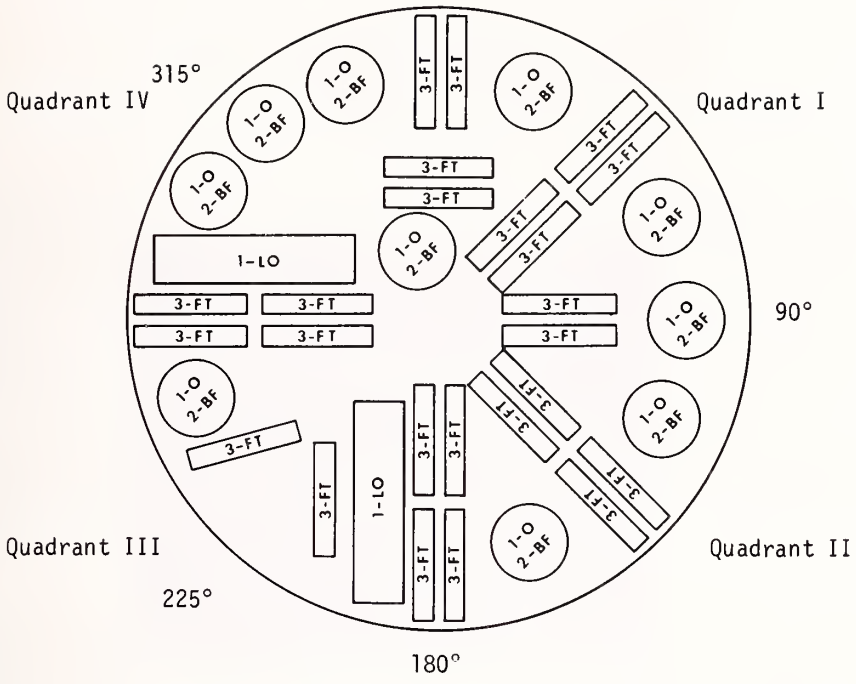

Figure 1. Polytran® hot forged NaCl specimen layout as delivered by Harshaw.

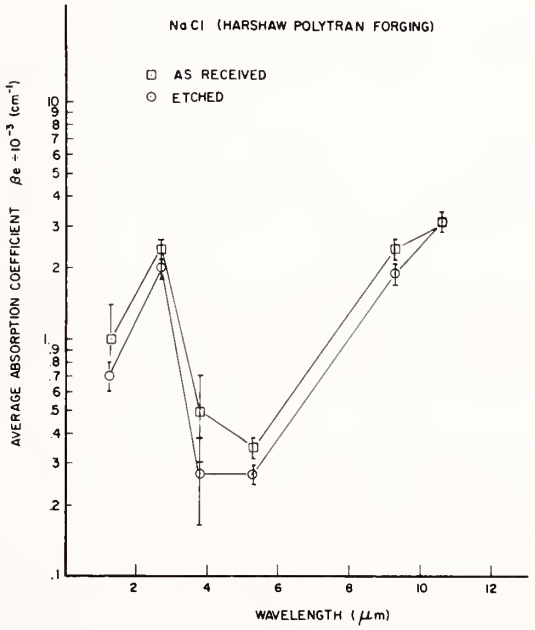

Figure 2. Absorption coefficients at various wavelengths for as-received and etched specimens taken from Polytran® NaCl forging.

MICROSTRUCTURE

HARSHAW HOT FORGED NaCl
(POLYTRAN ®)

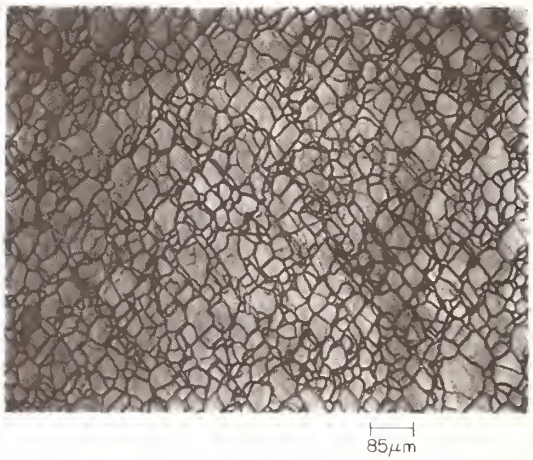

Figure 3. Typical microstructure of Polytran® NaCl forging.

OPTICAL, THERMAL, AND MECHANICAL MEASUREMENTS ON CO_2 LASER-IRRADIATED ZnSe

J.A. Detrio, J.A. Fox, and J.M. O'Hare
University of Dayton Research Institute
Dayton, Ohio 45469

The laser power dependence of the temperature distribution, optical distortion, and strain have been measured for specimens of ZnSe with absorption values between 0.006 and 0.020. For a well behaved Gaussian beam profile we observe a thermal lensing effect which changes the location of the beam waist but which does not significantly increase the minimum beam diameter. The predicted and measured temperature rise agree for laser powers of 230 and 705 watts and beam diameters of 2.1 mm and 4.2 mm, respectively. The identification of factors which influence the departure of predicted from measured response are discussed. The precision of the model is also examined.

Key words: Absorption; calculated performance; CO_2 laser; holographic interferometry; measured performance; optical path difference; temperature profile; thermal distortion; thermal lensing; ZnSe

1. Introduction

The goal of this work is to assess the accuracy of the prediction of the optical, thermal, and mechanical responses of ZnSe to CO_2 laser radiation. The accuracy of the model in predicting the performance will depend upon the accuracy of the input data and upon the adequacy of the theoretical model.

The validity of the prediction model is tested by comparing the measured response to the predicted response. The optical performance includes the thermally induced optical path differences, OPD, and the changes in the far field irradiance (focal plane spot size) produced by the thermally distorted window. The thermal response of the window includes the temperature distribution within the window and the time rate of rise of the edge temperature.

The scope of this work includes three different specimens of CVD ZnSe with different measured absorption and the use of two different CO_2 lasers. Thus the influence of variation in absorption and the influence of different laser power and beam diameters can be assessed. The study is limited to a single material and to the use of only one computational model.

In a previous paper [1][1] the effects of laser irradiation on ZnSe at a single power level (230 W) was assessed. The present study extends the measurements to higher power levels (705 W) and includes some refinements in techniques. Because reference 1 may not be readily accessible to the reader some of the relevant details will be repeated here for completeness.

---

[1]Figures in brackets indicate the literature references at the end of this paper.

2. Calculational Model

The primary response of a window to laser radiation is thermal; as energy is absorbed the temperature rises. The results of this temperature rise are thermally induced stresses and thermally induced distortion. The primary quantity of interest is therefore the distribution of temperature within the window as a function of time, T(r,z,t).

The temperature distribution is the solution to the heat conduction equation:

$$\rho C_p(\partial T/\partial t) = \kappa \nabla^2 T + Q(r,z,t).$$

The heat input Q(r,z,t) (W cm^{-3}) is assumed to be proportional to the laser beam intensity profile, I(r,t) (W cm^{-2}) and the absorption, $\beta_e(cm^{-1})$.

The absorption can be distributed between the surface, a_s (fractional absorption) or the linear absorption coefficient, $\beta(cm^{-1})$. This model assumes a homogeneous absorber and neglects scattering. The boundary conditions that apply include heat loss from the surfaces

$$F(r,t) = \kappa(\partial T_s/\partial p) + hT_s = a_s I(r,t)$$

where $(\partial T_s/\partial p)$ are directional derivatives normal to the surface, h is the heat transfer coefficient for the surface at temperature T_s. The surface absorption is explicitly included in these boundary conditions.

The total energy absorbed by the specimen is given by:

$$E_a = (\beta \ell + 2a_s)\, P_o t_p = \beta_e P t_p$$

where t_p is the irradiation time and P_o is the total laser power obtained by integrating the incident intensity distribution.

The solution of the time dependent heat equation for a Gaussian beam profile and the given boundary conditions is obtained by the use of a computer program "THERM" written by Dr. John Loomis [2] and modified by Dr. J.M. O'Hare [3]. The program is described in UDR-TR-78-76 dated August 1978.

The computations yield the following output:

$T_e(t)$	Edge temperature as a function of time
T(r,t)	Average temperature as a function of radial position versus time
$\sigma_r(r,t)$	Radial stress versus position and time
$\sigma_t(r,t)$	Tangential stress versus position and time
$\Phi(r,t)$	OPD versus position and time
I(r,z)	Intensity distribution at axial location z

The materials parameters used in these calculations are summarized in table 1.

Table 1. Properties of CVD ZnSe employed in calculations

Mechanical		
Poisson's Ratio	ν	0.28
Young's Modulus (psi)	E	9.75×10^{6}
Thermal		
Heat capacity (j/gK)	C_p	0.355
Thermal conductivity (W/cmK)	κ	0.17
Thermal expansion (K^{-1})	α	7.8×10^{-6}
Physical		
Density (g cm^{-3})	ρ	5.27
Optical		
Refractive Index	n	2.41
Thermooptic Coefficient (K^{-1})	dn/dT	6.17×10^{-5}
Elasto-optic	p_{11}	-0.08
Coefficients	p_{12}	0.02

3. Experimental Details

Three specimens of Raytheon's Chemical Vapor Deposited (CVD) ZnSe with different absorption values were selected for study. The specimens were polished by PTR Optics of Waltham, MA. The specimens are 38 mm in diameter, approximately 4 mm thick with a 1 degree wedge angle. The surfaces are flat to $\lambda/10$ at 6328Å with a 50/20 scratch/dig specification.

These specimens were selected because they had absorption values that were significantly different but with the same visual appearance. The absorption values have been measured at various times during the course of this work. The absorption data are summarized in table 2.

Two CO_2 lasers were used in these studies: A Coherent Radiation Model 41 with 4.2 mm Gaussian beam at 230 W and a Sylvania Model 971 with 9.6 mm Gaussian beam at 705 W. The nominal power levels used were selected to give the most stable laser output and to give a 3:1 power ratio.

The experimental layout is shown in figure 1. This is the same basic arrangement used in Ref. 1. The laser power is measured with a CRL Model 213, or Model 201 power meter with the output recorded on one channel of a strip chart recorder. A typical strip chart trace is shown in figure 2.

The edge temperature is monitored with a copper-constantan thermocouple and recorded on one channel of the four-channel chart recorder. For the 705 W studies an aluminum heat sink is placed between the specimen and the thermocouple to minimize the effect of scattered radiation. If this thermal mass is not used, the scattering is absorbed by the thermocouple and produces a larger temperature rise in the specimen at the point of contact. The Aℓ block reduces the transient heating effect by distributing the scattering over a larger thermal mass.

Table 2. Absorption coefficients, β_e for CVD ZnSe at different laser powers, times, and with different strain gauge attachment conditions

Sample No.	Average laser power (watts)							
	10-20			230		705		
1105	3.3	6.5	7.2	5.43	8.5	4.0	3.7	2.8
1246	10.3	10.4	14.0	11.7	18.0	12.1	13.1	11.4
1244	18.7	19.6	25.3	23.5	28.0	24.0	25.2	19.4
Date	5/77	5/78	7/79	10/78	5/78[a]	3/79	5/79	7/79
No. of Gauges	0	1	2	1	1	2	2	2

[a]Incident power only was measured. For this situation

$$\beta_e = (mC_p/\ell)\,(\Delta T/\Delta t)_{Net}/P_i$$

where P_i is the incident laser power.

A holographic interferometer is used to measure optical path differences. The interferograms are obtained by photographing the specimen image, as viewed through the reference hologram. The 35 mm photographs are made at selected times during irradiation while the entire interaction is recorded on video tape. Each 35 mm frame is photographically enlarged and printed, then the fringe positions are plotted with the aid of a Tektronics graphics tablet.

The $\Phi(r,t)$ function of position is obtained at HeNe wavelengths. This function is interpreted to give the corresponding temperature distribution $T(r,t)$. The interferograms are analyzed to measure the rms deviation of the wavefront from a plane or a spherical reference surface, the Strehl ratio, and the effective focal length of the best fit quadratic surface.

The beam diameter is measured by a moving knife edge technique. The method is based on the fact that the integral of a Gaussian intensity distribution leads to an error function of the form

$$1 - 2T = \mathrm{erf}(\sqrt{2}\, y_o/\rho),$$

where T is the fraction of the total beam power passing the knife edge, y_o is the position of the knife edge and ρ is the beam radius. The transmittance is measured every ten microinches and we use a graphical solution which transforms this function to a straight line when T is plotted against y_o (if the beam is Gaussian). The beam diameter is the distance 1/e points in the distribution (13.5% and 86.5%).

A procedural change over the work of reference 1 has provided more accurate information on the presence of thermal lensing. In the earlier work the beam diameter was only measured at the primary focus; now we measure the diameter as a function of position along the mirror axis. This procedure allows us to separate defocusing effects from distortion.

The earlier work used two Micromeasurements (M≡M) Type EA-06-062AQ-350 gauges installed on opposite sides of each specimen; one gauge oriented to measure the radial strain component, the other to measure the tangential strain. An improved T-rosette gauge from M≡M; Type EP-08-062TH-120 was installed for the high power measurements. These latter gauges represent a better match to the ZnSe materials expansion coefficient.

Two strain amplifiers were used—a custom-made differential amplifier described in reference 1 and a Vishay Model P 350 from M≡M. The gauges were connected in a bridge circuit using the radial gauge as one input and the tangential gauge as the reference. This configuration provides the algebraic difference of the signals (sum) while subtracting the thermal effects. This latter point is essential because of the heating effect of scattered radiation. The measured strain ε is related to the stress according to:

$$\varepsilon_r - \varepsilon_t = [(1+\nu)/E](\sigma_r - \sigma_t).$$

The calibration of the gauges and amplifiers were verified using a beam with known loads.

4. Data and Results

The response data will be discussed in three categories: thermal, optical, and mechanical. The specimen characterization data will be presented first. The customary equation for obtaining the effective absorption from the thermal rise data is:

$$\beta_e = (mC_p/\ell)\ (\Delta T/\Delta t)_{Net} \left(\frac{2n}{n^2+1}\right) \Big/ P_T\ ,$$

which relates the absorbed power to the materials parameters and the power circulating within the specimen. P_T is the transmitted power and the factor $2n/(n^2+1)$ relates the transmitted power to the power within the sample.

The temperature measurements consist of edge temperature versus time and the temperature profile derived from the holographic interferometry. The validity of edge temperature measurements made with the Aℓ heat sink was verified by comparing measurements made with and without the heat sink. The measured values of temperature rise differed by less than 4%.

The thermal rise data for the three specimens when irradiated by each laser are shown in figure 3. The calculated thermal rise curves are also shown for comparison.

The thermal profile data are shown in figure 4. The temperature difference is related to the fringe distortion, according to prior interferometric measurements [4], as 1.713°C per fringe at 6328Å. The refractive index of ZnSe at the HeNe wavelength is 2.59. The calculated temperature distribution and the 230 W laser beam profile are also shown in figure 4.

The optical response data are derived from the holographic interferograms and from the beam diameter measurements. The holograms are reproduced in figure 5. Since the OPD versus position is correlated with the thermal profile of figure 4 a separate presentation is unnecessary. The spot size data are of special interest. In figure 6 the beam diameter measurements are shown as a function of position for the high power measurements.

The measured strain is shown in figure 2 for a typical data trace on the 4-channel recorder. The strain data represent the practical state-of-the-art for resistance strain gauge techniques. This problem is compounded by the thermal contributions. The data are summarized in table 3 which includes selected data for both kinds of strain gauges. The calculated values are also given in the table. The results are independent of the gauges or amplifiers used. The new gauges provided a smaller standard deviation in the measurements. The uncertainty in these measurements is between 30% and 100%.

Table 3. Comparison of measured and calculated microstrain for ZnSe discs irradiated with a CO_2 laser of 230 W and 705 W power for one minute

Specimen No.	Absorption $\beta_e(cm^{-1})$	120Ω Gauge 705 W		350Ω Gauge 705 W		230 W	
		Meas.	Calc.	Meas.	Calc.	Meas.[a]	Calc.
1105	0.0065	5.6	7.4	6.3	6.7	2.5	2.3
1246	0.0104	11.6	11.8	9.9	10.7	3.2	3.7
1244	0.0191	29.6	22.4	40.8	19.6	4.5	6.8

[a]Reference [1]

5. Discussion and Correlations

Two kinds of comparisons can be made: one to assess the consistency of the input data (materials parameters), and the second to assess the validity of the predicted response. Graphical presentations of these comparisons are especially helpful and are used repeatedly; the measured response is plotted as a function of the measured absorption or the laser power to ascertain the consistency of the input data, or the measured reponse is plotted against the calculated response to test the accuracy of the predicted response.

5.1. Optical

In figure 7 the fitted spot size data from figure 6 are superimposed at the axial position corresponding to the minimum beam waist to show that the spot size is not significantly altered by the thermal lensing. The distance to the minimum spot size (effective focal length) is plotted as a function of the effective absorption in figure 8. The fit to a quadratic dependence of this function is shown.

The diffraction limited spot size for a Gaussian beam is given by

$$d = \frac{4}{\pi} \frac{\lambda f}{D} \quad .$$

In these experiments the focal length f is approximately 524 mm, the wavelength, λ, is 10.6 μm and the beam diameter D is 4.2 mm and 9.6 mm for the 230 W and 705 W laser, respectively. The corresponding minimum spot sizes are 1.6 mm and 0.71 mm. The performance calculation assumes diffraction limited optics; however, the measured spot sizes with no specimen in place are approximately twice the diffraction limit. For this reason we compare the measured change in spot size to differences between the calculated spot size and the diffraction limited spot size. The data for measured spot size versus absorption are shown in figure 9.

The calculation of the focal plane response assumes that the window is located at or near the focusing element. In the experimental configuration the window is approximately 220 mm from the mirror.

5.2. Thermal

The calculated and measured edge temperatures observed after one minute of irradiation are plotted as a function of the measured absorption in figure 10. Both the 230 W and 705 W data are shown. The calculated values which are based on the low power measurements of absorption are well behaved; a linear fit to these quantities intercepts the origin and correlates well with the measured absorption. The high power data are consistently overestimated while the low power data are generally underestimated by the calculation. The low absorption specimen showed the greatest variability.

The peak center-to-edge OPD is shown as a function of absorption for two sets of measurements made at 230 W in figure 11. The earlier data show excellent correlation, but some discrepancies in the later date indicate the spread in such measurements.

The history of the specimen absorption values is found in table 2. The influence of strain gauge mounting is evident by the increased absorption. The mechanism which explains the increased absorption is the absorption of scattering by the strain gauge which then heats the specimen. This internally scattered radiation would normally escape from the specimen if the gauges were not attached.

5.3. Mechanical

The strain measurements are clearly the most difficult and uncertain of the response characterizations made. The difficulties are related to the very small signals available and to the effect of temperature changes produced by the heating of the specimen and the absorption of scattering by the gauge. Other sources of error are damage to the gauges and leads, the effect of humidity and aging on the gauge response, and differences in the quality of the bond between the gauge and the specimen.

The measured and calculated strains are compared in figure 12 which uses selected data. The uncertainty in these measurements is between 30% and 100%. The data were selected for cause; in most cases a contact was damaged which rendered the data unusable; in some cases the data for one specimen were suspect without any identifiable cause.

5.4. Validity

The overall validity of the model is assessed by its ability to predict the edge temperature. The results are shown in figure 13. Only one data point deviates significantly from the ideal correlation; that for the lowest absorbing specimen (number 1105). The difficulty probably lies with the measured absorption which fluctuates with the number of strain gauges attached and with the condition of the surface. This difficulty is expected since good absorption measurements are required and they are difficult to make for low absorption specimens.

The comparison of spot size measurements to the predictions of the model is shown in figure 14. The two slopes correspond to the two different beam diameters at the different power levels. The correlation is linear but not ideal. It appears that the model is sensitive to the laser beam diameter or mode structure with the small diameter results being underestimated by the theory, while the high power data are overestimated.

6. Summary

The response of ZnSe to an axisymmetric CO_2 laser beam is adequately predicted by the analytical mathematical model used for these studies. The model is valid for laser powers up to 700 W. The agreement between the predicted and measured response depends upon the materials or laser parameters involved and upon the techniques used to measure the response. The results are summarized in table 4.

In general the response correlates well with the effective absorption. The thermal response provides the best agreement. The optical characterizations are well correlated, but the quantitative agreement suffers from an inability to match the experimental conditions to the theory. The agreement between predicted and measured strain is the least precise of the response characterizations. Further strain measurements are being made to refine these data.

Table 4. Summary of the comparison of the response of CO_2 laser irradiated ZnSe to the performance predicted by the thermal model

Response	Correlation with absorption	Agreement with prediction (approx. %)
Thermal		
$T_e(t)$	Excellent	±15%
$T(r,t)$	Good	-20%
Optical		
$\Phi(r,t)$	Good	-20%
$I(r,z)$	Excellent	Not matched to theory.
Mechanical		
$\sigma_r(r_o,t)$-$\sigma_t(r_o,t)$	Good	±30%-100%

7. Acknowledgments

This work is supported by the Air Force Materials Laboratory, Wright-Patterson Air Force Base, Ohio 45433. The authors are pleased to acknowledge the assistance of their colleagues at the University of Dayton. The fringe data were analyzed with the aid of a computer program written by Mr. Richard Harris. The graphical method for measuring the beam diameter was provided by Mr. D.D. Preonas. The strain gauges were installed by Mr. Dale Grant.

8. References

[1] Detrio, J.A., Petty, R.D., O'Hare, J.M., and Fox, J.A., published in *Proceedings of the High Power Laser Optical Components Meeting*, 14-15 Sept 1978, Part 1, June 1979. Compiled by James L. Stanford, NWC TP 6111 Part 1, pp. 148-157.

[2] Loomis, John S., "Computer Program for Calculating Thermal, Mechanical, and Optical Properties of Discs Heated by Laser Radiation," July 1977.

[3] O'Hare, J. M., UDR-TR-78-76, 21 August 1978.

[4] Harris, R.J., Johnston, G.T., Kepple, G.A., Krok, P.C. and Mukai, H., Appl. Optics, V. 16, #2, 1977.

9. Figures

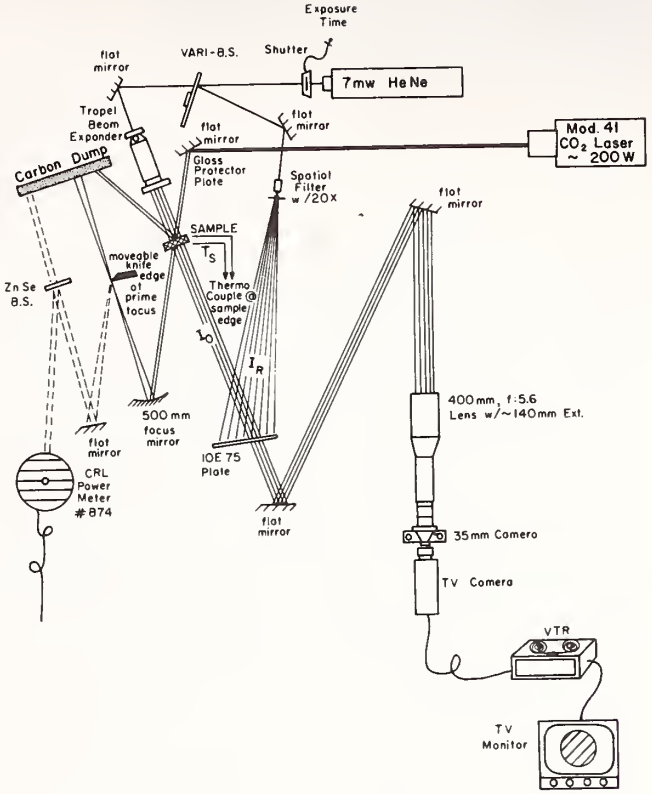

Figure 1. Experimental arrangement for the measurement of edge temperature, and strain versus time; holographic interferometry, focal spot size measurements, and laser power monitoring. The apparatus is shown as configured for the 230 W experiments. A similar arrangement is used at 705 W, but the positioning of some components must be altered.

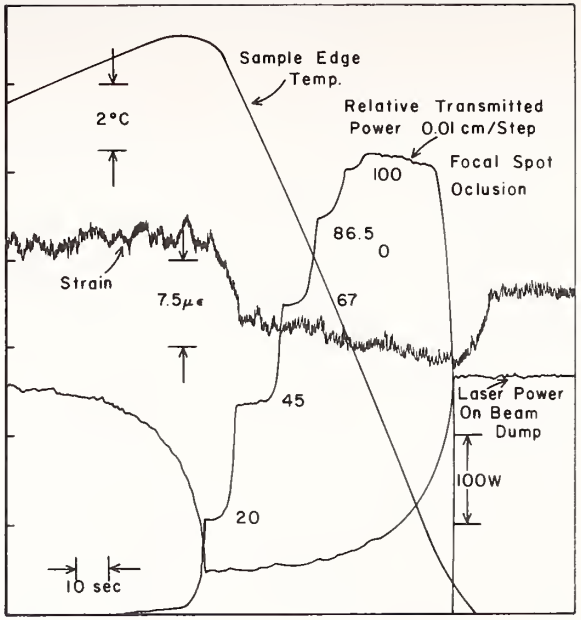

Figure 2. An example of the 4-channel recorder trace when the complete set of data are recorded simultaneously.

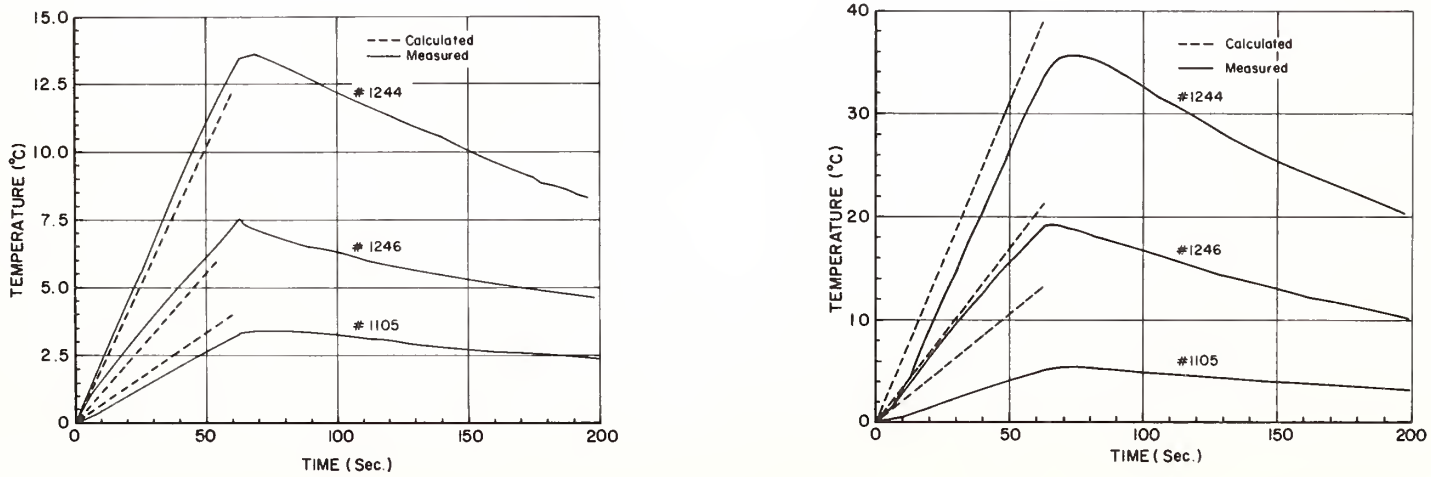

Figure 3. Comparison of the thermal response predictions and measurements for 230 W (a) and 705 W (b).

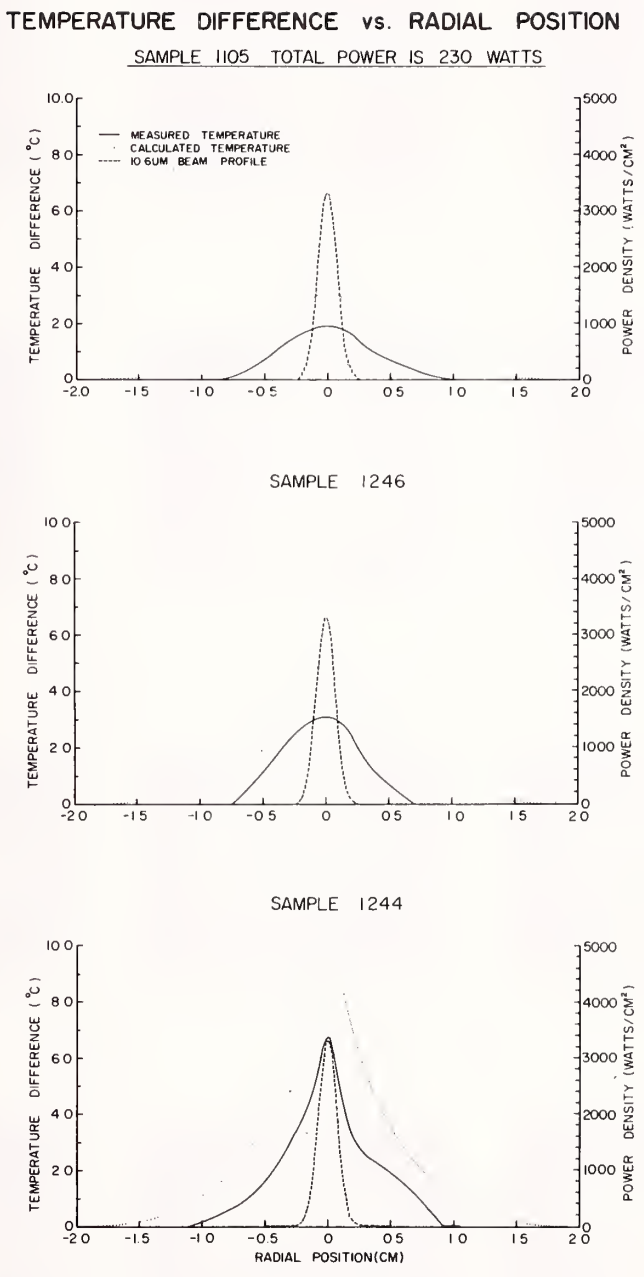

Figure 4. Thermal profile measurements and predictions are compared for the three ZnSe specimens at 230 W. The laser beam profile is also shown. Some of the differences between the measured and calculated temperature profiles are due to the choice of the reference background fringe pattern. Some of the differences are due to artifacts in the fitting process when there is an unequal number of fringes on each side of the maximum distortion.

HOLOGRAPHIC INTERFEROMETRY SUMMARY

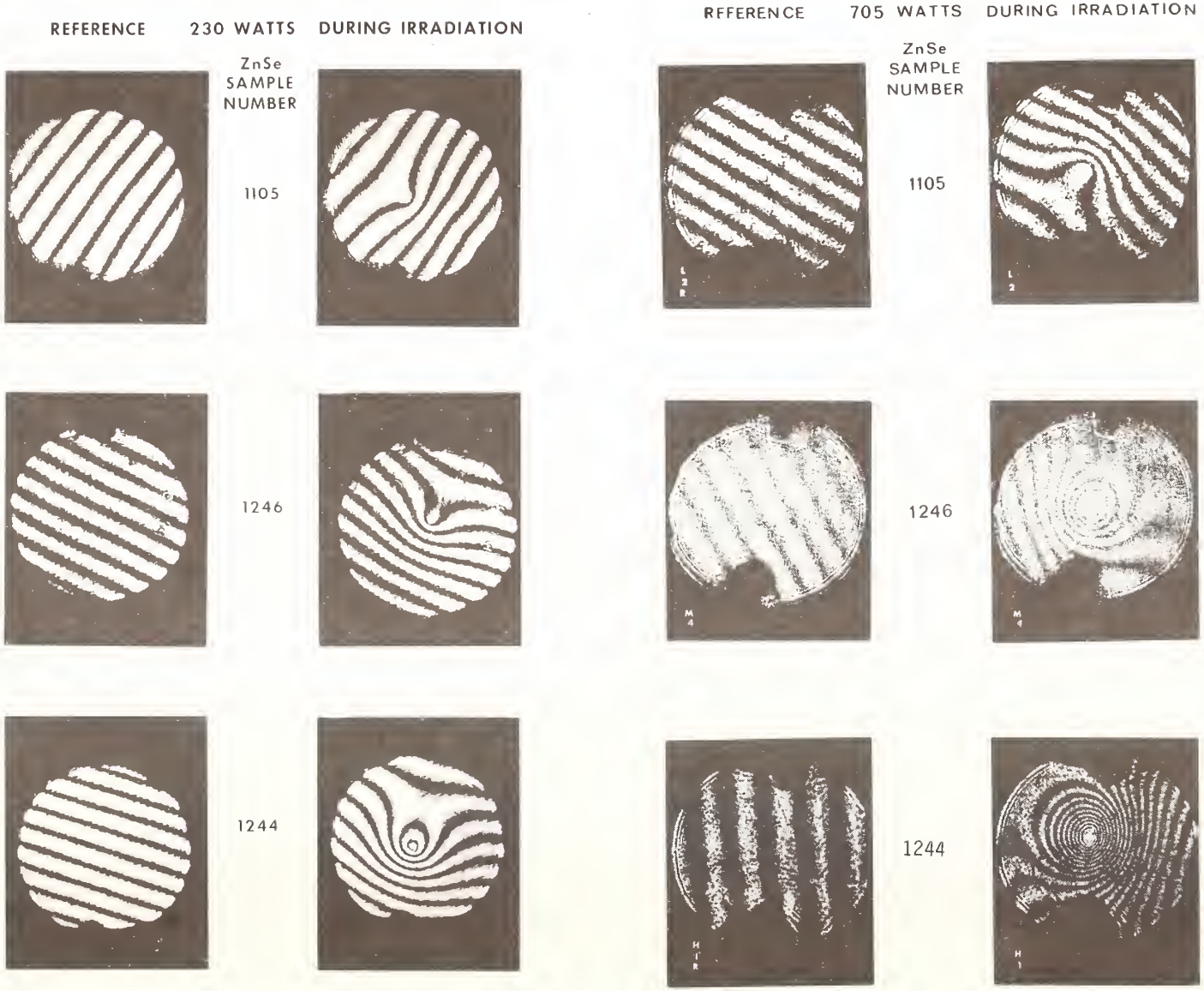

Figure 5. Examples of the holographic interferograms made at 230 W and 705 W. The presence of vibration near the 1 kW laser has degraded the high power interferograms.

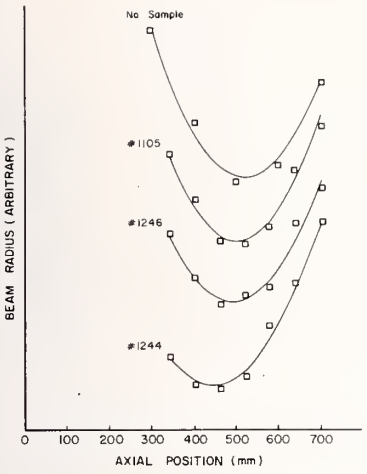

Figure 6. The moving knife edge measurements of the beam diameter near the focus for the case of the three ZnSe specimens and the case with no window in place are shown for the region near the focus.

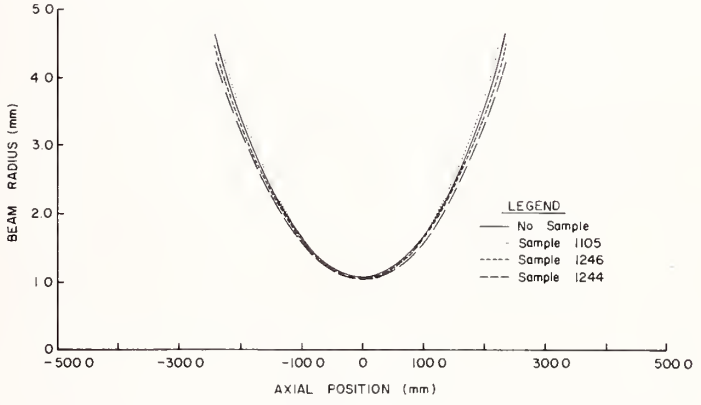

Figure 7. The beam diameter versus axial position near the focus for the four cases plotted in Figure 6 are superimposed with the fitted curves adjusted along the z-axis to align all of the minimum. The significance of this presentation is that the minimum spot size is unchanged by the windows; however, the focal position changes.

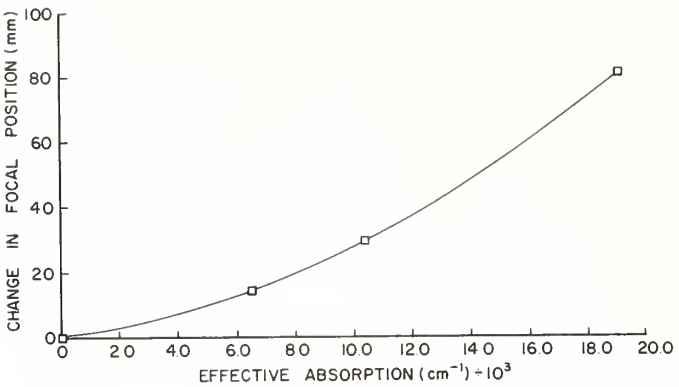

Figure 8. The distance from the focusing mirror to the position of the minimum spot size is plotted as a function of the specimen absorption. The continuous curve is a quadratic fit to the experimental data. The fit is excellent and the quadratic dependence is expected.

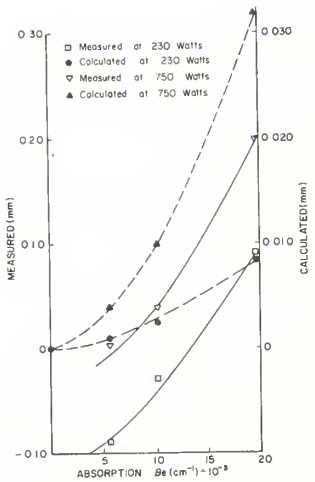

Figure 9. The change in the measured and predicted spot size for the three specimens is plotted as a function of absorption. This presentation illustrates the difficulty of predicting the minimum spot diameter for the non-ideal optical system used in the experiment.

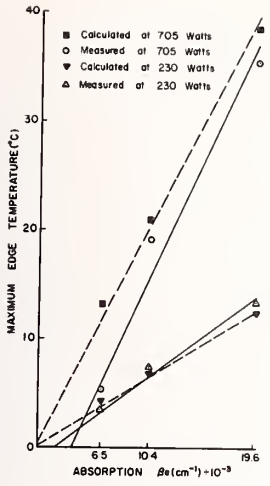

Figure 10. Comparison of the measured and calculated edge temperature plotted as a function of absorption. Both 230 W and 705 W data are shown.

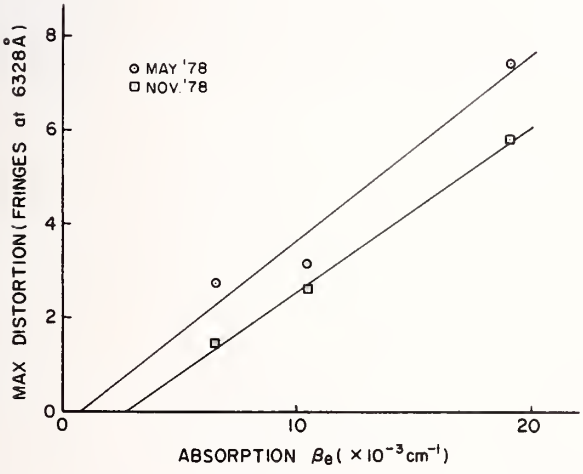

Figure 11. The peak optical path differences for several measurements at 230 W are summarized. The primary purpose of showing these data is to illustrate the experimental error that can occur. Part of the variability is due to the factor discussed in the caption to Figure 4.

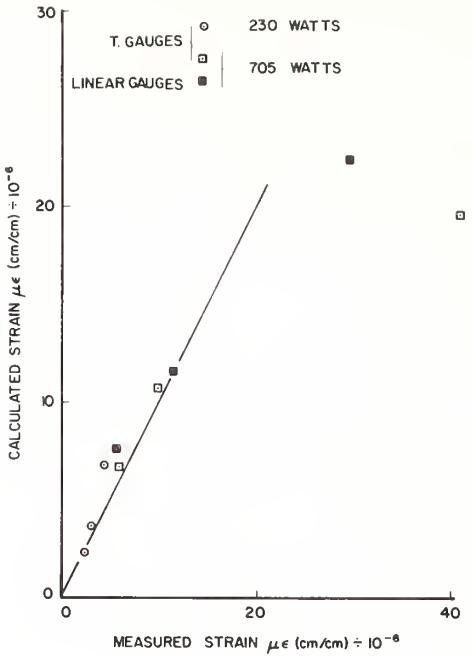

Figure 12. A comparison of the measured and calculated strain for selected strain data at 230 W and 705 W. The data shown were selected because no obvious cause for rejecting the values could be identified such as a damaged lead or amplifier malfunction. The accuracy of the measurement was therefore difficult to assess; based on all of our data the uncertainty is between 30% and 100%.

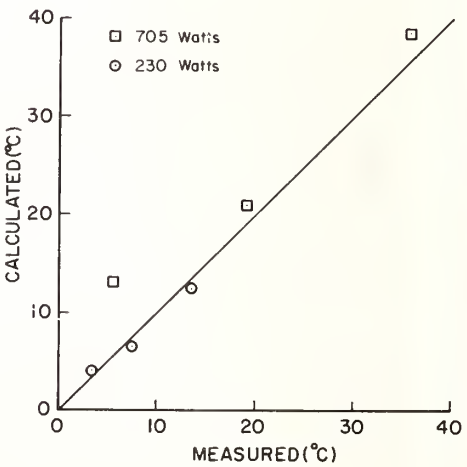

Figure 13. A comparison of the measured and calculated peak edge temperature rise for both 230 W and 705 W experiments is shown. These data summarize the most successful application of the model. Only the lowest absorption specimen deviated from the predicted value and most of this deviation can be attributed to the increased absorption due to the strain gauges.

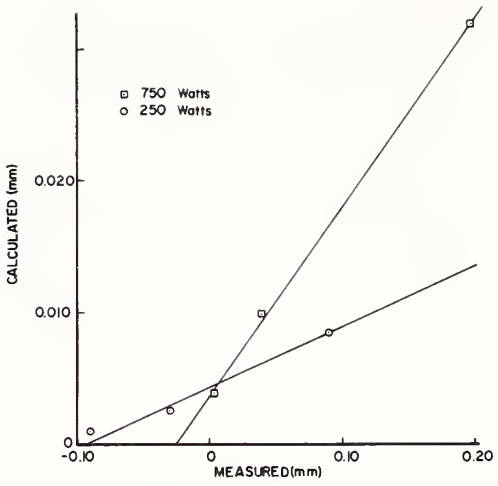

Figure 14. A comparison of the measured and calculated change in spot size. The data do not lie on a single line because of the difference in the beam diameter and the lasers used at 230 W and 705 W.

ELECTRONIC, NUCLEAR AND TOTAL NONLINEAR INDICES OF LIQUIDS

David C. Brown, J. M. Rinefierd, S. D. Jacobs, and J. A. Abate
Laboratory for Laser Energetics
University of Rochester
Rochester, New York 14627

We have extended the work previously reported to this conference on the nonlinear indices of a wide variety of liquids. Based upon measurement of linear indices and calculation of the Abbé value, we obtained the electronic contribution to the total nonlinear index. Using measurements tabulated recently by Hellwarth we are then able to calculate the nuclear and total nonlinear indices.

Agreement between the total nonlinear index and measurements reported in the literature will be discussed as will the correlation with Abbé value and linear index.

Key words: Abbe value; coolant; index-matching liquids; nonlinear refractive index; self-focusing.

1. Introduction

It is well known that the principle mechanism limiting the achievable peak power from Nd: Glass lasers is small scale self focusing, arising from the existence of a cubic nonlinear index, a subject which has been thoroughly addressed in the literature [1,2].[1] A major development in understanding such effects was the work of Boling, Glass and Owyoung, [3], which for the first time allowed one to calculate the electronic part of the nonlinear index n_2^e for a wide variety of transparent solids using only the linear index at the location of the Na "d" lines n_d and the Abbé value ν_d, both easily measurable quantities. With few exceptions the agreement between calculated values and experimental measurements has been excellent; the reader is encouraged to see the recent excellent article by Weber, Milam, and Smith [4]. An assessment of the nuclear contribution n_2^n to the total nonlinear index n_2^T in fluoroberyllate glasses has been made recently by Weber, Cline, Smith, Milam, Heiman, and Hellwarth [5].

It has been realized for some time by a number of workers that the same formalism used to calculate n_2^e for solids should be equally applicable to liquids. Preliminary measurements and calculations of n_2^e were presented at the 1978 Conference on Laser Induced Damage in Optical Materials [6]. Interest in the use of such liquids for applications in high peak power Nd: Glass laser systems has heightened in recent years. For example, there is interest in using a liquid to cool the front face of an active-mirror amplifier, in index matching and cooling various zero axial-gradient high-repetition-rate amplifiers, and in index matching for large aperture Pockels cell devices.

We present below measurements and calculations of n_2^e for a number of liquids. It will be seen that by combining that information with a recent tabulation of nuclear parameters by Hellwarth [7], it is possible to find the nuclear n_2^n and, thus, the total nonlinear index n_2^T as well. We will discuss the dependence of the total nonlinear index on various optical parameters as well as implications for high peak power system design.

2. Theoretical Background

One can show that the total nonlinear index n_2^T is related to the third order susceptibility $\chi^{(3)}_{1111}$ through [3]

[1] Figures in brackets indicate the literature references at the end of this paper.

$$n_2^T = \frac{12\pi}{n_d} \mathrm{Re}[\chi^{(3)}_{1111}(-\omega,\omega,\omega,-\omega)] \tag{1}$$

where ω is the laser angular frequency, n_d the linear index, and Re denotes the real part. The total index may be written as

$$n = n_d + n_2\langle E\rangle^2 = n_d + \gamma I \tag{2}$$

where E is the electric field, $\langle\ \rangle$ denotes the time average, γ the nonlinear coefficient, and I the intensity. $\langle E\rangle^2$ is related to I in electrostatic units through

$$I = \frac{n_d}{4\pi c}\langle E\rangle^2 \tag{3}$$

where c is the speed of light. Since the value of n_2 is usually quoted in electrostatic units (esu), γ is given by

$$\gamma = \frac{(4.19 \times 10^{-3})n_2}{n_d} \tag{4}$$

Two major effects account for the third order nonlinearity in solids and liquids, namely the electronic part n_2^e due to nonlinear distortion of the electron clouds around the nucleus, and the nuclear part n_2^n which is due to the nuclei as they attempt to minimize the total matter-field interaction. Both mechanisms are extremely fast ($<10^{-12}$sec.) and therefore operative for picosecond duration pulses. Then we write the total nonlinear index n_2^T as

$$n_2^T = n_2^e + n_2^n \tag{5}$$

We consider here only the nonlinear index for linear polarization. It has been shown that the nonlinear index for circularly polarized light is less than that for linear polarization [7], and in glass is lower by a factor of 1.44 [8].

To calculate n_2^e for a solid or liquid one may use the theory developed in Reference [3] to show that n_2^e is given by

$$n_2^e = \frac{K(n_d - 1)(n_d^2 + 2)^2}{\nu_d\{1.517 + [(n_d^2 + 2)(n_d + 1)\nu_d/6n_d]\}^{1/2}} \tag{6}$$

where n_d and ν_d are the values of the linear index and Abbé values at the location of the Na "d" lines, and K a normalization constant determined by fitting to experimental data. Although eq. (6) is limited since it ignores the dispersion or frequency dependence of n_2^e, it has nevertheless been extremely useful in finding n_2^e for solids at 1.06μ based only upon measurements of n_d and ν_d. The Abbé value, a measure of the reciprocal dispersion is formally given by

$$\nu_d = \frac{n_d - 1}{n_F - n_C} \tag{7}$$

where n_d, n_F and n_C are the linear indices measured respectively at the corresponding wavelengths λ_d = 5876Å, λ_F = 4861Å, and λ_C = 6563Å. A low value of n_2^e can thus be obtained by using a material with a low n_d and large ν_d.

For linear polarization, Hellwarth [7] has shown that it is possible to write n_2^T as

$$n_2^T = \frac{2\pi}{n_d}\left(\frac{3}{4}\sigma + A_o + B_o\right) \tag{8}$$

where σ, A_o, and B_o are Born-Oppenheimer coefficients which describe the electronic (σ) and nuclear (A_o,B_o) contributions. Then from eq. (5) we see that

$$n_2^e = \frac{3\pi\sigma}{2n_d} \tag{9}$$

and

$$n_2^n = \frac{2\pi}{n_d}(A_o + B_o) \tag{10}$$

Formal expressions for A_o and B_o, available from Raman scattering data, may be found in the article by Hellwarth [7].

It is also useful to separate the total third-order susceptability $\chi^{T(3)}_{1111}$ into electronic ($\chi^{e(3)}_{1111}$) and nuclear parts ($\chi^{n(3)}_{1111}$),

$$\chi^{T(3)}_{1111} = \chi^{e(3)}_{1111} + \chi^{n(3)}_{1111} \tag{11}$$

and to write n_2^e and n_2^n as

$$n_2^e = \frac{12\pi}{n_d} \mathrm{Re}(\chi^{e(3)}_{1111}) \tag{12}$$

and

$$n_2^n = \frac{12\pi}{n_d} \mathrm{Re}(\chi^{n(3)}_{1111}) \tag{13}$$

For liquids [7], it can be shown that $A_o = -\frac{1}{3} B_o$, so n_2^n may be written

$$n_2^n = \frac{4\pi B_o}{3n_d} \tag{14}$$

In what follows below, we will also calculate for liquids the fraction f_e of the total nonlinear index which is electronic in origin, given by

$$f_e = n_2^e / n_2^T \tag{15}$$

3. Measurements

In order to calculate n_2^e from eqs. (6) and (7), we have measured n_d, n_F, and n_C for all of the liquids shown in Table 1 where n_d and ν_d are tabulated. The measurements were performed using a Hilger-Chance refractometer with a tunable dye laser source. To calculate n_2^e it is necessary to determine the value of the normalization constant K in eq. (6). Normally, one would obtain it by a least squares fit to experimental data, however, little data is available at present. Instead, we have set the value of K by normalizing to the well known values for benzene. In particular, we have used the values determined by Levenson and Bloembergen [9] and Owyoung [10] for χ^{3e}_{1111} and used eq. (12) to find $n_2^e = 4.62 \times 10^{-13}$ esu and $n_2^e = 5.02 \times 10^{-13}$ esu respectively. Taking the average value ($\bar{n}_2^e = 4.82 \times 10^{-13}$ esu) one then obtains K = 101.5. This value for K along with n_d and ν_d enabled us to calculate n_2^e for all the liquids shown in Table 1. n_2^e varies from 0.40×10^{-13} esu for FC-104 to 13.44×10^{-13} esu for 1-bromonapthalene. The efficacy of this procedure is unknown at present due to the paucity of experimental data on χ^{3e}_{1111} or n_2^e. A more precise value for K could be obtained when such data becomes available.

Using eq. (9), we have also calculated the electronic coefficient σ as shown in Table 1. For nine of the liquids listed there, we show data taken from a compilation by Hellwarth [7] for $(\sigma + B_o)$. Thus we can then find B_o and from eqs. (14) and (5) the values of n_2^n and n_2^T, with the results shown in Table 1. It should be noted that for three of the liquids (cyclohexane, acetic acid, CCl_4) $B_o < 0$. As pointed out by Hellwarth [7], theoretically $B_o \geq 0$ always, hence the data here should be treated as only preliminary, a reflection of uncertainties in the normalization procedure mentioned above, and in the measurement of $(\sigma + B_o)$. It is likely that as more precise values of n_2^e and B_o are obtained from measurements this situation will be resolved. It is obvious that at present it is impossible to assign error bars to the obtained values of n_2^e, n_2^n or n_2^T.

The lowest value of n_2^T obtained is for H_2O (1.36×10^{-13} esu), not unlike that of typical optical glasses, while the largest value is for CS_2 (9.67×10^{-13} esu); the fraction of electronic nonlinear index (f_e) varies from 0.12 for CS_2 to 0.61 for H_2O.

In figure 1 we show the calculated total nonlinear index n_2^T as a function of n_d for

the nine liquids in Table 1. Recently Veduta and Kirsanov [11] published data (n_2^T) obtained from a number of liquids, including benzene, toluene, water, acetone, and ethanol. Normalizing the calculated value of benzene to that obtained in reference [11], we found the value of n_2^T shown in Figure 1 for comparison to the calculated ones. It can be seen that even with the uncertainties mentioned above the agreement is good for toluene, H_2O, and acetone. More importantly, one may observe in Figure 1 the trend that as the linear index n_d increases, so does n_2^T, in agreement with earlier work on solids. The trend would be even more pronounced if the cause of the negative values of B_o for CCl_4, cyclohexane, and acetic acid can be found. In Figure 2, we show the calculated n_2^T as a function of ν_d, and again one observes as in solid materials, the trend that as ν_d increases (low dispersion) one obtains low values of n_2^T.

In Figure 3 we show n_2^e and n_2^n as a function of n_d in an attempt to view their scaling behavior. While it is generally true that a larger n_2^e is associated with a larger n_2^n, it is impossible at present to draw any firm conclusions; again it is evident that the values for CCl_4, cyclohexane, and acetic acid are affected by the negative values of B_o. The study of scaling is important since if it can be shown that the nuclear part scales with the electronic contribution it is possible to describe the total nonlinear index by an equation such as (6) with a suitably adjusted constant, K, as has been done in the case of solid transparent optical materials [3].

Finally, while we have not explicitly considered the effect here, it is necessary to examine the absorption spectra or energy level structure of each liquid to insure that the calculated nonlinear index is not enhanced by a two photon resonance. It is well known that if the optical material is operating at a laser frequency ω and possesses a bandgap energy, E_B, then the condition

$$2\hbar\omega \gtrsim E_B \tag{16}$$

leads to the onset of two-photon absorption as well as an enhanced non-linear index near the frequency ω.

4. Conclusions

We have applied the Boling, Glass, and Owyoung [3] theory to the calculation of n_2^e for a variety of interesting liquids. By using the tabulated values of B_o [7], n_2^n and n_2^T may also be found. n_2^T may be comparable to optical glass in some cases, and as large as $\simeq$ x10 greater in others. One consequence of this is that in calculating the nonlinear phase distortion or "B integral" for a high power beam, formally given by [1]

$$B = \frac{K}{\lambda n_d} \int_o^L n_2^T I(z) dz \tag{17}$$

where K is a constant, relatively small thicknesses of liquid ($\sim$ mm) will have the same nonlinear phase distortion as ($\sim$ 1cm) of optical glass for high index or low Abbé value liquids.

The correlation of total nonlinear index with n_d and ν_d previously observed in solid optical materials has also been observed here and agrees well with available measurements of n_2^T.

The question of scaling n_2^n with n_2^e will await accurate measurements of n_2^T and B_o for liquids.

5. Acknowledgments

The authors acknowledge conversations with M. Weber, N. Boling and A. Glass, all of whom knowingly or unknowingly contributed to this work. The authors would also like to thank all of the many people who aided in this work.

This work was partially supported by the following sponsors: Exxon Research and Engineering Company, General Electric Company, Northeast Utilities, Empire State Electric Energy Research Corporation, and New York State Energy Research and Development Authority.

References

[1] Laser Program Annual Report, UCRL-50021-73, Lawrence Livermore Laboratory [1973].

[2] Laser Program Annual Report, UCRL-50021-74, Lawrence Livermore Laboratory [1974].

[3] N. L. Boling, A. J. Glass, A. Owyoung, IEEE Jour. Quant. Elect. QE-14, 601 [1978], and UCRL-75628 [1974].

[4] M. J. Weber, D. Milam, W. L. Smith, Optical Engineering, 17, 463 [1978].

[5] M. J. Weber, C. F. Cline, W. L. Smith, D. Milam, D. Heiman, R. W. Hellwarth, UCRL-80434 [1977].

[6] J. M. Rinefierd, S. D. Jacobs, D. C. Brown, J. A. Abate, O. Lewis, H. Appelbaum, Laser Induced Damage in Optical Materials: 1978, NBS Special Publication 541

[7] R. W. Hellwarth, Prog. Quant. Elect., 5, 1 [1977].

[8] S. D. Jacobs, Laboratory for Laser Energetics, University of Rochester, unpublished results.

[9] M. D Levenson and N. Bloembergen, Phys. Rev. B 10, 4447 [1974].

[10] A. Owyoung, Optics Comm. 16, 266 [1976].

[11] A. P. Veduta, and B. P. Kirsanov, Soviet Physics JETP, 27, 736 [1968].

Table 1. Summary of Data and Calculations

LIQUIDS	n_d	ν_d	n_2^e ($\times 10^{-13}$esu)	σ ($\times 10^{-13}$esu)	$\sigma+B_o$ ($\times 10^{-13}$esu)	B_o ($\times 10^{-13}$esu)	n_2^n ($\times 10^{-13}$esu)	n_2^T ($\times 10^{-12}$esu)	$f_e=\frac{n_2^e}{n_2^T}$
α-Chloronapthalene	1.631	22	11.72	4.06	36.0	31.94	82.03	9.375	0.13
CS_2	1.624	22	11.50	3.96	37.0	33.04	85.22	9.672	0.12
Benzene	1.502	31	4.82	1.54	6.0	4.46	12.44	1.726	0.28
Toluene	1.495	31	4.71	1.49	9.0	7.51	21.04	2.575	0.18
CCl_4	1.458	24	6.09	1.88	0.5	−1.38	−3.96	0.213	
Cyclohexane	1.424	53	1.67	0.50	0.1	−0.40	−1.18	0.049	
Acetic Acid	1.369	46	1.68	0.49	0.3	−0.19	−0.58	0.110	
Acetone	1.356	51	1.37	0.39	1.0	0.61	1.88	0.325	0.42
Water	1.334	67	0.83	0.23	0.4	0.17	0.53	0.136	0.61
1-Bromonapthalene	1.656	21	13.44	4.72					
Tricresyl Phosphate	1.556	33	5.19	1.71					
$ZnBr_2$	1.555	35	4.74	1.56					
$ZnCl_2$	1.536	41	3.54	1.15					
DC-710	1.533	33	4.84	1.57					
C5040	1.511	39	3.53	1.13					
C5610	1.510	36	3.96	1.27					
σXylene	1.503	31	4.84	1.54					
Dimethyl Sulfoxide	1.479	40	3.07	0.96					
Glycerol	1.474	59	1.69	0.53					
1,2 Dichloroethene	1.442	49	2.00	0.61					
Ethylene Glycol	1.432	62	1.36	0.41					
Ethenol	1.359	60	1.09	0.31					
D_2O	1.327	55	1.08	0.30					
Methanol	1.326	54	1.11	0.31					
FC-104	1.273	91	0.40	0.11					

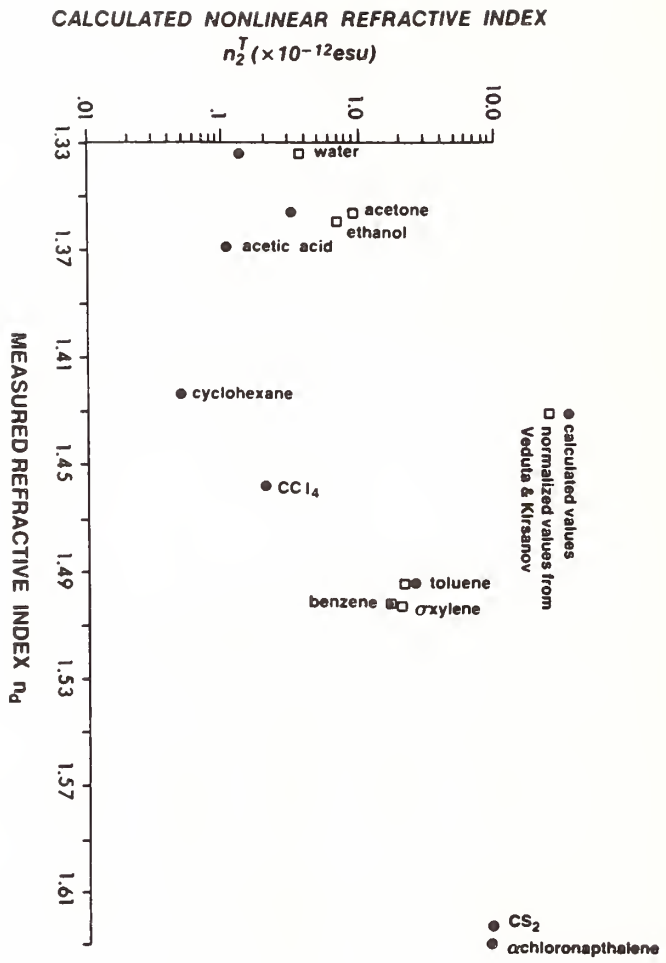

Figure 1. Calculated n_2^T versus n_d

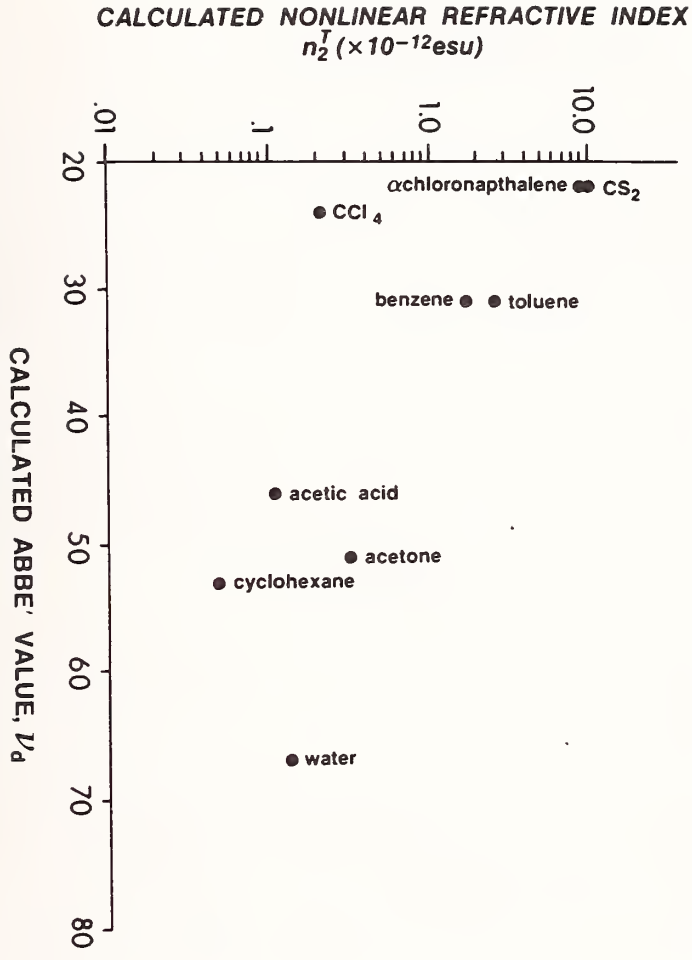

Figure 2. Calculated n_2^T versus Abbe value

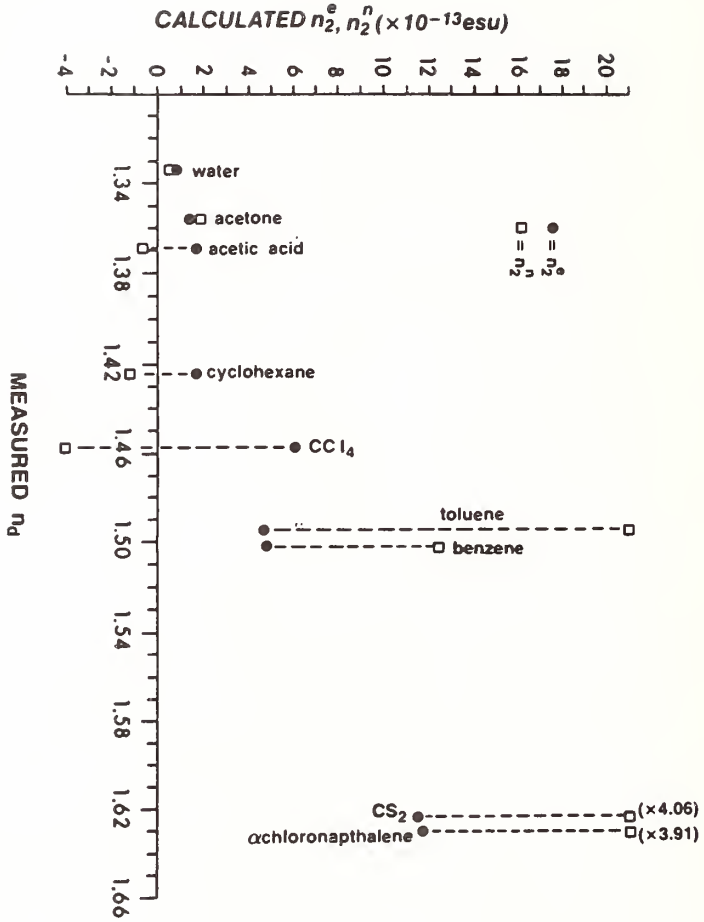

Figure 3. Calculated n_2^e and n_2^n versus n_d

WAVELENGTH MODULATION SPECTROSCOPY OF HIGHLY TRANSPARENT SOLIDS*

Rubin Braunstein, Ryu K. Kim
Department of Physics
University of California
Los Angeles, California 90024

and

Morris Braunstein
Hughes Research Laboratories
Malibu, California 90265

We have used wavelength modulation spectroscopy to measure the absorption in highly transparent solids at levels of 10^{-5} cm^{-1} in the spectral region from 2 to 12.0 μm. For the first time, it is now possible to obtain the continuous spectral distribution at this level of absorption where previously the only measurements have been laser calorimetric measurements at a few discrete wavelengths. We have used wavelength modulation techniques in conjunction with laser calorimetry to study absorption in the ultraviolet and visible regions. In the present work, a new wavelength-modulated spectrometer system was constructed so as to encompass the dominant HF, DF, CO, and CO_2 laser wavelengths. The richness of structure observed throughout this spectral region provides a possible identification of surfaces and volume contaminants as well as intrinsic absorption processes in solids. Results on KBr and other alkali halides are presented that demonstrate the versatility and power of this technique.

Key words: Extrinsic infrared absorption; volume and surface impurities; wavelength modulation spectroscopy; KBr; KCl; laser windows.

1. Introduction

The requirements for low-loss optical components for high-power laser, fiber-optic, and other light-guiding systems have stimulated the development of material growth and surface preparation techniques to yield materials with absorption levels on the order of 10^{-5} cm^{-1}. Interest in a particular spectral region of transparency has varied depending on the proposed applications of particular laser wavelengths. These material requirements have created a need for instrumentation to measure low-level absorption over an extended spectral region. A variety of sensitive techniques have been developed to measure absorption at discrete wavelengths of existing laser lines [1,2,3].[1] Many of these methods employ a high-power laser in some calorimetric configuration and can realize sensitivities that vary from 10^{-2} to 10^{-5} cm^{-1}. To ascertain intrinsic and extrinsic absorption mechanisms as well as to identify specific impurities, it is clear that it would be desirable to perform measurements over an extended spectral range.

Previously we have used wavelength-modulation techniques in conjunction with laser calorimetry to study absorption in the ultraviolet and visible regions [4]. At present, we report on the operation of a newly developed infrared wavelength modulation system operating between 2.5 to 12.0 μm that can measure the absorption in highly transparent

*Supported by the Air Force Office of Scientific Research.

1. Figures in brackets indicate the literature references at the end of this paper.

solids at levels of 10^{-5} cm^{-1} for a 1-cm path length. Since our system encompasses the dominant HF, DF, CO, and CO_2 laser wavelengths, the spectral distribution of absorption bands in this technologically important region can be observed. Measurements have been performed on a variety of alkali halides and semiconductors in the study of intrinsic and extrinsic absorption processes. The results on KBr and KCl are presented in some detail since an extensive literature exists concerning laser calorimetric measurements [2,3] on these technologically important infrared laser window materials. For the first time, it has been possible to obtain the continuous spectral distribution of the absorption at levels of 10^{-5} cm^{-1} and so provide a possible identification of surface and volume contaminants.

2. Experimental Technique

We have previously described the use of wavelength-modulation techniques to obtain the derivative and the subsequent integration of the absorption spectra in the visible and ultraviolet regions in laser-window materials [4]. The derivative spectra were obtained by sweeping the output wavelength of a monochromator across the exit slit by vibrating the output diagonal mirror at a depth of modulation that can be continuously controlled. Since the wavelength modulation measures not only the derivative of the transmission of the sample, but the derivative of the background as well, it is necessary to subtract this background to obtain the actual derivative of the absorption of the sample. In the visible-ultraviolet system [4], the modulated beam was directed alternately between the sample and a reference channel; since a single detector was used, it was necessary to use gating circuits that allowed independent measurement of the sample and a reference channel. The resulting spectra were normalized for the background variation by a servo-system. Although such an analog servo-system can be used to normalize background using photo-multiplier detectors, it is difficult to employ with infrared photoconductive detectors due to the dark current of these detectors.

To extend wavelength-modulation techniques into the infrared, we have modified a grating monochromator by oscillating an output diagonal mirror similar to the system employed in the visible-ultraviolet system [5]. This method of modulation is equally good for any spectral region of the monochromator. However, the system to subtract the background is different. This wavelength-modulated monochromator is used in conjunction with on-line digital techniques employing a PDP 11/20 computer. A sample-in sample-out procedure is used, the wavelength and sample position are under stepping-motor control, and provision is made for multiple scans for signal averaging. The digital data of background intensity, derivative of the background intensity, and the transmitted intensity through the sample and its derivative are independently recorded and are used in the on-line computation of the derivative of the spectral absorption. The wavelength-modulation technique yields essentially the energy derivative of the absorption coefficient. The absolute value of the absorption coefficient is obtained by integrating the observed derivative spectra, with the constant of integration supplied by a direct absorption measurement in the same apparatus at wavelengths where the absorption can be measured directly with good precision. Alternatively, the constant of integration can be supplied by a laser calorimetric measurement at a fixed wavelength.

Figure 1 shows a block diagram of the system implementing the above operation. The detector employed in the present work was a liquid-nitrogen-cooled PbSnTe detector and the source was a globar. This system can be used in the ultraviolet, visible, or infrared regions with appropriate changes of source, grating, and detector [6].

3. Experimental Results

A detailed study was made on a series of KBr and KCl samples selected for their low level absorption as indicated by laser calorimeter measurements at HF, DF, CO, and CO_2 laser wavelengths [2,3]. These crystals were obtained from various sources (Hughes Research Laboratories, the Naval Research Laboratory, and Oregon State University). The material was selectively ion filtered and reactive gas treated for purification prior to crystal growth. The samples were surface ground, polished with a slurry of Linde A in ethanol or propanol, and then dried under a heat lamp; this is the standard procedure for polishing alkali halides. Measurements were performed with the samples in the laboratory atmosphere

as well as in a dry N_2 atmosphere. The data were obtained initially in the form of the logarithmic derivative of the transmitted intensity with respect to energy with and without the sample. The energy derivative of the absorption coefficient was subsequently obtained by determining the constants of proportionality of the instrument by a computer correlation procedure to uncorrelate the background derivative [6]. The change in the absorption coefficient ΔK in cm^{-1} was then determined by a standard trapezoidal integration. Although the derivative data contain all the physical content of the spectral distribution of the absorption, the data in this report are presented in integrated form to facilitate comparison with the literature.

The absorption spectra of a typical KBr sample obtained with a conventional double-beam spectrometer are shown in figure 2. As can be seen, virtually no absorption structure is present above the noise level of the instrument, confirming the relative purity of the sample.

Figure 3 shows the integrated derivative spectra of a KBr sample taken with the sample in the laboratory atmosphere. The richness of the observed spectra should be noted in contrast to the featureless spectra shown in figure 2 for the same sample. The right hand ordinate in figure 3 indicates the absorption coefficient at 3.8 μm as inferred from a laser calorimeter measurement with a DF laser; the left hand ordinate indicates the relative change of absorption obtained by integrating the wavelength modulation derivative data. The depth of modulation of the monochromator frequency used to obtain these data was 10 cm^{-1}. The zero of the ΔK cm^{-1} wavelength modulation result is registered with the absorption calibration point of 0.4×10^{-4} cm^{-1} obtained by laser calorimetry. Therefore, to obtain the actual absorption coefficient at a particular wavelength, one merely adds or subtracts the appropriate ΔK value at a given frequency to the 0.4×10^{-4} cm^{-1} value. This type of representation of the data allows us to display the fine structure excursions in absorption above and below the calorimetric point. A point of caution is necessary in comparing a calorimeter measurement to our wavelength modulation results. Most calorimetric measurements are made with multi-line lasers, and, as our data show, the laser lines can straddle absorption lines. Successive runs on this sample reveal that the structure shown in figure 3 is reproducible within a mean deviation of $\Delta K \sim 10^{-6}$ cm^{-1}. Consequently, the noise level of the sample is at levels of the width of the drafting lines. The data points were taken at 5 cm^{-1} frequency intervals. The sample thickness was 4 cm.

When this sample is placed in a dry N_2 atmosphere, a continuous change in the spectral distribution of the absorption is observed until the spectra stabilize after the sample has been in this gaseous ambient for an hour. The dominant features of the spectra of this sample when in the laboratory atmosphere displayed in figure 3 are: a band near 2.5 μm with fine structure, multiple structure between 3 to 4 μm with fine structure, a sharp strong band at 4.2 μm, a band at 5 μm, and multiple structures between 6 to 12 μm. The data shown in figure 4 are for this same sample in a dry N_2 atmosphere. Although there is a distinct change in the spectra in figure 4 compared to figure 3, some of the original prominent features can still be recognized. The sharp peak at 4.2 μm is greatly reduced, and the band at 5 μm is gone, while some of the original structure between 5.8 and 12.0 μm is still present; however, a valley develops around 9 μm.

The absorption spectra for another KBr sample are shown in figures 5 and 6, taken in the laboratory and a dry N_2 ambient, respectively. It is possible to recognize the general spectral features in figure 5 that were seen in figure 3 despite the different relative intensities of the bands. Again, when the sample is in a dry N_2 atmosphere, as shown in figure 6, some of the features of figure 5 remain. It is interesting to note that both of these samples in dry N_2 show similar spectra (see figs. 4 and 6); again, a valley develops at 4.8 μm in both samples in this ambient.

Figures 7 and 8 display the spectra in a laboratory atmosphere for two other KBr samples. Although the details of the structure are different in these samples, there is a great deal of similarity with the general features in figures 3 and 5. However, it should be noted that the band observed at 4.8 μm in figures 3, 5, and 7 is absent in figure 8.

The spectral distribution of the absorption of all samples of KBr have the same dominant features. However, one can distinguish slight differences in the spectra from sample to sample, despite the fact that the same preparation techniques were used in the growth of these samples. Thus, our measurements can reveal as yet unknown subtle differences in growth conditions.

The integrated derivative spectra of KCl in the laboratory and dry N_2 atmosphere are shown in figures 9 and 10, respectively. Again for this substance, we observe changes in spectra as a function of gaseous ambient with some of the prominent features remaining in both spectra.

4. Discussion and Analysis of Data

In general, for the spectral region from 2.5 to 12 μm, the samples of KBr in this work show structure at 2.5 μm, multiple structures between 3 and 4.0 μm, a sharp peak at 4.2 μm, a band centered at 4.8 μm, multiple structures between 6 and 8 μm, a valley near 9 μm, and a peak at 10.6 μm at levels of absorption coefficient of 10^{-5} cm^{-1}. Since the relative magnitudes of these structures differ in different samples, the indications are that these bands have an extrinsic origin. Although the spectra differ in detail, the clustering of the spectra lines in similar spectral regimes indicates a common origin of the spectra. The magnitudes and line widths of some of the bands vary when the samples are in a dry N_2 atmosphere compared to a laboratory ambient, indicating that a portion of the absorption is due to surface physical adsorption. The structures that persist even when the samples are flushed in dry N_2 may be due to surface chemi-adsorbed species or volume impurities. The above measurements were made on 1- to 4-cm-thick samples. The surface character of some of these bands was confirmed by performing similar measurments on 1-mm-thick samples. Absorption coefficients on the order of 10^{-5} cm^{-1} were observed on thick and thin samples with slight differences in the spectral distribution. Due to the complex superposition of bands, it was difficult to unambiguously distinguish which bands would scale with thickness and which would identify volume absorption. The 4.2-μm band was observed with the same intensity for all thicknesses, confirming a surface origin. The continuous variation of the spectral features with thickness of sample that remain at 10^{-5} cm^{-1} levels indicates that at this level of absorption we have a combination of volume and surface absorption or there is an inhomogeneous distribution of volume impurities.

Correlation-type charts have been published that represent a tabulation of molecular-ion vibratonal frequencies as a means of identifying possible surface and volume impurities in alkali-halide laser window materials [7,8]. If one considers a frequency overlay of possible impurities that can be present in concentrations of 0.1 ppm, one finds that a quasi-continuum absorption would be expected throughout the 2.6- to 12.0-μm region due to the overlap of the Lorentzian tails of the various absorption bands. It has been felt that a heterogeneous distribution of a conglomeration of chemical compositions which can be deposited on the surface from the environment would produce a uniform absorption throughout the infrared spectral region [8]. However, the distinct absorption bands observed in this work indicate the possibility of specifically identifying dominant absorption centers.

Rather than considering the multiplicity of possible impurities that are displayed in the vibrational correlation charts [7,8], it is instructive to consider: (1) the "historical" two principal impurities, OH^- and CO_3^{-2}, which have been involved in the infrared absorption in the alka-halides [9,10,11]; (2) the C-H bands [12]; and (3) the surface carbonates [13]. The dominant bands for these groups are shown in figure 11.

The region between 2 and 4 μm reveals several structures, while previous measurements by laser calorimetry have indicated a peak near 2.7 μm (see fig. 12, reproduced from the literature [14]), which has usually been associated with the stretching frequency of the "isolated" OH^- radicals [14]. However, laser calorimetry measurements are performed with multi-line lasers at a few discrete wavelengths and so can only infer a broad band with the great possibility of missing peaks or valleys.

In the present work, a prominent peak is observed at 3850 cm^{-1}, which is shifted from the peak that is observed at 3610 cm^{-1} in deliberately doped KBr [15]. It is not clear that such a large shift could occur due to different crystallographic locations of OH^- in the lattice. The magnitude and line width of this peak shifts from sample to sample; in addition, placing a sample in a dry N_2 environment results in spectral changes that indicate that part of this band may be due to surface adsorption. However, there is a shoulder in this line (as can be seen in figs. 3, 5, 7, and 8) near 3700 cm^{-1} that persists in dry N_2 ambient and can be associated with adsorbed H_2O.

The region between 3 and 4.0 μm shows a superposition of structures that could be attributed to various C-H bonds (see fig. 11). The origin of these groups can result from surface contaminants due to the alcohol that is used to disperse the grinding compounds used in the surface polishing of the crystals. However, some of these bands may be due to volume absorption since some of the spectra scale with sample thickness. Volume absorption due to C-H bands can be due to carbonaceous fractions, which can result from organic materials such as water-soluble alcohols that decompose on melting and are incorporated in the crystals.

A classical example of physical adsorption taking place on a surface of KBr is seen at 4.2 μm. This strong narrow band with varying intensity is observed at 2358 cm^{-1} on all samples of KBr. This is close to the gas-phase value of 2349 cm^{-1} for the CO_2 vibration. Since this band is easily suppressed by flushing with dry N_2, it is readily identified as due to a physically adsorbed species. It is interesting to note that the CO_2 adsorption varies from sample to sample for the laboratory ambient, as can be seen from figures 3, 5, 7, and 8; it is not unreasonable to expect physical adsorption to depend on surface variations or impurities in the substrate.

The band at 4.8 μm is most likely due to surface-adsorbed "liquid" water as the absorption in this region is markedly reduced in a dry N_2 ambient; some of the additional structure in the 2.7 μm region can be due to the virational structure of water as it is also reduced by dry N_2 flushing. The absence of the 4.8 μm band in figure 8, even when the sample is in a laboratory ambient, indicates that H_2O adsorption depends on the condition of the substrate.

The bands between 5.5 to 8 μm are the most persistent of all structures seen in all the KBr samples. Measurements on thin samples still reveal these structures, which lends evidence that these are due to surface chemical adsorption. The positions of these bands are consistent with the vibrational frequencies of various surface carbonate complexes [13].

It is interesting to note that our data reveal in general a peak in absorption at 10.6 μm and a valley around 9 μm. It is possible to identify the 10.6 μm peak as due to the C-C vibration. It is our interpretation that laser calorimetry data indicate a possible minimum in absorption near the CO_2 laser line at 9.27 μm [16]. Our wavelength modulation data definitely establish this valley. The absorption between 5.5 to 8 μm seems to be due to surface carbonates. However, the absence of absorption at 1070 cm^{-1} signals that the species are in the form of carboxylates. Therefore, we can infer the presence of chemisorbed "carbonates" not only by the presence of absorption in the 5.5 to 8 μm region but also by the absence of absorption at 9.27 μm!

If one examines the data for KCl shown in figures 9 and 10 in the light of the discussion of the identification of the bands seen in KBr, similar features can be discerned. It is interesting to note that the physically adsorbed CO_2 band is markedly suppressed in KCl relative to KBr. The structures in the 6- to 8-μm region are still present together with the tendency for a valley at 9 μm. However, the valley at 5 μm in KBr that opens up in a dry N_2 ambient due to the possible desorption of H_2O is not seen in KCl. The wavelength modulation results confirm the similarity of the extrinsic absorption in KCl and KBr, which has been formerly inferred from laser calorimetric data [2,3].

5. Conclusion

A powerful new method of infrared optical derivative spectroscopy was developed that is capable of measuring the absorption coefficients at levels of 10^{-5} cm^{-1} for a 1-cm path length in the spectral region from 2.5 to 12.0 μm. This instrumentation has enabled us, for the first time, to measure the complete spectral distribution of low-level absorption in highly transparent materials. The richness of the observed structure enabled us to identify volume and surface impurities in KBr and KCl. The spectral distribution of the absorption of all samples of KBr and KCl have the same dominant features. However, we can distinguish slight differences in the spectra from sample to sample, despite the similarity in crystal growth; thus our measurements can reveal as yet unknown subtle differences in material synthesis.

6. Acknowledgments

The authors wish to thank Michael Burd for aid in the computer programs, James A. Harrington for laser calorimetric measurements, and Lloyd DeVaux for fabricating the exellent PbSnTe detector without which this work could not have been performed. We add our appreciation to Bradly Bobbs and Donald Deal for several helpful discussions.

References

[1] Deutsch, T.F., Laser window materials — an overview, J. Electron. Mater. 4, 663 (1975).

[2] Hass, M., and Bendow, B., Residual absorption in infrared materials, Appl. Opt. 16, 2882 (1977).

[3] Mitra, S.S., and Bendow, B., Residual absorption in infrared materials, Appl. Opt. 16, 2882 (1977).

[4] Harrington, J.A., Bobbs, B.L, Braunstein, M., Kim, R.K., Stearns, R., and Braunstein, R., Ultraviolet-visible absorption in highly transparent solids by laser calorimetry and wavelength modulation spectroscopy, Appl. Opt. 17, 1541 (1978).

[5] Welkowsky, M., and Braunstein, R., A double beam single detector wavelength modulation spectrometer, Rev. Sci, Instrum. 43, 399 (1972).

[6] To be published.

[7] Duthler, C.J., Extrinsic absorption in 10.6 m-laser-window materials due to molecular-ion impurities, J. Appl. Phys. 45, 2668 (1974).

[8] Flannery, M., and Sparks, M., Extrinsic absorption in infrared laser-window materials due to moleuclar-Damage in Optical Materials; 1977, 4-6 October 1977, Boulder, Colo., ed. by A.J. Glass and A.H. Guenther, NBS Special Publication 509, U.S. Government Printing Office, Wash., D.C. 1977, p. 5.

[9] Wedding, B., and Klein, M.V., Infrared absorption of the hydroxyl ion in alkali halide crystals, Phys. Rev. 177, 1274 (1969).

[10] Lipson, H.G., Larkin, J.J., Bendow, B., and Mitra, S.S., Molecular-impurity absorption in KCl for infrared laser windows, J. Electron Mater. 4, 1 (1975).

[11] Harrington, J.A., Gregory, D.A., and Otto, Jr., W.F., Infrared absorption in chemical laser window materials, Appl. Opt. 15, 1953 (1976).

[12] Palik, E.D., Gibson, J.W., Hass, M. Braunstein, M., and Garcia, B., Infrared characterization of surfaces and coatings by internal-reflection spectroscopy, Appl. Opt. 17, 1776 (1978).

[13] Hair, M.L. Infrared Spectroscopy in Surface Chemistry (Marcel Dekker, New York, 1967).

[14] Hass, M., Harrington, J.A., Gregory, D.A., and Davisson, J.W., Infrared absorption limits of HF and DF laser windows, Appl. Phys. Lett. 28, 610 (1976).

[15] Handler, P., and Aspnes, D.E., Electric-field modulationof the vibrational absorption of OH^- in KBr, Phys. Rev. Lett. 17, 1095 (1966).

[16] Rowe, J. M., and Harrington, J.A., Extrinsic absorption in KCl and KBr at CO_2 laser frequencies, J. Appl. Phys. 47, 4926 (1976).

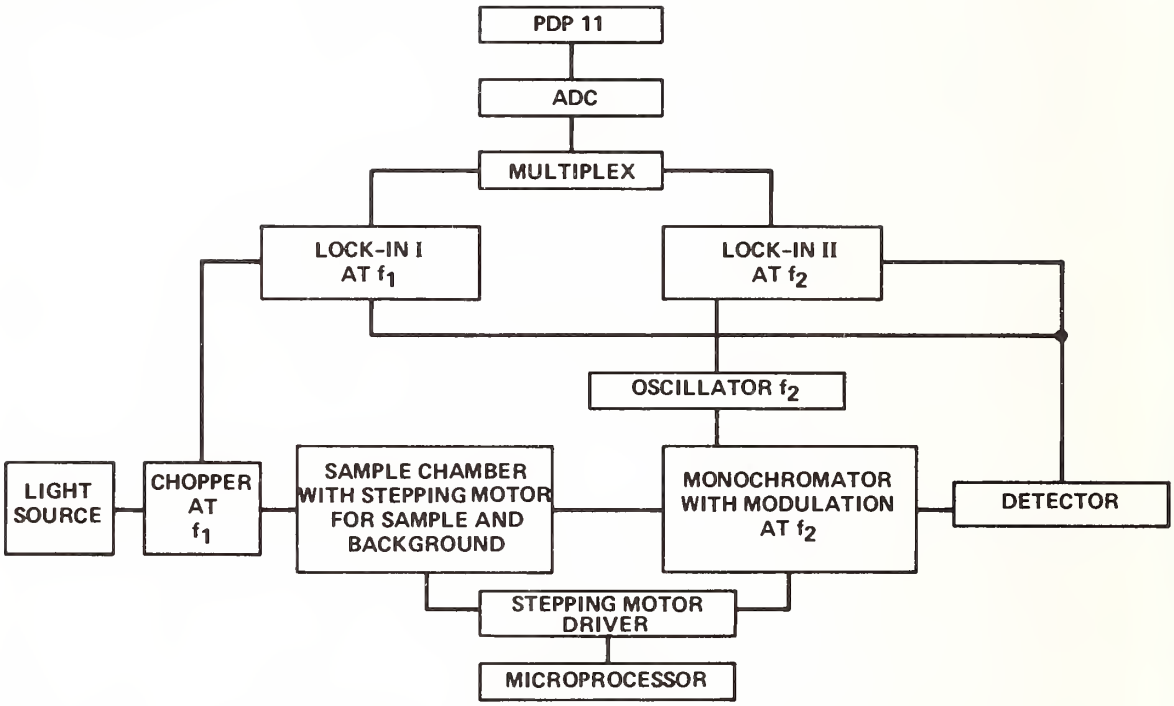

Figure 1. Infrared wavelength modulation system.

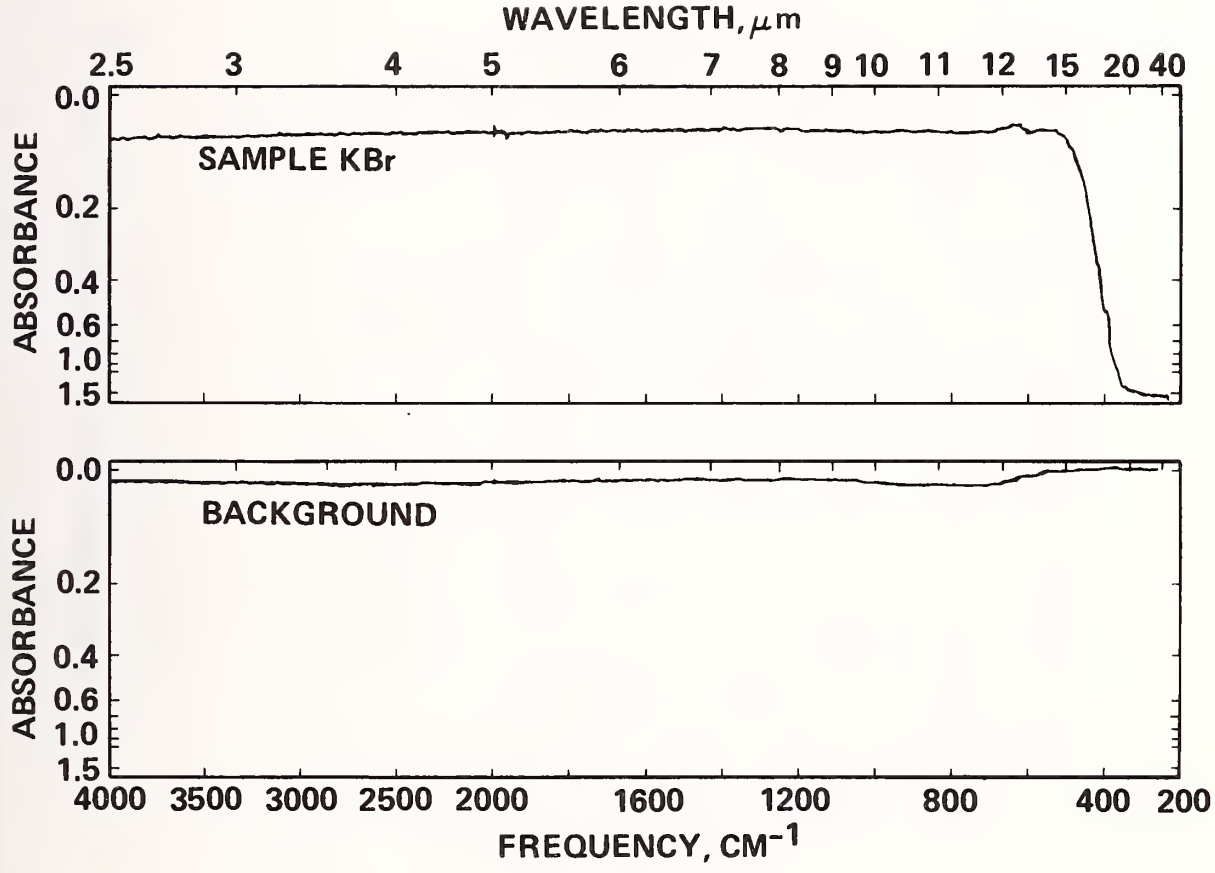

Figure 2. Absorbance of KBr measured with a conventional double-beam monochromator.

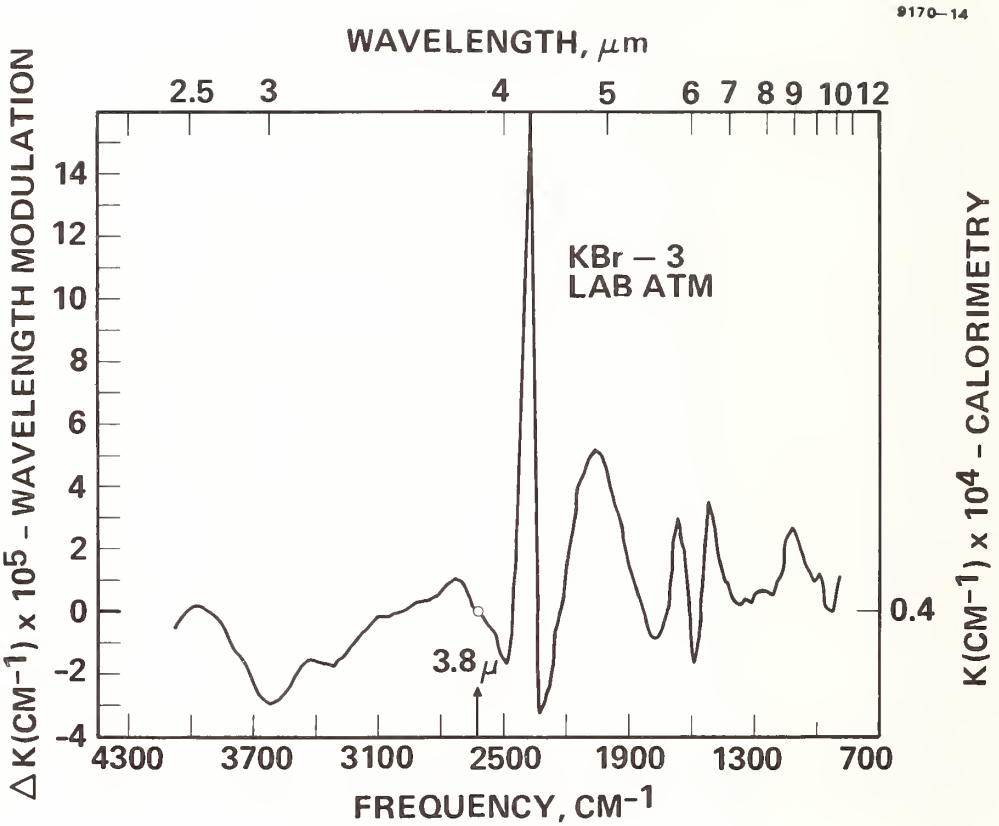

Figure 3. Wavelength modulation spectra of KBr in the laboratory atmosphere.

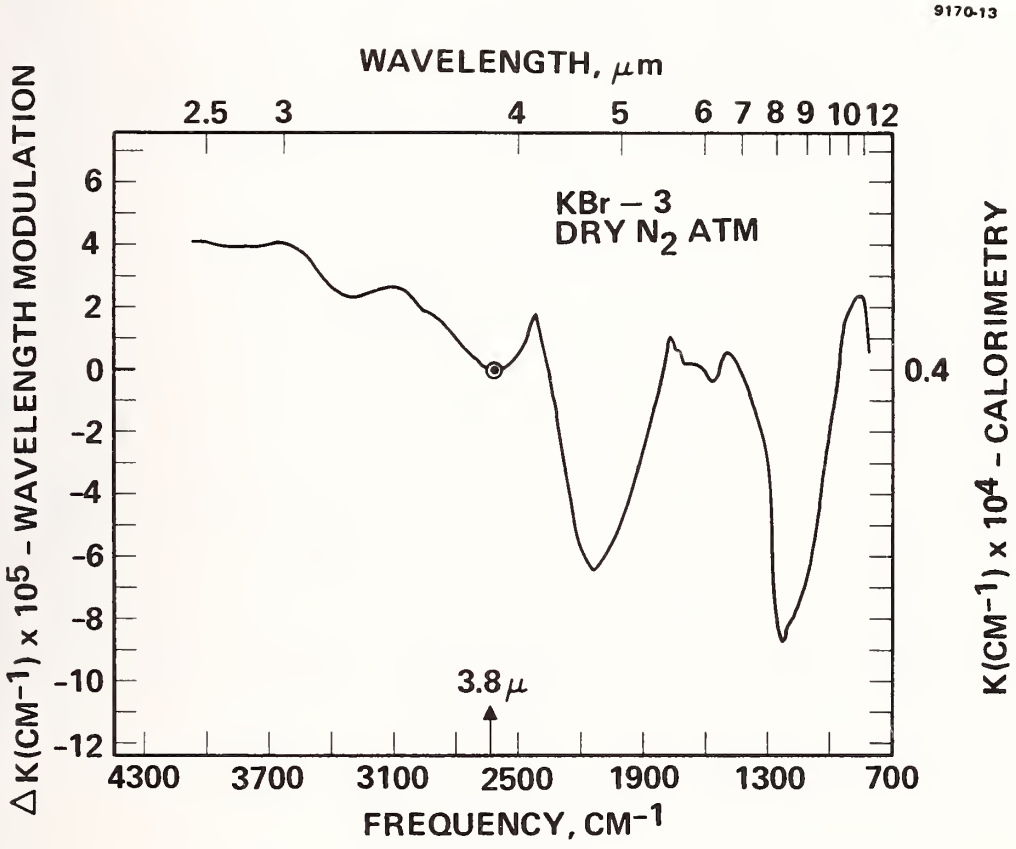

Figure 4. Wavelength modulation spectra of the sample of KBr in figure 3 in a dry N_2 atmosphere.

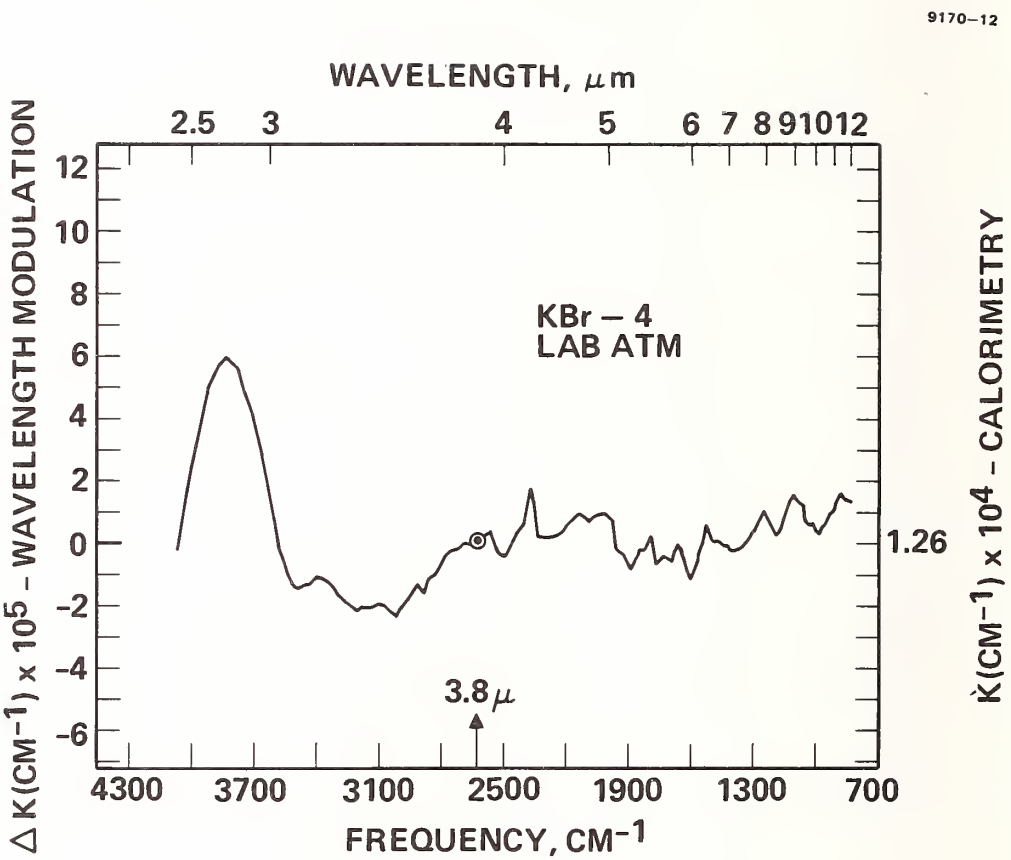

Figure 5. Wavelength modulation spectra of KBr in the laboratory atmosphere.

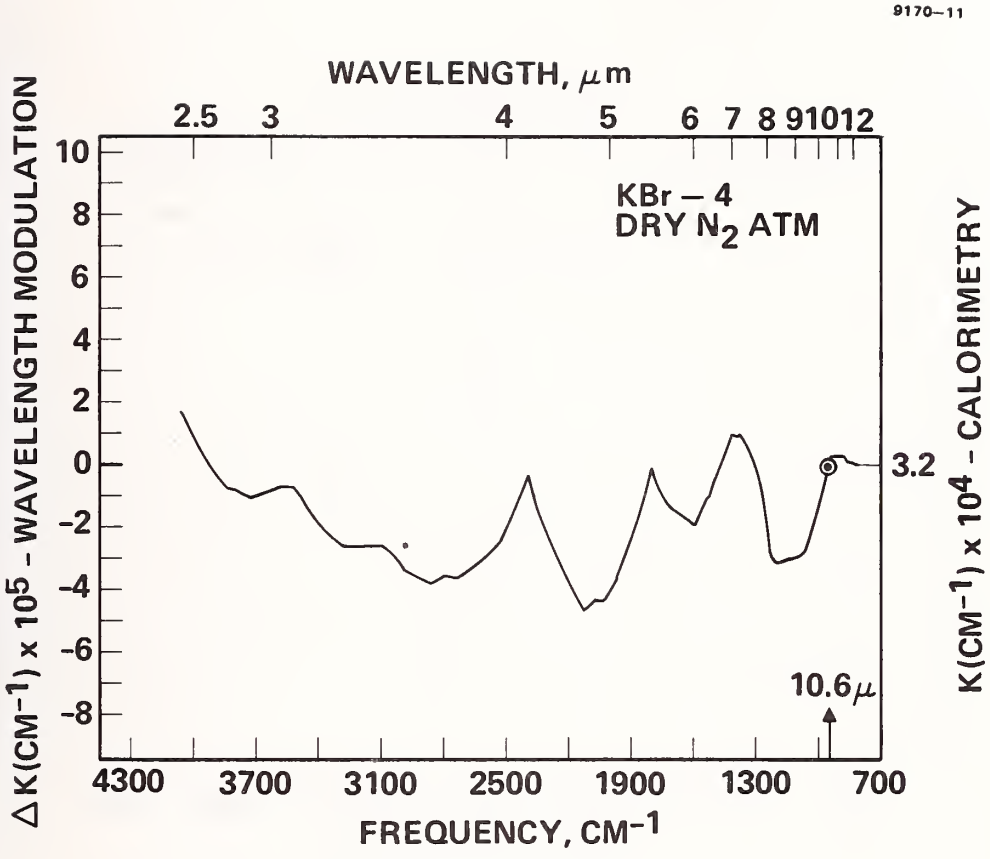

Figure 6. Wavelength modulation spectra of the sample of KBr in figure 5 in a dry N_2 atmosphere.

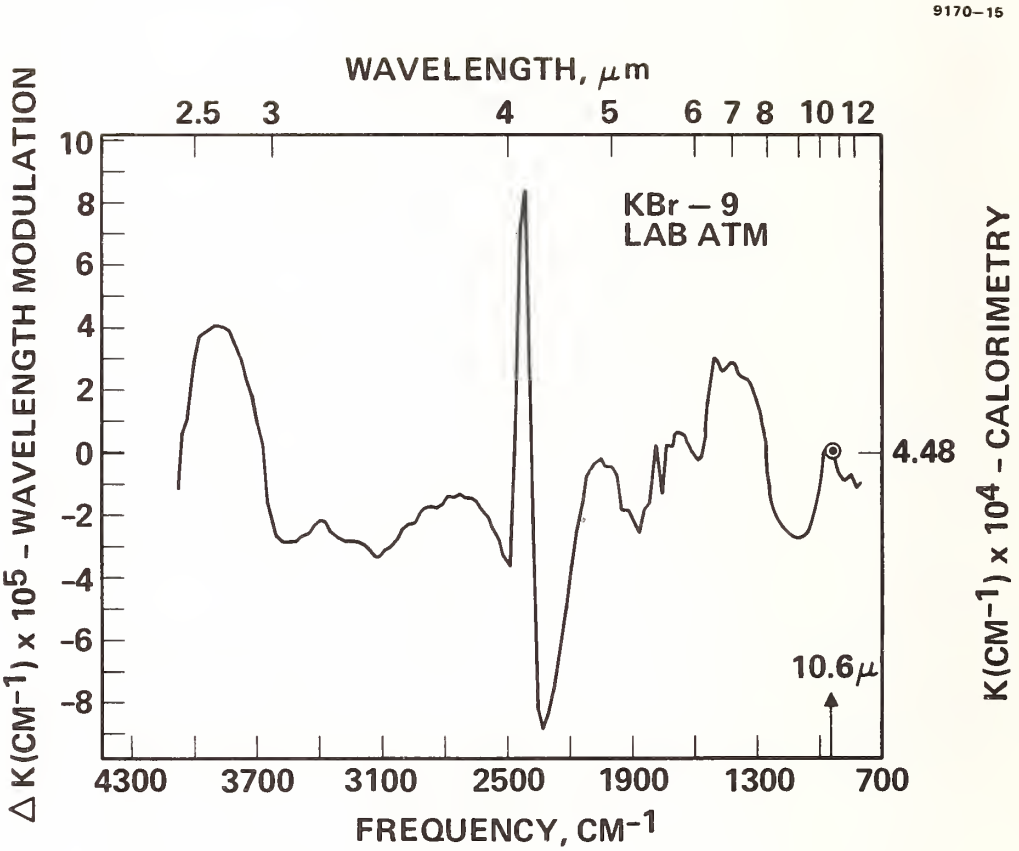

Figure 7. Wavelength modulation spectra of KBr in the laboratory atmosphere.

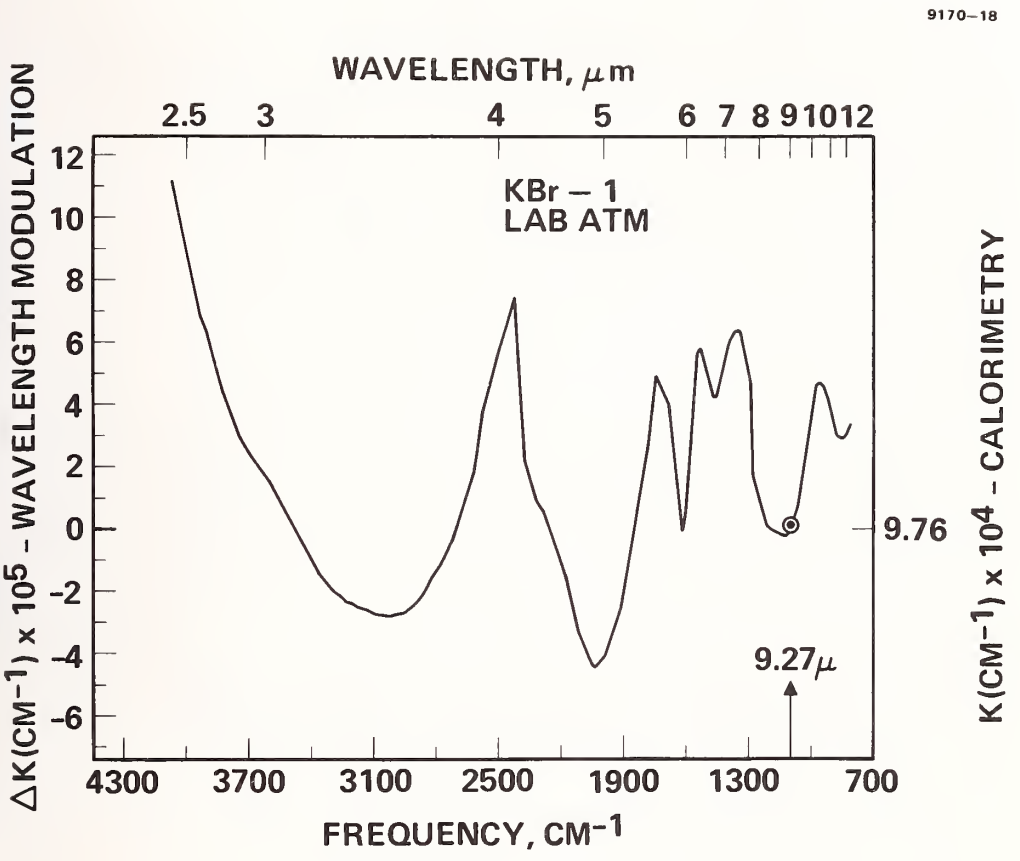

Figure 8. Wavelength modulation spectra of KBr in the laboratory atmosphere.

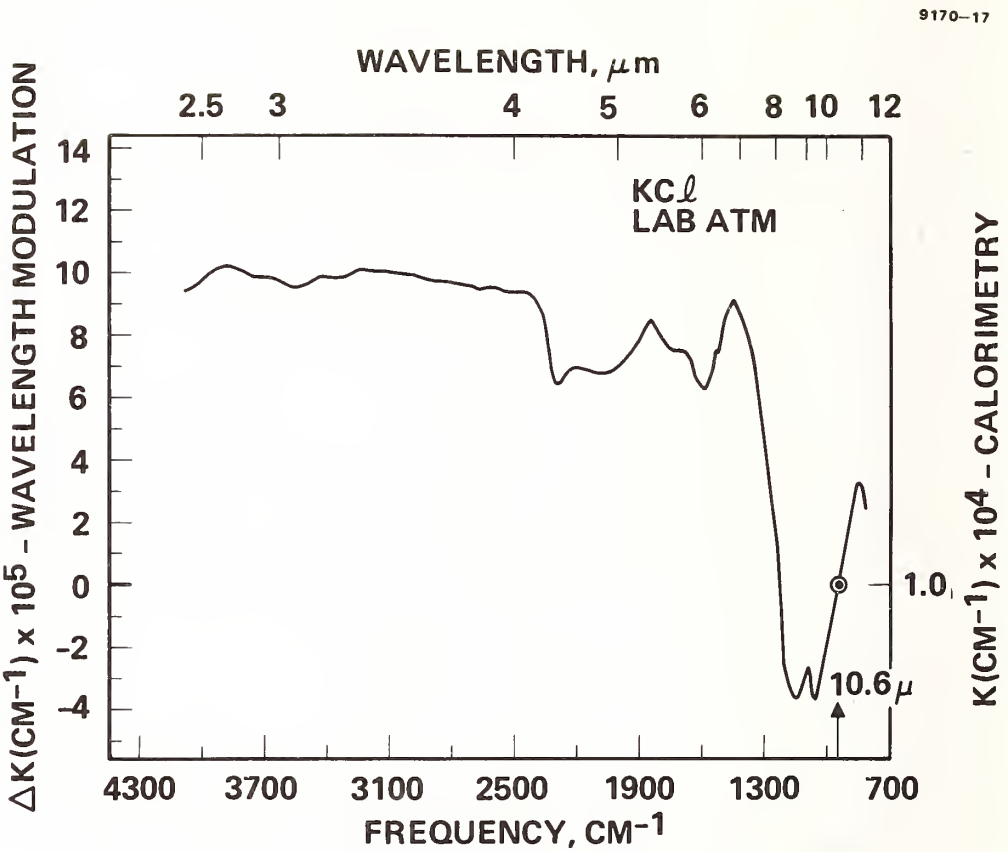

Figure 9. Wavelength modulation spectra of KCl in the laboratory atmosphere.

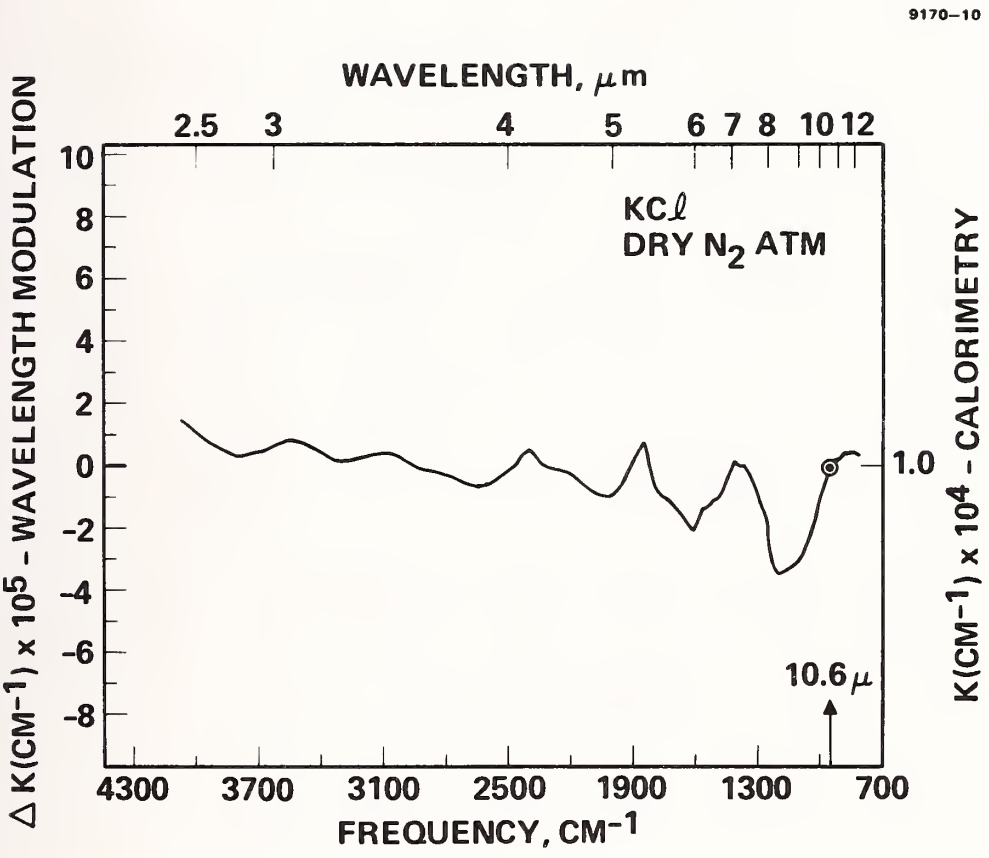

Figure 10. Wavelength modulation spectra of the same sample in figure 9 in a dry N_2 atmosphere.

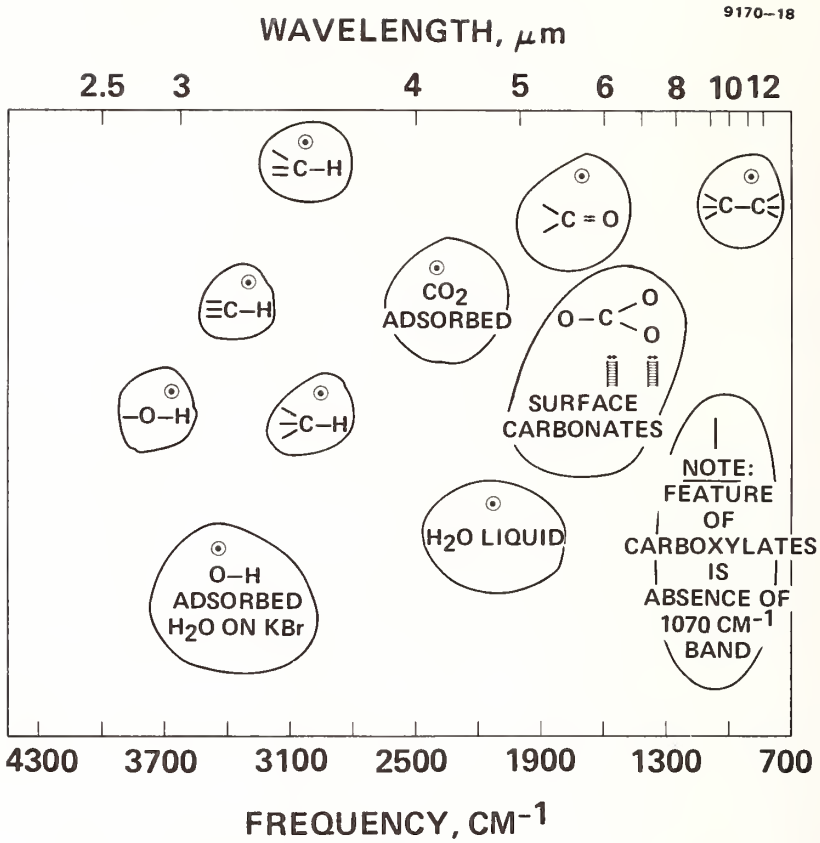

Figure 11. Correlation chart of bond frequencies of volume and surface impurities for KBr and KCl.

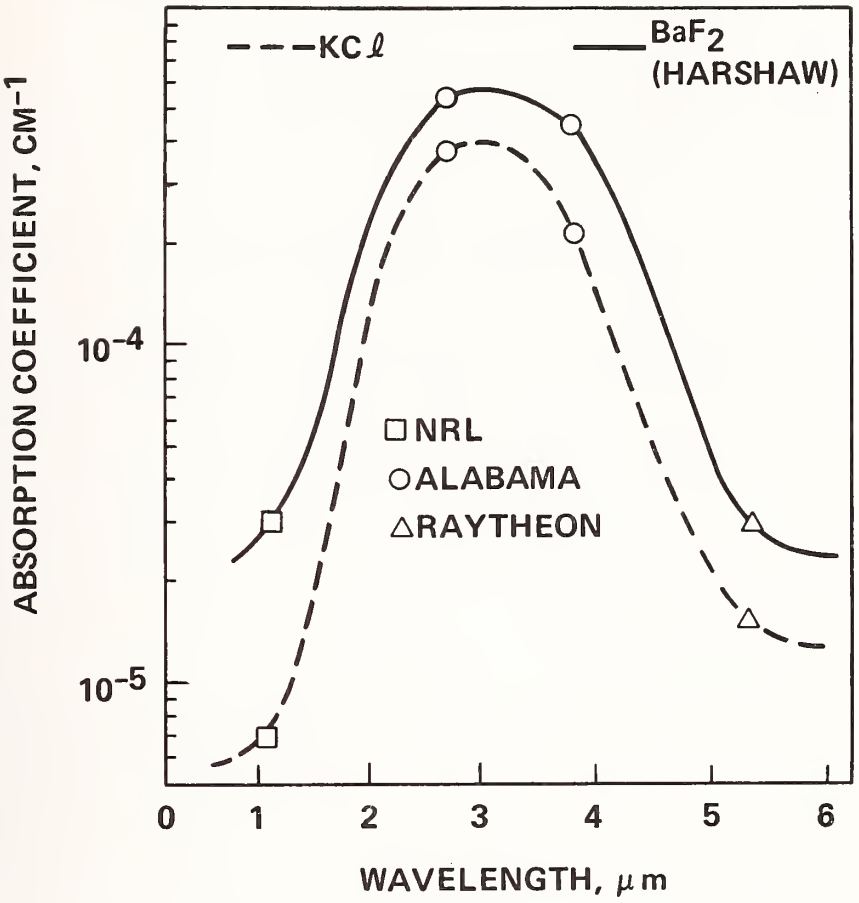

Figure 12. Absorption of KCl and BaF_2 by laser calorimetry [14].

This paper was subject to extensive discussion. The speaker expressed concern about the baseline data provided by multi-mode laser calorimetry. Among the concerns regarding laser calorimetric data is the problem of data obtained with multi-mode lasers in which the mode structure of the laser can straddle the particular line features in the absorption spectrum of the sample. In response to a question concerning the application of this technique to coated surfaces, the speaker indicated that it had been applied to silicon samples on which an oxide layer had developed. There was rather lengthy discussion on the problem of the adsorption and desorption of surface contaminants. The speaker commented that the detectability of surface contamination by this method showed the importance of carrying out measurements on samples in vacuum with careful surface preparation. It was observed that the physi-adsorption depended on the techniques of sample preparation. Adsorption and desorption of atmospheric water was observed in the 2.8 and 4-6 micrometer regions.

SYNCHROTRON RADIATION STUDIES OF BERYLLIUM FLUORIDE GLASS

R. T. Williams, D. J. Nagel, and P. H. Klein
Naval Research Laboratory
Washington, DC 20375

and

M. J. Weber
Lawrence Livermore Laboratory
Livermore, CA 94550

We report measurements of the reflectance of pure BeF_2 glasses in the range 9 eV to 120 eV, as well as photoelectron spectra in the valence band region. Based on these data, which should be regarded as preliminary, the lowest-energy reflectance peak is at 12.8 eV, implying an exciton resonance at about 13.1 eV, in close correspondence to LiF. Photoelectron spectra for the bulk glass show a valence band which is roughly symmetrical and about 5.8 eV wide (FWHM), with a tail of states extending into the gap.

Key words: BeF_2 glass; exciton resonance; photoelectron spectra; reflectance; synchrotron radiation; vacuum ultraviolet.

1. Introduction

Beryllium fluoride glasses are of current interest as possible materials for high power laser systems because of their very low nonlinear refractive indices [1] . In addition the linear refractive index of BeF_2 is extremely small, (e.g., n=1.275 at 587.6nm), so that it may be attractive for use in multilayer coatings for the ultraviolet. Photoemission spectra of evaporated films of BeF_2 have indicated that the valence level binding energy (center of the F^-2p peak relative to the vacuum energy) is 17.2 eV, compared to 12.8 eV in LiF [2]. These data suggest that the intrinsic band gap of pure BeF_2 should be comparable to or greater than that of LiF. In further support of this expectation, figure 1 shows empirical trends of the valence exciton energy in the alkali fluorides and alkaline earth fluorides.

Aside from interest in the possibility of using BeF_2 for vacuum ultraviolet optical components, knowledge of the intrinsic band gap and fundamental electronic structure is useful in predicting the wavelength dependence of multiphoton absorption coefficients, in understanding the source of near-uv linear absorption, and in obtaining a more complete spectrum of the refractive index. Absorption measurements on presently available bulk BeF_2 glasses have indicated a practical transmission limit of 150 nm [1], but until the present work no determination of the intrinsic band gap or far-uv properties had been made.

We have measured reflectance of pure BeF_2 glasses in the range 9 eV to 120 eV, as well as photoelectron spectra of the bulk glass in the valence band region. Ultraviolet reflectivity and photoemission are useful measurements for indicating the ultimately achievable transmission edge since they sample very high densities of states, assumed intrinsic in nature. On the other hand, both methods probe only the near-surface region, and so the hygroscopic nature of BeF_2 presents a problem. We have used an argon sputter etching gun to clean the samples in ultra-high vacuum prior to measurement.

2. Experiment

Glass samples were prepared at Lawrence Livermore Laboratory by melting pure BeF_2 in graphite crucibles. A typical impurity analysis is shown in table 1. Polished pieces about 0.5 mm thick and 1 cm^2 in area were prepared. Since pure BeF_2 is hygroscopic, preparation and subsequent handling were conducted in a dry environment.

The measurements of UV reflectance and photoemission were made using radiation from the Synchrotron Ultraviolet Radiation Facility of the National Bureau of Standards (Gaithersburg). The UHV experiment chamber and related measurement apparatus have been used in previous NRL investigations of the reflectance, fluorescence, and photoemission of alkaline earth fluorides [3] and other materials. The monochromator used in this work is a toroidal grating instrument providing useable flux from roughly 10 to 135 nm, with a 0.6 nm bandpass chosen for this work. The monochromator is not optimized for high flux in the 8-15 eV range which is of greatest interest in the present work, nor for resolution at the highest photon energies, so that there are uncertainties on either extreme of the spectrum. Continuing work is addressing these spectral ranges more thoroughly.

Reflectance was measured using an aluminum photocathode which could be moved to intercept the incident or reflected beams. Photoelectron spectra were measured using a double-pass cylindrical mirror analyzer (PHI Model 15-255-G). Since these were bulk insulator samples, it was necessary to provide charge neutralization when making photoelectron measurements. This was done by means of a filament serving as a flooding source of low-energy electrons. The pressure in the experiment chamber was typically 5×10^{-9} torr in these measurements.

3. Results and Discussion

The reflectance of sample number B815 (pure BeF_2) in the energy range 9 to 120 eV (roughly 135 to 10 nm) is shown in figure 2. The maximum reflectance in this figure is about 10%. This is lower than one expects based on other alkaline earth fluorides. Since specular reflectance is measured in this experiment, we assume surface roughness may be a significant factor, but have not yet characterized the diffuse scattering experimentally. Sample B815 appears fairly smooth to the eye, but sample P-71 shows obvious roughness. The reflectance of sample P-71 exhibits essentially the same features as B815, though at a lower absolute value (about 5% maximum). For the time being, absolute reflectivities should be regarded as tentative, but the spectral features can be discussed. We have marked locations of spectral features in figure 2 which are attributable to transitions originating in the F^-2p, F^-2s, and $Be^{++}1s$ levels.

In figure 3, we show the low-energy portion of the reflectance spectrum on an expanded scale, and suggest 13.1 eV as the energy of a resonance (assumed to be the valence exciton) responsible for the first reflectance peak. When we have more complete data, a determination of the optical constants will be made to locate the absorption resonance more precisely. For the time being. we assume that the exciton resonance is located slightly to the high-energy side of the first reflectance peak. The sources of the reflectance peaks at 15 and 17.5 eV are not known at present.

Figure 4 shows a photoelectron energy distribution curve corresponding to the valence band of BeF_2 sample number B815 (after sputter cleaning) for an incident photon energy of 50 eV. The filament used as a "neutralizing" source of electrons was in fact operated at a current sufficient to charge the sample to a negative potential. Hence, the observed photoelectron energies extend above 50 eV. For constant photon energy and flux of the incident radiation, the energy scale should be rigid (i.e. relative energies are meaningful), although floating in the sense that absolute energies relative to vacuum are not known. In order to establish an estimated scale of binding energy (est. E_b), we have assigned the center of the valence peak the same binding energy as was found for thin evaporated films of BeF_2 by Poole et. al. [2]. The peak in figure 4 is more symmetrical than that found in the thin film work, however. There is an apparent tail of valence states out to about 7 eV on the binding energy scale. This is roughly consistent with the observation that the practical transmission limit is 150 nm (8.3 eV).

4. Acknowledgment

The support of DARPA, DOE, and ONR is gratefully acknowledged. We wish to thank the NBS Synchrotron Ultraviolet Radiation Facility for providing beam time and technical assistance.

References

[1] Weber, M. J., Cline, C. F., Smith, W. L., Milam, D., Heiman, D., and Hellwarth, R. W., Measurements of the electronic and nuclear contributions to the nonlinear refractive index of beryllium fluoride glasses, Appl. Phys. Lett. 32, 403 (1978).

[2] Poole, R. T., Szajman, J., Leckey, R. C. G., Jenkin, J.G., and Liesegang, J., Electronic structure of the alkaline-earth fluorides studied by photoelectron spectroscopy. Phys. Rev. B12, 5872 (1975); Poole, R. T. Jenkin, J. G., Liesegang, J., and Leckey, R. C. G., Electronic band structure of the alkali halides. I. Experimental parameters, Phys. Rev. B11, 5179 (1975).

[3] Williams, R. T., Nagel. D. J., and Kabler, M. N., Reflectance, fluorescence yield, and photoelectron spectroscopy of CaF_2 in the 10 to 100 eV range, J. de Physique (to be published).

Table I. Impurity analysis of sample SS-1643: pure BeF_2 melted in graphite.

K	5000 ppm (by weight)
Ca	300
Al	200
Mg	30
Si	30
B	6
Mn	4
Cr	3
Sr	2

Elements not detected:

Na	< 300 ppm
Fe, Nb, Sb, Zr	< 30
Ba, Cd, Pb, Ti, Zn	< 10
Bi, Co, Cu, Mo, Ni, Sn, V	< 3
Ag	< 1

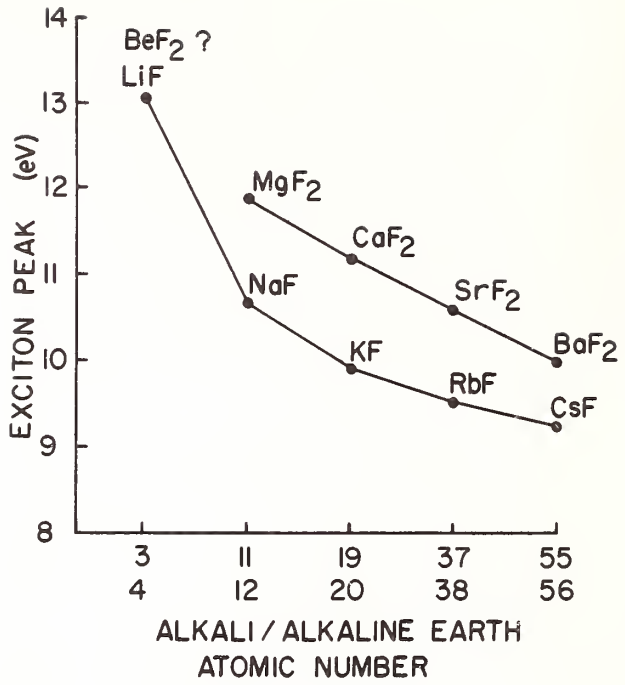

Figure 1. Empirical trends of the valence exciton peak energy in alkali fluorides and alkaline earth fluorides.

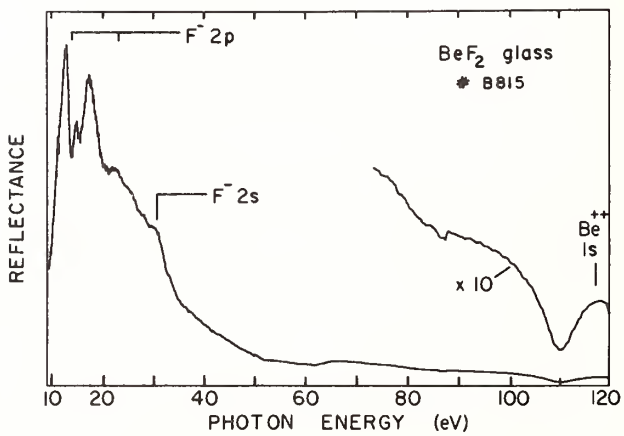

Figure 2. Reflectance of BeF_2 glass with probable atomic-level origin of features noted.

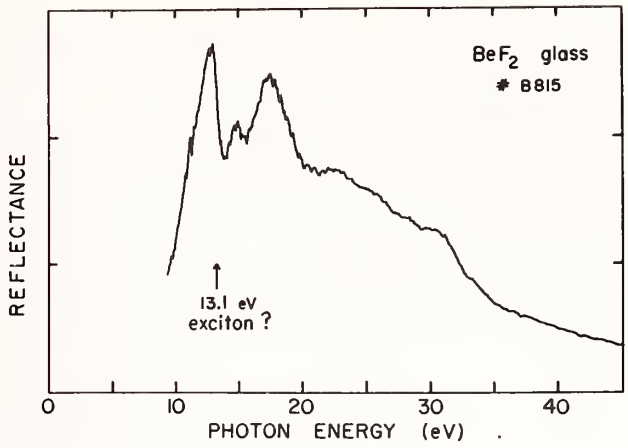

Figure 3. Reflectance of BeF_2 glass showing suggested position of the lowest exciton resonance.

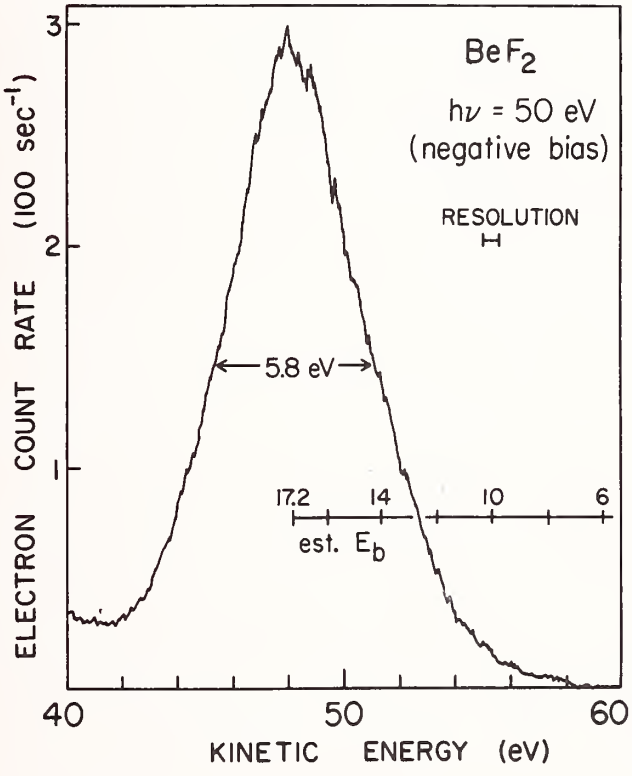

Figure 4. Energy distribution curve of photoelectrons excited from BeF_2 glass by 50 eV photons, under conditions of negative sample charging by an electron flood source (filament). The binding energy scale is estimated by comparison to Ref. 2.

THE ROLE OF Fe IN LASER-INDUCED DAMAGE IN ULTRAPURE KBr

D. F. Edwards and B. E. Newnam
Los Alamos Scientific Laboratory
Los Alamos, NM 87545

and

W. J. Fredericks
Oregon State University
Corvallis, OR 97331

ABSTRACT

The laser-damage threshold has been measured for several samples of ultrapure KBr crystals. Induced neutron activation analysis and thermal light scattering measurements indicate the major impurity to be Fe^{2+} with concentrations in the range .04-.095 ppm and radii in the 17-20 Å range. Other impurities either do not contribute to the scattering or are in concentrations 100 ppb or less. The measured damage threshold values were found to have the functional dependence on particle radius and pulse width predicted by the theory of Bennett.[1] Oxygen treatment to the KBr during the crystal growth process is observed to effect the damage threshold values. This suggests a damage mechanism that is related to a species derived from carbon. As an example, carbon present in the sample in ppb concentrations might be converted to CO which is covalently bound to the Fe. In this bound state the Fe no longer contributes to the laser damage.

NOTE: The authors withdrew this paper from publication in these proceedings in order to repeat the scattering measurements without the complication of surface-scattering contributions. When completed, these results will be published separately in the appropriate technical literature.

The speaker commented that no correlation was observed between the observed laser damage threshold and the iron concentration in the samples. He also remarked that he was aware of the difference in the damage thresholds observed in this work from those reported by Manenkov, but could not explain the difference. It was obvious that the source of the material used in the two experiments was different.

[1] H. S. Bennett, J. Res. NBS 75A (4), 261 (1971).

PROPERTIES AND FABRICATION OF CRYSTALLINE FLUORIDE MATERIALS FOR HIGH POWER LASER APPLICATIONS

T.M. Pollak, R.C. Folweiler, E.P. Chicklis, and J.W. Baer
Sanders Associates, Inc.
Nashua, NH 03061

and

A. Linz and D. Gabbe
Massachusetts Institute of Technology
Cambridge, MA

Crystalline fluoride materials exhibit certain desirable properties for applications in advanced laser technology. Fluorides are characterized by excellent ultraviolet transmission, low values of nonlinear index of refraction (n_2) and high optical damage resistance. Crystal growth temperatures of fluorides are relatively low; and scaling of growth to large diameters has been achieved, demonstrating fabrication capabilities of large apertures of high optical quality material.

This paper describes the fabrication and properties of two fluoride crystal families which exhibit a natural rare earth site. Two crystalline fluorides, Yttrium Lithium Fluoride (YLF), or $LiYF_4$, and Potassium Yttrium Fluoride (KYF), or KY_3F_{10}, have specific desirable properties for high power laser applications.

The optical performance of materials is very dependent upon the fabrication processes. Advanced material processing techniques have been developed, including feed purification and crystal growth techniques, which have been employed to fabricate fluoride crystals exhibiting excellent transmission, low scattering, and high resistance to laser damage. In addition, recent crystal growth developments have scaled the crystal growth of YLF to 100 mm diameter. Growth parameters were optimized to maintain proper crystal-melt interface to minimize the formation of defects. In addition, technical problems were addressed in scaling the crystal growth of YLF to 40 cm diameter.

Key words:
Advanced laser materials; Crystal growth; Crystalline fluorides; Faraday rotator; High power laser materials; Optical damage threshold; Top-seeded solution technique; Two photon absorption; Uniaxial crystal; Yttrium lithium fluoride

1. Introduction

The general materials requirements for advanced laser applications include high peak power and, in some cases, high average power propagation, together with material availability in large apertures of excellent optical quality. Crystalline fluoride materials exhibit certain properties inherently suited to these requirements. Furthermore, certain classes of these materials exhibit favorable spectroscopic, magneto-optic, or laser properties for specific component applications in advanced laser technology.

Optical materials for high power lasers are required for both passive components and active components. Passive components include lenses and windows; active components are laser materials and faraday rotators. The common requirements of all these components for high power propagation are related to the following specific material properties:

a. Nonlinear index of refraction (n_2): Low values of n_2 (the change in refractive index at high intensities) minimize the tendencies for self-focusing and beam breakup.

b. Optical transparency: Transparency at the operating wavelength and its harmonics is important to minimize two photon absorption and associated damage effects.

c. Material purity: Lack of inclusions which can become damage sites is essential for high power applications. These extrinsic defects can be a result of impurities in feed material or growth atmosphere.

In addition to the above properties, active components require appropriate spectroscopic properties for specific applications. Generally, these properties are obtained by including a dopant (active) ion in the crystal structure. Among the specific applications of interest are laser materials and faraday rotators. For such applications the dopant ion with the appropriate properties are trivalent rare earth ions. A host material with a natural lattice site for such ions is desirable to accommodate a wide range of dopant ion concentrations.

2. Crystalline Fluorides

Crystalline fluoride materials exhibit low values of n_2; transparency over large spectral ranges, and high optical damage thresholds. In addition, growth temperatures of fluorides are relatively low, enabling growth of crystals with minimal induced thermal stress. Crucible solubility at the growth temperatures is undetectable and will not lead to inclusions or defect centers. Generally, fabrication techniques of fluorides are well advanced and are capable of producing large diameter single crystals displaying high optical quality.

Two crystalline fluorides, YLF ($LiYF_4$) and KYF (KY_3F_{10}), have specific desirable properties for high power laser applications. YLF has been noted as a very unique laser host. More YLF laser transitions have been documented than in any other host. KYF, although still under development, displays excellent potential as a laser host and as passive elements due to its isotropic nature. The cubic structure of KYF allows the potential use of hot forging techniques to expand aperture size. In addition, the scalability of crystal growth for these materials has been demonstrated in recent programs at Sanders. As a result, YLF and KYF have excellent potential for use as active and passive elements for high power lasers.

3. Properties of YLF and KYF

The properties of the crystal families of YLF and KYF are desirable with respect to the established criteria for optical elements, passive and active. Tables 1 and 2 summarize some of the properties of these materials. The calculated n_2 for YLF and the estimated n_2 for KYF are very low. YLF also exhibits one of the shortest ultraviolet cutoff wavelengths of the high power compatible materials. In addition, laser damage resistance appears very high. At 1.06μm, YLF displays the highest threshold damage of all neodymium laser hosts [1][1]. Additionally, recent measurements by Liu, et al [2], reported that the two photon absorption coefficient (β) for YLF was undetectable at 266 nm. These data all conclude that YLF will transmit high peak power, far into the UV wavelengths with minimum loss.

[1]Figures in brackets indicate the literature references at the end of this paper.

Table 1. Properties of YLF and KYF.

	$LiYF_4$(YLF)	KY_3F_{10}(KYF)	
STRUCTURE	TETRAGONAL (SCHEELITE)	CUBIC	
UV EDGE	120 NM	< 200 NM	
N_2 (ESU)	0.6×10^{-13}	0.6×10^{-13} (EST)	M. WEBER LAWRENCE LIVERMORE LABORATORY
k (W/CM-K)	0.06	0.03	
GROWTH TEMPERATURE (C)	820	1030	
APERTURES GROWN	10 CM	3 CM	
$\frac{\partial N}{\partial T}$ (λ = 442 NM) ($^oC^{-1}$)	-3.0×10^{-6} π POLARIZATION -0.8×10^{-6} σ POLARIZATION	-	J. RINEFRIERD, UNIV OF ROCHESTER
β_{TPA} (CM/MW)	$< 4 \times 10^{-6}$* λ = 266 NM	-	

*P. Liu, R. Yen, N. Bloembergen, "TWO PHOTON ABSORPTION COEFFICIENTS IN U.V. WINDOW AND COATING MATERIALS.

Table 2. Properties of KTb_3F_{10} and $LiTbF_4$.

	KTb_3F_{10}	$LiTbF_4$
CRYSTALLINE STRUCTURE	CUBIC (FLUORITE)	TETRAGONAL (SCHEELITE)
OPTICAL		
INDEX OF REFRACTION λ = 633 nm	1.50	n_e = 1.473 n_o = 1.502
NONLINEAR INDEX n_2 (10^{-13} esu)	~0.7 *	~0.7 *
- VERDET CONSTANT V (MIN/Oe-cm) λ = 633 nm T = 295°K	0.40 *	0.425 *
RELATIVE FIGURE OF MERIT** nV/n_2 λ = 633 nm	4.3 *	4.9 *

*Marvin Weber, Lawrence Livermore Laboratary

** Where Hoya FR-5 is 1

As a uniaxial crystal, YLF has two distinct optical directions. When oriented with its "C" axis parallel to incoming radiation, the YLF acts as an isotropic window. With its "C" axis in the plane of the window, YLF displays a polarization effect.

Unlike YLF, KYF exhibits a cubic structure which is advantageous for several applications. The UV transmission of KYF, although not accurately known, is expected to be similar to YLF. The KYF is presently under development and its performance will be further elevated.

Both YLF and KYF allow free substitution of rare earth ions (RE^{+3}) and little (if any) host interaction with the active ion. The established criteria for laser materials has indicated that both YLF and KYF are excellent candidate materials for high power laser application.

4. Crystal Growth

Sanders employs the top-seeded solution growth (TSSG) technique as described by Linz, et al [3], for growth of YLF and other fluorides. The TSSG method is a modification of the Czochralski growth technique. Various fluorides have been grown employing TSSG, including YLF, KYF, KTb_3F_{10}, and Ho:ErF_3.

The Czochralski technique, or modification of this technique, displays inherent advantages over other growth techniques in the fabrication of high optical quality crystals. Top-seeded techniques allow growth of crystals unrestrained by crucible walls, unlike many "bottom seeded" techniques; i.e., Bridgmen. The absence of physical contact can eliminate defects and residual stress caused by the restraint. The mixing performed by the rotation of the crystal in the top-seeded methods enhances impurity and dopant distribution within the melt and the crystal. This factor is especially critical with dopants with distribution coefficients much less than one; i.e., neodymium. Single crystal materials grown by these techniques typically display wavefront homogeneity and low scatter.

The concept of crystal growth with the TSSG technique can be illustrated employing the phase diagram of the LiF - YF_3 system, figure 1. The compound $LiYF_4$ is incongruently melting, meaning that upon solidification of the stoichiometric composition, a phase transformation would occur at a temperature of about 819^{o}C. To avoid this destructive transformation, excess LiF "flux" is added to the melt to form a "solution". The resulting growth temperature is lowered below the temperature of the phase transformation.

The design of the crystal growth module illustrated in figure 2 is specifically to grow optical quality fluorides. The furnace uses commercial vacuum components for basic construction and seals. This provides a system that can effectively prevent any interchange between the internal and external atmospheres for an extended period. The furnace is composed of two units connected by an isolation valve, allowing manipulation of the seed rod without disturbing the lower working chamber. System control is maintained with a digital process computer receiving inputs from thermocouples and an optical sensor. This system detects a bright spot reflected from the meniscus between crystal and melt, using a He-Ne laser indicating the position of the crystal edge. This signal is processed and a correction is made to the system proportional to the diameter of the crystal. This looping process allows fine, continuous control of the growth process for periods over 200 hours unavailable through manual operation.

Materials for application as optical components in high power lasers must not only display uniformity, but must be free of impurity ions to avoid absorption leading to damage or scattering from inclusions. Sanders has developed advanced material handling techniques to purify and maintain purity levels in fluorides for crystal growth. Raw materials are purchased in the highest commercial purity, and processed through wet chemical, zone refining, and hydrofluorinating processes. Purification methods are used which are applicable to removal of a broad spectrum of suspected impurities from commercial alkali, alkali-earth, and rare earth compounds. When the input feed is an oxide, carbonate, or water

soluble compounds, purification involves aqueous solution chemistry followed by synthesis of a solid purified fluoride. Starting with a commercial fluoride on the other hand, zone refining is the purification method applied. The final step is rigorous hydrofluorination to remove remaining anionic impurities.

Crystal growth atmosphere is as critical to the complete process as any components. Since fluorides easily convert to oxides at the growth temperature, a reducing or inert atmosphere must be employed during growth. Growth in a vacuum is not possible due to the typical high vapor pressures of fluorides. We employ high purity argon as a growth atmosphere. Argon will maintain melt purity as well as being noncorrosive to furnace elements.

This fluoride crystal growth facility produces optically uniform, low scatter crystals. A photograph of Nd:YLF laser material in wide usage is shown in figure 3. Crystal growth of boules of Nd:YLF occur in periods of 200 hours or longer. The automatic growth facility maintains fine control of growth parameters throughout the entire process. As a result, laser materials are routinely fabricated displaying adequate properties for high power laser applications.

5. Scaling of Crystal Growth

Scaling of the crystal growth process has been achieved in recent development work. Specific materials grown were RE:YLF, however, the process is adaptable to other fluorides. The initial advancement in the growth scaling program has produced single crystals of YLF to a diameter of 10 cm. Figure 4 illustrates a crystal of Er:YLF during the growth process.

The approach to growth scaling was to expand the previously described fabrication techniques. The TSS growth technique was applied by increasing the crucible diameter to 20.5 cm, figure 5, at its mid-height. Sanders has observed with fluorides along with other investigators of both silicon [4] and gadolinum-gallium-garnet [5] that a maximum crystal diameter/crucible diameter ratio of 0.5 to 0.6 is suitable to maintain uniform circulation patterns in the melt. Proper melt circulation is required to keep a homogeneous melt composition, and prevention of defect formation as a result of impurity segregation at the crystal interface.

Parameters utilized for the growth of smaller crystals were employed as the baseline for parametric development. Special attention was paid to the thermal gradient achieved, and its effects on the crystal-melt interface. Growth rate and crystal rotation rate were used as compensating factors to achieve stability throughout the entire process. Figure 6 displays two 6.5 cm boules of Tm:YLF and a 10 cm single crystal boule of Er:YLF.

Initial evaluation of the Tm:YLF crystals indicated that they are of good optical quality. Polariscopic examination of polished discs did not reveal any low angle grain boundaries. Preliminary interferometry indicated that the crystals have two or three waves (633 nm) of distortion in a 2 cm thick, 6.5 cm disc, but that most of this is in surface irregularities. Polishing is in progress to improve the surface figure and evaluate the bulk homogeneity.

6. Applications for YLF and KYF

YLF is a versatile material and is being used in a variety of systems. Over twenty transitions have been demonstrated to date in this host, ranging from 300 nm [6] to 3.9 μm [7]. Nd:YLF operating at 1.047 μm or 1.053 μm is a good spectral match for the advanced laser glasses and is used as an oscillator in laser fusion systems [8, 9].

Tm:YLF, pumped by an XeF laser, and emitting at 453 nm [10], is an efficient storage laser and is being developed for laser fusion applications. Ce:YLF [6] is a tunable UV laser whose range extends from 300 nm to 350 nm.

The terbium analogs of both YLF and KYF display excellent magneto-optical rotary power; i.e., high verdet constants, and low values of n_2. The combination of these two properties results in the highest figures of merit of all known faraday rotator materials.

Because of its transparency, low n_2, and its high optical damage threshold, YLF has great potential as high powered laser windows. As its UV cutoff is 120 nm, it may be suited to many of the new UV and VUV lasers being developed. As a uniaxial crystal, YLF exhibits birefringent properties; potential applications include wave plates and polarizers.

At the present time both the measurement of the properties and the technology of crystal growth of YLF and KYF are progressing. Growth scaling will continue towards the goal of 40 cm diameter. This effort will press the limits of top-seeded solution growth technology and involve evaluation of other crystal growth techniques.

Acknowledgment

The authors would like to thank the Department of Energy, Office of Laser Confinement Fusion, for the financial support of the crystal growth scaling development work.

References

[1] Birnbaum, M., DeShazer, L., Engineering design of repetitively Q-switched solid state lasers for precision range in applications, Contract NASA-23698.

[2] Liu, P., Bloembergen, N., Two-photon absorption coefficients in UV window and coating materials, Appl. Opt., 18, 7, 1015 (1979).

[3] Linz, A., Belruss, V., Kalnajs, J., and Folweiler, R.C., Top-seeded growth of oxide crystals from non-stoichiometric melts, Mat. Sci. Bull., 6 (1971).

[4] Wilson, R., Varian Associates (private communication).

[5] Brandle, C.D., J. of Appl. Phys., 49 (3), 1855 (1978).

[6] Ehrlich, D.J., Moulton, P.F., Osgood, R.M., Jr., Tunable UV solid state Ce:YLF laser at 325 and 309 nm, Technical Digest IEEE/OSA Topical Meeting on Excimers, Charleston, SC, Sept 11-13, 1979.

[7] Esterowitz, L., Echard, R.C., Allen, R.E., Long wavelength stimulated emission via cascade laser action in Ho:YLF, Appl. Phys. Lett., 35 (3), 236 (1979).

[8] Zimmerman, J., et al., Proc. Topical Meeting on Inertial Confinement Fusion San Diego, Feb, 1978.

[9] S.E. Stokewski, et al., Proc. Topical Meeting on Inertial Confinement Fusion San Diego, Feb, 1978.

[10] Baer, J.W., Knights, M.G., Chicklis, E.P. and Jenssen, H.P., XeF pumped Tm:YLF an excimer excited storage laser, Technical Digest IEE/OSA Topical Meeting on excimers, Charleston, SC, Sept 11-13, 1979.

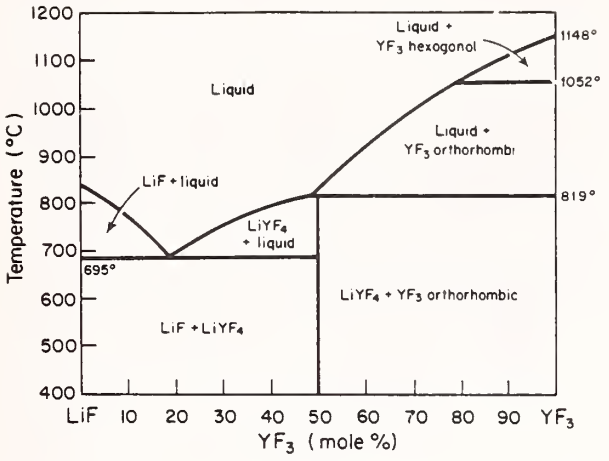

Figure 1. Phase diagram of LiF-YF_3.

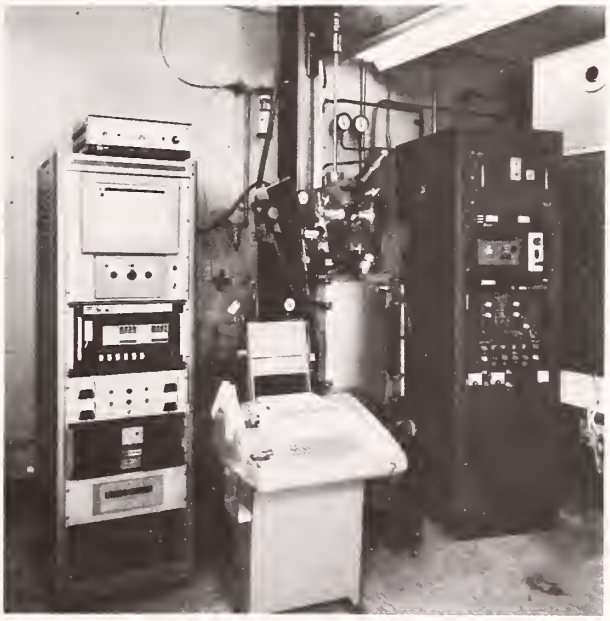

Figure 2. Crystal growth module.

Figure 3. Single crystal Nd:YLF laser material.

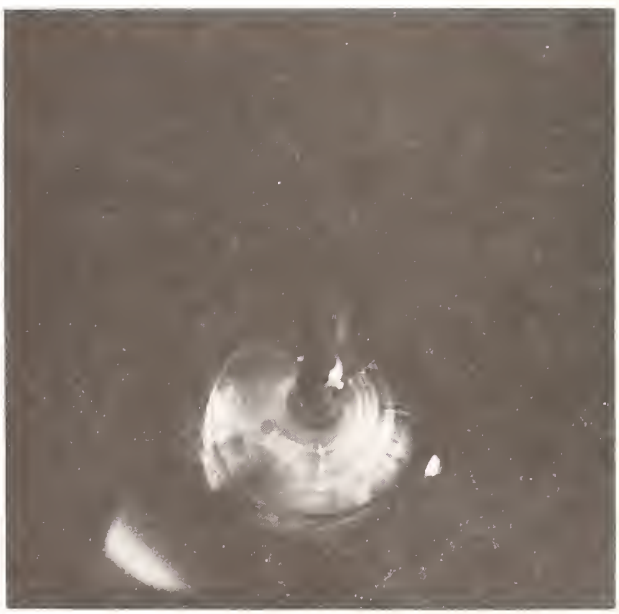

Figure 4. Er:YLF crystal during the growth process.

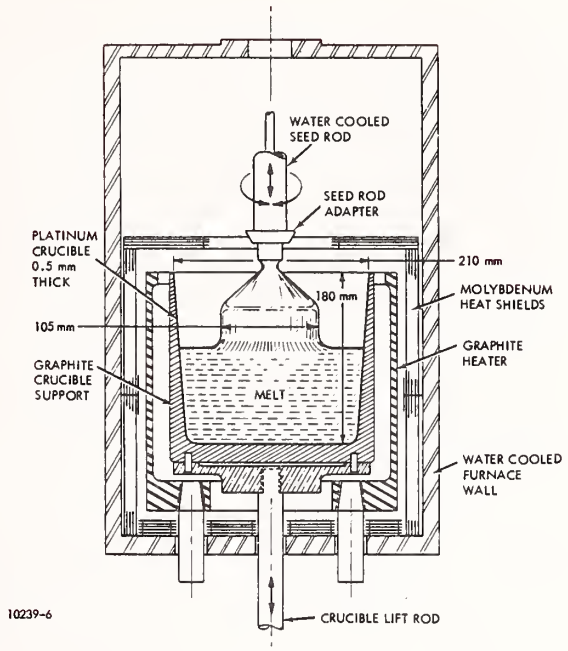

Figure 5. Crucible and furnace interior for growth scaling experiments.

Figure 6. Single crystals of rare earth doped YLF from growth scaling experiments.

LASER DAMAGE IN YTTRIUM ORTHOPHOSPHATE*

R. Allen, L. Esterowitz, and P.H. Klein
Naval Research Laboratory
Washington, DC 20375

V.O. Nicolai
Office of Naval Research
Arlington, VA 22217

and

W.K. Zwicker
Philips Laboratories
Briarcliff Manor, NY 10510

Preliminary laser-damage experiments on single-crystal blades of yttrium orthophosphate (xenotime, YPO_4) have been performed. Crystals, measuring about 15 X 3 X 0.7 mm were grown at Philips Laboratories by slow cooling of a flux containing lead pyrophosphate ($Pb_2P_2O_7$). Optical absorption is small from about 300 nm to about 3200 nm, approximating the transmission of calcite. A 1.06-μm Nd:glass laser with Q-switched pulse duration of 17 ns was used for damage measurements. The laser beam (0.025 cm FWHM) was focussed on the large face of the YPO_4 crystals. Visible damage was always observed at front and back crystal surfaces following exposure to pulses averaging 3.6 GW/cm^2 or more. No visible damage was found in YPO_4 at power densities less than 2.2-2.4 GW/cm^2. Calcite crystals showed damage at somewhat smaller power densities.

Key words: Absorption spectra, calcite, flux growth, laser damage, neodymium:glass, polarizer, pyrophosphate, yttrium orthophosphate, yttrium phosphate, xenotime.

1. Introduction

Its optical and mechanical properties combine to make mineral calcite the most popular polarizer material for use with laser systems. Optical-grade calcite has not been grown in the laboratory. As applications for lasers increase in number, optical-grade calcite becomes ever scarcer. The need for a replacement material with equivalent properties becomes correspondingly pressing.

Pertinent properties of calcite are compared with those of some other polarizers in Table 1. Soda-niter has an even greater birefringence than calcite, can readily be grown in the laboratory, but is too soft to polish readily and is extremely soluble in water. It has never been seriously suggested for widespread use with lasers. On the other hand, zircon has been proposed [1][1] as a laser polarizer. Its chief drawback is its relatively small birefringence, about one-fourth that of calcite.

Yttrium orthophosphate is twice as birefringent as zircon, harder than calcite, and insoluble in water. We report here some results of growth, spectroscopic, and laser-damage studies which give YPO_4 promise as a laboratory-grown, laser-tolerant polarizer material.

*Work supported in part by the Office of Naval Research.
[1] Figures in brackets indicate the literature references at the end of this paper.

Table 1. Properties of some polarizer materials.

Polarizer	Structure	At 589 nm: n_e	$n_e - n_o$	Moh's Hardness	Solubility
Calcite, $CaCO_3$	Hexagonal	1.4865	-0.1720	3.	Low
Soda-niter, $NaNO^3$	Hexagonal	1.2261	-0.2513	1.5-2.0	High
Zircon, $ZrSiO_4$	Tetragonal	1.968	+0.045	7.5	Low
Xenotime, YPO_4	Tetragonal	1.827	+0.107	4-5	Low

2. Crystal Growth

Yttrium orthophosphate was prepared by solution of yttrium oxide in excess lead pyrophosphate, and slow cooling of the melt. (Pyrophosphate conversion of yttrium oxide to the orthophosphate is well known, potassium pyrophosphate having been employed nearly a century ago [2].) A mixture containing 14 mole per cent of yttrium oxide and 86 m/o of lead pyrophosphate ($Pb_2P_2O_7$) was heated in a 100-ml covered platinum crucible at a rate of 300 C/h. When the upper surface of the melt reached 1400 C, heating was discontinued. The temperature was held constant for 2-6 h, with the bottom of the crucible 80 C cooler than the surface of the melt. The surface temperature was then lowered to 970 C at a rate of 4 C/h, maintaining the 80-C vertical gradient throughout the five-day cooling period. The crucible was then furnace-cooled to 100 C.

Crystals were removed from the flux by soaking in hot water. Blade-like specimens measuring 15 X 3 X 0.7 mm were common. The optic axis was found to lie parallel to the 3-mm dimension. The largest faces were optically smooth, and could thus be used without polishing for spectroscopic and damage experiments.

3. Absorption Spectroscopy

Ultraviolet, visible, and infrared absorption spectra were determined with a 0.7-mm-thick YPO_4 crystal. Surfaces were as grown. Surface contaminants were removed by rinsing with isopropyl alcohol just prior to measurement. Spectra were recorded in the range 210-2000 nm on a Cary Model 17 spectrophotometer. From 2.5 to 8.0 micrometers, spectra were recorded on a Perkin Elmer Model 283B spectrophotometer. All spectra were obtained with unpolarized light.

As shown in Fig. 1, the region of greatest transparency extends from 800 to 3000 nm. There are two prominent absorption bands, near 2000 cm^{-1} and 3000 cm^{-1}. These appear to be overtones of the 1000-cm^{-1} fundamental absorption, ascribed to P-O vibrations in the phosphate ion [3].

4. Laser Damage

Q-switched pulses from a 100-mJ Nd:glass laser were used for damage studies. Pulse length was 17 ns (FWHM). The beam was focussed to a 0.025-cm (FWHM) spot at the front surface of the sample by placing the sample 15 cm behind a plano-convex lens whose focal length was 18 cm. Polarization was parallel to the long crystal dimension for some measurements, perpendicular for others.

No damage was observed in YPO_4 unless accompanied by electrical breakdown of the air at the front surface. Damage was difficult to detect without a microscope. Only the front surface was damaged at low power densities, but both front and back surfaces were pitted at high power densities. For a given power density, occurrence of two-sided damage was somewhat dependent on polarization. With polarization parallel to the long (15 mm) dimension, two-sided damage took place about 90% of the time. With polarization parallel to the short (3 mm) dimension - the optic axis - two-sided damage was found only about 75% of the time. No difference was detected between results of N-on-1 and 1-on-1 studies.

For comparison, two types of calcite specimen were also subjected to damage. One group consisted of cleaved pieces of about the same thickness as the YPO_4 specimens. The surfaces of these had visible steps on them, which sometimes could not be avoided by the beam. The other group was a series of thicker slices, cut from a calcite polarizer assembly. These were then polished on a wax lap with 0.03-micrometer aluminum oxide (Linde A), using triacetin as a lubricant. Results are shown in Table 2.

Table 2. Damage with 17-ns pulses of 1.06-micrometer radiation.

Crystal	YPO_4	$CaCO_3$	$CaCO_3$
Surface	As-grown	Cleaved	Polished
Thickness, mm	0.7	0.6-0.7	1.4
Power density, GW/cm^2	Occurrence of damage		
Under 2.0	Never	Frequent	Rare
2.1-2.4	Never	Certain	Frequent
2.5-3.0	Occasional	Certain	Certain
3.1-3.5	Frequent	Certain	Certain
Over 3.6	Certain	Certain	Certain

As the table shows, yttrium orthophosphate crystals studied here appear to withstand more intense irradiation than do calcite specimens. Repeated measurements, on larger crystals of YPO_4 and on optically-finished calcite, will be needed to establish this conclusion. Work in progress, whose aim is preparation of larger YPO_4 crystals, may make it possible to perform the experiment.

5. Acknowledgement

We are grateful to R.C. Eckardt for supplying the calcite polarizer which was dissected for these measurements.

6. References

[1] Nicolai, V.O., Light polarizing prism of zircon, U.S. Patent 3,700,308, issued October 24, 1972.

[2] Duboin, A., On some double phosphates of yttrium and of potassium or sodium, Compt. rend. 107, 622 (1888).

[3] Nakamoto, K., Infrared and Raman Spectra of Inorganic and Coordination Compounds, 3rd edition, John Wiley and Sons, New York, 1978, p. 173.

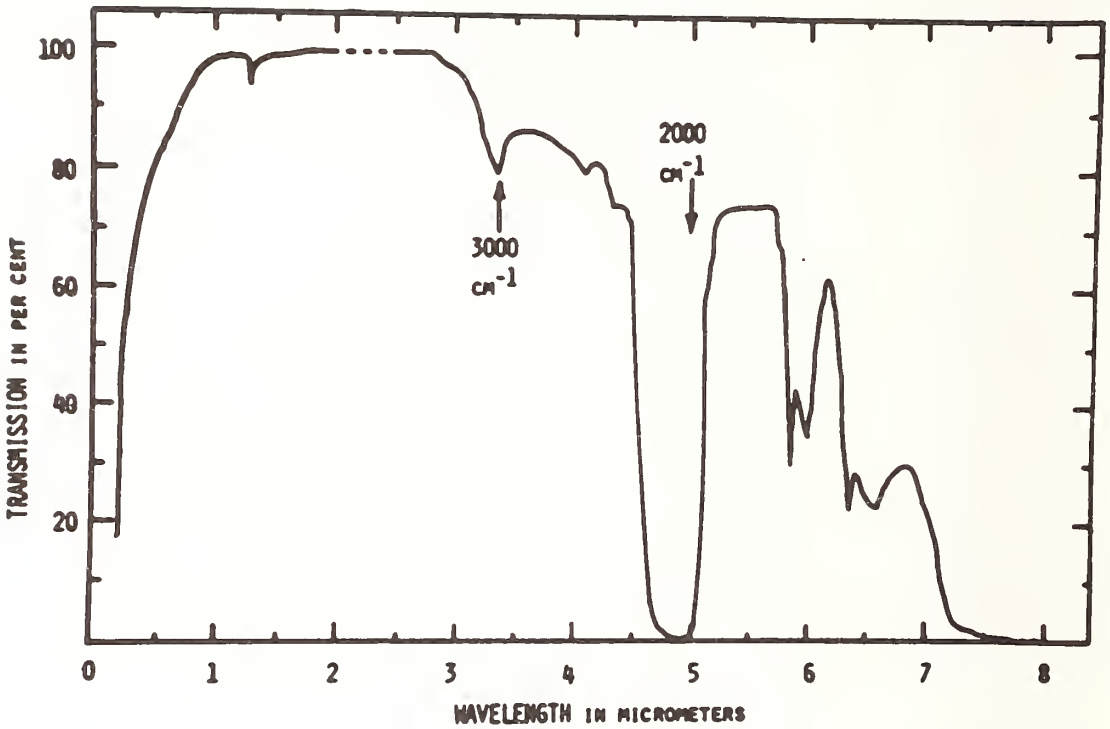

Figure 1. Absorption spectrum of yttrium orthophosphate.

The speaker indicated that yttrium orthovanadate should also be an attractive material, but that it has shown a tendency to hydrolize, whereas yttrium orthophosphate has not.

COMPRESSIVE FAILURE IN SAPPHIRE UNDER CO_2 LASER HEATING *

P. A. Miles and J. Gallagher
Raytheon Missile Systems Division
Bedford, MA 01730

and

R. L. Gentilman
Raytheon Research Division
Waltham, MA 02154

Irreversible changes have been observed in sapphire crystals subjected to surface heating by CO_2 laser irradiation at levels above 300 watts/cm^2. They are interpreted as due to plastic flow under compressive stress at temperatures above 900°C. The recognition of possible compressive failures in refractory oxides is of importance in defining laser tolerance levels in high power optics, in the design of laser heating experiments to assess the thermal shock resistance of materials, and possibly in the field of laser assisted machining of ceramics.

A detailed thermo-mechanical analysis has been carried out to predict the temperature and stress conditions throughout disk samples as a function of time, heat flux level and flux distribution. These calculations show that compressive stresses in excess of 200,000 psi were generated in our experiments. They also show that compressive failure is likely to precede tensile fracture in most experiments where partially heated disks are used.

Key words: Sapphire; plastic flow, compressive failure; laser damage; thermomechanical analysis.

1. Introduction

The mechanical failure of optical components exposed to high power laser radiation has been discussed and analyzed repeatedly since the first observations of distortion and fracture of NaCl windows in CO_2 lasers.[1-5] Attention has usually focused on the limits set by fracture under thermally induced tensile stresses at the cold edges of centrally heated windows. At the other extreme, the use of highly focused laser beams for the melting, evaporation or sublimation of a wide range of metals and other materials, the most recent example of which is the laser annealing ion implanted semiconductors,[6,7] can lead to the complete change in the physical state of the system without any evidence of tensile failure per se. These contrasting behaviors are explainable first in terms of the relatively low level of tensile stresses in the cold region surrounding very small heated regions, and second because of the lower ductility found in materials used as optically transmissive components. Although plastic flow in NaCl laser windows is well known,[1] it comes as a surprise to find conditions wherein laser heating over a relatively large area of a nominally brittle material such as sapphire can cause a 'failure' by induced ductility. A second example is the irreversible change observed in local heating of another ostensibly brittle material, CaF_2.[8] In retrospect, the explanation is quite straightforward - heat deposition at the material surface produces both high compressive and shear stresses in a region whose temperature is well above the ambient, and whose mechanical properties are different from those measured at room temperature. The purpose of this paper is simply to document our experiments on sapphire, and to set out a first order analysis of the temperature and stress fields developed in these tests.

* This work is supported by the Air Force Materials Laboratory, Wright-Patterson AFB, OH 45433 under Contract No. F33615-77-C-5280.

2. Experimental

The original purpose of these experiments was to demonstrate the superior resistance of sapphire to thermally induced stresses, as compared to other materials such as MgF_2, that are transparent in the mid-infrared range out to 6 μm wavelengths. To accomplish this, 2 inch diameter disks of sapphire, 1/8 in. thick, were exposed to a 10.6 μm CO_2 laser beam. The laser intensity was relatively uniform over a circle of 0.5 in. diam., centrally located on the disk (Fig. 1). Due to the very high absorption coefficient of sapphire at a wavelength of 10.6 μm, laser heating was confined to the first few microns at the surface. Heat deposition rates at the center varied between 100 watts/cm^{-2} and 10 kW/cm^2 for exposure times between 0.5 sec. and 10 secs. The appearance of the sample was recorded both by a video camera and videotape with a 16.6 msec frame time, as well as a high speed movie camera with a frame time of 10 msecs. In addition, a microphone was placed near the sample disk to record the sounds during or preceeding the point of fracture.

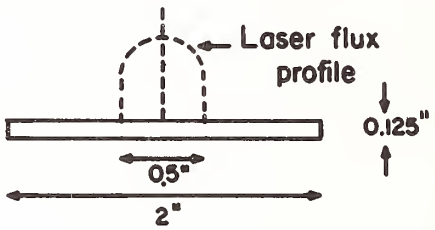

Figure 1. Sample and Laser heating geometry.

The results outlined in this paper are confined to the effects observed at input flux levels below 3 kW/cm^2. In this regime, two distinct effects were observed prior to the fracture and overall distintegration of the sample disk. The first of these was the appearance of a faint haze at the center of the heated region (Fig. 2a) that proved to be scattering of the light coming from the movie spot lights and indicative, therefore, of a change in the structure of the sapphire. The second effect was the appearance of a bright incandescence at beam center (Fig. 2b).

In contrast to these first two effects, the times-to-fracture showed the wide statistical variation expected from an effect that depends on the presence of preexisting structure defects. However, the average time-to-fracture did not follow the locus originally expected for tensile failure in a material whose thermo-mechanical properties were those as measured at room temperature, but, instead, lasted for relatively longer times at the higher incident flux levels. This result implies that the actual levels of tensile stress developed in the unheated region of the disk are lower than those predicted by a model that assumes a purely elastic behavior of sapphire at all temperatures.

Examination of the TV tapes showed that the initiation times for each of the first two effects was very consistent from one sample to another, and that as a function of the average laser intensity H (w/cm^2), each initiation time τ followed closely a relationship of the form (Fig. 3):

$$H^2 \tau = \text{const.}$$

Since the appearance of incandescence is itself an indication that a specific surface temperature has been reached, it is reasonable to associate each of the two lines with the expression for the temperature rise (ΔT) after a time, t, in a surface-heated dielectric of density, ρ, thermal conductivity, K, and specific heat, C, namely

$$(\Delta T)^2 = \frac{4H^2 t}{\pi K \rho C}$$

or

$$H^2 \tau = \frac{\pi}{4} K \rho C (\Delta T)^2$$

In fact, for the temperature changes experienced in these experiments, the value of K is reduced significantly from its value at room temperature (Fig. 4). In such cases, while steady state temperature profiles in locally heated regions can be treated analytically,[9,10] dynamic analyses require the numerical computations summarized in the next section.

Attempts were made to obtain samples that showed the initial scatter change, for later examination. This was done by shutting off the laser immediately after the appearance of scatter - an act that usually resulted in the immediate fracturing of the central region (Fig. 5). One such sample remained intact and showed obvious optical distortion in the central region and increased transmission under crossed polarizers before it,too, fractured. The evidence all points to the plastic deformation of the heated region under the action of compressive and shear stresses, followed by a tensile failure on cooldown.

Samples were all cut from Linde Czochralski-grown ingots with faces parallel either to the crystal basal plane (0001),* a rhombohedral plane (1012) or a (1123) plane. The onset of incandescence showed no dependence on sample type but the onset of scatter did so (Table 1). Whether these effects, which imply a temperature and stress change of 12%, were ones of visual perception only, or represented a distinct change in the plastic limits because of differences in resolved shear stress about the various crystal planes is uncertain. As it turns out, twinning under stress has been observed extensively in sapphire over a wide range of temperatures, but usually above 1000°C,[11-13] and can take place about both the basal and rhombohedral planes.

Table 1. Average onset times for scatter and incandescence at 650 W/cm ^{2}.

Sample Plane	Surface Scatter	Incandescence
$(10\bar{1}2)$	0.93 sec.	1.3 sec.
$(11\bar{2}3)$	0.67	1.3
(0001)	0.87	1.3

3. Analysis

The calculations of the temperature and stress fields in a sapphire disk with localized surface heating were carried out by computer in two stages using finite element techniques and modified codes AMGO 65 and AMGO 54,[14] respectively. First, a nonlinear heat flow analysis was performed which took into account the change in thermal conductivity over the range 0°C to 1700°C. Three specific values of input heat flux, namely 100 W/cm^2, 300 W/cm^2, and 1000 W/cm^2 were assumed for each such case. The resultant temperature profiles were then used to calculate the corresponding stress field in a perfectly elastic material whose (αE) value was constant, and set equal to an appropriate average value for sapphire at temperatures between 0°C and 1000°C, namely αE = 580 psi/°C. In fact, the elastic constants for sapphire depend on crystal orientation, and furthermore the most significant demonstration of these experiments is that its stress-strain curve must be nonlinear at high temperatures. Thus our calculations provide only an estimate of the stress levels at which plastic flow occurs, and, necessarily, give an overestimate of the tensile stresses existing near the point of fracture.

In order to simulate our specific experiment wherein a 2 inch disk was heated over the central 0.5 inch diam., the first calculations used this precise geometry, but with the simplification that the level of heat flux was held constant over the heated circle. Two other calculations that simulated surface heating over circles of 1.0 and 1.5 inch diam. were also made to explore the variation of stress field with heating geometry. The results of all three calculations are summarized briefly in figures 6-15.

The nonlinear aspects of the sample heating are most obvious for the highest heat flux, 1000 W/cm^2. Figure 6 shows the temperature generated on-axis in the top (irradiated) surface for this case. The upward deviation of the calculations from the line corresponding to the relationship

* Indices based on hexagonal unit cell with c/a = 2.73.

$$\Delta T = \sqrt{\frac{4t}{\pi K \rho C}}$$

derived from the linear theory is clearly seen over the range 0°C-1000°C and at times up to 0.5 second. By contrast, the downward curvature of the line at times beyond 0.5 second is a result of lateral diffusion of heat out of the region directly heated by the laser beam. In the temperature regions up to 1000°C, however, there is no signficant dependence on laser spot size between 0.5 and 1.5 inch.

The resultant stress fields are exemplified by the profiles of hoop stress (Figs. 7-12) at two specified times, namely 0.1 sec and 1 sec for each heating geometry and plotted for each of three parallel planes in the sample, the top surface (curves labelled 3, 40), the central plane (3, 30), and the back surface (3, 21). At all times, the maximum compressive stress is found on-axis in the top surface. The maximum shear stress also occurs at this point and is very close to one-half of the maximum compressive stress at all times. The stress on-axis in the central plane is weakly tensile at short times, changing to an intermediate compressive stress when significant heat diffusion through the sample thickness has taken place.

The maximum tensile stress occurs, as expected, as a hoop stress in the top surface at a point outside the circle heated directly by the laser. The radial profiles of stress clearly show the effects of lateral heat diffusion at t = 1 sec. For the 0.5 in. spot size, the magnitude of the tensile stress at the edge of the sample is some 35% of the tensile stress at the maximum, but these two stresses are virtually equal for the 1.5 inch spot at t = 1 sec. Indeed, the original choice of a 0.5 in. spot size in our experiments was made for this very reason, to minimize the chance that tensile fracture would be initiated by edge defects before failure could occur near the circle of maximum tensile stress.

It is instructive to plot out the time dependence of the maximum compressive and tensile stress levels (Fig. 13). At times up to 1 sec the former grows almost exactly as $\sigma_c \sim \sqrt{t}$, following, roughly, the actual temperature of the heated region. The tensile maximum, however, is expected to be proportional to the total heat input at short times, and therefore to vary linearly with time at times less than 10^{-3} sec, varying more slowly at later times as a the result of heat diffusion. By inference, the ratio of compressive/tensile stress maxima increases as the laser heating time decreases, so that tensile stress should be of little concern in short pulse heating, especially for small spot sizes. This latter point is brought out by comparing these curves with the compressive/tensile ratios for the other two cases (Figs. 14, 15). As the spot size increases, the compressive maximum decreases progressively, while the tensile maximum rises.

To return to our experiment, the computer models can be used to estimate the temperatures reached with 1000 W/cm^2 heating at which the scatter effect and the incandescence were seen. Adjusting for the fact that the actual laser flux on-axis is 25% higher than the average flux indicated in figure 3 gives values of 900°C and 1200°C, respectively, for these two effects. The levels of compressive and shear stress at the onset of scatter are estimated to be near, 200,000 psi and 100,000 psi, respectively.

4. Conclusion

The conclusions to be drawn from these efforts are more salutary than profound inasmuch as they are typical of a variety of experiments wherein intense heating is applied to small samples in an attempt to simulate the thermally induced tensile stresses experienced in domes, plates and cylinders exposed to conditions such as aerodynamic heating, jet exhausts and the like. Stress fields depend on geometry, size, and boundary conditions, and are not easily scaled. Small scale experiments, in general, require greater temperature differences in order to generate critical levels of stress. In turn, these elevated temperatures can lead to mechanical properties of the test piece that differ significantly from those observed in more normal operating regimes. As a consequence, conclusions drawn from small spot laser experiments as to the thermal shock resistance of materials are highly suspect. Experiments of this type can be useful only if the temperature dependence of mechanical properties are accurately taken into account.

A possible way out from this dilemma is the use of a partially inverted temperature nd stress distribution in flat plates produced by applying laser heating to an outer annulus, eaving the center of the disk unheated. This ensures that the edge of the disk is always n compression and further, that critical levels of tensile stress will be reached at the center f the disk before the edge is heated sufficiently to induce a failure in shear.

References

1] Horrigan, F. A., et al., Final Report, Contract DA-AH01-67-1589, Sept. 1968.

2] Sparks, M., J. Appl. Phys. 42, 5029 (1971).

3] Sparks, M., J. Appl. Phys. 44, 4137 (1973).

4] Sparks, M., and Chow, H. C., J. Appl. Phys. 45, 1510 (1974).

5] Miles, P. A., Infrared Laser Window Materials Meeting, Boulder, Colorado, 1976, p. 27.

6] Kachurian, G. A., et al., Sov. Phys. Semicond. 10, 1128 (1976).

7] Gat, A. et al., Appl. Phys. Lett. 33, 775 (1978).

[8] Detrio, J. A., and Petty, R. D., Laser Induced Damage in Optical Materials, NBS Spec. Publ. 541 (1978), p. 78.

[9] Lax, M., J. Appl. Phys. 48, 3919 (1977).

[10] Lax, M., Appl. Phys. Lett. 33, 785 (1978).

[11] Kronberg, M. L., Acta. Metal 5, 507 (1957).

[12] Conrad, H., J. Am. Ceram. Soc. 48, 195 (1965).

[13] Heuer, A. A., Phil. Mag. 13, 379 (1966).

[14] Brisbane, J. J., Tech. Rpt. S-198. US Army Missile Command Contract DAAH01-68-C-0891.

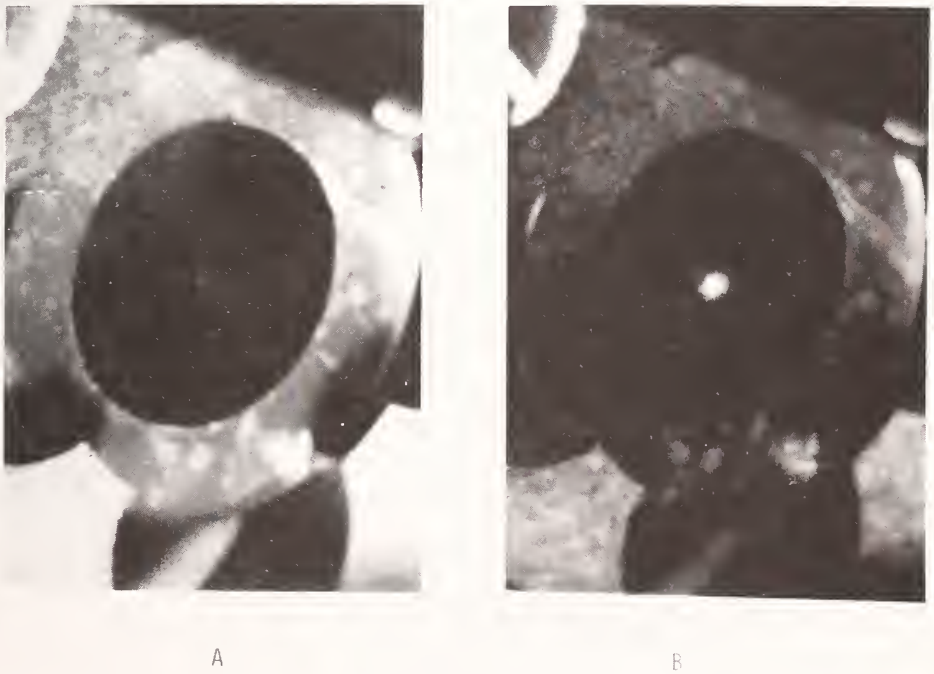

A B

Figure 2. Initial scatter and incandescence observed in laser heated sapphire. (A) scatter, (B) incandescence.

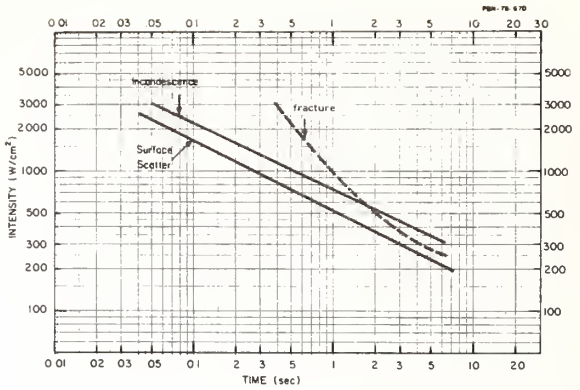

Figure 3. Loci of thresholds for scatter and incandescence and for the average time to fracture for laser heated sapphire disks.

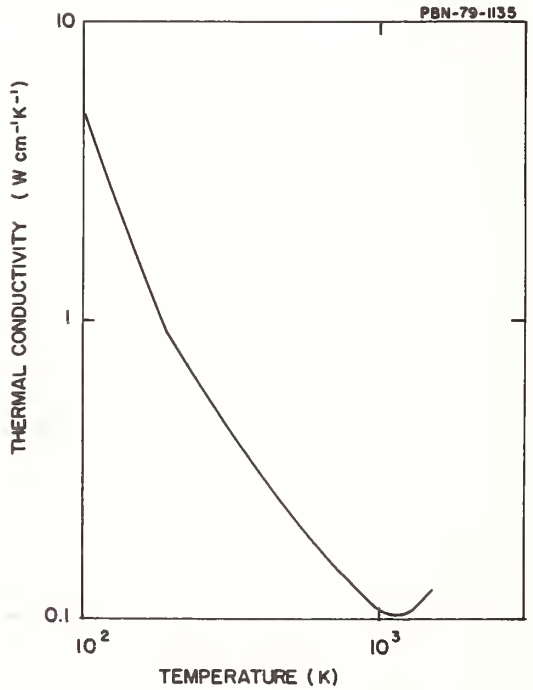

Figure 4. Temperature dependence of the thermal conductivity of sapphire.

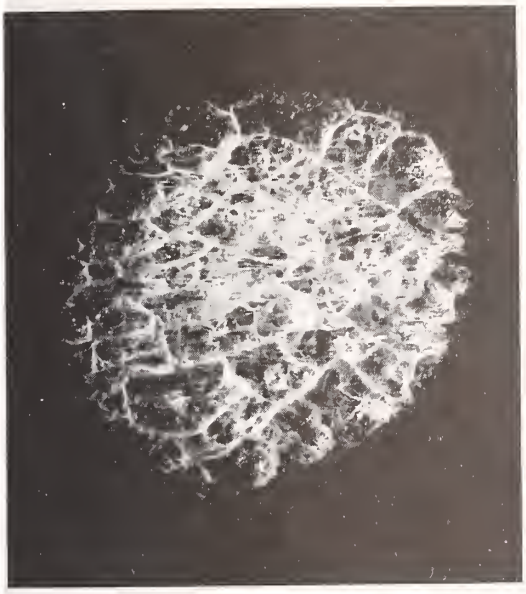

Figure 5. Fracture pattern in sapphire induced by cooling after laser shutdown.

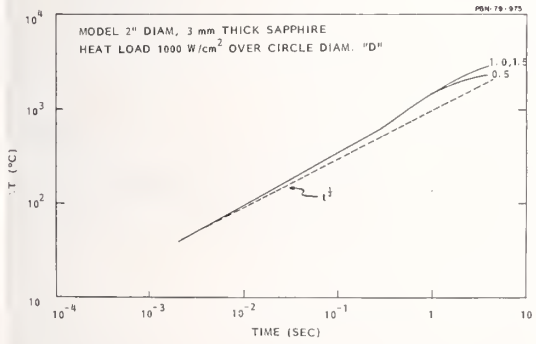

Figure 6. Temperature versus time for the on-axis central maximum of surface heated sapphire. Laser spot diameters 0.8, 1.0 and 1.5 in., respectively.

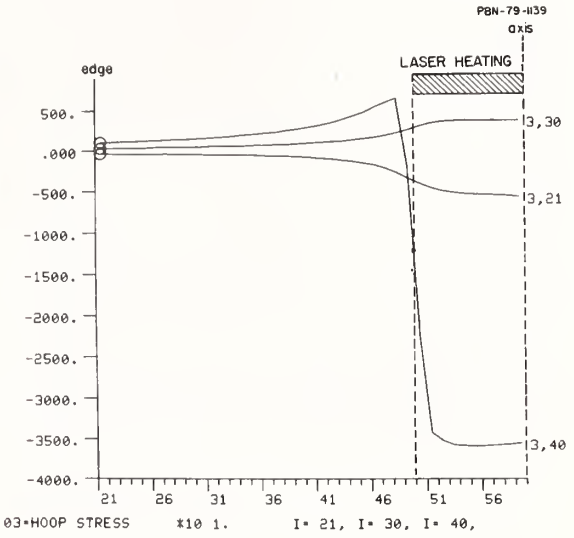

Figure 7. Hoop stress profiles for 0.5 in. diam. laser spot at t = 0.01 sec., stress scale factor 10.

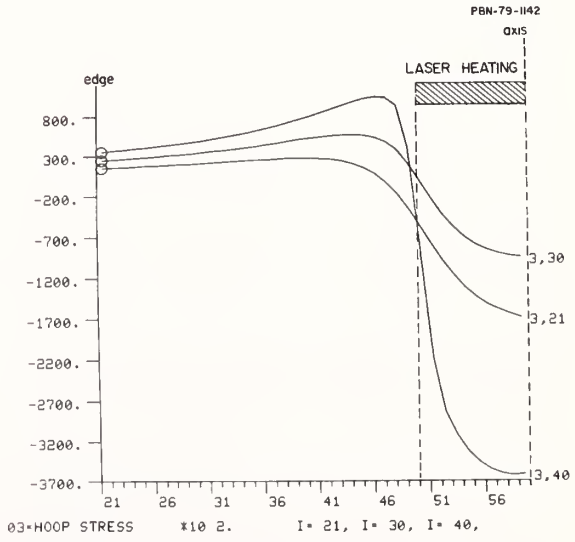

Figure 8. Hoop stress profiles for 0.5 in. diam. laser spot at t = 1 sec., stress scale factor 10^2.

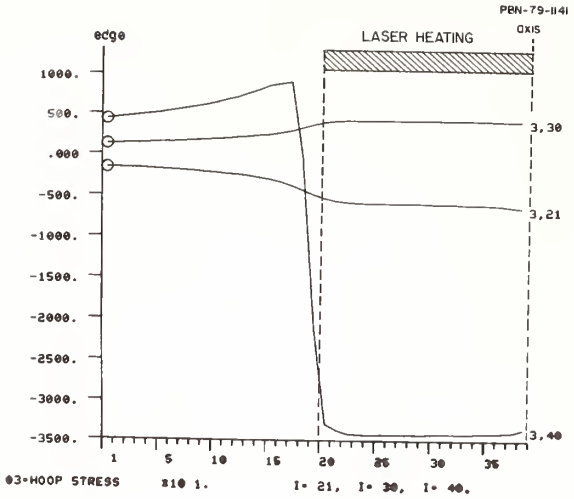

Figure 9. Hoop stress profiles for 1.0 in. diam. laser spot at t = 0.01 sec., stress scale factor 10.

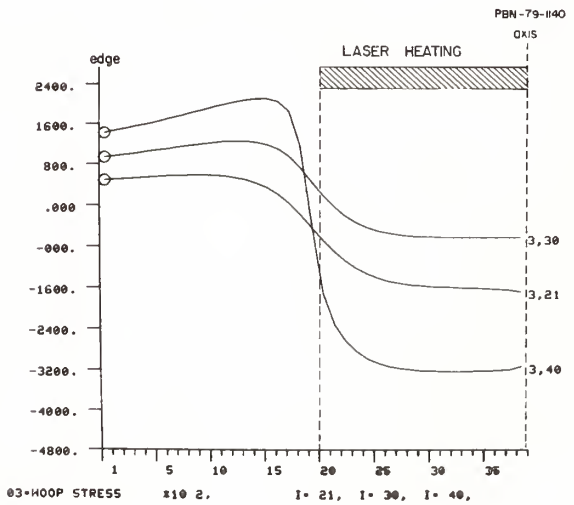

Figure 10. Hoop stress profiles for 1.0 in. diam. laser spot at t = 1 sec., stress scale factor 10^2.

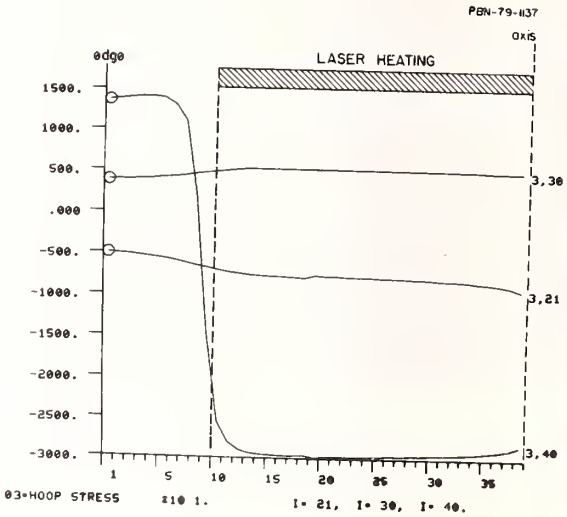

Figure 11. Hoop stress profiles for 1.5 in. diam. laser spot at t = 0.01 sec., stress scale factor 10.

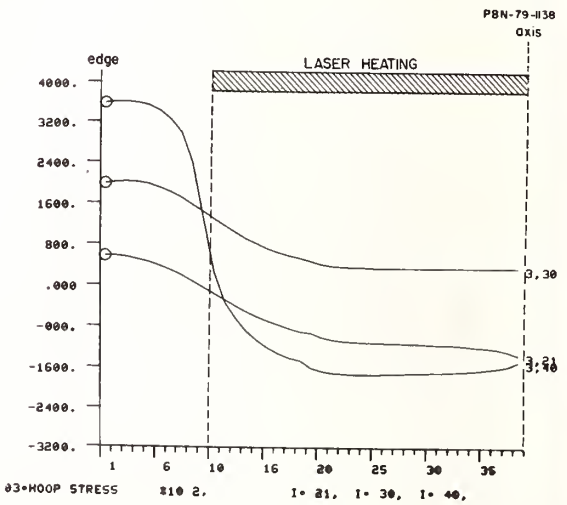

Figure 12. Hoop stress profiles for 1.5 in. diam. laser spot at t = 1 sec., stress scale factor 10^2.

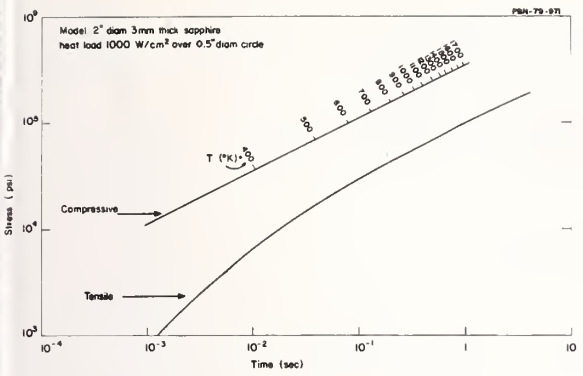

Figure 13. Time dependence of compressive and tensile stress maxima for a laser spot of 0.5 in. diam.

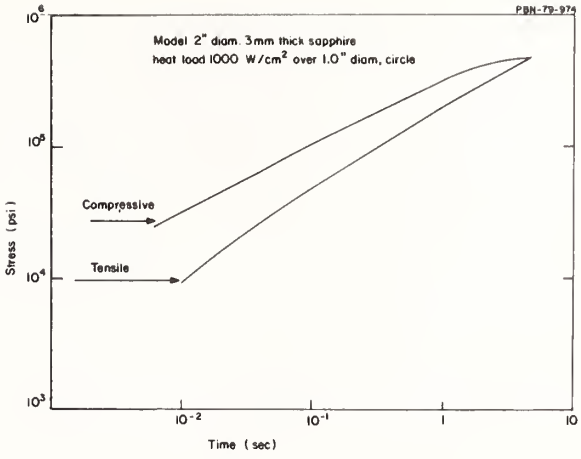

Figure 14. Time dependence of compressive and tensile stress maxima for a laser spot of 1.0 in. diam.

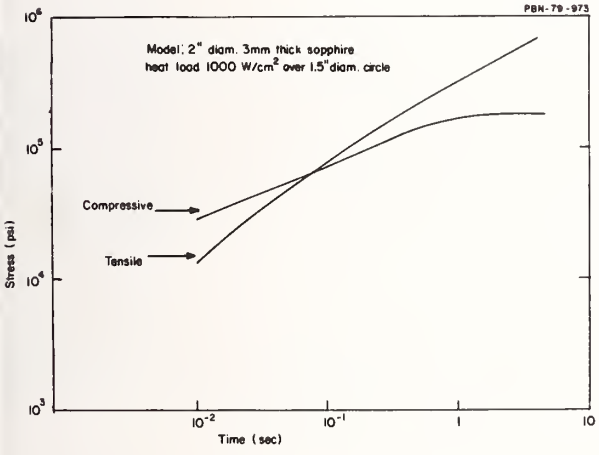

Figure 15. Time dependence of compressive and tensile stress maxima for a laser spot of 1.5 in. diam.

The speaker indicated that the sapphire used in these experiments was commercially-obtained Linde sapphire, and that although the observed incandescence was not sensitive to the orientation of the crystal samples, the fracture observed did depend on the crystal orientation. He remarked that zero-degree cuts were stronger than 60-degree cuts and the fracture was observed in rhombohedral planes. He indicated that the observed scattering seemed to come from induced variations in crystal structure on or near the sample surface.

FAILURE CRITERIA FOR LASER WINDOW MATERIALS

John A. Detrio, George A. Graves
University of Dayton Research Institute
Dayton, Ohio 45469

and

James M. Wimmer
AiResearch Mfg. Co.
Phoenix, Arizona

The brittle mechanical behavior of laser window materials must be considered in the establishment of failure criteria for selecting candidate materials and in the design of window components. The statistical techniques employed in brittle materials design and analysis are reviewed. The influence of the limited plasticity observed for the alkali halides, which exhibit fracture failure, is also discussed.

Key words: Brittle failure; failure criteria; flaws; fracture; K_{Ic}; laser windows; Weibull; yield stress

1. Introduction

The selection of a laser window material for a specific application usually results in the consideration of trade-offs between optical and mechanical properties [1,2].[1] To date, the two material properties usually considered in the trade-off are the thermally-induced optical distortion coefficient and the ultimate strength. The optical distortion, which is dominated by the temperature dependence of the index of refraction (dn/dT) or stress optics effects, has been explored in detail elsewhere [2-4]. The purpose of the present paper is to examine the mechanical failure criteria for window materials in greater detail since all of the infrared laser window materials of current interest exhibit brittle fracture when subjected to tensile stresses.

Completely brittle materials are characterized by the lack of any appreciable ductility prior to catastrophic failure by fracturing. The failure of brittle materials is controlled by the presence of defects or flaws, the size of which determine the "strength" of a window. Since these defects are the result of a chance occurrence in use, growth, or fabrication, the strength is a statistical property of the finished part.

These three elements; the absence of yielding, flaw sensitivity, and the statistical nature of failure require a different approach to the interpretation of the strength of a brittle window material. Specifically, the failure criteria must be stated in statistical terms, i.e., in terms of the reliability required of the window. One of the most important consequences of this statistical nature of failure is that the prediction of survival of full-sized components from data obtained on small test specimens requires an appropriate theoretical model.

2. Failure Criteria

The emphasis of this work is on the failure criteria for brittle materials and is therefore especially relevant to ZnSe and CaF_2 which are completely brittle at room temperature. The type of failure observed in alkali halides, will be briefly discussed first and then a criteria for brittle materials will be presented.

[1] Figures in brackets indicate the literature references at the end of this paper.

The alkali halides frequently fracture upon cooling following laser irradiation [5]. This phenomenon is generally thought to occur by the following mechanism [6]. When the relatively small central portion of the window is heated by absorption of the laser radiation, this material expands against the cooler outer region which constrains the expansion, resulting in localized compressive stresses. The compressive forces produce shear stresses that exceed the yield strength of the material and this yielding is the primary failure mechanism. The failure is detected on cooldown because the plastically deformed region cannot relax to its original configuration resulting in tensile forces which produce fracture.

The ultimate failure of KCℓ and NaCℓ, even with the limited ductility, is of a brittle nature. The fracture process requires flaws or cracks, and tensile forces which tend to open the cracks. Based on experimental observation, the best failure criterion for the alkali halides is the critical resolved shear stress, τ_{ys}. This stress is related to the yield stress, τ_{ys}, found in simple tension or compression experiments according to

$$\tau_{ys} = \sigma_{ys}/2 \ .$$

3. Brittle Fracture

Materials that fracture without exhibiting plasticity are defined as brittle. The failure of these materials is assumed to initiate at preexisting flaws and the "weakest link", i.e. the largest flaw, defines the failure stress. As a result, specimens prepared from the same lot of material demonstrate a distribution in fracture stress which is best described in a statistical fashion.

According to the Griffith theory [7] the flaw size is related to the fracture stress according to

$$\sigma = \frac{1}{Y} [(E\gamma/a)]^{1/2} \qquad (1)$$

where, Young's modulus, E, and the fracture surface energy, γ, are the material parameters which describe the fracture process. The flaw size, a, is a material fabrication or handling related quantity while Y is a geometrical factor related to the flaw type and location. An example of the relationship between stress and critical flaw size is shown in figure 1.

Flaws may have a variety of orientations relative to the applied stress but for brittle material those stresses which tend to open or lengthen the crack are of primary importance. Therefore, a flaw whose crack plane is normal to a tensile stress field is in the most favorable position for initiating fracture.

The driving forces acting at the crack tip and tending to propagate the crack can be described in terms of the stress intensity factor, K. Three stress intensity factors are required to describe the driving forces for a crack at an arbitrary angle, $90° > \theta > 0°$, to a tensile stress. K_I describes simple Mode 1 crack opening, while K_{II} and K_{III} describe the two shear modes of crack propagation. In brittle materials, fracture always propagates normal to the tensile stress, i.e. by Mode I crack opening although Mode II and III may influence the fracture initiation site.

The relationship between K_I and the normal stress is

$$K_I = Y\sigma a^{1/2} \ . \qquad (2)$$

When the stress intensity reaches the critical value (K_{Ic}), then fracture occurs. The critical stress intensity factor, K_{Ic}, is a material parameter and describes a material's resistance to fracture initiation. Comparing eqs. (1) and (2) it is evident that K_{Ic} can

be described in terms of the elastic modulus and fracture surface energy. Equation (2) can be used to determine K_{Ic} experimentally by one of a number of fracture mechanics tests. In general, these tests determine the stress required to propagate a macrocrack of known size and geometry for which a value of Y is available. For the case of a notch placed perpendicular to the length across the tensile surface of a 4-point flexural test bar, Y is given by [8]

$$Y = 1.99 - 2.47(a/h) + 12.97(a/h)^2 - 23.17(a/h)^3 + 24.8(a/h)^4 \qquad (3)$$

where a = notch depth
h = specimen thickness.
This type of fracture toughness specimen is referred to as a single edge notched beam (SENB) specimen.

4. Failure Predictions

The statistical properties of the failure of brittle materials under load can be described by a mathematical model due to Weibull. The distribution function is general in describing a wide range of material responses, but it was derived on the assumption of a random distribution of flaws with a distribution of sizes. The material is assumed to fail when the stress in the weakest region (worst flaw) reaches the critical value.

Because of the distribution of flaws, large specimens are more likely to contain a large flaw than small specimens. The Weibull model provides a procedure for scaling between parts of different sizes. A form of the Weibull model which applies to isotropic materials under uniaxial loads is described by the following equation. This equation predicts the distribution of strength as controlled by flaws within the volume of the material.

$$F(n) = 1-\exp\left\{-\int_V [(\sigma_n-\sigma_u)/\sigma_o]^m \, dV\right\} \quad . \qquad (4)$$

The parameters have the following definitions: F(n) is the cumulative fraction of failures observed at the applied stress σ_n. σ_u is the "zero strength" location parameter which is the stress level below which there will be no failures. σ_o is a scale parameter, m is the shape parameter which conveys the dependence of the distribution function on the flaw population. This latter parameter is also referred to as the flaw density exponent. The reliability, R equals 1 - F. An analogous expression can be written for surface flaws by replacing the volume integral with an area integral. Figure 2 shows some typical failure versus stress data for several brittle window materials.

Equation (4) explicitly describes the scaling rule through the volume integral. The quantities σ_u, σ_o and m are material parameters. In practice the parameters do not scale in the same manner as predicted by parameters obtained from small test specimens. This lack of predictability results from the relief of localized residual stress during the cutting and polishing of small test specimens that may remain in a large piece of material used to fabricate full size windows.

Figure 3 illustrates the fundamental differences between scaling the response of ductile materials (metals) and brittle materials. Both kinds of materials are described by a Weibull distribution. The difference between the two kinds of material is in the value of m, the shape parameter. Metals generally have values of 40 or more while a typical brittle material may have a value of 5. The example shown assumes equal mean strength values for small volume test specimens. Note that upon scaling the volume by two decades (volume of 100) the strength of the ductile component is only slightly degraded while the brittle material will, on the average, fail at less than half the applied stress.

In the window materials of primary interest fracture has been observed to usually initiate at surface flaws [9]. Two principal stresses can exist at the surface and, unlike the uniaxial stress distribution assumed in the elementary Weibull case, the total reliability will depend in general upon the effect of both stresses.

One approach to calculating the reliability in the case of biaxial stresses is to assume that each principal stress acts independently. The reliability can then be taken as the product of the reliability associated with each principal stress. In the case of a varying stress distribution the surface area can be divided into elements over which the principal normal stresses are essentially constant. The reliability of the i^{th} element is then given by

$$R_i = R(\sigma_1)\, R(\sigma_2)$$

where σ_1 and σ_2 are the principal stresses. The total reliability of the surface is then given by

$$R_{total} = R_1 R_2 \ldots R_i \ldots R_n \ .$$

Since the independent stress assumption may be nonconservative in some cases, alternate approaches [10] to reliability predictions may be preferable.

5. Flaws

There are at least three sources of flaws that may influence the survival of a laser window. They may be introduced in manufacturing, in handling, and in use. Manufacturing flaws can be present on the surface or in the bulk of the material. Surface flaws usually originate during grinding and polishing steps while volume flaws consist of such defects as inclusions or porosity and are related to the initial processing of the material. The manufacturing flaws are accounted for in the survival prediction if the witness specimens are properly selected and prepared. The major assumption (which should be verified) is that the same flaw population controls the strength of both the test specimens and the optical component. The flaws introduced by improper handling should be guarded against by the establishment of good handling procedures, special fixtures, and installing an awareness of the nature of brittle fracture in those responsible for handling the optical component. Handling flaws can be accounted for in the survival prediction if the window is inspected and proof-tested periodically. Flaws that are introduced in use, especially during irradiation represent a special problem because of their unpredictability. The flaws generated in use can result from the heating of intrinsic defects such as small absorbing inclusions which are not relevant to the mechanical strength when not irradiated or they can result from extrinsic defects such as dust motes which land on the window and are subsequently irradiated. The irradiated defect acts as a local stress rise and may initiate a larger crack. The influence of a proof-test on survival probability is illustrated in figure 4.

6. Stresses

The stresses which result in fracture of a brittle material are always tensile in nature although, as noted above, the alkali halides can be damaged by compressive forces. The stresses of primary interest are the result of thermal gradients introduced into the window by the absorption of the laser radiation. The thermal gradients can exist on two scales; localized which we define to be on the order of the size of a critical flaw or macroscopic in which the stresses are distributed over a large area or volume of material. In large windows localized stresses can be responsible for the formation of cracks or for the initiation of crack propagation although the distance traveled is small due to the limited extent of the stress field. The macroscopic stresses provide the energy required for fracture propagation and the ultimate catastropic failure of the window. The stresses on the two scales may work together to fracture the window.

The overall temperature rise in the center of a sample creates thermally induced stresses while a heated defect acts as a stress riser and crack nucleation site. Ring fractures are frequently associated with surface contaminants on brittle materials. In those cases in which the strain energy from overall heating is large, the ring fractures will nucleate cracks which propagate across the sample. In some cases, the heated defect will nucleate a crack which is kept closed by thermally induced compressive stresses, but which propagates when the specimen goes into a state of tensile stress upon cooldown following the irradiation. The tensile stresses may develop either through rapid surface cooling which is unlikely in a typical window configuration which does not involve an active cooling system; or, more likely, the tensile stresses develop when the surface has been permanently deformed by compressive stresses which produce yielding while the beam is on. Once permanent deformation has occurred, the material cannot relax to its former dimensions without generating large tensile forces.

The observation of yielding due to compressive stress is not inconsistent with the brittle nature of the material. Under a tensile load fracture would occur before the stress reaches the value required for yielding while under a compressive load, fracture is suppressed and yielding may occur. The amount of plasticity is restricted by several factors. A single crystal or large-grained material requires that an active crystallographic slip system be favorably oriented in the stress field. A polycrystalline material requires that slip be transmitted from grain to grain; this can occur only if the material has five active slip systems.

7. Other Factors

The calculation of the reliability of a brittle component is complicated by several additional factors. The most troublesome problem is slow crack growth which generally takes place by a stress corrosion mechanism. It is believed that this mechanism is responsible for the sudden failure of windows which have previously performed without any detectable mechanical problems [11]. The corrosive agent for many window materials is water or water vapor. In most practical situations the corrosive agent will tend to concentrate at the crack tip where the stresses are greatest. Since both stress and the corrosive medium must be present, slow crack growth usually occurs only under load.

Residual stresses introduced during forming or fabrication processes also tend to complicate reliability predictions because they are usually not well characterized and are not necessarily obtained from an analysis of the failures of small test specimens. The useful application of the scaling law therefore requires that the flaw distribution and material itself be the same in both the small test specimens and the large component.

The effect of cyclic loading and vibratory loads may be a problem in certain window applications and environments. Vibratory loads of low amplitude do not necessarily represent a serious problem in laser windows but the total load, static stress plus peak cyclic stress must be considered in establishing the reliability of a window.

Mounting stresses are also of practical importance in the use of brittle materials. Care should be used to avoid transmitting stresses from structural members to the windows and a rigid bezel or mounting frame should be used to minimize the transmission of flexural deflections to the window. A thick resilient mounting gasket is also desirable to minimize the transmission of environmental stresses. The procedures used to fasten the window in place should be carefully tested to minimize the generation of mounting stresses by the application of unequal torque or bending. Stress risers should be carefully avoided as should any type of localized stress at window-to-metal contacts which can result in Hertzian-type damage.

8. Acknowledgments

The support of the Air Force Materials Laboratory, Wright-Patterson Air Force Base, Ohio is gratefully acknowledged. The contractual effort concerning the mechanical characterization of infrared window materials is monitored by Mr. Charles Strecker. The optical characterization of laser window materials has been monitored by Dr. G. Edward Kuhl and Dr. Walter Knecht. The authors especially wish to thank Dr. John Wurst of UDRI for many informative and helpful discussions.

9. References

[1] Sparks, M., J. Appl. Phys. 42, 5029 (1971).

[2] Sparks, M., and Cottis, M., J. Appl. Phys. 44, 787 (1973).

[3] Klein, C.A., Infrared Phys. 17, 343 (1977).

[4] Klein, C.A., Infrared Phys. 18, 251 (1978).

[5] Klein, C.A., This Conference.

[6] Loomis, J.S., *Fourth Conference on High Power Infrared Laser Window Materials 1974.*

[7] Griffith, A.A., Phil. Trans. Roy. Soc. (London) A221, 163 (1920).

[8] Brown, W.F., Jr., and Srawley, J.E., "Plane Strain Crack Toughness Testing of High Strength Metallic Materials," ASTM Special Tech. Publ., No. 410, ASTM, Philadelphia, PA, 1966.

[9] Freiman, S.W., Mecholsky, J.J., Jr., Rice, R.W., J. Am. Ceramic Soc. 58, 406 (1975).

[10] Batdorf, S.B. and Heinisch, H.L., Jr., J. Amer. Ceramic Soc. 61, 355 (1978).

[11] Arnett, C.H., Optical Spectra, May 1979, Letter to the editor.

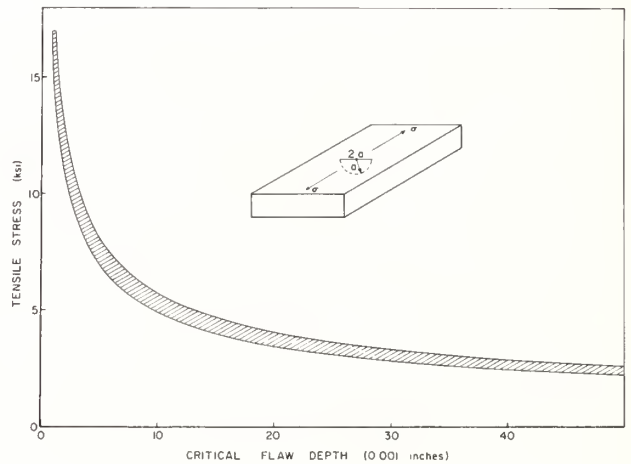

Figure 1. The relationship between Mode I tensile stresses and the critical flaw size is shown for ZnS. The graph is generated by the use of experimental K_{Ic} data in conjunction with eq. (2).

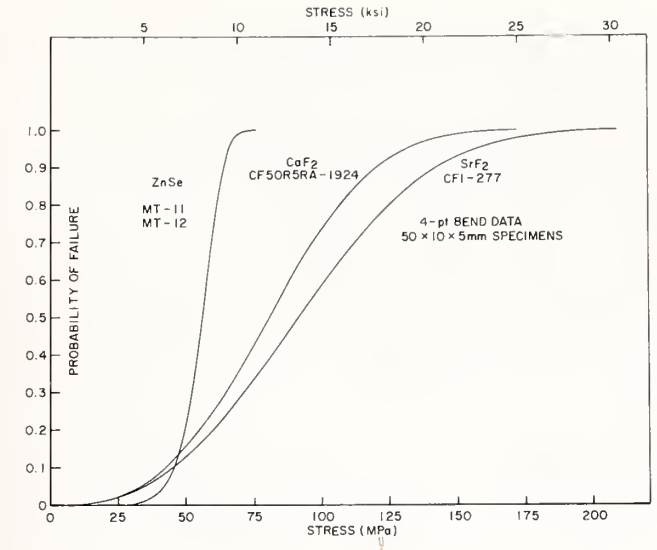

Figure 2. The results of fitting experimental data obtained from small coupon bend specimen testing are shown for CVD ZnSe, fusion cast CaF_2 and SrF_2. The fluorides have significantly higher mean strengths (stress at 50 % probability of failure) but a larger variation in failure stress.

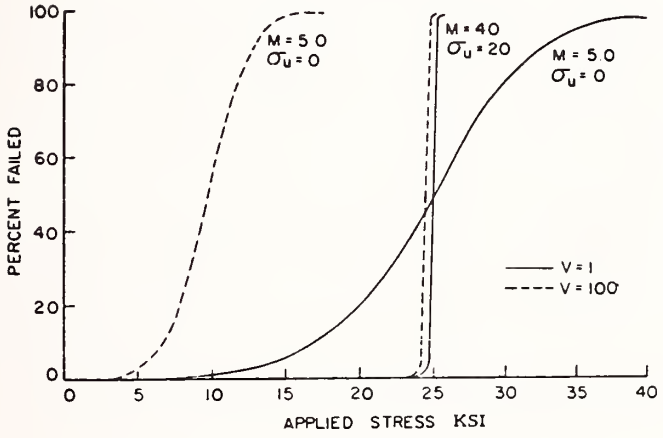

Figure 3. The effect of increasing the volume by a factor of 100 is shown for parts made with materials having equal mean strengths for small test coupons but different m parameters (standard deviation). The significant point being made is that in scaling the volume by a factor of 100 the mean strength of the brittle materials, which frequently have small m values, is greatly degraded.

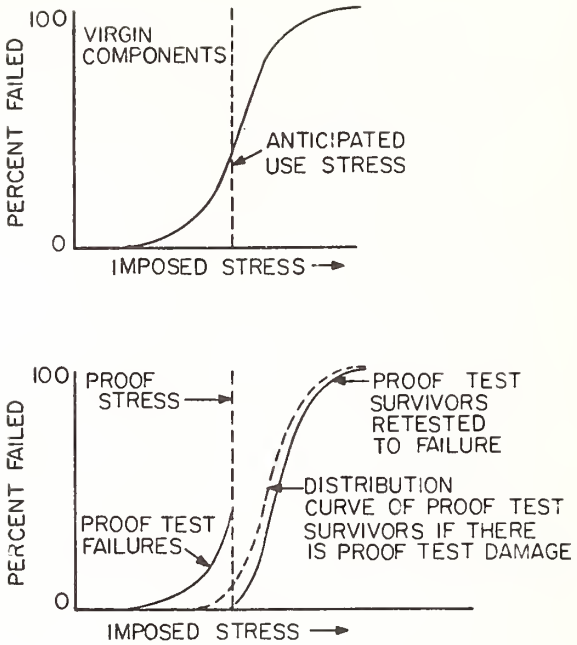

Figure 4. Brittle material can be proof-tested to eliminate those parts containing critical flaws. At the expense of sacrificing some of the parts the reliability of the survivors can be improved significantly. The stress level at which the proof-test is carried out should be determined by consideration of the required reliability and the slow crack growth properties of the material in the use environment. Proof-testing is not addressed in this paper but it is an important practical consideration in the use of brittle materials.

THERMOMECHANICAL STRESS DEGRADATION OF METAL MIRROR SURFACES UNDER PULSED LASER IRRADIATION*

Henry M. Musal, Jr.
Lockheed Palo Alto Research Laboratory
Palo Alto, California 94304

Progressive degradation of the optical surface of metal mirrors in pulsed laser applications can result from cumulative plastic deformation under thermomechanical stress caused by relatively small temperature excursions during irradiation. An analysis of the transient stress-strain behavior of the near-surface region shows that elastic response is maintained below a limiting surface temperature rise (ΔT_y), which depends on the yield stress, modulus of elasticity, Poisson's ratio, and coefficient of thermal expansion of the metal. This temperature rise defines the threshold for first-pulse plastic yield at the surface. An elastic-plastic model of metal behavior shows that the increment of plastic strain accumulated during each successive laser pulse will be proportional to the temperature rise above $2\ \Delta T_y$. This plastic strain will appear at the surface as slip bands and intergranular slip that progressively degrades the optical quality of the surface. The surface temperature rise of metal mirrors under pulsed laser irradiation depends on both the metal optical and thermal properties as well as the laser pulse parameters. The peak temperature excursion produced by a constant-flux (rectangular) pulse is expressed in terms of the optical absorptance, pulse fluence, pulse duration, thermal conductivity, density, and specific heat. Using this relationship, the pulse fluence threshold (F_y) for first-pulse plastic yield is derived. The threshold for multipulse accumulation of plastic deformation is $2\ F_y$. Numerical values of these thresholds are calculated for copper under CO_2 laser irradiation. The appearance of well-defined slip bands on the surface of copper mirrors after irradiation by a mode-locked CO_2 laser pulse burst has been experimentally demonstrated. The theoretical quantification of thermomechanical stress degradation presented here is used to calculate the expected behavior of copper under the reported experimental conditions, and these results are correlated with the available experimental data.

ey words: Cu mirrors; damage thresholds; laser damage; laser-induced stress-strain; lastic deformation; surface degradation.

1. Introduction

The expanding application of high output power/energy repetitively pulsed lasers, and the ecessity for compact beam control optics, places severe demands on optical components with espect to flux/fluence handling capability. The service life of these components is an mportant design consideration. Degradation of optical performance under operational condi-ions for which no direct test data are available must be predicted, using experimentally alidated theoretical analyses and/or physically appropriate extrapolations of existing data. he thermomechanical stress degradation of metal mirror surfaces under pulsed laser irradia-ion is considered here, with specific emphasis on the threshold for onset of cumulative ffects.

Surface damage of metal mirrors in pulsed laser applications is directly related to the ransient surface temperature rise caused by the small (but unavoidable) fraction of the inci-ent laser radiation that is absorbed. Thermal expansion of the metal, resulting from this emperature rise, causes distortion (strain) in the near-surface region and thereby induces tress. If this induced stress exceeds the yield stress of the metal, plastic (irreversable) train will occur. This plastic strain will appear at the metal surface in the form of slip ines and bands, which introduce surface roughness that can degrade the optical quality of

*Work supported by Lockheed Palo Alto Research Laboratory Independent Research funds.

the surface by increasing nonspecular scatter and/or absorptance. In repetitivey-pulsed operation, plastic strain effects can become cumulative, resulting in progressive degradation to unacceptably high levels of scattering and/or absorption, and ultimately leading to fatigue failure (cracking) of the metal at the surface.

Many complicated physical phenomena and analytic difficulties are involved in the problem of transient inelastic thermomechanical effects. Only a simple model of these phenomena and a first-order analysis, with no pretense of comprehensive treatment, is presented here. However, this model and analysis do provide a basis for specification of operational limits, or optimization of materials selection and fabrication, to avoid premature metal mirror failure due to excessive plastic strain accumulation.

2. Thermomechanical stress and strain

2.1. Physical description

Consider the physical response of the near-surface heated region of a metal under short-pulse large-spot laser irradiation (figure 1). As a result of the rapidly rising temperature, the metal tends to expand but is restrained by inertial forces (stresses). In the direction normal to the free surface, the stress relaxes to near zero very fast via a small outward displacement of the free surface. On the other hand, displacement (strain) in directions parallel to the free surface is inhibited by the inertia of the surrounding material. Very large compressive stresses can be induced in these directions. They will exceed the elastic limit of the metal if the temperature rise and coefficient of thermal expansion are large enough. In this situation the metal suffers plastic compressive deformation. This is a permanent strain that will remain even after the metal has cooled down to the initial ambient temperature. As a result of this compressive plastic strain, tensile stresses are generated during cool-down. If the compressional plastic strain was large enough, these tensile stresses will also exceed the elastic limit of the metal and tensile plastic yield will occur. Thus, during temperature cycling due to repeated pulse irradiation, both compressive and tensile plastic strain can accumulate. This strain is manifest as surface roughness and intrusion-extrusion hillocks where slip planes and bands intersect the free surface.

To quantitatively bound the response regime under consideration here, it is useful to define several characteristic dimensions. Dynamic stress relaxation is limited by the speed of propagation of acoustic waves, hence a measure of the time required for stress relaxation to occur over some distance is simply the time required for an acoustic wave to traverse this distance. The acoustic wave speed in most metals is approximately 5×10^5 cm/s. Hence, transient stress effects propagate over a distance of approximately 1 cm in 2 μs, or 5 μm in 1 ns. Put another way, regions having dimensions of the order of microns, or centimeters, have transient stress relaxation times of the order of nanoseconds, or microseconds, respectively. The thermal penetration depth (section 3) is a measure of the thickness of the near-surface region that is substantially heated during pulsed laser irradiation. It can be shown that in most metals acoustic waves can travel across distances greater than the thermal penetration depth given times in excess of approximately 15 ps. Hence, it can reasonably be assumed that transient stress relaxation will exist normally through the near-surface heated region at times substantially greater than 15 ps. However, stress relaxation in directions parallel to the free surface is determined by the size of the structure, or the heated spot. For transverse dimensions of a few centimeters, the transverse relaxation time will be of the order of a few microseconds, as pointed out previously. Short-pulse large-spot irradiation signifies that the heated region has transverse dimensions substantially larger than both the thermal penetration depth and the transverse stress relaxation distance, for the pulse duration under consideration.

The analysis presented here is confined to the short-pulse large-spot interaction regime, where normal stress relaxation exists through the heated near-surface region of a metal, but there is inertial confinement of the metal in directions parallel to the free surface. It is applicable to pulsed laser irradiation conditions ranging from a 1-ns duration pulse applied over at least a 10-μm diameter spot up to a 10-μs duration pulse applied over at least a 10-cm diameter spot, if only the response during heating is considered. If the response during cooling after the pulse terminates is to be included, the required spot sizes must be increased by a factor of approximately 25 in order to remain within the

transverse inertially confined regime. If the spot-size criterion is not met, the transverse inertial confinement approximation will not be applicable. Although similar physical behavior will still occur, the quantitative relationships derived here will not be valid.

2.2. Elastic response

The transient mechanical response of materials under rapid heating conditions, in a number of specialized circumstances, has been previously investigated. For example, Mura [1][1] considered both a semi-infinite block and a semi-infinitely long cylinder where the plane surfaces were subjected to an instantaneous temperature change. Boley and Tolins [2] considered a half-space whose free surface was subjected to instantaneous changes of stress, strain, or temperature. White [3] analyzed a semi-infinite body whose surface abosrbs harmonically varying power density. Zaker [4] considered both a half-space and a finite slab where the power deposition was a step-function in time and exponential in distance from one surface, assuming negligible heat conduction. Bushnell and McCloskey [5] considered heat addition at the interface between two semi-infinite regions, neglecting heat conduction. Duley [6] has summarized and referenced more recent work involving laser irradiation of material surfaces where surface vaporization, plasma pressure, and normal stress waves are emphasized. None of these analyses directly addresses the specific situation of interest here. However, they do support the earlier assertation that the normal stress in the near-surface region relaxes very quickly to the free surface value.

The transient stress-strain response of a plane metal surface under short-pulse large-spot laser irradiation is based on the analysis of a metal half-space subjected to a time-varying temperature rise that is a spatial function of only the distance below the free surface. The basic dynamical thermoelastic response equations follow from the Duhamel-Neumann law and the equation of motion [7, 8]. With the imposition of the transverse inertial confinement constraint and the boundary condition of zero normal stress at the free surface itself, the governing equations are:

$$\frac{(1 - 2\nu)}{E} \tau_N (X, t) = \frac{(1 - \nu)}{(1 + \nu)} \epsilon_N (X, t) - \alpha \Delta T (X, t) \quad (1)$$

$$\frac{(1 - 2\nu)}{E} \tau_T (X, t) = \frac{\nu}{(1 + \nu)} \epsilon_N (X, t) - \alpha \Delta T (X, t) \quad (2)$$

$$\frac{\partial \tau_N (X, t)}{\partial X} = \rho \frac{\partial^2 u_N (X, t)}{\partial t^2} \quad (3)$$

$$\epsilon_N (X, t) = \frac{\partial u_N (X, t)}{\partial X} \quad (4)$$

where E, ν, α, and ρ are the modulus of elasticity (Young's modulus), Poisson's ratio, coefficient of thermal expansion, and density of the metal, $\tau_N (X, t)$, $\epsilon_N (X, t)$, and $u_N (X, t)$ are the normal (in the direction X into the metal) stress, strain, and displacement, and $\tau_T (X, t)$ is the transverse (in both orthogonal directions parallel to the free surface) stress. The four variables (normal stress, strain, and displacement and transverse stress) are all functions of time (t) and distance (X) below the free surface, as is the driving temperature rise $\Delta T (X, t)$. This system of partial differential equations can be manipulated so as to give a single nonhomogeneous wave equation for any one of the variables. The remaining variables can then be expressed in terms of this primary variable. Detailed solution of the wave equation for the primary variable can be complicated, as can be seen from the typical specific cases considered in references [1] through [5]. Fortunately, it is unnecessary to do this if the behavior of only the near-surface region of the metal is of concern.

[1] Figures in brackets indicate the literature references at the end of this paper.

Within the near-surface region of the metal, where the normal stress is relieved rapidly compared to temporal changes in the temperature, it is approximately correct to set τ_N (X, t) equal to zero. With this approximation, the governing equations reduce to

$$\epsilon_N (X, t) \cong \frac{(1 + \nu)}{(1 - \nu)} \alpha \Delta T (X, t) \tag{5}$$

$$\tau_T (X, t) \cong - \frac{E}{(1 - \nu)} \alpha \Delta T (X, t) \tag{6}$$

$$\frac{\partial}{\partial X} u_N (X, t) \cong \frac{(1 + \nu)}{(1 - \nu)} \alpha \Delta T (X, t) \tag{7}$$

Equation (7) can be integrated to give

$$u_N (0, t) \cong - \frac{(1 + \nu)}{(1 - \nu)} \alpha \int_{X=0}^{X \to \infty} \Delta T (X, t) \, dX \tag{8}$$

where the boundary condition $u_N (X, t) \to 0$ as $X \to \infty$ has been used. The negative algebraic signs in eqs. (6, 8) indicate a compressive stress and a displacement of the free surface in the negative X-direction (expansion of the metal), respectively, for a temperature increase. Thus, eqs. (5, 6, 8) provide adequate description of the strain, stress, and free surface displacement for an arbitrary temperature rise variation in space and time within the near-surface region.

2.3. Plastic yield threshold

In the near-surface region of the metal, the dominant stresses (τ_T) are parallel to the free surface, and the normal stress (τ_N) is negligible. These stresses are the principal stresses. The stresses parallel to the free surface are compressive during temperature increases, and vanish when the temperature returns to its initial value as long as the magnitudes of these stresses remain small (elastic response). Equation (6) shows that the magnitudes of the transverse principal stresses are proportional to the temperature rise, coefficient of thermal expansion, and Young's modulus.

For large values of the principal stresses, the metal will yield plastically. That is, during the initial part of the temperature increase the metal will be subject to compressive stress within its elastic range, but upon reaching its yield stress it will suffer plastic compression. This will take the form of "extrusions" of material out of the plane of the free surface (figure 1). The maximum shear stresses occur along planes inclined at 45° to the free surface, hence plastic slip will take place along favorably oriented crystal planes or grain boundaries nearest to these maximum shear stress planes. The extrusion "steps" will therefore have sides oriented at approximately 45° to the original free surface. Now, upon cooling, the metal will contract elastically at first. If the compressive plastic yield was small, elastic behavior will continue all the way down to the initial temperature, but the metal will be left in a state of tension in the near-surface region that compensates for the plastic (irreversible) compressive strain that occurred during heating. If the compressive plastic strain was large, this tensile stress may also exceed the yield stress, thus causing tensile plastic yielding during cooling down to the initial temperature. The morphology of the plastic slip in this case will be similar to that during heating, except the extrusion sides will be slanted oppositely relative to the original free surface.

The Mises-Hencky criterion [9] defines the onset of plastic yield as the condition where the octahedral shear stress exceeds the critical value $\sqrt{2}\, Y/3$, where Y is the tensile yield stress of the material. For the specific configuration considered here, the octahedral shear stress is just $\sqrt{2}\, |\tau_T|/3$; therefore, the yield threshold is defined by $|\tau_T| = Y$. The surface temperature rise at which plastic yield will first occur at the free surface follows directly from eq. (6), and is

$$\Delta T_y \cong \frac{(1 - \nu)\, Y}{E\, \alpha} \qquad (9)$$

Thus, the threshold for plastic deformation is expressed in terms of the surface temperature rise.

As an example, consider the surface temperature rise threshold for plastic deformation of a copper mirror surface. For pure copper, $\nu = 0.345$, $\alpha = 1.67 \times 10^{-5}\ K^{-1}$, and $E = 1.23 \times 10^{11}\ N/m^2$ (1.79×10^7 psi) are well-established numerical values [10]. Equation (9) then becomes $\Delta T_y = 3.18 \times 10^{-7}\ Y$, where ΔT_y is in degrees K and Y is in units of N/m^2. Selection of an appropriate numerical value for Y is not trivial because the yield stress depends critically on the heat-treatment and work-hardening histories of the particular sample. However, experimental studies [11 to 17] of the fatigue failure of pure copper under alternating stress-strain conditions consistently show that a fatigue life greater than 10^6 cycles is achieved if the maximum equivalent tensile stress is kept below $\pm\ 6.2 \times 10^7\ N/m^2$. Using this value as the yield stress gives $\Delta T_y = 20$ K.

2.4. Elastic-plastic model

To quantify the inelastic behavior of the near-surface region of a metal under pulsed laser irradiation, it is necessary to model the mechanical response of the metal in terms of elastic and plastic modes of deformation. Although this response can be very complex, for the purpose of this discussion a simple linear-elastic/perfectly-plastic model is chosen to represent the dominant features of the behavior. Figure 2 illustrates the stress-strain diagram for this model. It is convenient to couch the discussion here in terms of strain as the principal independent variable. Thus, in the linear elastic regime AOA', stress increases linearly as strain is imposed. The behavior is perfectly reversible for excursions between points A and A'. However, if a strain greater than the yield strain is imposed, as illustrated by excursion OAB, the stress increases to the yield stress and then remains constant during plastic contraction from A to B. Now, upon returning to its original dimensions (zero strain) the material follows the path BC (parallel to AOA'), and is left with a residual stress OC. Subsequent cycling along the path CB occurs elastically with no further plastic strain.

It is clear from the diagram that if the plastic strain AB is greater than the elastic yield strain, then the return path must also include plastic strain, as shown in OABDFGE. In this path plastic strain GE occurs during the return to zero strain. Note that strains ABDF and GE are contractions and elongations, respectively, and usually do not occur along the same slip planes. Hence, although no net strain remains at point E, there has been an accumulation of plastic strains, and the material is in a tensile stressed condition.

The stress-strain behavior at a metal surface under pulsed laser irradiation is given by eqs. (1) through (4) for the linear elastic regime, under the constraint that the net strain in directions parallel to the surface is zero. This constraint imposed the condition

$$\alpha\, \Delta T\, (\chi, t) + \frac{1}{E} \left[(1 - \nu)\, \tau_T\, (\chi, t) - \nu\, \tau_N\, (\chi, t)\right] = 0 \qquad (10)$$

where the first term is the transverse thermal strain $\epsilon_{TT}\, (\chi, t)$ caused by the temperature rise and the second term is the resultant transverse mechanical strain $\epsilon_{TM}\, (\chi, t)$ induced by the inertial constraining forces. It has been shown that in the near-surface region, the normal stress is negligible (it is actually zero at the free surface itself). Thus, to good approximation,

$$\epsilon_{TM}\, (\chi, t) \cong \frac{(1 - \nu)}{E}\, \tau_T\, (\chi, t) \cong -\alpha\, \Delta T\, (\chi, t) \qquad (11)$$

This relationship exists for each of the orthogonal transverse directions, and is consistent with eq. (6). Equation (11) describes the stress-strain relationship within the metal near

the surface in the linear elastic regime. This regime ends, and the plastic regime begins, when the octahedral shear stress reaches the value $\sqrt{2}\ Y/3$. This occurs when $|\tau_y| = Y$. The required temperature rise (ΔT_y) has already been given in eq. (9), and the concomitant strain magnitude is $(1 - \nu)\ Y/E$. These considerations are illustrated in the stress-strain diagram shown in figure 2. Note that either mechanical strain or temperature rise can be considered to be the independent variable in this situation, because $\epsilon_{TM} \cong -\alpha \Delta T$ in both the elastic and plastic regimes.

Now consider the effects of cyclic temperature excursions caused by repeatedly pulsed laser irradiation. If the maximum temperature rise (ΔT_{max}) is less than ΔT_y, the material at the surface will experience a maximum strain less than the yield strain and the stress-strain path will lie along line OA in figure 2, which represents perfectly reversible elastic behavior. For values of ΔT_{max} between ΔT_y and $2\Delta T_y$, the stress-strain path will be similar to OABC in figure 2, with plastic yield AB on the first pulse and elastic behavior on all subsequent pulses with equal or smaller values of ΔT_{max}. If ΔT_{max} is greater than $2\Delta T_y$, the stress-strain path on the first pulse will be OABDFGE, as shown in figure 2. Plastic strain will occur during heating (ABDF) and during cooling (GE). In subsequent pulses with the same value of ΔT_{max}, the path EDFGE will be followed, again producing plastic strain during both heating and cooling on each cycle. The increment of plastic deformation that is produced by each pulse after the first is apparent from figure 2. Point D is located at twice the yield strain ($-2\ \alpha\ \Delta T_y$) and point F is located at a strain of $-\alpha \Delta T_{max}$, hence the magnitude of the contraction strain increment ($\Delta\ \epsilon$) along the path segment DF is

$$\Delta \epsilon = \alpha\ (\Delta T_{max} - 2\ \Delta T_y) \tag{12}$$

The same magnitude increment is accumulated along path segment GE, but in elongation. The same plastic deformations will accumulate in both orthogonal transverse directions.

When a metal is subjected to alternating strains in excess of the yield strain, such as described above, the plastic deformation tends to occur along closely spaced slip planes that form slip bands. These bands widen across the surface and form more prominent extrusion and intrusion steps as plastic deformation accumulates. Thus, roughening of the surface is related to plastic strain accumulation. Eventually fatigue cracks occur at the slip bands. Thus, the fatigue life of a metal under cyclic deformation also depends on the total accumulated plastic strain.

3. Metal surface heating

The temperature rise of a metal surface under pulsed laser irradiation depends on both the optical and thermal properties of the metal as well as the laser pulse parameters [18]. Absorbed laser radiation is deposited (converted to heat) within the near-surface region (electromagnetic skin depth) of the metal. The skin depth in metals at temperatures between normal ambient and melting, for radiation within the ultraviolet to near-infrared wavelength range, lies between 10 and 100 nm. This heat is rapidly transported deeper into the metal by thermal conduction. An approximate measure of the depth d to which thermal conduction will transport heat energy during a time interval t is given by $d = 2\ (K\ t)^{1/2}$, where K is the thermal diffusivity of the metal. For most metals, K is of the order of 1 cm^2/s. Thus, the thermal penetration depth is larger than the skin depth for irradiation periods longer than 25 ps. Consequently, in thermal analyses of metals under pulsed laser irradiation, absorbed laser radiation is well represented as a surface heat source when the pulse duration is at least an order of magnitude larger than 25 ps. In this regime, the temperature rise is dominantly controlled by the thermal conduction mechanism. If the optical absorptance of the metal surface and the thermal properties of the bulk metal are independent of temperature (which is a reasonable approximation for small temperature changes), and the irradiated spot size is large (an order of magnitude or more larger than the thermal penetration depth for the pulse duration under consideration) with a spatially uniform illumination, then the surface temperature rise $\Delta T\ (0, t)$ can be expressed in terms of a

onvolution integral of the form

$$\Delta T\ (0,\ t) \ = \ \frac{A}{(\pi\ k\ \rho\ C)^{1/2}} \int_{\eta=0}^{\eta=t} \frac{f\ (\eta)}{(t\ -\ \eta)^{1/2}}\ d\eta \qquad (13)$$

here k, ρ, and C are the thermal conductivity, density, and specific heat of the metal, A s the optical absorptance, and f (t) is the time-varying incident radiation flux at the urface.

For a rectangular (constant-flux f) pulse of time-duration T_p, the maximum temperature xcursion (ΔT_{max}), which occurs at the end of the pulse, is

$$\Delta T_{max} \ = \ \frac{2\ A\ f\ T_p^{1/2}}{(\pi\ k\ \rho\ C)^{1/2}} \ = \ \frac{2\ A\ F}{(\pi\ k\ \rho\ C\ T_p)^{1/2}} \qquad (14)$$

here $F = f\ T_p$ is the pulse fluence. For a parabolic-shaped pulse, the maximum temperature ise is

$$\Delta T_{max} \ = \ \frac{4}{5}\left(\frac{3}{2\sqrt{2}}\right)^{1/2} \frac{2\ A\ f\ T_p^{1/2}}{(\pi\ k\ \rho\ C)^{1/2}} \ = \ \frac{4}{5}\left(\frac{3}{2\sqrt{2}}\right)^{3/2} \frac{2\ A\ F}{(\pi\ k\ \rho\ C\ T_p)^{1/2}} \qquad (15)$$

here now f is the peak flux, T_p is the FWHM pulse duration, and $F = 2\sqrt{2}\ f\ T_p/3$ is the ulse fluence. These expressions, in conjunction with the expression for ΔT_y, can be used to xpress the plastic yield threshold in terms of the pulse parameters. Thus, the pulse luence (F_y) at which the plastic yield threshold is reached is

$$F_y \ \cong \ \frac{(\pi\ k\ \rho\ C\ T_p)^{1/2}}{2\ A}\ \Delta T_y \ \cong \ \frac{(1\ -\ \nu)\ (\pi\ k\ \rho\ C\ T_p)^{1/2}\ Y}{2\ A\ \alpha\ E} \qquad (16)$$

or a rectangular pulse. The threshold for continued accumulation of plastic strain is $2\ F_y$.

As an example, the threshold for inelastic behavior of a high-quality copper mirror sur- ace under rectangular pulse CO_2 laser irradiation is $F_y\ T_p^{-1/2} \cong 1.1 \times 10^4$ J/cm^2-s$^{1/2}$, here the yield stress has been assumed to be 6.2×10^7 N/m^2 (ΔT_y = 20 K). This relation- hip is shown in figure 3, where both the threshold fluence for initial (first-pulse) plas- ic yield (F_y) and cyclic accumulation of plastic strain ($2\ F_y$) are shown as functions of he pulse duration.

The absorbed laser radiation resides within the metal as heat, which is evidenced by the emperature rise of the metal. At any time t, the energy input per unit surface area (F_{abs}) s

$$F_{abs}\ (t) \ = \ \int_{\eta=0}^{\eta=t} A\ f\ (\eta)\ d\eta \qquad (17)$$

his is equal to the heat added to the metal, which is

$$F_{abs}\ (t) \;=\; \int_{\chi=0}^{\chi\to\infty} \rho\, C\, \Delta T\ (\chi,\ t)\ d\chi \tag{18}$$

If the thermal capacity (ρ C) is independent of temperature and spatial position, it follows that

$$\int_{\chi=0}^{\chi\to\infty} \Delta T\ (\chi,\ t)\ d\chi \;=\; \frac{1}{\rho C} \int_{\eta=0}^{\eta=t} A\ f\ (\eta)\ d\eta \tag{19}$$

from which the elastic free surface displacement can be expressed as

$$u_{\chi}\ (0,\ t) \;\cong\; -\,\frac{(1+\nu)}{(1-\nu)}\ \frac{\alpha}{\rho C} \int_{\eta=0}^{\eta=t} A\ f\ (\eta)\ d\eta \tag{20}$$

Bennett [19] has presented a similar expression that does not include the $(1 + \nu)/(1 - \nu)$ factor which arises due to the transverse inertial constraint that has been imposed here. The numerical value of this factor is approximately 2 for most metals. Because the elastic response regime extends over only a small temperature excursion, the optical absorptance will be essentially constant and can be removed from the integral in eq. (20). The integral is then simply the incident fluence up to the time of concern. For a high-quality copper mirror surface under CO_2 laser irradiation, the predicted free surface displacement will be approximately 0.6 nm per incident J/cm^2 in the elastic response regime.

4. Theoretical-experimental correlation

Direct correlation of theoretical predictions based on the analysis presented here with presently available experimental data is difficult for several reasons. Early evidence [20] of plastic yield under pulsed laser irradiation was obtained under small-spot conditions, where transverse heat conduction and stress relaxation effects would be active. Furthermore, the incident fluence levels were high enough to cause surface melting. However, plastic yield effects were observed outside of the melt zone, as would be expected. Later studies [21] of plastic deformation caused by pulsed laser-induced thermal stress were not significantly influenced by transverse heat conduction. However, the fluence levels were above the melt threshold, transverse stress relaxation was not negligible, and a complex temporal pulse shape (mode-locked pulse-burst) was employed. Here plastic yield effects were seen both within and around the melt zone. Recent characterization [22] of the thresholds for inelastic effects still are not clearly in the large-spot regime with respect to transverse stress relaxation, and were obtained with a mode-locked pulse-burst. The first condition allows the transverse stress to relax somewhat during the pulse, which has the effect of raising the temperature and pulse fluence thresholds. The second experimental condition (pulse shape) makes it difficult to properly assign a simple pulse duration to the energy input so that correlation with the thresholds illustrated in figure 3 can be made. Nevertheless, a correlation of some of these latest experimental results with theoretical predictions has been made.

The irradiation temporal profile in the experiments of Porteus et al. [22] was approximated by a sequence of individual pulses of 10-ns FWHM, spaced 20-ns apart, and contained within a 100-ns duration envelope, as shown in figure 4. Both the individual pulses and the envelope were given parabolic shapes for convenience. Also shown in the figure is the single-pulse equivalent of the pulse train (same total fluence and overall duration; parabolic profile with a 71-ns FWHM). The surface temperature rise responses to irradiation by both the pulse-burst and the equivalent single-pulse are illustrated in figure 5, where the heat input has been treated as a surface source, the absorptance was assumed to be independent of surface temperature, and the thermal response was considered to be heat-conduction dominated. For copper, under CO_2 laser irradiation, the scale factor between the surface

mperature rise and the incident fluence was $7.2^{o}K$ at the temperature peak per J/cm^2 incint on the surface in the pulse-burst irradiation condition. It can be seen that use of e equivalent single pulse predicts an erroneously lower peak temperature. Thus, using the lue of $20^{o}K$ for ΔT_y, the predicted threshold fluence for plastic yield is 2.8 J/cm^2 for the lse-burst. It should be remembered that fluence values above this are required to produce y plastic strain. The experimentally measured fluence at which plastic strain effects re observable on the surfaces of single-crystal and bulk (polycrystalline) copper were 9 d 18 J/cm^2. The polycrystalline samples were either optically polished or diamond-turned, d therefore would be expected to have higher initial yield stresses as a result of the ld-working (strain-hardening) effect of these surface finishing processes. Hence, the gher pulse fluence thresholds for these samples are not unexpected.

The predicted transverse stress-strain history of an annealed copper surface undergoing e temperature rise history depicted in figure 5, at an incident fluence level of 9 J/cm^2 hich produces a predicted peak temperature rise of $65^{o}K$), is traced out in figure 6 ssuming linearly-elastic/perfectly-plastic behavior in the inertially confined regime). ring the first temperature rise OA, and subsequent fall AA', the metal responds elastically the compressive stress. However, on the second temperature rise A'B the compressive plas- yield point Y is exceeded, and an increment of plastic strain YB is accumulated. Cooling om B to B' generates an elastic response, and subsequent heating to C causes elastic comession B'B plus inelastic compression BC. Cooling to C' again generates an elastic sponse. Heating from C' to D causes elastic compression C'C plus inelastic compression . Cooling from D to D' and subsequent heating to E generate only elastic strains. The nal cool-down from E generates elastic response to Y' (which occurs at approximately) ns) followed by tensile inelastic strain from Y' to the end point at ambient temperature. e total compressive plastic strain is 7.3×10^{-4}, the tensile plastic strain is 3.9×10^{-4}, that the total accumulated inelastic strain is approximately 1×10^{-3} for the entire cle. Whether this is the minimum observable inelastic strain (measurable threshold contion) is a moot point at this time.

5. Discussion

The governing equations that describe the transient thermomechanical stress-strain havior of metal surfaces under short-pulse large-spot laser irradiation have been set rth. It has been shown that detailed solution of these equations can be avoided if only e near-surface region is of interest. This is where the transverse stresses and strains e largest and, therefore, is the most important region with respect to surface damage.

In the near-surface region, the induced stresses and strains (both inelastic and plas-) have been related to the temperature rise caused by absorption of laser radiation, ing a linear-elastic/perfectly-plastic model of material response. The surface tempera-re rise thresholds at which the metal surface begins to yield plastically during heating, d at which plastic yield also occurs during cooling, have been quantified in terms of this del. Cyclic temperature excursions that exceed the second of the above-mentioned thresh-ds, such as produced under repeatedly pulsed laser operation, lead to an accumulation of astic strain. This will be evidenced by the appearance of slip lines and bands at the al surface that should be directly correlated to the total accumulated slip [17]. Ultiely, fatigue crack failure of the metal may occur. Numerical results indicate that the mperature rise threshold for inelastic behavior is quite small, and therefore the short-lse laser fluence at which inelastic effects begin to appear is also small.

These predictions apply to the metal at the surface. Because the temperature excursions e smaller deeper within the metal, the strains and resultant stresses will also be smaller d plastic deformation will cease at some distance below the surface. The thickness of the eld zone will depend on the maximum surface temperature and the laser pulse duration. If minimum thickness yield zone is required to produce observable effects at the surface, en for very short duration pulses a higher surface temperature rise (requiring a larger lse fluence) than predicted here will be necessary.

Some of the detailed results presented here will be altered in the case of metals that display significant work hardening as a result of plastic deformation, and/or exhibit strain-rate sensitivity of the yield stress at very high strain rates. Work hardening may be the result of prior mechanical treatment, such as machining and polishing, or may be the direct result of accumulated plastic strain during repeated laser pulse irradiation. This raises the yield stress of the metal. It should also be pointed out that plastic deformation increases the electrical resistivity of metals, which will be evidenced by an increase in the optical absorptance [18]. The principal effect of both increased yield stress and strain-rate sensitivity is to raise the temperature rise and pulse fluence thresholds for plastic yield and cyclic accumulation of plastic strain, while increased absorptance lowers the fluence thresholds for these effects.

The modeling and analysis of thermomechanical stress degradation presented here is also applicable to mirror coating failure caused by plastic yield of the underlying metal substrate, when an appropriate adjustment is made for energy actually absorbed by the substrate. Even tightly bound natural oxide layers are subject to this kind of "failure". Compressive plastic yield of the metal substrate usually causes localized delamination of the coating, and tensile plastic yield usually causes cracks in the coating at the yield sites.

There is a need for more experimental data on the threshold for thermomechanical stress degradation and the relationship of progressive plastic strain accumulation to increased surface roughness, nonspecular scattering, and optical absorptance in the short-pulse large-spot regime. As pointed out earlier, observation of plastic strain effects requires that the thresholds be exceeded by an as-yet-undetermined increment. Sensitive measurements of plastic yield are needed. Baxter [23] has used ultraviolet-enhanced exoelection emission microscopy in this role. The onset of exoelection emission may be a good indicator of the onset of plastic slip. Correlation of the time-resolved emission current with the expected surface temperature rise history could be used to validate the model and analysis of progressive accumulation of plastic strain. Concomitant measurement of surface roughness, nonspecular scattering, and optical absorptance changes with progressive accumulation of plastic strain are also needed to complete the thermomechanical degradation picture.

6. Conclusions

Several specific conclusions may be drawn from the results presented here.

- The surface temperature rise at which a metal surface under short-pulse large-spot laser irradiation will begin to yield plastically due to thermomechanical stress is relatively small. This plastic yield threshold temperature rise (ΔT_y) is of the order of $20^{\circ}K$ for pure copper.

- A simple scaling relationship, namely $F_y T_p^{-1/2}$ = constant, expresses the plastic yield threshold in terms of pulse parameters. For a high-quality copper mirror irradiated by a rectangular (constant-flux) CO_2 laser pulse, the numerical value of the constant is approximately 1×10^4 J/cm^2-s$^{1/2}$. This scaling relationship is shown in figure 3.

- Repetitive pulse irradiation will cause accumulation of plastic strain on each successive pulse if $2\,\Delta T_y$ (or, equivalently, $2\,F_y$) is exceeded during the pulse. The increment of plastic strain accumulated during a pulsed heating-cooling cycle is proportional to the temperature rise in excess of $2\,\Delta T_y$, and consists of both contraction and extension in both of two orthogonal directions along the surface. It will be manifest as progressive surface degradation in the form of slip bands, intergranular slip, and fatigue cracks.

These specific conclusions are necessarily based on the simple model for elastic-plastic response of a metal used here, and consequently are subject to modification as a result of more realistic evaluation that incorporates the complicating details that have been omitted in this model. However, it is expected that the basic behavior and effects will be the same.

7. References

[1] Mura, T., Thermal strains and stresses in transient state, Proceedings of the 2nd Japan National Congress for Applied Mechanics, pp. 9 — 13 (1952).

[2] Boley, B. A., and Tolins, I. S., Transient coupled thermoelastic boundary value problems in the half-space, Journal of Applied Mechanics, 29, pp. 637 — 645 (1962).

[3] White, R. M., Generation of elastic waves by transient surface heating, Journal of Applied Physics, 34, pp. 3559 — 3567 (1963).

[4] Zaker, T. A., Stress waves generated by heat addition in an elastic solid, Journal of Applied Mechanics, 32, pp. 143 — 150 (1965).

[5] Bushnell, J. C., and McCloskey, D. J., Thermoelastic stress production in solids, Journal of Applied Physics, 39, pp. 5541 — 5546 (1968).

[6] Duley, W. W., CO_2 Lasers: Effects and Applications, Academic Press, pp. 341 — 351 (1976).

[7] Sokolnikoff, I. S., Mathematical Theory of Elasticity, McGraw-Hill, pp. 358 — 362 (1956).

[8] Shames, I. H., Mechanics of Deformable Solids, Prentice-Hall, pp. 126 — 128 (1964).

[9] Ibid, pp. 100 — 102.

[10] Gschneidner, Jr., K. A., Physical properties and interrelationships of metals and semimetallic elements, Solid State Physics, 16, Academic Press, pp. 275 — 426 (1964).

[11] Wadsworth, N. J., Work hardening of copper crystals under cyclic straining, ACTA Metallurgica, 11, pp. 663 — 673 (1963).

[12] Wood, W. A., Cousland, S. McK., and Sargant, K. R., Systematic microstructural changes peculiar to fatigue deformation, ACTA Metallurgica, 11, pp. 643 — 652 (1963).

[13] Laufer, E. E., and Roberts, W. N., Dislocation structures in fatigued copper single crystals, Philosophical Magazine, 10, pp. 883 — 885 (1964).

[14] Laufer, E. E., and Roberts, W. N., Dislocations and persistent slip bands in fatigued copper, Philosophical Magazine, 14, pp. 65 — 78 (1966).

[15] Lukas, P., Klesnil, M., Krejci, J., and Rys, P., Substructure of persistent slip bands in cyclically deformed copper, Physica Status Solidi, 15, pp. 71 — 82 (1966).

[16] Lukas, P., Klesnil, M., and Krejci, J., Dislocations and persistent slip bands in copper single crystals fatigued at low stress amplitude, Physica Status Solidi, 27, pp. 545 — 558 (1968).

[17] Roberts, W. N., Persistent slip bands in fatigued copper, Philosophical Magazine, 20, pp. 675 — 686 (1969).

[18] Musal, Jr., H. M., Influence of laser pulse shape on metal mirror damage, Proceedings of the International Conference on Lasers '78, pp. 267 — 273 (1978).

[19] Bennett, H. E., Thermal distortion thresholds for optical trains handling high pulse powers, Laser Induced Damage in Optical Materials: 1976, NBS Special Publication 462, pp. 11 — 24 (1976).

[20] Haessner, F., and Seitz, W., Laser-induced dislocation structures in copper single crystals, Journal of Materials Science, 6, pp. 16 — 18 (1971).

[21] Porteus, J. O., Soileau, M. J., and Fountain, C. W., Slip banding in Al single crystals produced by 10.6 μm laser pulses, Applied Physics Letters, 29, pp. 156 — 158 (1976).

[22] Porteus, J. O., Fountain, C. W., Jernigan, J. L., Faith, W. N., and Bennett, H. E., Pulsed-laser stress phenomena on highly reflecting metal and alloy surfaces, Laser Induced Image in Optical Materials: 1977, NBS Special Publication 509, pp. 204 — 214 (1977).

[23] Baxter, W. J., Laser scanner for exoelectron display and measurement of fatigue damage, Journal of Testing and Evaluation, 5, pp. 243 — 250 (1977).

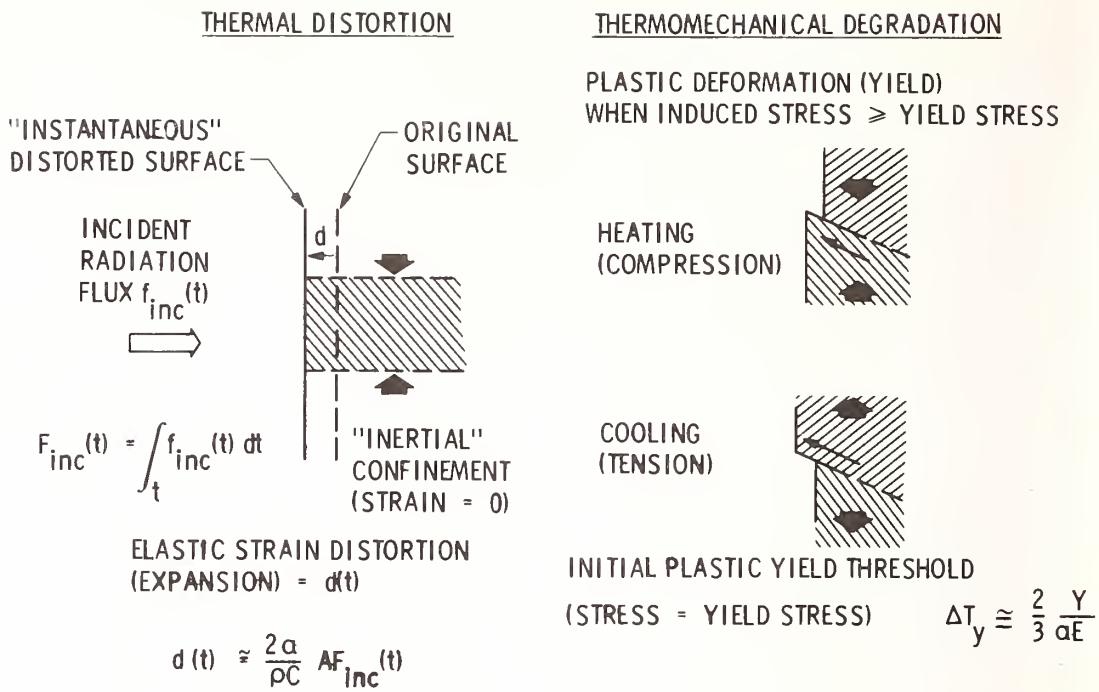

Figure 1. Metal surface thermal distortion and thermomechanical degradation

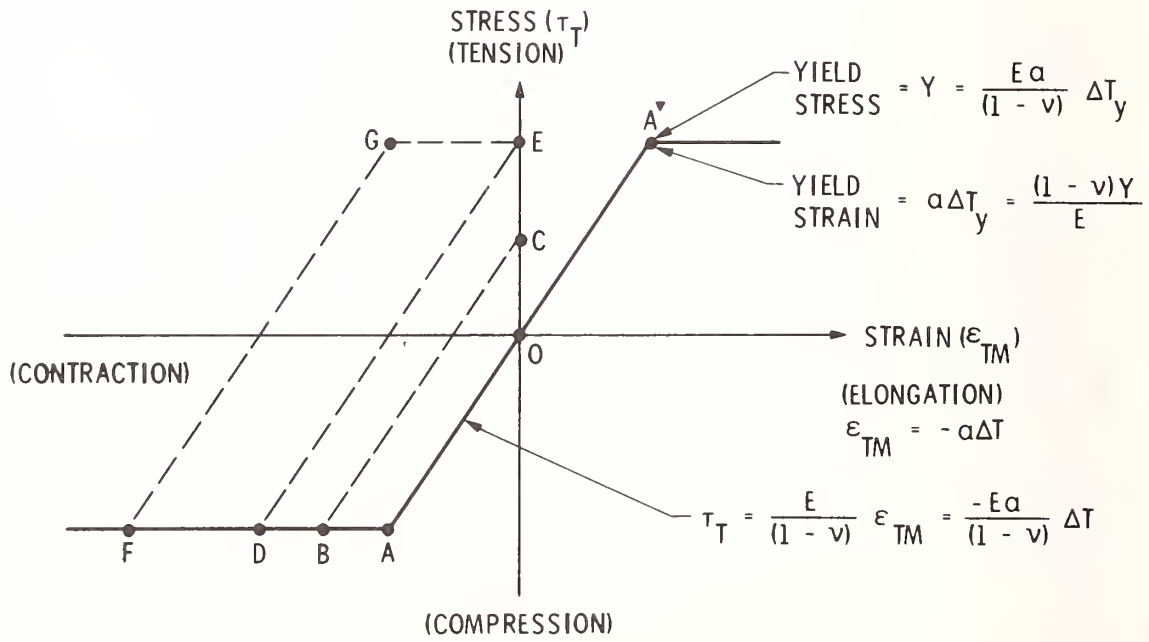

Figure 2. Linear-elastic/perfectly plastic stress-strain diagram for metal surface under pulsed laser irradiation.

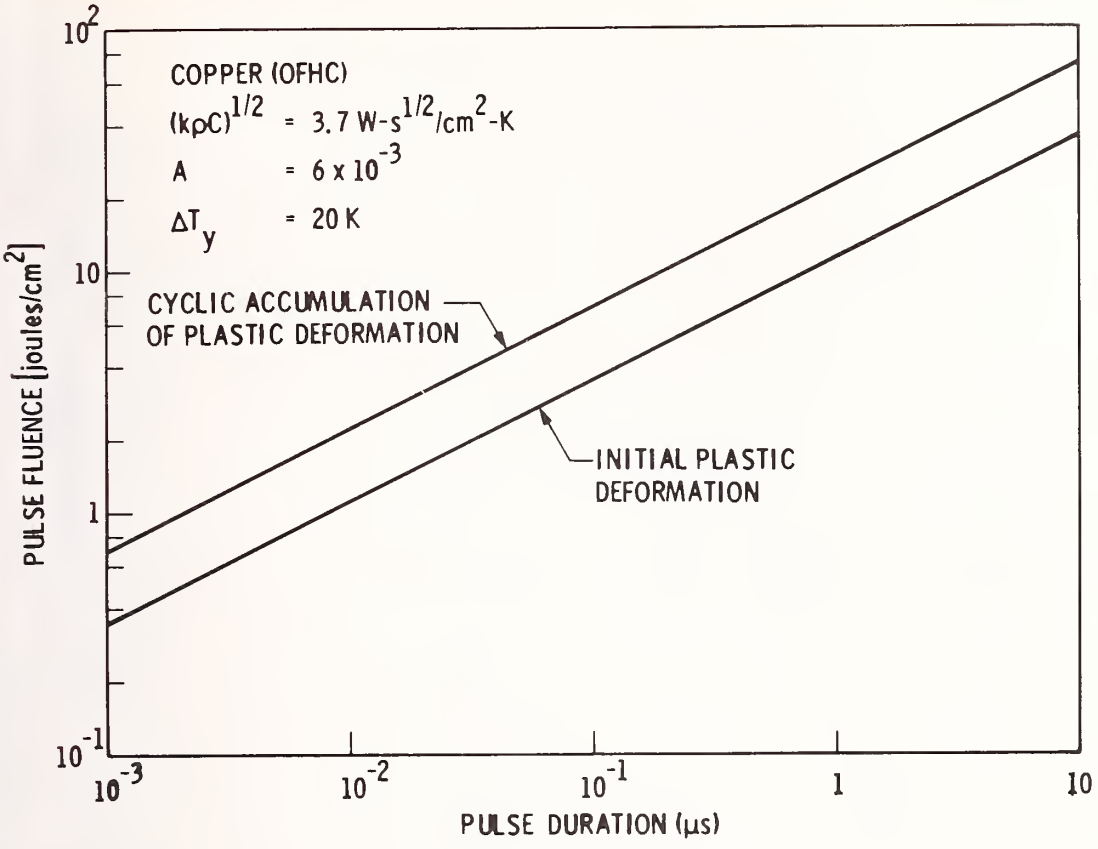

Figure 3. Thresholds for copper surface plastic deformation under pulsed CO_2 laser irradiation

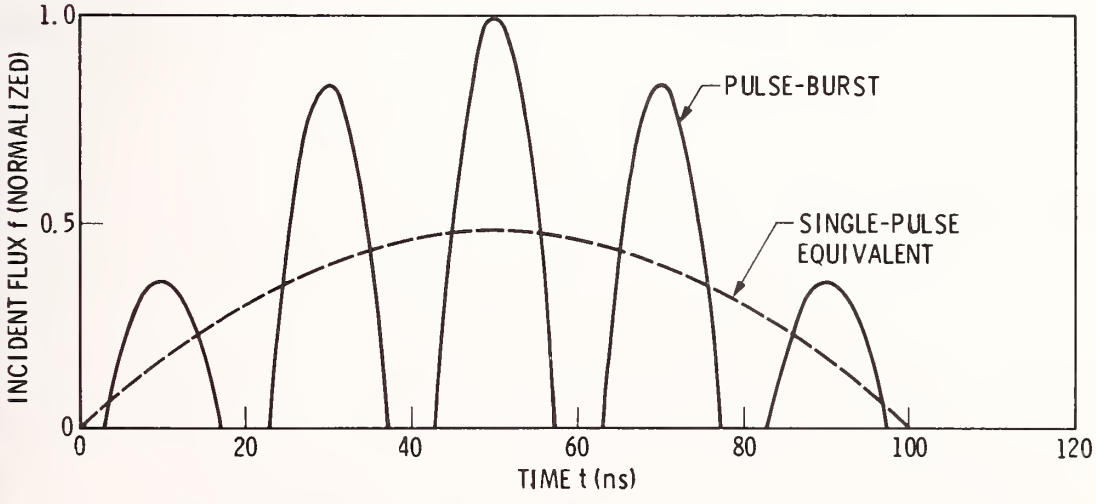

Figure 4. Mode-locked pulse-burst and single-pulse equivalent

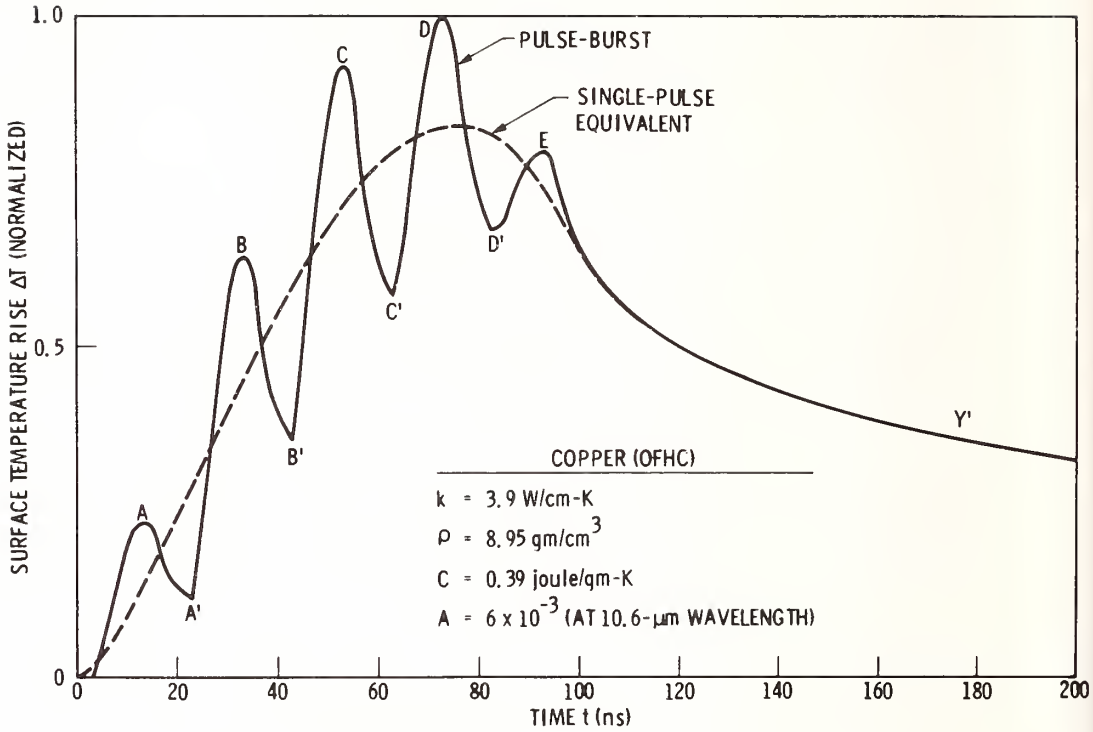

Figure 5. Copper surface temperature rise under CO_2 laser irradiation

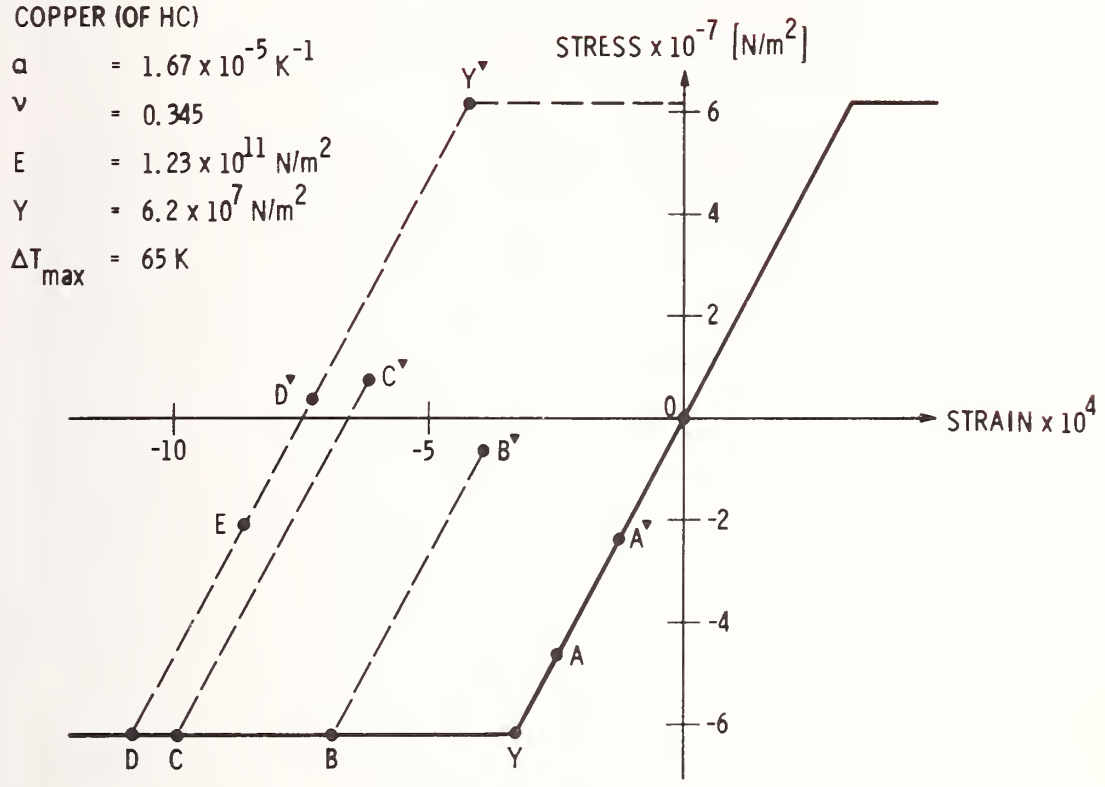

Figure 6. Stress-strain response of copper surface to pulse-burst temperature rise history

DEFECT-DAMAGE-RESISTANT COPPER MIRRORS

J. O. Porteus, D. L. Decker, D. J. Grandjean, S. C. Seitel, and W. N. Faith*
Michelson Laboratory, Physics Division
Naval Weapons Center, China Lake, California 93555

The calculated threshold for 10.6-μm laser-induced melting of intrinsic crystalline copper is found to be in excellent agreement with the latest experimental value when the 100-nsec pulse shape and temperature-dependent material properties are properly modeled. Melt thresholds of diamond-turned copper mirrors recently produced and tested at the Naval Weapons Center are found to be very nearly intrinsic. However, laser-induced pitting related to surface defects often causes failure at a considerably lower level. Selection of starting material and technique of surface finishing are shown to be important factors influencing laser damage related to surface defects and disorder. A well-defined inverse relationship between the thresholds for laser-induced slip and melting is demonstrated and provides a good indication of surface disorder on polished, as well as diamond-turned mirrors. Mirrors prepared by vapor deposition of copper on polished silicon carbide are found to be remarkably free of defect and visible (thermal) damage but have lower melt thresholds than good bulk copper mirrors. Thermal modeling indicates that the premature melting can be avoided by improving the thermal conductivity of the substrate.

Key words: Cu mirrors; crystalline disorder; diamond turning; laser-induced slip; polishing; ripples; SiC substrates; surface defects; thermal diffusivity; vapor-deposited mirrors.

Introduction

The threshold for 10.6-μm, 100-nsec pulsed laser-induced melting of intrinsic crystalline Cu is well established, both experimentally and theoretically [1,2][1]. Melt thresholds of good diamond-turned Cu mirrors are very close to the intrinsic value [3]. However, laser-induced pitting often causes spatially selective damage at considerably lower levels. Pitting is believed to result from random bulk defects which may trap optically absorbing contaminants when exposed at the mirror surface. Such defects can also reduce damage thresholds of dielectric mirrors prepared on metal substrates. The roles of material selection and surface finishing with respect to laser damage are not completely understood. In this paper we examine these variables in relation to damage associated with defects and crystalline disorder. Three different varieties of oxygen-free, high-conductivity (OFHC) Cu are intercompared in terms of damage morphology, multithreshold damage characteristics [2], and pit formation frequency. On diamond-turned surfaces the dependences of melt and slip [4] thresholds on the type of cut and top-rake angle are examined. The well-defined relationship between these two thresholds, as governed by surface disorder, is demonstrated. A polished mirror is evaluated for comparison with the diamond-turned samples. A mirror prepared by vapor deposition of Cu on a polished SiC substrate is also evaluated and found to be remarkably free of laser-induced pits and visible slip. However, the melt threshold is substantially below that of intrinsic Cu as a result of the less effective heat dissipation in the SiC.

Experimental Apparatus and Procedure

Measurements are made in a previously reported laser damage facility (fig. 1) where comprehensive target monitoring and careful beam characterization are key features [5]. The experiments were performed in vacuum in order to simplify the discussion of basic phenomena. The ultrahigh vacuum (UHV) test chamber was equipped with the following essential monitoring apparatus for the present work: (1) 20-power microscope; (2) Faraday cup

* Work supported by the Air Force Weapons Laboratory and by Navy Independent Research funds.
[1] Figures in brackets indicate the literature references at the end of this paper.

with grounded entrance grid (10 mA/sr detection sensitivity at 35 degrees off the laser beam axis) for sensing of sample-emitted ions and neutrals having sufficient energy to produce secondary electrons; and (3) Auger analyzer with electron imager which is sensitive to work-function variations ~ 0.1 eV over the target surface and to changes in surface roughness. The 10.6-μm laser beam is focused on the sample by a ZnSe lens having a focal length of 24 cm. This produces a Gaussian spatial intensity distribution 350 μm in diameter at $1/e^2$ of the maximum. Temporally, each pulse consists of a train of mode-locked spikes which form an envelope of 100 nsec nominal duration. Thresholds quoted here are peak thresholds, i.e., they refer to the energy density of the damaging pulse (fluence) at the point of maximum spatial intensity. The Lumonics CO_2 TEA laser used here is capable of delivering a maximum fluence of 300 J/cm^2 on the axis of the focused beam. The fluence is inferred from the measured pulse energy on the basis of pinhole scans of the focused beam. In the present work, a standard sample was tested on a daily basis to maintain relative calibration uncertainties to within an estimated ±5%.

Multithreshold measurement and analysis procedures have been reported in detail [6]. Briefly, the sample to be analyzed is exposed to one pulse at each of approximately 50 sites spaced at 1-mm intervals along its surface. Pulse energies, which are measured for each pulse, are uniformly distributed over a range which includes the thresholds for each of the damage effects of interest. The occurrence of light emission (flash) and pit formation are noted by an observer as they occur, while damage features which are more difficult to identify, e.g., slip, melting, and cratering, are categorized with the aid of more sophisticated optical microscopy, i.e., dark field and Nomarski, after the sample has been removed from the test chamber. The data are reduced by entering the peak energy density and a code representing observed damage features for each site into a computer and performing a statistical analysis. This gives an average threshold for each effect, together with its standard deviation, the latter being a measure of the threshold uniformity over the surface. Results are presented in the form of a bar chart called a damage profile. Examples are given below.

Intrinsic Damage

In addition to melting, slip bands due to thermal stress [4] appear in intrinsic Cu at about one-fifth of the energy density required to produce melting. Pitting rarely occurs below the melt threshold. The process of laser-induced melting in intrinsic crystalline Cu is straightforward for pulse lengths ≧ 100 nsec. Table 1 compares measured thresholds with those calculated from thermal diffusion theory. The experimental value 76.6 ± 8.6 J/cm^2 was obtained on a sample prepared in UHV by the best techniques available for producing a clean, well-ordered, defect-free surface, although without an optical finish [3]. The present value is higher than that previously reported by a factor of 1.69 as a result of corrections for systematic errors in our earlier beam scan measurements [2]. The first calculated value in table 1 for a 100-nsec square pulse was obtained earlier this year by Sparks and Loh [1] by solving the heat flow equation exactly. We were able to reproduce their result within 2% using a finite difference solution [7], which permits greater flexibility in modeling the actual pulse shape and the temperature-dependent material properties. Replacing the square pulse with a more representative pulse having a linear rise and exponential decay increases the calculated melt threshold from 53.2 to 67.2 J/cm^2. Including the temperature dependence of the specific heat, thermal conductivity and density, and the nonlinearity of the temperature-dependent optical absorption further raises the calculated melt threshold to 76.1 J/cm^2, in excellent agreement with experiment. This also verifies a calculated value of the 74 J/cm^2 which we reported two years ago [4].

Material Dependence of Damage

Three varieties of bulk Cu were used in this study, all OFHC: (1) AVCO, a high-density forged Cu produced specifically for AVCO Corporation to their specifications; (2) Naval Weapons Center (NWC), a commercial grade purchased from Ducommun Metals and found to have good characteristics for diamond turning; and (3) Y-12, commercial grade Cu from a reliable supplier commonly used by the Union Carbide Oak Ridge Y-12 diamond-turning facility.

Table 1. Comparison of measured and calculated melt thresholds for intrinsic bulk copper.

Experimental value (Porteus and Decker, 1979)	76.6 ± 8.6
Calculated values	
Absorption linear with T; other properties constant	
1. Square pulse	
Exact solution (Sparks and Loh, 1979)	52.2
Finite difference solution (FDS)	53.2
2. Exponential pulse (FDS)	67.2
T^2 Absorption term; T-dependent properties	
Exponential pulse (FDS)	76.1

One 1.5-inch-diameter sample of each material was prepared in the NWC diamond-turning facility [8]. Samples 1.5 inches in diameter were individually turned to center using the same tool under identical conditions. A constant spindle speed of 500 rev/min was used. Cleaning was done immediately after turning using a freon degreaser and a series of ultrasonic rinses in clean acetone. Samples were then blown dry with nitrogen. Just before testing, the surfaces were wet with acetone and dried by drawing lens tissue over them.

Figure 2 compares micrographs of laser damage morphology on the three materials. The energy in each case was sufficient to produce slip bands, melting, intergranular slip [4], and well-developed pitting, accompanied by emission of ions and visible light. Large pits often occur along grain boundaries, particularly on the NWC and Y-12 samples. This is less apparent in the AVCO Cu, although the overall density of small pits is higher than in the other two materials. Also, laser-induced ripple patterns [9] are generally more developed on the AVCO Cu.

Figures 3 - 5 compare damage profiles of the three materials. There are no striking differences, and variations are generally within the reproducibility of results on a given sample. Melt thresholds are very close to intrinsic in all three cases. On the AVCO sample the standard deviation for light emission extends somewhat below that for pits, which is consistent with plasma formation at pits too small to resolve with the 20-power microscope. Also, the intergranular slip threshold is lowest on the AVCO Cu. This may imply that the grain boundaries are less effectively pinned as a result of a lower concentration of defects along grain boundaries.

The pit threshold gives a good indication of the onset of pitting where the mean distance between pits is not substantially larger than the 0.35-mm focal spot diameter. However, the pit threshold is not a reliable indicator of low density pitting, which may occur at lower fluence levels. This may be a serious limitation for large beam applications. To obtain information on low-fluence pit density we conducted a comparative pit frequency study, the results of which are given in table 2. Each of a large number of test sites, given in the first row of the table, was shot once at a fixed fluence. The percentage of sites on which pitting was observed is given in the second row. The fixed fluence was chosen as 67% of the threshold for ion emission on each of the three materials. The ion threshold provides a convenient reference, eliminating the necessity for removing the sample from the test chamber for microscopy or for source calibration with a standard sample. Ion emission is somewhat less sensitive to pitting than light emission and is therefore a more appropriate reference.

The results of this study indicate that the pit frequency is substantially higher on the AVCO sample, indicating a higher density of defect sites. On the other hand, this sample exhibited no visible defects at any test site before laser damage, while four were observed on both the NWC and Y-12 samples, as indicated in the last row of table 2. Our interpretation is that the special processing of the AVCO Cu has reduced defect concentration at individual sites, but has produced a larger number and more uniform distribution of defect sites. The above-mentioned prominence of ripple patterns, the smaller average pit size, and the lower intragranular slip threshold are consistent with this interpretation.

Table 2. Pitting frequency compared on three varieties of Cu at 67% of the ion emission threshold.

	AVCO	NWC	Y-12
Sites tested	316	203	192
Percent pitted*	25.4	12.0	6.1
Visibly defective sites**	0	4	4

*At 67 percent of ion threshold
**Before laser damage.

Influence of Diamond Turning

To determine the influence of surface finishing on laser damage, comparative studies similar to the above on samples which were diamond turned under different conditions and on a polished sample were made. Diamond-turned samples which were individually turned to center were compared with others which were flycut in pairs. Flycutting differs from center turning in that the cut is interrupted as the tool passes between the two samples. The cutting (surface) speed was approximately 1200 in./min. Flycut samples were prepared at top-rake angles of +5, -5, and -10 degrees in order to investigate this variable. All center-turned samples, including those discussed in the preceding section, were turned with a top-rake angle of -5 degrees. The same diamond tool set at a side-rake angle of 0 degrees was used in all cases. Cleaning procedures were as described above.

The melt thresholds measured on the diamond-turned samples are presented without standard deviations in figure 6. It is clear that center turning yields higher thresholds, other conditions being equal. Among the flycut samples the -10 degree rake angle produces somewhat better results than the more positive angles. Figure 7 presents the same information for slip thresholds. Notice that the trends in slip thresholds are generally opposed to the trends in melt thresholds exhibited in figure 6. This is a consequence of the inverse relationship between slip and melting, which is caused by surface disorder. Here (fig. 7) lower slip thresholds indicate better surface order, so that conclusions regarding surface quality agree with those from figure 6. Evidently, the interrupted cut, higher cutting speed, or a combination of both tend to degrade surface quality. Possibly, a large negative top-rake angle reduces the shock of the interrupted cut, thus reducing disorder in the samples flycut at -10 degrees.

The inverse relationship between the thresholds for slip and melting becomes more apparent when the data are plotted in terms of these variables, as demonstrated in figure 8. In addition to the data from the diamond-turned samples, data points corresponding to intrinsic crystalline Cu and polished AVCO Cu have been included. A data point from an earlier, relatively poor-quality, diamond-turned sample is also included at the far right. The curve was drawn merely to indicate the data trend, which is consistent with our understanding of crystalline disorder effects. Surface disorder introduced by diamond machining, or polishing, increases the number of dislocations. This in turn tends to inhibit slip and raise the slip threshold. However, additional dislocations also tend to increase the scattering of conduction electrons, thereby raising the surface absorption and reducing the melt threshold. Points at the upper left, such as that for UHV-prepared Cu, therefore indicate better surface order than points at the lower right, such as those for Cu which has been polished or diamond turned under less favorable conditions. The slope of the data trend is about -0.6, indicating that the slip threshold is roughly a factor of two more sensitive than the melt threshold to the state of surface order. The fact that some of the diamond-turned samples, particularly the center-turned samples, are so close to intrinsic in terms of effective surface order is quite remarkable and indicates that diamond turning can be accomplished with a minimum of cold working.

Unfortunately, a study of low-fluence pit frequency in relation to diamond turning variables was precluded by time limitations. In order to give some indication of this relationship, we show in figure 9 the minimum fluence at which pitting was observed in the ordinary 50-site multithreshold damage test on each of the various diamond-turned samples.

As a group, the flycut samples show more pitting at low fluences. However, the cutting method and rake angle have a less consistent influence on pitting than on uniform melting and slip.

Influence of Polishing

In order to determine the influence of polishing on defect damage, a pit frequency study was performed on a sample of AVCO-polished AVCO Cu. Results are compared with those from diamond-turned AVCO Cu (cf table 2) in table 3. A substantial gradation in pit frequency was observed on the polished surface, as indicated by results from two different areas given in the first two columns of the table. In area A no advantage over diamond turning was observed. In fact, the pit density is somewhat higher than on the diamond-turned sample. In area B, however, the pit frequency is only half that shown in the last column. This tends to substantiate the view [2] that under optimum conditions the disordered layer generated by polishing can effectively "heal" small defects present in the starting material. The polished sample exhibited no visible defects at any of the test sites before laser damage.

Table 3. Pitting frequency on two areas of AVCO-polished Cu compared with that on NWC-diamond-turned Cu at 67% of the ion emission threshold. Both samples are of AVCO Cu.

	Polished		Center turned
	Area A	Area B	
Sites tested	78	78	316
Percent pitted*	35.9	12.8	25.4
Visibly defective sites**	0	0	0

*At 67 percent of ion threshold
**Before laser damage.

The increased surface disorder introduced by polishing is quite evident when one compares the resulting damage profile (fig. 10) with that of a diamond-turned surface of the same material (fig. 3). The substantially higher slip threshold and lower melt threshold on the polished sample are in accordance with increased disorder, as discussed in connection with figure 8. The large standard deviations for pits and light emission reflect the large variability in pit density indicated in table 3.

Vapor-Deposited Cu

As an alternative to bulk Cu, we have also evaluated mirrors formed by vapor deposition of Cu on polished silicon carbide substrates [10]. These samples were prepared by the Westinghouse Research and Development Center. The absence of pitting and laser-induced slip in the damage morphology is remarkable (fig. 11). This is substantiated by damage profile data (fig. 12), which also shows the excellent uniformity of these samples. Defect damage resulting in spatially selective pitting is indistinguishable from uniform melting as indicated by the equivalent thresholds for melting and pits. The lack of slip effects is believed to be a result of small crystallite size, which provides numerous channels for stress relaxation. A difficulty with these mirrors is the relatively low threshold for melting, which is well below the 76 J/cm^2 value for intrinsic bulk Cu, and varies with the thickness of the copper layer. Using the thermal modeling methods described in connection with table 1, it is concluded that the substrate thermal conductivity, which is substantially below that of Cu, is mainly responsible [10]. The possibility of raising the substrate conductivity by using improved SiC or alternative materials offers much promise for this type of mirror.

Conclusions

A number of important conclusions can be made as a result of this study. First of all, the theoretical intrinsic crystalline Cu melt threshold is in excellent agreement with latest experimental results when the 100-nsec pulse shape and temperature dependence of material properties are properly taken into account. We have also shown that special processing of the starting material can have an important influence on the size and density of defects which lead to pitting. Such processing has little apparent influence on surface crystalline order, which is modified mainly by the method of surface finishing. The effective state of surface order on bulk (coarse-grained) mirrors can be determined quite accurately from a well-defined inverse relationship which exists between the thresholds for slip and for melting. Based on this relationship, center-turned bulk Cu can be remarkably close to intrinsic in terms of its nonselective damage characteristics. Flycutting is less desirable, but the adverse effect on surface order can be moderated by using a large negative top-rake angle (-10 degrees). Under optimum conditions, polishing can reduce pitting, apparently by "healing" small defects with disordered material. However, results can vary widely, even on the same sample, and the melt threshold is invariably degraded. Vapor-deposited Cu mirrors on polished silicon carbide substrates show remarkable resistance to pitting and slip damage, but melt thresholds are relatively low. Calculations indicate the possibility of significant improvement by use of substrate materials with better heat transfer characteristics.

References

[1] Sparks, M., and Loh, Jr., E., J. Opt. Soc. Am. 69, 847 (1979).

[2] Porteus, J. O., and Decker, D. L., in Laser Induced Damage in Optical Materials (Academic Press), to be published.

[3] Porteus, J. O., Decker, D. L., Jernigan, J. L., Faith, W. N., and Bass, M., IEEE J. Quantum Electron. QE-14, 776 (1978).

[4] Porteus, J. O., Fountain, C. W., Jernigan, J. L., Faith, W. N., and Bennett, H. E., NBS Spec. Publ. 509, 204 (1977).

[5] Porteus, J. O., Soileau, M. J., and Bennett, H. E., NBS Spec. Publ. 435, 207 (1975).

[6] Porteus, J. O., Jernigan, J. L., and Faith, W. N., NBS Spec. Publ. 509, 507 (1977).

[7] Gaski, J. D., Fink, L. C., and Ishimoto, I., "Systems Improved Numerical Differencing Analyzer," TRW Systems Report #11027-6003-RO-00.

[8] Decker, D. L., and Grandjean, D. J., NBS Spec. Publ. 541, 122 (1978).

[9] Temple, P. A., and Soileau, M. J., NBS Spec. Publ. 462, 371 (1976).

[10] Porteus, J. O., Choyke, W. J., and Hoffmann, R. A., Appl. Opt. (in press).

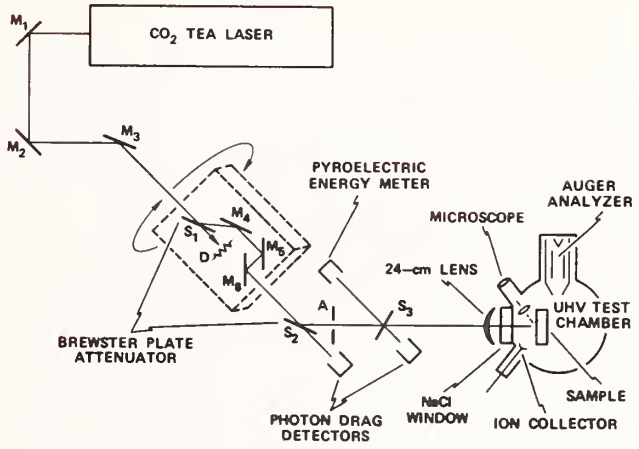

Figure 1. Laser damage facility. M_1-M_6 are bare Cu beam turning mirrors. S_1 and S_2 are ZnSe Brewster plates used for controlling incident fluence. S_1 and M_4-M_6 may be rotated as a unit about the beam axis, while S_2 remains fixed. D is a beam dump. S_3 is a NaCl beam splitter.

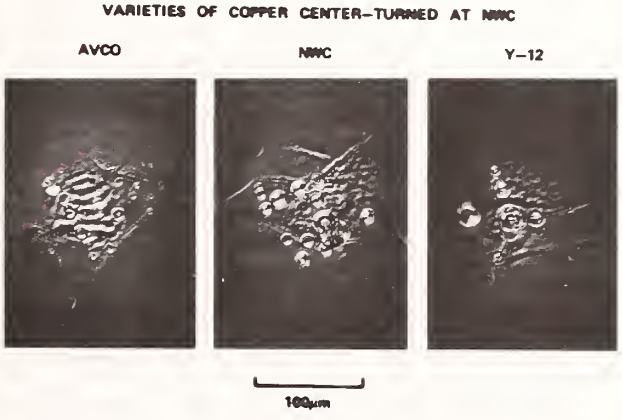

Figure 2. Damage morphology compared on bulk Cu mirrors diamond turned to center. Three varieties of OFHC Cu are represented. Laser fluence was sufficient to produce uniform melting accompanied by flash and ion emission in each case.

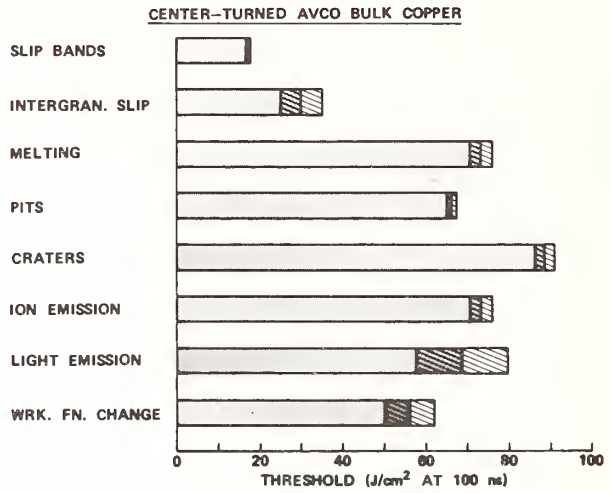

Figure 3. Damage profile for AVCO Cu, diamond turned to center. A shaded bar for each damage characteristic indicates the corresponding threshold averaged over approximately 50 damage sites on a single, representative sample. Hatched blocks represent corresponding standard deviations, which mainly indicate nonuniformity of the sample surface.

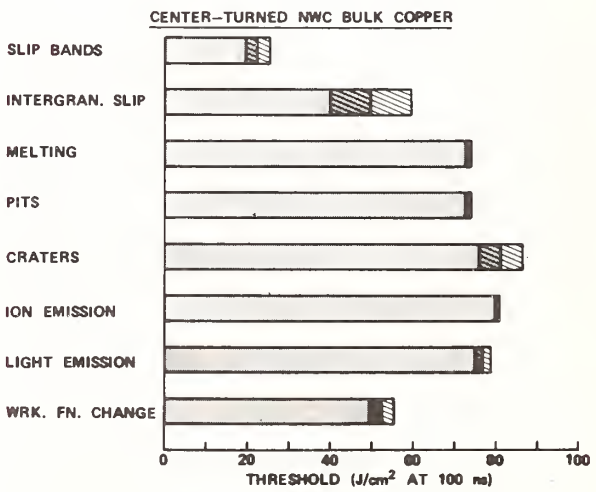

Figure 4. Damage profile for NWC Cu, diamond turned to center.

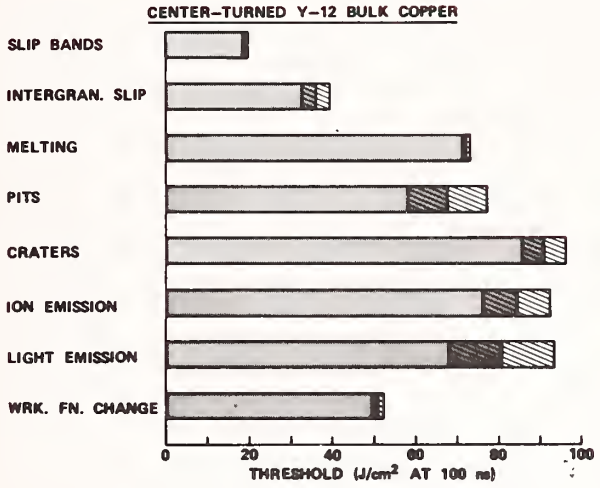

Figure 5. Damage profile for Y-12 Cu, diamond turned to center.

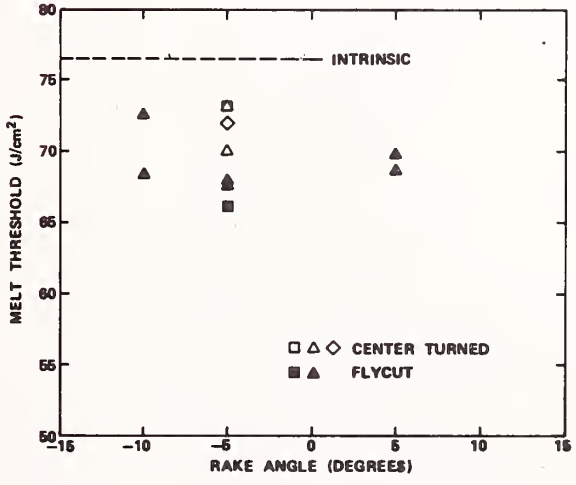

Figure 6. Melt threshold vs. top-rake angle for diamond-turned bulk Cu. Each data point represents a different sample. In addition to the type of cut, the point symbols also show the type of material as indicated in figure 9.

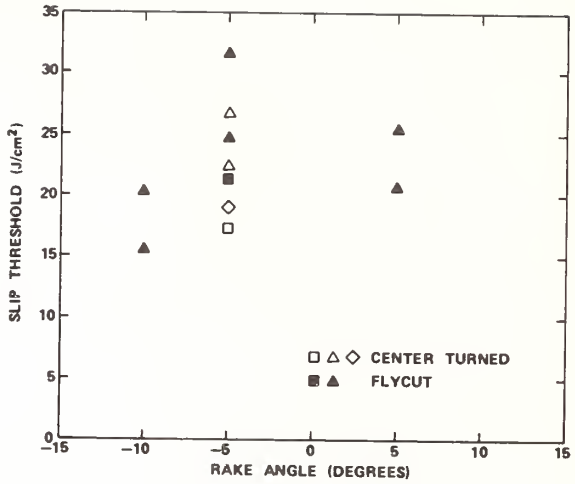

Figure 7. Slip threshold vs. top-rake angle for diamond-turned bulk Cu. Point symbolism corresponds to the preceding figure.

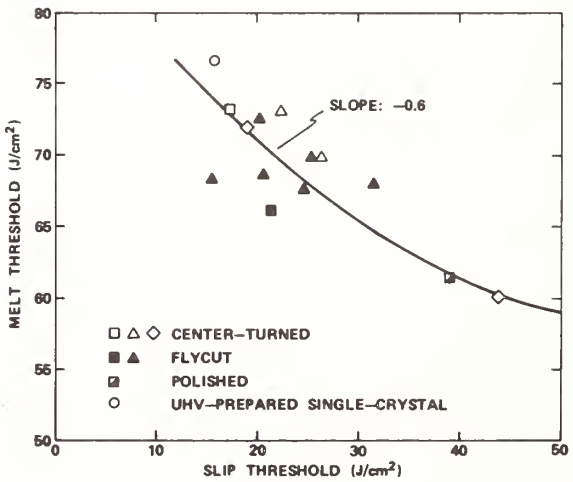

Figure 8. Melt vs. slip thresholds for diamond-turned, polished and intrinsic Cu samples. Point symbolism corresponds to the preceding figure for the diamond-turned samples. The data point at the far right is from an earlier batch of Y-12 Cu which was center turned with a tool in relatively poor condition.

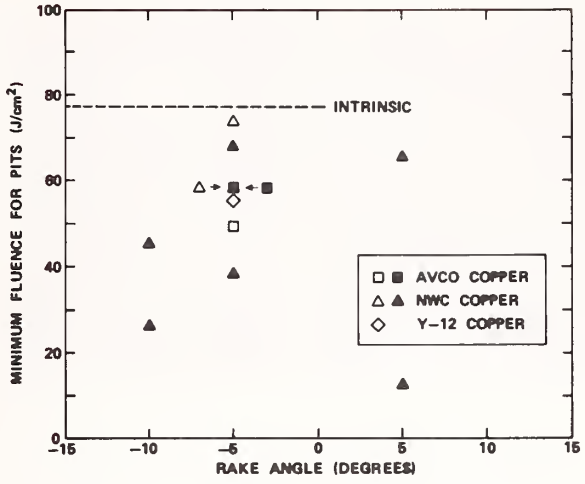

Figure 9. Minimum fluence for pit formation on diamond-turned samples. Data is based on an ordinary 50-site multithreshold damage test in each case. Light and dark symbols represent center-turned and flycut samples, respectively, as in the preceding three figures.

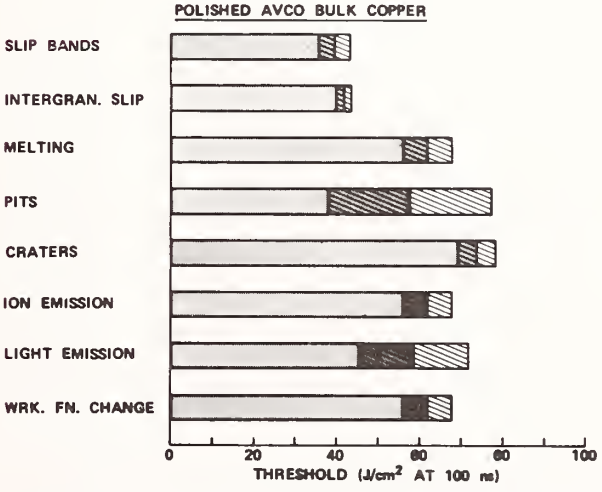

Figure 10. Damage profile for AVCO Cu polished by AVCO. Surface disorder compared to a diamond-turned surface of the same material (fig. 3) is high, as indicated by thresholds for slip and melting. See also figure 8.

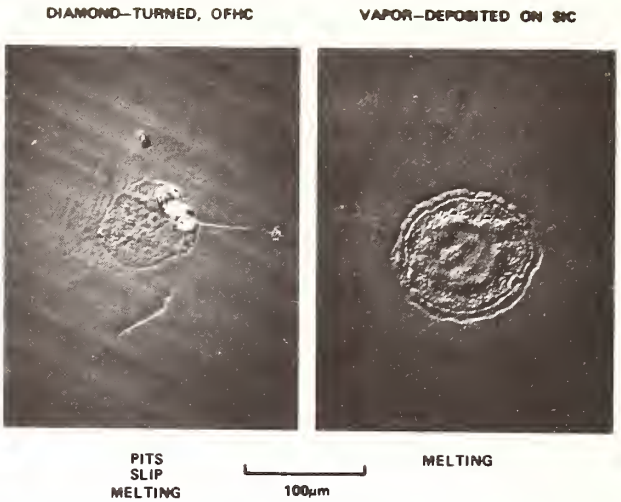

Figure 11. Damage morphology of vapor-deposited Cu mirror (right) compared with that of a diamond-turned bulk OFHC Cu mirror (left). Slip bands, intergranular slip faults and pits, which can be seen on the left, are absent from the vapor-deposited sample.

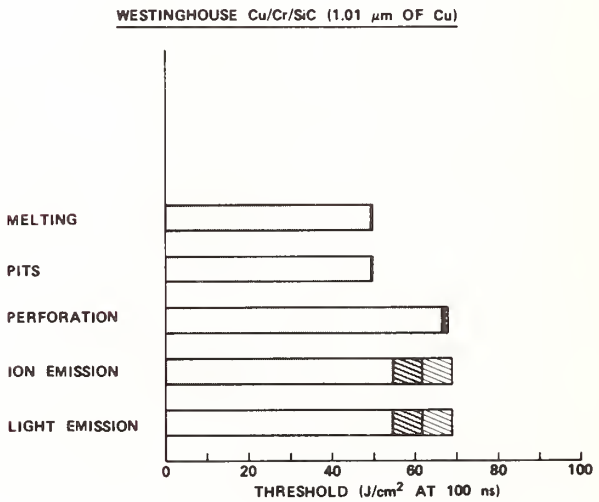

Figure 12. Damage profile of a vapor-deposited Cu mirror having a 1.01-μm thickness of Cu. The excellent uniformity is indicated by the extremely small standard deviations of the thresholds for melting and pits.

LASER-DAMAGE RESISTANT COPPER SURFACES WITH HIGH REFLECTIVITY AFTER OXIDATION

M. Oron†, L.G. Svendsen, and G. Sørensen
Institute of Physics, Iniversity of Aarhus
DK-8000 Aarhus C, Denmark

Ion implantation of aluminum into copper has been used to produce mirror surfaces with improved properties with respect to pulsed-laser damage. Upon oxidation of implanted samples, they show a much higher reflectivity of the laser pulse compared to non-implanted samples. The oxidation has been followed by Rutherford backscattering technique and nuclear reactions, and the improved surface properties are explained by the presence of compound oxide layer beneath the surface, which shows greater stability against decomposition than the pure metal oxide. This novel coating technique, comprising ion implantation and oxidation, may be advantageous in improving surface properties such as reflectivity of metal mirrors.

Key words: Laser damage; ion implantation; corrosion inhibition; mirror surfaces.

1. Introduction

Development of damage-resistant mirrors for high-power pulsed lasers is of crucial importance. As far as metal mirrors are concerned, Porteus et al. [1][1] have performed an evaluation for high-power applications. They found that oxidation preferentially lowers the threshold for plasma formation, which produces transient optical degradation in addition to permanent damage. Goldstein et al. [2] have studied pulsed-laser damage to uncoated metallic reflectors and indicate a ranking of material with copper being the optimum one followed by silver and gold. However, copper as well as other metals will oxidize, which lowers the threshold for laser damage, and the reflectivity may thus deteriorate due to thermal decomposition of the oxide layer. By alloying, it is possible to inhibit the oxidation of metals, and in recent years, ion implantation has been used as a tool for surface alloying [3].

Copper possesses excellent thermal conductivity and good reflectivity. Oxidation of copper has been the subject of several papers, e.g., [4], and recently, ion accelerators have been applied to surface alloying with the purpose of obtaining corrosion inhibition [5,6]. It has been reported that ion implantation of aluminum results in a build-up of a protective layer consisting of a mixture of oxides of aluminum and copper located somewhat beneath the surface [7]. In the present study, ion implantation of aluminum into copper has been used as a tool to inhibit oxidation and thus improve the surface properties with respect to reflection of high-power laser pulses. A detailed study of the oxidation of copper influenced by various dopants (Ti, Cr, etc.) and their ability to build up protective surface layers will be published in detail elsewhere.

As far as metal mirrors for high-power lasers are concerned, there is a need for a suitable surface coating, which inhibits oxidation and, if possible, creates a thermally stable oxide in the surface layers. Although ion implantation is an expensive coating technology, the application may be justified when the production cost of laser mirrors is considered.

Ion implantation offers several advantages as a coating technique, and it should be emphasized that this technique does not introduce a definite boundary layer as evaporation

---

†Permanent address: Soreq Nuclear Research Centre, Yavne, Israel.

1. Figures in brackets indicate the literature references at the end of this paper.

techniques. The thermal conductivity is supposed to remain good in the surface layers; hence the coated layers are not burned off due to the laser power. Even though the surface may become oxidized, the formation of a thermally stable surface oxide with a mixed composition might also improve the properties of the metal with respect to laser damage.

It has been the scope of the present study by a combination of ion implantation of aluminum into copper and subsequent surface oxidation to create a coating in a copper-mirror surface, which consists of a mixture of various oxides of aluminum and copper, with a good stability against thermal decomposition. Aluminum was chosen as a dopant because it can be considered a getter material in view of the reaction $2Al+3Cu_2O \rightarrow 6Cu+Al_2O_3$. According to the literature, Al_2O_3 is more passivating than Cu_2O, but it should also be possible to synthesize mixed oxides such as $CuAlO_2$ and $CuAl_2O_4$ with good thermal and passivating properties. The deterioration of an oxidized copper surface is particularly crucial due to the low decomposition temperatures of copper oxides. Thus an improvement of the thermal stability of copper-metal surfaces might expand the application to mirror purposes.

2. Experimental procedure

The first part of the experimental procedure concerns ion implantation of aluminum into copper and a study of the oxidation processes, while the second part deals with a study of the damage to the metal-oxide surfaces made by a high-power laser.

Pure copper was electropolished prior to ion implantation, which was performed at 60-80-keV ion energy, utilizing the isotope separator at the Institute of Physics, University of Aarhus. Ion beams of Al^+ were produced by the carbon-tetrachloride method, where an oxidized aluminum foil was placed in a heated quartz tube, through which there was a flow of CCl_4. Ion currents of 10-30 μA were usually obtained. To make the implantations homogeneous, the ion beam was swept electronically. Doses between 10^{17} and 2×10^{17} ions/cm^2, which correspond to an alloying percent of 10-20% if equal sputtering of the alloying compounds is assumed, were used. Concerning the penetration of the energetic aluminum ions into copper, the projected range can be theoretically estimated, as shown by Lindhard et al. [8]. For 60-keV Al^+ in copper, the theoretically estimated projected range corresponds to 28 μg/cm^2, which is equal to 310 Å. However, implantation of high doses usually leads to a larger penetration with a rather constant dopant distribution in the surface. In this case, the range profile of the implanted aluminum was measured by comparing Rutherford backscattering (RBS) spectra with similar spectra from pure copper, using a 3-MeV He^+ beam, which was scattered 150° by the sample into a solid-state detector. The aluminum-implanted region was found to extend ∿1300 Å from the surface, which is considerably more than the theoretically estimated projected range of 310 Å [8] that, assuming a certain straggling, could account for a penetration of ∿400 Å. Further, it was found that the alloying percentage was rather constant within the total penetration depth.

The copper samples were then oxidized by isochronal annealing in atmospheric air. In the present communication, only results obtained at 200°C or below have been included, while high-temperature oxidation temperatures will be published elsewhere. The oxide thicknesses obtained at a time scale of hours at 200°C or days at 100°C are comparable with oxide thicknesses obtained by a long-term oxidation at room temperature or at temperatures slightly above room temperature. In the present study, the oxidation of metals and the distribution of dopants were traced using nuclear-reaction techniques ($^{16}O(d,p)^{17}O$) and Rutherford backscattering (RBS), and these two techniques can map the elemental distribution in the surface layer [9]. The aluminum implantations covered an area of 4×4 mm, which appeared more grey than the non-implanted regions. After oxidation, it was easy to observe that aluminum implantation did indeed form a considerable protection against oxidation. After some time of oxidation, the grey, implanted area regained its red copper colour, while the non-implanted area was tarnished.

Reflectivity measurements are very sensitive to the surface treatment. In the present study, the effect of ion implantation was found by performing measurements of laser-pulse reflection from the particular samples implanted and from non-implanted areas. A conventional technique was used. The neodynium-glass laser (wavelength 1.06 μm) was Q-switched with a Pockels cell, having a variable pulse length from 10 μs (free-running mode) to 50-100 ns (Q-switched). The laser power in the pulse could be varied up to 5 J with an exposed area of ∿1 mm^2. The signal from the two photodiodes was visualized on a storage scope, and thus

the ratio between the incoming and reflected laser pulses was evaluated. For the long pulse length, the values of reflectivity could be put on an absolute scale via a measurement from a silver mirror of known reflectivity. The laser-pulse power was measured calorimetrically.

3. Experimental results

It is possible from an analysis of Rutherford-backscattering spectra to obtain information on the elemental distribution on the surface, and a detailed description on the analytical technique will be published elsewhere [9]. In the case of copper, the backscattering yield will be qualitatively lowered by the presence of lighter elements such as oxygen and aluminum. Figure 1 shows three stages of oxidation at 200°C of a copper sample which, previous to oxidation, was implanted with a dose of 2×10^{17} aluminum ions/cm^2. The RBS spectra for unoxidized samples are shown for comparison. In figure 1, the dip in the curves shows that as the oxidation proceeds, a copper-deficient layer beneath the surface is created. This is in contradiction to what is known from the oxidation of pure copper, where the surface composition is almost CuO, while deeper layers to a larger degree consist of Cu_2O. The presence in the implanted samples of a copper-deficient zone therefore indicates the presence of Al_2O_3. In Table 1 are listed the measured oxide thicknesses in atoms

Table 1

Oxidation, days at 200°C	Copper sample			Aluminum-implanted copper sample (2×10^{17} ions/cm^2)		
	Thickness of O layer ($\times10^{18}$ Cu at/cm^2)	Composition, average	Composition, surface	Thickness of O layer ($\times10^{18}$ Cu at/cm^2)	O composition, average	O composition, surface
5	3.0	Cu_2O	CuO	0.7	CuO	-
10	3.1	Cu_2O	CuO	0.7	CuO	-
15	3.2	Cu_2O	CuO	0.5	$CuO_{1.5}$	-

of copper and average as well as surface composition of the oxide layers. The implantation of aluminum to a dose of 2×10^{17} ions/cm^2 inhibits oxidation by a factor of 4-6. It should be noted that after implantation, the aluminum concentration was almost constant, but after oxidation, the aluminum was concentrated at a depth of ∿400-600 Å beneath the surface. Hence diffusion processes may play a role in the formation of the aluminum-rich passivating layer.

The samples used for reflectivity measurements were implanted at 80 keV with 10^{17} ions/cm^2 of aluminum. In the region without the amplifier, the laser pulse was in the 0.1-0.2 Joule/pulse region. With the amplifier, reflectivity of laser pulses in the 1 Joule/pulse region was measured.

Experiments with a laser pulse of 0.2 Joule were performed in aluminum-implanted samples, which had been oxidized for 24 h at 100°C and 150°C, respectively. At the low temperature, the reflectivity of the implanted and non-implanted areas was almost identical. However, at 150°C, a marked difference was noticed. While the reflectivity for the aluminum area was measured to be 98%, the non-implanted region showed a decrease in reflectivity of 66%. A number of aluminum-implanted samples were oxidized at 200°C for different periods prior to the reflectivity measurements (laser pulse 0.2 Joule), and the results are shown in figure 2. Since the reflectivity may vary from sample to sample due to the polishing procedure, figure 2 shows the decrease in reflectivity for individual samples of the non-implanted area normalized to the implanted area. It is observed that thicker oxide layers exhibit a considerable decrease of the reflectivity in the cases where aluminum was not implanted prior to the oxidation process.

For a laser pulse of the order of 1 Joule/pulse over an area of ∿3 mm diameter, the reflectivity measurements based on the pulse itself appear to be more complex. One reason may be the presence of aluminum impurity atoms in the surface plasma created. A copper sample was implanted with 10^{17} Al/cm^2 and oxidized at 100°C for 7 days. A laser pulse of 1 Joule/pulse will melt and decompose the surface layer. Figure 3 shows SEM pictures (mag-

nification 2000) from such oxidized copper samples in the center of the laser spot and in the border region. While the surface layer appears to have been totally melted in the center, the picture looks quite different in the border region of the laser spot. Here doughnut-shaped craters are found, which may be taken as an evidence of thermal-spike melting combined with gas evolution from the oxide decomposition. Now the samples were used as reflector of 1.2, 1.5, and 1.0 Joule on the non-implanted and 1.6, 1.7, and 1.6 Joule on the implanted area. Although the total laser power in this case is 25% higher for the implanted area, the visible damage is much less, as shown in figure 4, where the total laser spot with a magnification of 40 in a scanning electron microscope is displayed. When looking at a magnification of 450 (fig. 5), it is observed that also the character of the damage is different. The non-implanted area appears to have been totally melted on the surface, while the implanted area has characteristic doughnut-shaped structures, indicating that there has been local melting around spikes in the laser profile.

4. Discussion

The experimental findings of the present study indicate that by ion implantation of aluminum into copper, it is possible to improve the reflectivity of polished surfaces that have been oxidized in air at a temperature of 200°C or less. At these low temperatures, the RBS supports the idea of formation of a protective aluminum-oxide layer beneath the surface. Whether this layer consists of $CuAlO_2$ or mixtures of the respective oxides cannot be verified at present. However, the experiments show that after oxidation, aluminum is present in the outer surface layer (fig. 1) only to a small extent. This finding is also supported by preliminary SIMS measurements using the CAMECA probe at A.E.R.E., Harwell, and a computer unfolding of the RBS spectra [9]. By such an unfolding procedure, it is found that a copper sample, after aluminum implantation (2×10^{17} at 80 keV) and oxidation for two hours at 300°C, shows a two-layer structure consisting of a $\sim2.7\times10^{17}$ CuO mol/cm^2 layer on top of a $1.5\text{-}1.9\times10^{17}$ $CuAlO_2$ mol/cm^2 layer. The presence of such a two-layer oxide could explain the experimental observation that high-power laser pulses develop deeper craters in non-implanted areas. When a laser pulse is reflected from a metal surface, the power and the wavelength is of crucial importance because most surfaces are covered with oxide layers, where the power is absorbed. In the case of copper oxides, these are not thermally stable, and before melting of the metal, the oxides are decomposed. The present study shows that for oxides containing aluminum in the surface layer, the reflectivity is decreased much less for powers in the region of a few tenths of a Joule per pulse. When the samples were oxidized for some hours at 200°C prior to the reflection of the laser pulse (fig. 2), it should be noted that the largest improvement is observed for thick oxide layers. For thin oxide layers, only a slight improvement is observed because the laser pulse cleans the surface without further damage. It is also observed that for the same reason, the reflectivity of the non-implanted area after some pulses does not change compared to the implanted area. For the lowest reflectivity measured, the implanted areas showed a reflectivity roughly a factor of two better than did the non-implanted areas.

Reflection of laser pulses in the region above 1 Joule per pulse appears to be a complicated process. Thus Zavecz and Saifi [10] have studied the reflectivity from copper single crystals and found a drop in reflectivity to values much lower than can be ascribed to dielectric-like behaviours of the molten zone. As shown in figure 5, the ion implantation of aluminum reduces the melting of the surface; hence it must be expected that also at very high high power levels, the reflectivity of metal surfaces may be increased by ion implantation.

In the present study, the feasibility of producing a thermally stable surface coating has been demonstrated, but it should be noted that such a compound oxide might also change the hardness of the surface, and possibly a metal surface of copper and other metals could be hardened by ion implantation, oxidation, and laser annealing. Thus the combination of ion implantation, surface oxidation, and laser annealing might open up a number of possible new applications in the micro-metallurgy of solid metal surfaces in order to improve also other metal-surface properties than the reflectivity.

5. References

[1] Porteus, J.O., Decker, D.L., Hernigan, J.L., Faith, W.N., and Bass, M., IEEE J. Quant.Electronics 14, 776 (1978)

[2] Goldstein, I., Bua, D., and Horrigan, F.A., in: Laser-induced damage in optical materials, NBS special publication 462, 41 (1976)

[3] Dearnaley, G., in: Applications of ion beams to metals, eds. S.T. Picraux et al., (Plenum Press, 1974) p. 63

[4] Rönquist, A., and Fishmeister, H.F., J. Inst.Met. 89, 65 (1960)

[5] Naquib, H.M., Kriegler, R.J., Davies, J.A., and Mitchell, J.B., J.Vac.Sci.Tech. 13, 396 (1976)

[6] Rickards, J., and Dearnaley, G., in: Application of ion beams to metals, eds. S.T. Picraux et al. (Plenum Press, 1974) p. 101

[7] Svendsen, L.G., Corrosion science, in press (1979)

[8] Lindhard, J., Scharff, M., and Schiøtt, H.E., K.Dan.Vidensk.Selsk.Mat.Fys.Medd. 33, No 14 (1963)

[9] Børgesen, P., and Svendsen, L.G., to be published

[10] Zavecz, T.E., and Saifi, M.A., Appl. Phys.Lett. 26, 165 (1975)

6. Figures

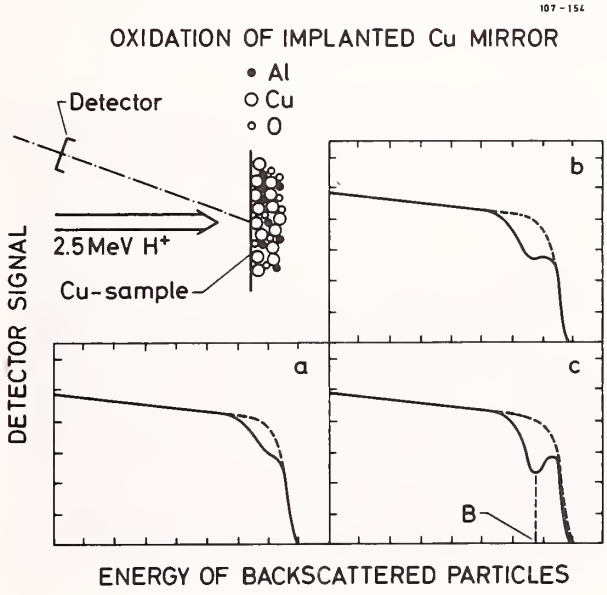

Figure 1. The backscattering yield of 3-MeV He^+ backscattered 145° from Al-implanted Cu (2×10^{17} ions/cm^2 at 60 keV). The samples have been oxidized at 100°C for (a) 5 days, (b) 10 days, and (c) 15 days. Solid curves represent oxidized samples and dashed curves non-oxidized samples (shown for comparison).

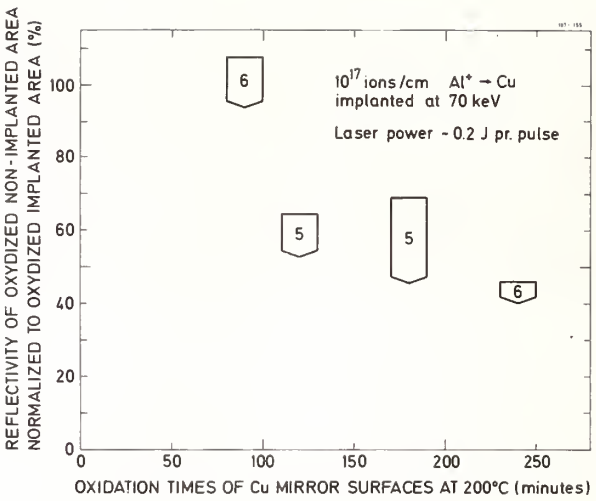

Figure 2. The change in reflectivity of an oxidized Cu area normalized to an oxidized Al-implanted area (10^{17} ions/cm^2 at 70 keV). The framed areas show the range in reflectivity change caused by the number of pulses ($\sim$0.2 J), which is indicated by the figure in the frame.

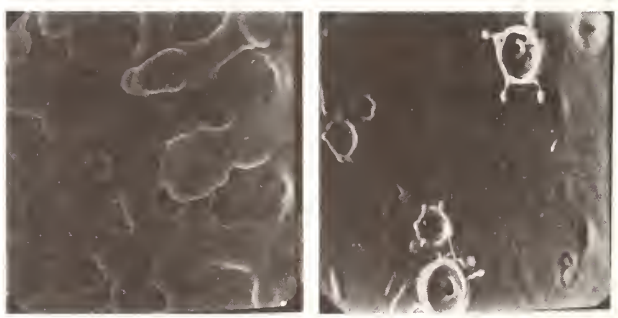

Figure 3. Scanning electron-microscope picture (magnification 2000) of a Cu surface exposed to a laser pulse of 1 J after oxidation in atmospheric air for 7 days at 100°C. Left-hand part shows center of laser spot. Right-hand part shows the border of the laser spot.

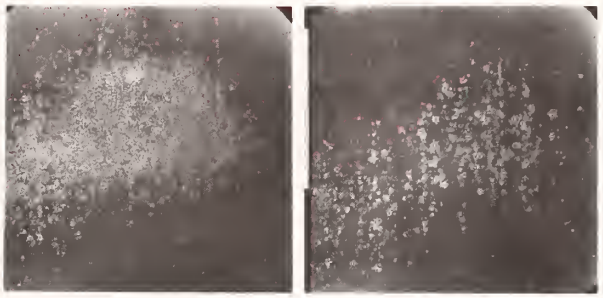

Figure 4. Scanning electron-microscope picture (magnification 45) of laser spot caused by three pulses (each ∿1.5 J). Prior to laser exposure, the sample was oxidized for 7 days at 100°C. Left-hand part shows non-implanted area. Right-hand part shows implanted area (10^{17} ions/cm^2 Al).

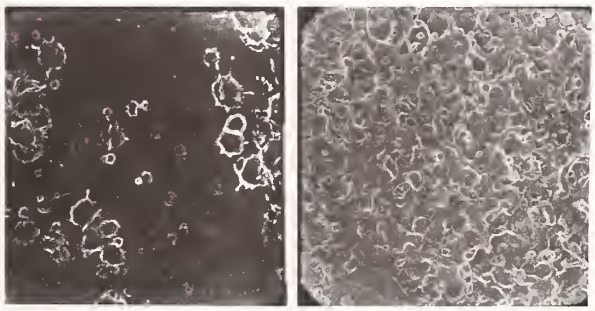

Figure 5. Larger magnification of figure 3. Left-hand part shows oxidized, non-implanted area. Right-hand part shows implanted area (10^{17} ions/cm^2 Al$^+$).

The speaker indicated that samples were exposed for several minutes to ion currents of up to 30 microamperes.

LASER-INDUCED BREAKDOWN OF DIAMOND-MACHINED WINDOW SURFACES*

M. J. Soileau, J. O. Porteus, and D. L. Decker
Michelson Laboratory, Physics Division
Naval Weapons Center, China Lake, California 93555

Previous work on diamond-turned KCl at 10.6 μm has shown that this technique has significant promise for improving the resistance to laser damage over that of polished surfaces. This work examines the particular characteristics of turned surfaces on CaF_2 and SrF_2 which influence the pulsed laser damage thresholds at 2.7 and 3.8 μm. We consider (1) polarization dependence due to the periodic nature of the surface roughness of turned surfaces, (2) damage to the material produced by the turning process, and (3) residual contaminants introduced by machining. The laser source is an HF-DF TE laser which produces plane-polarized, single-mode 120- and 90-nsec pulses at 2.7- and 3.8-μm wavelengths, respectively. The spatial distribution of intensity on target is Gaussian to the $1/e^2$ points. Detailed morphology is obtained from Nomarski and dark-field optical microscopy. The effect of laser conditioning is examined by comparing thresholds and surface characteristics on areas of the surface exposed to nondamaging laser pulses (n-on-1 effect). The so-called n-on-1 effect was found to be wavelength selective with a much larger effect seen at 2.7 than at 3.8 μm. This result provides information on machining damage and may have important implications for laser processing as a possible means of improving the performance of machined optical surfaces.

Key words: Diamond turning; infrared windows; laser breakdown; polishing; surface damage.

Surfaces prepared by precision diamond machining are compared with surfaces prepared by conventional polishing. The results indicate that the diamond-machined surfaces have as high or higher failure resistance under high fluence loading as surfaces prepared using conventional techniques. Failure of both types of surfaces is strongly dependent upon surface structure and surface contamination. Laser conditioning experiments indicate that absorbed surface water is a significant contributor to surface failure under high fluence loading at 2.7 μm.

Diamond machining has been shown to be an effective means of producing high quality optical surfaces on metal mirrors [1][1]. The technique has been applied to relatively soft dielectrics such as KCl and NaCl with promising results [2]. In this work, diamond-machined surfaces were produced on single-crystal SrF_2 and CaF_2 and polycrystalline MgF_2 (Irtran II).

Disc-shaped specimens, which had previously been polished using conventional techniques, were turned on-center with a single-point diamond tool [3]. Part of the polished surface was left intact for comparison with the machined surfaces. The tightly focused output of a pulsed HF/DF laser was used to probe the surfaces. The critical laser parameters are given in table 1. Further details of the laser facility are given elsewhere [4].

Table 1. Laser parameters.

Laser	Pulse energy (J)	Wavelength (μm)	Pulse width (nsec)	e^{-2} Focal spot diam. (μm)
HF	0.2	2.7	125	53
DF	0.2	3.8	95	57

* Work supported by the Office of Naval Research
[1] Figures in brackets indicate the literature references at the end of this paper.

The thresholds for visible spark, increased visible scatter and/or truncation of the beam transmitted through the sample, were measured in air for both the diamond-machined and conventionally polished surfaces. Changes in the surface were monitored with a 20-power microscope. The threshold for a particular effect was defined as that flux which produced the effect in 50% of the sites when irradiated with a given laser intensity. Unless otherwise noted, each site was irradiated only once.

The results of the threshold measurements are summarized in table 2. The failure of single-crystal surfaces was manifested by a visible spark, increased visible scatter, and abrupt truncation of the beam transmitted through the sample. Failure near threshold occurred at the peak of the pulse. This type of failure is suggestive of an avalanche breakdown process. The failure of the polycrystalline MgF_2 surfaces was characteristic of thermal processes, i.e., near threshold the visible scatter increased, but there was no visible spark or truncation of the transmitted beam.

Table 2. Summary of 1-on-1 damage thresholds.

Specimens	Machined low scatter	Machined high scatter	Polished
	HF thresholds (10^9 W/cm^2)		
CaF_2	7.04	4.4	6.75
SrF_2-4	2.86	3.86	6.74
SrF_2-2	6.84	3.95	4.68
MgF_2 (poly)	0.32	....	0.34
	DF thresholds (10^9 W/cm^2)		
CaF_2	10.6	7.99	9.37
SrF_2-4	5.22	3.97	12.0
SrF_2-2	8.20	....	6.34
MgF_2 (poly)	0.51	....	0.47

The most significant features of the results given in table 2 are: (a) Thresholds for the diamond-machined surfaces are of the same order as those of the polished surfaces; (b) thresholds for the polycrystalline MgF_2 are an order of magnitude lower than those of the single-crystal materials, (c) for all the surfaces studied, the HF (2.7 μm) thresholds are lower than the DF (3.8 μm) thresholds, and (d) thresholds are dependent on the surface quality of the materials.

The single-crystal samples showed alternating azimuthal regions of high and low visible scatter which were apparently determined by the relationship of the cutting direction to the crystallographic axes [3]. Thresholds were generally found to be 50% lower in the high scatter regions.

The lower thresholds at 2.7 μm as compared to 3.8 μm is suggestive that absorbed surface water is contributing to the failure of both the polished and diamond-machined surfaces. More evidence for the influence of surface water is seen in the results of N on experiments given in table 3. The so-called N-on-1 thresholds were determined by first irradiating a site five times at a flux equal to 80% of the damage threshold for single irradiations and then increasing the flux until damage results. Note that for all cases where an N-on-1 effect is seen, the effect (an increase in damage threshold) is greater at 2.7 μm than at 3.8 μm. These results suggest that selectively absorbing contaminants, e.g., water, are being removed from the surface. The peak of the water absorption band corresponds to the strongest HF line (2.7 μm), and thus absorbed surface water is a likely contributor to surface damage at HF frequencies.

Table 3. N-on-1 effect (percent increase).

Specimens	Machined HF	Machined DF	Polished HF	Polished DF
CaF_2	54	40	47	26
SrF_2-4	0	..	..	..
SrF_2-2	21	13	0	..
MgF_2 (poly)	21	14	0	..

The effect of the orientation of the residual machining grooves with respect to the laser electric field was investigated. The threshold was measured with the linearly polarized laser field parallel to and normal to the machining grooves. Polarizable defects normal to the incident field should enhance the coupling of the laser energy to the surface and lower the threshold [5]. The threshold was approximately 10% lower for the case of the field normal to the grooves than for the field parallel to the grooves. This decrease in threshold is as predicted by theory and is of little consequence for these low index materials. However, for high index materials such as GaAs, Si, ZnSe and Ge, the effect could be significant. Figure 1 illustrates the effects of the interference of the induced polarization field and the incident laser field for the case of the incident field normal to the residual machining grooves.

In summary, diamond-machined surfaces on SrF_2, CaF_2, and polycrystalline MgF_2 have HF/DF laser damage thresholds of the same order as polished surfaces on these materials. The mechanism of failure for single-crystal CaF_2 and SrF_2 appears to be electron avalanche breakdown initiated by defects and impurities for both diamond-machined and polished surfaces. The mechanism of failure for polycrystalline MgF_2 appears to be absorption by defects present throughout the material. The lower thresholds at HF frequencies compared to those at DF frequencies and the larger N-on-1 effect at HF frequencies indicated that absorbed water has a significant effect on the surface damage thresholds.

References

[1] The following review article summarizes the work on diamond-turned metal surfaces and is a good guide to work in this area: Porteus, J. O., in Laser Induced Damage in Optical Materials (Academic Press), to be published.

[2] Soileau, M. J., et al., NBS Spec. Publ. 462, 149 (1976).

[3] Decker, D. L., et al., NBS Spec. Publ. 562, 293 (1979).

[4] Van Stryland, E. W., et al., NBS Spec. Publ. 509, 118 (1977).

[5] Temple, P. A., and Soileau, M. J., NBS Spec. Publ. 462, 371 (1976).

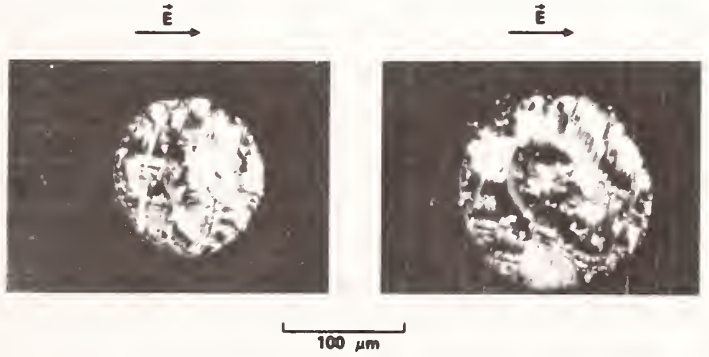

Figure 1. "Laser-Induced...Window Surfaces", Soileau et al.

OPTICAL AND SURFACE PHYSICAL CHARACTERISTICS OF DIAMOND-MACHINED INFRARED WINDOW MATERIALS*

D. L. Decker, D. J. Grandjean, and J. M. Bennett
Michelson Laboratories, Physics Division
Naval Weapons Center, China Lake, California 93555

This paper presents the results of the diamond turning of surfaces of a wide range of single-crystal and polycrystalline infrared window materials, including Ge, CaF_2, MgF_2, SrF_2, KCl, and GaAs. These surfaces were obtained from an advanced air-bearing, diamond-turning machine recently brought to an operational state at the Naval Weapons Center. The surface characterization performed includes a wide range of optical and surface physical examination including an analysis of scattered and absorbed light, and a surface micro-topographic examination by diamond profilometry, phase contrast interference (Nomarski), and scanning electron microscopy. These data are compared with earlier results and are related to the characteristics of the Naval Weapons Center diamond-turning machine and to the machining parameters. A companion paper at this conference discusses the laser damage resistance of these surfaces with implications for their use in laser applications.

Key words: Diamond single-point machining; dielectrics; infrared optical components; laser damage; optical properties.

Introduction

Diamond single-point turning or milling as a manufacturing method for precision optics has been demonstrated at a number of laboratories, notably the Energy Research and Development Administration complexes at Livermore, Calif., and at Oak Ridge, Tenn. [1,2].[1] The advantages of this technology over conventional methods include significant cost savings in many cases but, more importantly, the ability to readily generate aspheric surfaces which would be difficult or impossible otherwise. The materials which are amenable to diamond single-point machining are not limited to metals such as aluminum and copper and many of their alloys, but also include an impressive list of infrared window materials, useful as domes, windows, and lenses (see table 1). Much recent interest in diamond single-point machining is a direct result of the superior optical components for high energy laser application that can reliably be produced by this method. However, there are many low power laser or imaging optics applications for which the method offers significant system performance improvement over what can be done with conventional components [3].

This paper presents surface physical and optical characterization results for dielectric surfaces machined on the Naval Weapons Center (NWC) diamond-turning machine. The optical fabrication criteria outlined in table 2 are given as a reminder of the finishing requirements for a component. This paper is primarily concerned with surface microtopography and the directly related topic of scattered light [4,5]. Most of the previously reported work has been of a qualitative sort, and has not been followed up by detailed optical characterization or optimization of results [6]. This paper presents for the first time data relating to the mechanisms of material removal and the relationship of these mechanisms to the crystalline orientation of the work surface to the machining geometry.

*Work supported by Naval Weapons Center Independent Research Funds.
[1]Figures in brackets indicate the literature references at the end of this paper.

Table 1. List of dielectric materials which have been successfully diamond single-point machined as of 1979.

CaF_2	NaCl	ZnS
MgF_2	NaF	ZnSe
SrF_2	Si	$LiNbO_3$
KCl	Ge	GaAs
	acrylic plastics	

Table 2. Summary of the fabrication requirements which apply to most optical components.

Optical figure
Surface absorption
Scattered light
Damage threshold

Machining Technique and the Material Removal Process

The basic diamond-machining process discussed here is that of single-point turning or milling of a surface in the fashion of ordinary machine shop fabrication but using a very precise machine and special diamond tools (fig. 1). The diamonds used are of gem quality and are mounted and polished to a supersharp, highly accurate, radiused cutting edge. The overall view in figure 2 shows the tool and spindle slides of the NWC machine which are arranged in a T-base configuration [7].

In the case of a metal workpiece, material is removed by the tool in machining by shearing a chip from the surface. The idealized surface profile in a diametral plane perpendicular to the turned work surface is shown in figure 3. The tool nose radius r is typically 1/8 inch, and the tool feedrate is in the range of 10^{-4} inches per spindle revolution. The theoretical peak-to-valley roughness in this case is 10^{-8} inches. In actual practice, as the feedrate is made smaller the surface finish does improve as predicted; it approaches an asymptotic roughness controlled by material imperfection and irregularity in the machining process. The latter effects include very high frequency (10^6 Hz) chip vibration/surface interaction effects which are possibly excited by chip/tool friction [7,8]. Tools and feedrates typically used to machine dielectric surfaces are similar to those used to machine metal surfaces. In contrast with metal machining, there is strong tool/surface speed dependence to the resulting dielectric surface characteristics.

Material removal from most dielectrics examined in this paper occurs apparently as a consequence of brittle fracture. There is no evidence of plastic deformation in these cases, either on the resulting surface or on the machining debris. This statement is based upon scanning electron microscopy of the machined surfaces and machining debris. No subsurface examination has been made. A pitting effect occurs which is very sensitive to tool geometry and to crystallographic orientation. The location of "clear" and "cloudy" areas on diamond-turned surfaces of several materials is shown in figure 4. The visual effect of a cloudy area is a consequence of light scattering from microscopic pits. When turned on center, single-crystal materials develop a clear/cloudy pattern which will usually have the rotational symmetry of the crystallographic plane exposed by machining. The [331] axis in a cubic lattice is tipped only approximately 20° away from the [111] axis which, of course, has threefold rotational symmetry. Samples (a) and (b) of CaF_2 have virtually the same orientation, with sample (b) showing the expected symmetry, but (a) shows curious skewed twofold symmetry. The origin of the effect discovered in sample (a) is unknown, and this anomaly was observed only in this case out of several dozen samples of different materials and a variety of orientations which were turned in this study.

It is useful to examine these surfaces microscopically both with a light microscope and by electron microscopy at much higher magnification. Figures 5 and 6 are Nomarski interference contrast micrographs of an Irtran MgF_2 sample and single-crystal CaF_2 sample (b). In all cases, the samples were originally polished and were subsequently diamond turned, leaving a central polished spot for direct comparison. As shown in figure 5, the quality of the Irtran surface is substantially limited by voids remaining from processing of the material both in the polished and diamond-turned areas. In the case of single-crystal CaF_2 (fig. 6), the clear diamond-turned area is indistinguishable from the polished area. The scanning electron micrographs of figure 7 compare CaF_2 (b) polished and diamond-turned clear areas at

much higher magnification. The polished surface is defined by a superposition of scratches from the polishing grains. Most of the clear diamond-turned area is an extremely smooth, almost featureless, surface. The localized pitted areas often show the effects of multiple tool passes and a very interesting repetitive nature with a spatial period which varies from slightly less than 1 μm down to 0.5 μm (fig. 7). This variation is seen to occur even over a very small area and shows no correlation with position on the sample. Figure 8 shows the localized nature of the cloudy areas and a high magnification view of the pits in a cloudy area. There is no qualitative shape or size difference of the pits occurring in clear or cloudy areas--only concentration differences. The machined surface of a single-crystal Ge sample shown in figure 9 shows structure which is very similar to that displayed by CaF_2 in figures 7 and 8. Again, the difference in clear and cloudy areas is primarily in the pitting concentration. Often a decrease in spatial period can be correlated with a decrease in pit volume in a sequence of pits. The pit shape is, of course, strongly suggestive of an indentation mark made by the tool tip. However, the relative motion between the surface being turned and the tool tip is a factor of at least 40 smaller than the typical 1-μm-deep pit. A probable explanation is that the pits are produced by spalling as a result of a localized tensile load at the surface which exceeds the material strength following the release of the compressive loading at the cutting edge as the tool passes over the surface (fig. 10). The repetitive nature of the spall pit formation comes from a constructive interaction of the tool loading and a standing acoustic wave in the material which has been excited by the tool. The effect is similar to chatter often observed in an ordinary machine tool, except that it is not a machine structure resonant effect but an effect in the material itself. The effect is related to that observed in diamond machining of metal surfaces [7,8]. The standing wave may or may not be a consequence of a resonant effect. However, the temporal frequency of the material "chatter" is approximately 10^6 Hz which is on the order of the resonant frequency of a mass on a spring consisting of a spall fragment connected into the lattice of the work material. In this simple model, the resonant frequency would scale as the square root of the reciprocal of the volume of the spall pit. This relationship is at least qualitatively observed in the decrease in spall pit size and accompanying decrease in spacing. The spall pit sequence on the left of the superposition shown in figure 7 is a clear example of this effect. A resonant explanation thus seems likely.

In contrast to these brittle materials, the material removal mechanism for KCl is much different. There is no evidence of the pitting behavior either inside or outside of cloudy areas. Material is removed by shearing and plastic deformation much as in metal machining. The surfaces shown in figure 11 demonstrate that material removal tends to be very nonuniform and can result in a very ragged and rough surface. Other rather ductile dielectric materials such as GaAs have been observed to machine in a similar manner, with a chip flowing from the tool rather than fine dust as in the case of CaF_2. Clear and cloudy areas are due to subtle differences in surface texture.

As the cutting radius increases at constant rotational rate during machining, it has been observed in a number of cases that the spall tendency precipitously can decrease beyond a specific radius (surface speed). This may simply be due to the lack of constructive interaction of the tool and the resonant wave in the material. If so, the tendency to spall should occur in annular bands, depending upon surface speed. This effect has also been observed. Another possible explanation is that spall formation is dependent upon strain rate and hence surface speed. This explanation seems much less likely, however. The location of the greatest concentration of spall pits (the cloudy spoke areas on a single-crystal sample) is a direct consequence of the orientation of planes of easy cleavage in the material with respect to the tool. Due to the geometry of the tool, specifically its flat top, the normal surface loading force of the tool acts in a plane over the contact width of the tool. When this plane is parallel (or nearly so) to a plane of easy cleavage, the tendency to spall is greatly increased.

The tendency towards spall formation can be decreased by two known approaches: (1) higher or lower surface speeds and (2) large negative tool rake angle. By using a tool with a very large negative rake in the range of 20 to 45° very uniform surfaces have been turned on several dielectric materials including Ge and CaF_2. However, the success with both surface speed variation and tool geometry are very dependent upon the cutting edge characteristics of the tool being used. Edge sharpness and orientation and perhaps even the diamond bulk imperfection are involved in the resonant chatter effect. In machining ductile dielectric materials, the use of a lubricant such as triacetin is a definite advantage. A tool used near zero top rake and with low surface speeds, i.e., less than 300 in./min, has given the best results. Again, results depend very strongly on the condition of the tool edge.

Optical and Surface Physical Characterization

A diamond stylus profilometer has been used to examine the topography of the several diamond-turned surfaces reported here. The results shown in figures 12 through 15 were obtained from a Talystep profilometer, with a 1-μm-radius conical stylus. This instrument yields surface profile data along the track of the stylus with a lateral resolution on the order of a micrometer for the smoother, low slope surfaces examined here and with a height resolution of 3 Å. The output of the stylus transducer amplifier is digitized and subsequently processed to yield distribution functions for height, slope, and correlation [9]. In figures 12 and 13, unprocessed scans of polished and diamond-turned single-crystal CaF_2 are compared for two different scan lengths, 15 and 600 μm. The diamond-turned clear areas on the CaF_2 sample of figures 12 and 13 are a factor of three smoother than the corresponding polished surface on the same sample and have much less steeply sloped structure as well. The Irtran MgF_2 surface scans shown in figures 14 and 15 indicate a much rougher surface, the surface being substantially determined by voids still present in the hot pressed material. The diamond-turned surface is uniform and slightly rougher than the polished surface.

The surface profiles of the polished and clear diamond-turned areas thus are very similar in distribution of height and slope. Consequently, the light scattering from the two surface types will be similar. The magnitude of the total integrated scattered (TIS) light compared to that light specularly reflected, $\Delta R/R$, can be related to the rms roughness δ

$$\Delta R/R \cong (4\pi\delta/\lambda)^2 \quad ,$$

where λ is the wavelength of the incident light [10]. Table 3 gives values of TIS for Irtran MgF_2, CaF_2, and SrF_2 for light in the visible (0.647 μm) and in the near infrared (3.39 μm). There is little difference in the visible light scatter from the clear diamond-turned polished areas, with the cloudy diamond-turned areas on CaF_2 and SrF_2 scattering a factor of five more light than the clear areas. In the near infrared the differences between polished and clear diamond-turned scattered light are even smaller, with still a factor of roughly five difference between clear and cloudy. From an examination of the CaF_2 diamond-turned surfaces shown in figures 13 and 14, it is obvious that much debris from machining is present even after "cleaning." It is certainly true that much of the scattered light originates from these particles and that more complete cleaning would materially reduce the TIS, especially in the infrared. The presence of machining debris also has a negative impact upon the laser damage resistance of the machined surface, especially for short pulse lengths where dielectric breakdown is a predominant damage mechanism [11]. However, in a companion paper at this conference [12], no significant difference in laser damage thresholds for the polished and diamond-turned surfaces described in this paper were discovered for 100-μsec pulses of 2.7- and 3.8-μm wavelength laser radiation.

Table 3. Values of TIS at two different wavelengths, 0.647 and 3.39 μm, for three different materials which were diamond single-point machined in this study. Included is a comparison of polished and diamond-turned "clear" and "cloudy" areas on the same sample.

Material	Wavelength, μm	Polished	Diamond turned	
			Cloudy	Clear
MgF_2 (Irtran)	0.647	.02	.03	.03
	3.39	.006	.01	.01
CaF_2	0.647	.0007	.04	.001
	3.39	.00004	.004	.00003
SrF_2	0.647	.0008	.02	.004
	3.39	.0001	.0006	.0001

Conclusion

The diamond stylus profilometer results from diamond-turned dielectric surfaces are statistically not much different than surfaces produced by conventional grinding and polishing by loose abrasive. As a consequence, the TIS in the visible from a diamond-turned surface can be quite comparable to that of a high quality polished surface and, in some cases, even lower. For the materials examined in this paper, Irtran MgF_2, SrF_2, and CaF_2, the diamond-turned, surface-scattered light at 3.39-μm wavelength is on the order of that from the corresponding polished surfaces. As was shown, the diamond-turned areas are covered with a significant concentration of debris from turning, even after "cleaning." Much of the measured scattered light certainly originates from these particles. More elaborate cleaning must be accomplished. The scattering from the "cloudy" diamond-turned surfaces is much larger as a consequence of a much larger concentration of localized spall pitting. A full understanding of the latter effect and its elimination are important to the fully successful application of diamond turning to infrared optics. Some progress in this regard is reported in this paper. The Irtran MgF_2 results are very interesting and encouraging since this polycrystalline material is often used for low-cost infrared optics. There are no preferential cloudy diamond-turned areas on this surface, and the diamond-turned surface scatters only slightly more light than the polished area. It is thus demonstrated that under some conditions, diamond-turned dielectric surfaces can be quite comparable in optical quality to corresponding polished surfaces. The advantages that diamond single-point machining brings to the production of infrared optical components, high throughput, and ready generation of aspheric surfaces promise to revolutionize infrared optics production.

Acknowledgment

The authors of this paper acknowledge the contributions of many co-workers at NWC, notably P. C. Archibald for scattering measurements and Cliff Fountain for X-ray orientation of samples.

References

[1] Arnold, J. B., and Steger, P. J., "Diamond Turning on Advanced Machine Tool Prototypes" (SME Clinic on Industrial Application of Precision Machining and Gaging, 19-21 November 1974, San Francisco, Calif.) Report Y-DA-5975 (Union Carbide, Inc., Oak Ridge, Tenn., 1975).

[2] Bryan, J. B., et al., "A Practical Solution to the Thermal Stability Problems in Machine Tools," Technical Paper MR72-138 (Society of Manufacturing Engineers, Dearborn, Mich., 1972).

[3] Decker, D. L., Soileau, M. J., Porteus, J. O., and Bennett, J. M., NBS Spec. Publ. 462, 153 (1976).

[4] Decker, D. L., Bennett, J. M., Soileau, M. J., Porteus, J. O., and Bennett, H. E., Opt. Engr. 17, 160 (Mar/Apr 1978).

[5] Decker, D. L., and Bennett, J. M., SPIE Optical Coatings II, 140, 32 (1978).

[6] Arnold, J. B., Morris, T. O., Sladky, R. E., and Steger, P. J., SPIE Advances in Precision Machining of Optics 93, 96 (1976).

[7] Decker, D. L., and Grandjean, D. J., NBS Spec. Publ. 541, 122 (1978).

[8] Decker, D. L., Presented in a paper read before the Society of Manufacturing Engineers, Precision Machining Workshop, 27-29 June 1978, Williamsburg, Va.

[9] Elson, J. M., and Bennett, J. M., J. Opt. Soc. Am. 69, 31 (1979).

[10] Bennett, H. E., and Porteus, J. O., J. Opt. Soc. Am. 51, 123 (1961).

[11] Temple, P. A., and Soileau, M. J., NBS Spec. Publ. 462, 371 (1976).

[12] Porteus, J. O., Decker, D. L., Grandjean, D. J., Seitel, S. C., and Faith, W. N., "Defect-Damage-Resistant Copper Mirrors," this conference.

The speaker indicated that although several different machining fluids had been used in these experiments, no obvious effect on pitting or spalling had been observed. The dependence of the surface finish on the sample temperature was not examined. He further indicated that only preliminary studies of optical glasses were done in the course of this investigation. Initial results appear promising. The main effort on the diamond turning of optical glasses is being carried out at the Lawrence Livermore Laboratory. Sample preparation for the work reported here was carried out by mechanical polishing. The samples were initially machined to a depth of 4-5,000 angstroms. To remove the polishing layer, the final finished cut removed another 6-700 angstroms.

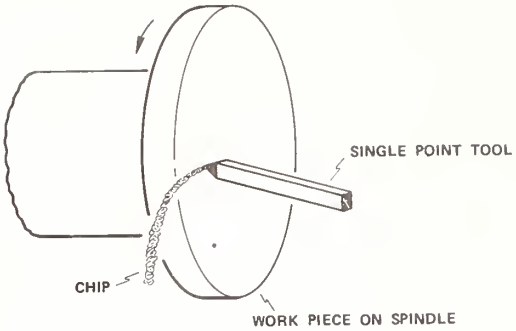

Figure 1(a). A schematic of the single-point tool machining process showing a part mounted on a rotating spindle being worked by a tool which is mounted on a slide mechanism capable of moving the tool over a controlled path in two dimensions.

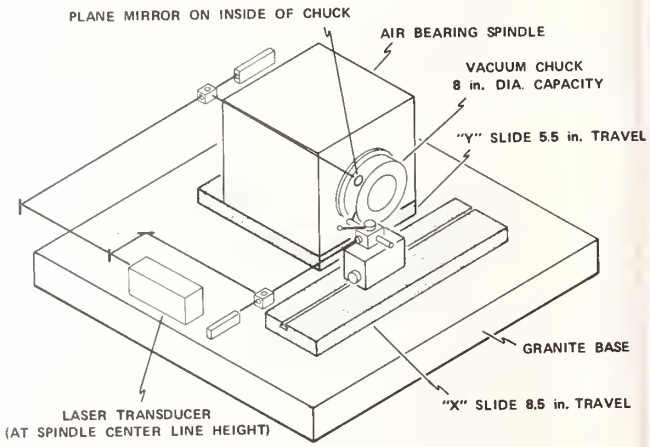

Figure 1(b). Isometric schematic of the NWC two-axis diamond-turning machine showing the placement of the spindle and tool slides in a T-base configuration. Also shown is a simple interferometer layout for measuring the primary motion of the slides.

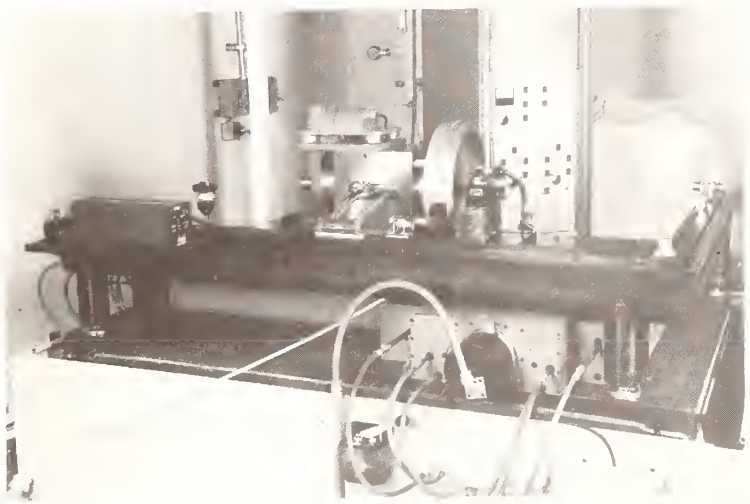

Figure 2. Photograph of the NWC machine showing the tool and spindle slides, the tool post assembly including precision height adjuster, chip/coolant guard, and spindle housing. A 6-inch-diameter copper flat is being machined.

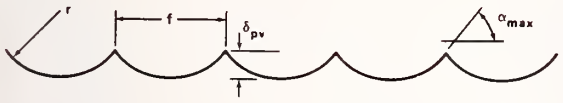

$\delta_{pv} \cong f^2/8r$ ASSUMING THAT $f/r << 1$

$\alpha_{max} \cong f/2r$

OR RMS VALUES:

$\delta_{rms} \cong \delta_{pv}/\sqrt{5}$

$\alpha_{rms} \cong \alpha_{max}/\sqrt{3}$

Figure 3. Ideal finish achieved by machining with a tool of nose radius r and a feedrate f. Both peak-to-valley (pv) and rms values are given.

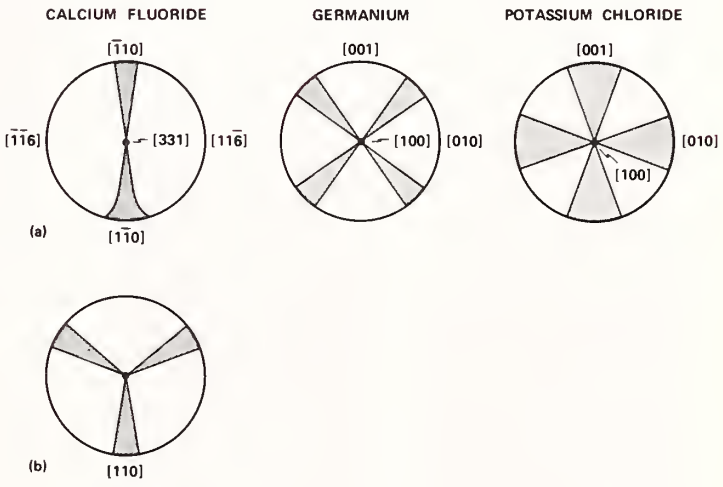

Figure 4. Schematic showing the locations of "clear" and cloudy structures resulting from diamond single-point machining relative to crystallographic directions for several different materials and orientations.

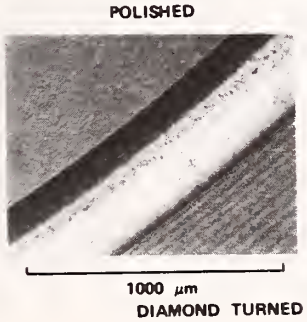

Figure 5. Nomarski phase contrast interference micrograph of a polished Irtran surface which has been partially diamond machined leaving a polished area for comparison.

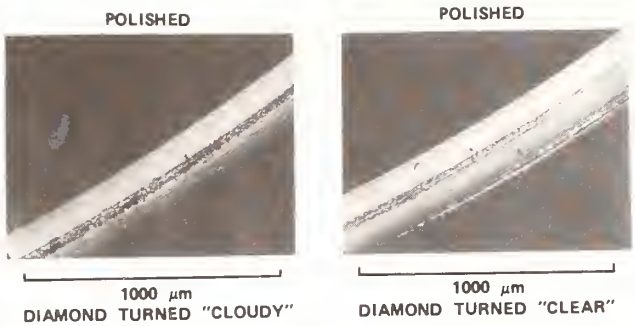

Figure 6. Nomarski phase contrast interference micrograph of a polished single-crystal CaF_2 surface which has been partially diamond machined leaving a polished area for comparison. On the left side is a representative "cloudy" area, and on the right is a "clear" area.

Figure 7. Scanning electron micrograph of the same single-crystal CaF_2 surface shown in figure 6. On the left side is a polished area, and on the right is an area selected from the clear diamond-machined portion showing localized pitting and some debris from turning.

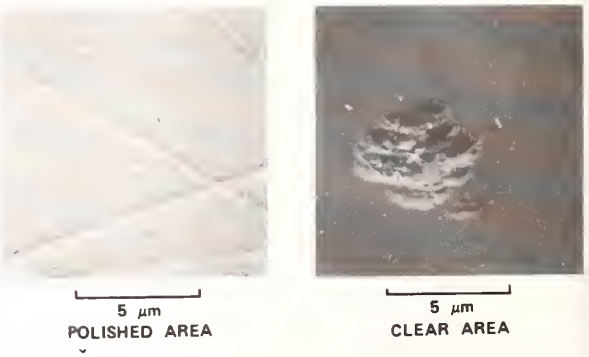

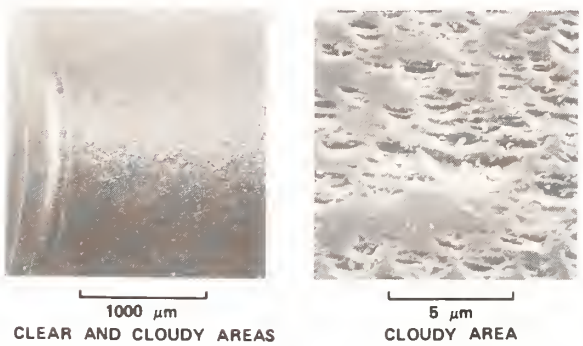

Figure 8. Scanning electron micrograph of the same single-crystal CaF_2 surface shown in figures 6 and 7. On the left side is a low magnification view of the localized "cloudy" spoke-shaped area as it is seen near the boundary between the polished and diamond-turned portions. On the right, at much higher magnification, is shown a representative "cloudy" area.

Figure 9. Scanning electron micrograph of a machined surface of a single-crystal Ge sample. The normal to sample surface is in the [100] direction. A low magnification view on the left shows one of the four spokes evident on this surface; the right shows the nature of the pitting which is prevalent in the cloudy spoke area.

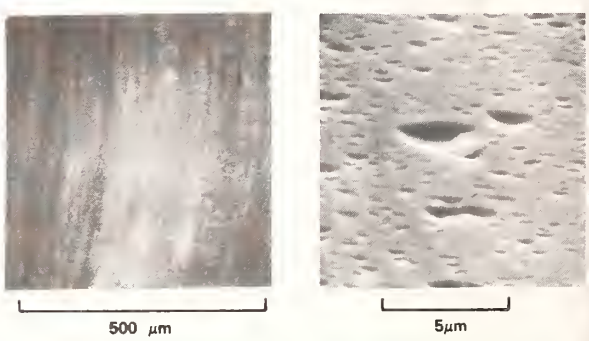

Figure 10. The mechanism of spall pit formation in brittle dielectrics is shown in these drawings. If the tensile strength of the material is exceeded when the compressive stress at the tip of the tool is released, a fragment will spall from the surface. The compressive stress is the resultant of a normal loading force and a frictional component schematically illustrated in the left-hand drawing.

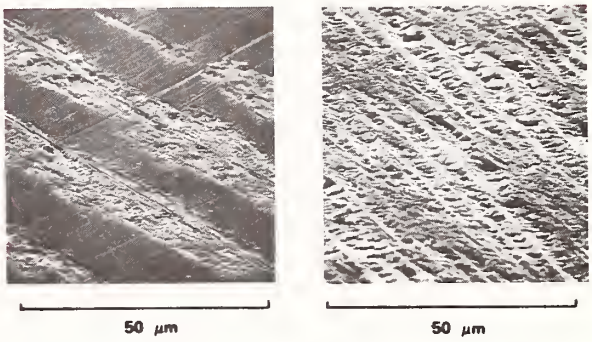

Figure 11. Scanning electron micrograph of a machined single-crystal KCl surface. The surface normal is in the [1,0,0] direction. On the left is shown a polished surface which has been contacted by the tool in several discrete, nonoverlapping passes; on the right is a surface produced by successive overlapping passes.

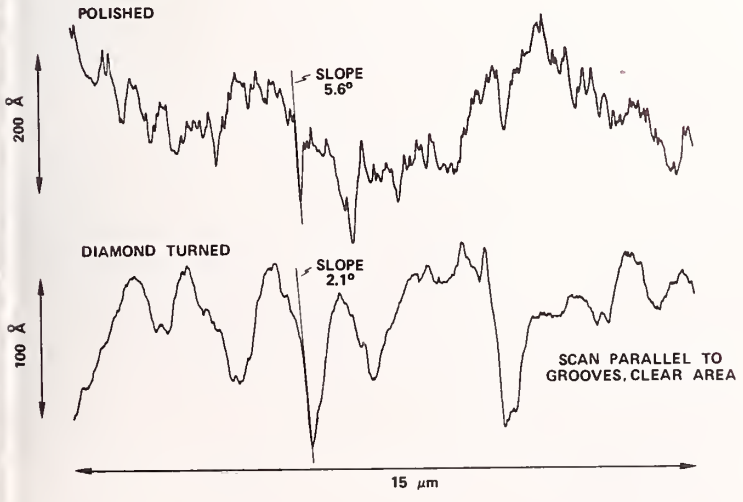

Figure 12. Unprocessed Talystep surface scan of 15-μm length on the CaF_2 sample previously shown in figures 6 through 8. Both polished and diamond-turned "clear" areas are shown.

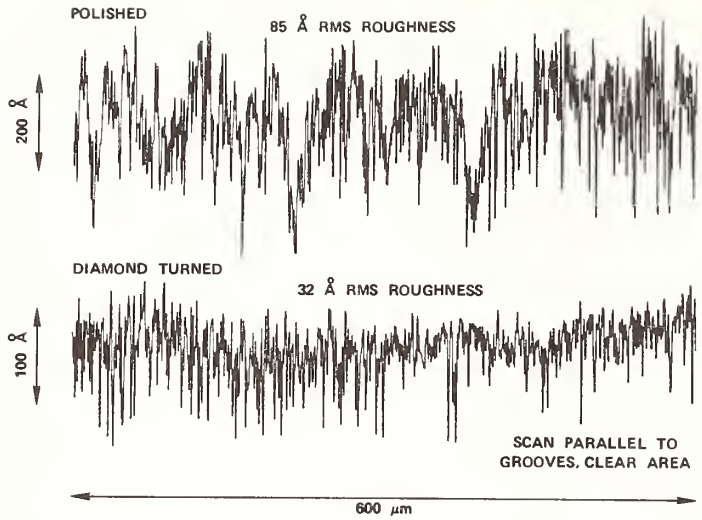

Figure 13. Unprocessed Talystep surface scan of 600-μm length on the CaF_2 sample previously shown in figures 6 through 8 and 12. Both polished and diamond-turned "clear" areas are shown.

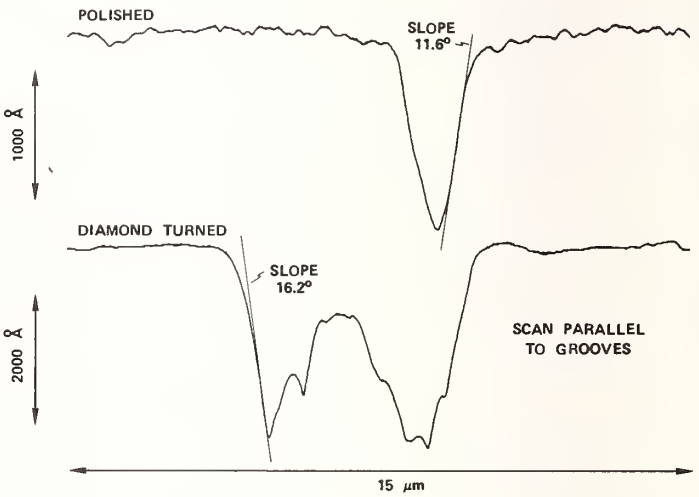

Figure 14. Unprocessed Talystep surface scan of length 15 μm on the polycrystalline MgF_2 previously shown in figure 5. Both polished and diamond-turned areas are shown.

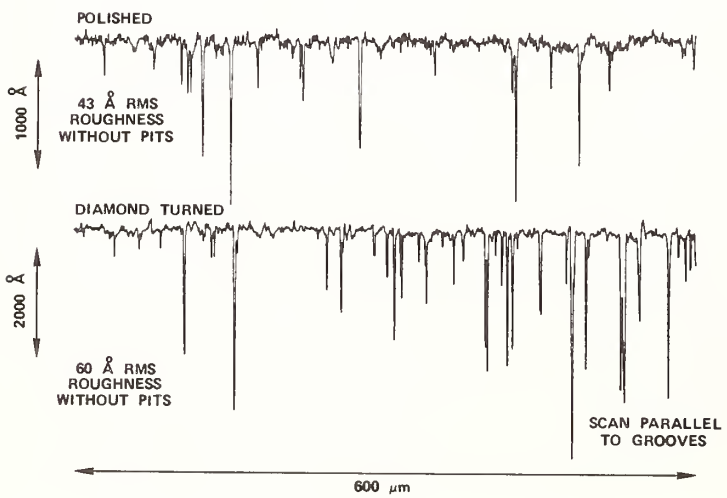

Figure 15. Unprocessed Talystep surface scan of length 600 μm on the polycrystalline MgF_2 previously shown in figures 5 and 14. Both polished and diamond-turned areas are shown.

SHORT-PULSE CO_2-LASER DAMAGE STUDIES OF NaCl AND KCl WINDOWS

Brian E. Newnam, Andrew V. Nowak, and Dennis H. Gill
Los Alamos Scientific Laboratory
Los Alamos, New Mexico 87545

The damage resistance of bare surfaces and the bulk interior of NaCl and KCl windows was measured with a short-pulse CO_2 laser at 10.6 μm. Parametric studies with 1.7-ns pulses indicated that adsorbed water was probably the limiting agent on surface thresholds in agreement with previous studies at long pulsewidths. Rear-surface thresholds up to 7 J/cm^2 were measured for polished NaCl windows, whereas KCl surfaces damaged at approximately 60% of this level. The breakdown electric-field thresholds of exit surfaces were only 50% of the value of the bulk materials. The pulsewidth dependence of surface damage from 1 to 65 ns, in terms of incident laser fluence, increased as $t^{1/3}$.

ey words: Alkali halides; CO_2 laser; KCl; laser damage; laser fusion; NaCl; nanosecond ulse; surface damage.

1. Introduction

Large-diameter NaCl windows are used extensively in the CO_2 amplifiers and target hambers of the Helios (10 kJ) and Antares (100 kJ, projected) fusion lasers at Los Alamos cientific Laboratory (LASL). Since these large windows (46-cm diameter, 8.5-cm thick) epresent a sizeable portion of the cost of building and maintaining these lasers, it is mperative that they have maximum optical damage resistance. In the experimental studies o be reported herein, we have examined some of the material and laser parameters that ffect the surface and bulk damage of NaCl (and KCl) for short (∿1 ns) pulses at 10.6 μm.

At the 1978 Laser Damage Symposium, Kovalev and Faizullov [1][1] presented substantial xperimental evidence that adsorbed H_2O is the limiting agent on the front-surface (f-s) amage thresholds of NaCl windows. They supported the hypothesis that this surface layer f water strongly absorbs the CO_2 radiation (10^3 cm^{-1} at 10.6 μm [2]), producing a rapidly xpanding vapor front which, when a sufficiently low density is reached, allows electric-ield breakdown as described by the familiar Paschen curve. Their experiments were carried ut with TEA CO_2 laser pulses having a high leading peak of 100-200 ns duration (∿150-ns isetime) and a long tail (1-15 μs) containing the majority of the pulse energy. Also, heir studies were on the entrance surface. Since pulsewidths of interest to laser fusion re much shorter, ∿1 ns, we conducted a series of short-pulse experiments on exit surfaces the most susceptible to early failure) to determine if adsorbed water is also the primary gent of surface damage for these conditions. These are described in section 5.

Since surface damage precedes bulk damage in NaCl windows, we have also made a care-ul comparison of the bulk and surface thresholds of crystals from four prominent manu-acturers to quantify the difference and learn how much potential improvement may be ossible over presently-used polishing methods. These results and a discussion are given n section 6.

As early as 1974, Stark and Reichelt [3] compared the damage resistance of Harshaw olytran KCl and NaCl window surfaces using 1-ns pulses. They measured a fluence ratio of .5 in favor of NaCl. In the past five years, however, significant advances in the tech-ology of crystal growth and surface polishing processes have occurred which suggested a ew and more extensive comparison of KCl and NaCl thresholds. These results appear in ection 7.

---

[1] Figures in brackets indicate the literature references at the end of this paper.

Finally, in section 8 we present our results for the pulsewidth dependence of exit-surface damage for NaCl and KCl windows.

2. Description of Test Specimens

Test specimens of NaCl and KCl were supplied by four prominent sources of high-quality ir crystals: Harshaw Chemical Company in Solon, Ohio (10 NaCl, 3 KCl), Naval Research Laboratory (NRL) in Washington, D.C. (1 NaCl, 1 KCl), Hughes Research Laboratories (HRL) in Malibu, California (1 NaCl, 1 KCl), and William Fredericks at Oregon State University (OSU) in Corvallis (2 NaCl). The details of these specimens are listed in table 11. To obtain a sufficiently long path length for conducting bulk-damage tests in the thin Harshaw windows, (without interference from concurrent front-surface damage) the perimeter of a few Harshaw windows were also polished flat. Also, two of the Harshaw windows were later cleaved in air to allow a direct comparison of cleaved and polished surface thresholds.

Table 1. Description of NaCl and KCl test specimens.

Supplier	Growth technique	Crystalline state	Surface state	Thickness
Harshaw	Stockbarger and Kyropoulos	single	polished with 0.3 μm Linde A	10 mm and 32 mm
HRL	Czochralski + CCl_4 RAP	single NaCl forged/polyxtal-KCl	polished 0.3 μm Linde A HCl etch-KCl	KCl: 9 mm NaCl: 34 mm
NRL	Czochralski + CCl_4 RAP	single	polished 0.3 μm Linde A	KCl: 55 mm NaCl: 53 mm
OSU	ion exchange	single	cleaved	33 & 23 mm

3. Experimental Apparatus and Procedure

Laser pulses of 1.7 ns to 65 ns (FWHM) at 10.59 μm (P-20) were emitted from a gain-switched CO_2 oscillator/double-pass amplifier in LASL's Gigawatt Test Facility. This laser provided a single-longitudinal mode, single-line, and gaussian spatial-profile output every 20 seconds which was ideal for these single-shot-per-site (1-on-1) tests. The short pulses were sliced out of the 65-ns oscillator emission by use of a double Pockel cell/spark gap arrangement. As illustrated in figure 1, the temporal shape of these short pulses was asymmetric (300-ps risetime, 1.5-ns falltime, 10-90% levels). A fairly large laser-beam spot size, 1-mm radius at the $1/e^2$ level, was used on the majority of the surface threshold tests. Samples were placed ahead of the focus of a 1-m F.L. plano-convex lens for these tests. For use in comparison of bulk and surface thresholds, a spot-size radius of 0.14 mm was obtained at the focus of a 19-cm F.L. lens. The spatial profile, measured periodically by a pinhole scan, approximated a gaussian dependence. The energy, temporal and spatial diagnostics, indicated in figure 2, have been previously described [4], and a summary of the laser test parameters is given in table 2.

Table 2. CO_2 laser damage test parameters.

Wavelength:	P(20), 10.59 μm, single-mode TEM_{oo}
Pulsewidths:	1 to 65 ns (FWHM)
Spot-size radius:	0.15 to 1.5 mm
1-on-1 irradiation:	40 to 60 sites
Test environment:	Air at 600 torr (2200 meters alt.)

The criterion for surface damage was permanent disruption (pitting or increased light scatter) visible under bright, white-light illumination with a 40X stereo microscope. Isolated microbubbles occurred at the threshold of bulk damage. Generally, microsparks preceded the occurrence of visible damage by a small margin.

Measurements of the exit-surface and bulk-thresholds were satisfactorily conducted in air rather than in the vacuum environment chosen by Faizullov and Kovalev [1] for most of their front-surface tests. Front-surface tests of high-threshold materials in air are often plagued by air breakdown at the pulse peak which effectively prevents energy in the tail of the pulse from reaching the surface. We determined that in measuring exit-surface thresholds, the interference of air sparks was not significant when viewing with the white light/ microscope method. Previously, Hayden and Liberman [5] had found the exit-surface thresholds of a NaCl window in vacuum and air to be essentially the same, 5.7 and 5.4 J/cm^2, respectively.

The transmitted temporal-pulse termination technique of detecting damage was not considered sufficiently sensitive in these tests with large millimeter-size beams. The area of the damage sites (microns in diameter) was judged much too small to block a significant fraction of the pulse energy.

Exit-surface rather than f-s damage was of primary interest in these studies since, for low-index materials like NaCl, the former almost always occurs first. This derives from the in-phase addition of the incident and reflected electric vectors at the rear surface as indicated in figure 3. However, for normal incidence of a coherent laser beam upon a window having parallel surfaces, the ratio of the front-to-rear-surface thresholds (in MV/cm) is dependent on the thickness and can range from 1 to n [6]. Therefore, in these tests the windows were oriented sufficiently off normal (several degrees) to preclude multiple-beam interference effects.

4. Damage Morphology

Threshold damage on the exit surfaces was in the form of one or a few shallow microspits, of the order of several microns diameter. Invariably, a separate microspark was associated with each damage site, but sparks did occur at lower laser fluences with no discernible damage. On some surfaces, the pits were elliptically shaped with the long axes parallel to polish sleeks.

Evidence of threshold damage in the bulk was in the form of one or a few tiny bubbles remaining after an incandescent microspark(s). High-magnification studies of these bulk sites were not completed upon this writing.

5. Influence of Adsorbed Water

In addition to schlieren photographs to establish the existence of an expanding vapor front at an irradiated NaCl surface, Kovalev and Faizullov [1] supported their assertion that adsorbed water determines the surface damage threshold with the following evidence:

1) As the laser spot size was varied over the range 0.12 to 1.12 mm radius, the f-s threshold of NaCl in vacuum was constant at 36 MV/cm^2 (2.2 J/cm^2). The tests were conducted at 10.6 μm with a 150-ns pulse risetime. This result was theoretically predicted by their eq. 5 for spot sizes larger than the thickness of an adsorbed water film uniformly absorbing over the surface.

2) The f-s threshold increased with pressure of the ambient gas. This was expected because the shock wave velocity of an expanding water vapor front is reduced at higher ambient pressures, and there is an increased frequency of electron collisions with neutral particles. Thus, for full development of an electron avalanche in the rarefied region, a higher electric field is required.

3) After an initial dramatic rise in threshold from 2.2 to 13.5 J/cm^2 by treating an NaCl surface with an HCl-acid etch, the threshold dropped, upon subsequent remeasurement at 20 minutes, to a value of 6.5 J/cm^2. This value appeared to be a steady-state level as determined from additional periodic measurements up to 3 months. Readsorption of an H_2O layer within 20 minutes was indicated.

4) Kovalev and Faizullov [1,7] observed large increases in the f-s threshold of NaCl when pre-irradiated at subthreshold fluences (N-on-1 effect). Removal of volatile absorbing contaminants, such as water, was indicated.

In view of these important results conducted with long pulses, the present study with 1.7-ns CO_2 pulses was motivated. To detect the possible influence of adsorbed H_2O on NaCl surface thresholds the following tests were conducted:

1. threshold versus spot size,
2. threshold of a cleaved surface versus time of ambient exposure, and
3. threshold versus total water content.

5.1. Threshold versus Spot Size

Figure 4 exhibits the exit-surface threshold measurements of one NaCl window for spot-size radii from 0.14 to 1.5 mm. The vertical bars for each point represent the threshold variation across the sample surface. Therefore, the solid line drawn through the points could as well have been drawn horizontally, i.e., no spot-size dependence was evident. Similar measurements on two other windows also revealed no definite dependence.

5.2. Threshold of a Cleaved Surface

The f-s threshold of an NaCl window cleaved in air (relative humidity of 35%) was determined within one hour to be 17.6 ± 0.6 J/cm^2. After ten days exposure, the threshold had dropped to 13.1 ± 1.5 J/cm^2, a decline of 26%.

These tests were performed on the front surface, instead of the rear surface as were all other of our tests, because rear-surface tests were not possible at these high-fluence levels. When the cleaved surface was oriented as the rear surface, the polished (front) surface damaged first, thereby shielding the rear surface of interest. Using the polished samples available, it was not possible to obtain satisfactory cleaved surfaces for both front and rear.

5.3. Threshold versus Total Water Content

The presence of OH^- ions in NaCl is revealed by the characteristic spectral absorption peak at 187 nm, near the uv band edge [8,9]. As seen in figure 5, there was a wide range of OH^- concentrations (bulk + surface) among the test specimens grown by the several techniques. OSU sample No. 1-65 was purposely grown with a slight water concentration. The 187-nm absorbance of the Harshaw sample, No. 1-48-14 greatly exceeded that of the other samples supplied by Harshaw. In table 2, we compare the absorbance with the exit-surface threshold. It is appropriate to compare the results for the cleaved and polished windows separately. The cleaved window with greater OH^- concentration did have a lower threshold, but the polished Harshaw sample with very high absorbance actually had a slightly higher threshold than the HRL sample with low OH^- content.

Table 2. NaCl exit-surface threshold versus absorbance at 187 nm.

Sample	Absorbance at 187 nm[a]	Exit threshold	
		J/cm^2	MV/cm
OSU - ion exchange 4-65 cleaved	0.10	7.0	1.19
HRL - RAP & forged Polished	0.10	5.3	1.04
OSU - ion exchange 1-65 cleaved	0.30	5.3	1.05
Harshaw - Stockbarger 1-48-14, heel, polished	1000	6.1	1.12

w = 1.0 mm, Δt = 1.7 ns (FWHM)

[a]See table 1 for sample thicknesses.

5.4. Discussion

The absence of a spot-size dependence and the decline of the surface threshold with time for our 1.7-ns pulses are similar to the results obtained by Kovalev and Faizullov [1,7]. Correlation of the total OH^- ion content (bulk + surfaces) was not as conclusive, however. Direct correlation of the surface absorption at 187 nm with surface threshold would have been better. Unfortunately, surface absorption measurements of these relatively thin samples was not accomplished. However, the one clearly valid comparison of the surface thresholds of the two cleaved OSU crystals was consistent with absorption in a surface layer of water. Thus, the results of our three tests do support the hypothesis that surface damage of NaCl, for 1-ns CO_2 pulses, results from OH^- absorption.

Our observation that microsparks were associated with the tiny damage sites was not unexpected. At surface defects (scratches, pits or included polishing residue) the local electric field is enhanced, resulting in early breakdown most likely in the expanding vapor. The presence of the localized plasmas causes total retro-reflection and a maximum standing-wave field of 2.0 at the exit surface, as described by Boling et al. [10]. Early damage is a natural consequence.

Self-focusing, as a contributor to early breakdown of the exit surfaces, was also assessed. As reviewed in the Appendix, the magnitude of this effect in the above tests and those yet to be described was negligible.

6. Surface versus Bulk Thresholds

In table 3, the bulk and surface thresholds of NaCl crystals from four sources are compared. In computing the listed values, the enhancement of the electric field at the exit surface (recall figure 3) was taken into account. It is remarkable that the same value, 2.1 MV/cm, was obtained for the bulk threshold for each of the first three samples listed. The ratio of exit-surface to bulk thresholds for these was also about the same, 0.5. In terms of incident laser fluence (J/cm^2), exit surfaces polished by standard methods survived approximately 20% as much as the bulk (25% for front surfaces).

Table 3. Comparison of bulk and exit-surface thresholds of NaCl single crystals.

Sample	Bulk	Surface	Ratio
	MV/cm	MV/cm	
Harshaw 6-8-16 Stockbarger	2.1 ± 0.2	1.03	0.49
IRL - RAP B-334	2.1 ± 0.1	1.15 ± 0.10	0.55
IRL - RAP 7B-175	2.1 ± 0.1	1.07 ± 0.03	0.51
OSU - ion exchange 20-2-13, 4-65	1.02 ± 0.03	1.20 ± 0.11 Cleaved, 14 years ago (1965)	1.17

= 0.14 mm
t = 1.7 ns (FWHM)
= 10.6 μm

The bulk threshold of the OSU crystal was much lower than anticipated, expecially since its concentration of impurities was very low [11]. Tiny scattering sites were visible in the bulk by use of a He-Ne laser (forward scattering, mainly). As this crystal was grown in an atmosphere of argon, it has been suggested (unconfirmed as yet) that the scattering sites were bubbles of argon gas [11]. For a spherical void in NaCl (n = 1.494 at 10.6 μm) an electric-field enhancement factor of 1.23 is predicted from Bloembergen's

analysis [12]. The remainder of the difference may be accounted for by breakdown in argon gas at some unknown pressure rather than in bulk NaCl. The threshold of this cleaved surface was unexpectedly high especially considering that the crystal was grown, cleaved and cleaned in 1965, 14 years ago!

There are several explanations why thresholds of surfaces are lower than in the bulk. Firstly, the E-field enhancement at the exit-surface results in earlier damage there than in either bulk or front surface. Secondly, the surface roughness produced by polishing results in enhanced electric fields and increased absorption. (At 1.06 μm, House et al. [13] found that fused silica surface-thresholds (MV/cm) were inversely proportional to the square root of the rms roughness.) Thirdly, polishing physically disrupts the crystalline order of a surface layer. Fourthly, polishing compounds and pitch are embedded and cleaning methods cannot be 100% effective. Fifthly, adsorbed gases, e.g., H_2O, absorb the laser energy. Adsorption is augmented by surface roughness and embedded impurities.

To quantify the deleterious effect of polishing on the damage threshold, we tested two samples cleaved in air. The results, given in table 4, provide a comparison of f-s thresholds of adjacent polished and cleaved surface areas. First, we note that the roughness of the cleaved surfaces (∿50 Å) was one-quarter that of the polished surfaces as measured with a profilometer. Therefore, it is not too surprising that the cleaved surfaces had much higher thresholds, by factors of 2.3 and 2.0, respectively in terms of laser fluence. The fact that these values were only 75 to 80% of the bulk electric-field thresholds (2.1 MV/cm) indicated that the finite roughness (50 Å) may have been a limiting factor. Sufficient moisture adsorbed during the one-hour test period may have also depressed the damage resistance. The reduced threshold after ten days exposure to ambient conditions was already discussed in section 5.2.

Table 4. Entrance surface thresholds of cleaved and polished NaCl (single-crystal).

Surface		Threshold		Ratio of surface to bulk
Polished, ∿ 200 Å RMS		J/cm²	MV/cm	
Linde A - 0.3 μm	A	8.4 ± 1.0	1.09	0.52
1 year storage	B	9.0 ± 0.4	1.13	0.54
Cleaved, ∿ 50 Å RMS				
Tested within 1 hour	A	19.4 ± 2.3	1.66	0.79
in 35% RH	B	17.6 ± 0.6	1.58	0.75
After 10 days	B	13.1 ± 1.5	1.37	0.65
in 35-40% RH				

w = 0.75 mm
Δt = 1.7 ns (FWHM)

Sample A: Harshaw K-24-20 (Kyropoulos)
Sample B: Harshaw 6-1-16, Heel No. 1 (Stockbarger)

The f-s thresholds given in table 4 may be compared with their exit-surface thresholds to obtain the ratio. For Sample A, these were 8.4/6.8 or 1.24 and for Sample B, these were 9.0/6.1 or 1.48. These compare well with the theoretical value of 1.44.

Addressing the problem of surface contamination by polishing compounds and pitch, we subjected two polished surfaces to Auger analysis. To our surprise, no evidence of Al was seen in the surface polished with Linde A (Al_2O_3), nor was carbon found in the surface polished with diamond paste! Examination with a more sensitive technique is suggested as the null result was unexpected. Previously, Turk et al. [14] had presented definite evidence of removal of an absorbing layer on a polished KCl surface removable by use of an etchant (see figure 6). Presumably, the absorbing impurities were the Linde A, pitch and water.

We measured no difference in the surface thresholds of Harshaw Polytran NaCl (forged, polycrystalline) and Harshaw single-crystal material. However, no measurement of the bulk threshold of Polytran was made.

7. KCl versus NaCl

7.1. Bulk and Surface Measurements

The bulk thresholds of both NaCl and KCl, measured with relatively large beams (w = 0.14 mm radius) and 1.7-ns pulsewidth, are presented in table 5. Included for comparison are the data of Soileau et al. [15] and Fradin et al. [16] both of whom tested Harshaw crystals with very small spot-sizes and longer pulseforms. Although the value for NaCl is consistently the same, 2.1 MV/cm, the thresholds for KCl varied more widely. Since Harshaw has not concentrated on the growth of KCl windows for high-power, short-pulse use to the extent that they have for NaCl [17], we believe that the NRL sample of KCl better represents the presently attainable damage resistance for that material.

Table 5. Comparison of bulk thresholds of single crystal NaCl and KCl.

Source	Test Conditions	Bulk Thresholds, MV/cm NaCl	KCl	Ratio
NRL - RAP	a	2.1 ± 0.1	1.66 ± 0.09	0.79
Harshaw - Stockbarger	a	2.1 ± 0.2	0.76 ± 0.01	0.37
Harshaw - Stockbarger	b	2.1	1.45	0.69
	c	1.95	1.39	0.71

[a] Δt = 1.7 ns (FWHM), w = 0.14 mm.

[b] Δt = 60 - 105 ns (FWHM), partially mode-locked train, w = 0.036 mm; data of Soileau et al. [15].

[c] Δt = 200 ns (FWHM), w = 25 μm; data of Fradin et al. [16].

As the exit-surfaces present the real limitation to high-power laser applications, we extended this comparison to polished surfaces of both crystals. The results, listed in Table 6, continue to show NaCl as having the advantage. Using the mean values for the sets of samples measured, a fluence ratio of 0.63 was obtained. The corresponding field ratio is then 0.79, which is the same as that derived from the highest bulk values in Table 5.

Table 6. Comparison of exit-surface thresholds of polished NaCl and KCl.

Source	Single-crystal NaCl J/cm²	KCl J/cm²	Ratio
Harshaw	6.0 ± 0.5[a]	3.6 ± 0.6	0.60
NRL	6.2 ± 1.0	4.1 ± 0.8	0.66
HRL	5.3 ± 0.4	3.7 ± 0.4 (forged)	0.70

$$\frac{KCl}{NaCl} = \frac{3.8^{b}}{6.0^{c}} = 0.63$$

w = 1.0 mm, Δt = 1.7 ns (FWHM), λ = 10.6 μm, 1-on-1.

[a] Mean value of eight samples.

[b] Mean value of three samples.

[c] Mean value of ten samples.

7.2. Discussion

Based on arguments involving medium polarizability and available electrons (in pure, defect-free crystals) to contribute to an electron avalanche, one would expect that the damage threshold (MV/cm) would scale proportionately to atomic density divided by $n^2 - 1$. Such a derivation was obtained by Bettis et al. [18]. The values of (At. Density)/(n^2-1) for KCl and NaCl at 10.59 μm are 0.288 and 0.362. The ratio of these values is 0.80, which is the same as that obtained from the experimental measurements. Using the data generated by Fradin et al. [16], we constructed a plot of E_{th}(MV/cm) versus the above expression as seen in figure 7. An exact linear relationship is not expected since some of the physical properties of the crystals (impurities, defects, mechanical strength, melting point) are not included in the derivation of the abscissa. However, the general trend is obvious. Such a dependence has been observed for crystals and thin film materials at other wavelengths, e.g., by Bettis et al. [18] at 1.06 μm and by Newnam and Gill [19] at 266 nm.

Using their recent theory of electron avalanche breakdown, Sparks et al. [20] have computed bulk thresholds for KCl and NaCl at 10.6 μm to be 0.63 and 0.8 MV/cm, respectively. These computed values are obviously too low in light of experimental values presented here, but their ratio, 0.8, is in agreement with our measurements.

8. Pulsewidth Dependence

The exit-surface thresholds of several samples were measured with 65 ± 3-ns pulses as well as the short, 1.7-ns pulsewidth used as the standard in this test program. The smooth temporal structure of both pulseforms is seen in figure 1. Due to a difference in the beam divergence of the laser in the long-pulse mode, a larger spot-size radius (1.4 mm) was inadvertantly used. However, as demonstrated earlier in figure 4, the thresholds were not spot-size dependent, so a direct comparison with the 1.7-ns results (1.0-mm spot size) was deemed appropriate. The results for three samples are plotted in figure 8. Consistently, a straight line drawn between the data points exhibited a $t^{1/3}$ fluence dependence. For a few other samples, not plotted here, a slightly less-rapid increase with pulsewidth was measured. Since tiny microsparks were generally associated with damage at isolated surface sites, it is not understood why the anticipated $t^{1/2}$ dependence (generally associated with diffusion processes such as plasmas) was not observed. Possible explanations include the rate of vapor expansion or the susceptibility of surface defects.

9. Summary

This study of the extrinsic surface and bulk thresholds of NaCl and KCl windows with millimeter-diameter, 1.7-ns CO_2 laser pulses at 10.59 μm has yielded some very significant results.

First, exit-surface damage, which occurs at 70% the fluence level of entrance-surface damage, was examined. Thresholds up to 7 J/cm^2 were measured for polished surfaces. In contrast, cleaved surfaces with one-quarter as much surface roughness damaged at twice the level of polished surfaces, but remeasurement after ten days found the advantage to have dropped to 50%. No spot-size dependence was observed for beam diameters from 0.3 to 3 mm. Correlation of the damage susceptibility with the total absorption (bulk + surfaces) at the OH^- ion absorption band at 187 nm was not totally conclusive. Overall, however, the results of these experiments support the hypothesis [1,7] that surface damage results from OH^- absorption, coupled with surface roughness.

That there is much room for improvement of the damage resistance of both NaCl and KCl surfaces was determined from comparative measurements of the bulk thresholds. Exit surfaces, with present state-of-the-art polish, damaged at only 50% of the electric-field threshold of the bulk, or at only a 20% level in terms of incident laser fluence (J/cm^2). For ideal surfaces, the thresholds at the exit could be as high as 70% of the bulk level (J/cm^2). Further work on surface preparation should be the first priority.

A comparison of the bulk and surface thresholds of KCl and NaCl produced by three vendors obtained a field ratio (MV/cm) of 80% in favor of NaCl. This is in agreement with theoretical predictions based on the electron-avalanche mechanism. Finally, a pulsewidth

dependence of $t^{1/3}$ was measured for a few samples of both materials from 1.7 to 65 ns, which was less than the anticipated $t^{1/2}$.

10. Acknowledgments

The authors are grateful for the cooperation of the following persons for supplying the test specimens: David Krus and Ontario Nestor of Harshaw, Roger Turk and James Harrington of HRL, William Fredericks of OSU and Philipp Klein of NRL. Additionally, one of the authors (BN) is indebted to the above and Guy Bastien and Virgil Straughan of Harshaw for thorough discussions about crystal-growth technology, window shaping and surface polishing. Thanks go to Vito Lazazzera and Linda Martinez of LASL for polishing assistance and Robert Springer for Auger surface analysis. Leon Sonntag and John Meier provided invaluable assistance in carrying out the damage tests.

References

[1] Kovalev, V. I., and Faizullov, F.S., "Investigation of the Surface Breakdown Mechanism in IR-Optical Materials," in Laser Induced Damage in Optical Materials: 1978, (A. J. Glass and A. H. Guenther, eds.), p. 318. NBS Spec. Pub. 541, U.S. Gov't. Printing Off., Washington, D.C., (1978).

[2] Hale, G. M., and Querry, M. R., "Optical Constants of Water in the 200-nm to 200-μm Wavelength Region," Appl. Opt. 12, 555 (1973).

[3] Stark, E. E., Jr., and Reichelt, W. H., "Damage Thresholds in ZnSe, A/R Coated NaCl and Micromachined Mirrors by 10.6 μm Multijoule, Nanosecond Pulses," in Laser Induced Damage in Optical Materials: 1974, (A. J. Glass and A. H. Guenther, eds.), p. 53. NBS Spec. Pub. 414, U. S. Gov't Printing Off., Washington, D.C., (1974).

[4] Newnam, B. E. and Gill, D. H., "Damage Resistance of AR-Coated Germanium Surfaces for Nanosecond CO_2 Laser Pulses," in Laser Induced Damage in Optical Materials: 1977, (A. J. Glass and A. H. Guenther, eds.), p. 298. NBS Spec. Pub. 509, U.S. Gov't Printing Off., Washington, D.C. (1978).

[5] Hayden, J. J. and Liberman, I., "Measurements at 10.6 μm of Damage Threshold in Germanium, Copper, Sodium Chloride, and Other Optical Materials at Levels up to 10^{10} W/cm^2." in Laser Induced Damage in Optical Materials: 1976, (A. J. Glass and A. H. Guenther, eds.), p. 173. NBS Spec. Pub. 462, U.S. Gov't Printing Off., Washington, D.C., (1976).

[6] Sam, C. L., "Laser Damage of GaAs and ZnTe at 1.06 μm," Appl. Opt. 12, 878 (1973).

[7] Kovalev, V. I., and Faizullov, F. S., "Influence of Adsorbed Water on the Optical Strength of Infrared Optics Elements," Sov. J. Quantum Electron. 7, 326 (1977).

[8] Etzel, H. W. and Patterson, D. A., "Optical Properties of Alkali Halides Containing Hydroxyl Ions," Phys. Rev. 112, 1112 (1958).

[9] Rolfe, J., "Hydroxide Absorption Band in Alkali Halide Crystals," Phys. Rev. Lett. 1, 56 (1958).

[10] Boling, N. L., Crisp, M. D., and Dube, G., "Laser Induced Surface Damage," Appl. Opt. 12, 650 (1973).

[11] Fredericks, W. J., Oregon State University, personal communication, 1979.

[12] Bloembergen, N., "Role of Cracks, Pores, and Absorbing Inclusions on Laser Induced Damage Threshold at Surfaces of Transparent Dielectrics," Appl. Opt. 12, 661 (1973).

[13] House, R. A., II, Bettis, J. R., and Guenther, A. H., "Surface Roughness and Laser Damage Threshold," IEEE J. Quantum Electron. QE-13, 361 (1977).

[14] Turk, R. R., Pastor, R. C., Timper, A. J., Braunstein, M., and Heussner, G. K., "Optical Finishing of KCl Windows to Minimize Absorption in the Infrared," in Proc. of the Fifth Conf. on High Power Infrared Laser Window Materials-1975, (C. R. Andrews and C. L. Strecker, eds.), p. 103, DARPA, (1976).

[15] Soileau, M. J., Bass, M., and Van Stryland, E. W., "Frequency Dependence of Breakdown Fields in Single-Crystal NaCl and KCl," in Laser Induced Damage in Optical Materials: 1978, op. cit., p. 309.

[16] Fradin, D. W., Yablonovitch, E., and Bass, M., "Comparison of Laser Induced Bulk Damage in Alkali-Halides at 10.6, 1.06, and 0.69 Microns," in Laser Induced Damage in Optical Materials: 1972, (A. J. Glass and A. H. Guenther, eds.), p. 27. NBS Spec. Pub. 372, U. S. Gov't Printing Off., Washington, D.C., (1972); also Appl. Opt. 12, 700 (1973).

[17] Krus, D. J., Harshaw Chemical Co., private communication, 1979.

[18] Bettis, J. R., House, R. A., Guenther, A. H., and Austin, R., "The Importance of Refractive Index, Number Density, and Surface Roughness in the Laser-Induced Damage of Thin Films and Bare Surfaces," in Laser Induced Damage in Optical Materials: 1975, (A. J. Glass and A. H. Guenther, eds.), p. 289. NBS Spec. Pub. 435, U. S. Gov't Printing Off., Washington, D.C., (1976).

[19] Newnam, B. E., and Gill, D. H., "Ultraviolet Damage Resistance of Laser Coatings," in Laser Induced Damage in Optical Materials: 1978, op. cit., p. 190.

[20] Sparks, M., Holstein, T., Warren, R., Mills, D. L., Maradudin, A. A., Sham, L. J., Loh, E., Jr., and King, F., "Theory of Electron-Avalanche Breakdown in Solids," in Laser Induced Damage in Optical Materials: 1979, (H. E. Bennett, A. J. Glass, A. H. Guenther, and B. E. Newnam, eds.), NBS Spec. Pub. 586, U. S. Gov't Printing Off., Washington, D.C., (1980).

[21] Wang, C. C., and Baardsen, E. L., "Study of Optical Third-Harmonic Generation in Reflection," Phys. Rev. 185, 1079 (1969), and Phys. Rev. B1, 2827 (1970).

[22] Maker, P. D., and Terhune, R. W., "Study of Optical Effects Due to an Induced Polarization Third Order in the Electric Field Strength," Phys. Rev. 137, A801 (1965).

[23] Smith, W. L., Bechtel, J. H., and Bloembergen, N., "Picosecond Breakdown Studies: Threshold and Nonlinear Refractive Index Measurements and Damage Morphology," in Laser Induced Damage in Optical Materials: 1975, op. cit., p. 321.

[24] Watkins, D. E., Phipps, Jr., C. R., and Thomas, S. J., "Ellipse Rotation in Germanium," in Digest of Technical Papers, 1979 IEEE/OSA Conf. on Laser Eng. and Applications, p. 31 (1979).

[25] Akhmanov, S. A., Sukhorukov, A. P., and Khokhlov, R. V., "Self-Focusing and Diffraction of Light in a Nonlinear Medium," Sov. Phys.-Usp. 10, 609 (1968).

[26] Kerr, E. L., "Transient and Steady-State Electrostrictive Laser Beam Trapping," IEEE J. Quantum Electron. QE-6, 616 (1970).

[27] Dawes, E. L., and Marburger, J. H., "Computer Studies in Self-Focusing," Phys. Rev. 179, 862 (1969).

[28] Marburger, J. H., "Self-Focusing Theory," Prog. Quant. Electr. 4, 35 (1975).

[29] Fradin, D. W., "The Measurement of Self-Focusing Parameters Using Intrinsic Optical Damage," IEEE J. Quantum Electron. QE-9, 954 (1973).

Appendix

Measurement of the extrinsic damage thresholds of NaCl and KCl with large laser beams (w = 0.14 mm for the bulk; 0.14 to 1.5 mm for surfaces) required substantial input powers. At these power levels, intensification of the laser radiation by self-focusing had to be carefully evaluated. Our analysis of the magnitude of self-focusing in the present tests included contributions from both fast (electronic) and transient (electrostrictive) nonlinear mechanisms. For the laser parameters and sample dimensions used, the computed nonlinear intensification was of negligible magnitude as we now review.

For a gaussian beam, the critical power for maintaining a constant shape is given by the familiar expression

$$P_1 = c\lambda_o^2 / 32\pi^2 n_2 \quad , \tag{1}$$

where $n = n_o + n_2 \bar{E}^2$, and where n_2 is a composite of nonlinear indices including n_{2e} and n_{2s}, representing the relatively prompt electronic and time-dependent electrostrictive material responses. For NaCl and KCl the values of n_{2e} used here were 4.6 and 3.7 x 10^{-13} esu, respectively. These values are the average of three sets of measurements in the visible and at 1.06 μm [21,22,23]. In a recent measurement at 10.6 μm of ellipse rotation in NaCl, Watkins et al. [24] also determined that n_{2e} was less than 6 x 10^{-13} esu, which was the limit of their experimental sensitivity. An expression for n_{2s} was derived by Ashkmanov et al. [25]:

$$n_{2s} = n_o(\rho dn_o/d\rho)^2/4\pi\rho v^2 \quad , \tag{2}$$

where ρ is the density and v is the radial sound velocity. At 10.6 μm, the values for NaCl are 8.3, 9.4, and 9.8 x 10^{-14} esu along the [100], [110], and [111] directions, respectively. For KCl, these values are 8.2, 11.1, and 12.6 x 10^{-14} esu. The self-focusing arising from electrostriction is incomplete until the compressive sound wave has transversed across the beam diameter.

For the electrostrictive mechanism, Kerr [26] determined two temporal regimes for the critical power P_{1s}, which for a paraboloidal temporal pulse shape, are

$$P_{1s} = 0.943\ P_1, \ \tau > 1, \qquad \text{(steady state)} \tag{3}$$

and

$$P_{1s} = 0.943\ P_1/\tau^2 \ , \ \tau < 1, \qquad \text{(transient)} \tag{4}$$

where

$$\tau = \Delta t v / w_o \quad , \tag{5}$$

with w_o being the spot size at the entrance of the medium for a collimated or gently focused beam. For the bulk tests with 1.7-ns pulses and w = 0.14 mm, the value of τ was 1.645 which, from eq. (4) yielded a power of 24 GW for P_{1s} for both NaCl and KCl along the

[100] direction. This is a factor of 1000 larger than P_{1e} (23 and 29 MW, respectively). indicating a negligible role for electrostriction in these tests. For the surface threshold tests at the same pulsewidth, electrostriction had even less influence. It had only 1% as large an effect as the electronic mechanism for the 65-ns surface tests.

From exact solutions of the nonlinear wave equation, Dawes and Marburger [27,28] suggested the use of another critical power, P_2, which gives an axial singularity at infinity for an initially plane wave. P_2 is 3.72 times larger than P_1, and for NaCl and KCl P_{2e} becomes 86 and 107 MW, respectively. To calculate the increase of the axial intensity due to self-focusing, we used formulas derived by Dawes and Marburger:

$$\frac{I(z)}{I(0)} = [(1 - z/R)^2 + 4(1 - P/P_2)z^2/k^2w_o^4]^{-1} \text{ for } P \leq 0.25\ P_2, \tag{6}$$

and

$$\frac{I(z)}{I(0)} = [1 - z(1/z_f + 1/R)]^{-\alpha/2} \quad \text{for } P \geq 1.5\ P_2, \tag{7}$$

where z is the path length within the medium, R is the focal length of the incident phase front within the front surface of the medium ($R = -w_o(dw/dz)_o^{-1}$, $R > 0$ for a converging beam), w_o is the spot-size radius ($1/e^2$ level), z_f is the self-focusing length and α is a numerically-derived exponent. For laser powers intermediate to the above, the graphic solutions of Dawes and Marburger were used.

In the bulk tests of NaCl, the laser power levels did not exceed 0.06 P_2 at which self-focusing produced a 0.5% intensification. In the exit-surface tests of NaCl, the ratio of P/P_2 was 0.67, or less, using a spot size of 1.0 mm. The resultant intensification was computed to be less than 1% (2%) for the 1-cm (5-cm) thick samples. Comparable, but smaller values were computed for KCl which has a smaller n_2.

Finally, we mention that Fradin et al. [29] and Smith et al. [23] have used a different formula for computing the intensification at the focal plane during bulk damage measurements:

$$\frac{I'(f)}{I(0)} = (1 - P/P_1)^{-1} \text{ for } P \leq 0.9\ P_1 \quad . \tag{8}$$

This formula predicts much greater intensification than is calculated from the above eq. (6) of Dawes and Marburger which describes their exact numerical solutions.

1.7-NS PULSE

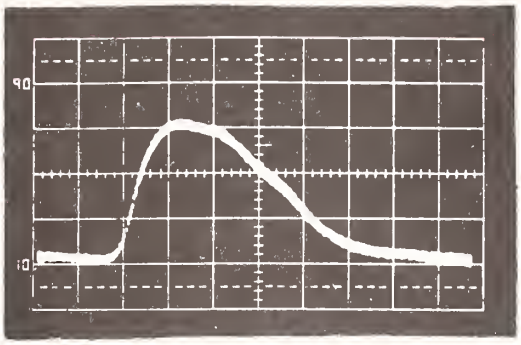

0.5 NS PER DIVISION

65-NS PULSE

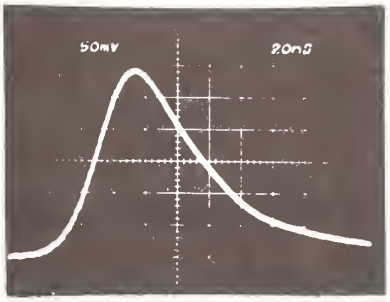

20 NS PER DIVISION

Figure 1. Oscillograms of CO_2 laser pulseforms.

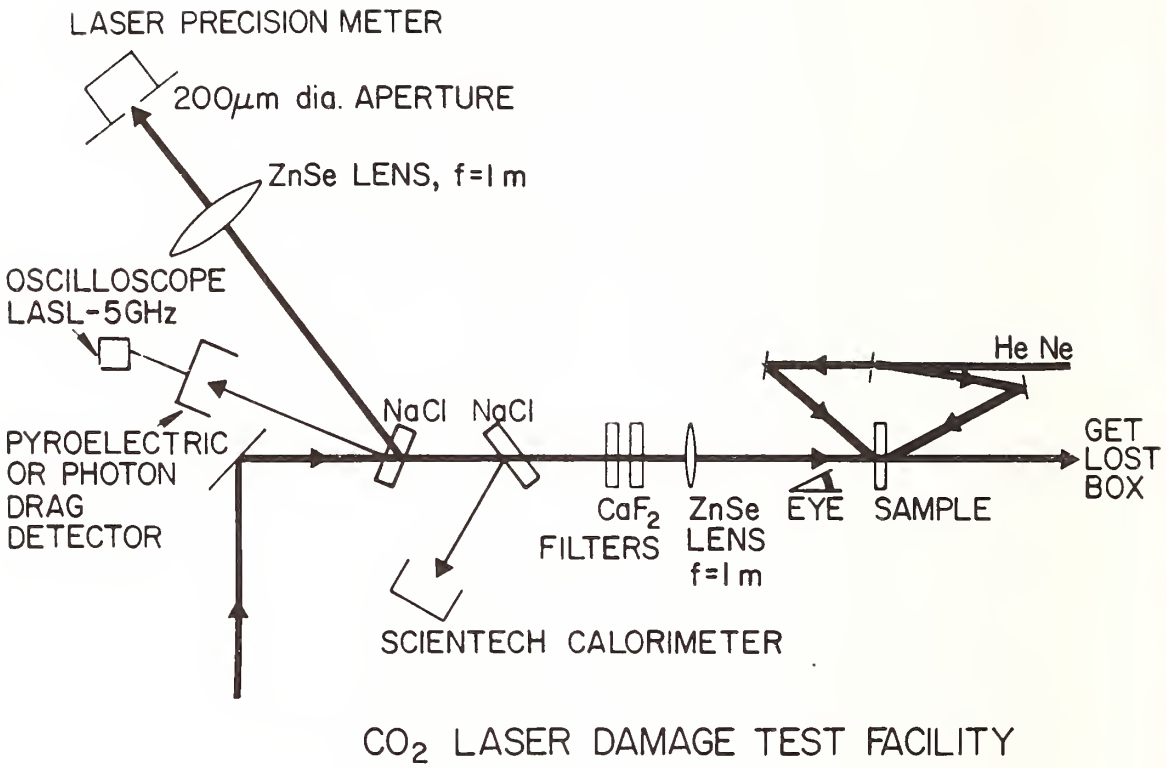

Figure 2. Schematic of CO_2 laser damage facility and associated diagnostics.

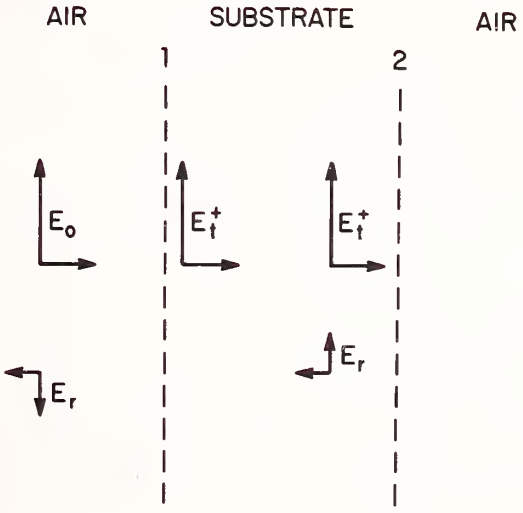

$$\frac{E\ (REAR)}{E\ (FRONT)} = \frac{2n}{|(n+1)+(n-1)\exp 2ikd|}$$

Figure 3. Electric-field vectors of a linearly-polarized laser beam at front and rear surfaces of a transparent dielectric.

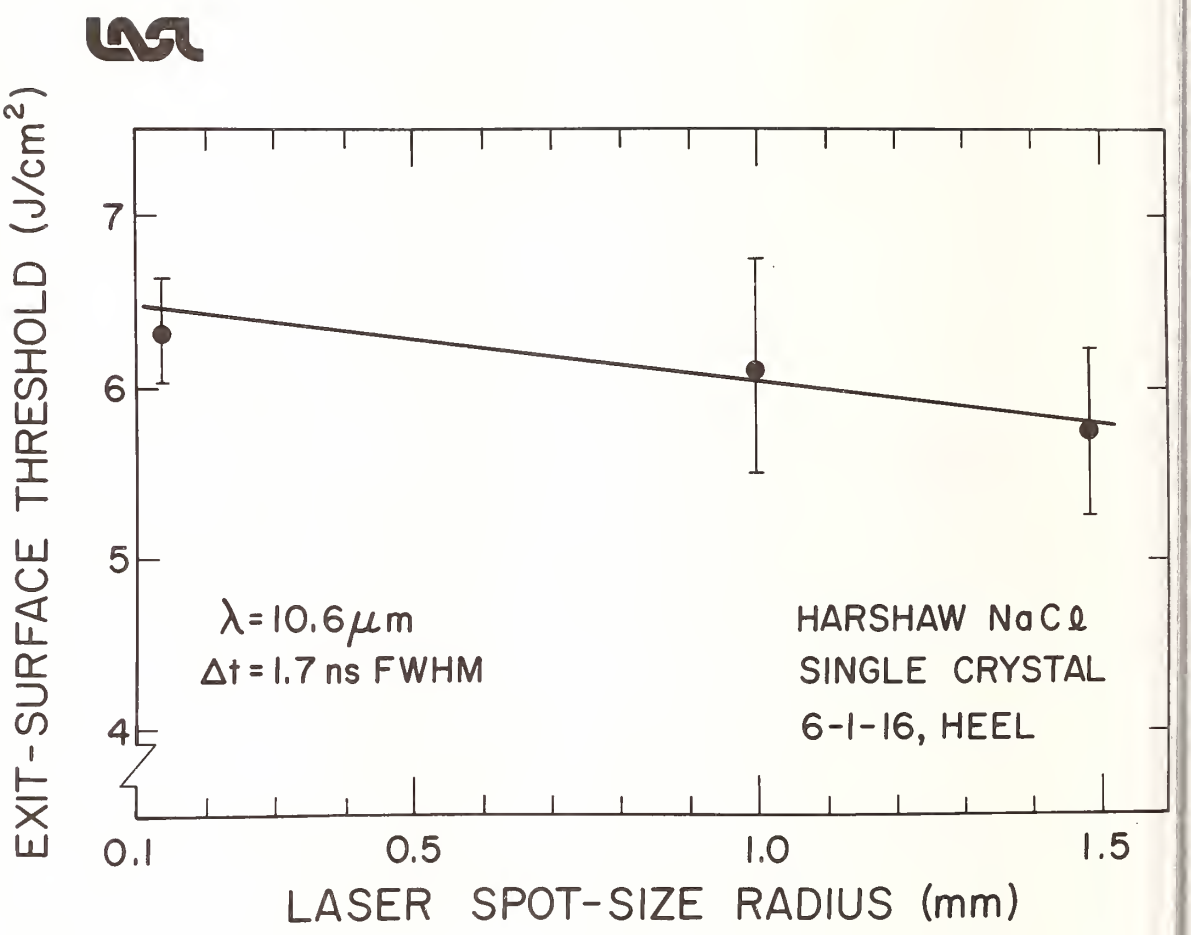

Figure 4. Exit-surface damage threshold of a single-crystal NaCl versus CO_2-laser spot-size radius.

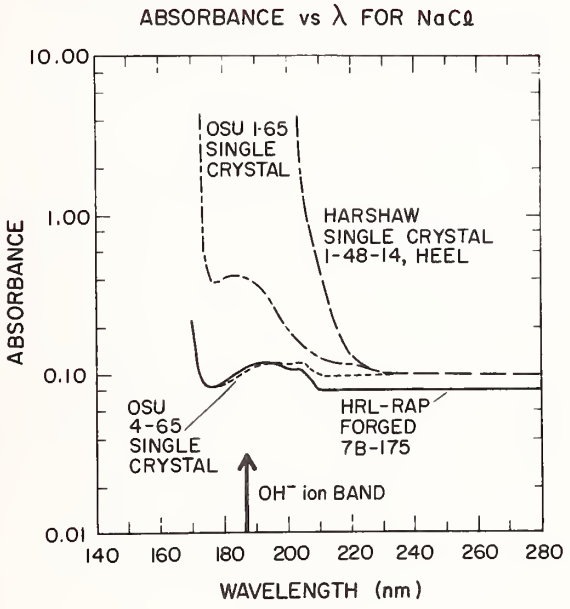

Figure 5. Ultraviolet absorbance for several NaCl windows with the OH^- ion band at 187 nm indicated. See table 1 for sample thicknesses.

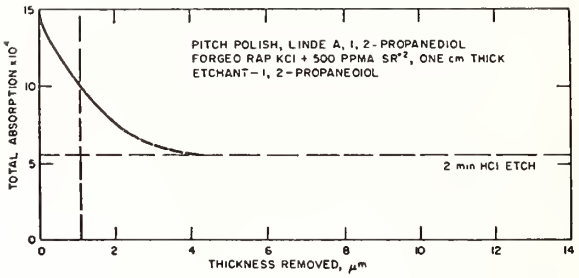

Figure 6. KCl absorption at 10.6 μm versus thickness of polished surface removed. After Turk et al. [14].

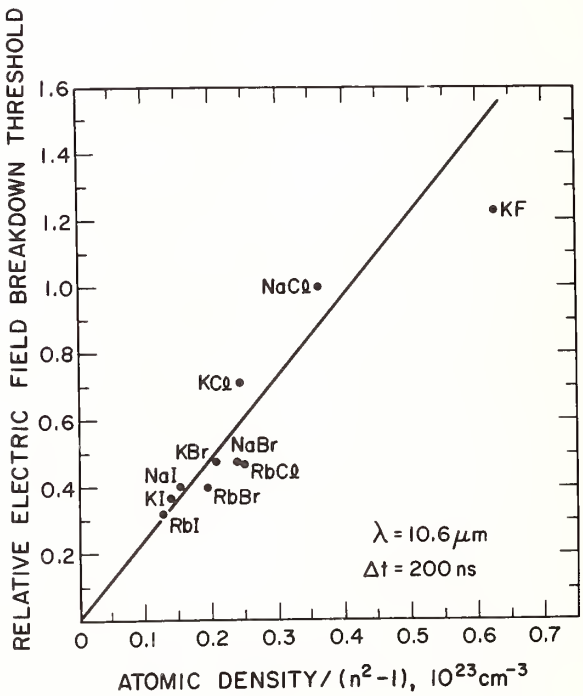

Figure 7. Bulk electric-field breakdown thresholds at 10.6 μm versus atomic density/$(n^2 - 1)$ for alkali halide crystals relative to NaCl (∿1.95 MV/cm). Data from Fradin et al. [16].

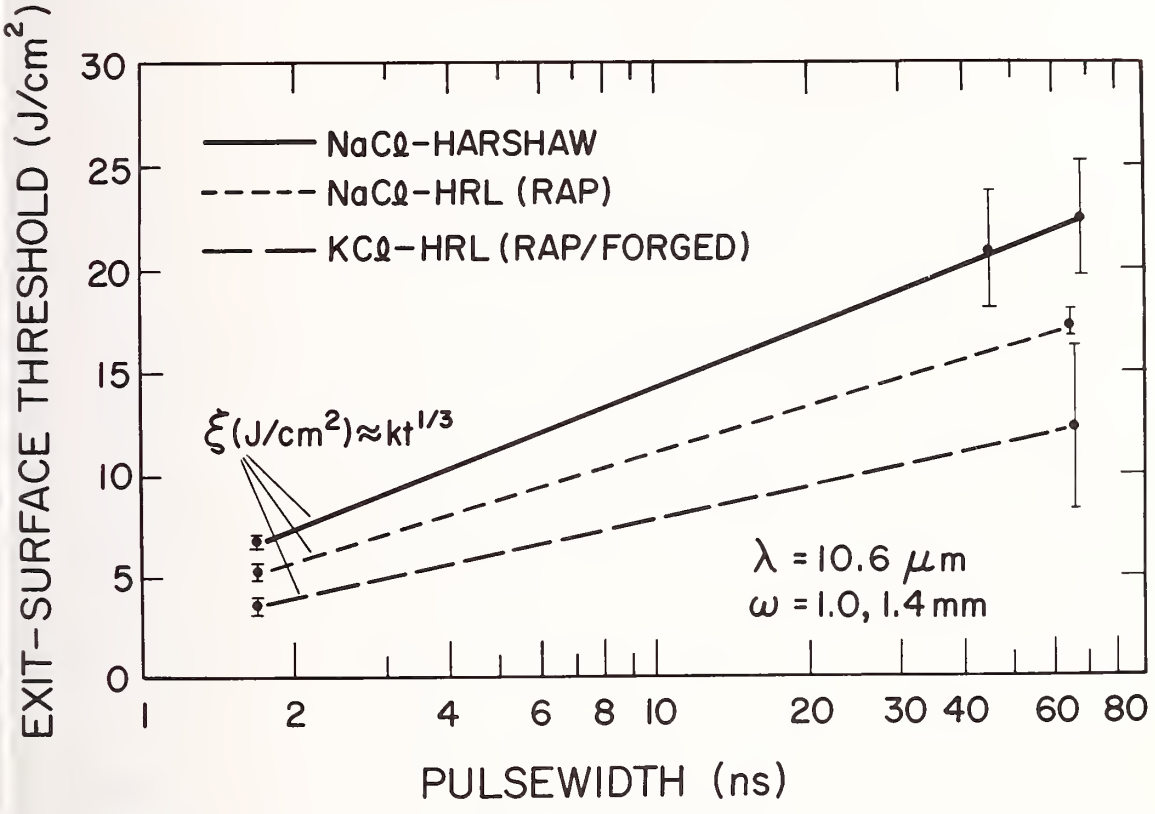

Figure 8. Exit-surface damage threshold versus CO_2 laser pulsewidth for NaCl and KCl.

The discussion of this paper centered around the question of whether or not the correlation between damage threshold and surface absorption was actually determined. The speaker indicated that a 20 to 50 percent increase in the observed damage threshold was generated by pre-irradiation of the surface at a power level lower than the damage threshold. The implication was that by this pre-irradiation process, adsorbed gases, water vapor and other contaminants were expelled from the surface. It was remarked that great variation could be seen from sample to sample in alkali halide materials, and that this might obscure any fundamental properties of individual materials. The speaker indicated that the samples used in this work were supplied specifically for damage studies, and represented the best samples available from commercial suppliers. The surface absorption measurements used in this work were made by the supplier and thus it was not possible for the speaker to verify the measured values. The consensus of the discussion appeared to be that the correlation between surface absorption and the observed damage thresholds was implied by the results of this work but not unequivocally established.

CO_2-LASER POLISHING OF FUSED SILICA SURFACES FOR INCREASED LASER DAMAGE RESISTANCE AT 1.06 μm*

P. A. Temple
Michelson Laboratory, Physics Division
Naval Weapons Center, China Lake, California 93555

and

David Milam and W. Howard Lowdermilk
Lawrence Livermore Laboratories
Livermore, California 94550

We have prepared bare fused silica surfaces by subjecting the mechanically polished surface to a rastered cw CO_2 laser beam. Analysis shows that this processing causes (a) removal of a uniform layer of fused silica and (b) a probable re-fusing or healing of existing subsurface fractures. The fused silica removal rate is found to be a function of the laser intensity and scan rate. These surfaces are seen to have very low scatter and to be very smooth. In addition, they have exhibited entrance surface damage thresholds at 1.06 μm and 1 nsec, which are substantially above those seen on the mechanically polished surface. When damage does occur, it tends to be at a few isolated points rather than the general uniform damage seen on the mechanically polished part. In addition to the damage results, we will discuss an observational technique used for viewing these surfaces which employs dark-field illumination.

Key words: Fused silica; laser damage; surface finishing; surface polishing.

Introduction

We have prepared fused silica surfaces by subjecting the mechanically polished surface to a cw CO_2 laser beam treatment. These surfaces are found to exhibit increased laser damage resistance to 1.06 μm, 1 nsec pulses. In addition to a description of the damage results, we will discuss some of the other physical properties of surfaces prepared in this way.

Surface Preparation

All the samples used in this set of measurements were Suprasil II, polished by Zygo Corporation. They were quite smooth with a Talystep rms roughness of under 10 Å. Figure 1 shows the setup used to treat these mechanically polished surfaces with a CO_2 laser beam. Since the wavelength of CO_2 radiation is much longer than the wavelength of the absorption edge of fused silica, CO_2 radiation is highly absorbed by fused silica. The result is intense local heating of the fused silica surface. Thus far only unfocused CO_2 radiation from a Coherent Radiation Model 41 laser has been used. By using a beam power of approximately 75 watts and a scan rate of $\sim$ 5 mm/sec, we have succeeded in achieving the desired result of modifying the fused silica properties without seriously degrading the figure of the surface. At this power and scan rate, the region under irradiation appears as a bright reddish-white spot about 2 to 3 mm in diameter. At higher laser powers or slower scan rates, sublimed SiO_2 is seen to come off the irradiated region and is redeposited as a white powder on the cooler parts of the sample just above the irradiated region. By scanning in a left-to-right motion and by beginning the scans on the lower part of the sample and making each successive scan 0.5 mm above the previous scan, this fine white powder is reevaporated, and the finished part does not have SiO_2 powder on the laser-polished portion.

* Work sponsored by Navy Independent Research funds and Department of Energy.

Surface Inspection

The techniques used to inspect the surfaces prepared in this study have been Nomarski microscopy and total internal reflection microscopy (TIRM) [1,2][1]. The latter technique has been described elsewhere and in a poster paper at this meeting [3]. In TIRM the transparent part is illuminated from within with a laser beam (fig. 2) at an angle just greater than the critical angle. Since total reflection occurs, no light escapes except where there has been some perturbation of the surface. The image seen through the microscope, then, is one of a dark background with bright regions where the surface has been disturbed.

Damage Results

Six samples prepared by CO_2-laser polishing have been damage tested at Lawrence Livermore Laboratory. These have all been front surface tests at a wavelength of 1.06 μm and a pulse length of 1 nsec. Damage is defined as the appearance of pits as seen in Nomarski microscopy. In general, the results have indicated that these surfaces exhibit a higher resistance to damage than do conventionally polished fused silica. This is evidenced by no pits appearing at energy density levels which would normally cause damage on a conventional part and fewer individual pits when damage finally does occur at higher energy density levels. Table 1 is a list of the results from two samples. Keeping in mind that typical polishing samples have a damage threshold which ranges from 10 to 20 J/cm^2, the laser-polished samples show a very high resistance to damage.

Table 1. Fused silica entrance surface damage.

Sample		J/cm^2	Comments
Z1-23		30.6	No light, 1 site
		40.7	Flash, 3 sites
		55.5	Flash, 3 sites
Z1-21		33.4	Flash, no damage
		23.0	Flash, minor damage
		40.1	Flash, minor damage
	Same site	29.0	Flash, no damage
	Same site	38.0	Flash, no damage
	Same site	42.3	Flash, damage

Of particular interest are the three shots on one site where the first two shots caused no damage.

Damage Morphology

Figure 3 is a set of three photographs taken of a conventionally polished fused silica surface which has been damaged on the entrance surface by a 15 J/cm^2 pulse. The typical dished-out damage pits are seen in the Nomarski photograph, while the TIRM photograph shows a great deal of structure unrelated to the occurrence of damage. The simultaneous photograph in the center shows that most of the damage pits do indeed have a small bright spot in the center, but certainly damage is more easily detected by Nomarski inspection.

Figure 4 shows Nomarski and TIRM photographs of a damage site on laser-polished fused silica. Here, while much damage is visible in the TIRM photo, only one pit is visible in the Nomarski photograph. As will be pointed out below, the surface was virtually featureless prior to damage. The pit, in addition, does not have the usual conical shape as seen on conventionally polished parts. Rather, it is quite sharp-edged. While it seems quite certain that the damage resistance of laser-polished fused silica is substantially better than conventionally polished fused silica, it is possible that damage may have taken place which went undetected by Nomarski microscopy but which would have been visible in TIRM if that technique had been visible during the damage tests.

[1] Figures in brackets indicate the literature references at the end of this paper.

Physical Properties of Laser-Polished Fused Silica

Shown in figure 5 are two TIRM views of a fused silica surface as seen before and fter laser polishing. From these photos it is seen there are residual marks on the mechan- cally polished part due to the mechanical polishing process, and that these are no longer een in the laser-polished surface. As indicated in the figure, this particular part was nitially very smooth, and, at least in the short run, laser polishing did not degrade this noothness. Shown in figure 6 are two TIRM views of a fused silica surface similar to that n figure 5 but after one-half-hour etch in 5% HF acid at room temperature. The absence of ny linear features in the laser-polished surface indicates that, at least on the surface, : has "forgotten" its past experience of being mechanically polished. While not shown, hese two surfaces reveal similar information in Nomarski microscopy. That is, the mechan- cally polished surface is quite highly decorated with scratches, while the laser-polished urface is quite uniform in appearance.

Figure 7 shows two Zygo interferograms of a fused silica part which has been laser olished by scanning at successively slower rates on widely separated regions. The figure n the left is the result of interference between the polished surface and a standard flat. n this case, changes in the interference pattern are exclusively due to changes in the urface profile. This figure indicates that the regions which have been laser polished are epressed below the mean surface. We have verified that this is so by Talystep measurements. n the case of the part shown in figure 7, the pass which resulted in a featureless appear- nce in TIRM had a measured maximum depression of 1500 Å. All passes with less depression till showed the marks characteristic of polishing, while those CO_2 scans which were made t a slower rate showed ever wider featureless regions.

The photo on the right of figure 7 was made by placing a second fused silica blank in ontact with the laser-polished surface of the first sample. The inner region was filled ith a fluid of index identical to that of fused silica. The existence of the fringe istortion coincident with the laser-polished scan lines indicates that the index of the aterial in the laser-polished region has increased. This is possible since the specific ravity of SiO_2 can range over a value of from 2.2 to 2.66, and the index ranges over a alue of 1.46 to 1.55, depending upon the crystalline state. Fused silica is, in addition, fairly open lattice material, and it may be collapsing to a more dense form under laser rradiation.

Mechanical tests on the surfaces of laser-polished parts indicate that these surfaces re under tensile stress. Surface tensile stress is expected to result from this type of apid heating and cooling of the surface of a cool substrate. However, tensile stress ould also result if the surface was indeed going to a more dense phase, as is suggested by he data in figure 7.

Damage Resistance

CO_2-laser-polished parts appear, by etching as shown in figure 6, to have fewer defects ssociated with mechanical damage from previous processing. This may be the reason for the ncreased damage resistance of laser-polished parts. Even in the case of laser-polished arts, however, it is quite possible that deeper, unhealed regions are the sites of subse- uent damage, if the part is subjected to a sufficiently high photon flux during damage esting. Figure 8 shows a damage site which is suggestive of this. Here, a laser-polished egion has been damaged. Both the TIRM and Nomarski photographs show a linear feature and amage along this feature.

Most damage sites do not reveal any particular linear pattern. In the usual mechani- ally polished surface there is literally a mat of scratches and fractures, and it is not urprising to see damage occurring in an essentially random fashion. Laser-polished parts, n the other hand, appear to have a much reduced surface microcrack density, and the laser lux required to cause damage to these deeper and less numerous defects is much higher, as hown in table 1.

Real Optics

The question of making useful optical components from CO_2-laser-polished parts will epend upon one's ability to retain optical figure during CO_2-laser polishing. This is not

unlike the situation which exists for flame-polished or acid-etched surfaces, both of which can show higher damage resistance than the mechanically polished surface. In the case of CO_2-laser polishing, however, the situation is more easily controlled. In addition, it appears as though a sufficient CO_2 polish to improve the damage threshold may not disrupt the figure too badly.

Conclusion

In this paper we have presented a method for the preparation of fused silica surfaces which results in increased surface damage resistance to 1.06 μm radiation. These surfaces are prepared by intense heating of the fused silica surface by an incident cw CO_2 laser beam. The resulting surface is essentially featureless, as seen in dark-field microscopy. Evidence was shown to suggest that many of the microscopic fractures present after mechanical polishing are removed by this polishing technique. The simultaneous removal of mechanical defects and increase in damage threshold was taken as evidence that surface fractures play a role in lowering the damage threshold of polished glass surfaces. Finally, we have noted that in its present state CO_2-laser polishing results in a degraded surface figure, but that it appears as though surface figure could be retained with careful CO_2-laser processing.

References

[1] Temple, P. A., "An Improved Dark-Field-Like Surface Inspection Technique Using Total Internal Reflection," presented at Conference on Optics '79, 23-25 May 1979, Los Alamos, New Mexico.

[2] Temple, P. A., "Total Internal Reflection Microscopy: A Surface Inspection Technique," submitted to Appl. Opt.

[3] Temple, P. A., "Examination of Laser Damage Sites on Transparent Surfaces and Films Using Total Internal Reflection Microscopy," this conference.

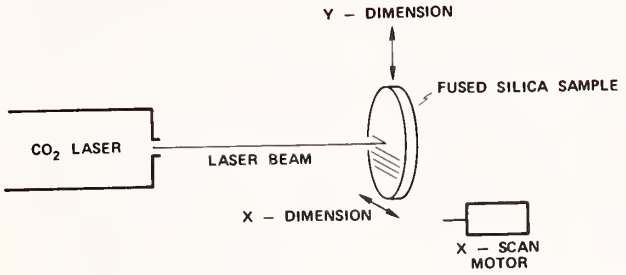

Figure 1. CO_2-laser-polishing apparatus. The laser is an unfocused Coherent Radiation Model 41 CO_2 laser. The sample is 3 meters from the laser. The sample is moved left and right by a variable speed motor and up and down by hand. The sample was unheated and in air during polishing.

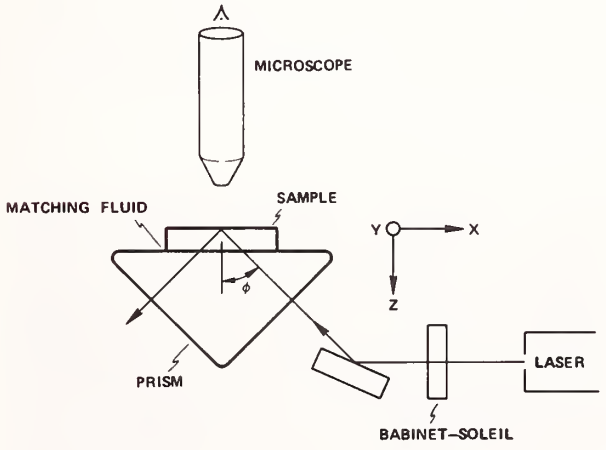

Figure 2. The total internal reflection microscopy (TIRM) used to inspect highly polished transparent samples. A polarized laser beam is coupled into the sample by a prism. The angle of incidence at the sample top surface is just beyond the critical angle. The sample is gripped by a microscope slide manipulator, and, since the sample is supported on an oil film on the prism, it can easily be moved about for inspection of the entire upper surface. The microscope used for the photographs in other figures was a Zeiss Nomarski microscope with the Nomarski illuminator turned off.

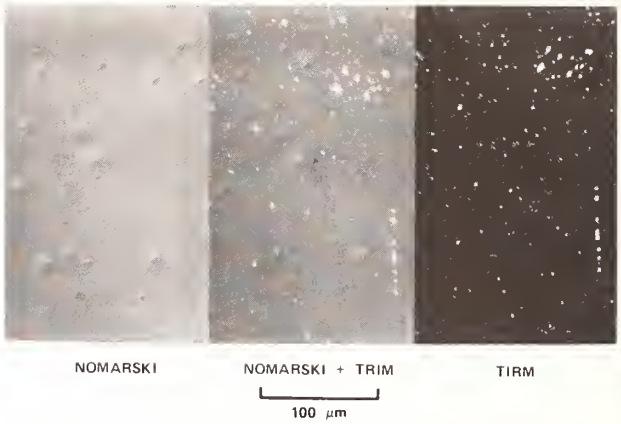

Figure 3. Three photos of the same region of a laser-damaged, conventionally polished piece of fused silica. The view on the left is a Nomarski photo showing several pits caused by a 15 J/cm^2, 1.06 μm wavelength, 1 nsec pulse length exposure. The photo on the right is a TIRM view. Since the part is mechanically polished, it has many features visible in this view which are not related to the damage shown in the left photo. The center view shows the Nomarski and TIRM illuminations simultaneously. It can be seen here that few of the TIRM features are actually identified with damage sites. Most of these features are mechanical damage due to the polishing process.

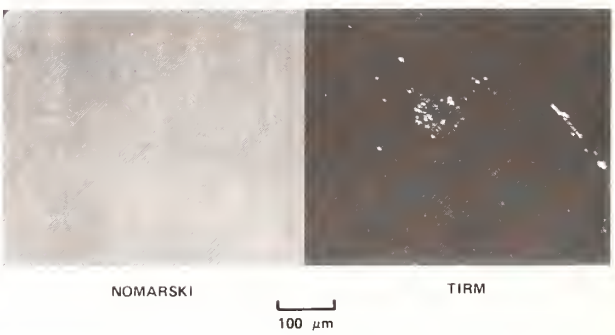

Figure 4. A Nomarski and TIRM view of the same damage site on a laser-polished surface. The laser-polished site was featureless before damage, and any features seen in the TIRM view are the result of damage, either as actual pits or as debris. Note that the damage is not easily detected on the Nomarski photograph.

Figure 5. A piece of fused silica before and after laser polish. This part is unusually featureless even as a mechanically polished part. The laser-polished part is totally featureless in both TIRM and Nomarski illumination.

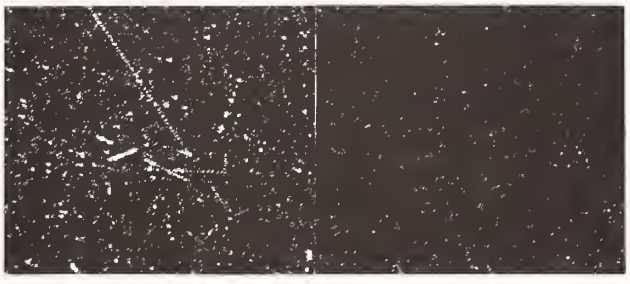

Figure 6. Two regions of the same fused silica sample as seen in TIRM after one-half hour of etching in 5% HF acid. The linear features, evident in the mechanically polished part, are totally lacking in the laser-polished part.

Figure 7. Two Zygo interferograms of a fused silica part which has been laser polished by six passes, evenly spaced, over the surface of the part. The scan rates were successively slower for scans nearer the right. The photo on the left demonstrates that there has been a reduction in the height of the surface where the surface was scanned. Talystep measurements verified this to be the case. The photo on the right shows that the material in the laser-polished region is of different optical density than the rest of the sample as a result of laser polishing in that region.

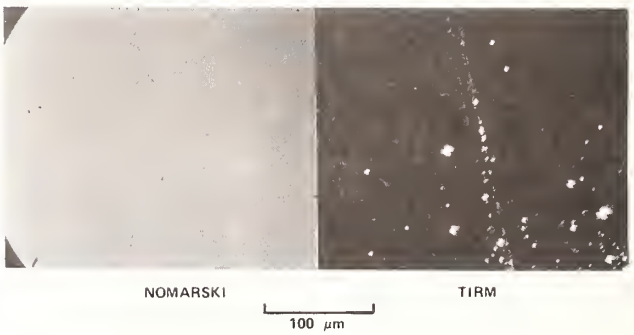

Figure 8. A Nomarski and TIRM view of a damaged region on a previously featureless laser-polished part. Of particular interest is the linear feature along which damage occurred. This is suggestive of that linear feature, probably a scratch introduced much earlier in the mechanical polish, being the nucleation site for damage.

The speaker indicated that the scan rates used in this work ranged from 1/10th to 1 centimet per second. He indicated that further evidence to support the contention that the surface c the sample was densified during the flam-polishing process was provided by samples that were scribed before surface treatment. In some cases, whole sections of these samples detached b spallation after the flam-polishing process, indicating the presence of very strong tension forces which would be consistent with the model of increased density.

THE RELATIVE IMPORTANCE OF INTERFACE AND VOLUME ABSORPTION BY WATER IN EVAPORATED FILMS*

T. M. Donovan and P. A. Temple
Michelson Laboratory, Physics Division
Naval Weapons Center, China Lake, California 93555

and

Shiu-Chin Wu and T. A. Tombrello
California Institute of Technology, Pasadena, California 91125

Previously, a precision adiabatic calorimeter has been used to make single line HF calorimetry measurements of surface, interface, and bulk absorption on wedge-shaped films. In this paper we correlate hydrogen concentrations and profiles measured using a nuclear resonant technique with these previous calorimetric measurements. Results show, for example, that H_2O is uniformly distributed in materials such as NaF and ThF_4 but occurs at the film-substrate interface in materials such as As_2Se_3 and ZnS. The relative effectiveness of encapsulation of NaF and ThF_4 by ZnS will be discussed. Good agreement is found between measured absorption and that calculated from measured hydrogen profiles.

Key words: Absorption; calorimetry; coatings; encapsulation; hydrogen; thin films; water; water absorption.

Introduction

In a program designed to develop multilayer coatings with minimal absorption for use with HF lasers, contamination by water was expected to be a major source of residual absorption at the laser operating wavelength, 2.8 microns. Further, as absorption in multilayer coatings is not always the same as would be predicted from measurements on single layers [1][1], contamination at surfaces and interfaces was expected to be a major source of residual absorption. In the effort to minimize this absorption by improving or optimizing deposition techniques, it was important to be able to measure not only the total coating absorption but the absorption as it occurs spatially within the multilayer design.

In previous papers [2,3] a single laser line calorimetric measurement technique was described from which values of surface bulk and interface absorption could be obtained directly from measurements on wedge-shaped films. In this paper we report the results of applying a nuclear resonant technique [4], developed for measuring hydrogen content and spatial profiles in solid samples, to measuring hydrogen content and distribution in 1- and 2-layer optical coatings. Values of absorption that we obtain, assuming the hydrogen is present as H_2O, agree in detail, both as content and distribution, with values measured by calorimetry, verifying that water contamination is responsible for residual absorption in these coatings at 2.8 microns. Results are presented for NaF, ThF_4, As_2Se_3, ZnS, SiO_x, and Al_2O_3 single-layer films. Finally, the reduction of H_2O in ThF_4 by encapsulation with ZnS is discussed.

Absorption in NaF Films

Single HF laser line absorption of NaF as measured by Temple [2,3] are listed in table 1, along with the absorption coefficient of bulk NaF at 2.73 microns [5] and the absorption of H_2O [6] in this spectral region. Two conclusions are immediately apparent from this data: First, NaF films have about four orders of magnitude more absorption than bulk NaF in this spectral range, and second, the ratios of absorption of the NaF film and H_2O from

* Work sponsored by the Materials Division of the Defense Advanced Research Projects Agency.

[1] Figures in brackets indicate the literature references at the end of this paper.

2.91 to 2.73 microns are identical. This ratio of absorption is shown more clearly in figure 1, where the H_2O absorption data have been normalized to the NaF data at 2.91 microns. These results show that the predominant absorption in the NaF film is due to H_2O contamination.

Table 1. Absorption of thin film and single crystal NaF and H_2O.

λ (μm)	NaF (film)(cm^{-1})	NaF (bulk)(cm^{-1})	H_2O (cm^{-1})
2.73	2.5	4.3×10^{-4}	1,472
2.76	5.5		3,050
2.79	9.6		4,684
2.83	14.4		7,104
2.87	17.6		9,851
2.91	19.4		11,660

In order to determine the spatial distribution of absorptance and, therefore, the distribution of H_2O in the film, measurements were made as a function of film thickness at both 2.73 and 2.91 microns [2,3]. The pronounced thickness dependence of absorption as shown in figure 2, particularly at 2.91 microns, along with the zero thickness extrapolation of the absorptance to approximately the uncoated substrate absorptance, indicates that the water contamination occurs throughout the film with some interface contribution present.

To verify that the excess absorption in the NaF film is due to H_2O and that the H_2O is uniformly distributed in the film, measurements were made of the H content and distribution in the films using the resonant nuclear reaction $^{19}F + {}^{1}H \rightarrow {}^{16}O + {}^{4}He + \gamma$, as described by Leich and Tombrello [4]. Hydrogen profiles measured for NaF films deposited in a helium cryopumped UHV system, an ion-pumped UHV system, and an oil-diffusion pumped system are shown in figures 3(a) and (b). The average H content in all cases is about 150 ppm, and the ratio of H atoms to NaF molecules is about 0.005. The distribution of H is uniform with some buildup at the film-substrate interface. Assuming the H is present as H_2O (secondary negative ion mass spectroscopy (table 2) measurements confirm that H is present primarily as H and OH ions), we estimate a quantity equivalent to a 25 Å H_2O to be uniformly distributed in a hypothetical 10 000 Å NaF film. Calculating the absorptance from the expression $A = \alpha d$, where α is the absorption coefficient of H_2O and d = 25 Å, gives $A = 2.9 \times 10^{-3}$ and $A = 3.6 \times 10^{-4}$ at 2.91 and 2.73 microns, respectively. These values compare reasonably well with values of 2.2×10^{-3} and 2×10^{-4} taken from the data of figure 2 at α = 1 micron for the above wavelengths. Thus, the nuclear resonance data confirm the calorimetric results that H_2O contamination is responsible for the anomalously high absorption in NaF films, and that the H_2O is uniformly distributed in these layers. The nuclear technique also provides a quantitative measure of the H (H_2O) content of the films.

Absorption in As_2Se_3 Films

The reported absorption coefficient of As_2Se_3 and As_2S_3 films is lower than NaF [7] at 2.8 microns. Measurements on wedge-shaped films of As_2Se_3 [2,3], as shown in figure 5, confirm the low film absorption of reference [7] and indicate there is little or no thickness dependence of the absorptance either at 2.73 or 2.87 microns. There is, however, a significant surface contribution at these wavelengths, as indicated by the difference between the absorptance extrapolated to zero film thickness and the measured substrate absorptance. Hydrogen profiles of As_2S_3 (As_2Se_3) films show a H content of about 10 ppm or less within the film volume and significant quantities, about 200 ppm, at the film-substrate interface. Calculation of absorptance with a 500 Å interface region and 0.02 H_2O to As_2S_3 molecular ratio yields an absorptance of $\sim 1 \times 10^{-3}$. The measured surface contribution at 2.87 microns, from figure 5, is 0.7×10^{-3}. Again, the agreement is good, indicating the interface absorption observed calorimetrically in As_2Se_3 is due to H_2O contamination at the film-substrate interface.

Table 2. Secondary ion mass spectroscopy (SIMS) analysis of NaF films prepared in ultrahigh vacuum and an oil-diffusion pumped system.

-Ions	UHV	Oil-diffusion	+Ions	UHV	Oil-diffusion
H	74	63	H	216	117
C	2	4	F	7	5
CH	5	6	Na	1000	1000
O	51	71	Si	153	70
OH	33	29	NaO	0.5	0.5
F	1000	1000	SiO	3	2
Na	1	1	Na_2	7	9
C_2H_2	1	4	Cr	.0.5	0.5
Si	0.5	0.5	Si_2	1	1
Cl	3	3	Na_2F	2	2
F_2	0.5	0.5	Si_2F	0.5	0.5

H Contamination in ThF_4 and ZnS and the Effect of Encapsulation

The nuclear resonant technique was used to measure H profiles in ThF_4 and ZnS and then to determine the added effect of encapsulating the ThF_4 layer by ZnS by sequential deposition of the two layers without breaking vacuum. These results are compared with calorimetric measurement of absorptance of quarter-wave pairs of alternating layers of ZnS and ThF_4 in two configurations: (1) high index layer ZnS on the outside and (2) ThF_4 as the outside layer.

A H profile of ThF_4 is shown in figure 6. Hydrogen is uniformly distributed throughout the film as in the case of NaF; however, the overall contamination level is higher, i.e., about 1000 ppm. If a freshly deposited 2000 Å film of ThF_4 is coated immediately without interruption of the vacuum by a 2000 Å film of ZnS, the result shown in figure 7 is obtained. The H content of the ThF_4 is reduced from 1000 ppm to less than 20 ppm, a reduction of about a factor of fifty in H content. The H content of the ZnS is about 10 ppm.

An independent experiment [8] in which two multilayer coatings consisting of five pairs of alternating quarter-wave optical layers of ZnS and ThF_4 were deposited simultaneously by the Optical Coating Laboratory, Inc., Santa Rosa, California, using an appropriate shuttering arrangement in the following configurations:

$$\text{substrate } (LH)^5 \text{ and substrate } (HL)^5 \quad ,$$

where H = ZnS and L = ThF_4. The single line HF laser absorptance of these coatings was 6×10^{-4} and 2×10^{-2} at 2.87 microns, respectively. The factor of thirty-five decrease in absorptance resulting from exchanging ZnS for the ThF_4 outer layer is in good agreement with the decrease predicted by direct measurement of H contamination of ThF_4 and encapsulated ThF_4. These data suggest that ThF_4 has a highly porous structure and H_2O is absorbed by the film on exposure to air. This is different behavior than we observed in NaF films where the air-exposed film has similar H content as the encapsulated ThF_4 film. The H profile of ZnS as a single layer (fig. 8) shows a H content of about 10 ppm in the volume of the film and a film-substrate concentration of 200 ppm. The interface contribution seen in the single-layer profile is not observed at the ZnS-ThF_4 interface, suggesting that it results from incomplete cleaning (chemical and vacuum bakeout) of the fused quartz substrate prior to deposition of the ZnS layer. Deposition on freshly deposited ThF_4 eliminates this contamination layer, at least at the ZnS-ThF_4 interface.

Absorption of Al_2O_3 and SiO_x Films

Al_2O_3 and SiO_x have been evaluated using both single line HF calorimetry and with the H profiling technique. The absorption results shown in table 3 for Al_2O_3 indicate a bulk or volume absorption of 39 cm^{-1} with a surface absorptance of 2 x 10^{-3} and a film-substrate absorptance of 4 x 10^{-3}. The measured H profile shown in figure 9, where H peaks of 250 and 500 ppm occur at the surface and film-substrate interfaces, respectively, and about 100 ppm H occur in the film volume. Calculated values of absorptance assuming 500 Å surface and interface layers are 0.6 and 1.25 x 10^{-3} for the surface and film-substrate, respectively. The calculated bulk film absorption coefficient is 50 cm^{-1}. These numbers are also in good agreement with measured values, considering the absorption and H concentration measurements were made on different films.

Table 3. Volume and interface absorption at 2.87 microns of several thin film coatings.

Material	β_F (cm^{-1})	A (x 10^4) (air film)	A (x 10^4) (film substrate)
NaF	17.5	...	...
SiO_x	10.0	25	0
Al_2O_3	39.0	21	40
As_2Se_3	0.5	0	5

The single line calorimetric measurements for SiO_x are also listed in table 3 and show a surface absorptance of 2.5 x 10^{-3} with a bulk absorption coefficient of 10 cm^{-1}. There is no suggestion of absorption at the film-substrate interface. The H profile for SiO_x shown in figure 10 shows a similar result with 300 ppm H at the surface and about 50 ppm within the film. The reason for the clean substrate-film interface region is not understood.

Conclusions

The results presented in this paper show that H_2O is a major source of contamination and hence absorption at 2.8 microns in a variety of coating materials. With hydroscopic materials such as ThF_4, as-deposited films absorb large quantities of H_2O when the coating is exposed to air. ZnS and As_2Se contain < 10 ppm. H_2O in the volume of the films are effective encapsulants capable of reducing the H_2O in these ThF_4 films to about 20 ppm. In materials with less affinity for H_2O than ThF_4, i.e., ZnS, As_2Se_3, Al_2O_3, and SiO_x, H_2O contamination occurs predominantly at air-film or film-substrate interfaces. Because of the variety of H profiles and one-to-one correspondence between H profile and absorptance profile as determined by calorimetry [2,3], we conclude that the H profiling technique is an excellent method for the identification of H_2O contamination and its spatial distribution in optical thin films and multilayers and complements the calorimetric technique with the capability of profiling multilayer structures. Both techniques will be valuable in assessing the effectiveness of improved deposition techniques designed to minimize the effect of H_2O, particularly at interface regions by application of *in situ* desorption techniques.

References

[1] Holmes, S., Final Report on Contract No. N00123-78-C-0627, Naval Weapons Center, China Lake, Calif. 93555.

[2] Temple, P. A., Decker, D. L., Donovan, T. M., and Bethke, J. W., NBS Spec. Publ. 541, 37 (1978).

[3] Temple, P. A., Appl. Phys. Lett. 34, 677 (1979).

[4] Leich, D. A., and Tombrello, T. A., "A Technique for Measuring Hydrogen Concentration Versus Depth in Solid Samples," Nucl. Instrum. Methods 108, 67 (1973).

[5] Harrington, J. A., et al., Proceedings Laser Window Conference, 1974 (AFML, Wright Patterson Air Force Base, Ohio, 1975).

[6] Rusk, A. N., Williams, D., and Querry, M. R., J. Opt. Soc. Am. 61, 895 (1971).

[7] Harrington, J. A., Rudisill, J. E., and Braunstein, M., Appl. Opt. 17, 2798 (1978).

[8] Beauchamp, W. T., Final Report on Contract No. N60530-78-C-0252, Naval Weapons Center, China Lake, Calif. 93555.

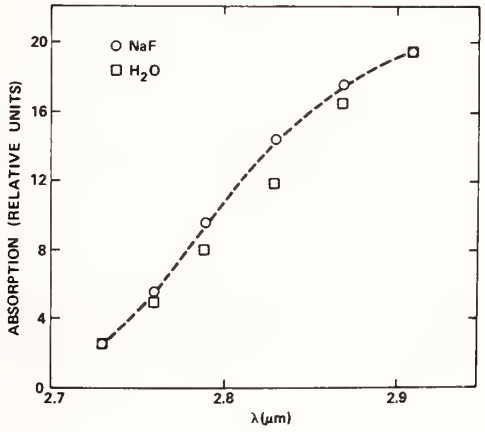

Figure 1. Spectral absorption in relative units of NaF film compared to H_2O. H_2O absorption data normalized to NaF data at 2.91 microns.

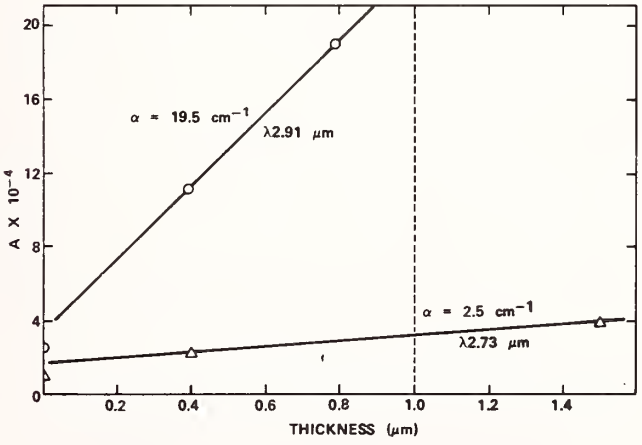

Figure 2. Thickness dependence of absorptance of NaF film for the two wavelengths, 2.73 and 2.91 microns.

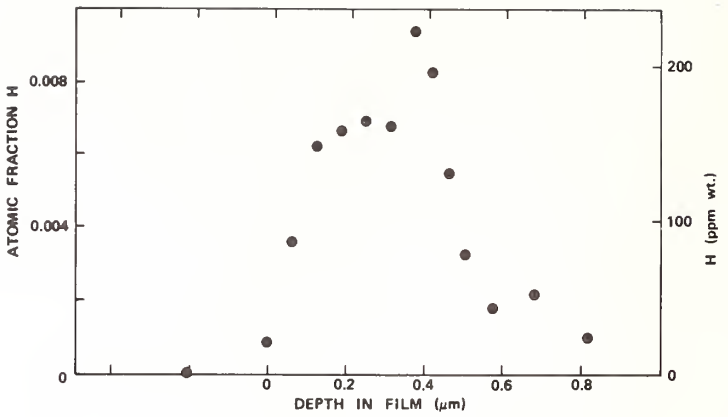

Figure 3(a). Hydrogen distribution of NaF film deposited in cryopumped ultrahigh vacuum system and measured using nuclear reaction $^{19}F + {}^{1}H \rightarrow {}^{16}O + {}^{4}He + \gamma$.

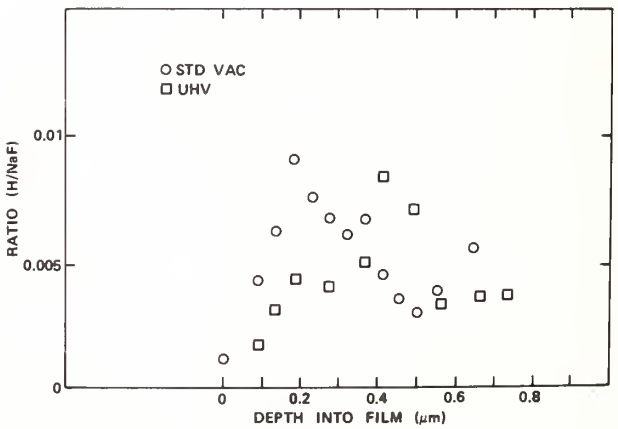

Figure 3(b). Comparison of hydrogen distributions in NaF films deposited in ultrahigh and standard vacuum.

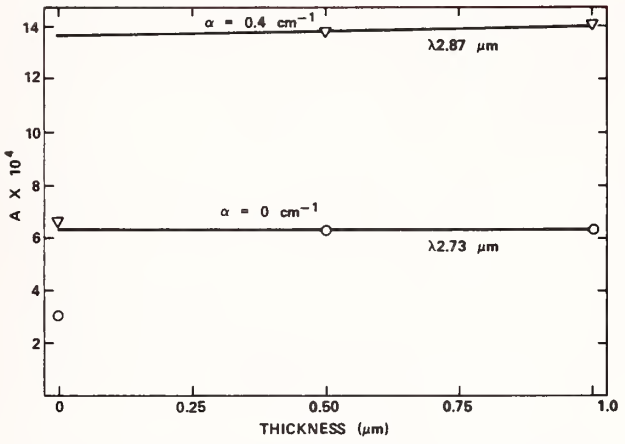

Figure 4. Thickness dependence of absorptance of As_2Se_3 film measured at 2.71 and 2.93 microns show low volume absorption and large substrate-film interface absorptance.

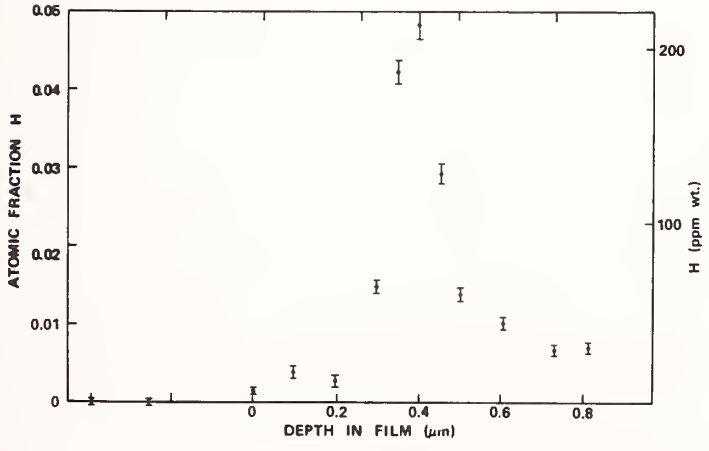

Figure 5. Hydrogen profile of As_2S_3 film showing large film-substrate interface contamination.

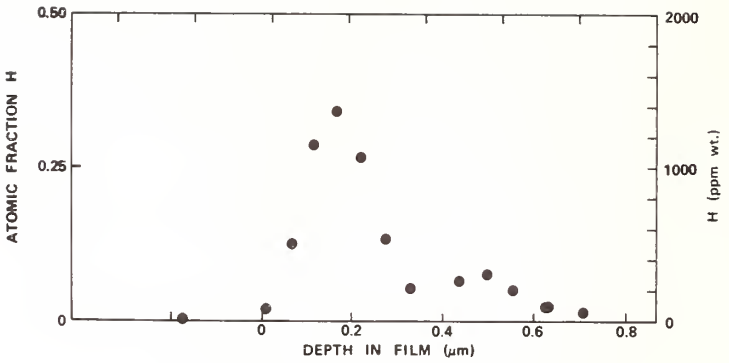

Figure 6. Hydrogen profile data of ThF_4 film.

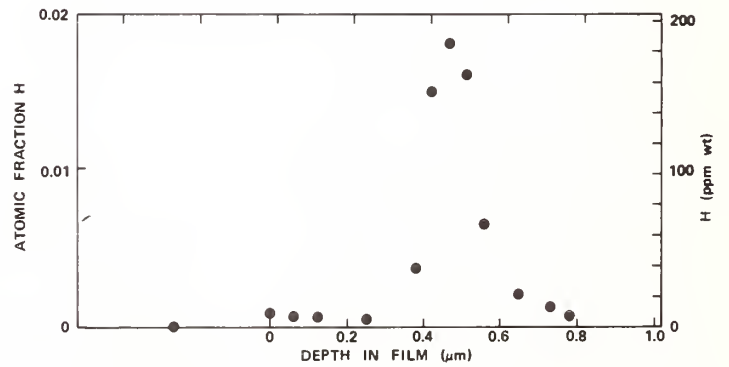

Figure 7. Hydrogen profile data of ZnS film showing large film-substrate interface absorptance.

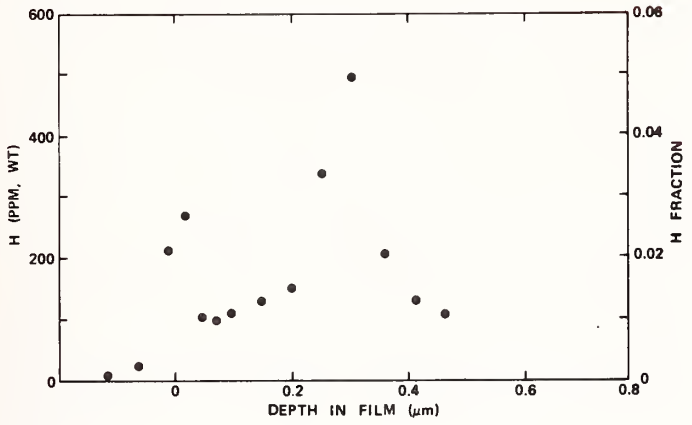

Figure 8. Hydrogen profile of ~ 2000 Å ThF_4 film overcoated with ~ 2000 Å of ZnS. H content of the ThF_4 is greatly reduced over single-layer film (Fig. 7). Film-substrate interface H of ZnS is greatly reduced over single-layer film (Fig. 8).

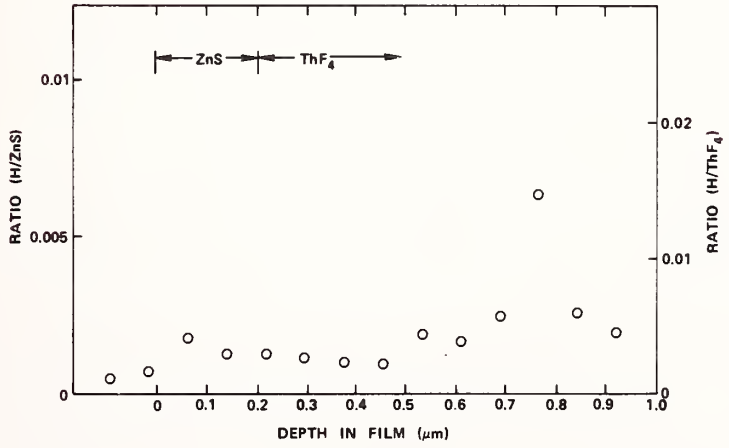

Figure 9. Hydrogen profile data of Al_2O_3 film showing large air-film and film-substrate concentrations.

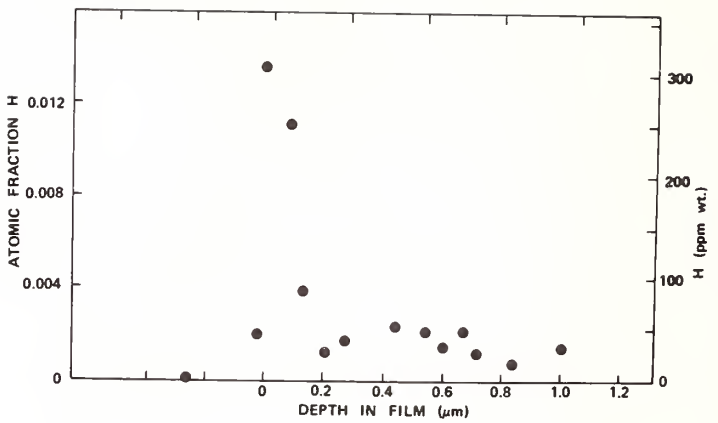

Figure 10. Hydrogen profile data of SiO_x film showing large surface concentration.

The speaker indicated that methods to avoid the presence of an interface contamination layer were under investigation. So far it had been determined that vacuum bakeout was not effective in removing an adsorption layer at the interfacial surface. It was pointed out in discussion that the absence of a water layer at the interface in the presence of materials like thorium fluoride was probably due to the fact that materials like thorium fluoride absorb water in bulk, and therefore water at the interface is redistributed within the coating layer.

CHARACTERIZATION OF SMALL ABSORPTIONS IN OPTICAL COATINGS

Wilford N. Hansen, Lee Pearson, and Galen Hansen
Utah State University
Logan, Utah 84322

and

Wayne J. Anderson
Physics Department
United States Air Force Academy, Colorado 80840

Probably the main causes of laser damage in thin films used as optical coatings are impurities and non-stoichiometry, especially at interfaces. This paper considers the problems of identifying absorbing species, locating them in the optical structure and measuring the amount of absorbing species present. The importance of an absorbing species at a given location in the structure is directly proportional to the relative electromagnetic field squared $\langle E^2 \rangle$ at that location. This fact is used both to avoid absorption when it isn't wanted and to enhance absorption when it is wanted, such as during analysis. Versatile and sensive spectroscopic procedures for locating and characterizing small absorptions are discussed. Our approach makes use of Poynting's theorem, viz., that the rate of conversion of electromagnetic to joule energy at any point in a medium is proportional to $\langle E^2 \rangle$ at that point.

Emphasis in this paper is on thorium fluoride, zinc sulfide, zinc selenide, and silicon monoxide films on silver, germanium, and zinc selenide substrates. Effects of $\langle E^2 \rangle$ field placement and intensity are illustrated. Significant absorbing foreign species were found in all films tested.

Key words: Internal reflectance spectroscopy; absorption; coatings; zinc sulfide; thorium fluoride; zinc selenide; silicon monoxide.

1. Introduction

At the present state of art, laser damage thresholds usually are not determined by the intrinsic bulk properties of the optical materials involved. Impurities, especially at interfaces, are still a main cause of damage because of their absorption bands at working laser frequencies. It is therefore important to identify these impurities, find their location in the multilayer optical system, and determine the amounts present. We show how this can be achieved using infrared reflection spectroscopy, and illustrate the procedures by a study of several important optical coatings. We also show how the stoichiometry of certain optical coatings can be studied by similar techniques coupled with a transformation to obtain the optical constants of the coating.

In this study it was found that large absorption may occur even in a perfectly intrinsic specular silver substrate. This will happen at certain frequencies where the average electromagnetic electric field squared, $\langle E^2 \rangle$, just inside the silver surface goes through a maximum. While this intrinsic phenomenon may or may not be important as a direct source of laser damage to mirrors, depending on circumstances, its rationalization is always essential to the understanding of infrared spectra of optical coatings on metals. This effect is large even for silver in the infrared. For other metals it will generally be much larger.

2. Experimental Procedures

In this study emphasis is on characterizing small absorptions. Therefore various techniques were used to enhance the sensitivity of the infrared absorption methods used. Multiple reflection spectroscopy, internal and external, was the choice. In addition to many beam encounters in series, angle settings and polarization choice were used to enhance sensitivity, by making $\langle E^2 \rangle$ large in the region of interest. For external reflection, two microscope slides on which were deposited the base metal and coating(s) were placed facing each other to permit multiple reflections in series. For internal reflection, a plate of high index material was used, either zinc selenide or germanium. The films of interest were deposited on both faces of the plate. Attachments such as those available from Harrick Scientific Corporation, Ossining NY, can be used to advantage. We used PE 180 and PE 621 spectrophotometers.

Detailed procedures and methods of analysis of the reflection spectra can be found in reference [1]. The large $\langle E^2 \rangle$ was placed at the air-film or substrate-film interface as desired and alternately it was arranged for $\langle E^2 \rangle$ to be very large in the film center and small at the two interfaces. This latter case is illustrated by figure 1. The beam "sees" a particular region in proportion to $\langle E^2 \rangle$ in that region. Thus we are able to locate the position of the offending species. The profile of $\langle E^2 \rangle$ depends on angle of incidence, and polarization as well as film optical thickness.

3. Results and Discussion

3.1 ThF_4 Films

ThF_4 films deposited by the AFWL, Kirtland AFB, NM, were investigated by internal and external reflection spectroscopy. Some films were deposited on silver. Others were deposited on germanium and zinc selenide internal reflection plates. The substrate was sometimes heated to 150° during deposition. A few of the films were capped with a 2μ layer of ZnS and some with ZnSe while still in vacuo. The films were then transported by mail and were exposed to the atmosphere for at least two days and up to one month in some cases before measurements were made.

Our spectra showed that all of the ThF_4 films including the capped ones contained large amounts of water which was found to be distributed throughout the films, and typically amounted to a liquid water equivalent of from 500 to 1000 Å in a 2.4μ ThF_4 film. The capped films had almost as much moisture as the uncapped films. The reason for this is not known. Surely ThF_4 can be deposited water free. And surely it can be kept anhydrous by capping. It may require special procedures, however, and needs to be investigated further while making use of these sensitive procedures to measure the moisture. It was further attempted to displace the moisture from the films by heating to about 107°C, in vacuo, while at the same time taking spectra. Only a few percent of the moisture was lost. It is suggested that a thermogravimetric analysis be run on hydrated ThF_4 to high temperatures to document the temperature(s) of water loss.

Hydrocarbon contamination was also found. It amounted to only a few monolayers at most, however, and was always at the external ThF_4/air interface. Water and hydrocarbons accounted for all of contaminant spectra seen except for a 100 Å layer of SiO which was deliberately placed in some of the samples under the ThF_4 to test the $\langle E^2 \rangle$profile. In all cases it showed up exactly when it should, and was invisible when the expected $\langle E^2 \rangle$ profile "said" it should be.

Examples of ThF_4 spectra are shown in figures 2-5. Photocopies of the actual spectra are used here because otherwise important detail is lost. Note that "transmittance" on the standard form paper used should be replaced by $(I/I_o)x100$. Figure 2 is dominated by water absorption in the regions of 3μ, 6.1μ, and beyond 10μ. ThF_4 also has a broad intense intrinsic absorption band with maximum about 25μ but beginning around 10μ. In figure 3 there is an additional SiO band at about 9μ. The atmospheric CO_2 bands at about 4.2μ should be ignored. Figure 4 shows interference minima at 770 and 2850 cm^{-1}. These are due to absorption in the silver itself and are large here because of the use of ⊥ polarization and large angle of incidence. As discussed below, the frequency position of these minima can be used to determine optical thickness.

3.2 ZnS and ZnSe Films

In the case of ZnS and ZnSe films small amounts of both water and hydrocarbon were found, amounting to a few monolayers each. They were both found to be concentrated at the substrate/film interface. Evidently they remained in spite of careful cleaning procedures. Again, the 100 Å SiO layer deliberately placed under the coating in some samples, showed up exactly as expected.

Examples of spectra are shown in figures 6 and 7. These multiple internal reflection spectra are extremely sensitive, making a single monolayer easily visible. Water bands in the 3μ region and the 6-7μ region are clearly visible. More than usual detail is seen in the water structure, especially in the case of ZnS, figure 7. Hydrocarbon in the 3.5μ region is clearly visible in both figures. The CO_2 dips near 4.2μ again should be ignored. Absorption beyond 10μ is due to the Ge plate itself and is of no interest here.

3.3 SiO Films

In figure 8 are shown spectra of a 0.5μ SiO layer on silver. Water and intrinsic SiO bands are seen. The first interference minimum for intrinsic absorption in the silver substrate is off scale to the left. The water contamination is much less than in the case of ThF_4, but much more than for the zinc compounds.

The complex dielectric constant, $\hat{\varepsilon}(\lambda)$, or complex refractive index, $\hat{n}(\lambda)$, can be calculated throughout the intrinsic SiO band from the spectra of figure 8. This can be done in several ways. It can be done by inverting $\perp$ and $\parallel$ reflection equations at wavelengths throughout the absorption band, or it can be done by transformation, [4], using either the $\perp$ or the $\parallel$ spectrum. The fact that the absolute position of the "no absorption" background is not at 100% doesn't preclude high accuracy. The trick is to compare the reflectance with what it would be, in the same spectrum, if the absorption band were electromagnetically bleached. Details are discussed in reference [1]. It is interesting to note the enormous difference in spectral shape and intensity for the two polarizations. These differences are rationalized completely when the $\langle E^2 \rangle$ values inside the film as a function of wavelength are considered.

3.4 Intrinsic Absorption in Film Covered Metal

Consider the external reflection spectra of figures 9, 10, 11. The dominant feature is the absorption in the silver itself, even though the silver is behaving nearly as ideal intrinsic silver should. And this is the infrared region where silver is one of the best reflectors in existence, with $\hat{n} \cong 3+i50$ at 1500 cm^{-1}. Clearly, absorption in the substrate metal must be accounted for in rationalizing reflection spectra. The shapes of these interference spectra change with angle of incidence, polarization and film thickness.

The absorption of the 100 Å SiO layer is clearly visible in the unpolarized spectrum of figure 9, and is enhanced in the $\parallel$ polarization spectrum of figure 10. It is completely absent in the $\perp$ polarization spectrum of figure 11. The reason for this absence is that $\langle E^2 \rangle$ at the SiO layer position is typically three orders of magnitude less for $\perp$ polarization than for $\parallel$ polarization at 45°. On the other hand, the $\langle E^2 \rangle$ values just inside the silver are comparable for the two polarizations.

The intrinsic absorption of zinc sulfide itself is seen best in figure 10. The well known absorption caused by the imaginary part of $\hat{\varepsilon}$, where $\hat{\varepsilon} \equiv \mathrm{Re}\hat{\varepsilon} + i\ \mathrm{Im}\hat{\varepsilon}$, is shown at about 270 cm^{-1}. The band at 340 cm^{-1} is less well known, and is due to the energy loss function, $\mathrm{Im}(-1/\hat{\varepsilon})$, and logitudinal excitation, [2]. It is completely absent at normal incidence and for $\perp$ polarization at any angle of incidence. These points are illustrated by figure 11.

The interference phenomena can be rationalized with relative ease if certain points are realized. The phase change for reflection at the dielectric/silver interface is approximately either 180° or 0° for these long wavelengths, depending on polarization. From equation 5a of reference [3] it can readily be shown that extrema in reflectance for

perpendicular polarization occur at

$$h/\lambda = n/4\xi \quad \text{(extrema)}$$

where h/λ is the film thickness/wavelength ratio, n is an integer, and $\xi \equiv (n_f^2 - n_1^2 \sin^2\theta_1)^{1/2}$ where f stands for film 1, for the incident phase and θ_1 is the angle of incidence. Odd n give the minima in reflectance, i.e.,

$$h/\lambda = (2n+1)4\xi \quad \text{(reflectance minima)}$$

and

$$h/\lambda = (2n)/4\xi \quad \text{(reflectance maxima)}$$

The minima are much sharper than the maxima, so they are the obvious choice for experimental determination of film optical thickness. Only one minimum is needed. When needed, corrections can be added to the above equations when the phase changes aren't exactly 0 or 180°.

4. Conclusions and Recommendations

One objective of this study has been to test some innovative procedures to see how effectively and efficiently they work. They have worked very well. Information obtained has been copious and to the point. The time, effort, and cost has been minimal compared to other projects for getting similar data, with which we have had experience. We believe that these procedures can with care, be used routinely in the laboratory.

All of the films studied were found to contain important absorbing species as contaminants. These species were identified and located. It was also shown that the amount present could be determined from the spectra.

Thorium fluoride films all contained large amounts of water in spite of modest efforts to avoid it. From our results it is apparent that avoidance of water in thorium fluoride films will require elaborate procedures. Undoubtedly, it can be done with proper procedures during preparation and with enough impervious overcoating to prevent contamination subsequently. It may not be worth the effort, however, and it is strongly suspected that the films would always be easy targets for moisture degradation. If the fluoride films <u>are</u> used, this work shows how to monitor the moisture content with ease and accuracy.

The zinc sulfide and selenide films were contaminated with water and hydrocarbon, but were otherwise clean. These contaminants were found to be present at the solid/solid interface, indicating a preparation problem. Surely they can be eliminated with feedback from spectroscopic testing. The amount of contamination was small, but large enough to be important if located in a large $\langle E^2 \rangle$ position.

Silicon monoxide contained moisture - much less than thorium fluoride, and much more than zinc sulfide or selenide. It was shown that such films can be characterized by taking polarized spectra. The procedures used are directly applicable to the characterization of silicon monoxide and silicon dioxide films. In fact, silicon oxide films of various stoichiometry could be studied conveniently by this method and their optical constants determined easily throughout the fundamental absorption region.

It is suggested that the procedures illustrated by the present study be used routinely in optical coating evaluation. It is hoped that this study has served to illustrate how this can be done. More extensive studies should include high temperature studies. Any absorption will surely change at high temperatures where laser damage actually occurs. Absorption bands tend to broaden. Even the intrinsic bands of the film may broaden in some cases enough to cause laser damage due to intrinsic absorption. This should be investigated systematically. It is recommended that broad band spectroscopy be used, like the spectra shown here from 2.5 to 50μ. It is important to have qualitative as well as quantitative information.

5. Acknowledgements

The support of this work by the Air Force Weapons Lab, Kirtland AFB, New Mexico, under contract F29601-79-R-0081 is gratefully acknowledged. Part of the work was done

at the Naval Weapons Center, China Lake, CA, with help from NWC personnel. Special thanks go to Drs. Hal and Jean Bennett for their valuable discussions and assistance.

6. References

[1] Hansen, W.N., Reflection Spectroscopy of Optical Coatings, J. Opt. Soc. Am. 69, 264 (1979).

[2] Kittel, C., Introduction to Solid State Physics, 5th ed., John Wiley and Sons, New York, 1976, pp. 328f.

[3] Hansen, W.N., "Electric Fields Produced by the Propagation of Plane Coherent Electromagnetic Radiation in a Stratified Medium", J. Opt. Soc. Am., 58 380 (1968).

[4] Hansen, W.N., Abdou, W.A., "Analysis of Solid-Liquid Interphase Spectra via Causal Transformation," J. Phys. (Paris) 38 C5-207 (1977).

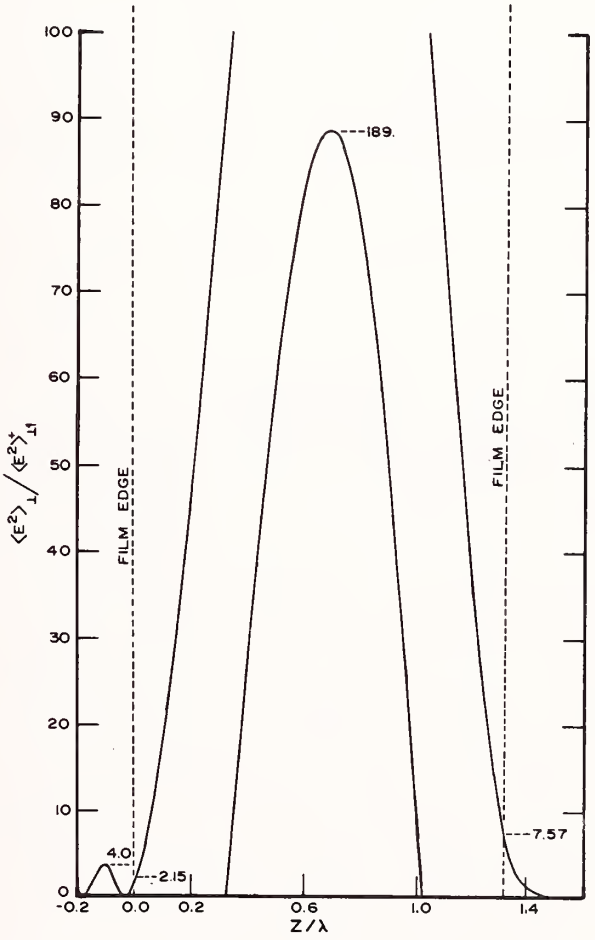

Figure 1. $\langle E^2 \rangle_\perp / \langle E^2 \rangle_{\perp i}^+$ for internal reflection in a germanium-film-air system. Phase one is Ge with $n_1 = 4.0$; phase two is a film, $h/\lambda = 1.3$, $n_2 = 2.0$; for phase three, $n_3 = 1.0$; $\theta_1 = 29.5^0$. Note that the fields are large at the film center.

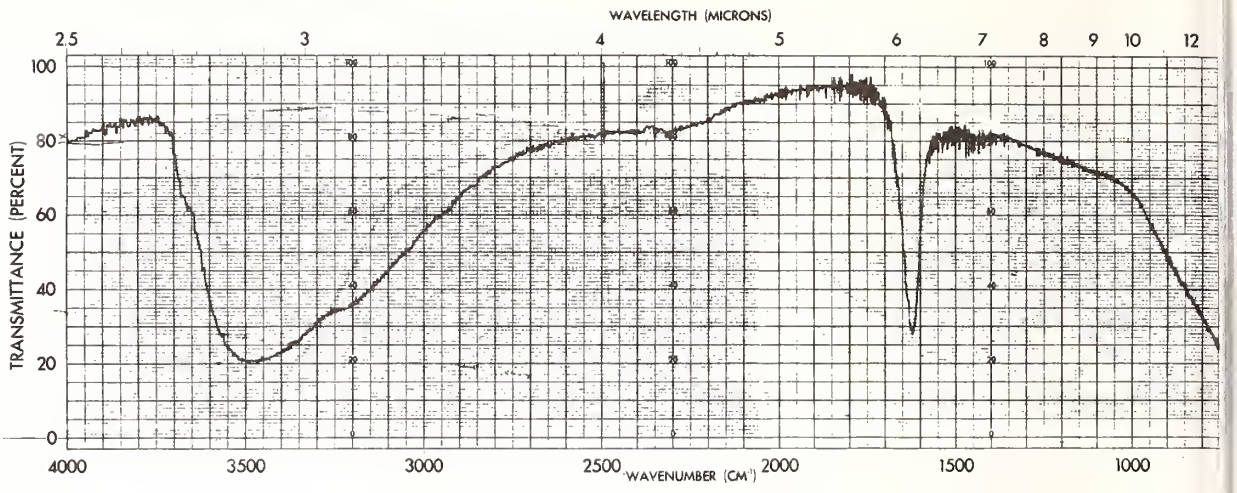

Figure 2. External reflection spectrum of 2.23μ ThF_4 film on silver, sample 4-A, 12.5 reflections at $\theta_1 = 45^o$; PE-621 spectrophotometer.

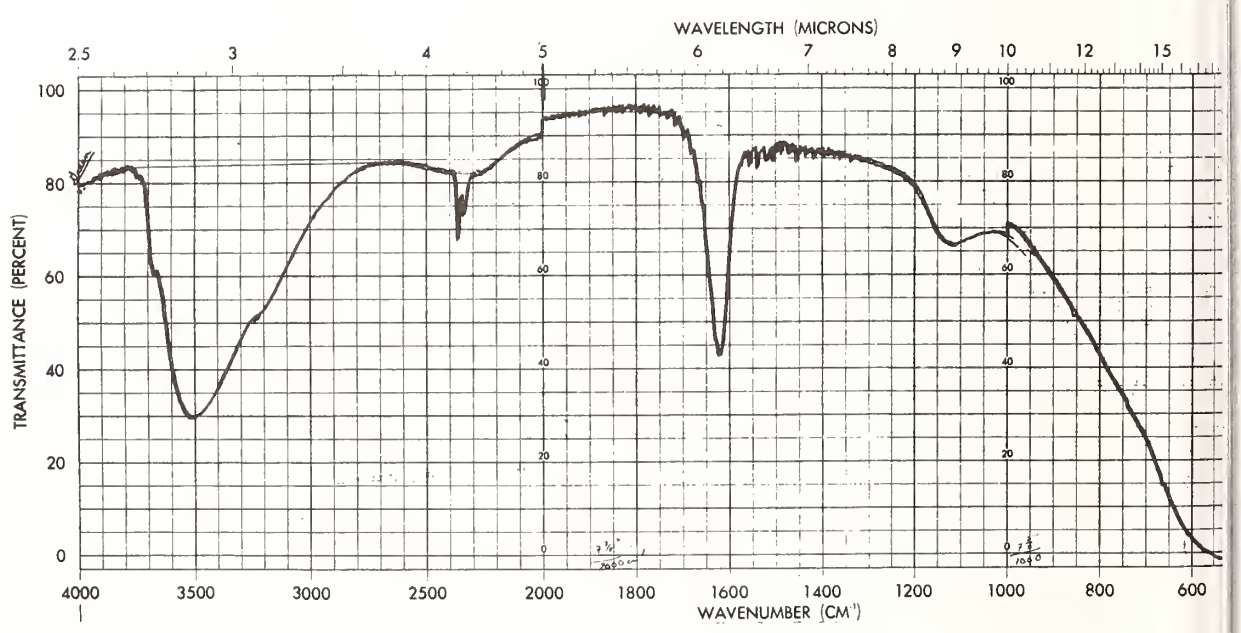

Figure 3. External reflection spectrum of 2.23μ ThF_4 films on silver plus 100Å SiO at silver/ThF_4 interface; sample 4-B, 12.5 reflections at 45^o; PE-180 spectrophotometer.

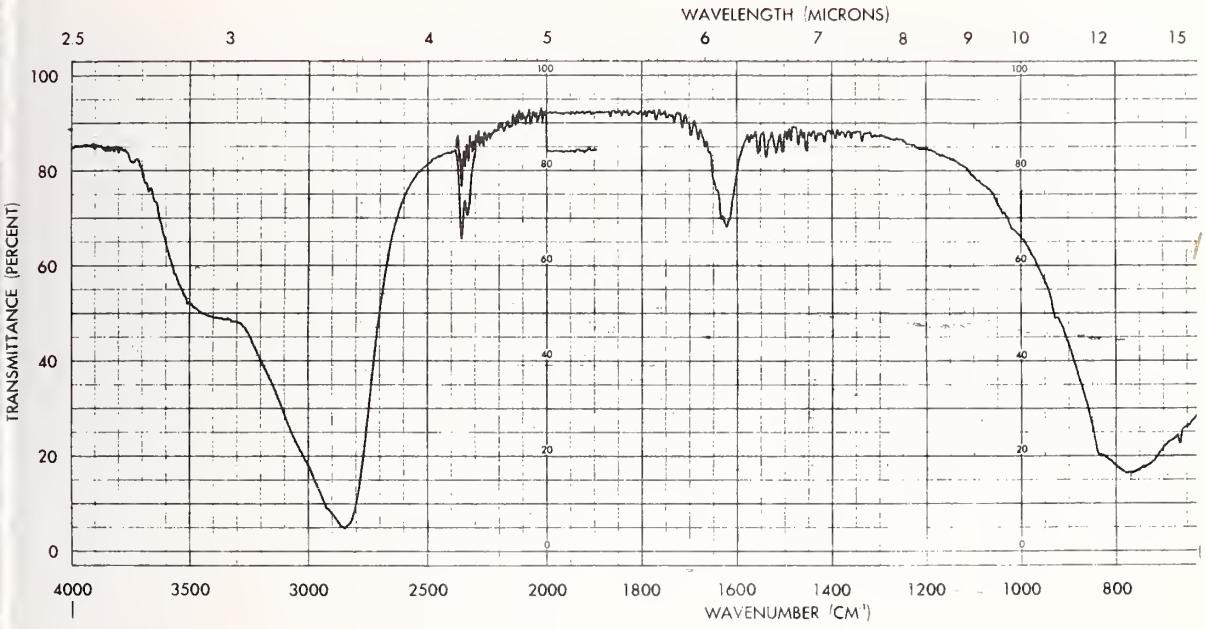

Figure 4. External reflection spectrum of 0.5μ ThF_4 on silver with 2μ ZnSe cap; 10 reflections at $\theta_1 = 67^o$, $\perp$ polarization, PE-180 spectrophotometer.

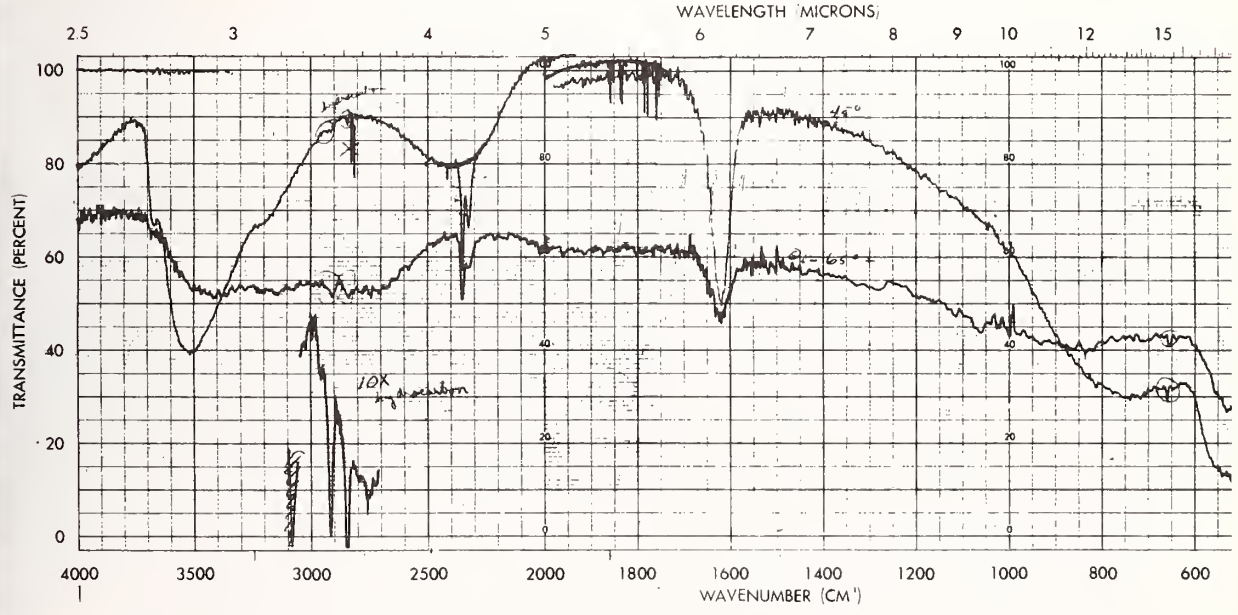

Figure 5. ThF_4 on silver, 0.2μAg/0.01μSiO/2.23μThF_4, external reflection, $\perp$ polarization using PE-180; top curve, $\theta_1 = 45^o$; bottom curve $\theta_1 = 65^o$; bottom short curve is 10X scale expansion showing hydrocarbon bands in 65^o spectrum.

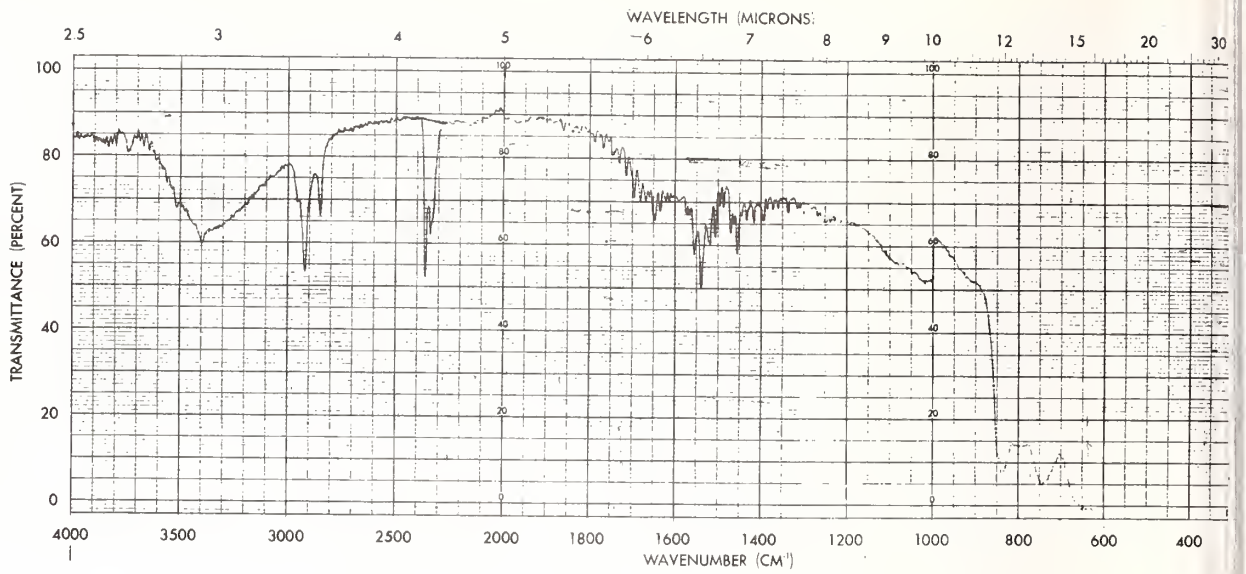

Figure 6. Internal reflection spectrum of ZnSe on Ge plate; 40 reflections at $\theta_1 = 30^{\circ}$; || polarization; PE-180.

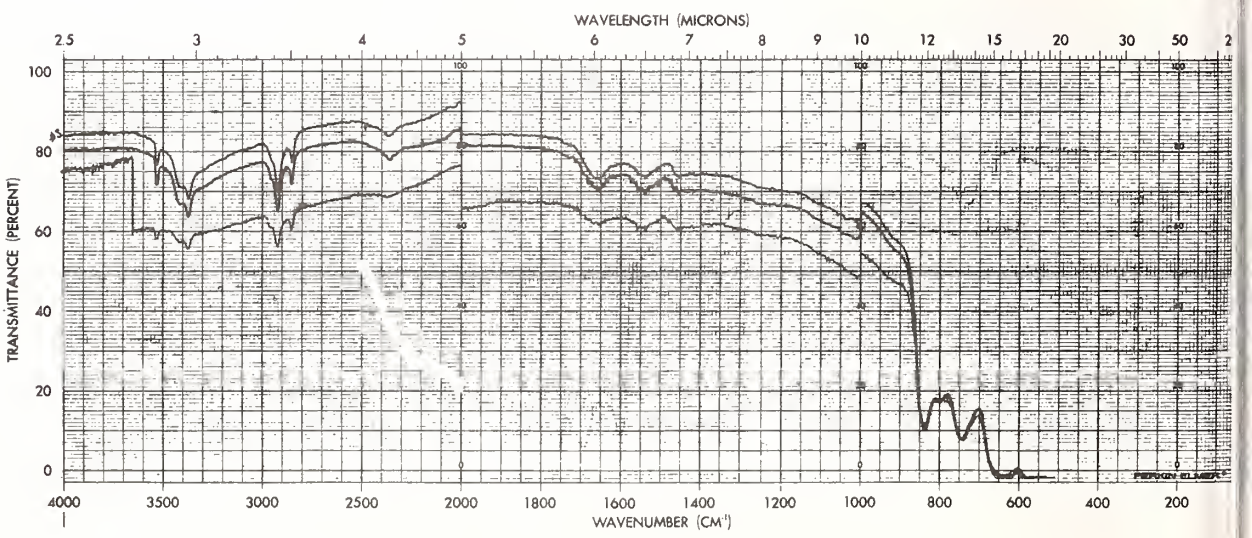

Figure 7. Internal reflection spectra of 0.5μ [illegible] film on Ge plate; top spectrum, $\theta_1 = 45^{\circ}$; middle spectrum, $\theta_1 = 30^{\circ}$, bottom spectrum $\theta_1 = 82^{\circ}$; PE-180.

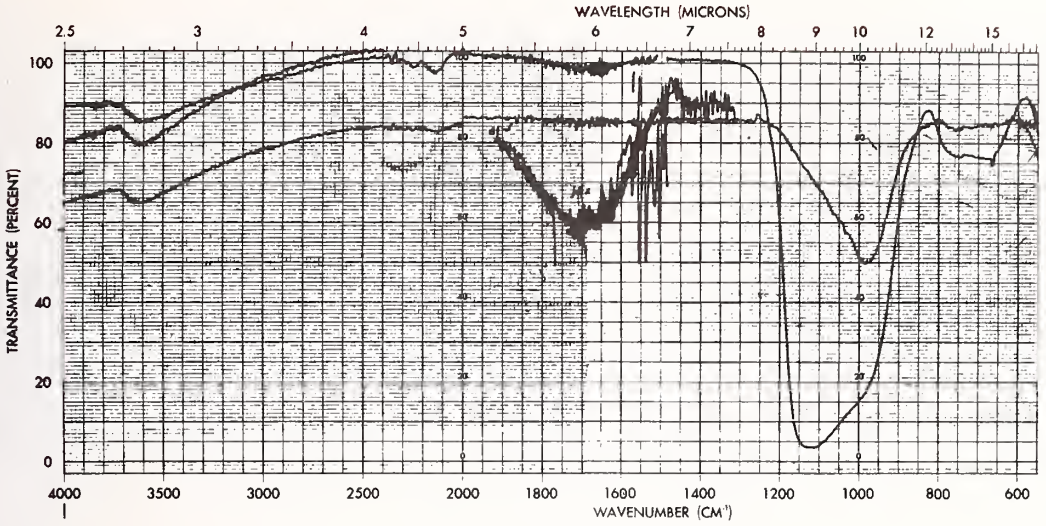

Figure 8. External reflection spectra of 0.5μ SiO on silver; 13 reflections at $\theta_1 = 45^{\circ}$; top is || polarization, bottom is $\perp$ polarization; PE-180. 10X expansion is for top, || polarization.

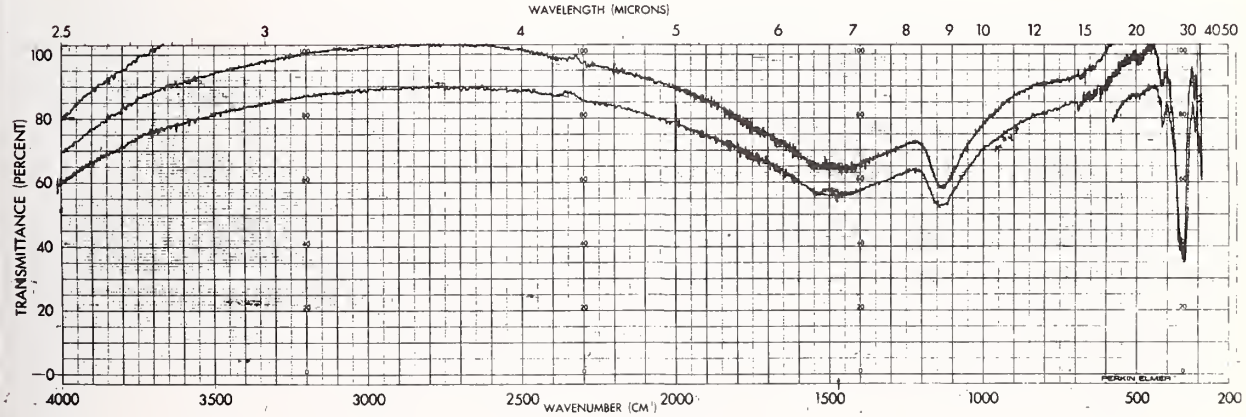

Figure 9. External reflection spectrum of ZnS on silver, sample 2-B; 12.5 reflections at 45°; PE-621.

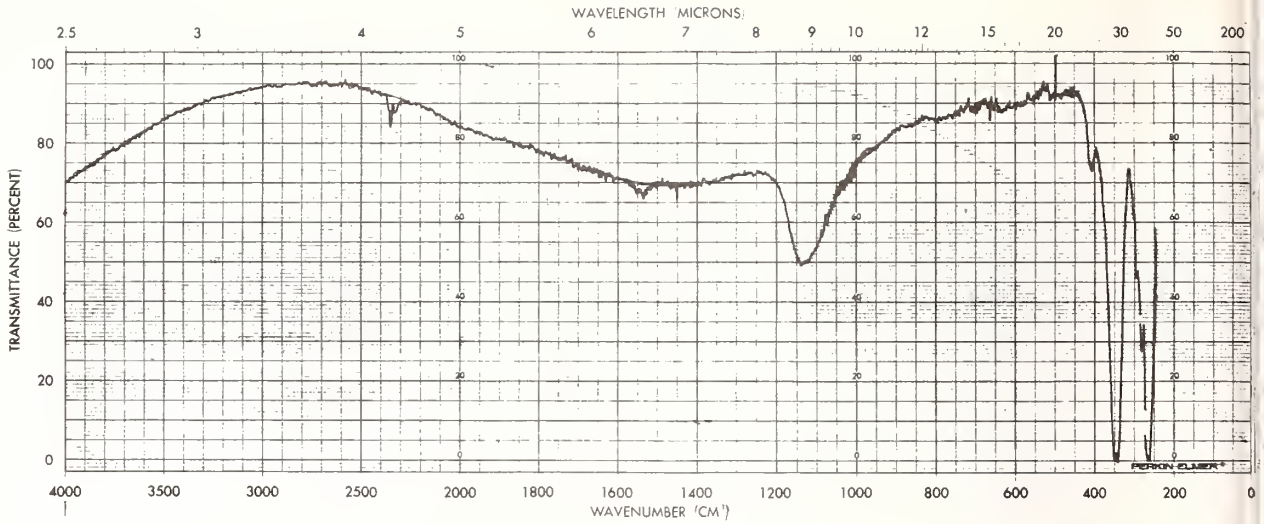

Figure 10. As in figure 9 but using || polarization, PE-180.

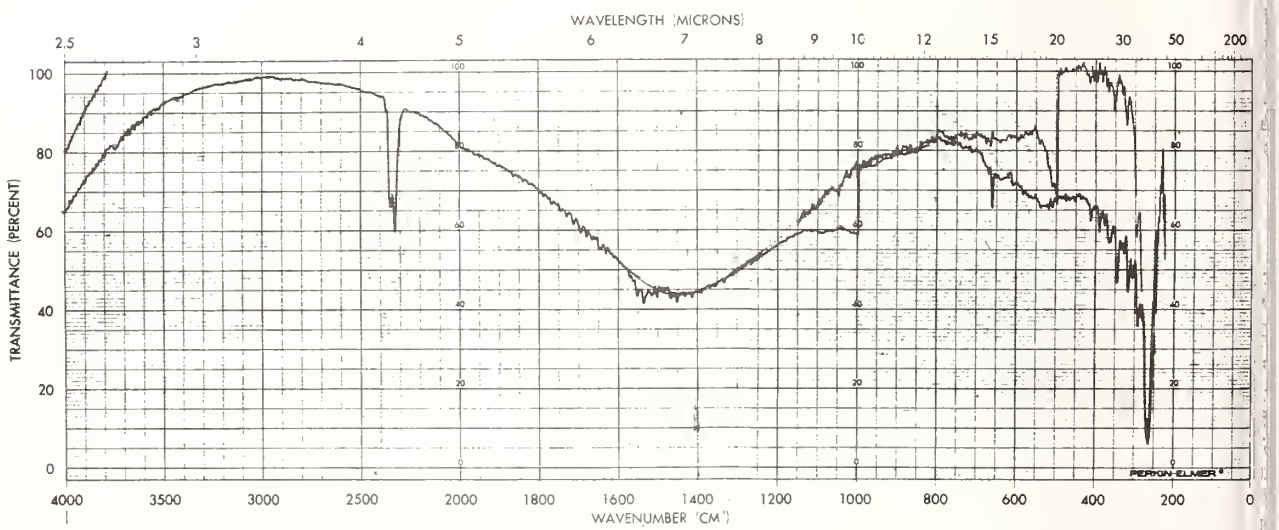

Figure 11. As in figure 9 but using ⊥ polarization, PE-180.

SURFACE MICROANALYSIS TECHNIQUES FOR CHARACTERIZATION OF THIN FILMS

T. W. Humpherys, R. L. Lusk, and K. C. Jungling
Air Force Weapons Laboratory
Kirtland AFB, NM 87117

With the advent of lower wavelength systems, increased sophistication of functional requirements, and higher incident radiation levels, more stringent demands have been placed on coating depositions with complimentary detailed chemical and physical characterizations being required. Scanning Auger Microscopy, X-ray Photoelectron Spectroscopy, and Secondary Ion Mass Spectroscopy techniques have been applied to thin film coatings to detect and identify compositional and structural irregularities. Impurity sites in ThF_4 and ZnS films, principle causes of poor coating performance, have been isolated and analyzed. Point maps, line scans, and depth profiles are shown to provide remarkable clarity with submicron resolution. Abnormal oxygen content in ThF_4 films indicates the presence of water and may eliminate its use as a coating material for HF systems. Although these surface analysis methods are destructive by nature, the validity of their use in analyzing thin film coatings is demonstrated and establishes a precedent for coating development programs.

Key words: Auger analysis; dielectric coatings, optical coatings; surface analysis; thin film characterization; thin film impurities.

1. Introduction

Auger Electron Spectroscopy (AES), Secondary Ion Mass Spectroscopy (SIMS), and X-ray Photoelectron Spectroscopy (XPS, often identified as ESCA) surface analysis techniques have been utilized to investigate structure, defects, and contamination in multiple layer thin film coatings. Schematic representations of these various techniques are shown in figure 1 with some typical performance parameters for each method [1]. The destructive nature of these techniques and the general lack of spatial resolution are considered problem areas, especially when analyzing films of submicron thickness. The results of a study to determine the validity of these types of analyses are presented with particular emphasis on analysis beam probe induced damage.

2. Experimental Approach

The experimental approach was to analyze the various layers of a multistack thin film coating as each of the layers was sputtered through using argon ions. Special thin films were fabricated to exercise various capabilities of the analysis techniques. The results presented are from ZnS and ThF_4 designs of which a typical example is illustrated in figure 2. Each layer was approximately 2000 Å thick in order to avoid excessive sputter times when profiling. The number of layers represents a typical functional coating design for an enhanced reflector including the base metal reflector and a chromium binder. Silicon wafers were utilized as substrates in order to provide a conducting medium which could also be cleaved resulting in a clean, uniform break in the coating for edge profiles. The samples were Ar^+ sputtered with SIMS data recorded during the sputtering process. AES and XPS data would be taken between sputtering sequences to produce profiles of the coatings. Analysis was conducted, when feasible, in the same vacuum chamber with a base pressure in the low 10^{-10} Torr range. A PHI Model 590 Auger system was used for most of the analysis presented in this paper with some sputtering accomplished in the PHI Model 550 ESCA system.

3. Results and Discussion

A specimen of the design specified in figure 2 was analyzed at various depths while profiling through the first layer of ZnS and into the ThF_4 layer. The secondary electron microscope (SEM) photographs in figure 3 display the various stages of the profile. Several prominent dust particles are evident on the otherwise featureless surface which provide a reference for the remaining photographs. After sputtering into the ZnS layer, several point defects or impurity sites appear. Further sputtering down to approximately 1500 Å exposes additional impurity sites, all of which are enclosed by a halo region. Each of these disk shapped areas house one of the impurity sites. This point defect and halo region remain intact even into the ThF_4 layer. Insulating properties of ThF_4 reduce, to some extent, the resolution of the SEM photographs. Sputtering of this specimen was terminated at this time in order to perform more detailed analysis. The final photograph in this set is a Nomarski micrograph of a typical area in the sputtered crater which illustrates that both the defects and corresponding halos are also visually observable. The micrograph indicates possible height differences between halo regions and the surrounding area. Height variations could be a consequence of different or biased sputtering rates. The geometrical patterns of the halos suggest that this anomaly is attributeable to the presence of the impurity sites.

A close-up SEM photograph of a single defect region, figure 4, depicts a typical area that was analyzed in greater detail incorporating various microanalysis techniques. The contrasting horizontal line extending through the halo region was electron beam induced during AES line scans. Although the halo itself may be an artifact of argon ion bombardment during the sputtering process, a similar consequence is apparent in the Auger analyzed areas which have been subjected to the electron beam. In addition, the surface is also disturbed, to a much lesser degree, however, during a typical SEM photograph acquisition sequence in which the incident electrons are substantially less energetic than the Auger probe electrons.

A three point (spatial) Auger analysis comprises figures 5 through 7. The survey in figure 5 was obtained when constraining the probe beam to an area outside of the halo region of figure 4 but remaining within the sputtered crater. Dominant amounts of Th and F are as expected since sputtering was terminated in the ThF_4 layer. In addition to these elements, however, there is a substantial amount of O present. The large amount of oxygen present, at least in comparison with other films such as ZnS, ZnSe, Ag, Cr, CeF, and Al_2O_3, indicates substantial water content in the ThF_4 film. This concurs with corresponding SIMS analysis in which both H and O are observable and also supports the conclusions of an independent study of several ThF_4 films in which spectral data confirms the presence of water throughout each of the ThF_4 layers [3]. The AES survey on the halo area, presented in figure 6, indicates this region to be F deficient and O enriched. Th signatures are relatively unchanged. The flux of incident argon ions during the sputtering process collide and interact with the ThF_4 compounds driving off some of the loosely bound flourine atoms. This dissociation and the abundance of oxygen readily allows $ThOF_2$ or ThO_2 type of compounds to form. In all ThF_4 layers analyzed, AES and especially XPS data taken on a newly exposed surface from sputtering indicate that the oxygen concentration increases as a function of time. This implies adsorption of water from the chamber onto the ThF_4 where it reacts to form thorium oxide compounds.

The submicron Auger probe beam was then positioned on the point defect with the resulting AES survey shown in figure 7. Again fluorine is deficient and oxygen dominates the energy spectrum. Additional differences occur in the 150 and 1000 EV energy ranges when compared to the survey on the halo. Both Zn and Na signatures are located near 1000 EV [2]. Variations in the low energy range suggest the presence of significant amounts of sulfur. Since the film is made of ZnS, it is proposed that the point defect is composed of or is a trap for ZnS.

Auger images, or spatial elemental maps, also provide useful information and verify many of the conclusions stated above. An F elemental map, figure 8, illustrates the lack of F in the halo region. The mapping technique displays four levels of elemental concentrations ranging from black, representing nondetectable amounts, to bright white, implying areas of high concentration. A surface AES survey was conducted in the large rectangular region below the halo. The pronounced absence of fluorine in this area dramatically exhibits the effect of the incident electron beam during Auger analysis. In comparison these regions are oxygen rich as shown in figure 9. The much more massive thorium atoms are much less mobile than the fluorine atoms and are not effected by the electron beam, nor is there any detectable difference in the halo region as seen in the Th elemental map in figure 10.

An additional technique involves a spatial line scan searching for predetermined elements. A scan was made across the halo region, through the defect point while monitoring the energy windows characteristic of the signatures of O and F. As expected, the O content increases, figure 11, as the beam transverses the halo while the F concentration decreases. The amounts detected radically change as the defect center is reached. This sequence is reversed as the probe beam moves beyond the halo. This is the process which produced the horizontal line in figure 4. Although the halo is most likely caused by the sputtering and analysis techniques, it is apparent that detection of point defects is enhanced through these processes.

Line scans across the edge of a film exposed after the silicon chip is cleaved are also possible provided the thickness of the thin film layers is greater than the resolving power of the analysis beam. This does occur for most films designed for operation in the infrared. To obtain an edge scan on the coating designed for and utilized in this study, the exposed film edge created upon sputtering during a SIMS profile was line scanned from the bottom of the crater, which was in the silicon substrate, outwards across the film boundaries to the outer surface consisting of the top ZnS layer. Figures 12 and 13 depict, respectively, a schematic representation of a sputtered crater and the various elemental line scans of the film. Contaminants can be followed in this manner also. Definite boundaries are evident indicating the compositional structure of the thin film stack. With a high resolution probe, point areas within layers can then be analyzed in much greater detail yielding stoichiometry of each of the layers in the film stack.

SIMS analysis was conducted on separate thin film stacks, one made with RAP processed ThF_4 and the other with Balzers ThF_4. Both were E-beam deposited. Each film was sputtered through the first layer of ZnS and well into the first ThF_4 layer where SIMS data was recorded. The results are presented in figure 14. The RAP film contains more of the impurities Na, Al, Li, and K. Similar comparisons were made on the bulk materials with the same conclusions. Independent analysis [4] on similarly coated films support, in general, the conclusions presented here. The exact history and handling procedures of these materials is not known and may have contributed to the observed contaminants.

Impurity sites observed in this study are not unique to a particular vender, supplier of basic coating materials, deposition techniques, or deposition facilities. Under a space radiation program conducted by NWC [5], several coatings of ZnS and ThF_4 were found to experience similar point defects with corresponding halos. Other films in a typical storage environment were found to deteriorate as a function of time. The latter degradation is probably from a different mechanism since the defect centers appear to be pores and the halo is not disk shaped but follows more of a structured pattern similar to a snowflake. Water vapor enters the film through the pores and interacts with the underlying ThF_4 layers. Nomarski photographs of some of these specimens comprise figure 15. The common denominator at this point appears to be ThF_4. The orgin of the impurity sites, however, could result from a number of other sources, such as improper substrate cleaning and preparation, inadequate deposition processes,

or contaminated coating materials.

3. Conclusions

Not all films analyzed exhibited numerous impurity sites with corresponding halos. None of the films studied, however, were totally free from point defects or impurity sites. It was obvious that any defect or impurity became readily apparent during the analysis process. Although the exact physical and chemical interactions are not yet well understood, the methods discussed enhance the detection of minute irregularities which degrade optical and mechanical properties of thin film coatings. Surface analysis techniques are fast becoming an integral part of the development and analysis of thin film coatings. Refined procedures and techniques for this type of usage should provide tremendous insight into understanding the poor performance of many thin film coatings.

4. Acknowledgments

The authors are indebted to Dr. T. Wiggins and Dr. A. Taylor for their assistance in gathering and interpreting much of the data. We also extend our gratitude to R. Espisito for many helpful discussions and for providing many of the specimens.

5. References

[1] Swingle, R. S., and W. M. Riggs, ESCA, in Critical Reviews in Analytical Chem., 5, 267 (1975).

[2] Davis, L. E., et. al., Hanbook of Auger Electron Spectroscopy, 2nd Ed., Physical Electronics Industries, Inc., 1977.

[3] Hansen, W. N., et. al., Characterization of Small Absorptions in Optical Coatings, this conference.

[4] Nelson, A. J., private communications.

[5] Donovan, T. M., private communications.

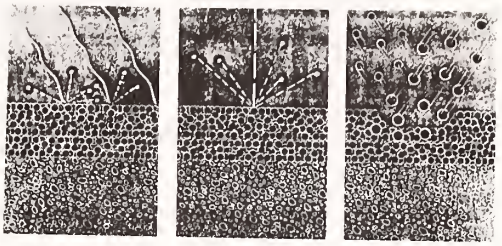

TYPE ANALYSIS	ESCA	AUGER	SIMS
SPUTTERED AREA	7X8 MM	1X1 MM	1X2 MM
ANALYSIS AREA	2X2 MM	0.2 μM	200 μM
INCIDENT BEAM	X-RAYS	ELECTRONS	IONS
ELEMENTS ANALYZED	Li UP	Li UP	1-300 AMU

SCHEMATIC OF THE VARIOUS SURFACE ANALYSIS TECHNIQUES EMPLOYED

Figure 1. Schematic representation of ESCA, Auger, and SIMS microanalysis techniques with typical characteristic parameters.

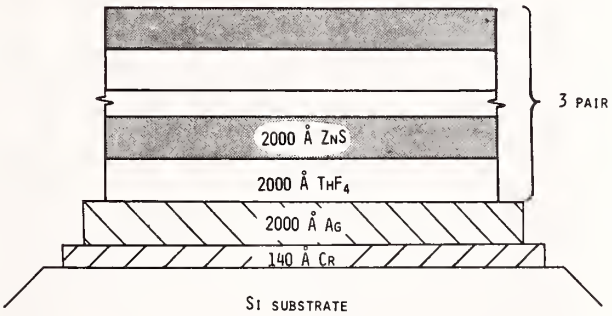

THIN FILM DESIGN FOR SURFACE ANALYSIS

Figure 2. Typical thin film design specifically fabricated for this study.

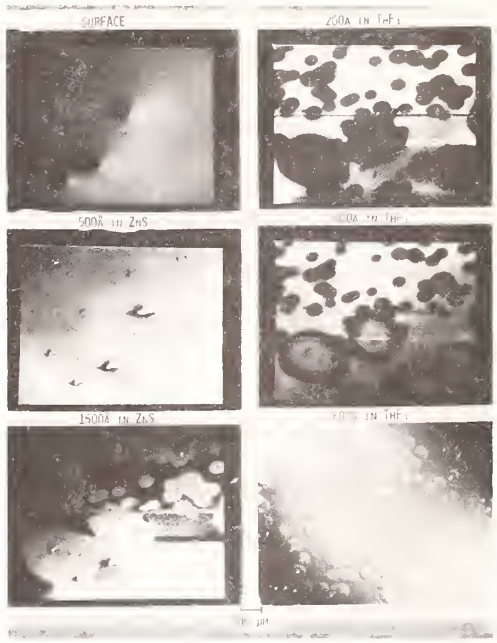

Figure 3. SEM and Nomarski photographs at various depths during profiling through the outer ZnS layer and into the first ThF_4 layer of a three pair stack.

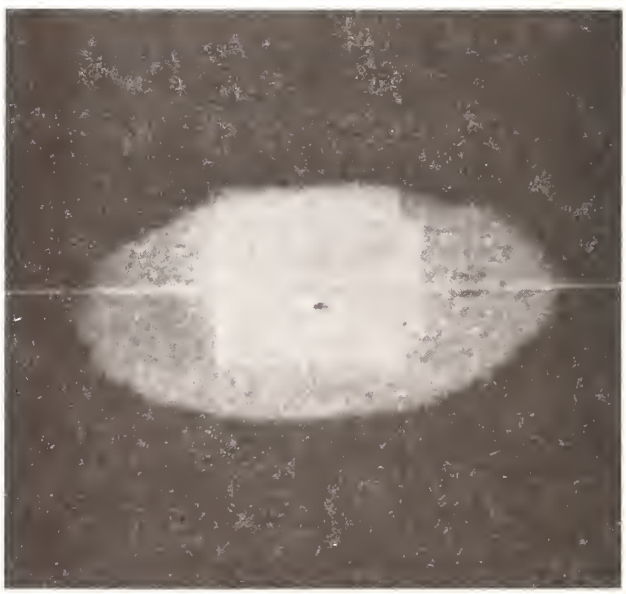

Figure 4. SEM photograph of a typical point defect and halo region.

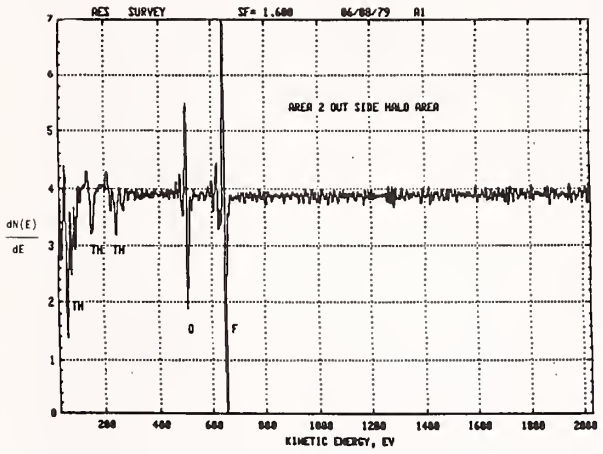

Figure 5. Auger survey outside of the halo region within the sputtered crater.

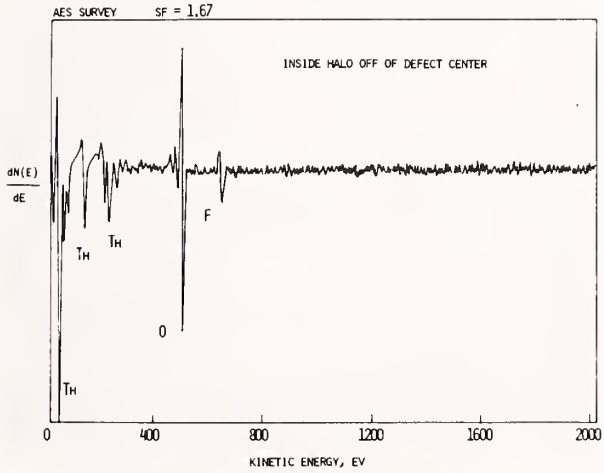

Figure 6. Auger survey inside the halo.

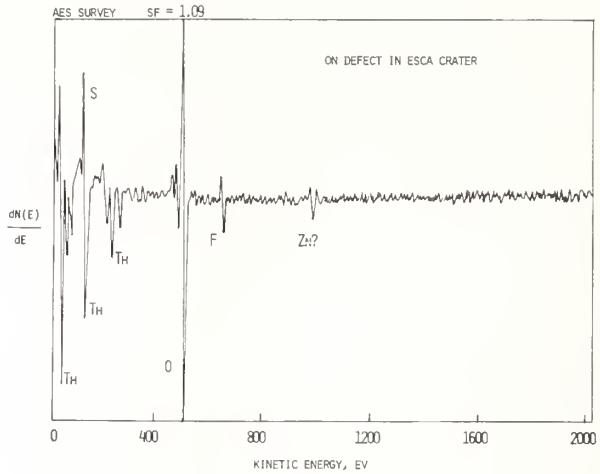

Figure 7. Auger survey on the point defect.

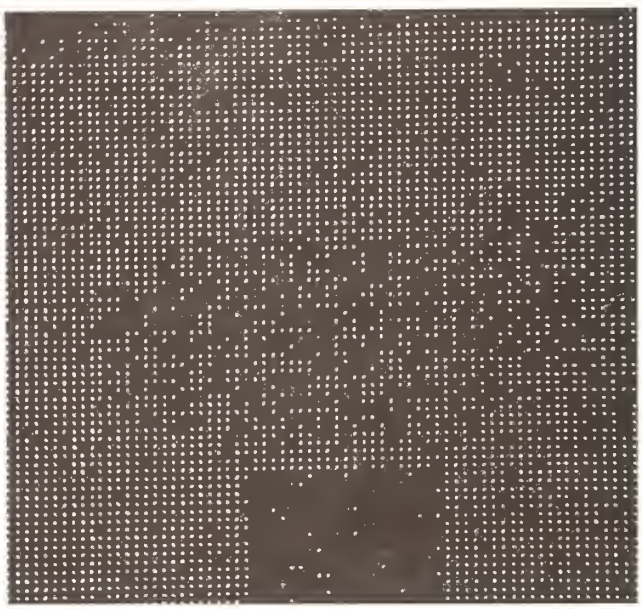

Figure 8. Flourine Auger map of halo region.

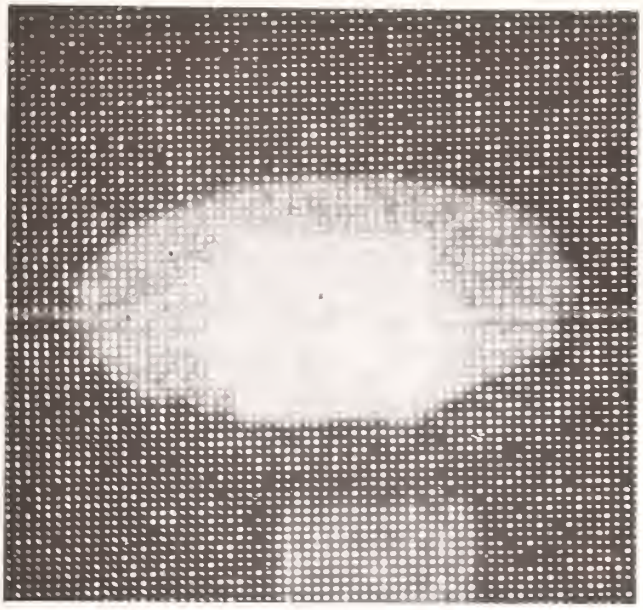

Figure 9. Oxygen Auger map of halo region.

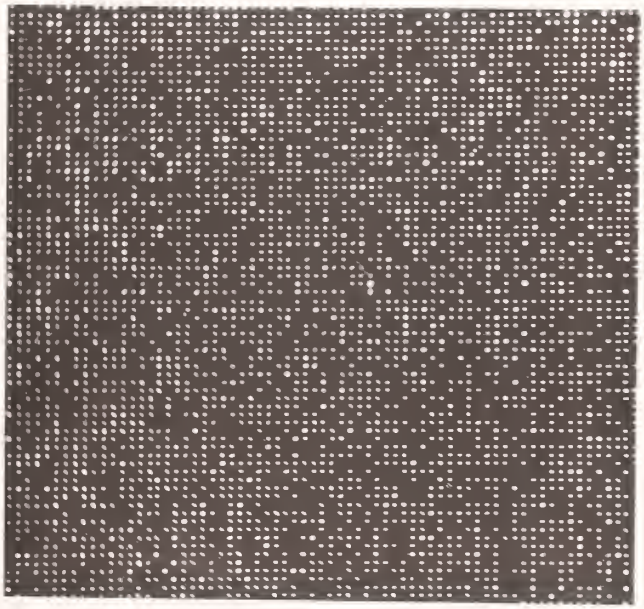

Figure 10. Thorium Auger map of halo region.

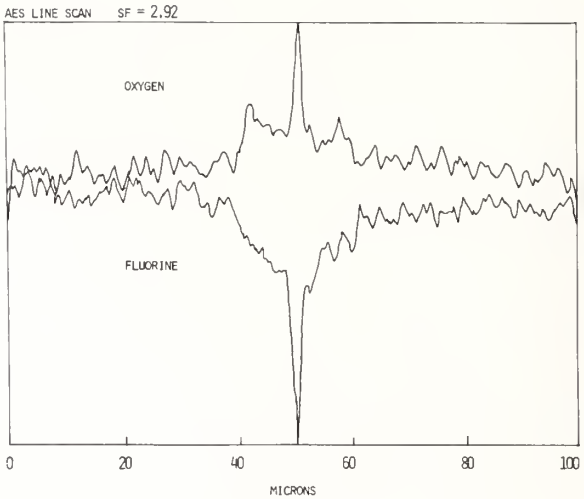

Figure 11. Oxygen and flourine line scans through halo region and across the point defect.

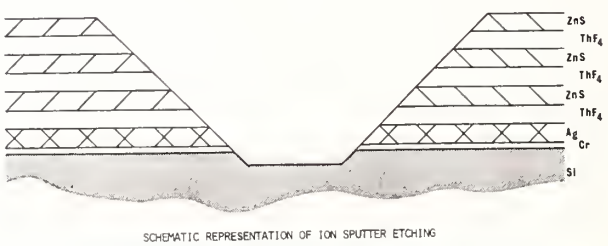

Figure 12. Schematic of a typical sputtered crater in a three pair ZnS/ThF_4 coating.

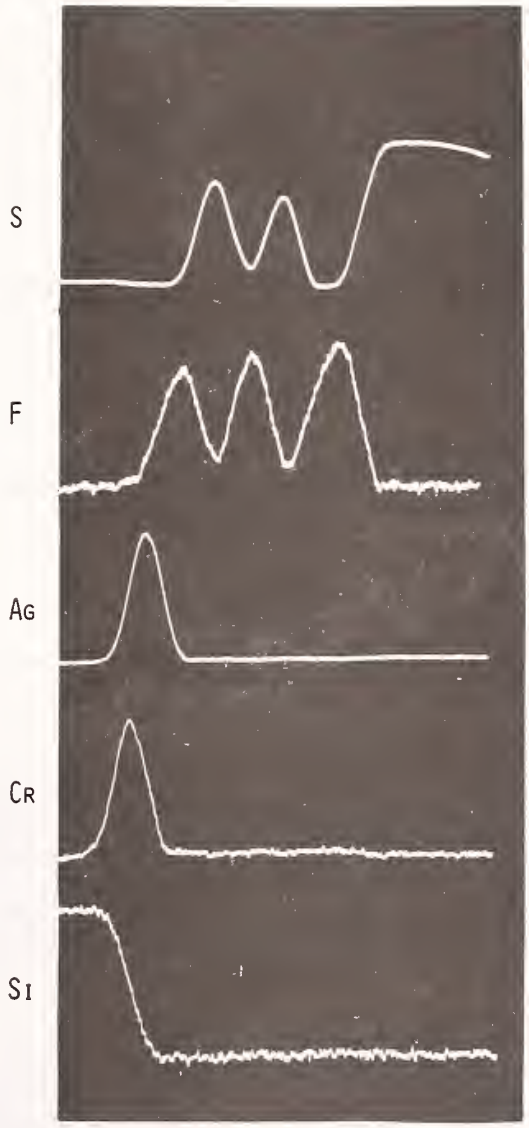

Figure 13. Elemental Auger line scans across the edge of SIMS profile crater depicting the various coating multilayer constituents.

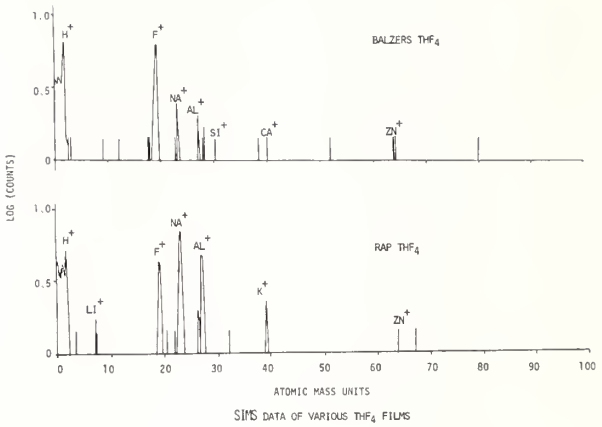

Figure 14. Comparison of Balzers and RAP ThF_4 films by SIMS analysis.

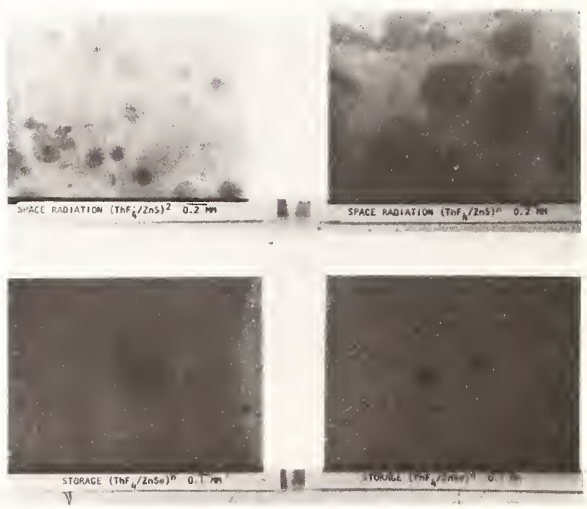

Figure 15. Nomarski micrographs of four coatings, two after space radiation (top) and two after storage (bottom).

PYROELECTRIC MEASUREMENT OF ABSORPTION IN OXIDE LAYERS AND CORRELATION TO DAMAGE THRESHOLD

H. Küster and J. Ebert
Institut für Angewandte Physik, Universität Hannover
Welfengarten 1, 3000 Hannover, Germany

The absorption of several oxide layers used in HP laser optics was measured by a fast pyroelectric detector in the range from 600 to 2000 °C. The layers of Al_2O_3, BeO, MgO, HfO_2, ZrO_2, Nd_2O_3, CeO_2, TiO_2 and SiO_2- thickness about 0.5/um - were electron gun evaporated on Suprasil I substrates.

Damage thresholds were obtained with 800 ns - pulses from an unstable resonator type Nd^{3+}-glass laser with a Gaussian farfield intensity profile. The occurence of damage is determined by electronic registration of laser induced scattering.

The results were analyzed to determine relations with layer absorption, absorption edge and thermal conductivity.

Key words: absorption edge; damage temperature; damage threshold; microsecond pulses; temperature depending absorption; unstable resonator.

1. Introduction

In general absorption is determined at ambient temperatures in a calorimeter using a cw laser. The temperature rise of the sample occurring in this kind of measurement is within the range of some degrees. In damage threshold experiments much higher temperatures may occur, some people reported even a melting of oxide materials, which means temperatures well above 1800 K. We have conducted our investigations to clarify the behaviour of temperature and absorption in damage experiments.

Assuming an uniform rate of heat deposition in the film by the laser beam, cooling only by the substrate, no radial heat loss and thermal constants for film and substrate approximately equal, then the equation for temperature rise of a thin absorbing layer on a thick substrate is

$$\Delta T = \frac{\alpha P d \sqrt{t}}{\sqrt{\pi c \rho k}} \qquad (1)$$

ΔT	temperature rise [K]	d	layer thickness [cm]
α	absorption coefficient [cm^{-1}]	c	specific heat [Ws/gK]
P	power density [W/cm^2]	ρ	mass density [g/cm^3]
t	time of irradiation [s]	k	thermal conductivity [W/cmK]

In figure 1 the solid line indicates the calculated square-root-dependence of temperature rise for a constant absorption of 100 cm^{-1}. That curve does not fit either the measured time dependence of the temperature nor the calorimetrically measured absorption coefficients, which are about 10 cm^{-1} for ZrO_2- layers at 1.06 µm. To fit both we have to regard the temperature dependence of the absorption coefficient. In semiconductors and insulators the electric conductivity increases exponentially with temperature. The conductivity again is directly proportional to the optical absorption [1] , so that the electric conductivity as well as the optical absorption increase with temperature as

$$\alpha(T) = \alpha(T_A) \cdot e^{-\frac{B}{T-T_A}} \qquad (2)$$

T_A ambient temperature [K]
B material constant [K]

The absorption coefficient versus temperature of a ZrO_2 sample is shown in figure 2. There is a fairly good agreement between the measured and calculated points. The exponential dependence of the absorption on the temperature seems to be a correct assumption. Now it is possible to explain a sudden layer destruction because each increase of temperature consequently results in an increase of absorption, which in turn results in an explosive heating with plasma formation and cracking, melting and vaporizing of the material.

2. Experimental Procedure

2.1. Lasersystem

Damage thresholds are measured at 1.06 µm using an acousto-optically Q-switched Nd-glass laser (fig. 3). The unstable resonator produces high output energy with a far field intensity which is fairly Gaussian without any intracavity aperture.

Table 1. Laser system data

Laser	Nd^{3+}-glass, λ = 1.06 µm
Output	8 J max.
Pulseform	max. 15 pulses 800 ns FWHM, nearly Gaussian temporal profile
Interpulse duration	regular 50 µs intervalls by acusto-optical Q-switch
Laser rod	Schott LG 630, diam. 12mm, length 220mm, cutted in Brewster angle
" head	gold plated double ellipse
Resonator	unstable, both mirrors high reflecting, output mirror coated on elliptic area 6/8 mm diameter

The laser beam is directed through a system of attenuators (fig. 4) and further onto a beamsplitter for energy detection. The detector produces a signal related to the energy incident on the sample and is adjusted by a calibrated joulemeter. The time resolved energy signal is stored in a transient recorder. The laser beam is further guided through a dichroic beamsplitter and finally through the focussing lens onto the sample. The spot diameter at the points of $1/e^2$ intensity is 0.5 mm. For damage detection a He-Ne laser beam is transmitted through the irradiated site. The resolution in transmission is better than 0.1 % and the transmitted signal is stored too.

2.2. Temperature measurement

The temperature radiation of the layer is collected by the focussing lens (fig. 5), the spectral range around 850 nm is reflected by the dichroic splitter. The outer part of the radiation cone is collected and directed through a filter system and an aperture of 0.5 mm diameter on a silicon diode. It is necessary to use the spectral range of 850 nm for detection because this is the range of maximum sensitivity of Si-diodes. Special filters are used to suppress laser radiation as well as shorter wavelength. In addition the inner part of the radiation cone is shielded to stop the laser radiation reflected and scattered under small angles.

The signal is converted by an analogous computer into a voltage corresponding to a temperature in centigrades. The temperature scale has been adjusted by a calibrated tungsten tape lamp assuming an emissive power of the layers $\varepsilon = 0.15$. For that fixed ε the reading error is within $\pm$ 1% over the entire range. But the different materials have slightly different emissive powers, which have been measured in the temperature range up to 1100° C using an electric oven. The change of ε between 0.1 and 0.3 in turn induces a relative temperature change at the lower temperature limit of -9% and +19% respectively. If ε is known, the accuracy of the pyrometrically determined temperature is better than $\pm$ 5%. The temperature radiation of the bare substrates has been taken into account. Only temperatures above 580° C are displayed because of the sensitivity limit and the signal noise.

The corresponding signals of energy, temperature and damage versus time are shown in figure 6. The pulsepower is calculated from the energy steps, absorption coefficients from temperature steps. Damage is detected by the change in the transmission signal, or from the occurence of plasma which are quite well correlated.

2.3. Evaporation process

The layers are deposited in a high vacuum evaporation plant using electron beam technique in a reactive atmosphere (figure 7). The thickness is optically monitored during the processes and adjusted to $4\lambda/4$ at 1.06 µm. The layer absorption at ambient temperatures is measured in a laser calorimeter similar to that described by Allen et al. (2).

Table 2. Evaporation process data

Substrate	Suprasil I, 25mm diam., 1mm thick
Substrate cleaning	vapour degreasing in $C_2Cl_3F_3$, lens tissue rub with isopropanol, draw off solidified collodium
Reactive evaporation	oxygen into electron beam, partial press. $2 \cdot 10^{-4}$mbar, substrate temperature 210° C, evaporation rate ca. 5Å/s
Activated reactive evaporation	for high refractive materials: ionized oxygen on substrates
Electron gun	6kV, rotating targets 60 mm Ø
Vendors of targets	Balzers and Cerac
Layer thickness	nd = 1.06 µm = $4\lambda/4$ at 1.06 µm

3. Results

From equation (1) the presumption arises that damage threshold is inversely proportional to absorption, if damage temperature of a substance is constant. Taking the absorption coefficients from the calorimeter measurement at ambient temperatures the relation does not apply at all. The threshold values as well as the absorption coefficients reported here correspond to layer temperatures of about 600°C and fit the proportionality satisfactory.

In figure 8 the damage threshold of ZrO_2-layers is shown depending on the absorption coefficient. There is a fair correspondence between the measured values and the relation proposed before:

$$D \cdot \alpha_{600^o} = \text{const.} = 25 \text{ GW/cm}^3$$

The constant is obviously a measure for the power absorbed per volume which causes destruction under the conditions in question. In this experiment we have changed the oxygen pressure to generate different absorptions, but in further investigations with diverse materials we used equal evaporation parameters (table 2). Doing this we are in some cases far away

from the best parameter combinations regarding minimum absorption and highest damage thresholds, but this is the objective method compairing materials. The absorption coefficients then scale the decomposition propability of the different materials.

In figure 9 the damage threshold of different coating substances depicted against the absorption coefficient at 600° C performs the required relation. Material properties like thermal conductivity do not seem to effect the damage threshold because BeO and SiO_2 for instance show no strong deviations, although BeO has a thermal conductivity 200 times higher than SiO_2. The damaging temperatures and the melting points seem to have more influence on the damage thresholds. Some materials with relatively low melting points (TiO_2, CeO_2) show a lower damage threshold than high melting materials (ThO_2, MgO).

Table 3. Average damage temperature of oxide layers on Suprasil I

Coating material	TiO_2	Ta_2O_5	CeO_2	Al_2O_3	Nd_2O_3	BeO	ZrO_2
Damage temp. (°C)	≈590	≈620	≈680	≈600	≈600	≈650	≈640
Melting point (°C)	1840	1880	1950	2015	2270	2530	2700
Dam. temp. (K) as part of melt. point (K)	0.41	0.41	0.43	0.38	0.34	0.33	0.33

The insulator type characteristics of the low melting materials are changed to semiconductor type at relative low temperature. So we have been looking for the part of the damage temperature to the melting point. As it can be seen from the values in table 3 there is no typical behaviour perceptible. Probably the damage of the layers strongly depends on the relatively low melting point of the substrate material SiO_2 and its vanishingly small expansion coefficient.

There is a remarkable point: changing the evaporation parameters for lowest absorption does not essentially change the product $D \cdot \alpha$ as you can see for ZrO_2 in figure 8. The tendency is always the same: points lying below the curve $D \cdot \alpha$ = const remain below it and so do the points situated above, because the damage temperature too does not change.

In addition to the material properties considered above the absorption edge at shorter wave lengths is correlated to damage threshold. Assuming, that the laser wave length is far away from the wave length of the absorption line the theory predicts the absorption α to be proportional to the resonant wave length λ_0^4. This can not be derived by the measurements shown in figure 10. The discrepancy to λ_0^4 occurs because we did not measure the wave lengths of the center of the absorption line but a longer one where the transmission of a 0.5 µm thick layer drops to 50%. A second reason for the divergence is the constant evaporation parameter which has not been the optimum for each material regarding the absorption coefficient.

The solid line in figure 10 indicates a possible relation to our measurements. We do not expect the indicated relation to be generally valid but we hope that there might be some derivable expression.

4. Summary

We tried to get some information about the connection of thin film absorption and laser induced damage. The main results have been achieved by using a fast pyrometer for the measurement of the layer temperature. The findings may be summarized as follows:

a. Absorption coefficients show a strong temperature dependence according to an exponential function.
b. Absorption coefficients near the destruction temperature are inversely proportional to damage thresholds.
c. The average damage temperature for oxide layers on fused silica substrates is far below the melting points.

5. References

1] Seitz, F., The Modern Theory of Solids, New York 1940, p. 192

[2] Allen, T.H., Apfel, H. a. Carniglia, C.K. "Laser Induced Damage in Optical Material", 1978, p. 33, NBS Special Publication 541

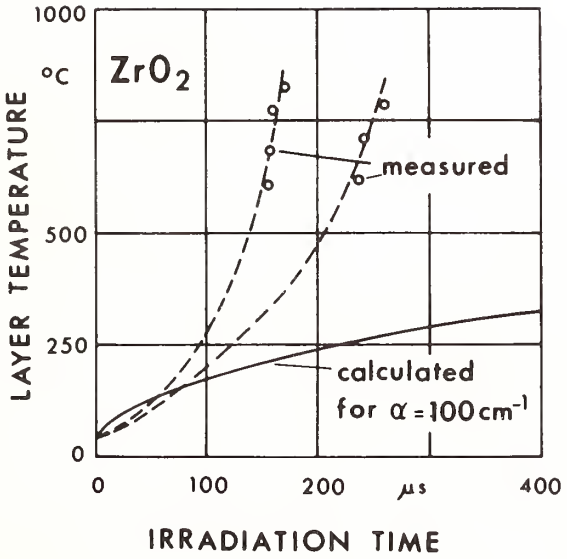

Figure 1. Temperature rise of ZrO_2-layers irradiated by constant intensity.

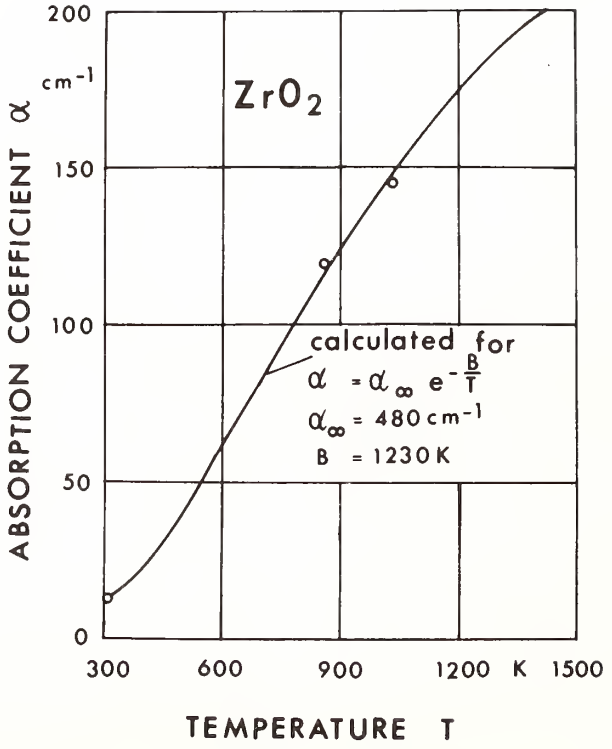

Figure 2. Temperature dependence of the absorption coefficient of ZrO_2, o measured points.

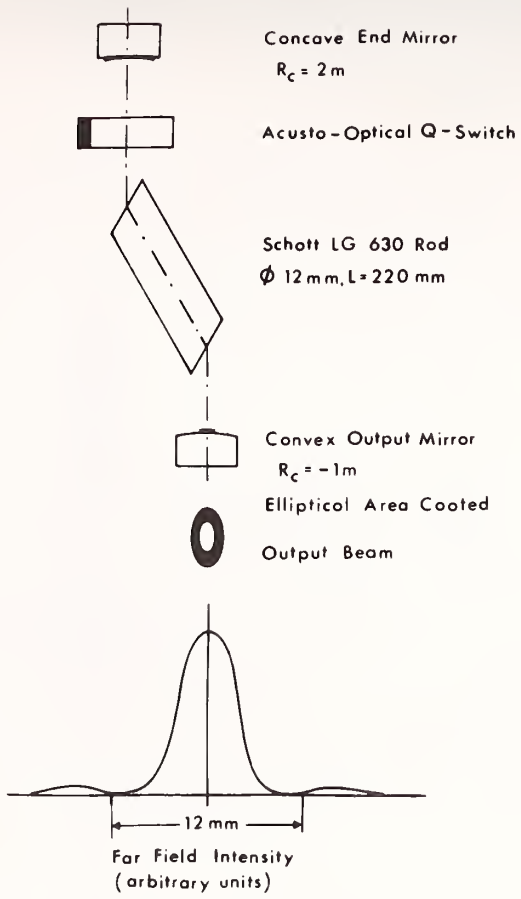

UNSTABLE RESONATOR TYPE Nd-GLAS LASER

Figure 3. Laser system.

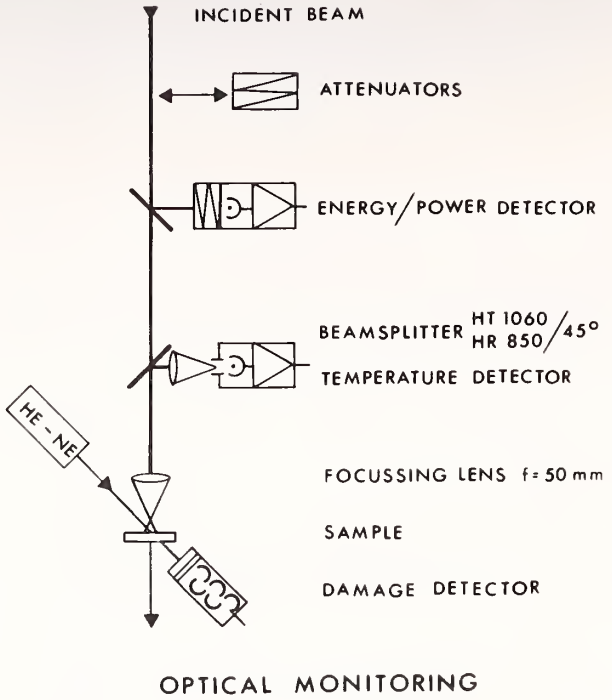

OPTICAL MONITORING

Figure 4. Damage test arrangement.

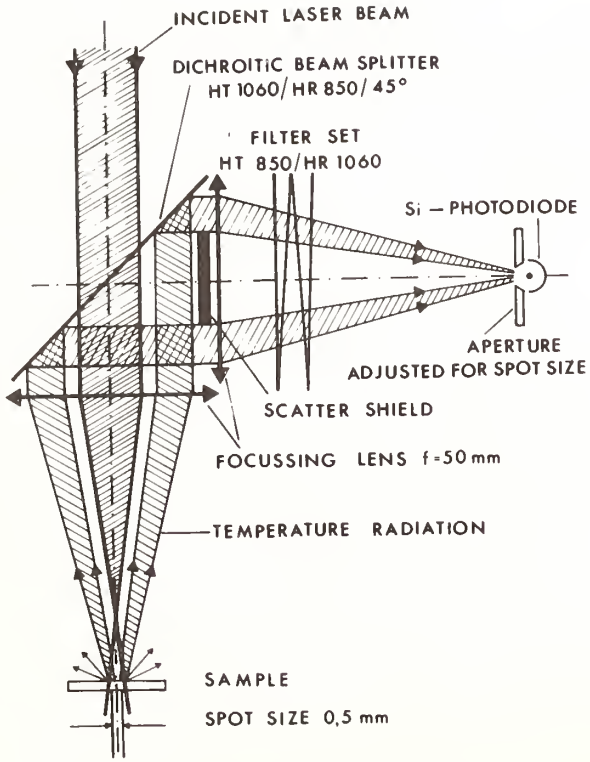

Figure 5. Pyrometer beam path.

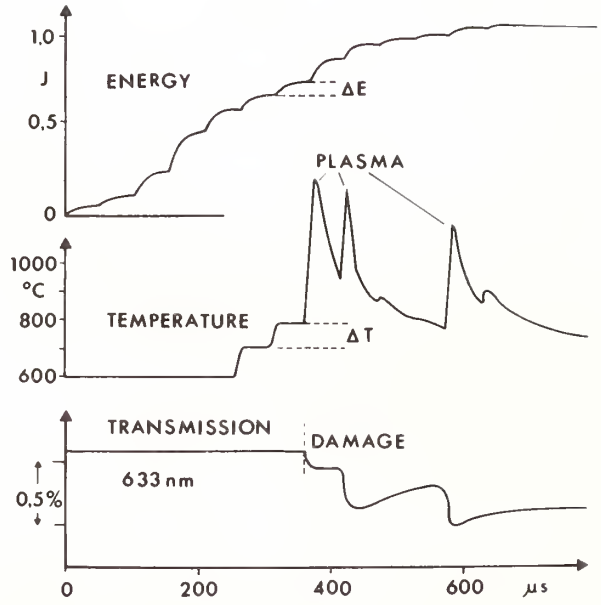

Figure 6. Typical plot of stored signals for calculation of damage threshold and absorption coefficient.

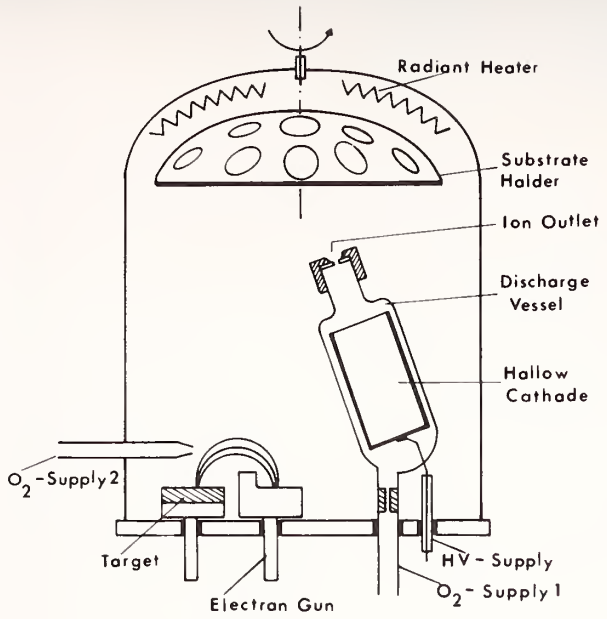

EVAPORATION CHAMBER

Figure 7. Evaporation plant.

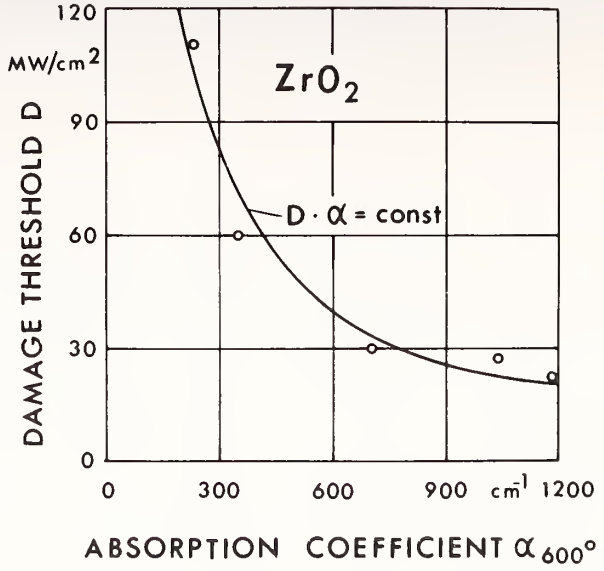

Figure 8. Damage threshold of ZrO_2-layers measured at 600° C. Layers evaporated in oxygen of 6, 4, 2, 1 and $0 \cdot 10^{-4}$mbar. const = 25 GW/cm³.

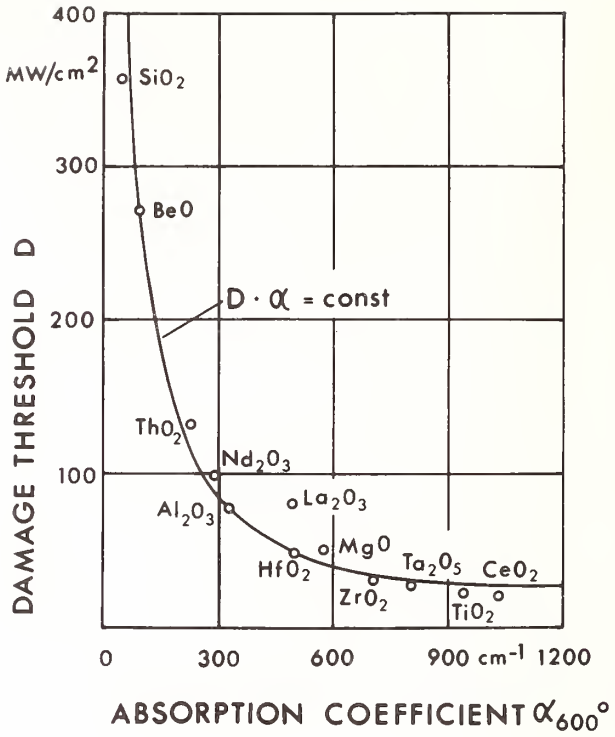

Figure 9. Damage threshold of oxide layers versus absorption coefficient measured at 600° C.

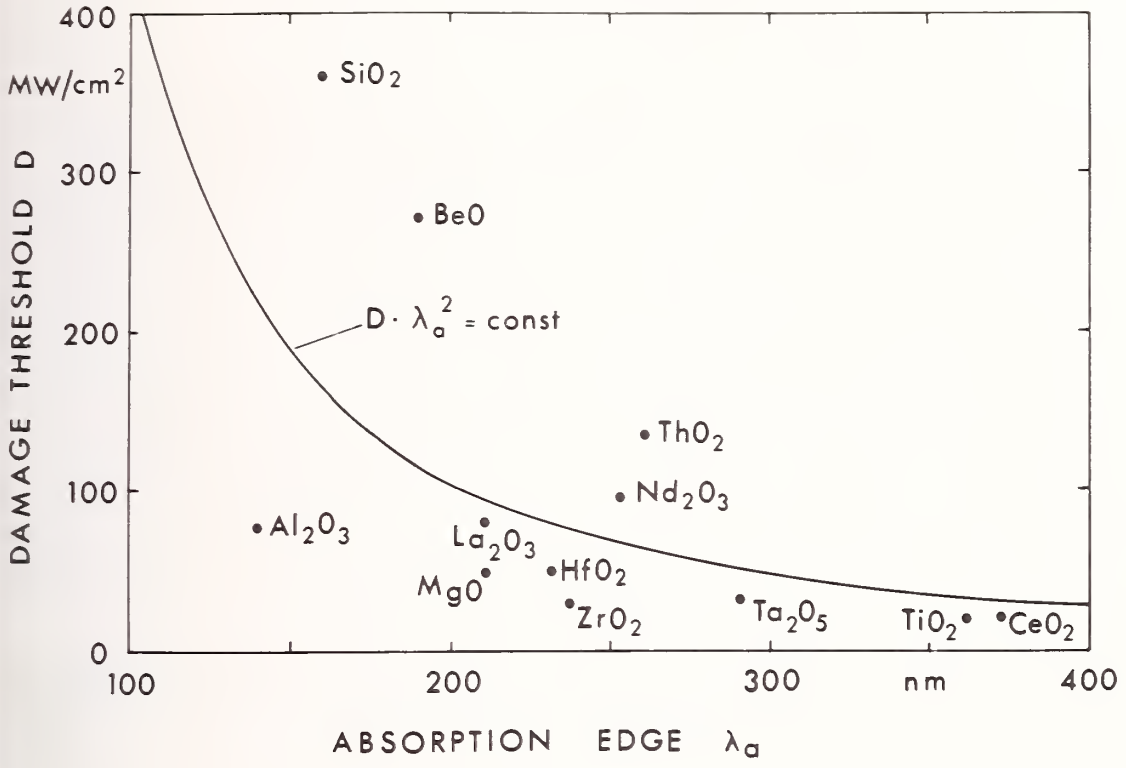

Figure 10. Damage threshold versus uv-absorption edge of oxide layers. Absorption edge λ_a is determined as wave lengths where the transmission of a 0.5 μm thick layer drops to 50% (α = 13 860/cm).

For a number of different samples, the damage temperature appeared to be about 600 degrees centigrade. Damage was assumed to arise from an absorbing layer at the interface between the oxide layer and the substrate. This was confirmed by the fact that in many experiments the oxide layer was disrupted. All data were taken at one pulse length, 800 nanoseconds. At this pulse length it was pointed out that standing-wave effects would no longer be important due to the effect of thermal diffusivity during the pulse duration.

HIGH-TEMPERATURE OPTICAL CHARACTERIZATION OF THIN FILM REFLECTOR AND ABSORBER LAYERS

M. R. Jacobson and R. D. Lamoreaux
Optical Sciences Center
University of Arizona
Tucson, Arizona 85721

We have developed a High Temperature Spectrophotometer (HTS) capable of measuring the temperature-dependent, reversible changes in reflectance and transmittance of thin films. The effective spectral range of the instrument - 0.38 to 15 microns - covers 98% of the solar Air Mass 2 spectrum, as well as 94% of the radiation from a 500 C blackbody. A tungsten-halogen,or globar source, provides two beams which are recombined before leaving the vacuum chamber. A Leiss sodium chloride monochromator disperses the radiation, which is detected by either a silicon ora thermocouple detector, depending on wavelength range. A microcomputer controlled sample-and-hold data acquisition system compares the two beams, corrects for background, and initiates data analysis. To minimize irreversible chemical changes in the films, a vacuum on the order of 5×10^{-6} Torr is maintained by a diffusion pump in the central chamber. Cartridge heating assemblies raise the sample substrate temperatures to 700 C in reflectance and 500 C in transmittance; chromel-alumel thermocouples embedded and cemented into the substrates monitor temperatures.

Key words: High temperature; infrared; optical instrumentation; reflectometers; spectrophotometers.

1. Introduction

Several developing energy and military technologies require optics that perform at elevated temperatures. The photothermal conversion of solar energy, for example, demands surfaces that both absorb well over the solar spectrum and reflect well in the thermal infrared. If such selective absorbers can maintain their optical performance at high temperatures, they will contribute to a higher thermodynamic efficiency for the total system. Our group at the University of Arizona's Optical Sciences Center has been developing high-temperature stable selective surfaces for the past several years under NSF-RANN, ERDA, and DOE funding. Measurements of optical properties at operating temperatures are crucial to the evaluation of these coatings. To this end, we have developed a High Temperature Spectrophometer (HTS) to measure reflectance and transmittance of coating samples over a spectral range of 0.38 to 15 microns. We shall describe the instrument in terms of its four basic systems: optical, environmental, electronic, and data analysis.

2. Optics

Shown from left to right in Figure 1 are the source optics, the vacuum chamber optics, and the monochromator optics; only one of the two beams is traced for clarity. The sources, a 500 W tungsten-halogen lamp and a diesel engine igniter globar, are mounted on a carousel for convenient interchange. The carousel structure also supports a cylindrical tube which acts as a lamphouse and a fan which cools the sources. A third sector is left vacant for an additional source. Pairs of spherical and flat mirrors transfer the beams to foci within the transmittance cell. Before entering the cell, the beams are alternately passed by a single chopper with one open 90 degree sector. The chopper is driven by an O-ring belt drive powered by a stepper motor, the speed of which is controlled by a pulse train from the electronics.

When used in the transmission mode, the beams enter through the twin sodium chloride windows of the transmittance cell, which is mounted on the large vacuum cavity. A substrate coated with the thin film to be measured is placed in the sample beam, while a nominally identical substrate is held in the adjacent reference beam to cancel substrate ef-

fects. In the reflectance mode, the entire transmittance cell can be replaced with a simple flange containing another pair of sodium chloride windows. Next, spherical and flat mirrors relay the beams to the reflectance cells on either side of the vacuum chamber. The sample reflectance cell, at the top of Figure 1, clamps the sample firmly between the heater block and the cell structure, by means of opposed stainless steel wedges. The unheated reference reflectance cell holds the aluminum reference mirror tightly, as well. Beyond these cells, the final sets of optics direct the two beams to the beam recombiner, which operates as illustrated in the inset in Figure 1. A set of microscope slides was beveled; they were glued together so that the slopes alternated. When aluminized, the recombiner interleaves the sample and reference beams into a single beam, which leaves the vacuum chamber through another sodium chloride window.

A Leiss Sodium Chloride Double-Prism,Double-Pass Monochromater follows. An entrance slit admits the beam from the vacuum chamber, after which it is dispersed by the first of two Littrow-mounted prisms. An intermediate slit blocks stray light and admits the beam to the second set of dispersing optics. Then, the beam exits the monochromator and is directed to the detectors by a flat,followed by a spherical,mirror. The spherical mirror can be rotated slightly to focus on either of two detectors, a two-color silicon photodiode-lead sulfide detector from Infrared Industries for the visible and near-infrared; or a thermocouple detector from Reeder for the mid-infrared.

3. Environmental

The samples must be heated to temperatures of interest and maintained at high vacuum. Furthermore, both temperatures and vacua must be monitored. Finally, cooling arrangements around the hot sample cells must be made to prevent undesirable effects on adjacent components.

Samples are heated by Watlow cartridge heaters inserted into closely machined copper blocks. The block in the sample reflectance cell contains a pair of 250 W, 1/2-inch diameter heaters. This block directly heats the back surface of the sample to about 700 C. A chromel-alumel, or K, thermocouple monitors the block temperature; a second K thermocouple is cemented into a hole in the corner of the sample itself. The transmittance cell carries two copper blocks, one for the sample and one for the reference beam. Each contains eight 3/8-inch diameter cartridge heaters dissipating a total of 1,000 W to heat the sample to about 500 C at its center; they are arranged around a circular hole in the block which admits the light beam. Heating of the transmittance samples is more difficult, because only the edges can be heated by conduction. Each transmittance sample is pressed against its block over the circular hole by a stainless steel holder. Again, K thermocouples are cemented to the blocks, while pairs of thermocouples, one in a corner and one near the center, monitor the samples' temperatures. All thermocouple wires are led out of the vacuum chamber via high-temperature junction strips,made of Macor machinable ceramic and chromel/alumel lugs,to vacuum thermocouple feedthroughs. Outside the instrument, a twelve-position thermocouple switch allows rapid access to the numerous temperatures under observation. All copper heating blocks are nickel-plated to prevent oxidation of the copper. A temperature controller unit can be incorporated into the system, as well.

A cooled copper baffle surrounds the sample reflectance cell, while the transmittance cell is a double-walled stainless vessel with feedthroughs for water circulation. A recirculating water chiller provides coolant in both cases.

A two-inch Edwards diffusion pump evacuates the main chamber to levels of around 10^{-6} Torr. To improve speed and prevent degradation of optics by pump oil, a chilled baffle is included above the pump. The usual thermocouple gauging for roughing pump vacua and hot filament ionization gauging for diffusion pump vacua are provided. An argon bleed line is used to prevent condensation in the chamber and oxidation of the hot sample after a run. To provide easy access to the samples and optics, the entire top of the vacuum chamber can be removed.

4. Electronic

In Figure 2, a simplified schematic shows the operation of the sample-and-hold electronics. Signals from the silicon photodiode circuit of the two-color detector and the thermocouple detector for wavelengths shorter and longer than one micron, respectively, enter preampliers located adjacent to the detectors. Then, longer cables relay the signals to the sample-and-hold electronics. A switch and one stage of amplification, not shown, precede the gate circuitry. The gates have inputs from both the LED/phototransistor pairs at the chopper, and a crystal clock. The former select the proper chopper phase from the three possibilities; while the clock defines the actual time period during which data is taken. Figure 3 depicts the phase synchronization system. The LED/phototransistor pairs, of which one is drawn, report when the open sector of the chopper blade admits light into the vacuum chamber. Pulses 250 ms apart are generated, as illustrated at the bottom of Figure 2. These pulses also set the crystal clock, which then opens the appropriate gate for 102 ms, thereby waiting for the slower thermocouple detector to reach a constant value. The second gate sends the integrated signal on to an A/D converter. The A, B, and C phases refer to the sample, black chopper blade, and reference phases.

The A/D converter sends its digital output on to the 6800 computer and also drives a four and one-half digit selectable display. When the computer has recorded the data at a particular wavelength, it commands the stepper motor at the monochromator to advance to the next wavelength. As we shall see in the next section, the microcomputer provides us with efficient and flexible data analysis.

5. Data Analysis

Our preliminary analysis routine uses the microcomputer to remove various sources of background noise and to plot the spectral reflectances. Later versions will calculate solar absorptances and thermal emittances at various temperatures, and may automatically allow the system to integrate for longer periods at wavelengths where the signals are weak. The operation is similar for both reflectance and transmittance modes. Four basic sources of error or noise are present: offsets in different channels of the sample-and-hold electronics; offsets in the preamplifiers; thermal emission; and stray light. The first problem can be eliminated by reading the output from each channel when both beams are blocked at the beginning of a run. The second and third are not modulated by the chopper, and will fall out when the sample and reference beams are compared by the microcomputer after each cycle. Stray light, however, can be generated by the sample and reference beams, and must be quantified and subtracted. This can be done by a means of standard samples. First, a run is made with first surface aluminum reflectors in both beams; this measures the response of the system to the maximum anticipated signal. Then glass samples with blackened first surfaces are introduced into both beams. These two measurements each provide observed signals for sample and reference beams, which consist of the actually reflected component and a stray light component. The stray light is assumed to be the same in each case; the reflectance of the blackened glass is known to be on the order of 1% of aluminum, depending on wavelength. This reduces the problem to two equations in two unknowns - which are the corrected aluminum reflectance and the stray light. When these unknowns are computed at each wavelength for sample and reference beams, we are ready to proceed. Then, corrected values of sample and reference aluminum mirrors are available at each wavelength for sample measurements.

At this point, the sample itself is introduced, and runs are made at ambient and higher temperatures. As before, the sample is always compared to the aluminum reference, and the dark phase values are subtracted from both. The adjusted values calculated above and stored in the computer correct the measured values at each spectral point, yielding the measured, corrected reflectance factor. Finally, reflectance values for aged aluminum are used to change the reflectance factor to absolute reflectance. [1]

The procedure is basically the same for transmittance measurements, except that the sample reflectance cell contains an aluminum mirror and is not heated. Approximately 340 points are taken while covering the 0.38 to 15 micrometer range (or alternately "μm range"); these scans take about 20 minutes each. Data are plotted by a strip chart recorder and are stored in the microcomputer.

6. Data and Research Plans

An example of data previously taken on the instrument follows in Figure 4. A 1.75 micron thick film of silicon was fabricated by chemical vapor deposition on a silver reflector and heated to 500 C in the HTS. The absorption edge shifts to longer wavelengths due to phonon-assisted transitions, while the interference fringes deepen due to increased free carrier absorption. The first effect increases solar absorption, while the second raises the thermal re-emission of the thin film stack. In this case, as shown in Figure 4, the reversible thermal effect causes the use of room temperature reflectance data, to produce an error of as much as 10% in the solar absorptance of a sample at elevated temperature. We are planning to use the HTS at the earliest opportunity to explore the high-temperature reflectance properties of both highly reflective and black molybdenum films. We also plan to observe the transmittance properties of carbon-alloyed amorphous silicon, which is stabilized against crystallization to temperatures of around 1000 C.

7. Acknowledgments

This work has been supported under the following contracts: "Chemical Vapor Deposition of Amorphous Silicon for Photothermal Solar Energy Converters," Department of Energy, Division of Materials Sciences, #ER-78-S-02-4899; "Chemical Vapor Deposition of Refractory Metal Reflectors for Spectrally Selective Solar Absorbers," Department of Energy, Advanced Technology Branch, #EY-75-S-04-3709; and "High Temperature Reflectance and Transmittance Measurements of Thin Films," Joint Services Optical Program, Air Force Office of Scientific Research, #F49620-77-C-0138.

6. References

[1] H.E. Bennett, J. M. Bennett, E.J. Ashley, JOSA, 52, 11, 1245 (1962).

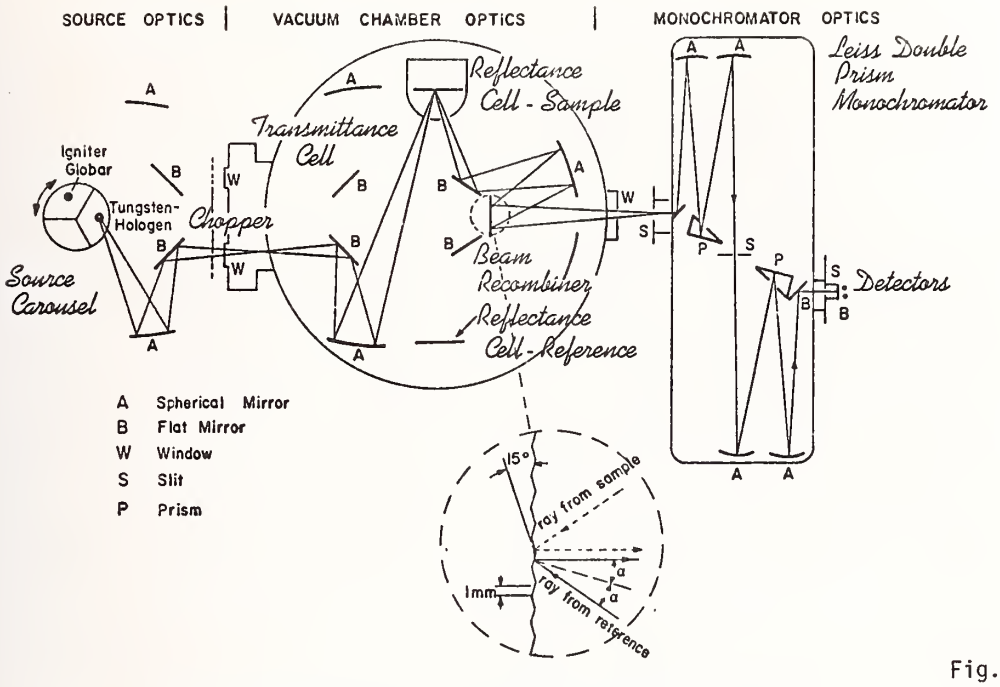

Fig. 1

HIGH-TEMPERATURE SPECTROPHOTOMETER OPTICS

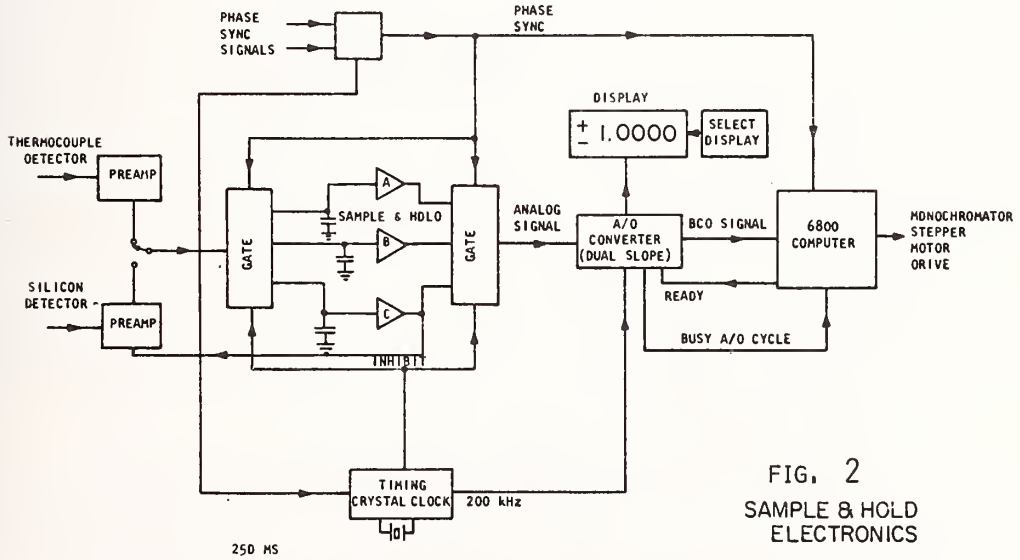

FIG. 2
SAMPLE & HOLD ELECTRONICS

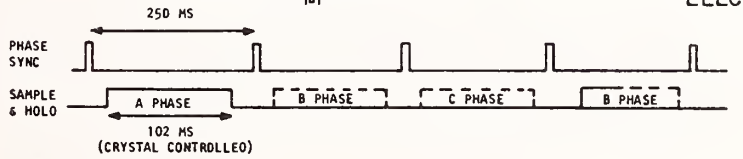

Fig. 2

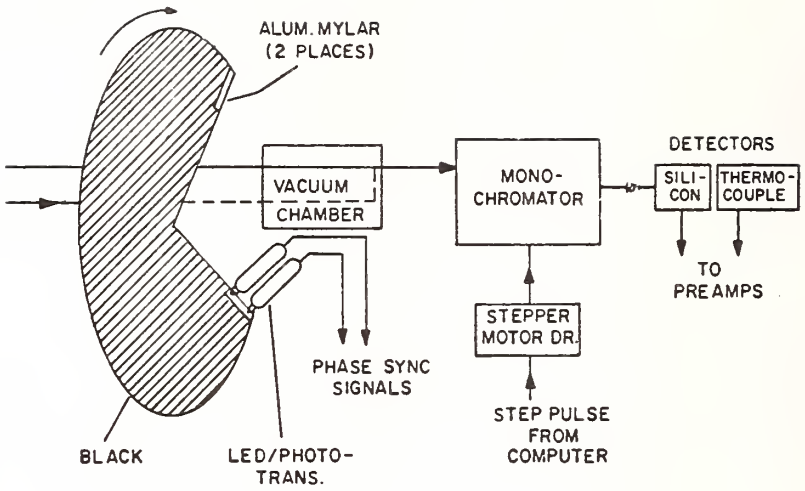

PHASE SYNCHRONIZATION SYSTEM IN HTS

Fig. 3

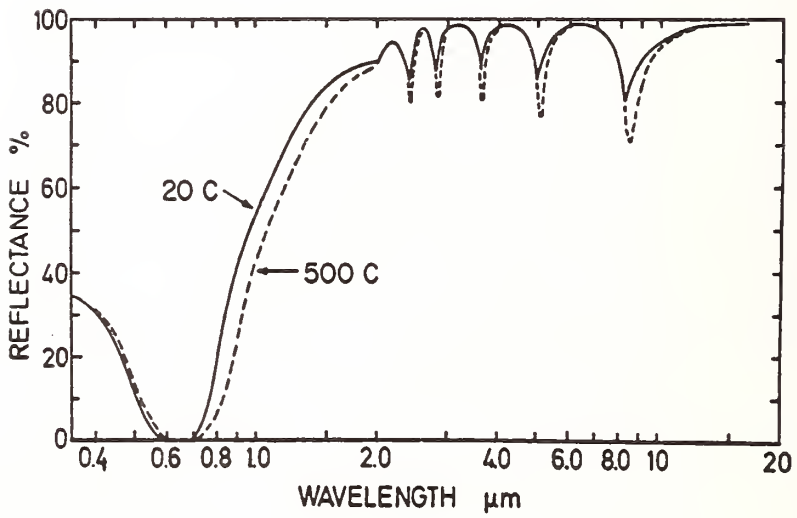

Figure 4. Change in reflectance of a 1.75 micron thickness silicon-on-silver selective surface due to heating from 20 to 500C in the HTS.

C V D MOLYBDENUM THIN FILMS FOR HIGH POWER LASER MIRRORS

G.E. Carver & B.O. Seraphin
Optical Sciences Center
University of Arizona
Tucson, Arizona 85721

Molybdenum thin films have been prepared by chemical vapor deposition (CVD) from both molybdenum carbonyl ($Mo(CO)_6$) and molybdenum pentachloride ($MoCl_5$). The crystal structure, grain size and composition of the films have been determined and related to their infrared reflectance. Post-deposition annealing raises the absolute reflectance of films deposited from the carbonyl to 98.73% at ten micrometers. The fact that these films are prepared without a polishing step may explain why their reflectance is 0.5% higher than that of super smooth polished bulk molybdenum. The higher reflectance and absence of a polish-induced damage layer could increase the damage thresnold of uncoated CVD molybdenum mirrors. Films deposited from the chloride have largely reproduced the optical properties of those prepared from the carbonyl, with grain sizes ranging from 0.03 to 0.5 micrometer. Polished bulk molybdenum substrates could be further smoothed by first overcoating them with, and subsequently polishing of, a several micron thick layer of fine grained CVD molybdenum.

Key words: Chemical vapor deposition; composition; crystal structure; grain size; molybdenum thin films; reflectance.

1. Introduction

High thermal conductivity, a low thermal expansion coefficient, and the relatively high damage threshold of molybdenum (Mo) suggest the use of Mo as a high power laser mirror [1,2][1]. The fabrication of low-scatter Mo surfaces by mechanical polishing is, however, difficult. Molybdenum thin films, on the other hand, can be much smoother if deposited on an appropriate substrate due to their small grain size than the polished bulk. Thin films of Mo generally have, however, anomalously low infrared reflectance [3,4]. Attempts to smooth bulk Mo by first overcoating with, and then polishing of, sputtered Mo thin films result in reduced damage thresholds [5]. This loss in stability has been related to the porosity of the sputtered films and interfacial problems between the film and the bulk [1]. Many applications dictate the use of reflectance enhancement coatings which also reduce the damage threshold of Mo-based mirrors. This paper reports on the production of Mo thin films which have a higher infrared reflectance than the reflectance of even super-smooth bulk Mo. We also report on the chemical vapor deposition of fine grained films which may prove useful in additional smoothing of bulk Mo substrates.

Refractory metal films prepared by CVD for use in photothermal solar energy conversion show promise through both high temperature (500 C) stability and high infrared reflectance [6]. Since the requirements are similar, our previous work in this area thus naturally extends itself into the high energy laser mirror field [7].

2. The CVD Process

Chemical Vapor Deposition occurs on substrates held above the threshold temperature of the pyrolytic decomposition or gas phase reduction of the reactant gas. As opposed to most PVD techniques, CVD films are therefore screened against failure at temperatures below this threshold and are at thermal equilibrium with the substrate during growth, resulting in temperature stable films of high packing density. If impurities and/or imperfections can be avoided, Mo films with very high infrared reflectance can be deposited [7,8]. In addition, CVD can coat complex shapes under one atmosphere without the need for ultra high

1. Figure in brackets indicates the literature references at the end of this paper.

vacuum. [9]

Two methods were used in this work to form Mo thin films: the pyrolysis of $Mo(CO)_6$, and the reduction of $MoCl_5$. The two reactions are as follows:

$$Mo(CO)_6 \xrightarrow{300\ C} Mo + 6\ CO \qquad (1)$$

$$2\ MoCl_5 + 5H_2 \xrightarrow{500\text{-}750\ C} 2\ Mo + 10\ HCl. \qquad (2)$$

Details on these two processes can be found elsewhere. [7,8].

All films reported here were deposited on fused silica substrates under one atmosphere of Argon carrier gas and were approximately 0.2 micrometer thick.

3. Optical and Metallographic Characterization Of CVD Molybdenum

A metallographic analysis must be carried out to explain why Mo thin films have different reflectance from that of supersmooth bulk Mo. We have therefore determined the composition of CVD Mo by Auger spectroscopy and electron microprobe techniques, the crystal structure by x-ray diffraction, and the grain size by electron microscopy.

Reaction (1) does not go to completion at 300 C. Higher temperatures result in powdery deposits if the reaction occurs under a pressure of one atmosphere. Films deposited from the carbonyl at 300 C therefore contain considerable amounts of carbon and oxygen and are only 54 ± 14 atomic % Mo. These films also exhibit an fcc-MoOC phase in grains which are less than 0.03 micrometer in diameter. As a result, the reflectance of films from the carbonyl is only 87% of the reflectance of Al at 10 micrometers. As shown in figures 1 and 2, post-deposition annealling increases the reflectance. The figures show that either 30 minutes at 750 C or five minutes at 1,000 C increases the reflectance of the Mo films up to the reflectance of Al. The fully annealled films contain as little as one atomic % carbon and two atomic % oxygen. The anneal also converts the films to the bcc-Mo phase and enlarges the grains to a diameter of 0.5 micrometer. Changes in composition, structure and grain size during anneal are summarized in figure 3. Even though these fully annealled films contain up to four atomic % Cr and two atomic % W, they still have an absolute reflectance of 97.4% at 10 micrometers. We have previously reported that this value is only 0.7% lower than the reflectance of supersmooth bulk Mo [7]. Since then, higher reflectance values have been attained on a new set of films deposited from purer $Mo(CO)_6$. After anneal, the new films contain about one-half the amount of Cr and W of the previous set, and have an absolute reflectance of 98.73% at 10 micrometers, now surpassing by 0.5% that of super-smooth bulk Mo. All of these absolute reflectance values were measured to within ± 0.1%, and were provided to us along with the super-smooth bulk Mo data, by Dr. J.M. Bennett of the Michelson Laboratory at China Lake, California.

The adsorption of oxygen or carbon monoxide on a Mo surface can reduce the reflectance [10]. Since our films,in transit to China Lake, California, were exposed to air for several days before the reflectance was measured, we may assume that the initial reflectance is even higher than the value measured after such exposure. The most reflective sample was remeasured twice after a period of several weeks to insure that the reflectance was not decreasing further in time. The results in Table 1 indicate that the reflectance is stable to within 0.1% over the observation period of 45 days.

TABLE 1

Absolute reflectance, R at 10 micrometers, versus time for annealled CVD Mo.

Deposition	-	day zero
R = 98.73		6 days

TABLE 1, (Continued)

R = 98.55	-	23 days
R = 98.64	-	45 days

The total integrated scatter (T.I.S.) from the most reflective film is 1.19 $\pm$ 0.59 x 10^{-3} for a wavelength of 0.6471 micrometer. This relates to an RMS roughness of 0.0018 micrometer while standard fused silica substrates have an RMS roughness of 0.0013 micrometer [11],indicating that the CVD film apparently is conformed to the quartz substrate. In addition, the as-deposited films do not roughen during anneal as evidenced by similar T.I.S. values of films before and after the anneal step.

Films deposited by reaction (2) at 750 C have similar optical and metallographic properties as the fully annealled films from the carbonyl reaction. Reaction (2) can produce, however, body centered cubic (bcc) deposits of equivalently pure Mo which have fine grains (0.030 micrometer) by depositing at 500 C. Presently, thin sputtered films of Mo are used to smooth bulk Mo substrates, but result in reduced damage thresholds of such mirrors. Even though CVD Mo must be deposited at high temperatures, a small grain size can result if the substrate temperature is low enough. If fine grained CVD deposits were formed on bulk Mo, the damage threshold may be higher than that of bulk Mo coated with sputtered Mo for two reasons. First, the CVD Mo is likely to be less porous than the sputtered Mo due to the deposition of the CVD film at thermal equilibrium with the substrate. Second, contaminants at the bulk-film interface can be partially removed by reaction with hydrogen at the temperature of deposition.

4. Discussion

In comparing them to the pure bulk phase, the anomalously low reflectance of refractory metal films was originally blamed on impurities and/or structural modifications. Improvements in the purity and structure of Mo films have been accomplished since the sputtered film of figure 4 was deposited in ultra-high vacuum two years ago [4]. Biasing during sputtering [12] and heating the substrates during evaporation [13] have increased the reflectance of PVD films to near bulk values. To our knowledge, however, only annealled CVD films have actually eclipsed the reflectance of super-smooth bulk Mo. This fact may be due to the absence of a polishing step during the preparation of our films. This hypothesis is supported by three facts. First, the literature acknowledges that mechanical polishing induces a damage layer in smoothed semiconductor and refractory metal surfaces [14,15]. Second, Saito observed increasing specular reflectance of polished bulk Mo with decreasing roughness until a certain RMS value was reached whereupon the reflectance began decreasing with decreasing roughness [2]. Third, polished bulk Mo which contains hardening agents (TZM) has exhibited a slightly higher reflectance than pure bulk Mo [1]. The hardened material may have a less extensive polish induced damage layer.

CVD Mo films deposited on an appropriate substrate without additional layers will become useful as mirrors for high-power lasers. Their high reflectance can possibly be raised even further by the following measures. First, CVD Mo could be isolated from gases which may be adsorbed at the surface. We have coated CVD Mo immediately after anneal with a CVD Si_3N_4 layer and improved their infrared reflectance [7]. Second, a substrate with a thermal expansion coefficient closer to Mo than fused silica, such as silicon carbide, may reduce elastic deformation upon cooling. Finally, residual amounts of Cr and W in our films could be further reduced through pre-purification of the reactant materials. Although not yet determined, CVD Mo should have a higher damage threshold than super-smooth bulk Mo, since the increased reflectance reduces the residual absorptance. Reducing the surface damage by the absence of a need to polish will help further. Support for this expectation is provided by the fact that diamond-turned copper has a higher threshold than mechanically polished copper [5].

5. Conclusions

Mo thin films have been deposited by chemical vapor deposition from both $Mo(CO)_6$ and $MoCl_5$. Post-deposition annealling has increased the reflectance of films from the carbonyl to 98.73% at 10 micrometer. The reflectance of these films is 0.5% higher than super-smoot bulk Mo. Films from the chloride have exhibited grain sizes ranging from 0.03 to 0.5 micro meter.

6. Acknowledgements

The authors wish to thank David Allred of the Optical Sciences Center, University of Arizona, for the electron microprobe measurements; Jean Bennett of the Michelson Laboratory, for the absolute reflectance and total integrated scatter measurements, plus the super-smooth bulk Mo data; Lou Demer of the University of Arizona for the electron microscopy; Tilak Raj of the University of Minnesota for the Auger spectroscopy determinations; and the entire Solar Energy Group of the Optical Sciences Center for assistance throughout this work.

This work has been supported by the Department of Energy under S.E.R.I. Subcontract #XH-9-8217-1.

7. References

[1] S.M. Wong, G. Krauss and J.M. Bennett, "Optical and Metallurgical Characterization of Molybdenum Laser Mirrors," in Laser Induced Damage in Optical Materials: A.J.Glass & A.H. Guenther, Eds., N.B.S., Washington, D.C. (1978) (NBS Spec. Publ. 541),132-163.

[2] T.T. Saito, "10.6 μm Absorption in Molybdenum Mirrors," in proceedings of ASME/AIAA Thermophysics and Heat Transfer Conference, Boston, Ma.: National Technical Information Service, Springfield, Va. (1974).

[3] H.S. Gurev, B.O. Seraphin, "Thin Film Reflectors of Improved Thermal Stability," in Proceedings of the High Power Laser Optical Components and Component Materials Meeting, Boulder, CO. (October, 1977) J.S. Harris & C.L.Strecker, Eds., Defense Adv. Research Projects Agncy, Arlington, Va.

[4] P.A. Temple, D.K. Burge, E.J. Ashley, Navel Weapons Center Annual Report No. 8,(1977) (unpublished) p.18.

[5] J.O.Perteus, C.W. Fountain, J.L.Jernigan, W.N.Faith, H.E.Bennett, "Pulsed-Laser Stress Phenomena on Highly Reflecting Metal and Alloy Surfaces," in Laser Induced Damage in Optical Materials: (1977) A.J. Glass & A.H. Guenther, Eds., N.B.S., Washington, D.C. (NBS Spec. Publ. 509),pp.204-214.

[6] B.O.Seraphin, J. Vac. Sci. Tech. 16, (1979) p.193.

[7] G.E.Carver, B.O.Seraphin, Appl. Phys. Lett. 34 (1979) p.279.

[8] G.E. Carver,"Thin Solid Films" 63, (1979) p. 169.

[9] W.M.Feist, S.R. Steele, D.W. Readey, "The Preparation of Films by Chemical Vapor Deposition," in Physics of Thin Films, Vol. 5 (1969) G. Hass & R.E. Thun, Eds., Academic Press, New York, pp. 237-322.

[10] J. Anderson, G.W. Rubloff, P.J. Stiles, "Solid State Communications," 12 (1973) p.480.

[11] H.E. Bennett, "Optical Engineering," 17 (1978) p.480.

[12] T. Raj, G.K. Wehner, "Composition Profiling of Solar Coating Materials," in proceedings, Second Annual Conf. on Absorber Surfaces for Solar Receivers, Boulder, Co (1979) Solar Energy Research Inst., Golden, CO, pp. 163-170.

[13] J.E. Nestell, Jr.,R.W. Christy, J. Vac. Sci. Technol. 16, (1978) p.366.

[14] T.M.Donovan, B.O.Seraphin, J. Elec. Chem. Soc. 109, (1962) p.877.

[15] J.H. Weaver, D.W. Lynch, C.G. Olson, Phys. Rev. B 7, (1973) p.4311.

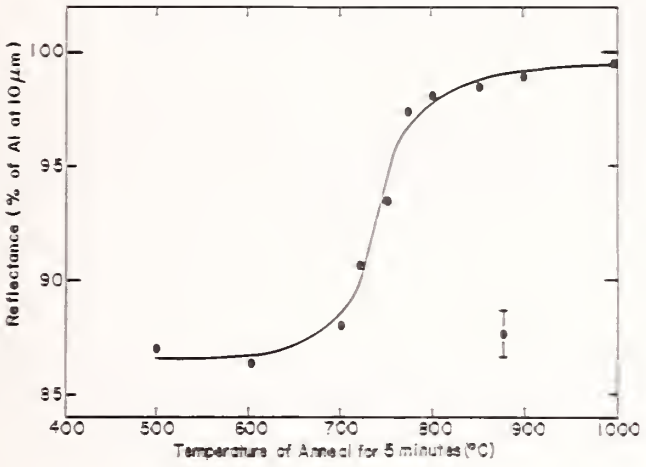

FIG.1. Relative reflectance, at 10 micrometers of CVD molybdenum films plotted against the temperature of a 5-min. anneal.

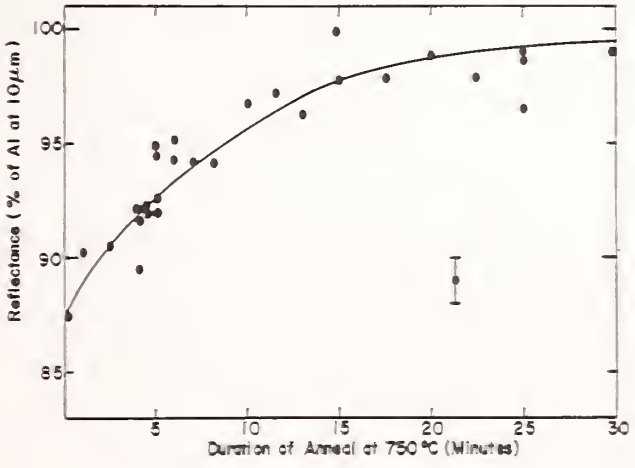

FIG.2. Relative reflectance, at 10 micrometers of CVD molybdenum films plotted against the duration of anneal at 750 C.

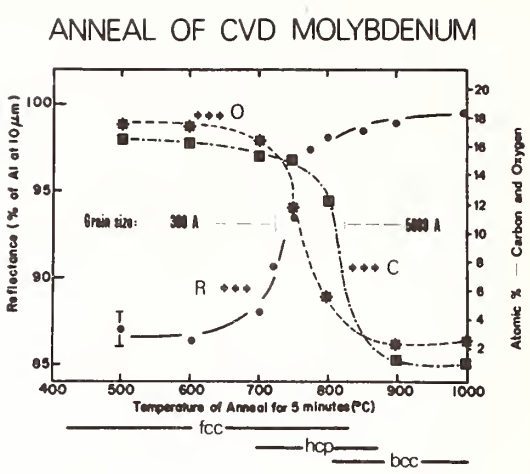

FIG.3. Relative reflectance of Fig.1 with changes of oxygen and carbon content, crystal structure, and grain size during anneal of a CVD Mo film.

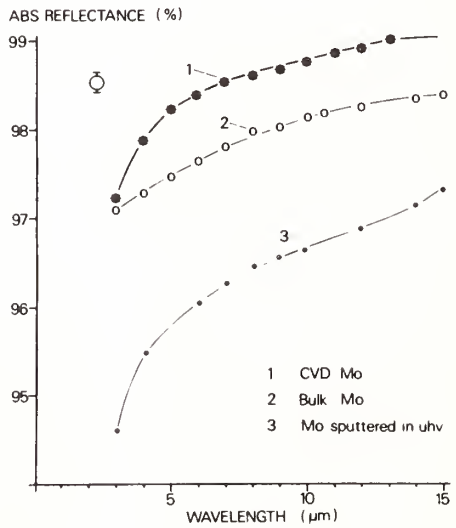

FIG.4. The absolute reflectance in the wavelength range 3-15 micrometers of (curve 1) annealled CVD Mo:(curve 2) Super-smooth bulk Mo: (curve 3) Mo sputtered in ultra-high vacuum.

PHOTOACOUSTIC EXPERIMENTAL STUDIES ON AN AR COATED LASER WINDOW AND SOME RELATED THEORETICAL CALCULATIONS

Nils C. Fernelius
University of Dayton Research Institute
Dayton, Ohio 45469

Experimental photoacoustic spectroscopy (PAS) amplitude and phase results on an AR coated ZnSe laser window were obtained at 10.6 μm as a function of chopping frequency. The PAS signal amplitude had an f^{-n} frequency dependence with n = 1.04. The PAS phase angle varied by 20° between 1000 Hz and 50 Hz; 7° between 1000 Hz and 100 Hz.

Theoretical calculations related to the situation were performed using the Bennett-Forman and Rosencwaig-Gersho PAS theories. The Bennett-Forman theory agreed with the PAS amplitude results for $r = \beta_{surface}/\beta_{bulk} \geq 0.05$ cm. A 7° phase change was obtained for r = 0.03 cm. The homogeneous sample Rosencwaig-Gersho theory did not fit either amplitude or phase angle data, yielding n = 1.5 and a phase angle of 45.0° which varied less than 0.04° over the frequency range measured.

Key words: Bulk optical absorption coefficient; optoacoustic spectroscopy; photoacoustic spectroscopy; surface optical absorption coefficient; ZnSe

1. Introduction

Photoacoustic spectroscopy (PAS) [1-9][1] is a recently revived technique which has promise for obtaining optical absorption coefficients from certain classes of materials which do not yield usable spectra by more conventional techniques. In addition to spectra obtainable by varying wavelength, information is obtainable by varying chopping frequency. In certain frequency ranges [10-11], the PAS amplitude changes from a f^{-n} dependence with n = 3/2 for predominantly bulk optical absorption to n = 1 for predominantly surface optical absorption. The PAS phase angle changes from a 45° phase lag for bulk absorption to a 90° phase lag for surface absorption. While the phase angle change is more pronounced in theory, due to the lack of knowledge of the actual phase zero one is forced to work with phase angle differences or other schemes.

2. Experimental

A Coherent Radiation Model 40A CO_2 laser set at 10.6 μm and with power output in the 20 to 25 watt range was used as the light source. The light was chopped with a Princeton Applied Research (PARC) Model 192 Variable Frequency Light Chopper. The signal from a GenRad 1961-Electret Detector microphone was detected by a PARC 5204 Lock-In Analyzer. The photoacoustic cell was arranged in a manner similar to that described elsewhere [11-12]. Thus the sample consisted of the entrance and exit windows of the cell.

The experimental results are given in figures 1 and 2. Laser rate calorimetry on the two windows yielded an average β_{eff} for the samples of 0.00707 cm^{-1}. The PAS amplitude results in figure 1 fitted an f^{-n} dependence with n = 1.04. The PAS phase angle results

---

[1] Figures in brackets indicate the literature references at the end of this paper.

yielded a phase angle difference of 20° between 50 Hz and 1 kHz and a 7° difference between 100 Hz and 1 kHz.

3. Theoretical Calculations

The chopping frequency dependence of the PAS signal was calculated using the Bennett-Forman [11], Rosencwaig-Gersho [10] and two-layer Rosencwaig-Gersho [13] theories. A more detailed account of this work can be found elsewhere [14]. Complex number FORTRAN IV computer programs were written to calculate PAS amplitude and phase for each theory. Representative thermal parameters which were inserted in these programs for ZnSe and other materials were taken from laser calorimetry work. Varying values for the optical absorption coefficient, in the range obtained from laser calorimetry experiments, were tried in the program to bracket real world experiments. For the ZnSe substrate β_B = 0.008, 0.004 and 0.001 cm^{-1} were used in all programs. The results of the Bennett-Forman and Rosencwaig-Gersho theories will be presented here. The results of the two-layer Rosencwaig-Gersho theory will be given in the companion paper.

3.1 Bennett-Forman Theory Calculations

The Bennett-Forman program calculates eq. (30) in ref. 11. After some calculations had been made, it was realized that the signal calculated was a product of terms dependent on the cell gas and dimensions times a term containing all the optical absorption coefficient dependence. This latter term can be written as

$$\beta_B[r+(1-j)\sqrt{\kappa_s/(2\omega\rho_s C_s)}] = \beta_s+\beta_B(1-2)\sqrt{\kappa_s/(2\omega\rho_s C_s)}$$

where β_B is the bulk optical absorption coefficient in cm^{-1}, $\omega/2\pi$ is the chopping frequency, r is the surface to bulk optical absorption ratio $r \equiv \beta_s/\beta_B$, β_s is the sample surface absorption (dimensionless), κ is the sample thermal conductivity, ρ the sample density and C the sample heat capacity. Thus all PAS amplitude plots have their scale set by β_B. The PAS phase angle values are solely determined by r and the sample thermal parameters.

A representative amplitude plot is given in figure 3. From this we see that an f^{-n} dependence with n = 1.00 for 50 Hz and higher is obtained for $r \geq 0.05$ cm. Since we measured n = 1.04 perhaps the lower limit should be extended a bit. PAS phase angle plots are given in figure 4. The curves near r = 0.05 cm appear to fit the data best. To avoid the problem of finding the zero phase setting, values of the phase angle difference between f_1 and f_2 with f_1 = 1000 and 500 Hz and f_2 = 100 and 50 Hz are plotted in figure 5. No value of r yielded a 20° phase change between 50 Hz and 1000 Hz. Roark *et al.* [15] noted in their work that the PAS phase angle changes more rapidly at low frequencies than expected by theory and less rapidly at high frequencies. Perhaps a better number to consider is the phase angle difference between 100 Hz and 1000 Hz. Using $\Delta\phi = \phi_{1000\ Hz} - \phi_{100Hz}$, the experimental value of 7° is obtained at r = 0.03 cm and 0.00015 cm. The value near r = 0.03 cm agrees with the amplitude comparisons. Using this value and the average laser calorimetry result of β_{eff} = 0.00707 cm^{-1} in $\beta_B = \beta_{eff}/(1+2r/\ell)$ where ℓ is the window thickness, we get β_B = 0.0066 cm^{-1} and β_s = 0.0002. Thus about 93% of β_{eff} is due to β_B. Yet the small amount of β_s is enough to make the PAS amplitude dependence to be near to that expected for surface absorption.

3.2 Rosencwaig-Gersho Theory Calculations

The Rosencwaig-Gersho program calculates the combination of eqs. (17) and (21) in ref. 10. The PAS amplitude results are shown in figure 6. All β value plots yielded n = 1.5 in $S = A f^{-n}$. The PAS phase angle calculated between 1 Hz and 10 kHz varied only between 45.04° and 45.00° in all cases. Thus a predominantly bulk-like absorption is predicted which is in direct conflict with experimental results.

The Rosencwaig-Gersho theory assumes a completely homogenous sample. To take into account the effects of a surface layer representing the AR coating a two-layer Rosencwaig-Gersho theory was developed [13]. Calculations based on it are discussed in the following paper.

4. Conclusion

Photoacoustic chopping frequency variation studies on AR coated ZnSe windows at 10.6 μm yielded PAS signal amplitudes and phase angle information. The signal amplitude had an f^{-n} dependence with n = 1.04. The phase angle variation between 50 Hz and 1000 Hz was 20°; between 100 Hz and 1000 Hz was 7°.

Theoretical calculations using the Bennett-Forman theory indicated that $r = \beta_{surface}/\beta_{bulk} = 0.03$ cm seemed to fit the data best. Using this value with laser calorimetry results of an average $\beta_{eff} = 0.00707\ cm^{-1}$ for these samples, a value of $\beta_B = 0.0066\ cm^{-1}$ and $\beta_s = 0.0002$ was obtained.

The homogenous sample Rosencwaig-Gersho theory predicted n = 1.5 for the amplitudes and almost no phase angle changes. Thus a two-layer Rosencwaig-Gersho theory was developed.

5. Acknowledgments

This work was supported by the Air Force Materials Laboratory, Wright-Patterson Air Force Base, Ohio.

6. References

[1] Bell, A.G., Am. J. Science 3rd Series 20, 305 (1880); Phil. Mag. Series 5, 11, 510 (1881).

[2] Rosencwaig, A., Physics Today 28 (9) (Sept. 1975).

[3] Rosencwaig, A., Analytical Chemistry 47 (6) 592A (May 1975).

[4] Rosencwaig, A., Rev. Sci. Inst. 48, 1133 (1977).

[5] King, A.A. and Kirkbright, G.F., Laboratory Practice 25 (6) 377 (1976).

[6] Munroe, D.M. and Reichard, H.S., Am. Laboratory 9 (2) 119 (Feb 1977).

[7] Harshbarger, W.R. and Robin, M.B., Accts. Chem. Res. 6, 329 (1973).

[8] "Optoacoustic Spectroscopy and Detection", edited by Yoh-Han Pao (Academic Press, NY, 1977).

[9] Rosencwaig, A., p. 207ff in "Advances in Electronics and Electron Physics, Vol. 46" edited by L. Marton (Academic Press, NY, 1978).

[10] Rosencwaig, A. and Gersho, A., J. Appl. Physics, 47, 64 (1976).

[11] Bennett, H.S. and Forman, R.A., J. Appl. Phys. 48, 1432 (1977) and references therein.

[12] Fernelius, N.C., Appl. Optics, 18, 1784 (1979).

[13] Fernelius, N.C., J. Appl. Phys., 50, (Oct. 1979).

[14] Fernelius, N.C., submitted to J. Appl. Phys.

[15] Roark, J.C., Palmer, R.A., and Hutchison, J.S., Chem. Phys. Lett. 60, 112 (1978).

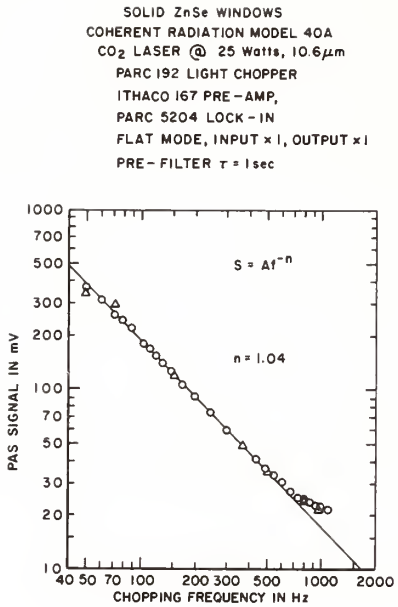

Figure 1. Photoacoustic signal amplitude versus chopping frequency on ZnSe laser windows using a 10.6 μm CO_2 laser source at 25 watts.

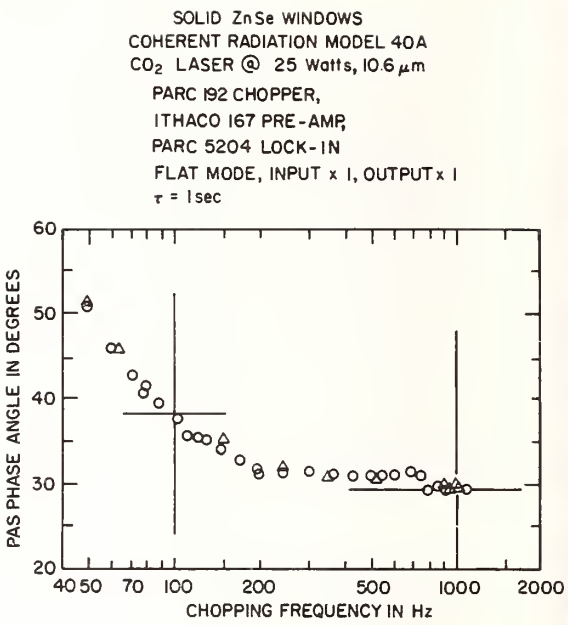

Figure 2. Photoacoustic phase angle versus chopping frequency on ZnSe laser windows using a 10.6 μm CO_2 laser source at 25 watts.

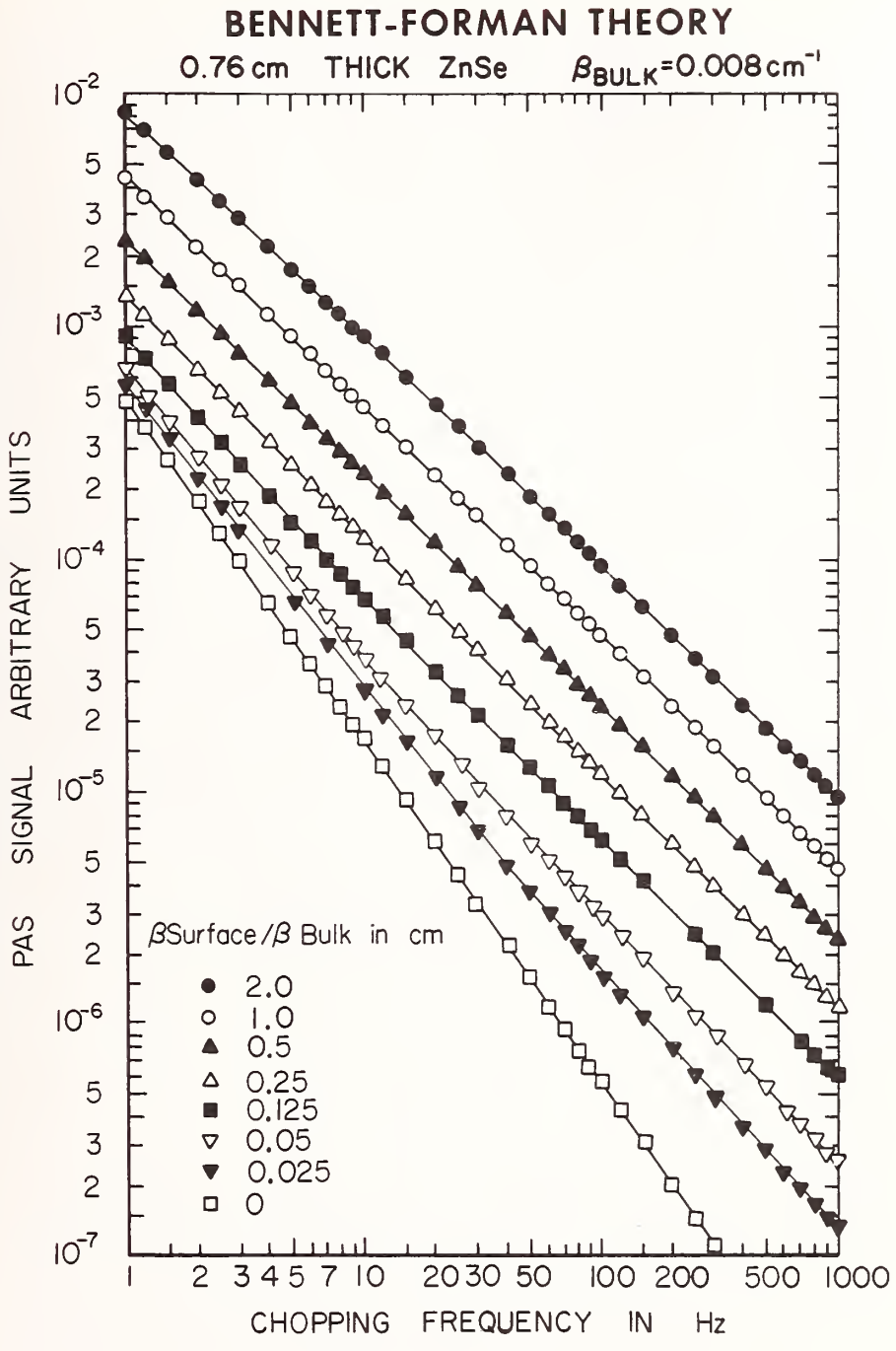

Figure 3. Theoretical PAS signal amplitude versus chopping frequency for a 0.76 cm thick ZnSe sample with β_{bulk} = 0.008 cm^{-1} for various $\beta_{surface}/\beta_{bulk}$ ratios using the Bennet-Forman theory.

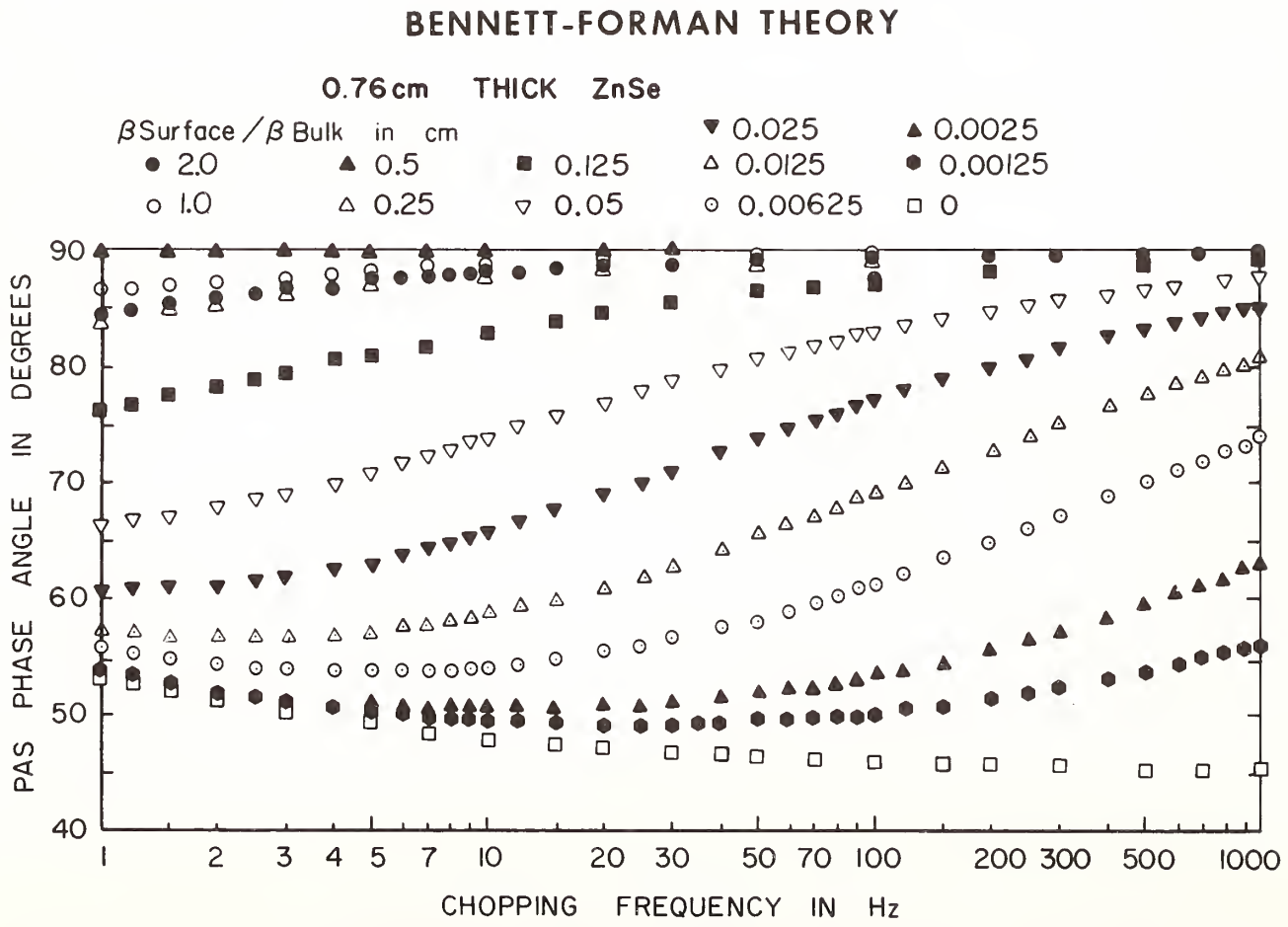

Figure 4. Theoretical PAS phase angle versus chopping frequency for a 0.76 cm thick ZnSe sample for various $\beta_{surface}/\beta_{bulk}$ ratios calculated using the Bennett-Forman theory.

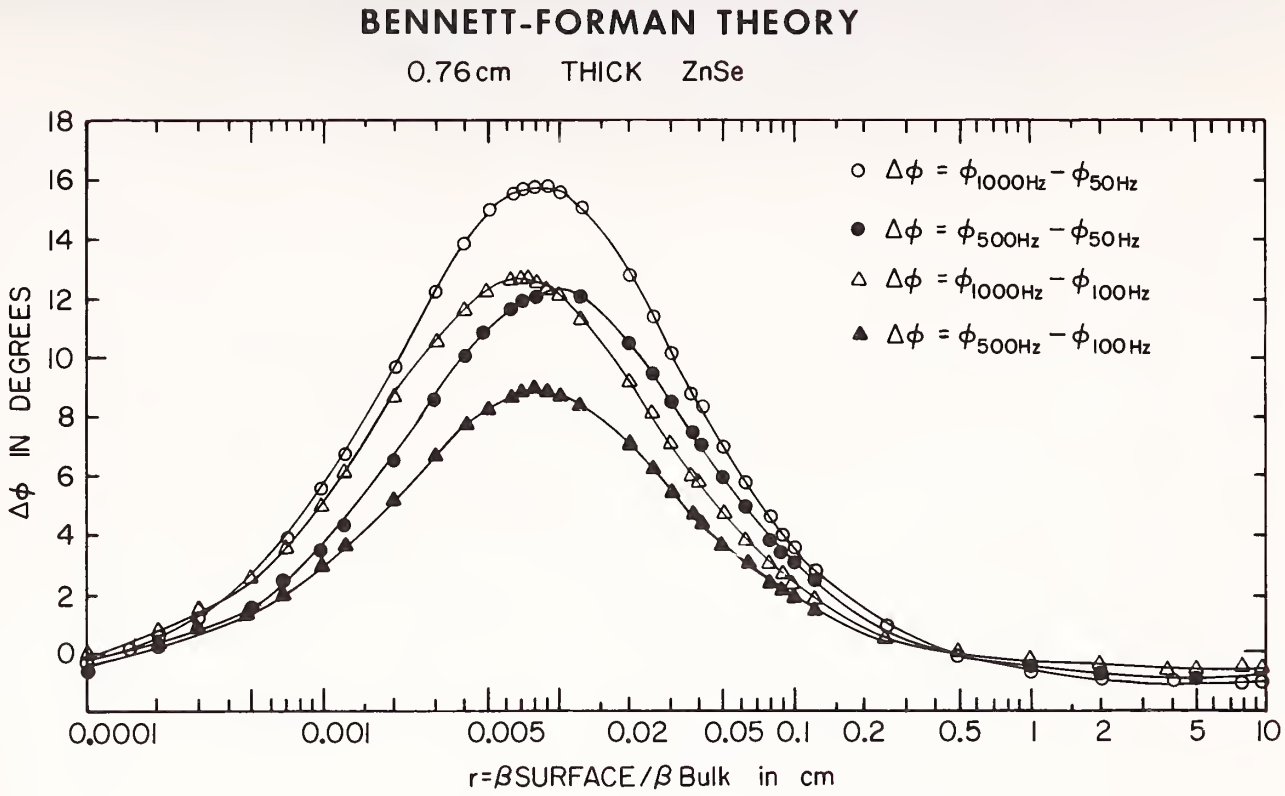

Figure 5. Calculated PAS phase angle differences versus $r = \beta_{surface}/\beta_{bulk}$ using the Bennett-Forman theory on a 0.76 cm thick ZnSe sample.

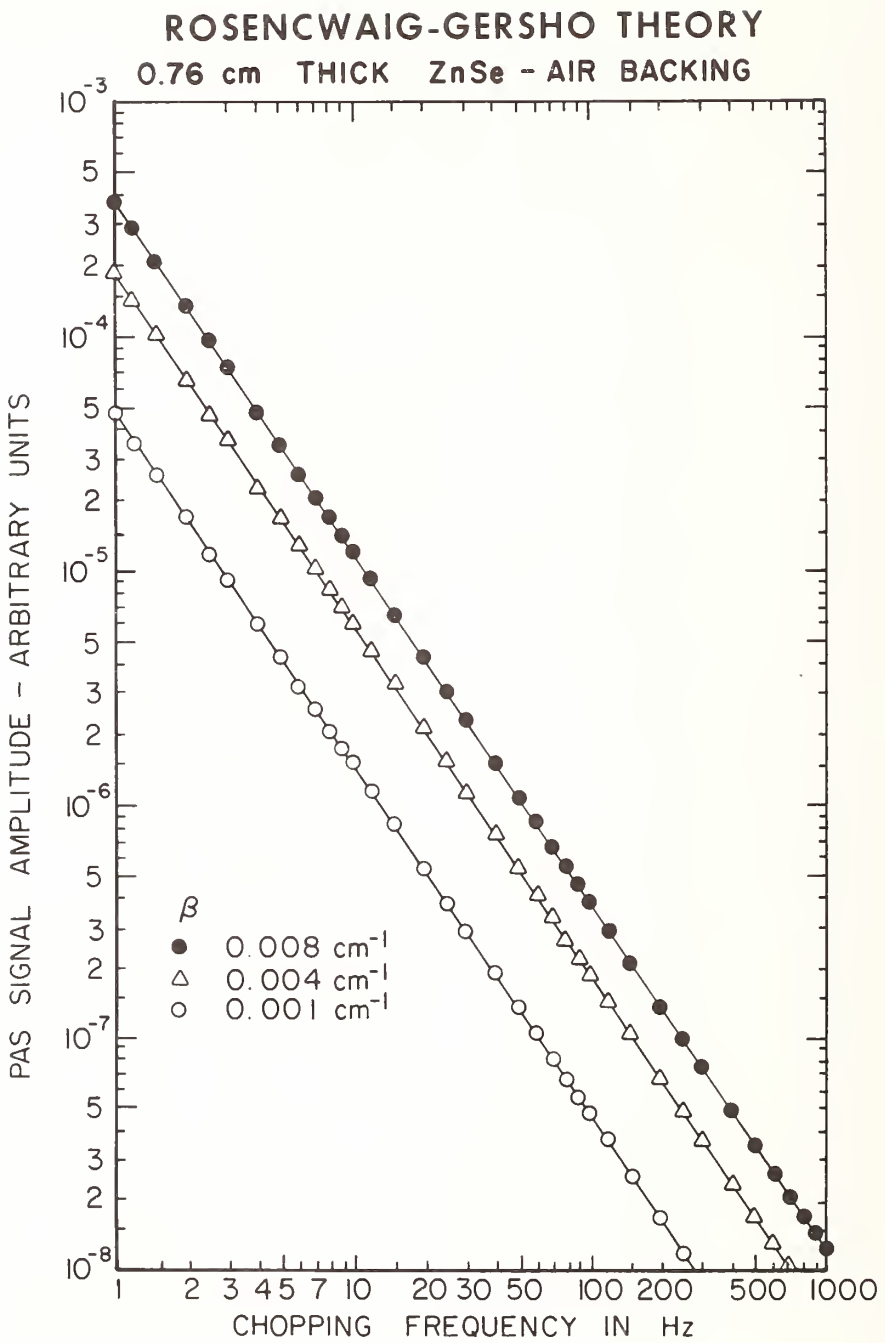

Figure 6. PAS signal amplitude versus chopping frequency calculated using the Rosencwaig-Gersho theory on a 0.76 cm thick ZnSe sample with air backing.

CALCULATIONS USING A TWO-LAYER ROSENCWAIG-GERSHO PHOTOACOUSTIC SPECTROSCOPY THEORY APPLIED TO AN ANTI-REFLECTIVE COATED LASER WINDOW

Nils C. Fernelius
University of Dayton Research Institute
Dayton, Ohio 45469

The ZnSe laser window studied experimentally had an AR coating consisting of a ZnS outer layer 0.32 μm thick with a ThF_4 inner layer 0.99 μm thick. Laser calorimetry experiments at 10.6 μm on other samples indicated that ThF_4 films have an appreciable optical absorption of ∿10 cm^{-1}.

Calculations were performed using a two-layer modification of the Rosencwaig-Gersho photoacoustic spectroscopy theory. A 7° phase change between 1000 Hz and 100 Hz was obtained for a coating bulk absorption of β_c = 2.7 cm^{-1}. Plots of this result along with the best fit using the Bennett-Forman theory in the previous abstract give similar amplitude and phase results. Examples of results for various β_c and coating thickness results are given.

Key words: Bulk optical absorption coefficient; optoacoustic spectroscopy; photoacoustic spectroscopy; surface optical absorption coefficient; ThF_4; ZnSe

1. Introduction

Calculations using the Rosencwaig-Gersho [1][1] photoacoustic spectroscopy (PAS) theory assumed the window to be pure ZnSe. Experimental results on an AR coated window disagreed significantly with the calculated results. As a first approximation to the real world, the AR coating is treated as a single layer with optical and thermal properties different from the substrate. A two-layer Rosencwaig-Gersho theory [2] was developed to handle this case. Mandelis *et al.* [3] have made a similar derivation. A schematic diagram of the PAS cell is shown in figure 1.

The ZnSe laser windows studied experimentally had an AR coating consisting of a ZnS outer layer 0.32 μm thick with a ThF_4 inner layer 0.99 μm thick. Conventional laser calorimetry experiments on samples with single coatings on ZnSe substrates indicate that at 10.6 μm some ThF_4 coatings have a bulk optical absorption coefficient, $\beta_B \sim 10$ cm^{-1}, and some ZnS coatings have $\beta_B \sim 15$ cm^{-1} [4]. If these values are applicable to our samples, then the ThF_4 layer would have an absorbance of $\beta_B \ell \sim 0.001$ and the ZnS layer would have $\beta_B \ell \sim 0.0005$. Laser rate calorimetry on our samples found an average β_{eff} of 0.00707 cm^{-1}. Assuming this is all bulk absorption in the substrate, then the substrate absorbance would be $\beta_B \ell \sim 0.007(0.76) \sim 0.005$. This shows that using the quoted β_B values the absorbance of the coatings would be an appreciable fraction of the substrate, at least 30%.

[1] Figures in brackets indicate the literature references at the end of this paper.

While a three layer sample treatment would be the proper way to treat this problem, the expressions for a two layer sample are already so complex that it was decided to use a two layer model as a first approximation to the experimental situation. The equations in the two-layer model are already about three times longer than the homogeneous Rosencwaig-Gersho results which were rather complicated. The absorbance of the ThF_4 layer is about twice that of the ZnS layer. The thermal conductivity of ZnS is 0.167 W/cmK which is about three times greater than the best estimate for that of ThF_4. Thus as a first approximation we neglect the absorbance of the ZnS layer and treat it as a thermal short. The layers are considerably thinner than the light wavelength so multiple reflection and interference effects do not occur.

2. Calculations

A complex number FORTRAN IV computer program was written to calculate equations (48) and (49) of reference 2. The outer layer was assumed to be ThF_4 on a ZnSe substrate 0.76 cm thick. In order to determine how various parameters affected the results, a variety of values were used. Calculations were made with substrate β = 0.008, 0.004 and 0.001 cm^{-1}. Results were obtained for thicknesses of the ThF_4 layer of h = 0.1, 0.2, 0.5, 1 and 2 μm and for bulk optical absorption coefficients of β_c = 20, 10, 5 and 1 cm^{-1}.

Examples of how these parameters affect amplitude and phase angle trends are given in figures 2-5. In figure 2 the outer ThF_4 layer is taken to be 1 μm thick. Plots are shown for the coating optical absorption coefficient of β_c = 1, 5, 10 and 20 cm^{-1} for the three substrate β values. When β_c = 1 cm^{-1} the differences in the substrate β values are readily apparent at low chopping frequencies. As β_c becomes larger, the coating absorption dominates the signal. The phase angle plots show almost bulk like absorption at low chopping frequencies for β_c = 1 cm^{-1} and β = 0.008 cm^{-1}. Again as β_c increases the phase lag approaches 90° over a larger range of the frequencies. Figure 3 shows similar results for h = 0.5 μm. In figure 4, h = 0.1 μm which is thin enough to exhibit considerable substrate effects even for β_c = 20 cm^{-1}. Figure 5 keeps the coating optical absorption at β_c = 5 cm^{-1} and varies the coating thickness. In this case for h = 0.1 μm strong substrate effects are seen while for h = 2 μm the coating provides most of the signal. Thus we see that for low β_c and small h values, the system resembles the substrate. For large β_c and h, the coating provides most of the signal.

Since h = 1 μm corresponds to the ThF_4 thickness in the coating, a number of calculations were made using that value and varying β_c. From these results a plot of $\Delta\phi = \phi_{1000Hz} - \phi_{100Hz}$ was made versus β_c. See figure 6. The experimental value of $\Delta\phi$ = 7° was obtained at β_c = 3 cm^{-1} for β = 0.008 cm^{-1}; β_c = 1.5 cm^{-1} for β = 0.004 cm^{-1} and at β_c = 0.38 cm^{-1} for β = 0.001 cm^{-1}.

If we assume that there is no surface or interface absorption, i.e. that all the optical absorption is due to the bulk ThF_4 layer and the bulk ZnSe substrate, then we can compare with the average β_{eff} = 0.00707 cm^{-1} measured by laser rate calorimetry. From the results in the previous paragraph we estimate the best fit to be β = 0.007 cm^{-1} and $\beta_c \simeq 2.7$ cm^{-1}. Using these values we get $\beta_{eff} = \beta + 2\beta_c h/\ell$ = 0.0077 cm^{-1} which is in good agreement with experimental results. Since $\beta_c h$ is not providing the dominant contribution in this region, we might take its value to be 2.7 cm^{-1} and subtract that from the measured β_{eff} to estimate β more precisely, i.e. β = 0.0071 - 0.0007 = 0.0064 cm^{-1}.

This compares with the best estimate of β_B for ZnSe using the Bennett-Forman theory in the previous paper which gave $\beta_B = 0.0066\ cm^{-1}$.

Fitting the PAS amplitude dependence to f^{-n} for $h = 1\ \mu m$, $\beta_c = 5\ cm^{-1}$ and $\beta = 0.008\ cm^{-1}$, a value of $n \simeq 1.04$ was obtained which is in exact agreement with the experimental value. Further details of this work have been given elsewhere [5].

3. Conclusion

A two-layer sample modification was made of the Rosencwaig-Gersho photoacoustic spectroscopy theory. Calculations using it were applied to the model of a ThF_4 coating on a ZnSe substrate made to approximate some AR coated windows measured experimentally by laser rate calorimetry and by photoacoustic chopping frequency variations. In addition some calculations were made to see how changing certain parameters affected the PAS amplitude and phase angles. For $\Delta\phi = \phi_{1000Hz} - \phi_{100Hz} = 7°$, the best values seemed to be $\beta_c = 2.7\ cm^{-1}$ and $\beta = 0.0064\ cm^{-1}$. This gave an $n \simeq 1.04$ in the f^{-n} amplitude dependence. Plots of these values along with the experimental results and the best fits using the Bennett-Forman theory in the previous paper are given in figures 7 and 8. The arbitrary amplitude and phase angle in the theory were chosen to agree with experiment at 100 Hz. The amplitude plots, figure 7, seem to be in excellent agreement below 700 Hz. Above 700 Hz the tail of a Helmholtz resonance in the cell [6] around 2 kHz distorts the experimental data. The two theories provide similar PAS phase angle results, as seen in figure 8, but both theories differ somewhat from the experimental results. These differences have also been noted by other researchers [7].

4. Acknowledgments

This work was supported by the Air Force Materials Laboratory, Wright-Patterson Air Force Base, Ohio 45433.

5. References

[1] Rosencwaig, A. and Gersho, A., J. Appl. Physics, 47, 64 (1976).

[2] Fernelius, N.C., J. Appl. Phys., 50 (Oct. 1979).

[3] Mandelis, A., Teng, Y.C., and Royce, B.S.A., J. Appl. Phys.

[4] Miles, P.A., Hopson, J.E. and Beauchamp, pp. 258-270 in *Proc. of the High Power Laser Optical Components and Component Materials Meeting, 1977*, editors J.S. Harris and C.L. Strecker.

[5] Fernelius, N.C., submitted to J. Appl. Phys.

[6] Fernelius, N.C., Appl. Optics, 18, 1784 (1979).

[7] Roark, J.C., Palmer, R.A. and Hutchison, Chem. Phys. Lett. 60, 112 (1978).

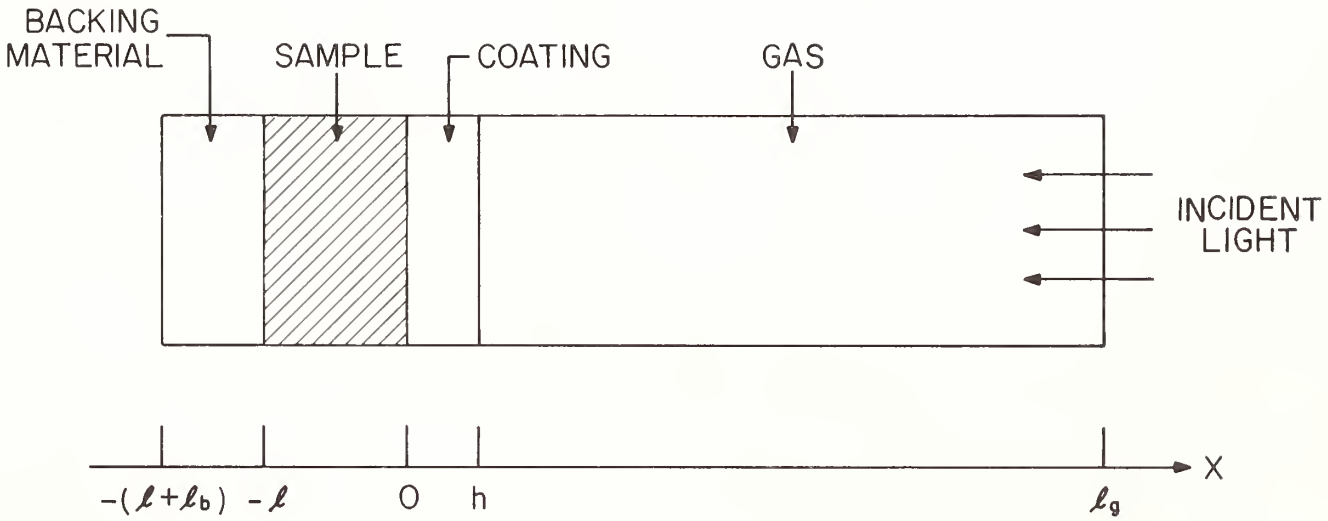

Figure 1. Model of PAS cell used in the two-layer Rosencwaig-Gersho theory.

TWO LAYER ROSENCWAIG-GERSHO THEORY
COATING THICKNESS, h = 1 μm
VARY OPTICAL ABSORPTION COEFFICIENT, β_c

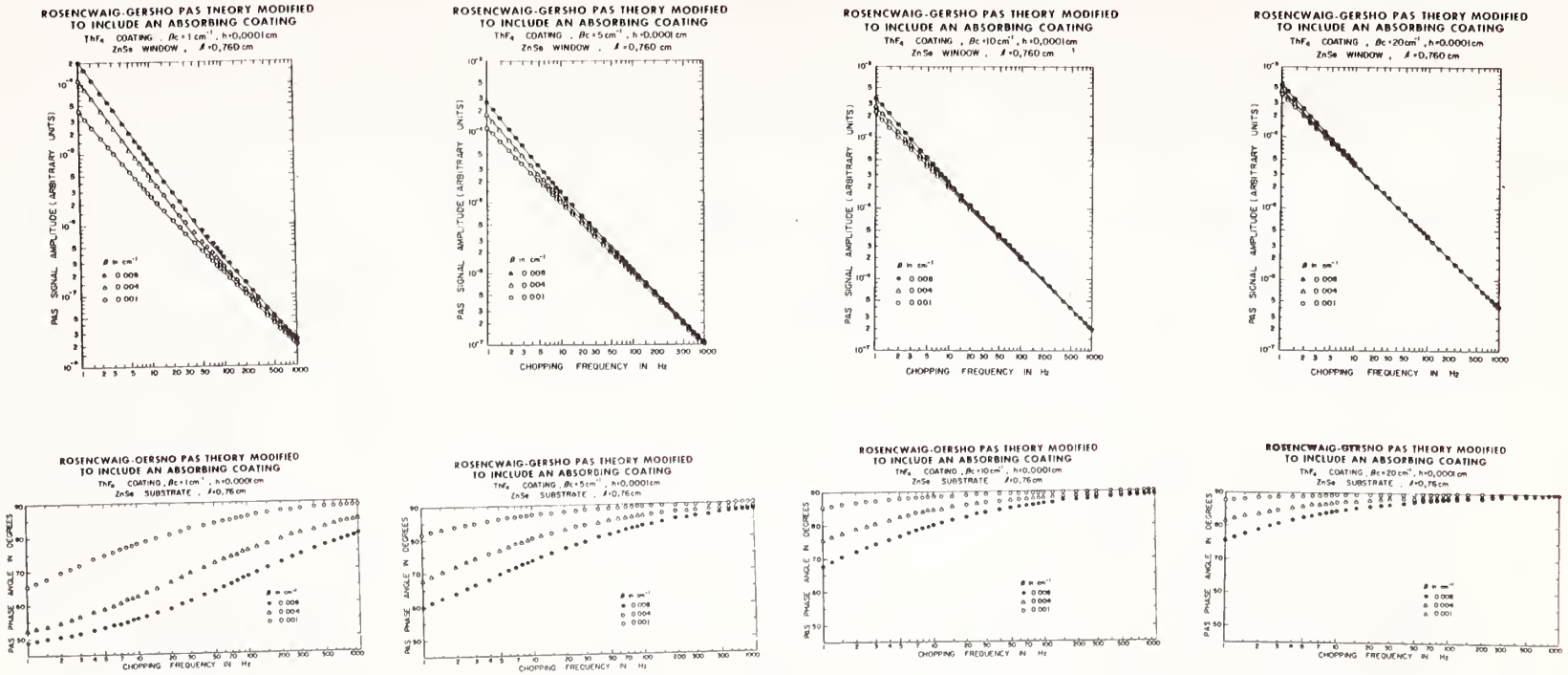

Figure 2. Calculated PAS amplitude and phase angle versus chopping frequency using the two-layer sample Rosencwaig-Gersho theory. For ThF_4 coating 1 μm thick on 0.76 cm ZnSe. Vary β_c.

TWO LAYER ROSENCWAIG-GERSHO THEORY
COATING THICKNESS, h = 0.5 μm
VARY OPTICAL ABSORPTION COEFFICIENT, β_c

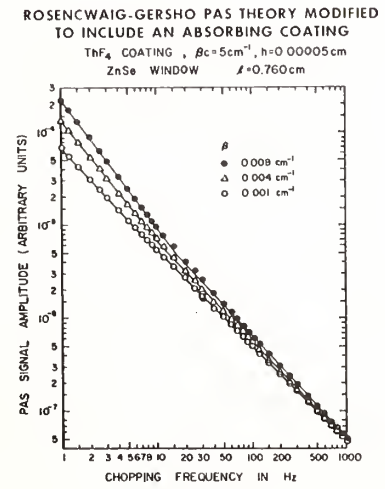

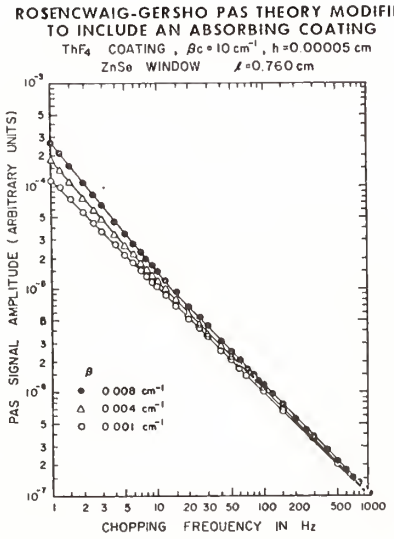

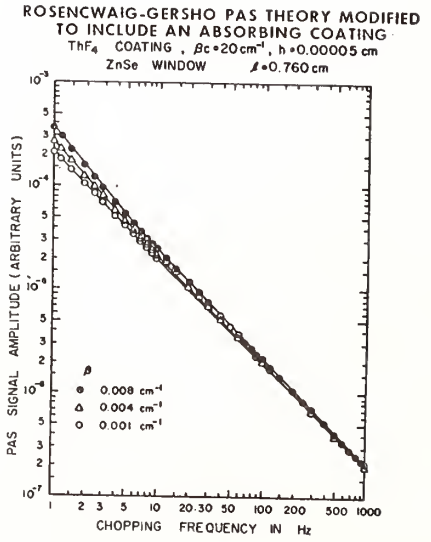

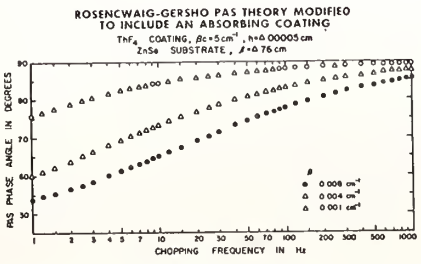

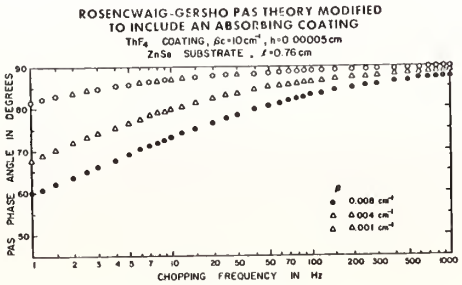

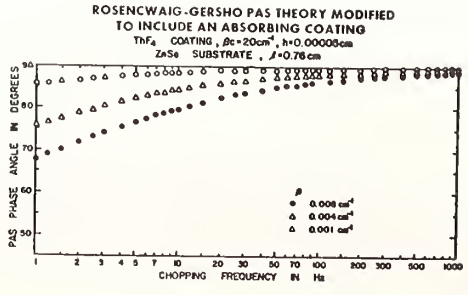

Figure 3. Calculated PAS amplitude and phase angle versus chopping frequency using the two-layer sample Rosencwaig-Gersho theory. For ThF_4 coating 0.5 μm thick on 0.76 cm ZnSe.

TWO LAYER ROSENCWAIG-GERSHO THEORY

COATING THICKNESS, h = 0.1 μm

VARY OPTICAL ABSORPTION COEFFICIENT, β_c

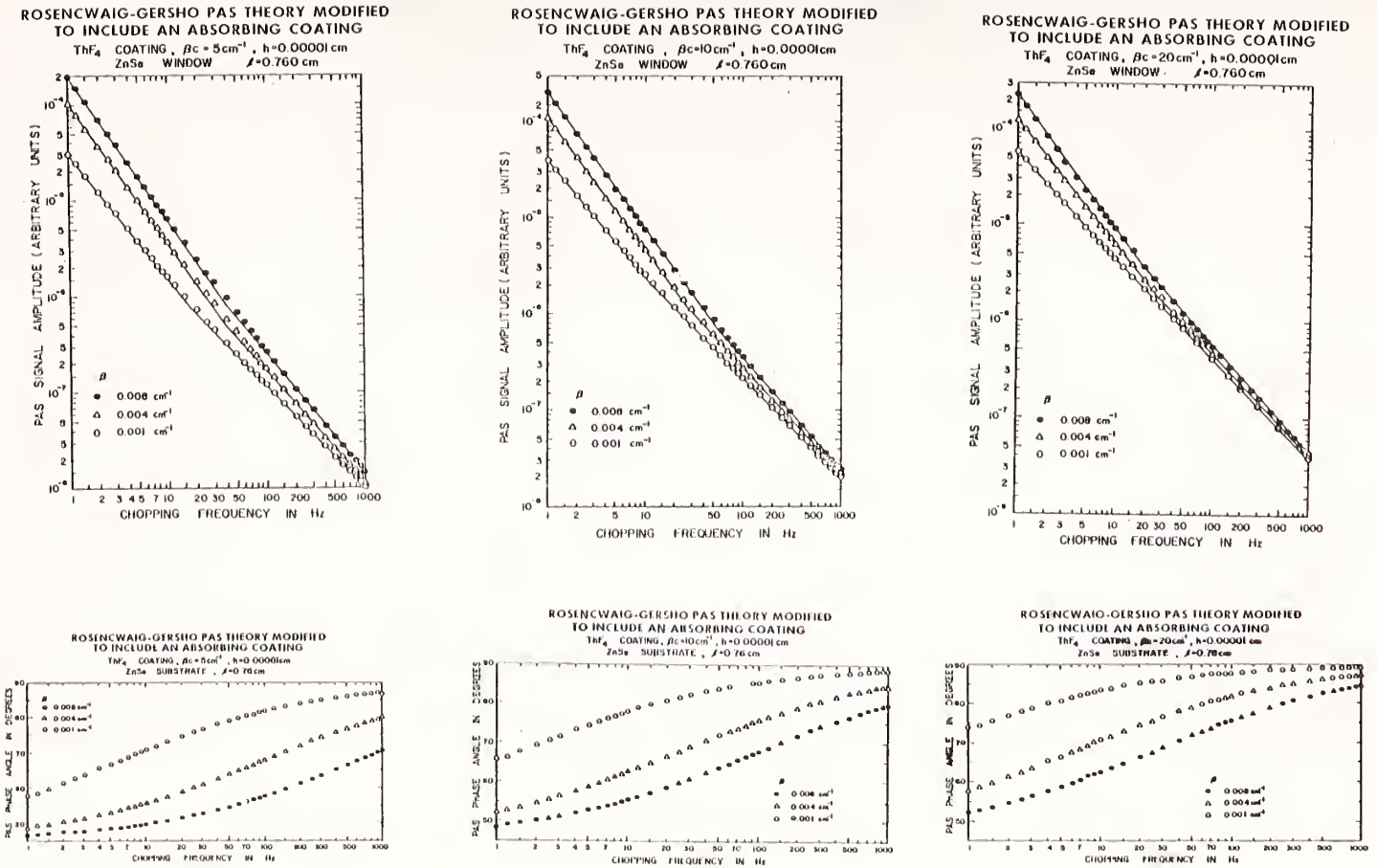

Figure 4. Calculated PAS amplitude and phase angle versus chopping frequency using the two-layer sample Rosencwaig-Gersho theory. For ThF_4 coating 0.1 μm thick on 0.76 cm ZnSe. Vary β_c.

TWO LAYER ROSENCWAIG-GERSHO THEORY
COATING BULK OPTICAL ABSORPTION COEFFICIENT, β_c = 5 cm^{-1}
VARY COATING THICKNESS, h

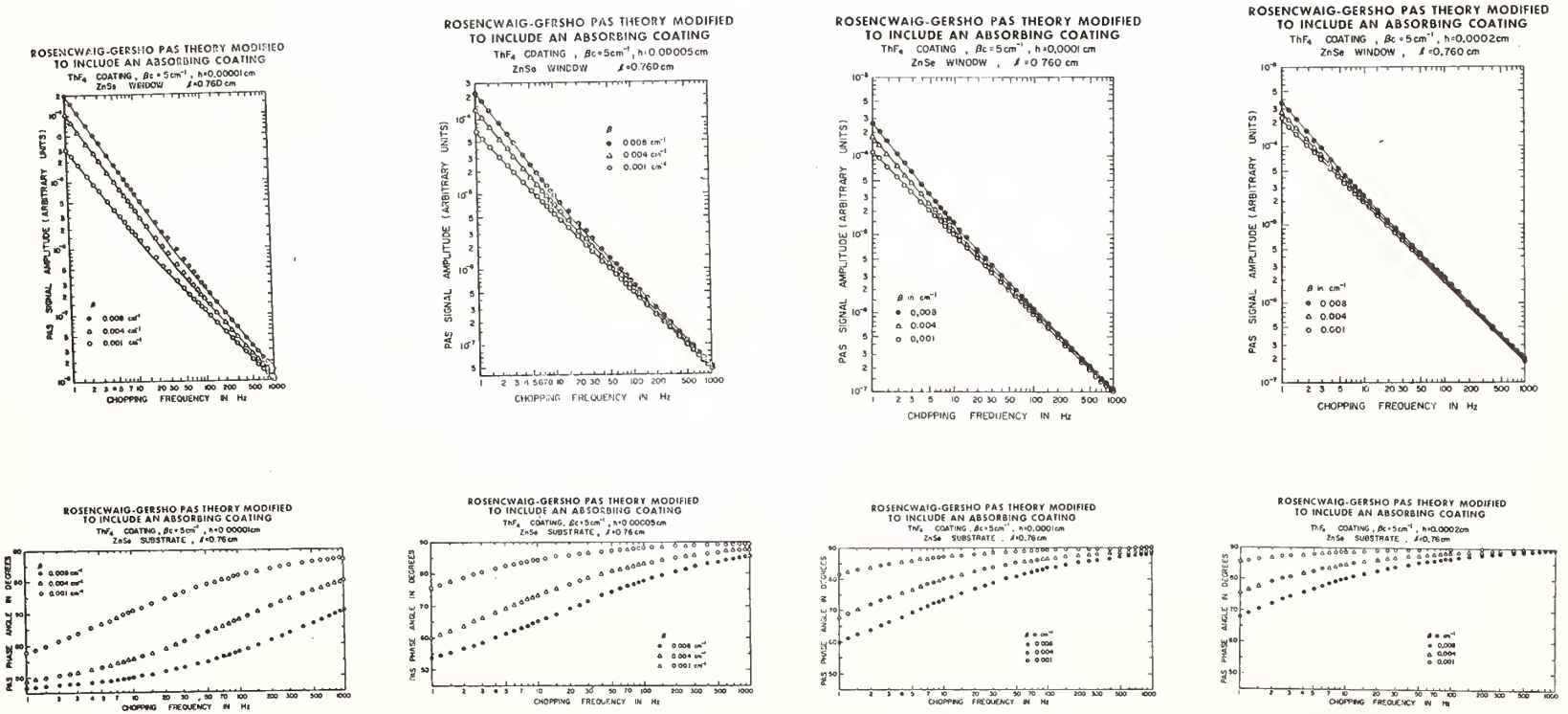

Figure 5. Calculated PAS amplitude and phase angle versus chopping frequency using the two-layer sample Rosencwaig-Gersho theory. 0.76 cm thick ZnSe substrate. ThF_4 coating β_c = 5 cm^{-1}. Vary thickness h.

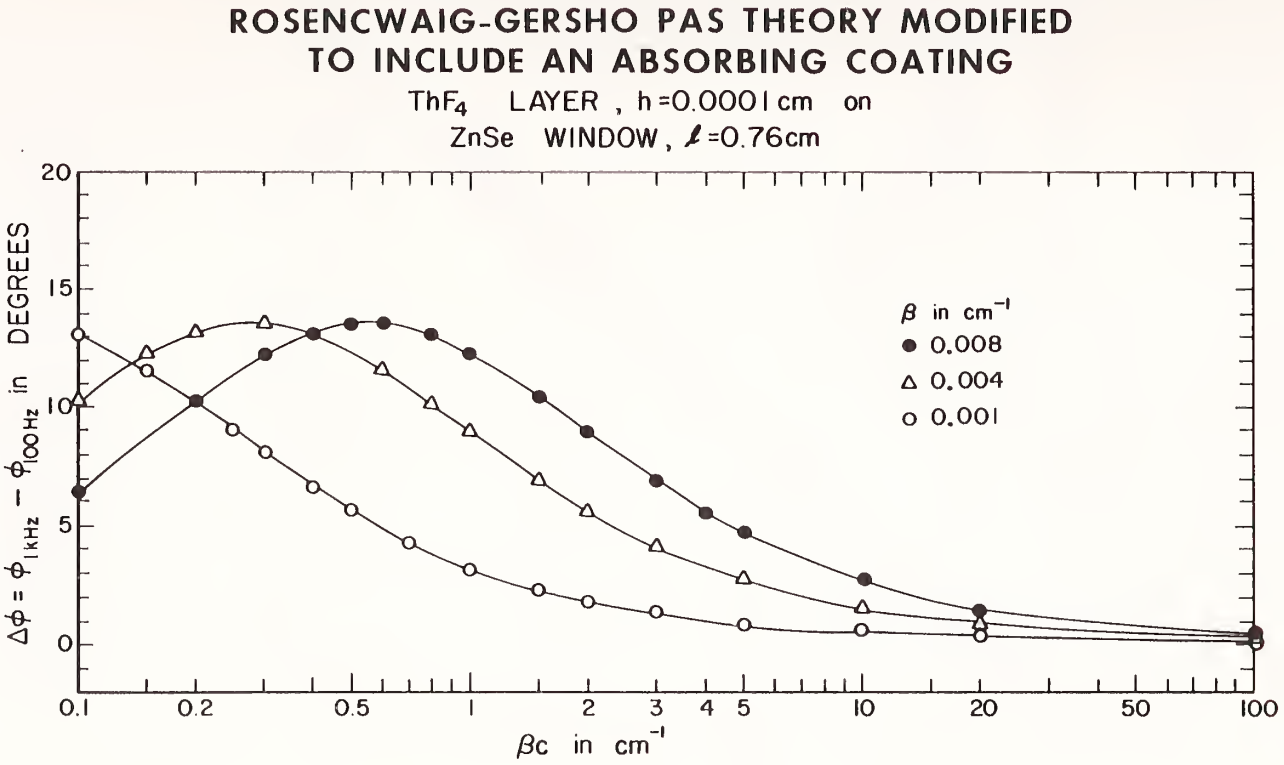

Figure 6. $\Delta\phi = \phi_{1kHz} - \phi_{100Hz}$ versus β_c calculated using the two-layer sample Rosencwaig-Gersho theory on a ThF_4 coating with h = 1 μm and ZnSe substrate with ℓ = 0.76 cm.

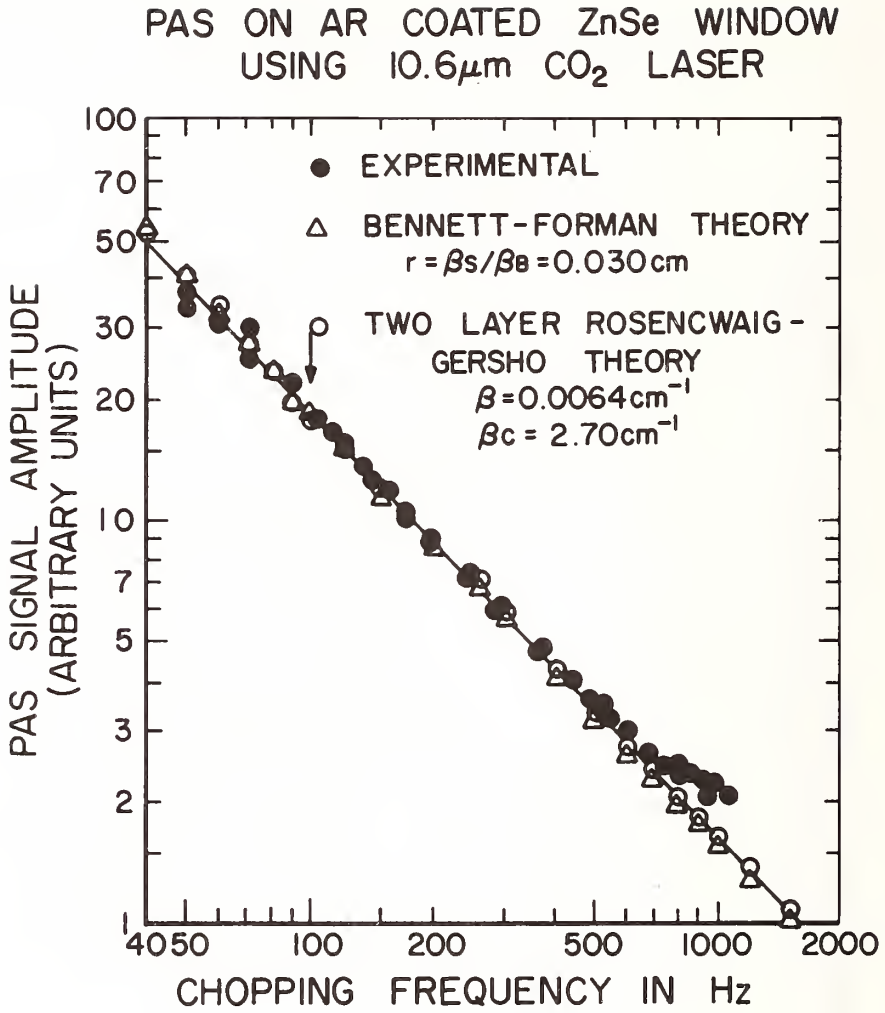

Figure 7. Plots of PAS signal amplitude versus chopping frequency for experimental data and best values of Bennett-Forman and two-layer sample Rosencwaig-Gersho theories on coated ZnSe windows.

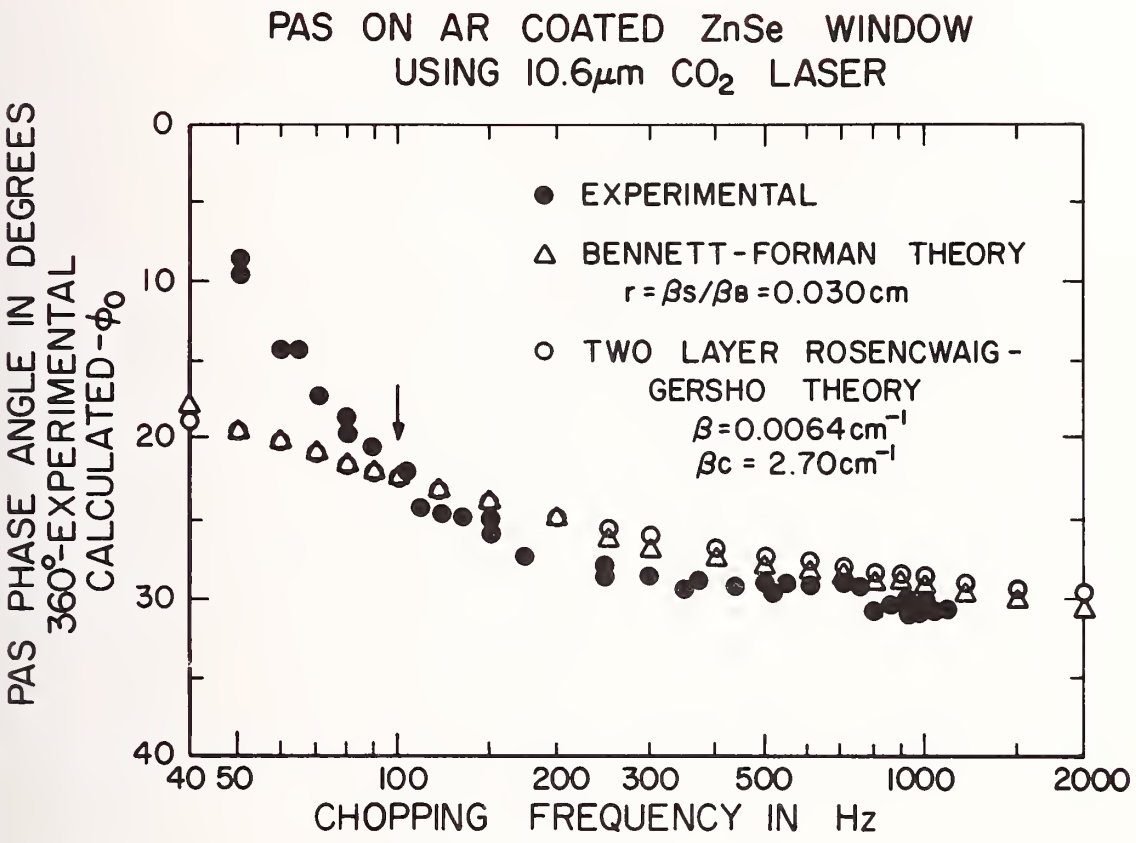

Figure 8. Plots of PAS phase angle versus chopping frequency for experimental data and best values of Bennett-Forman and two-layer sample Rosencwaig-Gersho theories on coated ZnSe windows.

PRE-PULSE IDENTIFICATION OF LOCALIZED LASER DAMAGE SITES IN THIN FILMS USING PHOTOACOUSTIC SPECTROSCOPY*

Robert P. Freese and Kenneth J. Teegarden
University of Rochester, Institute of Optics
Rochester, New York 14627

Scanning photoacoustic spectroscopy techniques were used to monitor optical absorption and inhomogeneity in thin films and substrates. Samples examined were 25 mm square by 2.5 mm thick germanium substrates which were partially coated with a thin film of germanium. Inter-sample thin film thicknesses varied from .65 um to 1.23 um. Raster scans made at 10.6 um using a 75 mW CO_2 laser indicate that thin film and substrate inhomogeneities as well as optical absorption may be nondestructively measured at rates in excess of 400 msec per resolution point. Average absorptance results are in good agreement with those obtained by laser calorimetry and transmission techniques. Chopping frequency studies indicate that some of the inhomogeneities are subsurface. Interference effects detected photoacoustically are used to compute the skew angle between the front and back surfaces. When the sample is exposed to a 40 nsec (FWHM) CO_2 laser pulse focused to a spot size of 3.5 mm, gross laser damage is found to occur where the interference effects were photoacoustically detected. An excellent correlation is also found to exist between the location of structure in the pre-damage photoacoustic mapping of the coated optic, and the location of isolated, low damage threshold "hot spots" found after the high power pulse irradiation.

Key words: Absorption; Ge; laser damage; optoacoustic spectroscopy; photoacoustic spectroscopy; thin films.

1. Introduction

Studies conducted on thin films indicate that, for long (>nsec) pulses, laser induced damage is extrinsic in nature and may be attributed to cracks, pores, defects, impurities, or other localized inhomogeneities [1,2][1]. However, the origin, identity, and control of these inhomogeneities is not well understood. One major hindrance is the lack of suitable nondestructive diagnostics which could detect localized thin film and substrate inhomogeneities and aid in their identification.

Recently, photoacoustic spectroscopy (PAS) has been shown to be a valuable tool in the investigation of highly transparent solids [3]. Kerr [4] and others [5] have demonstrated that absorptances on the order of 10^{-4} to 10^{-5} could be detected using PAS. Wong, et. al. [6], have recently shown that both surface and subsurface structure could be monitored with photoacoustic spectroscopy. Others [7] have used PAS to distinguish surface from bulk absorption in laser window materials.

* Work supported by the U. S. Department of Energy under Grant EY-76-S-02-4056*000

1. Figures in brackets indicate the literature references at the end of this paper.

In this work, we apply photoacoustic techniques to the study of absorption, inhomogeneity, and laser damage in thin films and substrates. Two dimensional raster scans were obtained from several coated germanium flats and indicate that thin film and substrate inhomogeneities as well as absorption and interference effects may be nondestructively monitored using this method. Laser damage threshold measurements were also performed on these samples using a 40 nsec (FWHM) 3.5 mm diameter CO_2 laser. Results to date suggest that a strong relationship may exist between the shape of the photoacoustic signal and the local damage threshold.

2. Generation of the Photoacoustic Effect

The photoacoustic effect refers to the generation of sound through the interaction of light with matter. Observation of the effect is typically accomplished by placing a sample in a specially designed (acoustically resonant or non-resonant) enclosed cell and illuminating the sample with amplitude modulated radiation. Light which is absorbed by the sample and converted into heat will create an intermittent flow of heat into the surrounding buffer gas, normally air. The resultant temperature fluctuation of the gas gives rise to a pressure fluctuation, i.e. the photoacoustic signal, whose phase and amplitude may be detected with a sensitive microphone and lock-in amplifier. Since the acoustic signal is directly related to the amount of heat transferred to the buffer gas, detection of the photoacoustic effect allows one to nondestructively extract information regarding the physical, thermal, and optical properties of the sample.

An alternative method of photoacoustic detection frequently employed involves the measurement of the elastic waves generated in the sample itself. In this method, a transducer is bonded directly to the sample, thus eliminating the need for a photoacoustic cell.

Several quantitative theoretical analyses of the photoacoustic effect have been recently published [8,9,10]. Most models treat the problem as a one dimensional heat flow analysis in the various sample, gas, and window regions of the cell. In general, these treatments are lengthy and will not be reproduced here. In the interest of giving the reader physical insight into the capabilities of the photoacoustic method, however, we present some of the more important results obtained from these investigations.

For a highly transparent ($\beta\ell \ll 1$), thermally thick ($d \ll \ell$) sample, the photoacoustic signal,S, is related to the following parameters: β, the optical absorption coefficient (cm^{-1}); d, the thermal diffusion length (cm); P, the average incident light power (W); and V, the irradiated volume of the sample. ℓ is the physical thickness of the sample (cm). In the case under consideration, it should be noted that, neglecting nonlinear absorption and saturation effects, S scales linearly with both β and P. Also, $V \equiv A \times d$, where A is the cross-sectional area of the incident light beam (cm^2). The thermal diffusion length is defined by $d = (K/\pi f \rho C)^{\frac{1}{2}}$, where K is the thermal conductivity of the sample (J/cm sec °C), f is the modulation frequency (Hz), ρ is the physical density of the sample (g/cm^3),and C is the specific heat (J/g °C). It should be noted that d essentially defines the sampling depth of the photoacoustic signal and may be varied by changing the modulation frequency of the light source.

These results may be exploited to nondestructively study both optical absorption and inhomogeneities in bulk and thin film materials. For example, if one mounted a perfectly homogeneous sample in an ideal photoacoustic cell (nonabsorbing gas; nonabsorbing, homogeneous window; nonabsorbing cell walls) and recorded the photoacoustic signal as a function of position, one would expect the magnitude of the signal to be everywhere constant. However, if the sample contained any spatially varying inhomogeneities within the diffusion length of the material, the signal would be altered. In particular, if the inhomogeneity were a scratch, void, pore, or other refractive index variation, the irradiated volume and possibly other photoacoustic parameters could be significantly

changed. Absorption or impurity sites would affect the amount of light absorbed. Various other physical, thermal, or optical defects (such as density) may also modify an important photoacoustic parameter. The net effect of any one or combination of these inhomogeneities would be, in general, to alter both the phase and magnitude of the photoacoustic signal. The spatial location of the defect could be found using focused beam scanning techniques. Its depth penetration might be found by changing the modulation frequency (and thus changing d). Impurities could be distinguished from pores using spectral analysis. Also, thin film effects might be distinguished from bulk effects by comparing the thin film photoacoustic signal to a substrate reference, or by scanning the substrate before and after thin film deposition.

3. Samples

The samples investigated in this study consisted of 25 mm square by 2.5 mm thick optical grade germanium sugstrates obtained from Eagle Pitcher Industries. The samples were polished flat to within $\lambda/80$ at 10.6 μm over the whole surface. The substrates were then cleaned with acetone and ethanol, and partially coated with a thin film of germanium at the Institute of Optics. Thin film deposition was accomplished using a resistance source in a conventional vacuum chamber. Thin film thicknesses were monitored during deposition using a calibrated Inficon crystal monitor. Sample to sample coatings varied from .65 μm to 1.23 μm. Care was taken to preserve clean and dust free surfaces at all times. However, it should be mentioned that polishing, cleaning, and thin film deposition procedures have not been necessarily optimized for these studies, and have been included for the sake of completeness. One should also note that the germanium on germanium samples were chosen primarily for demonstration and theoretical purposes. Nevertheless, these samples may be thought of as representative of substrate and thin film laser window materials encountered in infrared applications.

4. Photoacoustic Scanning Apparatus

A block diagram of the photoacoustic scanning apparatus is shown in figure 1. The light source consisted of an axial flow CO_2 laser operating in a single longitudinal mode (SLM) at 10.6 μm capable of providing 250 mW in the TEM_{00} mode. Amplitude modulation of the source was provided by a variable speed chopper, whose frequency could be varied from 10 Hz to 2 KHz. After passing through a NaCl beamsplitter, the beam was focused onto the mounted photoacoustic sample with the aid of an f/2 19 cm focal length Al coated front surface mirror. Registration of the CO_2 laser beam was accomplished using a collinear HeNe alignment laser. CO_2 laser power fluctuations were monitored with a Molectron P-3 pyroelectric detector.

A diagram of the photoacoustic cell, which was optimized for these experiments, is shown in figure 2. The interior dimensions of the cell were 12.7 mm in diameter by 1.4 mm thick. The microphone chamber and cell were connected by an 11 mm by .9 mm diameter channel. The total enclosed volume was approximately 240 mm^3. The cell itself was formed by clamping a Harshaw polycrystalline NaCl window and the sample against gaskets. Alternatively, the window and sample were sometimes sealed onto the cell with optical wax when a greater degree of permanence was desired. Interference effects between the window and sample were avoided by a 5° angle of tilt machined into the cell. Spurious absorption effects from the cell reported by others [11] were reduced by minimizing the cell wall thickness and by choosing the highly reflective metal aluminum for the cell material. Absorption effects from the NaCl were minimized by placing a brand new window on the cell immediately prior to each scan. Also, both the NaCl window and the cell were kept a few degrees above ambient room temperature to reduce the possibility of hygroscopic degradation. Optimization of the photoacoustic effect was accomplished mainly by minimizing the total cell volume. Air was normally used as a buffer gas.

The photoacoustic signal was detected by means of a B&K 4144 2.54 cm condenser microphone. A FET preamplifier provided an electrical gain of 10, thus establishing an overall sensitivity of 50 mV/μbar. The electrical signal was fed into an Ithaco Dynatrac 391A lock-in amplifier capable of tracking reference frequency fluctuations. The photoacoustic signal was normalized to laser power fluctuations by means of the Molectron pyroelectric detector, reference Dynatrac 391 lock-in amplifier, and ratiometer. The output of the ratiometer was displayed on a Honeywell chart recorder. The entire photoacoustic detection system was calibrated using a carbon black opaque sample and displayed a responsivity of 110 mV/W at a modulation frequency of 250 Hz.

Two dimensional raster scans were made using a synchronous motor driven scanner mounted on an Aerotech microprocesser controlled stepper motor translator. The photoacoustic cell was mounted on top of both scanners so that the sample moved while the laser beam remained stationary. In this manner, the angle of incidence of the laser upon the sample could be monitored and kept constant during the complete scan. Finally, both scanners and photoacoustic cell were placed on another Aerotech translator so that the mounted photoacoustic sample could be translated 5 cm to the high power laser damage apparatus without loss of registration. Scanning rates, which were determined mainly by signal to noise considerations, varied from 30 msec to 3 sec per resolution point.

5. CO_2 Laser Damage Facility

A block diagram of the high power laser damage apparatus is shown in figure 3. A Tachisto TAC II Model 215A TEA laser, capable of suppling 500 mJ of 10.6 μm radiation in a 40 nsec (FWHM) gain switched TEM_{00} pulse was employed as the high power laser source. The output of the TEA laser was monitored using several single shot diagnostics. The total pulse energy was measured by directing the Fresnel rear surface reflection of a wedged ZnSe beamsplitter into a calibrated Scientech Model 380-102 calorimeter. Alignment of the front surface reflection into a Rofin 7400 photon drag detecter (600 psec risetime) enabled the detection of the temporal profile. A permanent record of this profile could be made by photographing the trace off a Tektronix 7704A 250 Mhz oscilloscope, which was connected to the photon drag detector by means of a 50 Ω coaxial cable. Spatial profile of the beam was checked using either green liquid crystals, type 107 Poloroid film, and/or Thermofax paper. While the temporal profile of the laser varied somewhat from pulse to pulse, the total energy per pulse was found to be reproducible to $\pm$ 3%. The e^{-2} points of the TEM_{00} gaussian were reproducible to $\pm$ 5% in the short term and agreed well with calculated gaussian beam raytraces.

Alignment and registration of the CO_2 beam were accomplished by means of a collinear HeNe laser beam. Germanium samples reported in this paper were generally tested while still mounted in the photoacoustic cell. The irradiance of the high power CO_2 laser was varied by altering the distance between the sample and an f/10 760 mm focal length gold coated front surface mirror. The focused beam diameters (e^{-2} points) in the tests reported here were 3.5 $\pm$.2 mm.

6. Experimental Results

6.1 Photoacoustic Raster Scans

Two dimensional raster scans have been made on four germanium on germanium samples. Two representative rasters from these scans are shown in figure 4 and figure 5, where the average incident CO_2 laser power was 75 mW, the modulation frequency was 250 Hz, the thermal diffusion length was 213 μm, the lock-in time constant was 400 msec, and the thin film thickness was 1.23 μm. In figure 4, the scanning laser beam was defocussed by .5mm, while figure 5 shows the same scan with the beam brought to a 130 μm focus on the front surface of the sample. Raster scans such as those shown in figures 4 and 5 were highly reproducible providing one scanned along the identical path.

Comparison of the photoacoustic signals obtained from the thin film and substrate sides of the sample reveals that, on the average, the thin film signal is far greater than that of the substrate. Similiar results have been observed in all samples tested thus far. The increase in the average signal may be attributed to the increased absorption coefficient of the thin film in relationship with that of the bulk material. Indeed, knowing the response of the photoacoustic cell and neglecting any window or cell absorptions, it is possible to measure the thin film and substrate absorptances (within the diffusion length of the material) from the expressions:

$$A_{tf} = A_{tfs} - A_s \qquad (6.1\text{-}1)$$

$$A_{tfs} = S_{tfs} / R_o P\ (1\text{-}R_{tfs}) \qquad (6.1\text{-}2)$$

$$A_s = S_s / R_o P\ (1\text{-}R_s) \qquad (6.1\text{-}3)$$

where A is the absorptance, R is the Fresnel reflection coefficient for the first surface, R_o is the responsivity of the photoacoustic cell, and the subscripts tf,tfs,and s stand for thin film alone, thin film and substrate, and substrate alone, respectively. A comparison of the photoacoustically determined absorptances and the values measured prior to the scan using calorimetric and transmission methods is shown in Table 1.

Table 1. Absorptance Measurements

Location	PAS	Calorimetry / Transmission
Thin film "best"	.010 $\pm$ .001	----------
Thin film "ave"	.013 $\pm$ .001	.013 $\pm$ .001
Substrate alone	.007 $\pm$ .001	.008 $\pm$ .002

The good agreement between the photoacoustic and measured absorptances provides support for our initial assumption that cell wall and window contributions could be neglected. Uncertainty in the average photoacoustic measurements is due mainly to uncertainty in the cell responsivity, R_o. It should be mentioned that the ambient noise signal in this particular set of raster scans was $\pm$ 1 μV yielding a signal to noise ratio of approximately 50:1. We also found that the photoacoustic signal was a linear function of power from 30 mW to 120 mW. This indicates that our initial assumption neglecting nonlinear absorption was also justified.

Comparison of figures 4 and 5 demonstrate the improvement in resolution as the scanning laser spot size is reduced. Some of the photoacoustic peaks could be related to obvious surface flaws or scratches. However, many of the peaks occured in locations where no surface feature could be detected, even under the high magnification of a Nomarski or optical microscope. Such features may be related to localized inhomogeneities in the thin film or substrate. Indeed, chopping frequency studies performed on these features reveals that some of the inhomogeneities may be subsurface, as is shown in figure 6. For the top set of data points in figure 6 the photoacoustic signal varied as $f^{-.69}$. This frequency dependence is similiar to results obtained by others [12] for transparent media using a focused beam. In the lower set of data points, the signal varied as $f^{-.73}$ in almost an identical manner to the top set of points. However, at a frequency of approximately 400 Hz,where d=180 μm, the signal suddenly decreased. It remained low for frequencies greater than 400 Hz. We interpret the latter result as an indication of a subsurface inhomogeneity. In the first case, the defect was surface related and must have been at a depth of less than approximately 150 μm. In the second case, the photoacoustic signal dropped to a very low level for diffusion depths less than 180 μm, indicating that the inhomogeneity must have been located at a depth greater

than 180 μm. It should be noted that the vast majority of inhomogeneities investigated turned out to be of the surface variety. It should also be mentioned that, as a whole, there were far more photoacoustic features on the thin film side of the sample. Since one would expect roughly the same number of substrate defects regardless of position, it seems likely that the additional structure is due to thin film (or thin film interface) inhomogeneities.

The raster lines were scanned in a direction perpendicular to the thin film-substrate boundary line. A series of points obtained from these mappings was used to generate two scans in a direction parellel to the thin film-substrate boundary line. Results obtained in this manner for sample #4 are shown in figure 7. Inspection of this graph shows two periodic functions, one on the thin film side and one on the substrate side. While the amplitude of the thin film side is generally higher than its substrate counterpart, the two plots appear to be in phase with one another. Although this result was initially surprising, we believe that it may be attributed to interference effects between the internal incident beam and the Fresnel reflections off of the rear surface. The resultant constructive or destructive electric fields near the front surface give rise to increased (or decreased) absorption, which is detected photoacoustically. A diagram of the physical situation is presented in figure 8. The distance between successive maxima or minima is dictated by the skew angle between the front and rear surfaces, and is a result of the optical thickness of the sample increasing by $\lambda/2$. Using the average value of the spatial frequency, we find the photoacoustically measured angle of wedge to be .039° $\pm$ .003°. We also can predict that the wedge should only be in one direction, since the periodic fluctuations were detected in this direction only. A measured wedge angle of .042° $\pm$ .003° using retroreflection techniques confirmed both these results. It is also interesting to note that, using this analysis, the two periodic functions should be approximately in phase, since the additional optical thickness provided by the thin film is within 4% of exactly $\lambda/2$ at 10.6 μm.

6.2 Laser Damage Results

Sample #4 was left mounted in the photoacoustic cell and translated a known amount over to the laser damage apparatus using the Aerotech translator. The thin film side was then exposed to a CO_2 laser pulse containing a total of 183 mJ in a 3.5 mm diameter (e^{-2}) beam. Plasma formation was noted during the irradiation. A sketch of the resultant damage is shown in figure 9. Although the laser was definately in the TEM_{00} mode, two large (2.7mm by .8mm) elliptical damage sites were found. At these locations, the thin fi was often blown completely away or had partially seperated from the substrate. The positi of these gross damage sites coincided within half a raster width of the interference maxima previously discussed, as is diagrammed in figure 10. Similar results were obtaine in additional damage tests at different locations. This seems to conclusively indicate that the gross damage was mainly a result of the increased local electric field near the front surface. No laser damage was found to occur on the exit surface of the sample.

In addition to the gross damage, we found a number of localized isolated damage sites whose immediate neighborhood seemed to be unaffected by the laser pulse. The sizes of the "hot spots" varied from about 5 μm to approximately 65 μm (counting the cracks sometimes found in the thin film surrounding the site). In some cases, the surrounding thin film appeared to be left intact, while in other cases, the film was cracked and slightly raised from the substrate. The depths of the pits formed at these locations varied from 1 μm to 15 μm.

While the origin of these sites in not clear, an excellent correlation was found to exist between the position of these "hot spots" and the location of structure or peaks in the pre-pulse photoacoustic mapping of the sample. Of the 29 isolated damage sites greater than 5 μm in size, all were found to correlate with photoacoustic structure to within the spot size of the scanning laser. An excellent example is provided by raster scan #30, shown in figure 11, which represents an area located roughly 300 μm from the edge of the nearest gross damage site. All of the thin film peaks have been labeled

lphabetically and a physical description of any surface features seen at these locations nder a Nomarski microscope is given. Nomarski micrographs of some of the corresponding amage sites are presented in figure 12 along with a micrograph of part of the thin film nich was not irradiated with the high power laser. The latter micrograph may be taken s being representative of the thin film surface before damage, and shows scratches nich may have been associated with the polishing process.

It should be noted that while an excellent correlation is obtained between the ocation of photoacoustic peaks and isolated damage sites, there appears to be little elationship between the size of the damage site and the height of the peak. Also, here are more photoacoustic peaks than isolated damage sites, possibly indicating that otential damage sites may not have received sufficient irradiation, or that a localized efect which may have been detected photoacoustically has a threshold comparable to that f the material as a whole.

7. Conclusions

Scanning photoacoustic spectroscopy techniques have been used to monitor optical sorption and inhomogeneity in thin films and substrates at 10.6 μm. Average absorptance esults obtained photoacoustically are in good agreement with those obtained by lorimetric and transmission methods. Chopping frequency studies indicate that some the photoacoustically detected inhomogeneities may be subsurface. Interference fects have also been detected with this method. An excellent correlation has been und to exist between the location of structure in the pre-damage photoacoustic mapping the coated germanium sample and the location of isolated low damage threshold "hot ots" found after the coated optic was exposed to a 40 nsec CO_2 laser pulse.

8. Acknowledgements

The authors would like to gratefully acknowledge the assistance of Herb Graff for lishing the samples and measuring their wedge angles, David Lees for coating the mples, and Luigi Colombo and Pam Freese for assistance with the Nomarski micrographs.

5. References

]. Bloembergen, N., Role of cracks,pores, and absorbing inclusions on laser induced damage thresholds at surfaces of transparent dielectrics, Appl. Opt. 12, 661 (1973).

]. Guenther, A.H. and Glass, A.J., Laser induced damage in optical materials: tenth ASTM symposium, Appl. Opt. 18, 2112 (1979).

]. Hordvik, A. and Schlossberg, H., Photoacoustic technique for determining optical absorption coefficents in solids, App. Opt. 16, 101 (1977).

]. Kerr, E.L.,The alphaphone-a method for measuring thin film absorption at laser wavelengths, Appl. Opt. 12, 2520 (1973).

[5]. McDavid, J.M., Lee, K.L., Yee, S.S, and Afromowitz, M.A., Photoacoustic determination of the optical absorptance of highly transparent solids, J. App. Phys. 49, 6112 (1978).

[6]. Wong, Y.H., Thomas, R.L.,and Hawkins, G.F.,Surface and subsurface structure of solids by laser photoacoustic spectroscopy, Appl. Phys. Lett. 32, 538 (1978).

[7]. Hordvik, A. and Skolnik, L.,Photoacoustic measurements of surface and bulk absorption in HF/DF laser window materials, Appl. Opt. 16, 2919 (1977).

[8]. Rosencwaig, A., Theoretical aspects of photoacoustic spectroscopy, J. Appl. Phys. 49, 2905 (1978).

[9]. Bennett, H.S. and Forman, R.A., Absorption coefficients of highly transparent solids: photoacoustic theory for cylindrical configurations, Appl. Opt. 15, 1313, (1976).

[10]. McDonald, F.A., Photoacoustic determination of small optical absorption coefficients: extended theory, Appl. Opt. 18, 1363 (1979).

[11]. McClelland, J.F. and Kniseley, R.N. Photoacoustic spectroscopy with condensed samples, Appl. Opt. 15, 2658 (1976).

[12]. Fernelius, N., The use of photoacoustic spectroscopy to study laser window materials and thin film coatings, Proc. High Power Laser Optical Comp. and Comp. Matls, NBS, Boulder, Colorado (1977).

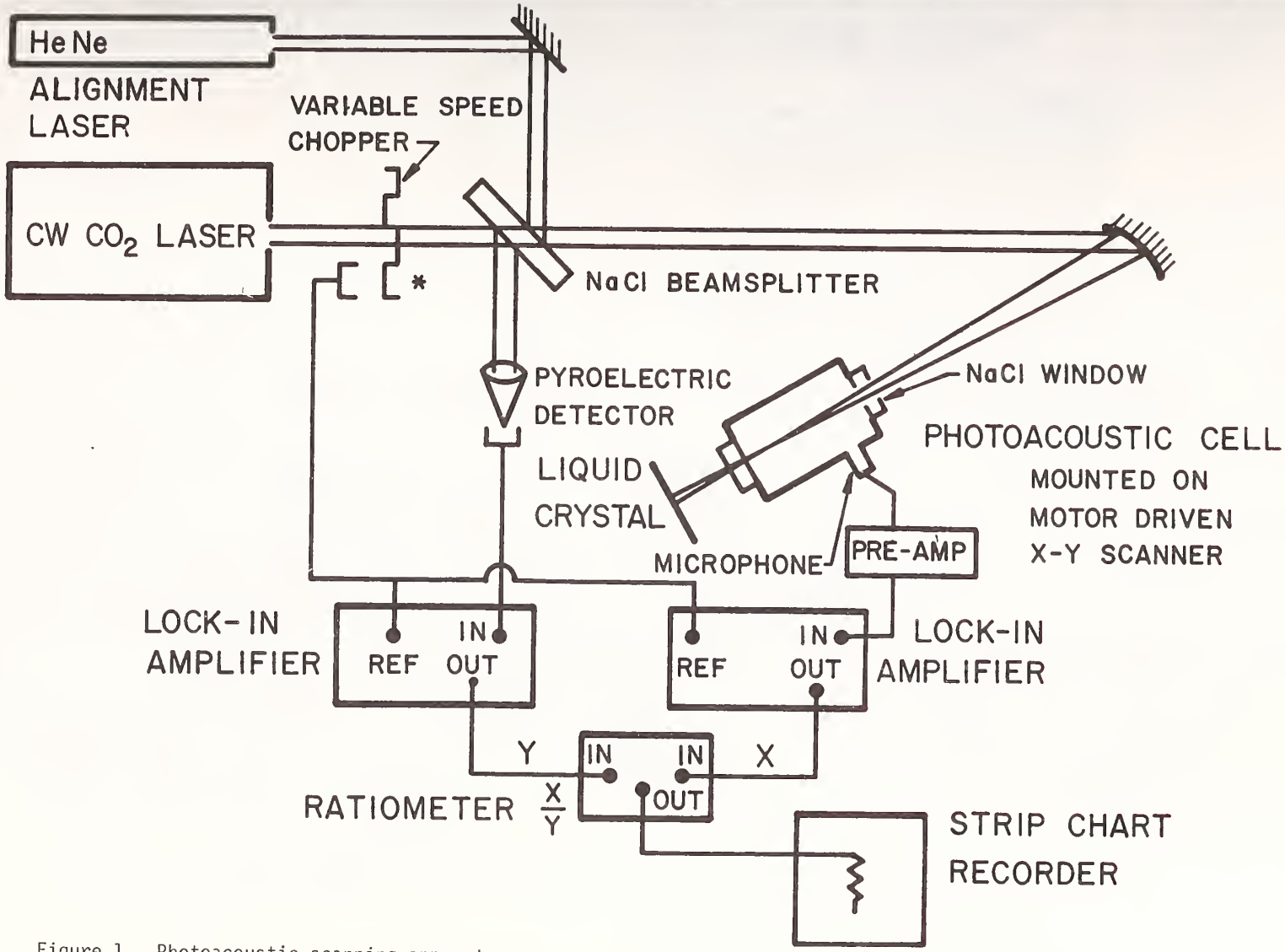

Figure 1. Photoacoustic scanning apparatus.

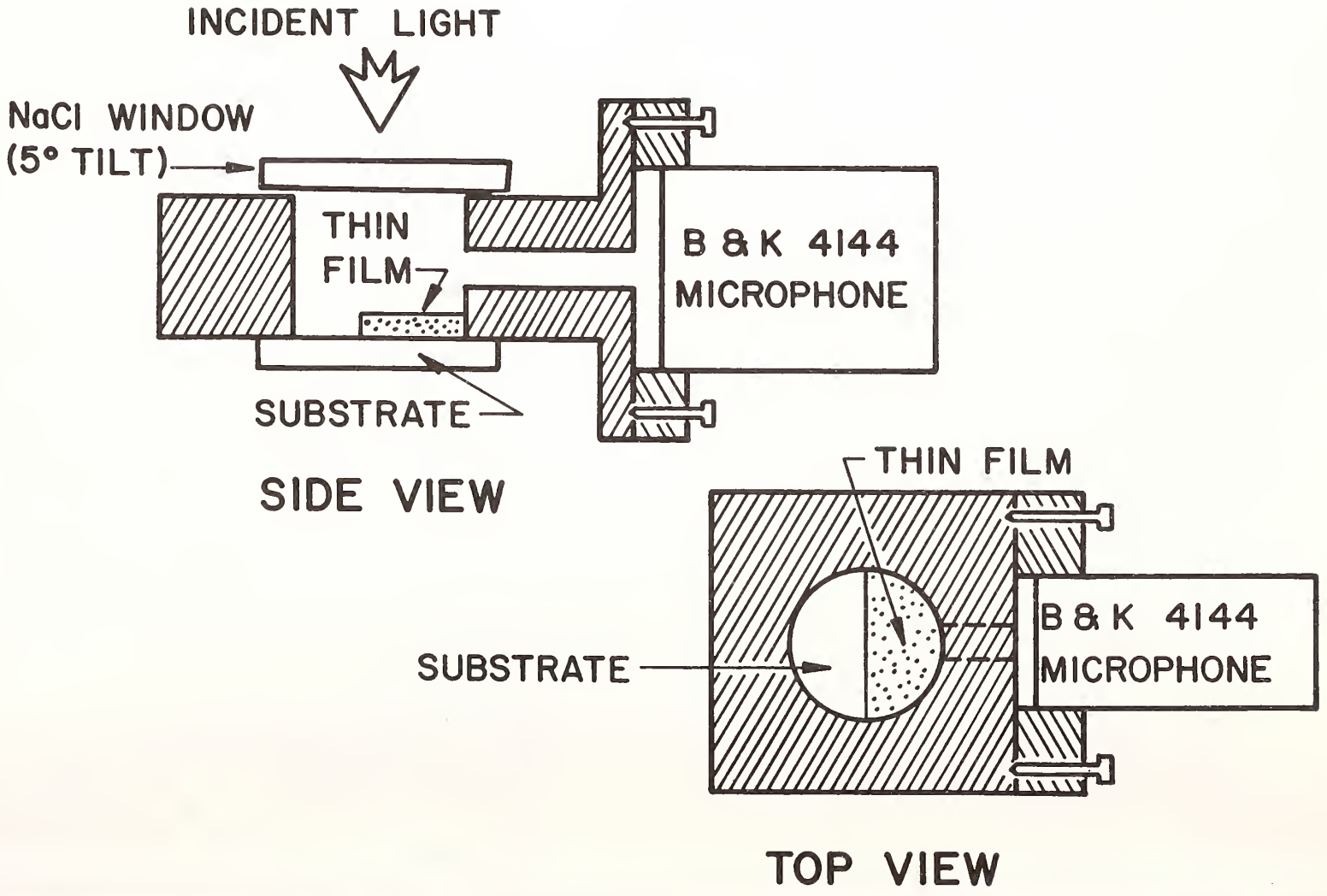

Figure 2. Diagram of the photoacoustic cell

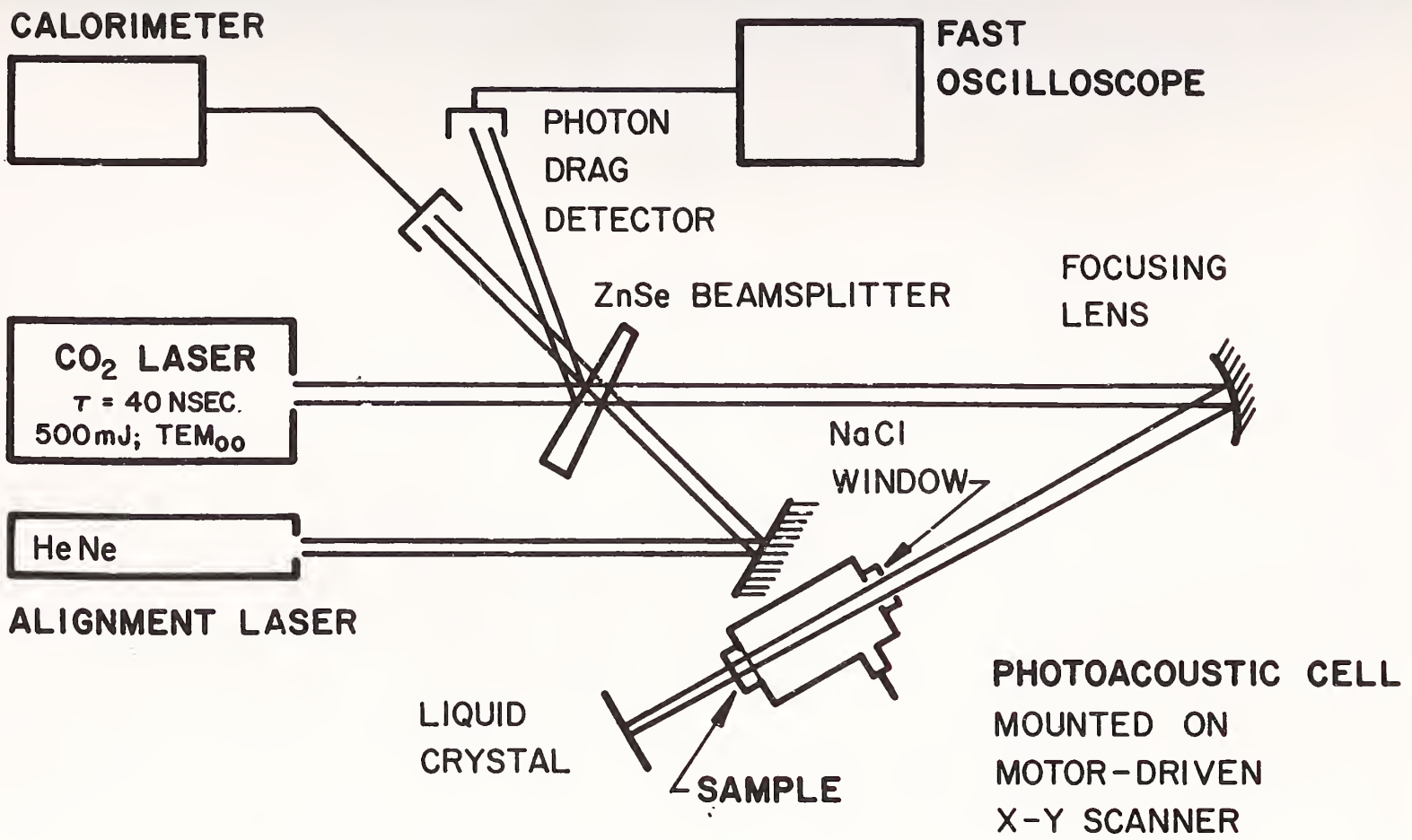

Figure 3. High power CO_2 laser damage apparatus.

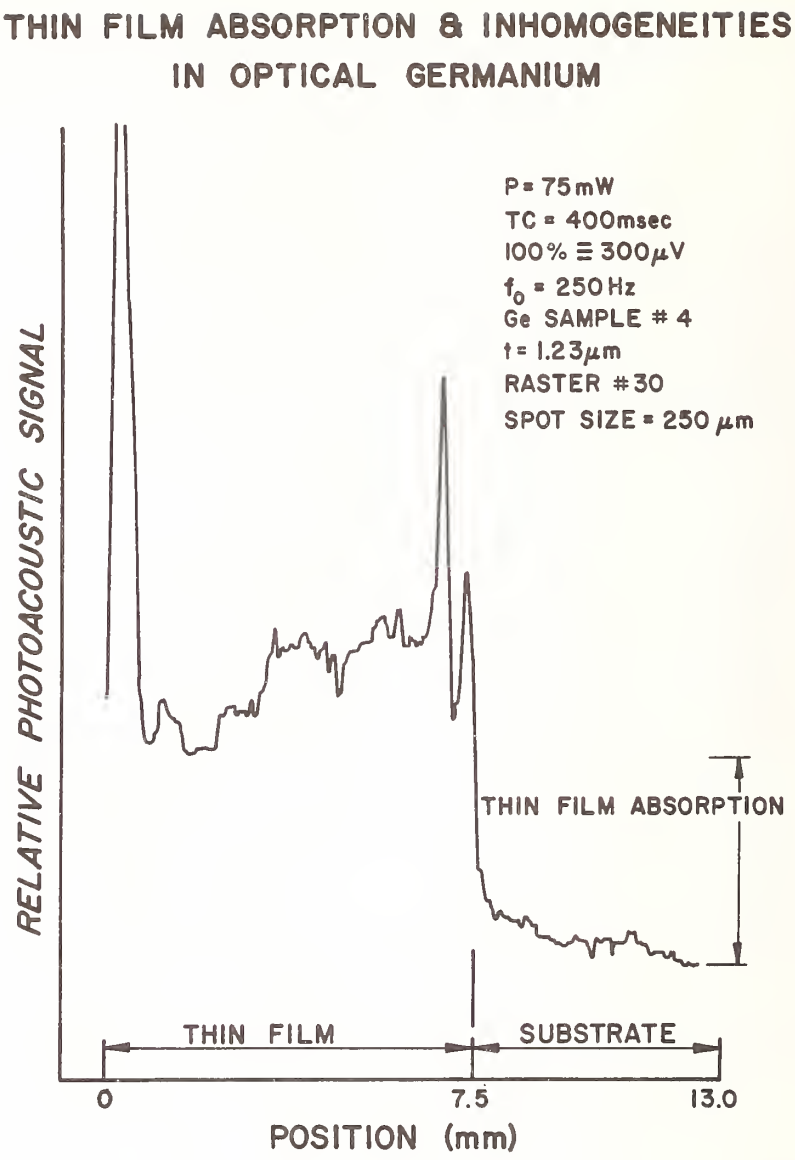

Figure 4. Photoacoustic raster scan using defocused laser beam.

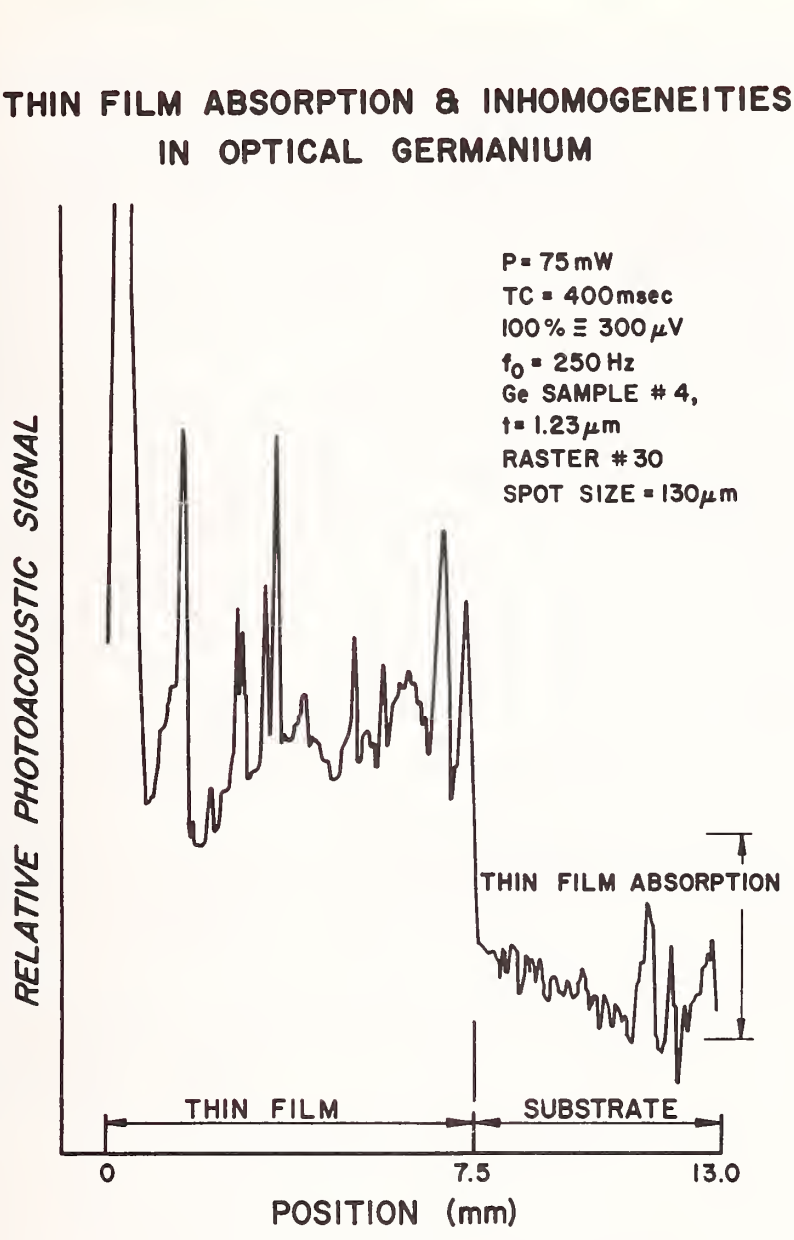

Figure 5. Photoacoustic raster scan using focused laser beam.

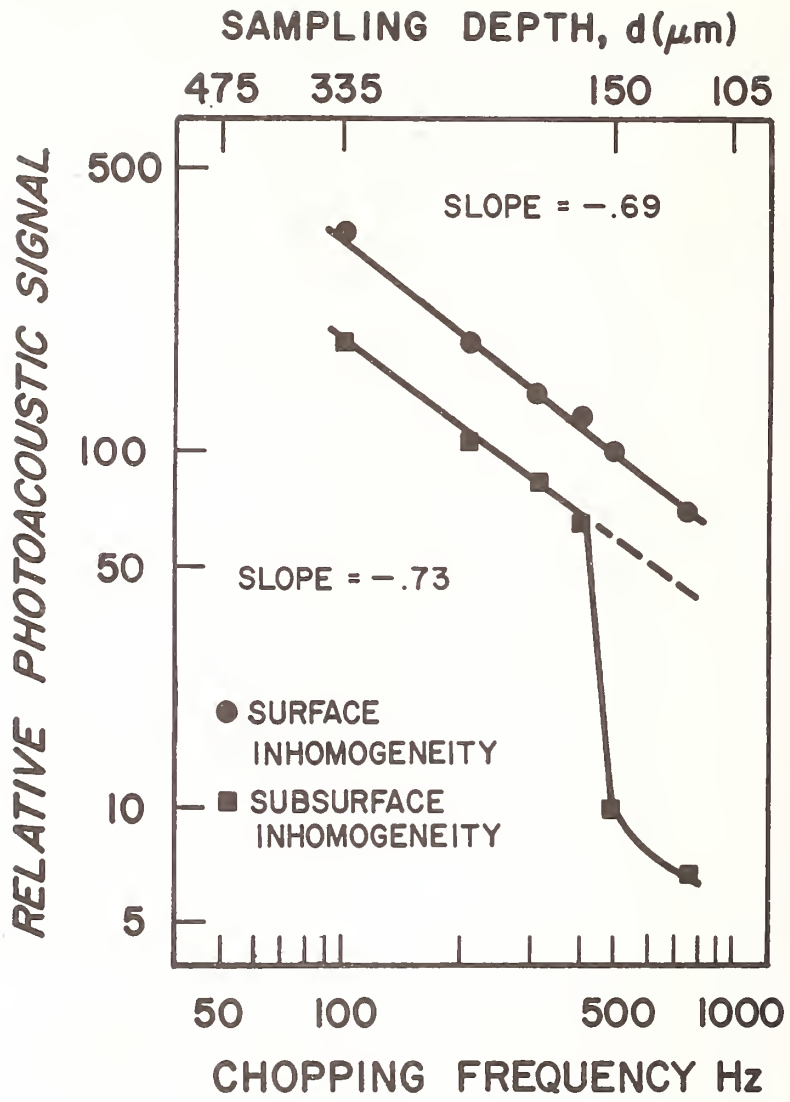

Figure 6. Photoacoustic signal vrs. chopping frequency for surface and subsurface inhomogeneities.

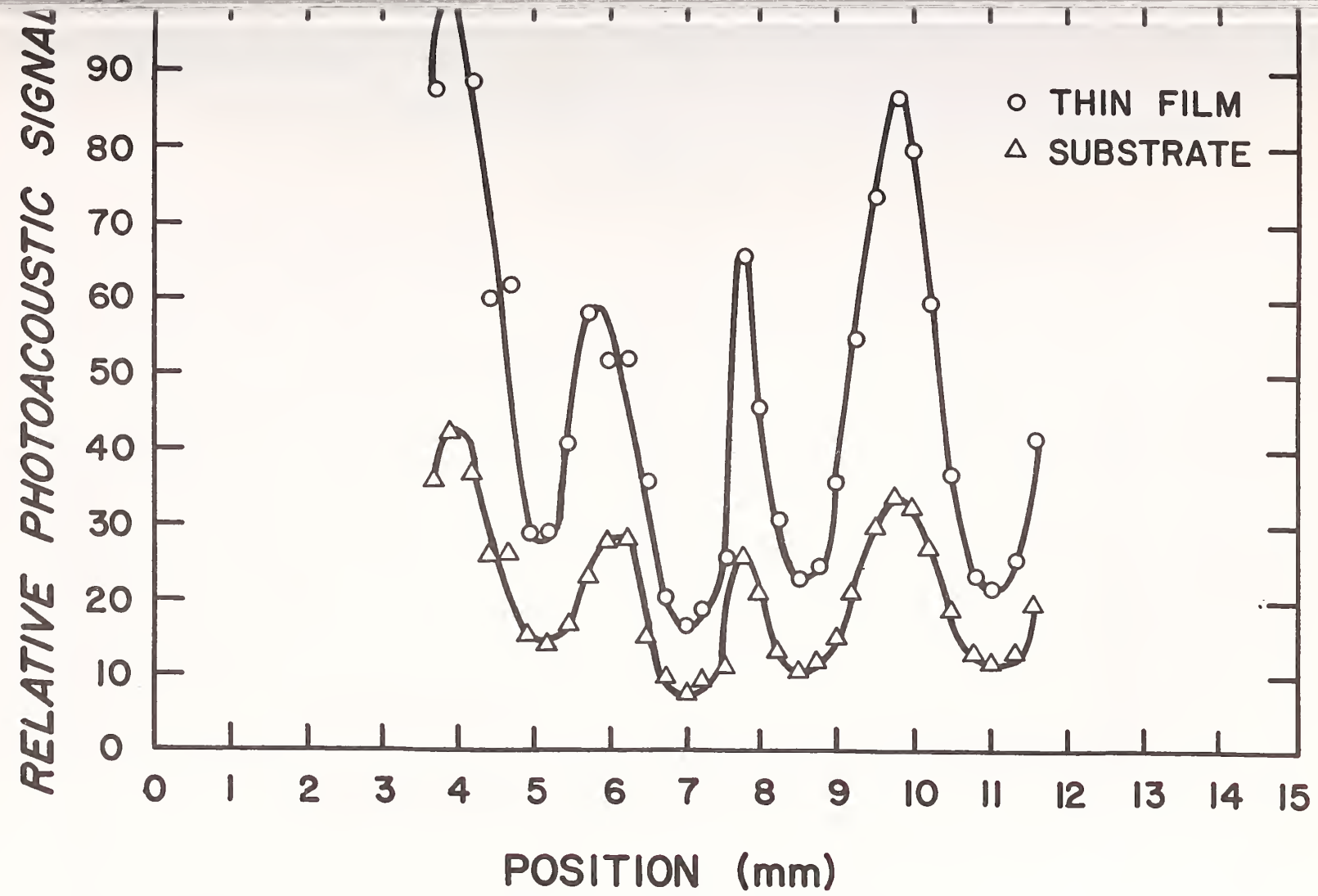

Figure 7. Photoacoustic signal as a function of position - direction parellel to the thin film - substrate boundary line.

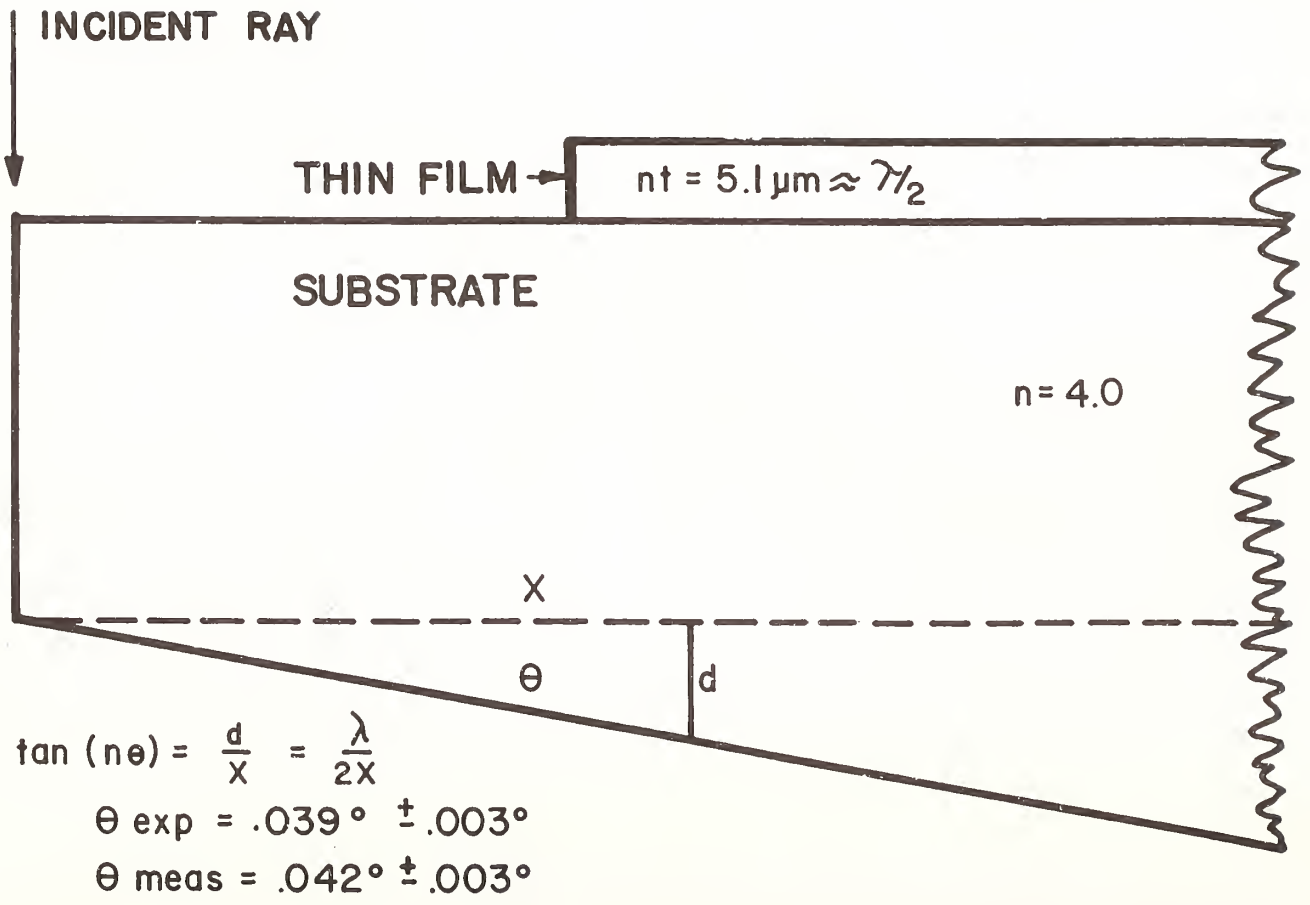

Figure 8. Sample interference geometry.

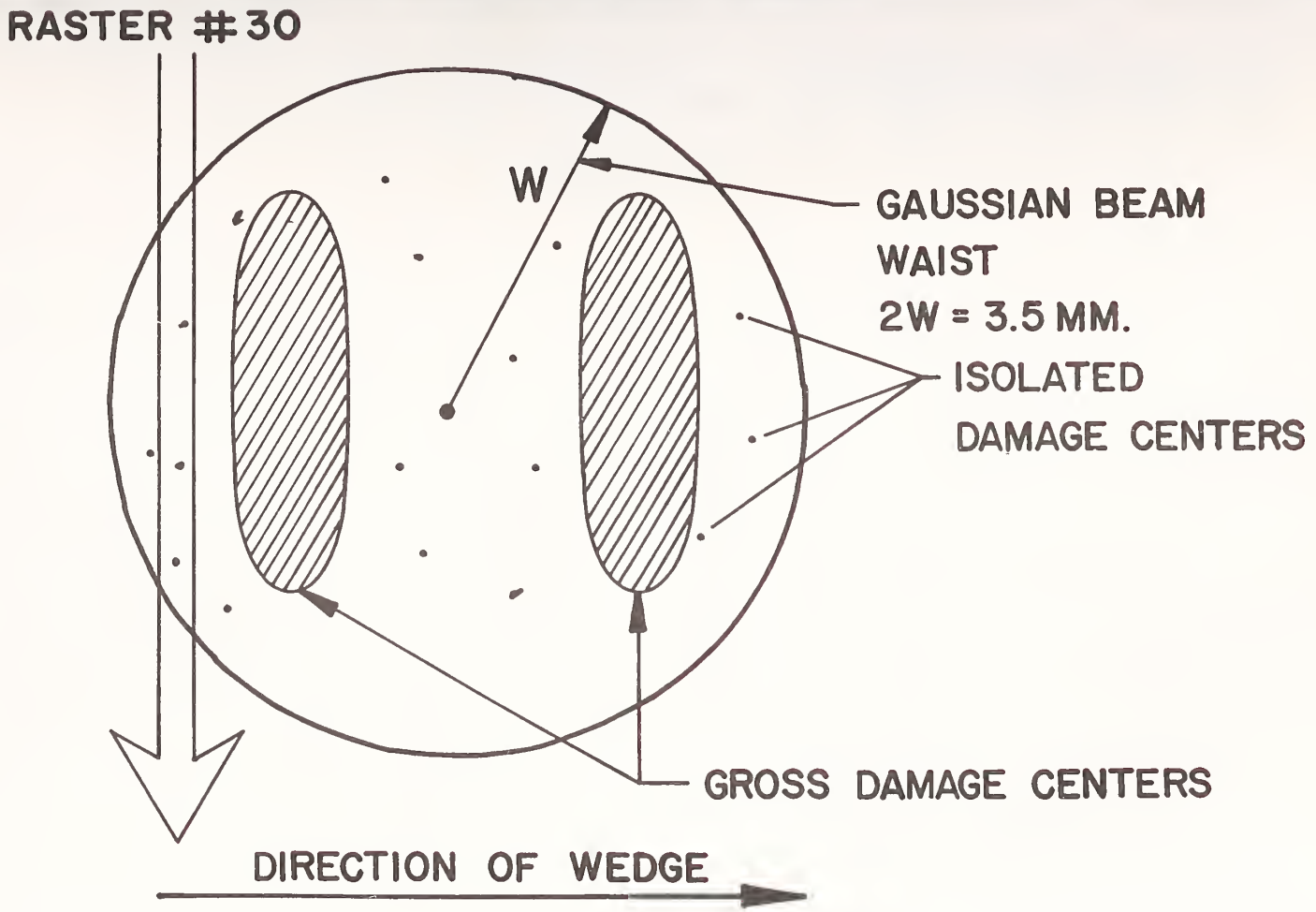

Figure 9. Sketch of single pulse CO_2 laser damage on germanium thin film.

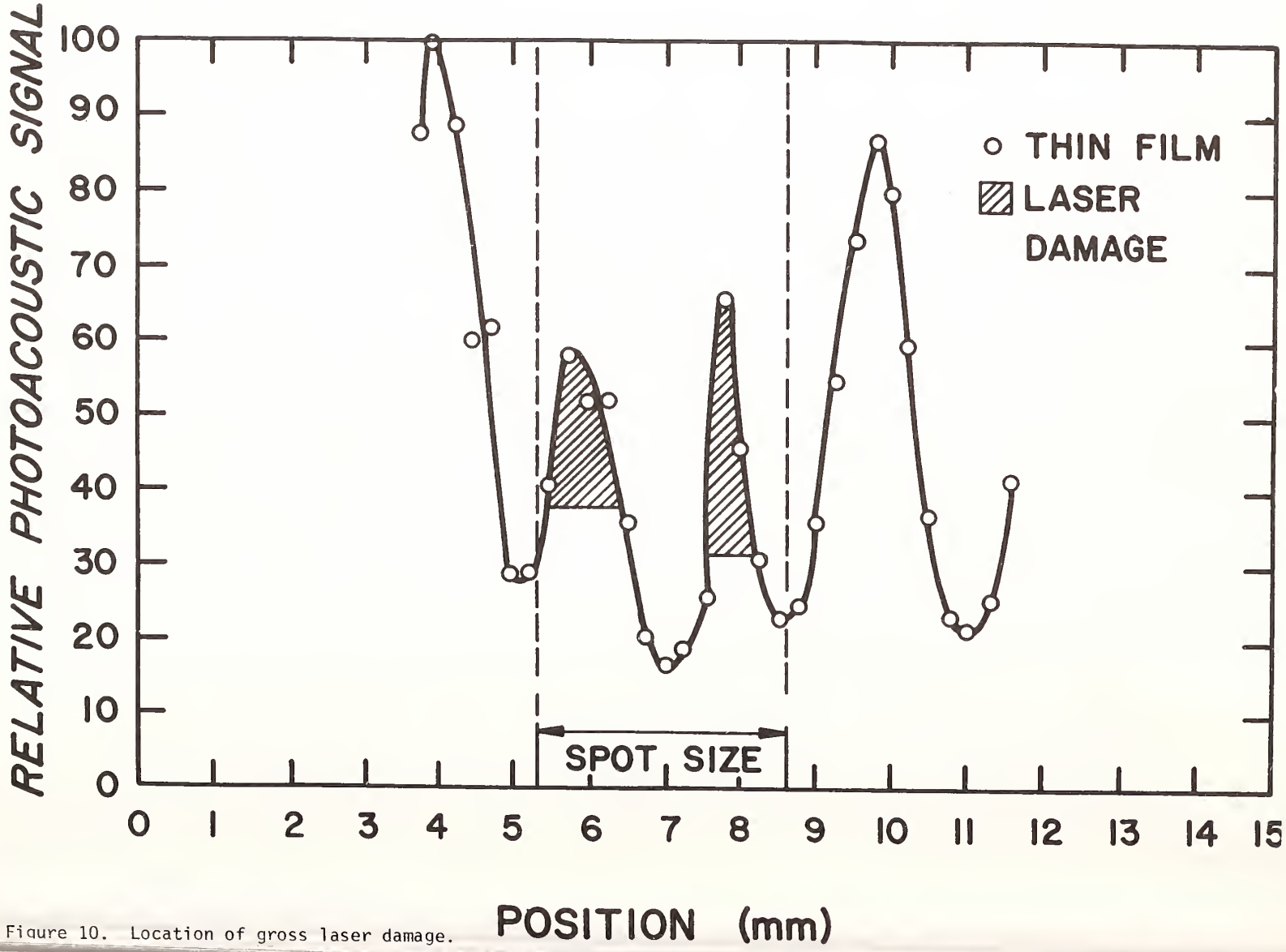

Figure 10. Location of gross laser damage.

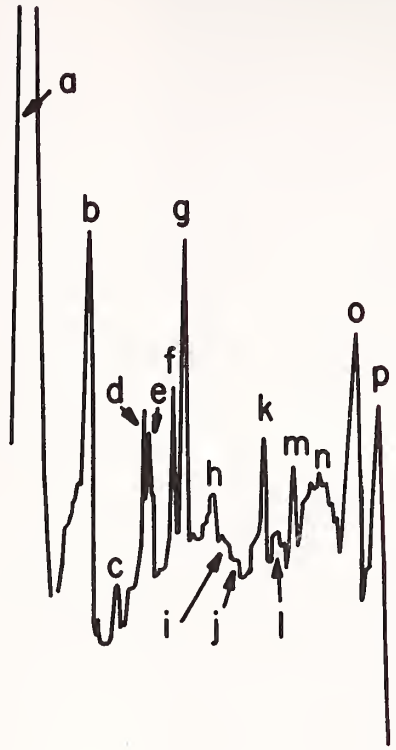

Peak	Laser Damage?	Physical Description of Location
a	no	surface scratch
b	yes	small group of isolated damage sites
c	yes	large (50 μm) damage site, film cracked
d	no	surface scratch } illustrates resolution of scanner (130 μm)
e	no	surface scratch
f	no	surface scratch
g	yes	two sites together
h	yes	isolated damage site
i	no	surface scratch
j	yes	two sites together - peaks resolved better in scans 29 and 31
k	yes	damage site, looks like cat's paw
l	no	no surface feature seen under Nomarski
m	yes	isolated damage site
n	no	no surface feature seen under Nomarski
o	yes	damage site the result of interference effects of thin film-substrate edge
p	yes	thin film - substrate boundary edge

Figure 11. Correlation between photoacoustic features and laser damage sites.

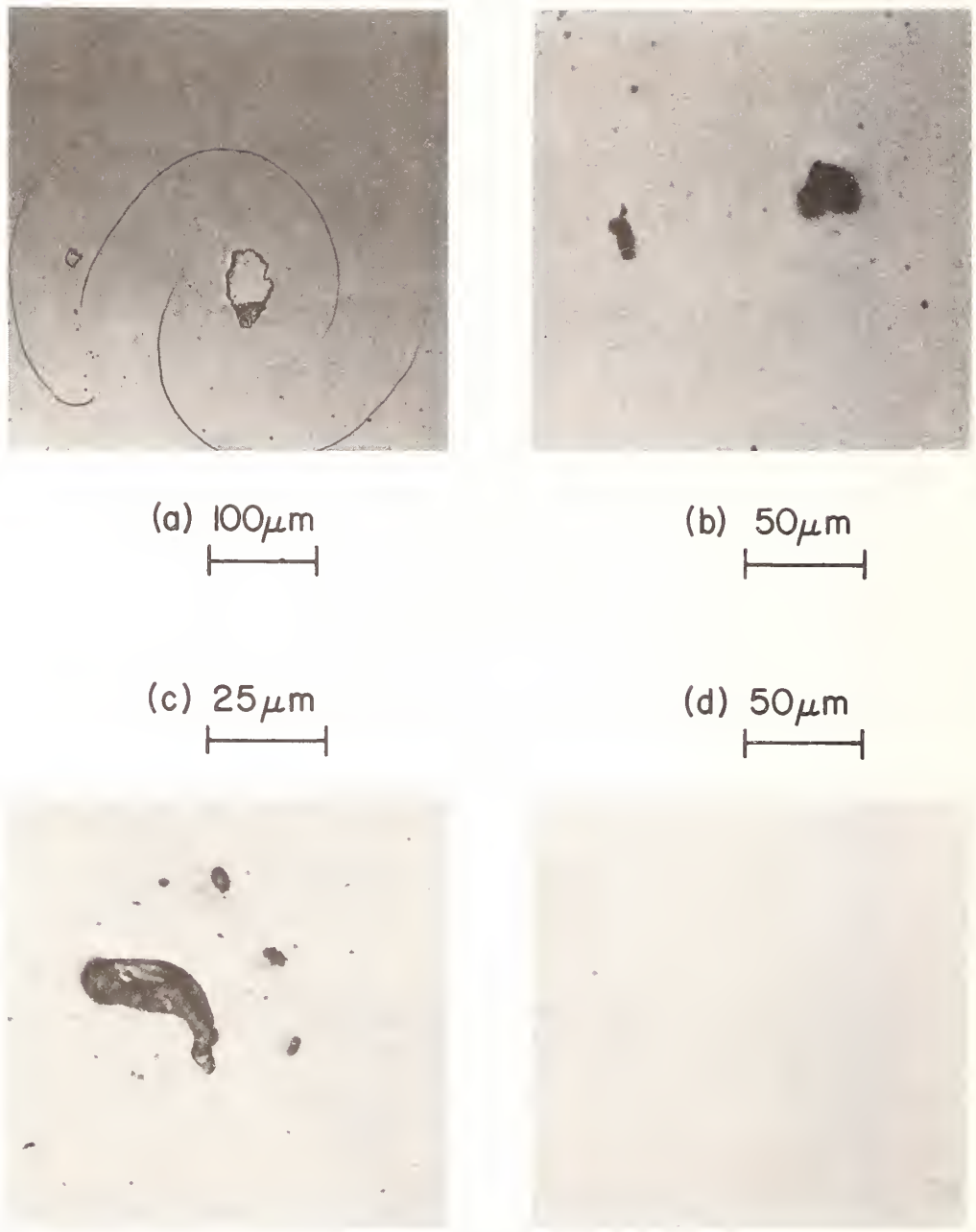

Figure 12. Nomarski micrographs of some of the isolated damage sites: a). PAS peak c; b) PAS peak g; c) PAS peak k; d) non-irradiated thin film surface.

EXAMINATION OF LASER DAMAGE SITES OF TRANSPARENT SURFACES AND FILMS USING TOTAL INTERNAL REFLECTION MICROSCOPY*

P. A. Temple
Michelson Laboratory, Physics Division
Naval Weapons Center, China Lake, California 93555

This paper describes total internal reflection microscopy (TIRM), a microscopic inspection technique useful in examining the laser-damaged surfaces of transparent samples. In this technique, the surface is illuminated from within the sample with a well-collimated polarized laser beam at an angle of incidence just greater than the critical angle. Since total reflection occurs, the illuminated region appears to be dark when viewed from outside the sample except for scatter caused by surface defects such as laser damage sites. We will describe two instruments used for TIRM inspection of samples. Finally, various damaged regions will be shown as they appear under TIRM inspection and under Nomarski microscopy. It will be seen that the two techniques are complementary, and that, on highly polished surfaces, TIRM shows somewhat more detail than does Nomarski microscopy. All of the damage sites shown will be the result of 1.06-μm, 1-nsec irradiation of fused silica or BK-7 surfaces.

Key words: Fused silica; laser damage; optical microscopy; total internal reflection.

Introduction

This paper describes a method of illuminating the region at and near the surface of a transparent sample or of a film on a transparent substrate [1-3][1]. The technique, total internal reflection microscopy (TIRM), has been useful in the inspection of polished glass surfaces and thin films both before and after laser damage has occurred. Also described are two microscopic setups, one of which makes use of a Zeiss Nomarski microscope for sequential viewing of the sample surface by either TIRM or Nomarski microscopy. The other is an in situ microscope for TIRM viewing of a part before and after laser damage testing has occurred. Finally, several photos will show the appearance of laser damaged surfaces as seen in TIRM and Nomarski microscopy.

TIRM Setup

The physical setup is shown in figure 1. In this technique the surface is illuminated from within the sample with a well-collimated polarized laser beam at an angle of incidence equal to or slightly greater than the critical angle [4][2]. In this configuration, since total reflection occurs, the only light which reaches the microscope objective is light which has been scattered into the z-direction by surface irregularities or inclusions; the field of view is dark in the absence of these perturbing sites.

In the study discussed in this paper, only s-polarized light was used. In this case there is an enhancement of the electric field at the surface for angles of incidence near the critical angle. Figure 2 shows the value of $\langle E^2 \rangle / \langle E_0^2 \rangle$ at the surface for internal illumination, as used in TIRM, and for external illumination, as used in the usual dark-field microscopy. As can be seen, at the critical angle nearly an order of magnitude enhancement exists for internal illumination over external illumination.

---

* Work supported by Navy Independent Research and Department of Energy funds.

[1] Figures in brackets indicate the literature references at the end of this paper.

[2] This configuration has been used by Parks' group (Ref. [4]). However, they have primarily monitored the transmitted beam intensity for changes induced by a disrupted surface caused by laser-induced damage. Their observation of the externally scattered light appears to have been fairly casual.

The illuminated area is viewed from above with a microscope. Only that light which is scattered into the small cone about the normal or z-direction is collected by the microscope objective. Two microscopes have been used in the study reported in this paper. The first, shown in figure 3, is a Zeiss Nomarski microscope. With the Nomarski illuminator turned off and the TIRM laser turned on, it is possible to use the Zeiss microscope as a simple magnifier. This is true even though a Nomarski objective is employed. Using this setup it is possible to view a surface under Nomarski conditions, under TIRM conditions, or under both types of illumination simultaneously. Figure 4 is such a set of photographs. Figure 4 shows a laser-damaged BK-7 entrance surface which had previously been mechanically polished. The laser used to illuminate the TIRM photographs was a 2-watt argon-ion laser. It can be seen that many features associated with mechanical damage to the surface from the polishing process are visible in the TIRM photographs but not in the Nomarski view. The laser damage sites are most easily seen as shallow pits in the Nomarski photograph. The Nomarski and TIRM view shows that there is a small sharp feature at the bottom of these shallow pits.

Figure 4 is an example of the complementary nature of these two microscopies. Nomarski microscopy shows slope changes very well. The pits seen in figure 4 are, in fact, very subtle features. There must be enough surface area involved, however, to show a contrasting region against the bright background. On the other hand, the features seen in the TIRM views may be very small in extent. The only requirement is that enough light is scattered to be seen against the dark background. Other measurements have verified that features a few hundred angstroms in extent are visible in TIRM.

Figures 5 - 7 show three views of a second TIRM microscope. This microscope is built around a Leitz laboratory instrument and employs a 3-mW HeNe laser for illumination. This low illumination power necessitated quite long exposure times but otherwise was satisfactory. Figures 6 and 7 show the instrument as used for microscopic viewing of the sample and as used for in situ damage testing. In the latter case, all the optics are removed from the beam path and the high power beam was incident from either the left or right for exit or entrance surface testing of the sample. With the microscope axis coaxial with the high power laser axis, it was possible to view a surface before and after damage testing.

Figure 5 is a detailed view of the sample stage of the microscope. Unlike the setup shown in figure 1, here the HeNe laser beam was coupled into the sample through a small prism. After the beam entered the sample, it was totally reflected off the bottom of the sample and then off the top of the sample, where it was viewed with the microscope. While provision existed for coupling the beam out of the sample with a second prism, it was not found to be necessary. The setup shown in figure 5, then, had the advantage of a clear aperture through the sample to allow for in situ laser damage testing. The sample was mounted in such a way that the coupling prism was held stationary while the sample could be moved for viewing and testing of various regions on the sample surface.

Observations

A companion paper given at this conference [3] shows several TIRM photographs of CO_2-laser polished and laser-damaged surfaces. It is suggested that this paper be consulted for the examples presented there. In addition to these photos, several other examples will be shown in the remainder of this paper.

Figure 8 shows two TIRM views of the same region of a fused silica sample taken before and after it was damaged by a laser pulse. This surface was prepared by ion milling a previously mechanically polished surface. The "undamaged" picture was taken with slightly lower magnification. These photos were not taken with the apparatus shown in figures 5 - 7. Figure 8 shows that all the damage occurred along the previously present scratches. It is characteristic of ion-milled surfaces for damage to occur along defect features made visible by the ion-milling process. Figure 9 is a pair of views of the same sample shown in figure 8. Shown in figure 9 is the scratch seen in figure 8, but in addition, a damage pit is shown. This pitted region was not photographed prior to damage, and it is not known if any features were visible at that site before damage occurred. The Nomarski view clearly shows the decoration brought out by ion milling along the scratch. However, it is not clear from the Nomarski photograph where subsequent laser damage has occurred. The increased scatter at damage sites, as seen in the TIRM view in this figure and in figure 8, makes it clear

where damage has in fact occurred. The single damage site in the upper right-hand portion of the photograph is unusual in that a large halo of spots occurred which is not evident in the Nomarski view. There are, however, two pits visible at this site in the Nomarski view of this surface.

Figure 10 shows two views of a BK-7 surface, before and after laser damage. These photos were taken using the microscope shown in figures 5 - 7. The exposure times are one minute in the "before" view and one-half second in the "after" view. This was an exit surface damage site, and the damage pits are very effective scatter sites in the case of exit surface damage. This figure is representative of several photographs taken in an effort to search for a correlation between features seen before damage and subsequent damage sites.

Figure 11 consists of two views of a 0.35-μm-thick SiO_2 film on a fused silica substrate. This film had a multitude of scattering sites more or less uniformly distributed throughout. This can be seen in the "before" view. The "after" view was taken with somewhat less exposure so that the bright spots in this view are damage sites, while the dim spots correspond to the sites seen in the "before" view. A careful inspection of these two photos shows that there is little correlation between the scattering sites seen before damage and the location of subsequent damage pits.

Conclusions

In this paper we have described a sensitive technique for microscopic viewing of surfaces before and after laser damage has occurred. This technique, called total internal reflection microscopy (TIRM), is complementary to Nomarski microscopy. Two microscopes employing two different illumination beam coupling techniques were shown. The first employed a Zeiss Nomarski microscope and allowed simultaneous viewing of the sample by either Nomarski or TIRM illumination. The second microscope described was an *in situ* microscope which allows viewing of a sample surface before and immediately after laser-damage testing. Finally, several photographs were shown which illustrated the nature of the microscopy made available by the TIRM technique.

References

[1] Temple, P. A., "An Improved Dark-Field-Like Surface Inspection Technique Using Total Internal Reflection," presented at Conference on Optics '79, 23-25 May 1979, Los Alamos, New Mexico.

[2] Temple, P. A., "Total Internal Reflection Microscopy: A Surface Inspection Technique," submitted to Appl. Opt.

[3] Temple, P. A., David Milam, and W. Howard Lowdermilk, "CO_2-Laser Polishing of Fused Silica Surfaces for Increased Laser Damage Resistance at 1.06 μm," this conference.

[4] Alyassini, N., and J. H. Parks, NBS Spec. Publ. 435, 284 (1975).

Figures

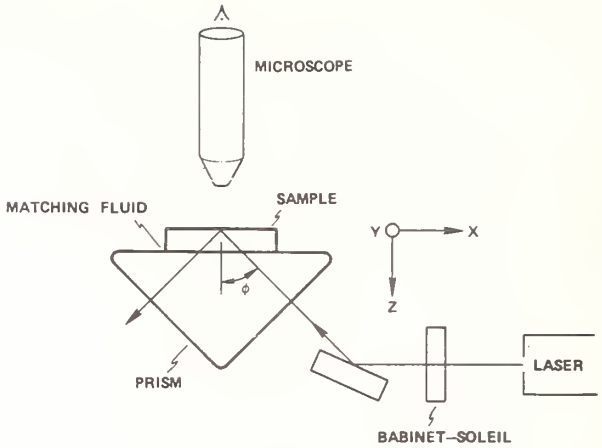

Figure 1. The physical setup used to illuminate transparent surfaces for microscopic examination. Not shown is a microscope slide manipulator used to grasp the sample and to slide it about on the oil-covered prism face. The laser used was an argon-ion laser.

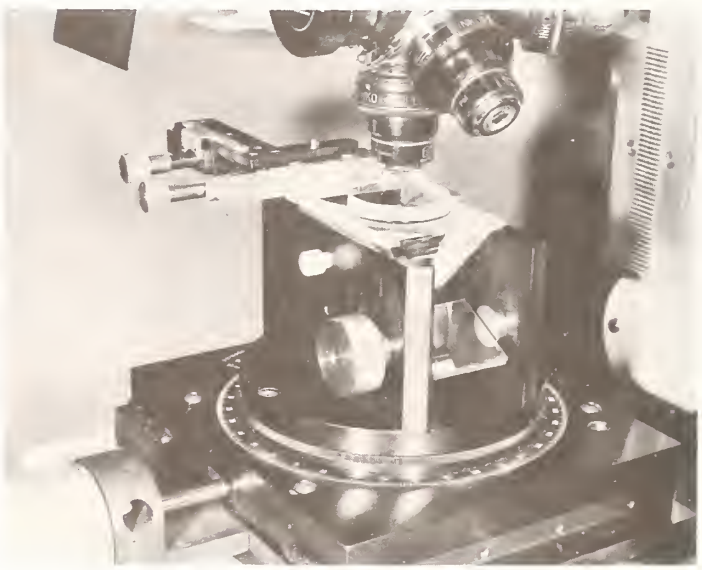

Figure 2. A fixture designed to implement the setup shown in figure 1. This fixture is shown mounted on the sample stage of a Nomarski microscope. The microscope slide manipulator, which is not shown in figure 1, can be seen grasping a 1-1/2-inch-diameter, 1/4-inch-thick sample.

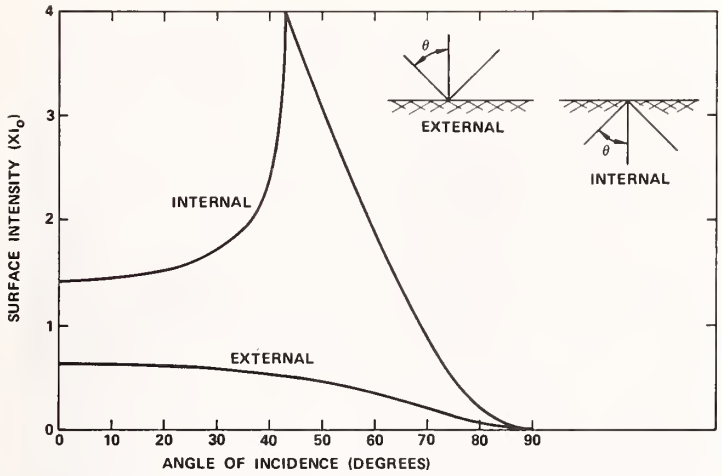

Figure 3. The value of $\langle E^2 \rangle / \langle E_0^2 \rangle$ for internal and external illumination using s-polarized light for various angles of incidence. The maximum value for $\langle E^2 \rangle / \langle E_0^2 \rangle$ is 4 and occurs at the critical angle for internal illumination.

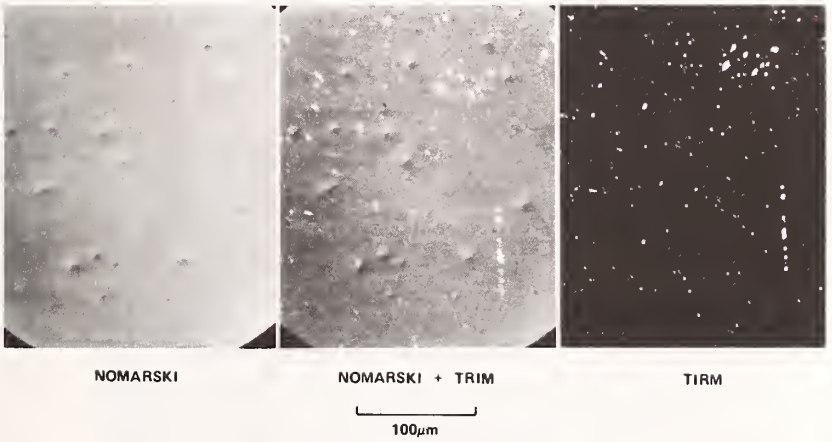

Figure 4. Three photos of the same region of a laser-damaged, conventionally polished piece of fused silica. The view on the left is a Nomarski photo showing several pits caused by a 15-J/cm^2, 1.06-μm wavelength, 1-nsec pulse length exposure. The photo on the right is a TIRM view. Since the part is mechanically polished, it has many features visible in this view which are not related to the damage shown in the left photo. The center view shows the Nomarski and TIRM illuminations simultaneously. It can be seen here that few of the TIRM features are actually identified with damage sites. Most of these features are mechanical damage due to the polishing process.

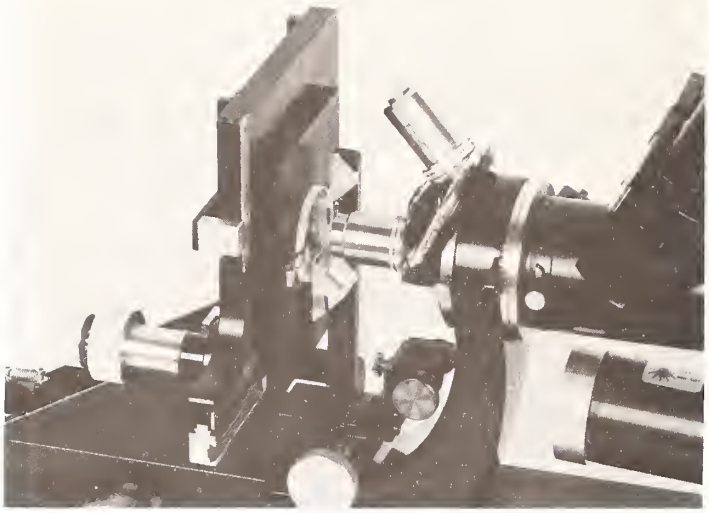

Figure 5. The sample holder and beam coupling prism for the in situ TIRM microscopy. In the center of the figure can be seen the sample with the coupling prism which is held in place with a small metal clip. The prism is optically attached to the sample by matching fluid. The sample is movable below the prism for viewing various regions of the sample.

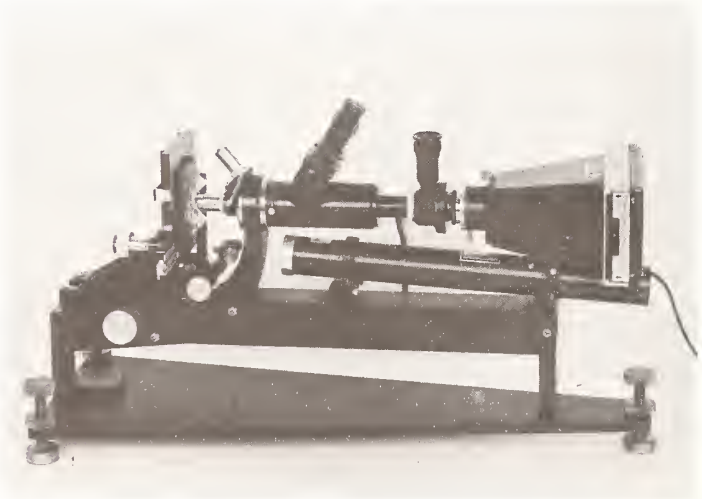

Figure 6. The TIRM in situ microscope as configured for TIRM viewing and photography. In this figure can be seen the 3-mW HeNe laser, the microscope viewing optics, the sample holding stage, and the polaroid camera. The base has adjustable feet for positioning the instrument in the high intensity laser beam.

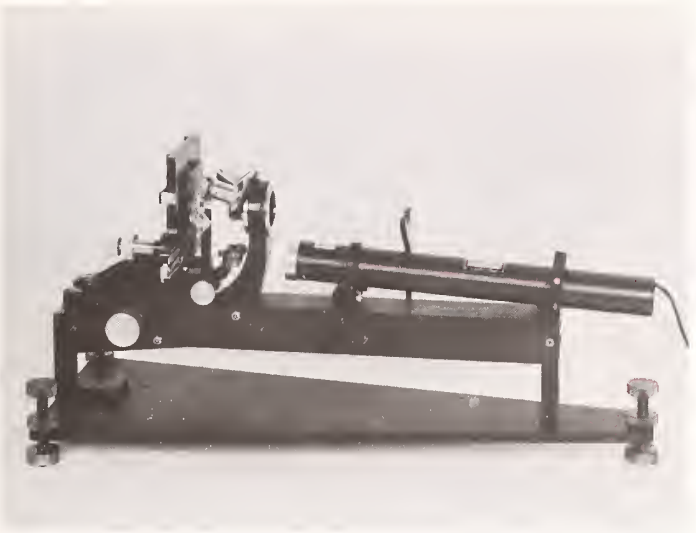

Figure 7. The TIRM microscope shown in figures 5 and 6 configured for laser-damage testing. The high intensity laser beam passes through the sample and through the empty space in the objective turret of the microscope.

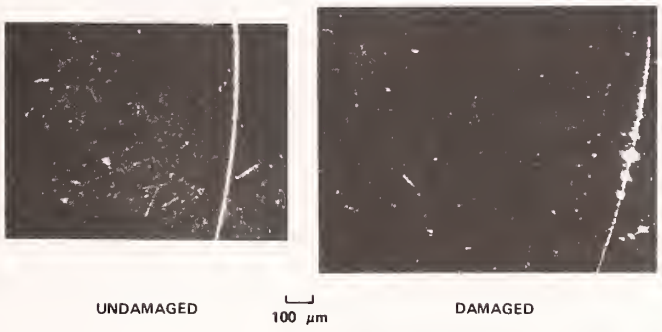

Figure 8. Two TIRM views of the same region of an ion-milled fused silica surface taken before and after it was damaged by a laser pulse. The "undamaged" picture was taken with slightly lower magnification. Note that all the damage occurred along the previously present scratch.

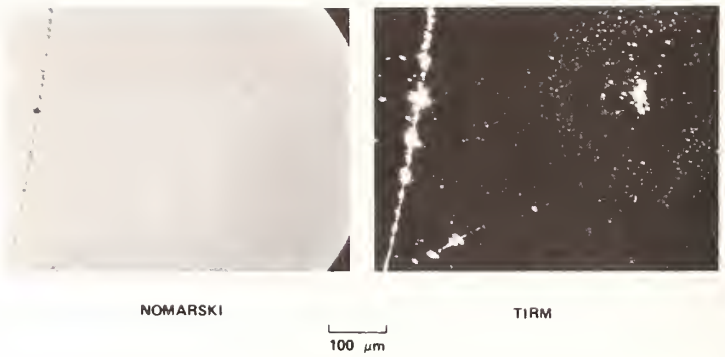

Figure 9. A Nomarski and a TIRM view of the same surface as shown in figure 8. The Nomarski view clearly shows the decoration brought out by ion milling. The single damage site in the upper-right-hand side of the TIRM view has a large halo around it. This halo cannot be seen in the Nomarski photograph.

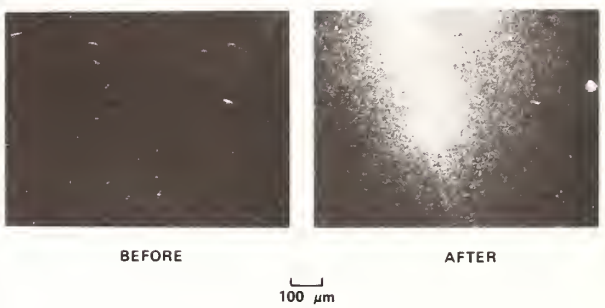

Figure 10. Two views of a mechanically polished BK-7 surface, showing its appearance under TIRM before and after laser damage. The exposure times are one minute in the undamage case and one-half second in the damaged case. This was an exit surface damage site, and the damage pits are very effective scatter sites in the case of exit surface damage.

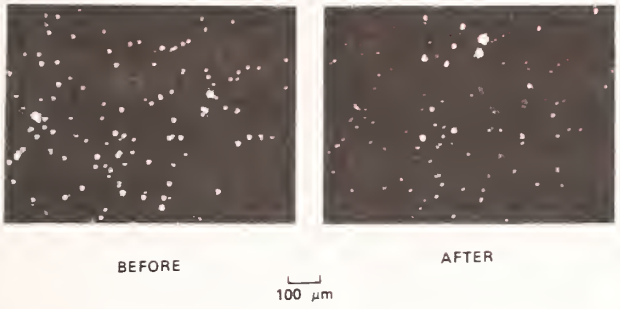

Figure 11. Two views of a 0.35-μm-thick SiO_2 film on a fused silica substrate. This film had a multitude of scattering sites prior to damage. The "after" view was taken with less exposure time, and the bright spots in this photo are damage sites, while the original scattering sites appear as dim spots. Very little correlation exists between the original film scattering sites and the subsequent damage sites.

PARAMETERS AFFECTING DAMAGE THRESHOLD IN THIN FILM INFRARED CHALCOGENIDE GLASS FOR APPLICATIONS IN LASER OPTICAL SWITCHING SYSTEMS

W. E. Kienzle
Science Applications, Inc. *
El Segundo, CA 90250

and

N. I. Marzwell
Rockwell International
Rocketdyne Division
Canoga Park, CA 91304

The study of process control of film deposition can be important in determining the threshold of film damage due to a laser pulse. This paper reports the optical properties of the infrared chalcogenide glass material $Tl_2SeAs_2Te_3$ as process parameters are varied. Several RF sputtered chalcogenide glass films of thickness varying from 0.6μm to 8.9μm were deposited on germanium and sapphire. The index of refraction and absorption coefficient were determined from the measured reflectance and transmittance curves for these samples. Further, these properties were measured for two different sputtering pressures, two sputtering voltages, twelve azimuthal target positions and three different substrate to target distances. The damage due to switching was assessed by subjecting different switches to CO_2 laser pulses with FWHM of 2 to 4 msec and energies up to 0.16 Joules which were focused on target spot diameter of 0.4 mm on the chalcogenide optical switch.

Key words: Absorption coefficient; Chalcogenide material; Deposition parameters; Index of refraction

1. Introduction

In recent years, the development of high power lasers in the infrared region has motivated studies of laser induced damage to infrared transmissive optical materials. Chalcogenide materials have been studied for use in optical components in laser systems operating in the spectral range from 2 to 10.6μm, RF payloads, thermal control and memory applications. In this paper we present preliminary measurements of the optical parameters that affect the damage threshold of a chalcogenide thin film. We discuss possible damage mechanisms and address the properties of these materials as they relate to their chemical composition and fabrication techniques.

Ovshinsky [1] identified the potential of chalcogenide systems for these types of applications. Subsequently, Bishop [2] fabricated and tested optical switches composed of amorphous glass material from the family $(Tl_2Se)_x (As_2Te_3)_{1-x}$. Aerojet Electrosystems Co. [3] has developed material and fabrication processes and characterized the performance of several types of switches, including the family $(Tl_2Se)_x (As_2Te_3)_{1-x}$. A typical chalcogenide switch is shown schematically in the upper right of figure 1, and consists of a thin (∿1-25μm) layer of switch material deposited on a wafer of substrate material (thickness ∿1-2mm) with one other wafer over this configuration to complete the switch configuration. Typical switch response is also shown in figure 1 where the initially transmitting switch rapidly becomes opaque when irradiated by a high intensity laser pulse.

2. Chalcogenide Characteristics

Chalcogenide glasses could be obtained from different combinations which have to be differentiated from oxide glasses whose composition includes sulfur, selenium and tellurium. It is those elements that act as glass formation inducers for other elements

* Work performed at Aerojet Electro Systems Co., Azusa, CA

such as thallium, antimony, bismuth...etc., for chalcogenide formation. The chalcogenide glasses could be made in a wide variety of physical, electrical and optical properties. A study of the electrical properties shows that the group of high-conductivity chalcogenides are typical electronic semiconductors with a hole conduction mechanism. The ability to crystallize is higher in chalcogenide glasses than in oxide glasses and it depends upon the composition of the various systems to a very large extent. Upon crystallization the electrical conductivity generally increases by as much as a factor of 10^{10}. The change in conductivity is connected with the long-range order and the different role impurities play in a glass and in a crystal. Zone purification of chalcogenide leads to a strong decrease in the electrical conductivity when it is in the crystal state while the electrical conductivity does not change when the chalcogenide is in the glass state. Chalcogenides also offer a smooth dependence of the absorption band edge upon change in composition. A similar smooth dependence of the absorption bands is seen also with composition. A chalcogenide glass alloy generally shows a smooth transition from the type of absorption of one component to the other component constituting the alloy. The laws established for crystalline substances can apparently be extended to vitreous substances. In certain cases transition from the glassy state to the crystal state goes through a gradual change from the short-range to the long range. The long wavelength cut off for the solid is usually determined by the lattice type absorption of the constituent elements. The beginning of transmission occurs at a wavelength corresponding to the energy of its forbidden gap (absorption edge).

The member of the chalcogenide compositional family $(Tl_2Se)_x (As_2Te_3)_{1-x}$ discussed in this paper is $Tl_2Se\ As_2Te_3$. This material is an amorphous semiconductor, which when irradiated by infrared radiation has a rate of energy absorption that increases with the temperature of the material. This runaway absorption results in a transmission change in the material. This transmission change is a result of free carrier optical absorption of the incident laser wavelength which causes thermal runaway, and subsequent opacity at the laser wavelength. As thermal runaway occurs, the material passes through a glass transition temperature at 353K and an order-disorder phenomena at 475K. Divitrification of the glass does not appear to occur during the switching action. Further description of the materials electrical, optical and mechanical behavior may be found in the list of references [4-6].

3. Thermal Irradiation Analysis

As part of a study to characterize the damage behavior of $Tl_2SeAs_2Te_3$ in a passive optical switch configuration, a three-dimensional transient model of the absorption of laser energy and its subsequent dissipation in the switch material was developed [3]. Passive means that a sufficiently large irradiance itself causes the switch to become opaque. Model predictions above 500K can only be taken as indicative of certain general trends since thermophysical data above 500K are not available.

The model assumes that below laser irradiance levels of 10^7 W/cm^2 the mechanisms of absorption and dissipation are thermal in nature. The configuration adopted here consists of three stacked disks of material. The center disk is the chalcogenide glass, one outside disk is a cover plate, and the other is the supporting substrate. Laser radiation is incident upon the cover plate. Reflections at the outer faces of the model switch were not considered since it was assumed that anti-reflection coatings would be used in the actual switch. Furthermore, internal reflections at the support chalcogenide interface were assumed negligible. The circumference of the layers is assumed to be held at the ambient temperature of the system.

The model requires knowledge of the absorption coefficient, heat capacity, thermal conductivity, and density of all the materials used. The power absorption per unit area within a thickness "d" of a material is assumed to satisfy

$$P = P_0 \exp(-\alpha d) \qquad (1)$$

where P_0 is the irradiance entering the volume. Internal energy of the glass, heat conduction, and radiation at the interfaces are the three mechanisms considered to dissipate the energy. Because of the exponential form of equation (1), an analytical solution of the heat equation is not possible and the method of finite differences was used to model the thermal transfer.

In discussing the results, it is useful to define the switching time, which is the time from first incidence of a laser beam until the switch power transmission has dropped to 1/e of its initial value. For the present chalcogenide materials used, the switch time is primarily the time (I) to heat the chalcogenide glass from the system ambient temperature to the temperature at which the temperature-dependent absorption coefficient begins to dominate. The additional time (II) for the temperature-dependent absorption coefficient to reach its maximum value is negligible by comparison.

If conduction and radiation effects are small, which is typically the case at the initial ambient temperatures, heating of the glass at a constant rate depends primarily on the heat capacity and absorption coefficient of the glass. The result is a linear increase in temperature during the time (I). As absorption proceeds, the temperature is highest at the middle of the chalcogenide film because of heat conduction from the chalcogenide film to the adjoining support materials. After the chalcogenide glass switches and becomes opaque, the highest temperature is at its front face because then absorption is so strong that it occurs all at the front face, figure 2. When a temperature of 475K is reached, the temperature-dependent absorption coefficient begins to dominate the total absorption coefficient resulting in a rapid increase in temperature and a corresponding rapid drop in transmission. Thus, below 475K, the switch is transmitting, and above 475K, it is opaque.

One of the problems of trying to match model performance with the performance of actual laboratory switches is the difficulty of accurately characterizing the thermophysical properties of the chalcogenide glass used. Consequently, it is preferable to describe trends rather than absolute magnitudes. The model has been very useful in understanding switch operation and what might be the optimum thermophysical values to be sought in the materials engineering of chalcogenide glasses.

Requirements for a variety of switch applications have been established as shown in figure 3 for one particular application. The thermal analysis model discussed above was used to calculate switch times for a chalcogenide switch with a thickness of 5μm for different values of the chalcogenide absorption coefficient. Previous results [7] have indicated that switch damage may occur above fluences of 60 J/cm^2 for pulses several milliseconds long. That threshold corresponds to a required switch time of approximately $2(10^{-5})$ sec as indicated by the horizontal bar in figure 3. Since the bulk chalcogenide material has an absorption coefficient of 15 cm^{-1}, it was clear that higher absorption coefficients would be necessary to provide the proper switch time. It was therefore necessary to determine the effect of various sputtering deposition parameters on chalcogenide film absorption coefficient.

4. Sample Preparation

Although a variety of techniques for depositing chalcogenide switch material have been examined as indicated in table 2, to date, the best process for fabricating chalcogenide switches appears to be the sputter technique. With this technique, high quality films of the proper composition can be fabricated. Previous efforts have identified a set of deposition parameters that are critical to film uniformity, compositional consistency, minimized film defects, and optimized deposition rate for different substrates. During the sample preparation the intent was to vary the set of deposition parameters that would possibly induce structural variations, and possible compositional variations as well. Parameters affecting structure are RF power and the target-to-substrate geometry. The parameters affecting compositional variations are the gas flow rate and gas pressure.

The $Tl_2SeAs_2Te_3$ target was synthesized from the elements, all of which had a purity of six 9's. The quartz tube was chemically cleaned and baked in a furnace at 400°C for at least 4 hours. Special effort was made to flush the quartz container with argon and remove air and moisture before sealing. The temperature was raised at the rate of 20°C each eleven minutes until it reached 550°C. The rocking furnace containing the quartz is then activated and the temperature rate of rise is increased gradually until the material has time to move completely from one end of the tube to the other. After twenty hours, the ampoule is quenched in air.

The sapphire and germanium substrates, 2mm and 1mm thick, respectively, were placed under the sputtering target. The argon bias voltage was varied between 0.6 and 1.4 kv. The distance between target and substrate was kept at two inches while the maximum sample temperature allowed was slightly above room temperature. An RF power at 50 watts forward with zero reflected resulted in deposition rates of 80Å. Prior to the deposition, samples were sputter etched clean. Once deposition was complete, the samples were maintained in a nitrogen dry box until the reflection and transmission measurements were performed. The particular sputtering conditions for each sample are shown in table 1. Aximuthal position refers to clockwise locations which are a fixed distance from a line drawn through the center of and normal to the target surface.

5. Results of Chalcogenide Switch Response Time

The switch time is defined in this document as the time for the transmitted pulse to reach i/e of its peak value. Integration under transmitted response curves indicates that the switch requires from 10^{-2} to 10^{-4} Joule/cm^2 to be activated. Results obtained indicate that submicron chalcogenide switching material undergo optical switching in nanoseconds to microseconds when exposed to intensities 10^4-10^5 watts/cm^2. The switch time varies approximately directly with switch thickness and inversely with incident intensity. Lowering the switch temperature generally increases the switch time, but the chalcogenide material does not show appreciable change until 170°. All thermally activated switching material including the chalcogenide material exhibits a certain degree of leakage due to the heat loss at the edge of the irradiated spot. This phenomena is more pronounced for Gaussian and non-uniform beams. Preliminary results show that a chalcogenide switch has an attenuation of 10^{-2} with a Gaussian beam.

6. Results of Optical Data Analysis

A Beckman IR4240 spectrophotometer was used to make reflection measurements on the film side, and in some cases transmission measurements from 2-12μm. All films measured were several quarter waves thick and homogeneous enough to produce interference effects. A typical resultant reflectance curve is illustrated in figure 4. Since the reflectance maximum occurs at an odd integral number of quarter wavelengths in optical thickness, a graph of integral value versus wave-number will be a straight line with slope given by four times the optical thickness. For the measurements reported here this non-linearity corresponds to a two percent change in index of refraction and is not critical to the conclusions. The results for the samples measured are listed in table 2.

Absorption data were also deduced for those samples where transmission measurements existed. For any assembly of thin films on a transparent substrate, the following relation is valid [8]

$$\frac{T}{1-R} = \frac{\eta_{\eta+1}}{\text{Real Part } (BC^*)} \tag{2}$$

where for a single film

$$\begin{pmatrix} B \\ C \end{pmatrix} = \begin{pmatrix} \cos\delta_F & (i\sin\delta_F)/N_F \\ iN_F\sin\delta_F & \cos\delta_F \end{pmatrix} \begin{pmatrix} 1 \\ \overline{n_s} \end{pmatrix} \tag{3}$$

and

$$\delta_F = \frac{2\pi n_F d_F}{\lambda} - \frac{i2\pi k_F d_F}{\lambda} \tag{4}$$

Furthermore, if k is small with respect to n, the above expressions may be combined near the turning points to yield

$$\alpha_F = \left(\frac{1}{d_F \left(\frac{n_F}{n_s} + \frac{n_s}{n_F} \right)} \quad \frac{1-R-T}{T} \right) \tag{5}$$

where the following definitions apply:

R	=	Reflectance of film and substrate
T	=	Transmission of film and substrate
n_{n+1}	=	Admittance of the film
$\begin{pmatrix} B \\ C \end{pmatrix}$	=	Characteristic matrix of the assembly
λ	=	Wavelength in free space
n_F	=	Refractive index of the film
n_s	=	Refractive index of the substrate
N_F	=	$n_F - ik_F$ = the complex index of refraction of the film
d_F	=	Film thickness

The absorption coefficients which were determined as described above are listed in table 1. Based on the results tabulated in table 3 and on the analysis of the reflection data, the following observations could be made: The index of refraction is basically constant from 20 to 10 μm to the accuracy of these measurements. An increase in sputtering pressure appears to produce a small decrease in the index of refraction.

There appears to be some dependence on substrate position as the number six position consistently has a lower index of refraction than the other positions. The refractive index of films on Al_2O_3 is lower than that on germanium (3.8 compared to 4.15). This is related to the equipment and the experimental set-up. Changing the voltage appeared to have no effect on the refractive index except when the voltage is reduced to 0.6KV. There seems to be little correlation of the index of refraction with thickness. The absorption coefficient appears to depend on the type of substrate as the value is much lower on Al_2O_3 than on germanium. The absorption coefficient seems to be independent of the voltage or sample position while an increase in sputtering pressure appears to increase the absorption coefficient as shown in table 2.

7. Results of Bidirectional Reflectance Measurements

For optical components and detector vulnerability applications, the scattering characteristics of the optical switch element is an important parameter. Measurement of the bidirectional reflectance distribution function (B.R.D.F.) and forward scattering distribution measurement does provide the necessary information. Scattering measurements versus temperature and angle of illumination remain to be evaluated. Until now we have measured the scattering for uncoated germanium substrate. The same substrate was remeasured after 9.9 μm of the $Tl_2SeAs_2Te_3$ was deposited by sputtering. The results shown in Table 3 indicates no considerable scattering due to 9.9 μm of chalcogenide on top of Ge substrate.

Table 3: I-R Measurements

Material	-θ-	BRDF/mm
Ge	1.5^{o}	$<6.10 \times 10^{-5}$
Ge coated with Chalcogenide (9.9μm)	1.5^{o}	3.20×10^{-3}

8. Switch Operation vs Laser Damage Effects

One of the important parameters for determining the performance of the chalcogenide was the power density versus optical transmission. The spatial distribution of the laser beam near the focal point of the input lens and the depth of focus of the lens were carefully measured. The beam as measured with a 0.001 inch slit had a diameter of 37μm and a depth of focus of approximately 0.2mm. For such a large depth of focus, the power density was uniform over a large enough region in space to make positioning of the switch less critical than in very short focus systems. The beam entering the focusing lens was checked out for maximum circular shape and minimum ellipticity and the power incident on the lens was typically 2.7 to 3.0 watts over the several days of the tests.

The data of relative transmission for the 7 micron test sample as a function of power density at three temperatures are shown in figures 5, 6, and 7. The relative transmission is the ratio of the signal amplitudes transmitted by the switch and incident on it normalized by the ratio of the detector outputs in the absence of the film and substrates but including all other elements in the optical train. The normalized signal amplitude ratio is only an approximation to the absolute transmission because of the unknown amounts of signal lost due to overfilling of lenses and beam splitters and losses due to scattering.

The relative transmission does not start at 1 for low power densities because of reflection losses from the two uncoated surfaces of germanium and the background absorption in the chalcogenide. These predict a relative transmission near 0.25 independent of thermal effects. Values significantly above or below this for low power densities may be due to surface irregularities or localized differences in film thickness. Movements of the switch through the laser spot showed adjacent areas of high and low transmission. For the test shown as figure 7, the sequence of trials starting with (1) was selected to have a low relative transmission for a small power density. It appears that something about the film must have changed as the power density was increased. From the collection of relative transmission curves, it is evident that absorption is a nonlinear function of power density probably through heating of the film as expected. The film of amorphous glass appeared to have a factor of 2 or 3 increase in absorption per decade increase in power density.

Some estimates of the damage threshold for the chalcogenide can be obtained from the relative transmission for increases in power density. The relative transmission continued to decrease with increasing power density until multiple pulses were applied at the highest power levels when the transmission increased, suggesting a change in the switch. The pulse lengths for the tests were approximately 6 milliseconds corresponding to an energy density of 6 joules/cm^2 for no change in relative transmission for repeated trials. The highest power levels corresponded to an energy density of 500 J/cm^2 where the switch showed the minimum transmission for several repeated pulses until it increased to a value between its previous value and the low power value. When the power level was reduced and the film was allowed to cool, the film appeared to heal itself and return to transmission at its previous lower power value. The self repair was probably due to a revitrification of the glass after being heated.

The chalcogenide film coating on the germanium substrate was found to survive laser irradiation and temperature cycling to 170 K with no apparent cracking, peeling, or separation of the glass material from the substrate. This was a positive contrast to one

sample in a previous test which separated and cracked. In each case, no damage to the substrate was detected.

Observation of the sample after testing revealed a regular pattern on the film surface that may have been related to variations in film thickness or structure. Figures 8 and 9 are typical views of the surface.

9. Conclusion

Presently, it is widely accepted that free electrons are the cause of laser induced damage to intrinsically transparent dielectrics in a self focusing free situation and in absence of absorbing inclusions. Although there is not broad agreement [9] on the process by which the free electron density increases in the presence of an intense laser field, it has been suggested [10] that the free electron density must reach 10^{18}-$10^{19}/cm^3$ in order to cause damage to the chalcogenide by heating due to the free electron absorption.

Such a density of free electrons will induce a detectable decrease in the refractive index of the chalcogenide film in addition to making it lossy. The decrease in specular reflectivity $\Delta n = 10^{-5} - 10^{-3}$ was measured for a BSC-2 glass which was subjected to a damaging Q-switched ruby laser pulse[11]. It was shown that the specular reflectivity decreases occured 2.4 nanoseconds prior to the onset of catastrophic damage and was caused by a laser induced increase in the free electron density with a measured average buildup time of 1.6 nanoseconds. The resulting free electron absorption can transfer a damaging amount of energy from the laser pulse to the sample causing at least melting of the irradiated surface site, as seen in this paper. Auger analysis revealed that for long pulse duration the material undergoes a chemical decomposition where the arsenic and selenium are sublimated from the laser exposed spot.

It appears that a viable switch, in terms of the requirements in figure 3, can be achieved with the sputtering techniques described above. It is also clear that variation of the sputtering deposition parameters will permit some control over the refractive index and absorption coefficient and that even more control over switch characteristics may be gained through a combination of process control and material selection.

Testing a 7 micron sample of chalcogenide on germanium at 299 K, 232 K, and 173 K revealed that the relative transmission is dependent on power density such as increasing power density produces a decrease in relative transmission. Switching was observed at 173 K. Further experimental work is needed to resolve questions of orientation in the laser beam and the relationship between surface appearance and performance.

ACKNOWLEDGEMENT

The authors would like to express their appreciation for the contribution of Ralph Somers of Aerojet Electro Systems Co., Azusa, CA. for his experimental and technical support.

References

[1] Ovshinsky, S.R., and Fritzsche, H., Amorphous semiconductors for switching, memory and imaging applications, IEEE Transactions on Electron Devices, Vol. ED-20, No. 2, Feb. 73.

[2] Stvom, U., and Bishop, S.A., Infrared optical switch-model and experiment, DOD Conference on Laser Hardened Material and Structures; NASA Ames Research Center, July 7-9, 1975.

[3] Marzwell, N., Somers, R., Dong, W., Kienzle, W., and Jefrey, J., Infrared Chalcogenide glass for applications in laser optical switching systems, High Power Laser Optical Components Meeting, Lowry Air Force Base, Sept. 15, 1978.

[4] Mitchell, D.L., Taylor, P.C., and Bishop, S.G., Free carrier optical absorption in vitreous $Ti_2SeAsTe_3$, Solid State Communications, Vol. 9. pp. 1833-1837, 1971.

[5] Taylor, P.C., Bishop, S.G., and Mitchell, D.L., Temperature Dependence of local order in the layer-type liquid semiconductors As_2Se_3 and $Tl_2SeAs_2Te_3$, Phys. Rev. Letters, 27, No. 7, p. 414, August 1977.

[6] Bishop, S.G., Taylor, P.C., Mitchell, D.L. and Slack, L.H., Far infrared and microwave conductivity spectrum of semiconducting $Rl_2AsSe_2Te_3$ glass, Journal of Non-Crystalline Solids 5, R351-359, 1971.

[7] Somers, R., Aerojet Electro-systems Co., private communications, August, 1978.

[8] Macleod, H.A., Thin Film Optical Filters, American Elsevier Publishing Co. Inc., New York, 1969

[9] Bass, M., and H.H. Barrett, "Avalanche breakdown and the probabilistic nature of laser induced damage" IEEE J. QE 8, 338 (1972).

[10] Bloembergen, N., "Laser-induced electric breakdown in solids", IEEE J. QE 10, 375 (1974).

[11] Alyassini, N., and Parks, J. , "Measurement of free electron density at the onset of laser induced surface damage in BSC-2. Laser Damage Conference 1977.

Table 1. The Optical Properties of $Tl_2AsSe_2Te_3$ for Various Sputtering Conditions

Substrate Material	Sputtering Voltage (kv)	Sputtering Pressure (μ)	Azimuthal Location	Film Thickness (μm)	n_F	Absorption Coefficient (cm^{-1})			
						3μm	5μm	7μm	1μm
Al_2O_3	BL	BL	BL	5.6	3.81	35	181	CO	CO
Al_2O_3	BL	BL	BL	0.6	3.71	571	459	CO	CO
Al_2O_3	BL	BL	BL	9.9	3.83	423	700	CO	CO
Al_2O_3	BL	BL	BL	9.9	3.91	797	1,343	CO	CO
Al_2O_3	BL	BL	BL	9.9	3.65	240	371	CO	CO
Ge	BL	BL	BL	5.6	3.42	---	---	---	---
Ge	BL	2.5	3	2.44	4.61				
Ge	BL	2.5	6	2.44	4.02	2,574	2,262	2,229	2,183
Ge	BL	2.5	9	2.44	4.56	2,035	2,005	1,985	1,852
Ge	BL	2.5	12	2.44	4.61	---	---	---	---
Ge	BL	5.0	3	2.07	3.74	---	---	---	---
Ge	BL	5.0	6	2.07	3.66	3,920	4,401	3,964	3,296
Ge	BL	5.0	9	2,07	3.86	3,602	3,164	2,956	2,593
Ge	BL	5.0	12	2.07	3.86	---	---	---	---
Ge	BL	BL	3	2.52	4.96	---	---	---	---
Ge	1.4	BL	6	2.52	4.06	2,033	1,440	1,061	1,496
Ge	1.4	BL	9	2.52	4.33	2,498	2,244	2,201	2,138
Ge	1.4	BL	12	2.52	4.25	---	---	---	---
Ge	0.6	BL	3	2.94	2.46	---	---	---	---

CO = Wavelength exceeds the transmission cut off in Al_2O_3

BL = Baseline parameters.

Table 2. Several deposition techniques have been considered for the chalcogenide material

Deposition Technique	Assessment
Chemical Vapor Deposition	Chemical reaction involved, anticipate stoichiometry problems
Sputtering	Technique has been used successfully
Evaporation	Attempts to date have not been used successfully
Oxidation	Not applicable
Reduction	Not applicable
Glow Discharge	Primarily for organic materials, stoichiometry considerations
Hot Press (Heat material above the softening temperature and control thickness mechanically)	Uniformity problems, not applicable for thinner switches (~25μm)

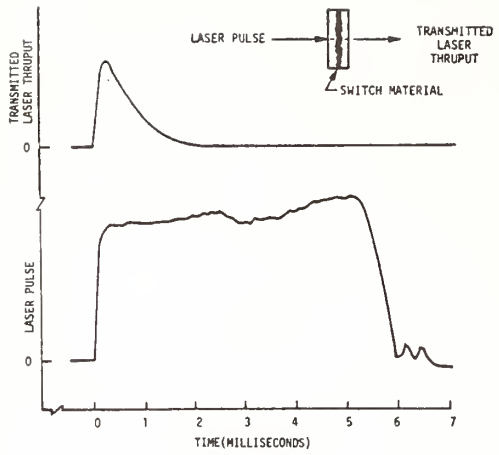

Figure 1. Typical switch configuration and response when irradiated by a high intensity laser beam.

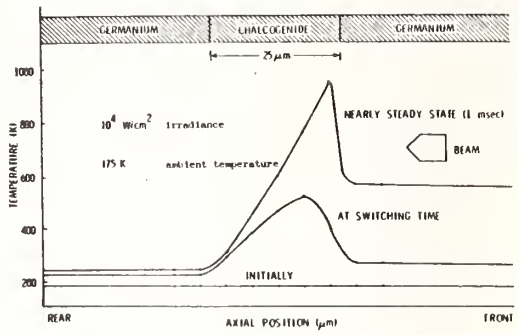

Figure 2. Axial temperature profile at switching time and later.

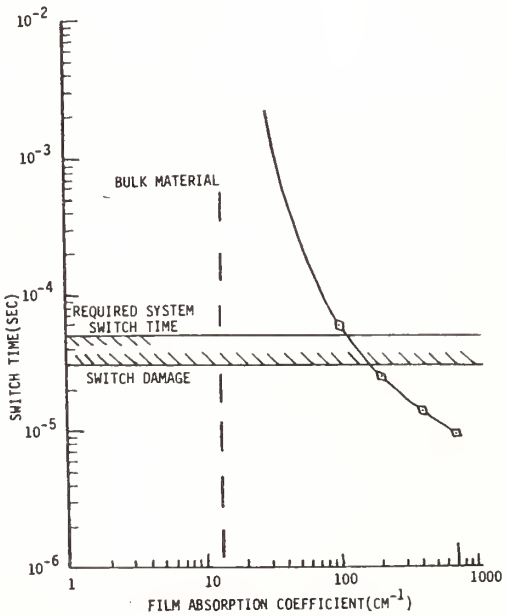

Figure 3. Acceptable switch times can be achieved by material process control of the absorption coefficient.

REFRACTIVE INDEX:

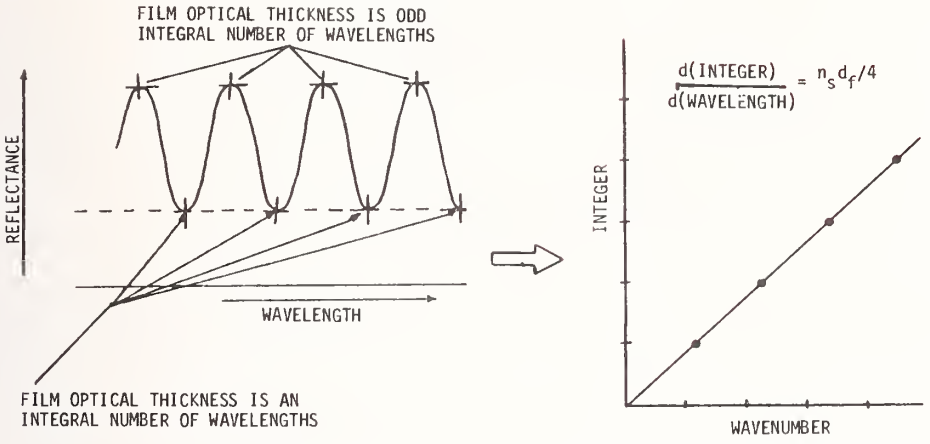

ABSORPTION COEFFICIENT NEAR THE TURNING POINTS:

$$\text{ABSORPTION COEFFICIENT} = \frac{1}{d_f\left(n_s/n_f + n_f/n_s\right)}\left(\frac{1-R-T}{T}\right)$$

Figure 4. The technique used to determine the refractive index and the absorption coefficient.

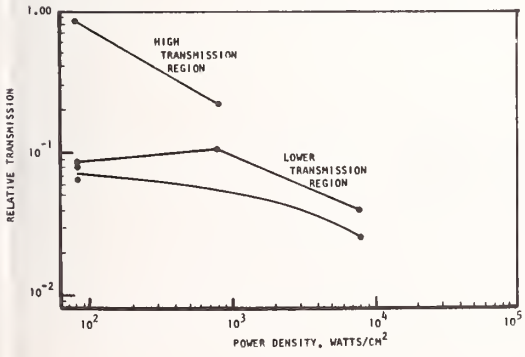

Figure 5. Power Density vs. Relative Transmission for a 7-mm Chalcogenide on Germanium (232°K).

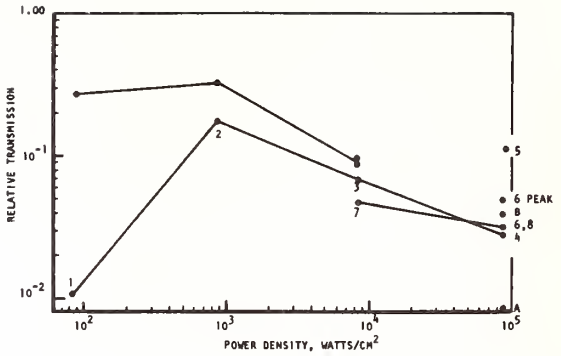

Figure 6. Power Density vs. Relative Transmission for a 7-mm Chalcogenide on Germanium (168°K to 173°K).

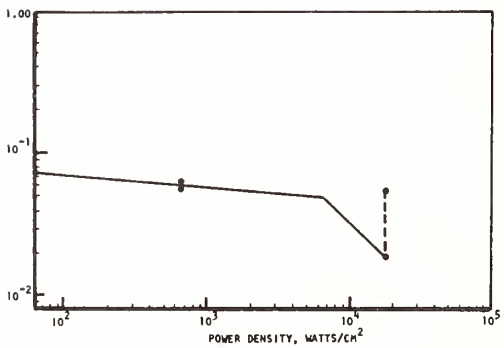

Figure 7. Power Density vs. Relative Transmission for a 7-mm Chalcogenide on Germanium (299°K).

IMPROVEMENTS IN CLARITY AND ENVIRONMENTAL STABILITY OF TLI-CONTAINING ANTIREFLECTIVE COATINGS

W.T. Boord, P.P. Chow
Honeywell Systems and Research Center
Minneapolis, Minnesota 55413

and

W.B. Harrison, J.E. Starling
Honeywell Ceramics Center
Golden Valley, Minnesota 55422

Clarity of Tll films in visible light was improved by masking the textures of polycrystalline KCl substrates with thin SrF_2 films. Also, the use of more environmentally durable fluoride films as replacements for KCl in the Tll-KCl-Tll 10.6 micron antireflective coating system was investigated.

Key words: Antireflective coating; deposition technique; environmental stability; masking layer; potassium chloride window; scattering; thallium iodide

1. Introduction

This KCℓ window coating study consists of two parts. The first is a study of the ability of strontium fluoride to mask the texture of KCℓ substrates in order to produce clear coatings. The second is a study of film absorptions produced by lead fluoride and sodium fluoride, which are more environmentally durable materials being evaluated as potential replacements for KCl in the TℓI-KCl-TℓI 10.6 μm antireflective coating system.

2. Substrate Preparation

Polycrystalline Eu-doped KCℓ, produced by hot forging, was used for the 3.81 cm diameter substrates in this work. Rough shaping of substrates was carried out with 600 grit silicon carbide abrasive. Intermediate polishing was then performed on a Pellon TAN-W pad using 0.3 alumina carried in kerosene-type liquid. This process removed approximately 100 microns of material from each face. Substrates were then etched in concentrated hydrochloric acid for 60 seconds to remove about 10 microns of material from each face. A final mechanical polish was then done on a beeswax lap with 0.3 micron alumina carried in triacetin.

3. Masking Layer Study

Four KCℓ substrates were used for the masking layer study. Single crystal strontium fluoride, obtained from Optovac, was evaporated from a Radak source. We found that because of higher efficiency of the Radak source the vacuum system did not heat up much during deposition. As shown in figure 1 each polished substrate surface was divided into quadrants, three of which were coated with strontium fluoride films of nominal thicknesses of 200, 400, and 600 Å. Substrates were then overcoated with thallium iodide of varying thickness.

Clarity was characterized by measuring the transmission of the 6328 Å He-Ne laser line through each quadrant. Table 1 shows the transmission data. It is seen that transmission was most improved by the 200 Å thick masking layers. The strontium fluoride layer modified the effect of the KCℓ substrate on the growth of TℓI films. It was noted that the TℓI films on the unmasked portion of the substrate tended to grow in orientations determined by the texture of the KCℓ substrate, resulting in visible striations. As shown in figure 2, this striation was not observed on the masked portion of the sample, indicating that uniform growth of TℓI was promoted by the presence of the masking layer.

Work is supported by AFWL, contract No. F33615-77-C-5038, Dr. G. Edward Kuhl project monitor.

4. Alternate Materials

Another task of this coating study was to investigate materials which might replace KCℓ in a three-layer AR coating design. Viable replacements would need to have low absorption coefficients and be less hygroscopic than KCℓ. Lead fluoride and sodium fluoride were chosen for this study. These films were deposited, using single crystal starting materials, over TℓI coated KCℓ substrates in the pattern shown in figure 3. Lead fluoride was evaporated from a Radak fixture with an alumina crucible. Uniform appearing films were deposited at 600 Å/min. Sodium flurodie was evapoarted using a chemically inert BeO crucible. Molten NaF tended to wet the wall of the crucible and run up and over the side of the crucible. By using a clean, new crucible, a NaF film was deposited by carefully adjusting the deposition rate.

Both lead fluoride and sodium fluoride are environmentally more stable than potassium chloride, but our absorption measurements indicated that their absorption coefficients are substantially higher. We believe this is partially due to the fluorides reacting chemically with crucible materials causing impurities to be incorporated into the films. The PbF_2 reacted with and damaged the alumina crucibles after two or three depositions. Refinement of the present deposition technique is likely to overcome this problem.

Table 1. SrF_2 masking layer results

Sample #	Tll Thickness (μm)						
6_5	0.3	SrF_2 Thickness (Å)	0	200	400	600	
		Transmission, %	0.53	0.55	0.54	0.52	
15_6	0.79	SrF_2 Thickness (Å)	0	200		650	850
		Transmission, %	0.48	0.51		0.49	0.49
10_6	1.29	SrF_2 Thickness (Å)	0	200	400	600	
		Transmission, %	0.34	0.43	0.42	0.42	
14_2	1.79	SrF_2 Thickness (Å)	0	200	400	600	
		Transmission, %	0.17	0.21	0.21	0.21	

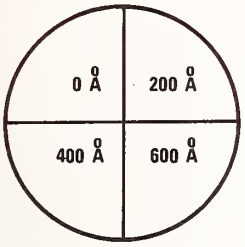

Figure 1. SrF_2 quadrant coating for masking study

Figure 2. Unmasked (upper-right) quadrant shows striation

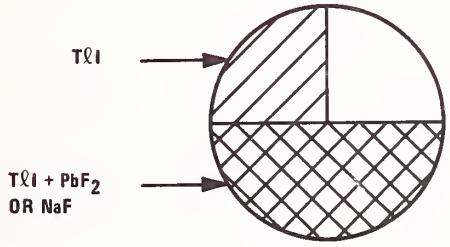

Figure 3. Fluoride coating for absorption measurements

REACTIVELY SPUTTERED OPTICAL COATINGS FOR USE AT 1064 NM*

W.T. Pawlewicz, R. Busch, D.D. Hays, P.M. Martin and N. Laegreid
Pacific Northwest Laboratory
Richland, Washington 99352

Optical coatings of TiO_2, $In_{1.9}Sn_{0.1}O_3$ (ITO), Ta_2O_5, Nb_2O_5, a-Si:H and SiO_2 have been prepared by reactive sputtering for use with lasers operating near 1064 nm. Damage thresholds of 7-10 J/cm^2 for TiO_2 and 5-6 J/cm^2 for transparent-conductive ITO were measured at Lawrence Livermore Laboratory for $\lambda/2$ coatings on fused silica irradiated with 1 nsec laser pulses. Sputtered Ta_2O_5, Nb_2O_5 and a-Si:H also appear to be promising high-index coating materials, but have not yet been damage tested. The reactive sputtering process is shown to allow precise control of coating crystalline phase and grain size. For TiO_2 both optical properties and damage threshold have been related to these materials properties, and glassy coatings are shown to be optimal.

Key words: Glassy structure; laser damage resistance; materials properties; oxide coatings; reactive sputtering; transparent-conductive coatings.

1. Introduction

Optical materials in thin film coating form have long been the most damage-sensitive elements in high power laser systems. Attempts to maximize coating damage resistance have traditionally involved its relationship to such deposition conditions as substrate temperature, deposition rate, partial pressure of reactive gas, etc. Although this approach is usually effective in optimizing coating performance, it relegates coating technology to the status of an art rather than a science. That is, the fundamental differences between an optimized coating and an unoptimized coating are never explored. The question "what makes a good coating good?" is not addressed. Thus experience gained in optimizing one coating material is of little assistance in optimizing a second. Further, knowing how a coating was made, rather than knowing the physical characteristics of the coating, is of little help in understanding the thresholds and mechanisms of laser-induced damage to that coating.

This paper reports results to date for a more fundamental approach to the optimization of optical coatings for high energy laser applications. Specifically, it deals with oxide optical coatings prepared for use at 1064 nm in neodymium:glass lasers. The approach is to study the dependence of damage threshold on the basic materials properties of a coating: crystalline structure and/or phase composition, grain structure (size, shape and orientation) and stoichiometry. Most of the work is being done for TiO_2. Other materials for which preliminary results are available are $In_{1.9}Sn_{0.1}O_3$ (ITO), Ta_2O_5, Nb_2O_5 and SiO_2. Amorphous Si:H alloys (a-Si:H) are also introduced as potential very-high-index coatings for use at 1064 nm. All of the coatings are made by rf diode sputtering which permits excellent reproducibility and precise control of coating materials properties through appropriate selection of deposition conditions. This materials-oriented approach has resulted in systematic optimization of the damage threshold of TiO_2 coatings, determination

*Work supported by the US Department of Energy, Offices of Inertial Fusion and Basic Energy Sciences.

of some key materials properties for high damage thresholds, and some potentially useful information for understanding damage mechanisms. Information gained with TiO_2 is now being extended to other metal oxides as well as novel materials such as a-Si:H.

2. Apparatus and Experimental Details

All oxide coatings are made by rf-diode reactive sputtering in an Ar/O_2 atmosphere. Figure 1 is a simplified schematic of a typical system used for this work. The oxides of Ti, Ta and Nb are made from metal plate targets. ITO coatings use a pressed-powder oxide target. Silica coatings are made with a Suprasil target. Si:H coatings are made by sputtering a vacuum-cast Si target in Ar/H_2 atmospheres. Substrates are fused silica discs. Both substrate and target electrodes are specially designed for operation over a wide range of gas pressures. A power-splitting network is used to distribute rf power to both the target for deposition and to the substrate for bias sputtering. The diode systems are mounted on conventional oil-pumped vacuum systems. Sputtering gas is mixed and pressures are measured with a capacitance manometer. Substrate temperature is measured with a thermocouple in the metal substrate holder. A quartz crystal thickness monitor is sometimes used to deposit coatings with a desired thickness. Principal deposition parameters affecting the materials properties are substrate temperature (20° to 700°C), oxygen or hydrogen partial pressure (0 to 10 Pa), and the rf-induced dc bias voltage applied to the substrate (0 to -500 V dc).

Crystalline structure, phase composition and grain size are determined for each coating using conventional x-ray diffractometer [1,2] and transmission electron microscopy (TEM) techniques. Optical properties are measured spectrophotometrically over the wavelength range from 200 to 2500 nm, and optical constants are deduced using the method of Manifacier, et al [3]. Laser damage thresholds are made by Lowdermilk, Milam, et al at Lawrence Livermore Laboratory, Livermore, CA (LLL) [4].

3. Results

3.1 Control of TiO_2 Materials Properties

For TiO_2 the important materials properties are grain size, phase composition (there are two crystalline phases, anatase and rutile) and stoichiometry. In this work phase compositions ranging from 40% rutile/60% anatase to 100% rutile are reproducibly obtained. Phase composition is influenced only by substrate temperature and O_2 partial pressure, as shown by the phase composition diagram of figure 2. Intermediate substrate temperatures of roughly 200 to 500°C result in mixed-phase coatings with rutile contents given by the numbers in the circles. The rutile content increases with the O_2 pressure. Rutile coatings are obtained for lower temperatures and higher temperatures. O_2 partial pressures less than 1.2 Pa always result in Ti metal coatings.

The occurrence of the rutile phase over a wide range of temperatures when high O_2 pressures are used permits deposition of coatings with grain sizes ranging from 10 to 60 nm through appropriate selection of the substrate temperature. For mixed-phase coatings, grain sizes are restricted to 10 to 30 nm since mixed-phase coatings are obtained only over a narrower temperature range.

Figure 3 shows the influence of substrate temperature on the average grain size of a rutile coating. Grain sizes near 10 nm are obtained for substrate temperatures between 20 and 250°C. Above 250°C grain size increases with temperature to about 30 nm near 600°C. Larger grain sizes can be obtained

at higher target power levels by capitalizing on plasma heating of the substrate, as shown in the inset for a nominal substrate temperature of 450°C. Grain size rises with power density to 60 nm near 8 W/cm^2. At still higher power levels grain size decreases due to inhibition of lateral grain growth by high deposition rates. The data in this figure were obtained both by x-ray diffraction and TEM techniques. Agreement between the two techniques is good for larger grain sizes and fair for the smaller.

Coatings with a predominatly glassy structure, or a grain size smaller than 10 nm, are obtained by applying 5 to 10% of the rf power to the substrate. With rf substrate bias, glassy coatings are obtained regardless of the substrate temperature used. Thus by using substrate bias, substrate temperature and target power in the right combination, microstructure can be controlled from essentially glassy to 60 nm grain size.

3.2 TiO_2 Optical Properties and Laser Damage Thresholds

Phase composition is found to have a small but significant influence on coating refractive index. Figure 4 shows the index at 1000 nm plotted as a function of rutile content. Since grain sizes in mixed-phase coatings are restricted to 10-30 nm, the data point shown for 100% rutile is the average index observed for these grain sizes only. Only a small variation of the index with phase composition is observed, due to the closeness of the refractive indices of rutile and anatase. The apparent variation of the index is only 3%, which is approximately equal to the scatter in the data points.

Phase composition does not appear to influence damage resistance. Table 1 summarizes damage thresholds for coatings having a grain size of 10 to 15 nm. Little difference is apparent between the two groups. There is also no obvious dependence of threshold on rutile content of the mixed-phase coatings.

Grain size, on the other hand, has been found to have a very significant influence on both the refractive index and the damage resistance of TiO_2 coatings. Figure 5 shows the influence of grain size on the refractive index at 1000 nm for 100% rutile coatings. For large grain sizes the ~ 2.5 index of bulk material is obtained. With decreasing grain size, the index drops to values as low as 2.0 for glassy coatings. The discovery of this relationship explains the wide range of index values reported in the literature for TiO_2 coatings. Knowing this relationship, it is possible to preselect the refractive index of a coating for a particular application by choosing deposition conditions that give you small, intermediate, or large grain size. Alternatively, by measuring the refractive index of a coating one can determine the grain size.

The influence of grain size on the laser damage resistance of TiO_2 coatings is shown in figure 6. There are two key results. First, damage resistance increases with decreasing grain size. Second, damage thresholds of 7 to 10 J/cm^2 are obtained for glassy coatings. It is also interesting to note that damage threshold increased consistently with the amount of bias applied to the substrate. Thresholds of 7 to 10 J/cm^2 are encouraging for single layers. They are very close to the values needed for the NOVA laser and are twice as high as the TiO_2 coatings presently used in the laser if the coatings are tested as single layers on fused silica substrates. Antireflection (AR) stacks of SiO_2 and e-beam evaporated TiO_2 coatings exhibit twice the threshold of single layer TiO_2 coatings. The same improvement in threshold for sputtered AR stacks may be possible.

The most outstanding difference between the glassy coatings and the polycrystalline coatings is a much lower surface roughness. Figure 7 shows both Nomarski and SEM surface micrographs for a glassy coating and coatings with grain sizes of 40 and 86 nm. The surface roughness scales with the grain size. Because of light scattering from the rough surfaces of polycrystalline coatings, the glassy coatings are of higher optical quality. The smoothness of the glassy coatings (figure 7) and their lower refractive index (figure 5) may be responsible for their higher damage resistance. A third possibility is that the glassy coatings, which are all bias sputtered, contain fewer impurities due to preferential resputtering of loosely bonded species from the substrate as the coating grows [5].

Recently, the first TiO_2/SiO_2 AR stacks were made using a glassy TiO_2 layer. The 2-layer design of 0.0833 λ TiO_2/0.333 λ SiO_2 illustrated in figure 8 was used with layer indices of 2.10 and 1.45, respectively. This stack can be reproducibily made with reflectance $\lesssim$ 0.1% near 1064 nm, as shown in the figure. The stacks were made both with and without a 0.5 λ SiO_2 underlayer between the stack and the substrate. Measurements are now in progress at LLL.

3.3 Other High-Index Coating Materials

In addition to TiO_2, the oxides of Ta and Nb are being studied. Excellent glassy coatings of Ta and Nb pentoxides can be made by reactive sputtering. It is found that glassy coatings do not scatter light like their polycrystalline counterparts. Shown in figure 9 are the transmission spectra and refractive indices near 1000 nm wavelength as compared to the glassy TiO_2. The coatings are smooth, the band edges are sharp and higher in energy than TiO_2, there is no absorption or scattering in the visible or near infrared, and the refractive indexes are close to that of TiO_2. The index of Nb_2O_5 is 5% higher than TiO_2, while Ta_2O_5 is 5% lower.

The very-high-index amorphous Si:H alloys are also being investigated. These alloys are potentially important for solar photovoltaic applications and may be useful for 1.06 μm polarizors. By depositing Si in an amorphous or glassy form and alloying it with hydrogen the optical band edge can be shifted from its crystalline value near 1.1 eV (1100 nm) all the way out to 2 eV. The refractive index drops to about 3.0 from its crystalline value of 3.45, but it is still so high as to make it a very attractive high index material. Damage testing of a-Si:H is planned soon.

3.4 Transparent Conductive ITO Coatings

Transparent conductive ITO coatings with high damage thresholds are also being prepared by reactive sputtering. These coatings can be used as the electrodes on electro-optic devices used in high energy lasers to suppress spurious laser radiation or to prevent retro-reflections from damaging the laser. Damage thresholds of 5.5 to 6 J/cm^2 were obtained for coatings with sheet resistances of 500 and 17,500 ohm/cm^2. These high threshold values are very impressive and may make possible significant improvement in the fabrication of electro-optic devices for HEL applications [6].

The sputtered coatings were found to have lowest beam attenuation due to scattering and absorption when compared with coatings from four commercial sources. Measurement results are summarized in table 2. These attenuation measurements were made by the Laboratory for Laser Energetics (LLE) at the University of Rochester [7]. The attentuation was found to increase with decreasing sheet resistance. For comparable resistances, the sputtered coatings show lowest attenuation.

4. Summary

Controlled variation of the materials properties of TiO_2 coatings has been demonstrated with the reactive sputtering process. Microstructure can be varied from glassy to 60 nm grain size. Phase composition can be varied from 60% anatase/40% rutile to 100% rutile. All the sputtered coatings are stoichiometric.

The relationship between refractive index and grain size has been established for rutile coatings. The index can now be preselected from 2.0 to 2.5 at 1000 nm, and 2.2 to 2.7 at 550 nm. The relationship explains the wide range of index values reported for TiO_2 in the literature. The variation of the index with phase composition has been determined to be small.

High damage thresholds of 7-10 J/cm^2 have been obtained for TiO_2 coatings prepared by rf reactive sputtering. Correlation of damage resistance with grain size indicates glassy coatings have highest resistance to laser-induced damage. Phase compositions between 40% rutile/60% anatase and 100% rutile result in the same damage thresholds. Two-layer TiO_2/SiO_2 AR stacks with less than 0.1% reflection loss at 1064 nm have been made, but damage testing results are not yet available.

Glassy coatings of Ta_2O_5, Nb_2O_5 and Si:H have also been made by the same reactive sputtering techniques and have been optimized for optical applications. Damage testing has not yet been done. These coatings have indices of 2.0, 2.2 and 3.0 at 1064 nm, respectively, and could be superior substitutes for TiO_2.

Finally, high damage resistance of 5-6 J/cm^2 and low attenuation have been demonstrated for reactively-sputtered, transparent-conductive coatings of ITO. The coatings appear promising for electro-optic device applications.

Acknowledgments

The authors gratefully acknowledge W.H. Lowdermilk and D. Milam of LLL for measurement of all damage thresholds reported in this paper, and S.D. Jacobs of LLE for providing the ITO attenuation data of table 2. They also thank I.B. Mann, E.L. McDonald and H.E. Kjarmo of PNL for technical assistance with coating preparation and characterization and H.R. Gardner for reviewing this manuscript.

References

[1] Hall, W.H., Proc. Phys. Soc. (London) A62, 741 (1949).

[2] Barrett, C.S., Structure of Metals, McGraw-Hill (New York 1952) 425-428.

[3] Manifacier, J.C., Gasiot, J., and Fillard, J.P., J. Physics E: Scient. Instr. 9, 1002 (1976).

[4] Milam, D., Appl. Opt. 16, 1204 (1977).

[5] Maissel, L.I., and Glang, R., Handbook of Thin Film Technology, McGraw-Hill (New York (1970) Chapter 4.

[6] Pawlewicz, W.T., Mann, I.B., Lowdermilk, W.H., and Milam, D., Appl. Phys. Letters 34, 196 (1979).

[7] Jacobs, S.D., private communication.

Table 1. Laser damage thresholds of TiO_2 optical coatings with the same grain size but different phase compositions. All coatings are single layers with half-wavelength thickness at 1064 nm (~ 230 nm) on fused silica substrates

Coating/ Substrate	Phase Composition[a]	Grain Size (nm)[a]	Damage Threshold (J/cm^2)[b]
54/S1-354	100% R	11	5.2 ± 0.8
57/S1-358	"	15	3.9 ± 0.6
85/S2-365	"	10	$\lesssim$ 2.5
55/S1-356	65% R/35% A	10/12	4.1 ± 0.7
68/S3-365	60% R/40% A	10/10	2.3 ± 0.5
56/S1-357	85% R/15% A	12/12	$\lesssim$ 2.0

(a) X-Ray Diffraction.
(b) Measured at LLL, 1 nsec pulses, 2 mm beam diameter.

Table 2. Laser damage thresholds and beam attenuation values for transparent-conductive coatings of various sheet resistance

Coating		Material		Sheet Resistance (Ω/cm^2)	% Attenuation at 1064 nm[a]	Damage Threshold (J/cm^2)[b]
25/S2-360	PNL	Sputtered	ITO	17,500	0.9	6.0 ± 0.5
23/S2-352		Sputtered	ITO	500	2.8	5.5 ± 0.5
20		Sputtered	ITO	19	7.0[c]	--
--	OCLI	Evaporated	ITO	12	--	3.5 ± 0.5
LCU-4		Evaporated	IO	100	4.4	2.5 ± 0.5
LCH-4		Evaporated	IO	20 ± 10	18.2	--
LC-4		Evaporated	IO	90	7.6	--
CC-1		Evaporated	IO	100	41.7	--
LCM-4		Evaporated	IO	200	6.2	--
LLE 481	OCC	Evaporated	ITO	15	14.4	--
LLE 461	Corning	Fired	--	15 - 100	39.7	--
LLE 468A	PPG	Sputtered	IO	5	48.3	--
LLE 468B		Sputtered	IO	20	25.5	--
LLE 468C		Sputtered	IO	100	9.6	--
LLE 468D		Sputtered	IO	300	8.0	--
LLE 468E		Sputtered	IO	500	14.1	--
LLE 469A		Fired	TO	20	37.9	--
LLE 469B		Fired	TO	80	20.9	--
LLE 469C		Fired	TO	180	14.1	--

(a) Measured at LLE, University of Rochester.
(b) Measured at LLL, 1 nsec pulses, 2 mm beam diameter.
(c) Measured at PNL.

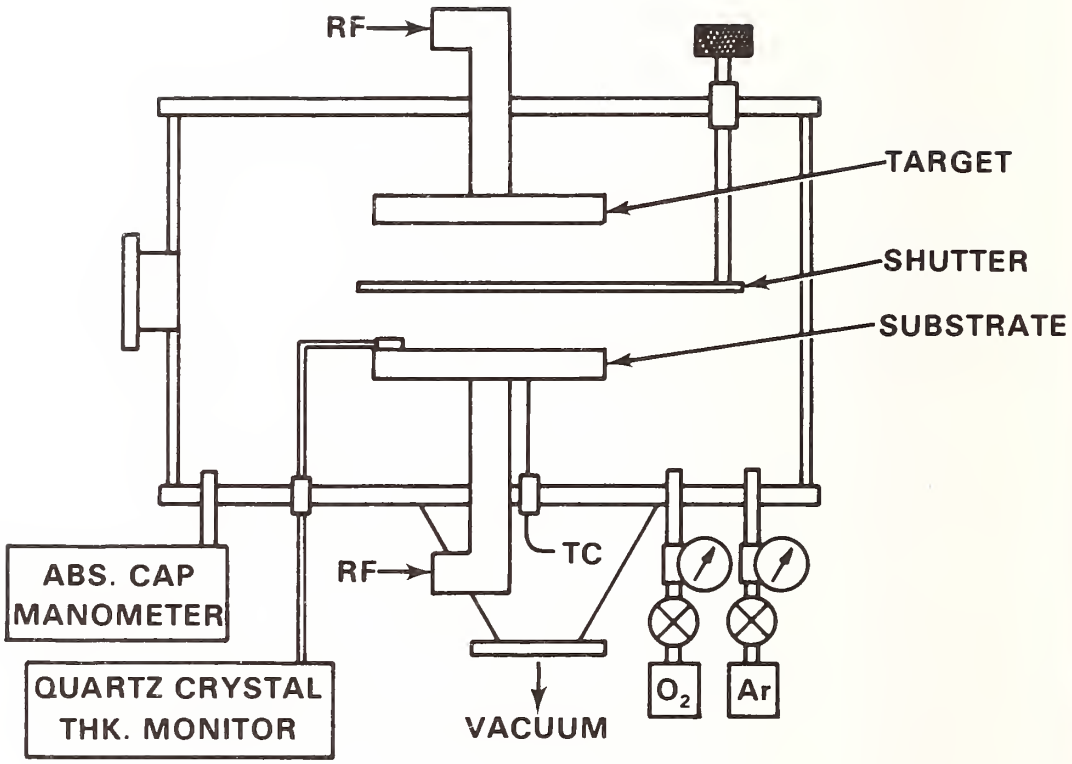

Figure 1. Features of rf diode reactive sputtering system used to deposit oxide coatings.

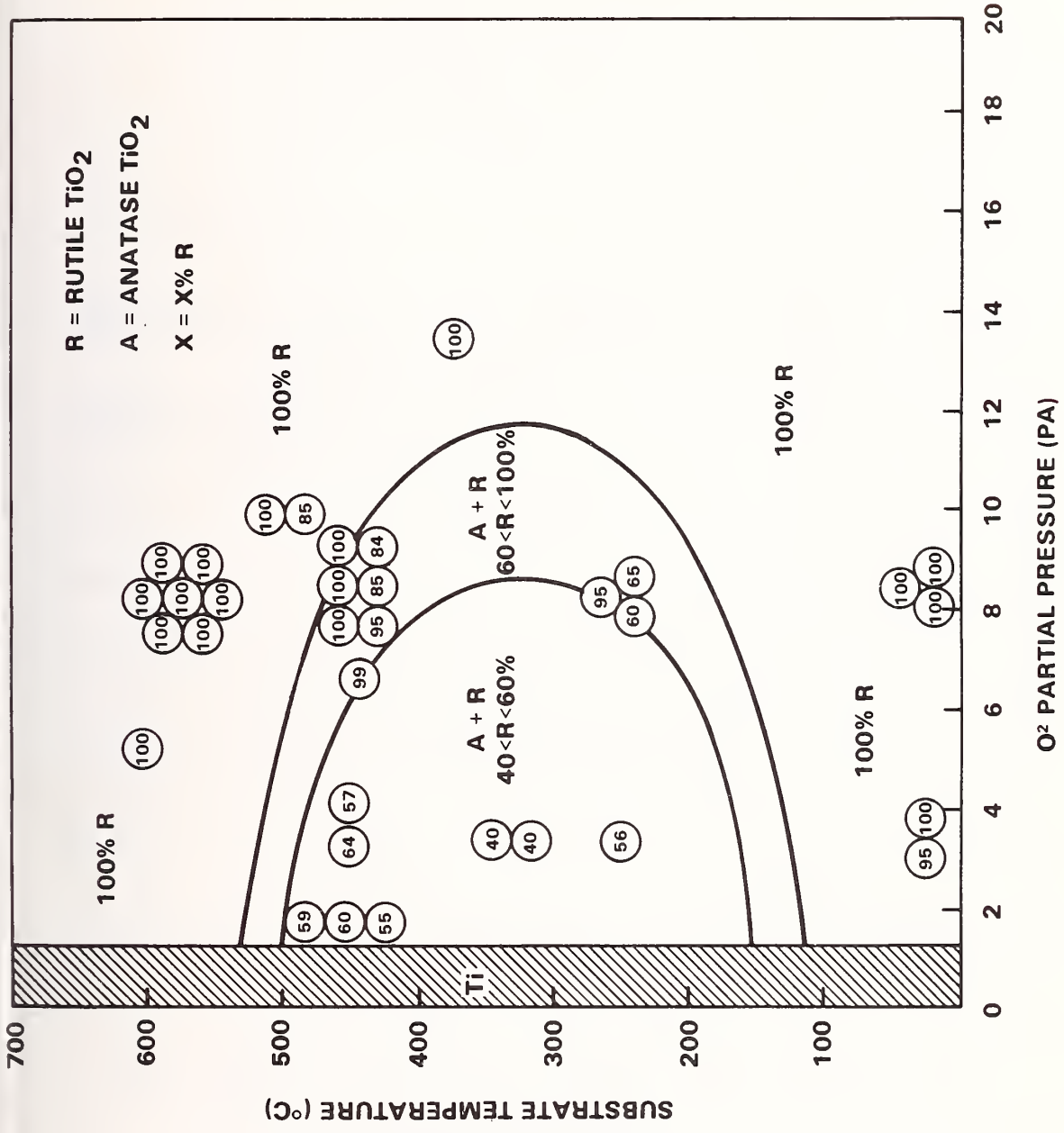

Figure 2. Phase composition diagram for TiO_2 coatings constructed from pertinent sputtering condition data. Diagram can be used to preselect the anatase/rutile composition of an optical coating.

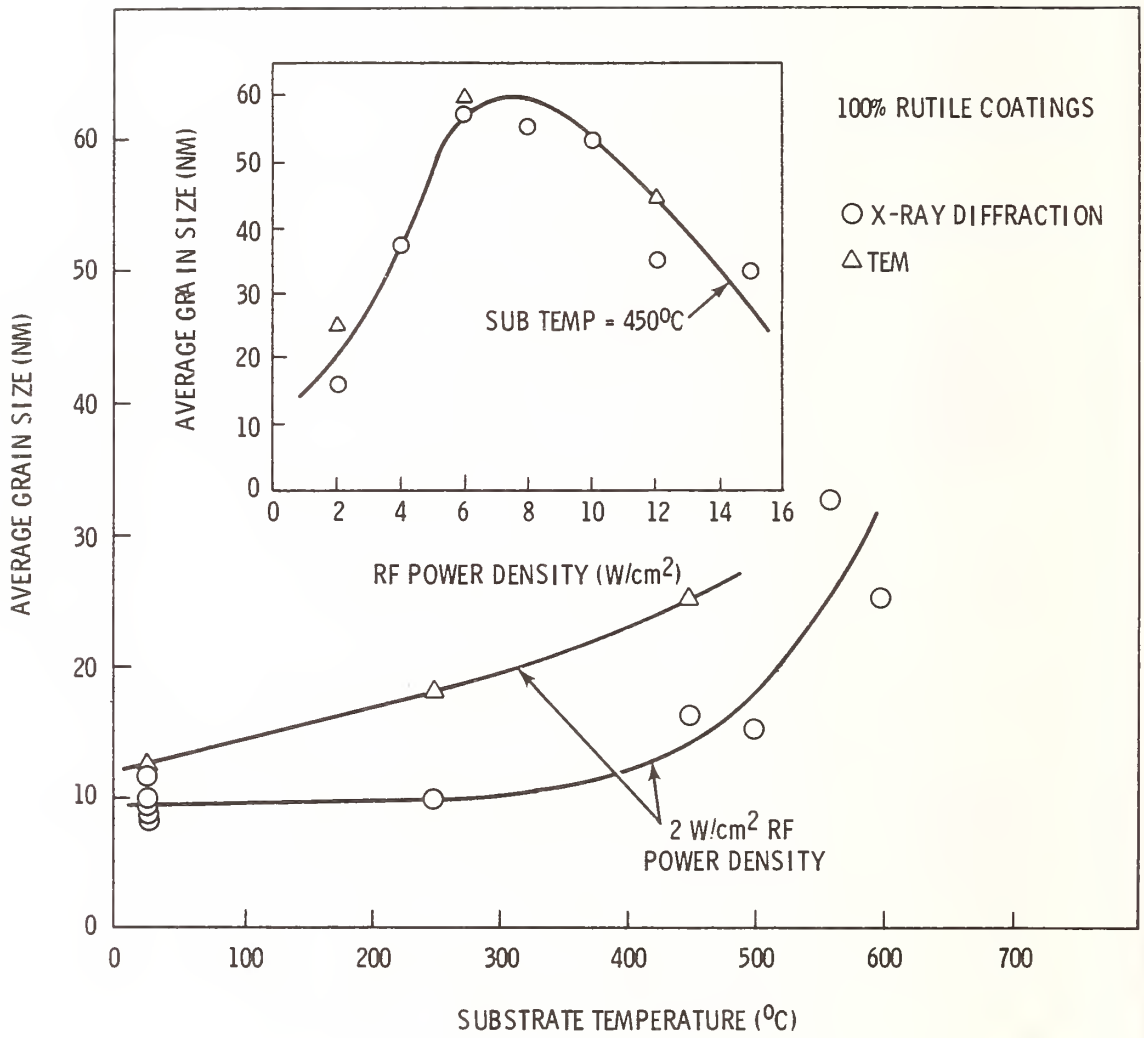

Figure 3. Influence of substrate temperature on the grain size of rutile coatings. Inset shows grain size enhancement by plasma heating during deposition.

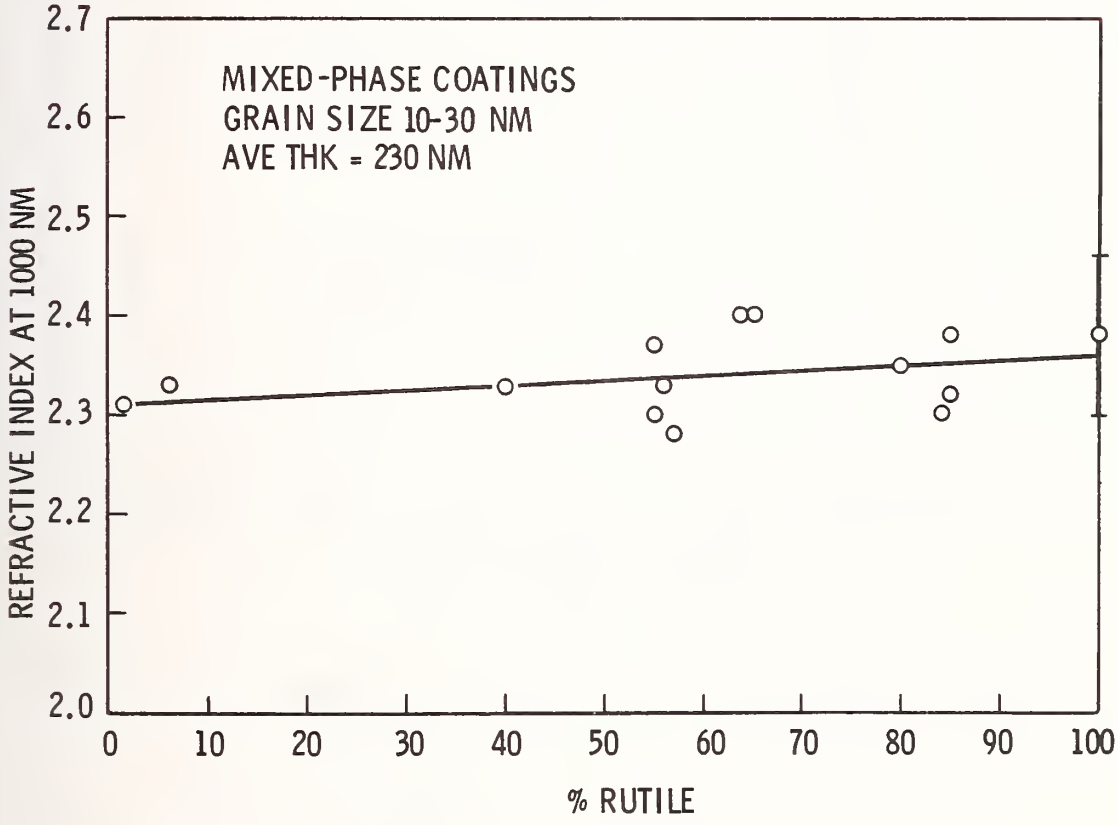

Figure 4. Influence of phase composition on the refractive index of TiO_2 coatings with intermediate grain sizes.

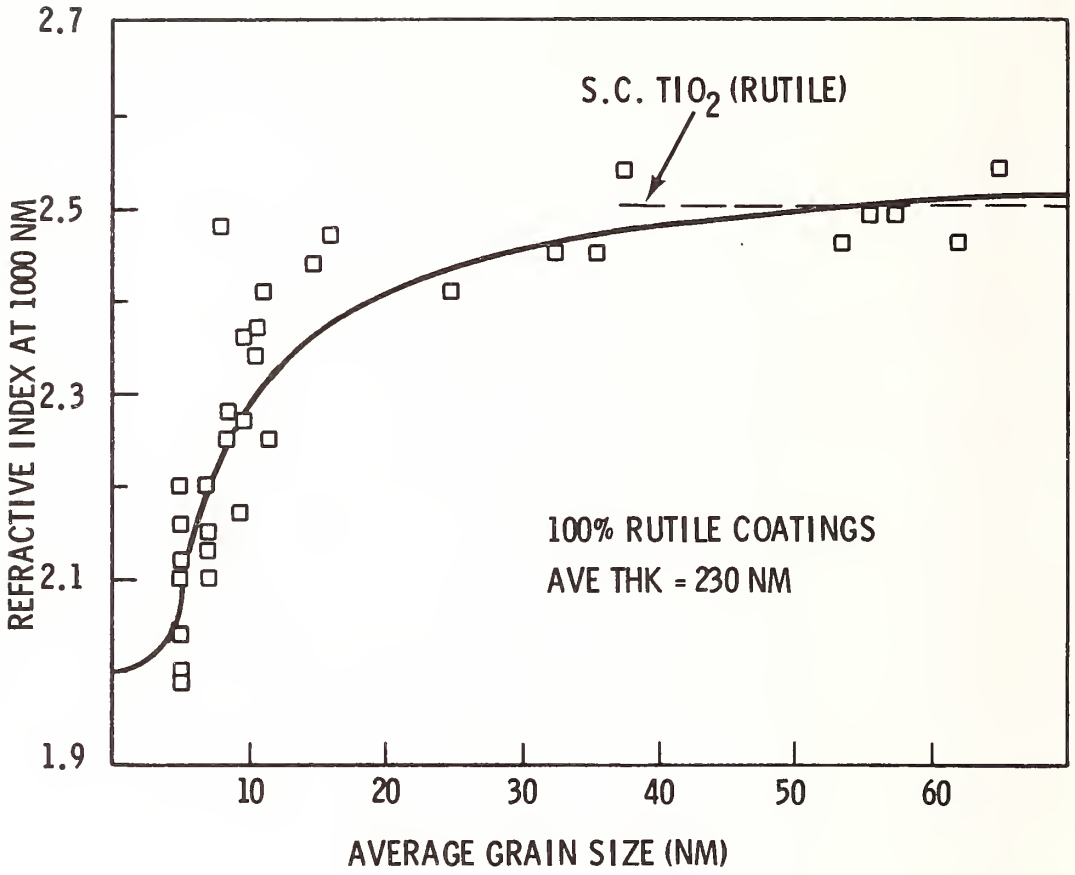

Figure 5. Influence of grain size on the refractive index of TiO_2 rutile coatings.

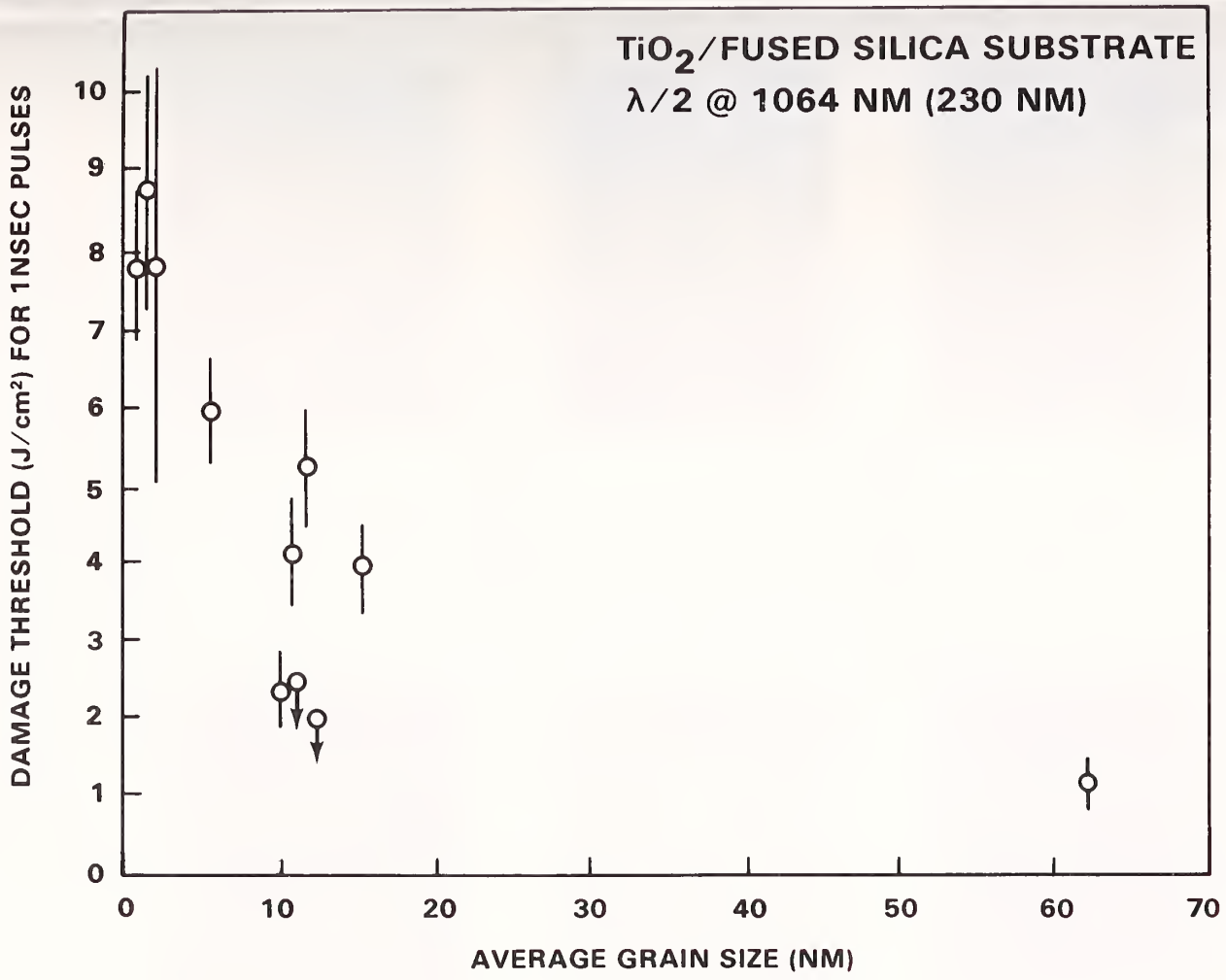

Figure 6. Influence of grain size on the laser damage threshold of rutile coatings. Highest thresholds are obtained for glassy coatings.

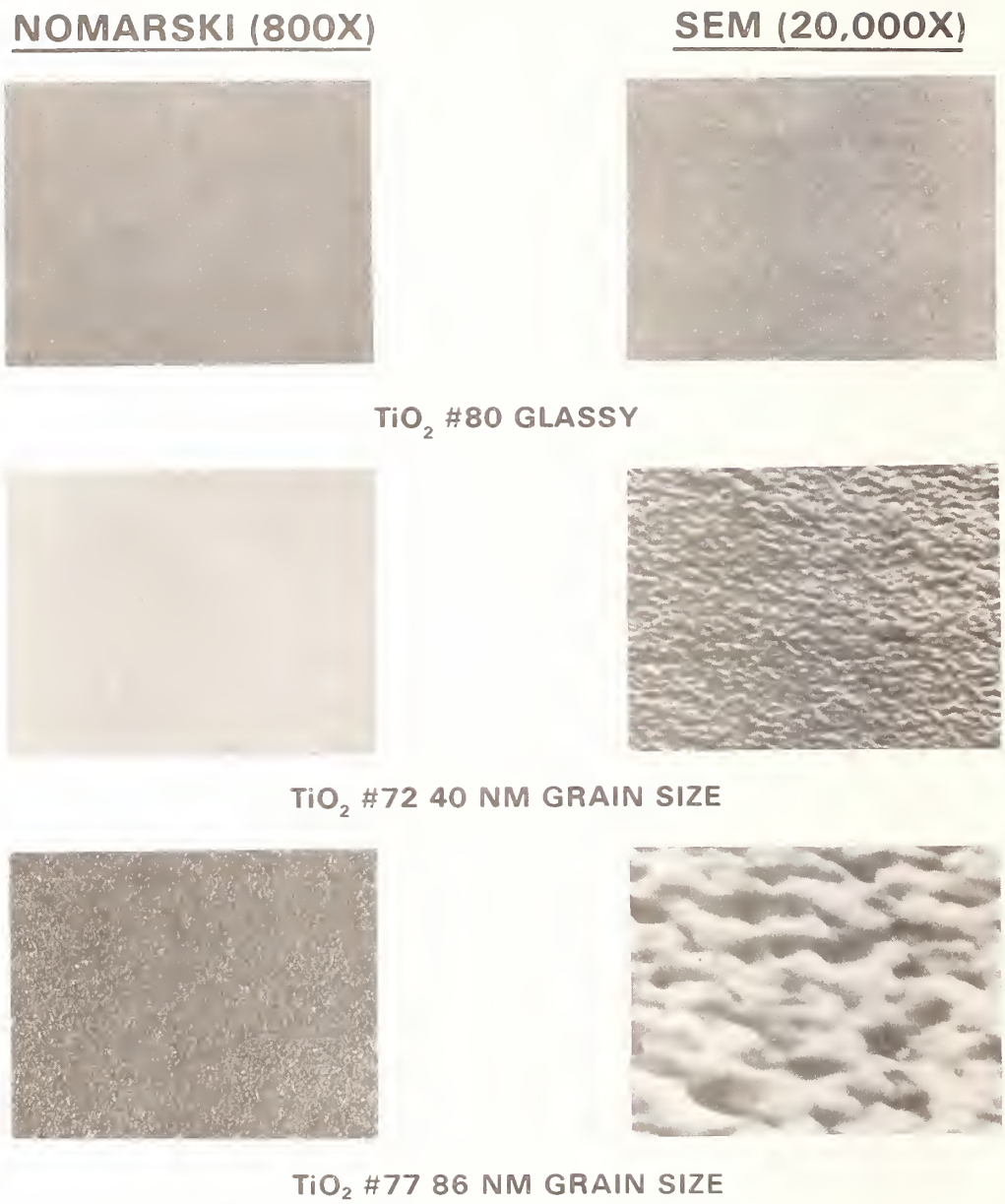

Figure 7. Surface topography of glassy and polycrystalline TiO_2 coatings measured by Nomarski microscopy and SEM.

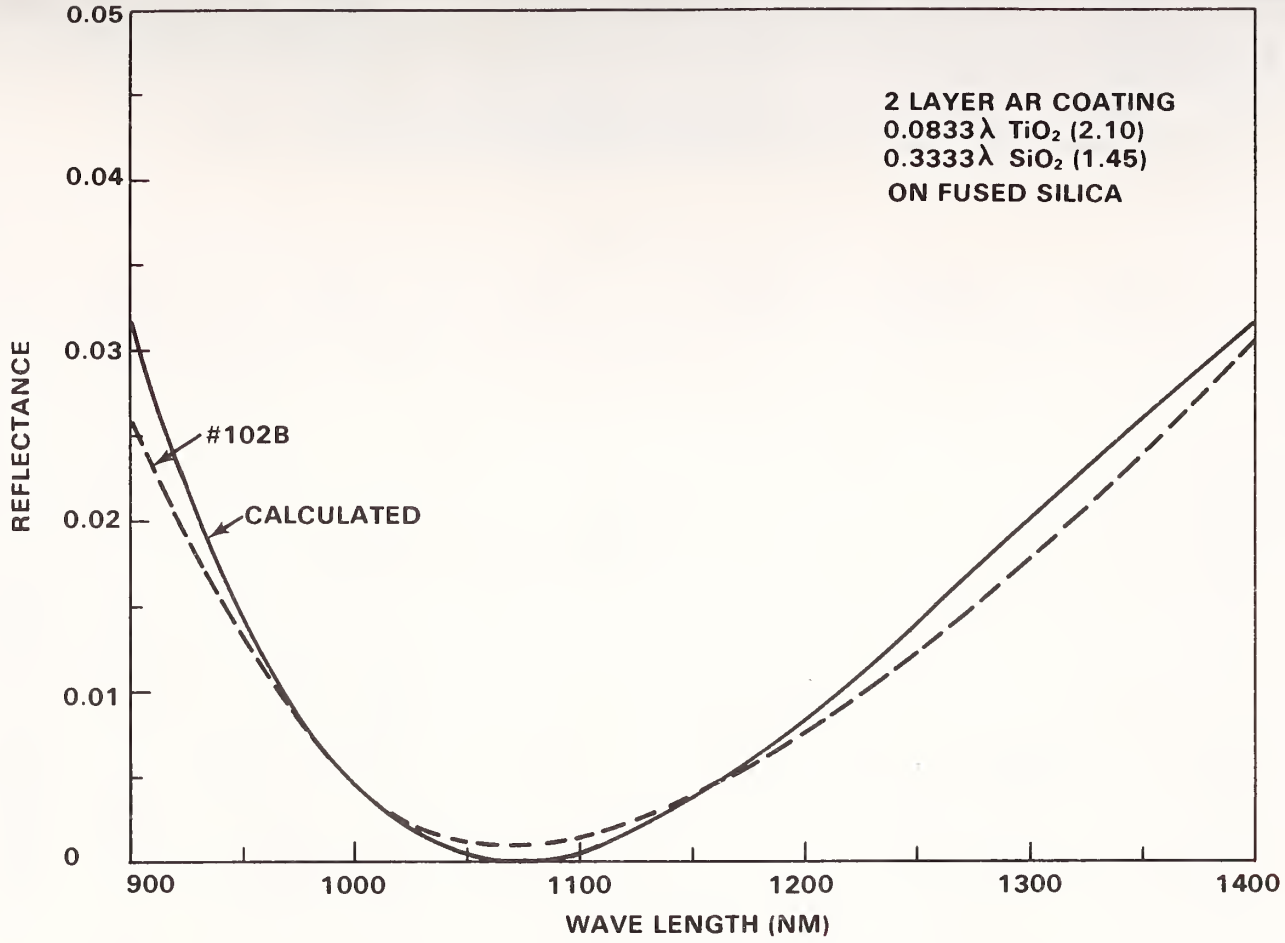

Figure 8. Calculated and measured spectral performance of two-layer TiO_2/SiO_2 AR coatings on fused silica.

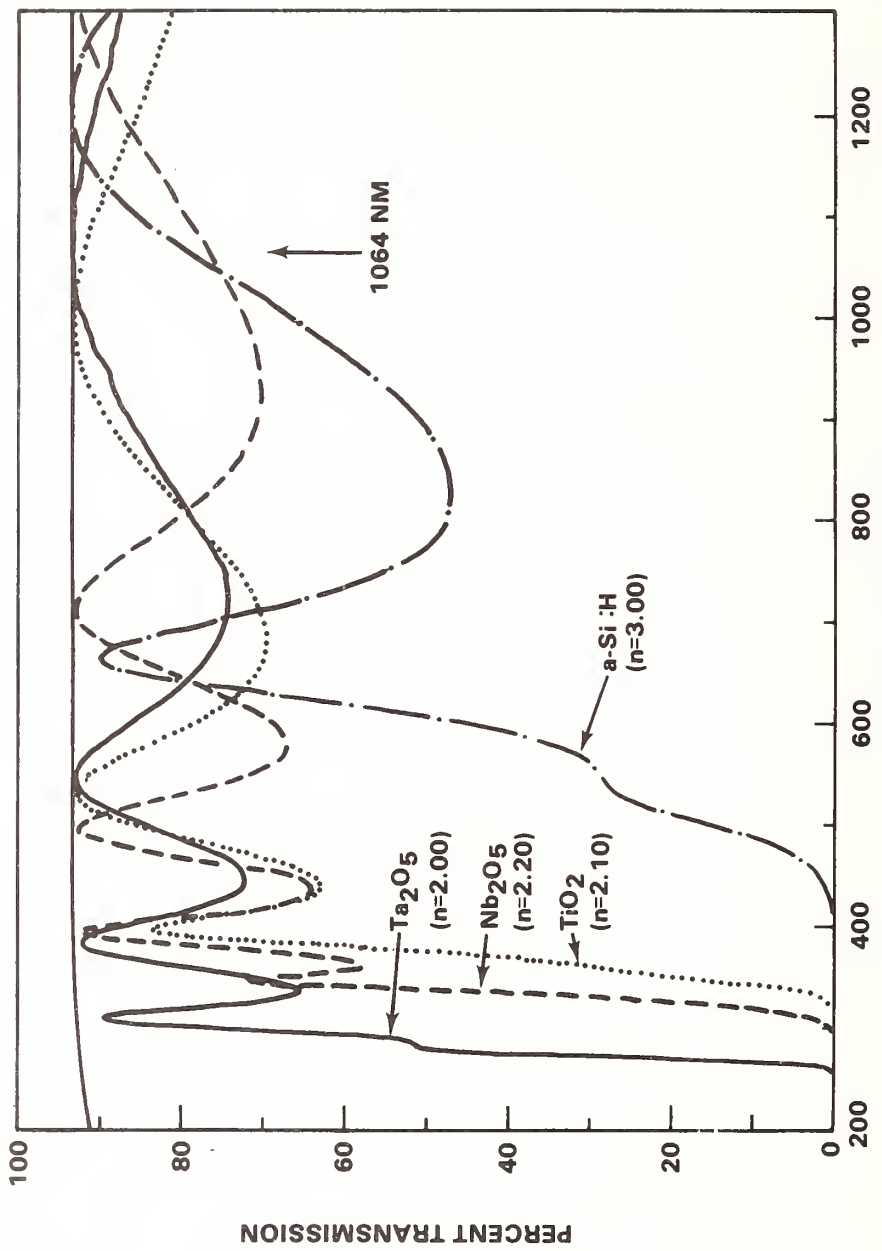

Figure 9. Transmission spectra and refractive indices for glassy coatings of four promising high-index materials.

t was pointed out that the distinction among the Braunstein, Basov and Keldysh formulae must e made not only in terms of allowed and forbidden transitions, but also in terms of the nclusion of interband and intraband transitions, both in the valence band and in the con- uction band. A complete theoretical treatment of two-photon absorption must include both nter- and intraband transitions, both in the valence and conduction bands. It was also ointed out in discussion that the calculation of absolute quantities in two-photon absorp- ion is very difficult, but that it might be preferable to calculate differential quantities uch as the variation of two-photon absorption with the orientation of the incident light or s a function of other experimental variables. These differential quantities would be menable to experimental test and would provide a more convincing test of theory than abso- ute calculations.

RECENT DAMAGE RESULTS ON SILICA/TITANIA REFLECTORS AT 1 MICRON

C. K. Carniglia, Joseph H. Apfel, T. H. Allen and Trudy A. Tuttle
Optical Coating Laboratory, Inc.,
Santa Rosa, California 95402

and

W. H. Lowdermilk, D. Milam and F. Rainer
Lawrence Livermore Laboratory
University of California
Livermore, California 94550

The results of several laser damage experiments involving 15 layer silica/titania high reflectors (HR) are reported. Damage testing was done by Lawrence Livermore Laboratory using 1 ns laser pulses at 1.06μm. The addition of a halfwave silica overcoat leads to a 50% improvement in HR damage threshold. An experiment to modify the electric field intensity distribution within the coating indicates that the determining factor is neither the peak field within the titania layers, nor the average field in the titania layers, but that the field at the titania/silica interface is important. An attempt to correlate damage threshold with absorption met with partial success. For absorptance values above 100 ppm, there is a strong correlation between damage threshold and absorption. However, for absorptance below 100 ppm, it appears that damage threshold is not related to bulk absorption in the coatings. Optical microscopy supports this conclusion.

Key words: Absorption; calorimetry; damage; electric field; high energy laser; laser damage; reflectors; thin film.

High reflector (HR) coatings usually have a higher damage threshold than other types of coatings commonly found in high energy laser systems, such as antireflection (AR) coatings and polarizing beam splitters. The rationale for further investigation of the damage characteristics of HR's is that such a study provides direct information about the damage resistance of the coating and coating materials without the complicating factors arising from the substrate on which the coating is deposited. In a typical HR design, the laser energy is concentrated in the outermost layers of the coating, with very little energy penetrating to the substrate interface. Thus, the observed laser damage should occur in the outer layers, and should reflect the properties of the coating materials.

In contrast, the interface between an AR coating and its substrate receives the full energy of the laser pulse. This interface is a natural weak link in the coating system. It can be affected by the polishing process, the surface finish, the cleaning process, and the residual surface contamination before and during the coating process. It has been demonstrated previously that laser damage to AR coatings tends to nucleate at this interface [1][1]. The resulting damage thresholds are significantly lower for AR's than for HR's.

---

1. Figures in brackets indicate the literature references at the end of the paper.

Thus, investigations which use AR coatings or halfwave layers to study the effects of variations in coating materials or process are more susceptible to variations in substrate preparation than are studies utilizing HR's.

The laser damage results reported here are for high reflectors consisting of 15 alternate layers of titania and silica, vacuum evaporated onto BK7-PH3 substrates. Each layer has an optical thickness equal to one quarter of the 1.06μm laser wavelength. Assuming refractive indices of 1.45 for silica and 2.2 for titania, the calculated reflectance for a 15 layer HR is 99.6%. The distribution of the time average of the electric field intensity within such a coating is shown in figure 1. The peak field within the coating occurs at the first titania/silica boundary and has a value of 0.82 relative to the incident beam. Note that the field maxima decrease with distance from the incident medium to a value of 0.002 at the coating/substrate interface.

The results of three different studies are reported here: (1) the effect of the addition of a halfwave silica overcoat to the basic 15 layer HR, (2) the effect of radical changes of the electric field distribution within the coating, and (3) the effect of large changes in the absorption of the titania layers. In addition, micrographs of typical damage sites are presented illustrating features of the damage morphologies.

The damage testing was done at Lawrence Livermore Laboratory. A 1.06μm laser and a pulse duration of 1 ns were used for all tests reported here. The parts were inspected and photographed using an optical microscope both before and after being irradiated by the test laser pulse. Each site was irradiated with only one pulse (one-on-one). A visible change in the surface of the part after irradiation by the laser indicated the occurence of damage. The accuracy of the damage threshold determination for a given part is ± 10%.

1. Halfwave Silica Overcoat

A variation on the 15 layer high reflector is the addition of a silica layer having a halfwave optical thickness. The addition of such an overcoat has no effect on the reflectance at the laser wavelength, nor does it affect the electric field distribution within the HR. The usual reason for the overcoat is that environmental durability is improved. This improvement carries over into the realm of laser damage as the following data indicate.

Figure 2 is a histogram summarizing the damage threshold measurements of 29 separate HR's: 17 without overcoat (indicated by horizontal shading) and 12 with overcoat (indicated by vertical shading). These reflectors repesent 15 separate coating runs carried out over a span of approximately one year. The average damage threshold of the overcoated parts is 14.4 joules/sq. cm, compared with 8.8 joules/sq. cm for the nonovercoated parts. The improvement due to the overcoat is greater than 60%.

Note that for 8 of the overcoated parts (representing 5 coating runs), there is a nonovercoated part, which was made in the same run, consisting of the same high reflector without the overcoat. This was accomplished by means of a masking system, which covered one or more of the parts for that portion of the run during which the halfwave overcoat was being deposited. For this subset of the data, the comparison between overcoated and nonovercoated parts is less sensitive to run-to-run variations in the coating process. For these 8 pairs of parts, the damage threshold with overcoat is 13 joules/sq. cm, compared to 9.4 joules/sq. cm without - a 40% improvement.

The data in figure 2 provide an indication of the effect of part-to-part (or coating run-to-run) variation on the damage threshold. The standard deviation of the data is 3.9 joules/sq. cm for the overcoated HR's and 2.8 joules/sq. cm for the nonovercoated HR's, in each case about 30% of the average value. It is fair to say that ± 30% is an indication of the variation of the damage levels to be expected when testing a series of HR coatings. This

result is useful for interpreting the results of damage experiments. It also indicates the advisability of testing several parts from several different coating runs to establish statistical reliability.

On the other hand, it should be pointed out that the three overcoated samples which damaged at levels above 19 joules/sq. cm represent the highest observed threshold values for coatings made by vacuum evaporation. This represents an achievable damage threshold level for titania/silica coatings at 1.06μm.

An additional conclusion that can be drawn from these damage data is that the silica layers themselves are not the weak link in the coating. This conclusion arises from the fact that the peak electric field intensity in the silica overcoat has a value of 1.9 relative to the maximum of 0.82 in the rest of the HR coating. Thus, the silica overcoat withstands over three times the energy as the silica layers in the nonovercoated parts at threshold. If the field within the silica layers were the determining factor, the overcoated parts would have a significantly lower damage threhsold.

The damage morphologies shown in section 4 indicate that there are pronounced differences between the overcoated and nonovercoated parts. The unanswered question relative to these data is why the overcoat improves the damage threshold even though the electric field distributions within the HR coatings (and in many cases the HR coatings themselves) are essentially identical. A possible explanation is that the silica overcoat protects the titania from degrading due to interaction with moisture or the atmosphere. Another possibility is that the silica layer adds mechanical strength to the coating.

2. Shifted Stack Center

If the wavelength of the incident radiation is shifted away from the design wavelength of the HR, the field distribution changes from that given in figure 1. As shown by Sparks and Flannery [2], it is possible to shift the majority of the laser energy into either the silica or the titania layers by an appropriate shift of the wavelength. If one of the coating materials is more absorbing than the other, there will be a corresponding change in absorptance with wavelength. The same effect can be achieved by shifting the design wavelength of the reflector relative to the laser wavelength. This approach is more suitable for laser damage experiments since the laser wavelength is fixed.

Three HR's were prepared simultaneously during a coating run. The thicknesses of the layers were controlled by partial masks, which the parts passed behind intermittently during evaporation. By this technique, HR's with center wavelengths of 1.19μm, 1.07μm, and 0.92μm were obtained. Figure 3 indicates that for the HR centered at 1.19μm, the electric field within the coating resulting from incident radiation at 1.06μm is greater in the silica layers, while figure 4 demonstrates that for the 0.92μm reflector, the field is greater in the titania layers. The field distribution in the 1.07μm stack is essentially the same as shown in figure 1. Table 1 compares the peak fields, the average fields, and the fields at the interfaces for the first few layers in these three designs.

Table 1 lists the reflectances of the three stacks. Note that as the stack center shifts away from the laser wavelength, the reflectance decreases. Thus, the reflectors centered at 0.92 and 1.19μm would not be practical for a laser system. It is possible to shift the peak fields in the outer layers without substantially decreasing the reflectance [3], but for the purposes of the experiment, the shifted stack centers is a more suitable approach.

Table 1. Comparison of reflectors with shifted stack centers.

Center Wavelength (μm)	0.92	1.07	1.19
Reflectance at 1.06μm	0.918	0.996	0.966
Peak Field within layers*			
1st (titania)	1.28	0.82	0.91
2nd (silica)	0.93	0.82	1.38
3rd (titania)	1.02	0.36	0.61
4th (silica)	0.76	0.36	0.90
Average Field within layers*			
1st (titania)	1.09	0.41	0.29
2nd (silica)	0.27	0.41	1.03
3rd (titania)	0.86	0.18	0.19
4th (silica)	0.22	0.18	0.67
Field at Interfaces*			
1st (air titania)	0.62	0.00	0.38
2nd (titania/silica)	0.93	0.82	0.91
3rd (silica/titania)	0.47	0.00	0.25
4th (titania/silica)	0.76	0.36	0.61
5th (silica/titania)	0.33	0.00	0.15
Calculated Absorptance† (ppm)	3700	720	950
Measured Absorptance§ (ppm)	3700	510	960
Damage Threshold (j/cm^2)	9.0	8.9	8.0

*Layers and interfaces are counted starting from the incident medium. The values of the field represent the time averaged square of the electric field relative to an incident beam of unit intensity.

†Calculated absorptance assumes that the silica layers are non-absorbing. A value of k = 0.00032 for titania is chosen to agree with the measured absorptance in the 0.92μm reflector.

§Measured on fused silica witnesses with the OCLI 1.06μm laser calorimeter.

The values for peak and average electric fields in table 1 quantify the differences between the coatings which are apparent from figures 1, 3, and 4. The peak field in the first titania layer of the 0.92μm stack is 40% greater than in either of the other two stacks. The peak field in the first silica layer (second layer of the stack) of the 1.19μm reflector is more than 40% greater than in either of the other two reflectors. The differences in terms of average fields within the layers is even more pronounced, being on the order of 3 to 1 between the various coatings.

For each reflector the largest value of the field at an interface occurs at the second interface (between the outer titania layer and the adjacent silica layer). The value of the field at this interface is nearly the same for each of the reflectors. In fact, the central wavelengths were chosen to produce the largest differences between the fields within the layers while maintaining the field at the second interface as constant as possible.

The absorptance of each reflector was calculated assuming that all of the absorption takes place in the titania layers. This is a measure of the average field summed over the titania layers. The 0.92μm reflector has nearly four times the absorption of the 1.19μm reflector and 5 times that of the 1.07μm reflector. For each stack the calculated absorptance assumes a value of $k = 0.00032$, which was chosen to agree with the measured value for the absorptance of the 0.92μm stack.

The absorptance was measured on the OCLI laser calorimeter, which has been previously described in detail [4]. The calorimeter utilizes a 1.06μm laser and has a sensitivity of a few parts per million (ppm) in absorptance. The absorptance was measured on 1" fused silica witness parts, which were made at the same time as the reflectors themselves. The excellent agreement between the calculated and measured values of absorptance at 1.19μm and the good agreement at 1.07μm provide very strong evidence that the measured absorptance is due to bulk absorption within the titania layers rather than to absorption concentrated at the interfaces between layers.

From the above measured and calculated data, one concludes that if absorption in the titania or average fields within the layers were the cause of damage, there should have been dramatic differences between the damage thresholds of these three parts. If the peak fields were the cause of damage, the differences should have been less dramatic but still measurable. As indicated in table 1, the measured damage thresholds for all three parts were essentially the same, between 8 and 9 joules/sq. cm, in agreement with the average of 8.8 joules/sq. cm reported in section 1 for nonovercoated reflectors. The only conclusion that can be drawn is that the field at the outer titania/silica interface plays a more important role in determining the damage threshold than either the average or peak fields in the coatings.

3. Absorption of Titania Layers

During the vacuum evaporation of titania layers, oxygen is usually introduced into the coating chamber to produce optical coatings with the desired characteristics. Too little oxygen results in highly absorbing coatings, while too much oxygen yields less durable or "softer" coatings. An intermediate value for the oxygen pressure is usually arrived at by experience.

For this portion of the HR study, a series of reflectors was made using various values of oxygen pressure during the evaporation of the titania layers. This resulted in a set of HR's having a wide range of absorptance values. The purpose was to investigate the relationship between absorptance and damage threshold.

The range of oxygen pressures used was 0.5×10^{-5} to 3.0×10^{-4} torr. At the lowest pressure, the measured absorption was in excess of 1% and the

parts were noticably dark. For pressures above 3.0×10^{-4} torr, the coatings were soft, consistently damaging after 20 rubs with an eraser. Six oxygen pressures, differing from each other by a factor of approximately 1.5, were used. The actual values of oxygen pressure are given across the horizontal scale of figure 5. At each oxygen pressure, two HR's were made, one with and one without a halfwave silica overcoat. (Two of each type were made at 1.5×10^{-4} torr and the damage data for this pressure presented below is an average of the results for two parts.)

The absorptance of each reflector was measured with the 1.06 laser calorimeter [4]. The absorptance data are represented in figure 5 by the "+" symbol, and the left scale gives the log of the absorptance. The solid curve connects the data for the overcoated parts. The dashed curve connects the data for the nonovercoated parts. The absorptance decreases monotonically with oxygen pressure from a maximum value above 0.01 at the lowest pressure to a minimum of 0.000014 (0.0014% or 14 ppm) at the highest pressure. The absorptances of the overcoated and nonovercoated parts are nearly equal at each pressure. Note the large range of absorptance values (over 3 orders of magnitude) for the small range of oxygen pressure (less than a full order of magnitude).

The corresponding damage thresholds are indicated by circles and are referenced to the right hand scale. There is a clear upward trend to the damage data as a function of oxygen pressure, indicating, in general, that higher absorption leads to lower damage threshold. On the other hand, all of the damage thresholds of the overcoated reflectors for pressures above 1×10^{-4} are within one standard deviation of the average value of 14.4 joules/sq. cm reported in section 1. Similarly, except for the last point, the thresholds for the nonovercoated parts level off at between 8 and 9 joules/sq. cm for pressures above 10^{-4}. Thus, the strongest conclusion that can be drawn with certainty is that for absorptances above 10^{-4}, the damage threshold decreases.

If one accepts that the correlation between damage and absorption extends beyond this limited range, then the question arises: Why does a variation in absorptance of three orders of magnitude result in a variation in damage threshold of less than one order of magnitude? The above data suggest that linear absorption by itself is not a sufficient damage mechanism to explain the observed damage thresholds. The damage morphologies discussed in the next section support this conclusion.

4. Damage Morphologies

An inspection of the morphologies of the damage sites using optical microscopy reveals several interesting differences between HR's of various types. The micrographs shown in figures 6-10 were all taken with a reflected Nomarski interference attachment. Table 2 summarizes the relevant data for the HR coatings shown in the micrographs: the presence or absence of halfwave silica overcoat, the measured absorptance in parts per million, the measured damage threshold for the part, and the actual laser energy for the site shown in the micrograph.

Figure 6 is a micrograph of a typical damage site on a highly absorbing HR. This part was made using an oxygen pressure of 5×10^{-5} torr during the evaporation of the titania layers (see figure 5 and section 3). The large damage crater has a diameter of about 1 mm and reflects the approximate size and shape of the laser beam used for damage testing. The removal of the coating from a large region of the part, which is apparent from the micrograph, is typical of what one would expect if bulk absorption were the cause of damage.

Table 2. Data for reflectors shown in Nomarski micrographs.

(See figures 6-10)

Figure	Overcoat	Absorptance (ppm)	Damage Threshold (j/cm^2)	Energy for site shown (j/cm^2)
6	No	13,000	3.2	5.9
7	No	39	13.5	18.7
8	No	39	13.5	18.7
9	Yes	65	8.6	19.9
10	Yes	12	12.5	26.4

Figures 7 and 8 show typical damage sites on a non ercoated HR having a more normal (low) value of absorption. In this case damage occurs in isolated sites which are 20 to 60μm in diameter. Thus, they are much smaller than the diameter of the laser beam. The damage sites are round and fairly well defined and appear blue in reflected light. Scanning electron microscope (SEM) pictures of the sites shown in figure 7 do not indicate that any of the layers of the coating have been removed. Rather the top surface of the coating has a "burned" or recrystallized appearance. Some of the damage sites appear to have small holes in the center. The second site from the left in figure 7 is such a site. It is shown at higher magnification in figure 8. The hole has a diameter of about 2μm and SEM micrographs show that it extends down several layers into the coating.

The damage morphologies for HR's with overcoat are much different, as figure 9 illustrates. This is a heavily damaged region, which demonstrates the two damage morphologies commonly found on overcoated HR's: Small "pits" ranging in diameter from 2μm to 10μm, and large ill-defined spots with diameters from 20μm to more than 100μm. The pits often form on defects which were visible as point scattering sites on the coating prior to the damage test. The damage threshold for the pits is generally lower than for the larger spots. SEM photographs of the pits show them as small craters typical of a thermal fracture of the type predicted by Duthler and Sparks [5]. Figure 9 is of a site with a large number of such pits. On a damage site nearer to threshold only a few of these pits are likely to be present.

The larger damage spots on overcoated HR's are visible as dark fuzzy round areas in figure 9. These spots are generally very difficult to see with the optical microscope. They tend to have a bluish color in reflected light. With the aid of Nomarski interference contrast, a faint ring of color can be seen around the central blue spot if one adjusts the Nomarski to be away from the null position. The site shown in figure 9 was investigated using SEM, but no visible features were observed at the positions of the large damage spots. However, if a thin layer of silver is added to the damaged part, a distinct pattern can be observed in reflected Nomarski. This layer of silver prevents light from penetrating the coating, and thus, experiencing the interference effects of the multilayer structure. The resulting Nomarski micrographs reveal the details of the morphology of the top surface of the coating. Figure 10 shows several such silvered damage spots from a site different from that shown in figure 9. The shading is due to the adjustment of the Nomarski attachment and indicates that the spot is depressed in the center and raised at the edges. (Compare the shading of the scratch.) Usually

no apparent break in the surface of the coating is apparent, although some sites do show a small break at the center of the spot.

The isolated nature of the damage sites in both the overcoated and non-overcoated HR's with low absorption indicates that bulk absorption is not the major cause of damage. Rather the damage is nucleating at isolated points. These points may contain impurities or some other type of local inhomogeneity of the coating. The circular nature of the damage indicates that the nucleation of the sites must be small compared to the final site size. Otherwise, one would expect more irregularly shaped sites, characteristic of the shape of the nucleating region.

The small pits usually observed on overcoated parts, and occasionally on nonovercoated parts, are apparently related to defects in the coating, which cause an absorption of energy and lead to a Duthler-Sparks type of failure. The larger spots seem to be caused by a different mechanism. A possible explanation for the spots on the nonovercoated HR's might be that the titania is heated, perhaps by a plasma, to a temperature high enough to cause recrystallization of the surface. The blue color might be due either to scattering by the recrystallized region or to an oxygen deficiency in the titania. With the overcoated parts, the heat generated by such a plasma would have to penetrate the overcoat to cause the recrystallization of the titania, thus requiring a higher incident energy. The profile of the surface observed for the overcoated parts could be due to: 1) a change in volume of the titania layer under the overcoat, 2) a delamination of the overcoat from the titania layer, or 3) a softening of the overcoat itself.

There remains the question of the cause of the nucleation of damage. Except for the small pit type of damage, there appears to be no correlation of the damage with observable defects in the coating. Presumably, the nucleation sites are small compared to a wavelength of light and will be difficult to detect.

5. Conclusions

The major conclusions of this study are:

(1) The standard deviation of the damage threshold measurement, due to part-to-part and coating-run-to-run variations, on a series of otherwise identical HR's, is about 30% of the average threshold value.

(2) A halfwave silica overcoat increases the average damage threshold of a series of HR's by about 50%.

(3) Neither the average field nor the peak field in the outer silica or titania layers correlates well with damage threshold. The field at the first titania/silica interface is the only electric field parameter that correlates with the damage thresholds.

(4) Damage threshold increases as absorption within the titania layers decreases. However, the results indicate that other factors play a role.

(5) Damage morphologies on highly absorbing parts indicate that bulk absorption plays a role in the damage mechanism. For parts with low absorption, the isolated nature of the damage sites indicates that bulk absorption is not a major factor.

6. References

[1] Carniglia, C. K., Apfel J. H., Carrier, G. B. and Milam, D., NBS Spec. Publ. 541, 218 (1978).

[2] Sparks, M. and Flannery, M., J. Opt. Soc. Am. 69, 933 (1979).

[3] Apfel, J. H., Appl. Opt. 16, 1880, (1977).

[4] Allen, T. H., Apfel, J. H. and Carniglia, C. K., NBS Spec. Publ. 541, 33 (1978).

[5] Duthler, C. J. and Sparks, M., NBS Spec. Publ. 414, 219 (1974).

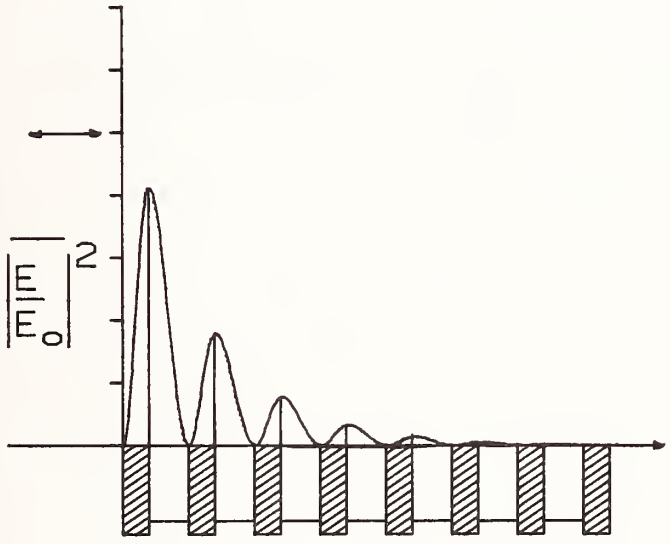

Figure 1. Time averaged square of the electric field strength for 1.064μm radiation incident from the left on a 1.064μm silica/titania quarterwave stack. The arrows indicate the electric field intensities of the incident, reflected and transmitted waves. The position of the layers is indicated below the field plot. The titania layers are shaded.

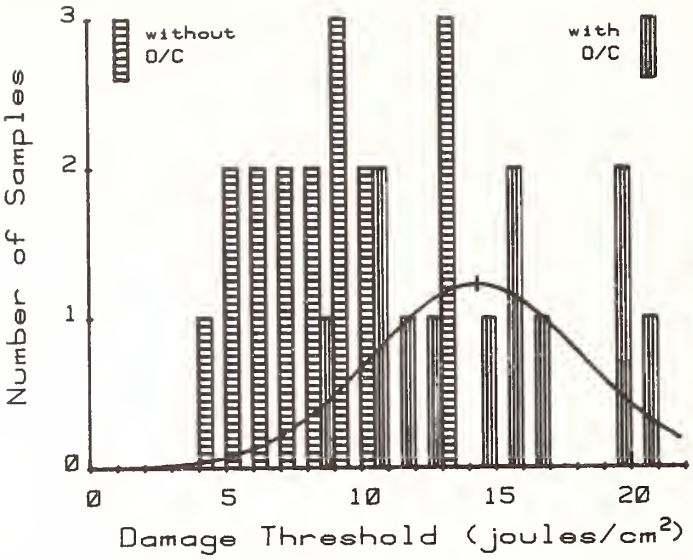

Figure 2. Histogram of damage data on 15 layer HR coatings with and without a halfwave silica overcoat.

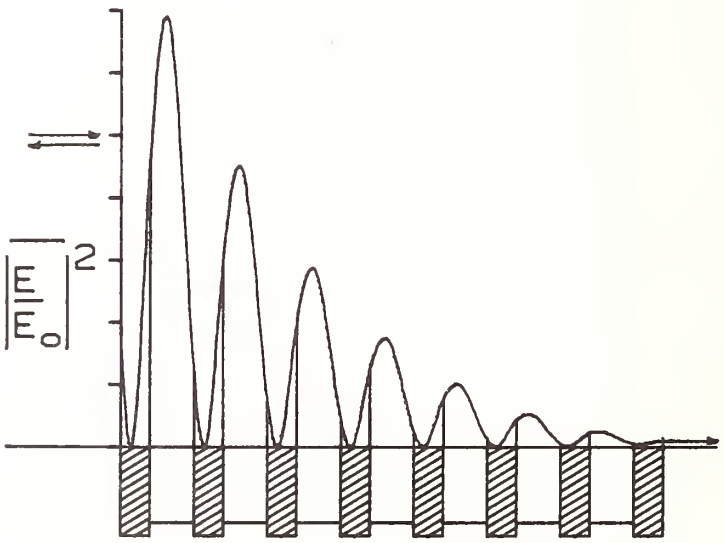

Figure 3. Similar to figure 1 for a quarterwave stack centered at 1.19μm.

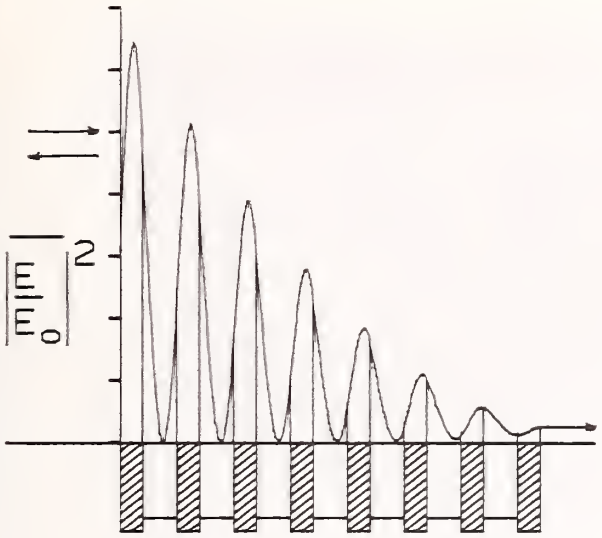

Figure 4. Similar to figure 1 for a quarterwave stack centered at 0.92 μm.

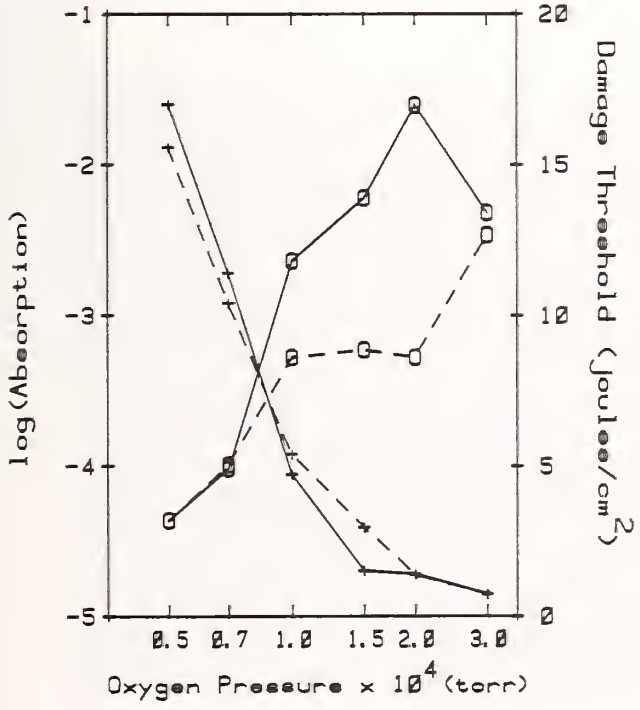

Figure 5. Absorption and damage data for high reflectors made using various values of oxygen pressure during the evaporation of the titania layers.

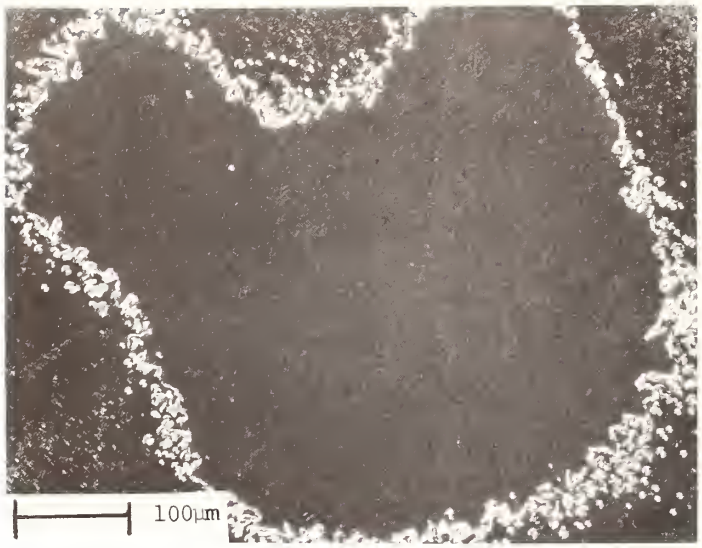

Figure 6. Nomarski micrograph of a damage site on a HR with high absorption.

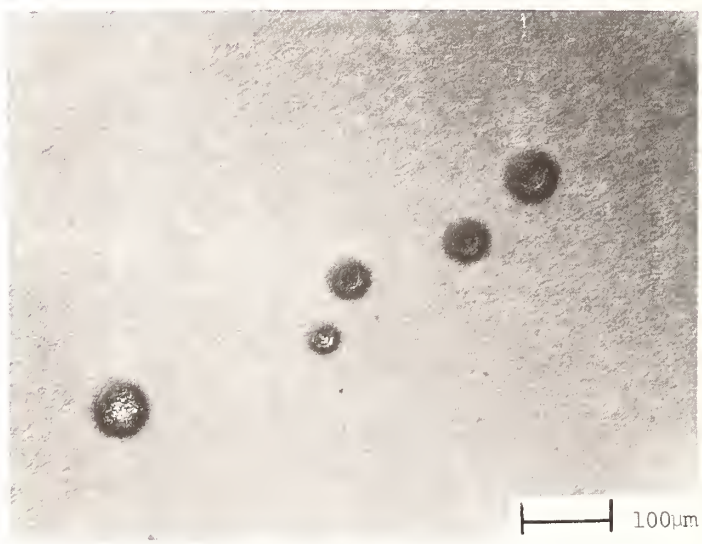

Figure 7. Nomarski micrograph of damage sites on a non-overcoated HR illustrating circular damage morphology.

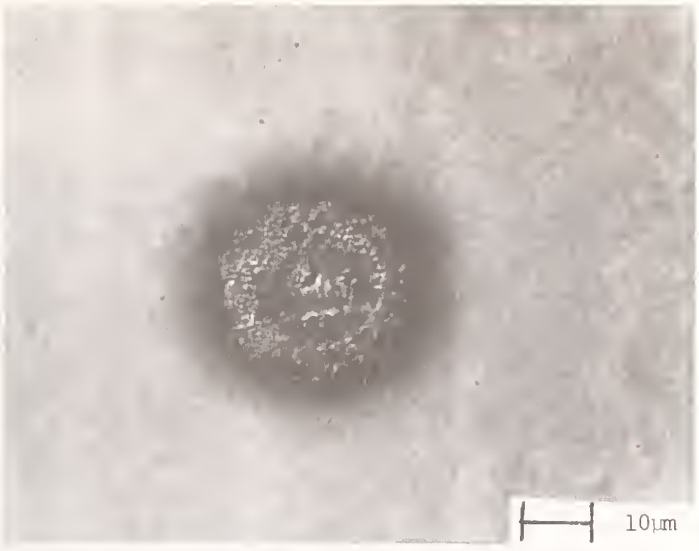

Figure 8. Nomarski micrograph of one of the damage spots of figure 7 showing a small hole in the center.

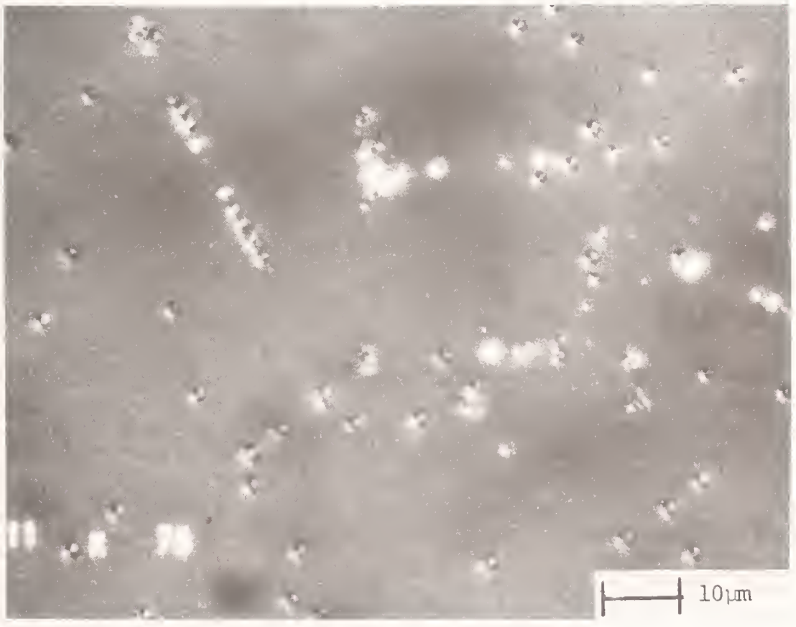

Figure 9. Nomarski micrograph of a highly damaged region on an overcoated HR, illustrating two damage morphologies: small pits and large blue (dark) spots.

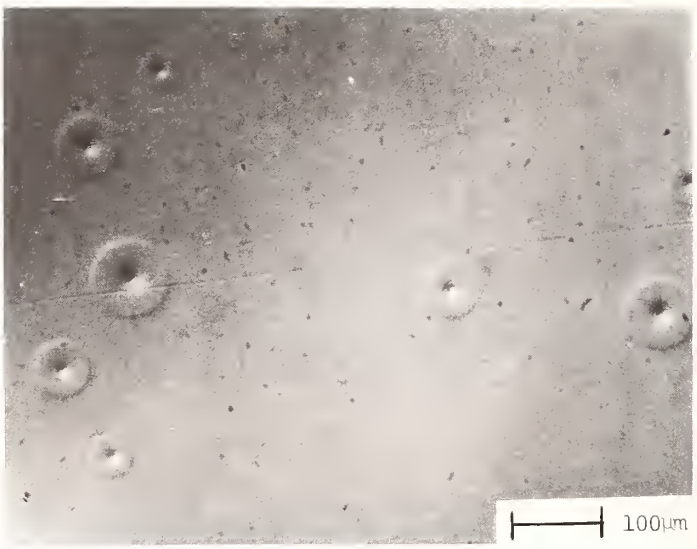

Figure 10. Nomarski micrograph of a damage site on an overcoated HR, which has been silvered after damage. Each damage site corresponds to a blue spot observed before silvering. The sites are raised at the edges and depressed in the center.

DAMAGE TO COATINGS AND SURFACES BY 1.06 μm PULSES

W. H. Lowdermilk, D. Milam and F. Rainer
Lawrence Livermore Laboratory
University of California
P.O. Box 5508
Livermore, CA 94550

Abstract

Damage thresholds for 1 ns, 1.06 μm laser pulses were measured for bare, polished surfaces and thin-film coatings prepared by several companies and laboratories. We discuss the origin and morphology of damage, review the experiments and summarize conclusions regarding the influence of substrate material, polishing compounds and processes, coating materials and deposition methods and the effects of absorption, electric-field strength, undercoats, overcoats and surface etching techniques.

Key Words: absorption; electric-field strength; film materials; impurities; 1 ns; 1.06 μm damage; overcoat; polished surfaces; pulsewidth dependence; thin-film coatings.

1. Introduction

Laser damage to uncoated (bare) and coated optical component surfaces determines the ouput and reliability of high-energy, high-power Nd:glass lasers. We have performed a variety of experiments in collaboration with other laboratories to improve damage thresholds and determine empirical scaling laws required for laser design. Accomplishment of these goals requires (1) accurate and reliable measurement of damage thresholds for different substrate materials, surface preparations, and coating materials and designs, (2) determination of the causes of damage and (3) identification and development of promising materials and processes.

The experiments reviewed here were coordinated by Lawrence Livermore Laboratory; designed and performed in collaboration with Optical Coating Laboratory, Inc. (OCLI), the Naval Weapons Center (NWC) and the Chemistry and Materials Science Department of LLL. Damage thresholds were measured at LLL using apparatus and methods described in detail elsewhere(1).

2. Cause of Damage

Near-threshold laser damage to bare surfaces and coatings of transparent, dielectric materials occurs as small, isolated pits which are randomly distributed over the irradiated surface. Damage must therefore arise from particulate inclusions, physical defects or chemical impurities. One mechanism for damage is absorption of laser energy by these sites, which heats a small volume of material to the melting temperature or to the point of thermal-stress fracture. A second mechanism is creation of an absorbing plasma by electron avalanche initiated by the free, or easily-liberated electrons.

Measurement of absorption coefficients for surfaces and thin films recently became possible using laser calorimetry(2) capable of detecting absorptions of 1 part in 10^5. Transparent, dielectric thin films have absorption coefficients of 1-10^3 cm^{-1}. Surface-layer coefficients are estimated as 10^{-3} - 10 cm^{-1} from extrapolation of absorption measured versus sample thickness. Comparison of these values with typical bulk-absorption coefficients of 10^{-3} cm^{-1} for BK-7 glass and 10^{-4} cm^{-1} for fused silica indicates the significantly higher concentrations of absorbing particles, impurities and defects in surface layers and coatings.

3. Damage to Polished, Uncoated Surfaces

We measured damage thresholds for a series of BK-7 glass substrates, polished by the standard materials and procedures specified for laser optical components. The surfaces had measured RMS roughness of 10 Å and surface etching revealed minimal subsurface fracture. Immediately before testing, the surfaces were cleaned by dragging an alcohol-wetted tissue across the surface. Cleaning the surfaces was important because dust on the surface will burn and induce damage at fluence levels below 14 J/cm^2. The distribution of thresholds measured for 14 samples is shown by the histogram in figure 1. The median 1 ns threshold was 16 J/cm^2 and 80% of the samples had thresholds above 14 J/cm^2. These threshold values are two to three times lower than the bulk damage threshold of BK-7.

A possible major cause of the surface threshold being significantly less than the bulk is that the optical grinding and polishing process leaves a physical-disturbed and chemically-contaminated surface layer called the Beilby layer, with thickness of 10-100 μm. Measurements of absorption as a function of the sample thickness indicate the absorption coefficient of this surface layer is 10^{-3} cm^{-1} to 10 cm^{-1}. Polishing compounds are an apparent, obvious source for absorbing surface-layer impurities. In fact, chemical analysis at LLL of a variety of common polishing compounds and lap materials found metallic impurities at concentrations of 10^3 ppm. Table 1 lists the species and concentrations which were measured. Later, a chemical analysis of the surface layer, removed by acid etch, demonstrated that these impurities did in fact become imbeded in the surface during polishing. We recently have obtained polishing compounds with metallic impurities reduced to 1-10 ppm concentrations, and are polishing glass with them.

Believing that surface-layer absorption limits damage thresholds, we also have explored removing the surface layer by various methods. Results have been largely discouraging, probably because the many processes for surface-layer removal recontaminate or physically damage the surface. Those methods which resulted in no increase and frequently a reduction of the threshold include sputter etching, ion planing and acid etching. Only one method applicable to optically-figured surfaces produced significant increase in damage threshold. In that method, a CO_2 laser beam was scanned across the polished surface of fused silica (3). Strong absorption of the CO_2 radiation caused melting and vaporization of material from the surface leaving it very smooth. Damage thresholds of these etched/annealed surfaces of more than two times the 16 J/cm^2 median threshold for polished surfaces has been observed. Possibly the improvement in threshold results from vaporizing impurities or annealing surface and subsurface microcracks. Additional samples will be tested to verify the result and determine the mechanism.

Numerous threshold measurements were made on freshly-fractured surfaces of BK-7 and fused silica. Suprisingly, the thresholds varied greatly among samples and many values were less than polished-surface thresholds. A possible explanation for the lower threshold of fractured surfaces is the fracture accompanied by micro-shattering which is leaves the surface littered with glass-particle debris. This debris, when irradiated, may easily melt and induce surface damage.

Although fractured surfaces would appear to be the logical beginning of detailed surface interaction studies, clearly additional work is required to characterize fractured surfaces. If, in addition, the cause of these large variations can be determined and controlled, the fractured surface could then be used to test the effect of impurities introduced in controlled quantity.

4. HR Coatings

4.1 Overcoat

Thin-film HR coatings consist of an odd number of quarter-wave thick layers, typically 15, alternating high-and low-index materials. The first and last layer are the high-index material. The most widely used materials for visible and near IR wavelengths are titania (TiO_2) and silica (SiO_2). Multiple reflections of the laser beam by a quarter-wave stack (QWS) creates a standing-wave electric field distribution which has a large maximum outside the coating and then alternating minima and maxima, with rapidly decreasing amplitude at the successive interfaces(4). The electric field at the substrate interface is very weak. This field distribution accounts for the fact that HR coatings normally damage at the first or second layer interface.

We have found that HR damage thresholds are significantly improved by addition of a half wave overcoat. The increase in damage threshold is not related to an alteration of electric fields. The overcoat layer does not affect the field distribution <u>in</u> the QWS. A large electric-field maximum falls in the overcoat layer.

Table 1 - Impurity concentrations (ppm) in polishing compounds measured by emission spectrometry.

Impurity Elements	MgO Code 920	SnO Av-116	Liquid 85[b]	ZOX CE-89	Al_2O_3 Microgrit 30T	Al_2O_3 Microgrit 9T	Reagent grade ZnO
Al	300	<5000	nd	nd	major	major	<100
Cu	6	1	10	10	4	nd	3
Si	600	1000	nd	nd	1 Wt%	1 Wt%	<2
Fe	200	600	≥1000	1000	1000	1000	nd
Ca	3000	100	2000	20	3000	3000	<2
Zn	<30	100	nd	<1	<30	<30	major
Ni	10	60	nd	<1	5	5	<3
Cr	<10	30	nd	1000	<10	<10	<10
Ag	<1	<1	nd	nd	<1	3	<1
Sr	10	1	≥1000	1000	100	1000	<1
V	<10	<10	nd	nd	40	20	<30
Pb	<10	<10	600	60	<30	<30	<10
La	nd	nd	nd	≥10 Wt%	nd	nd	nd
Ba	<100	<10	≥1 Wt%	5000	<30	<30	<100
Nb	<30	<30	≥1000	300	<30	<30	<100
Mn	10	<1	30	20	5	5	<10
Mg	nd	nd	≥1000	10	500	500	<1
Na	<300	nd	100	3000	3000	nd	nd
Ti	10	nd	nd	800	800	nd	<10
Ga	nd	nd	nd	30	30	nd	nd
Zr	<10	nd	≥1000	nd	nd	nd	nd

[a] nd means not detected.

[b] Y and Th level at 100-1000 according to x-ray fluorescence.

The distribution of 1 ns damage thresholds for a series of overcoated (OC) mirrors is given by the histogram in figure 2. We observed light emission at the OC mirror surface irradiated at fluences comparable to the nonovercoated (NOC) damage fluence. However examination by Nomarski microscope at one-hundred times magnification showed no evidence of physical damage to the OC surface. Table 2 compares thresholds for OC and NOC mirrors.

Table 2. Damage Thresholds (J/cm^2) for HR Coatings Measured with 1 ns Pulses.

	OC (12 Samples)	NOC (16 Samples)
Maximum	20.3	13.5
Minimum	8.0	5.0
Median	14.4	9.2

We studied the HR damage morphology using a scanning electron microscope (SEM). Threshold damage sites on NOC mirrors were circular spots, 10-70 μm in diameter, of material which appeared to have been melted and recrystallized. In the center of some spots there was a 1.5 μm diameter pit which was at least three or four layers deep. These damaged spots often occurred at the site of defects which had been visible by microscopy before irradiation.

Overcoated mirrors had a distinctly different morphology, with two different types of sites. Irradiation at fluences near threshold, produced small, circular pits with 1-5 μm diameters, at least three or four layers deep, and often located on existing defects. Irradiation with fluence 1.5-2 times the threshold fluence produced additional sites of 100-150 μm diameter which were located in apparently defect-free areas. These sites were not visible by SEM and barely visible by Nomarski microscopy. To enhance the visibility of these larger sites, a layer of silver was deposited on the coating. The sites could then be seen as areas where the overcoat had raised slightly, but not ruptured. Because the silica overcoat is under compressive stress, this morphology suggests the overcoat softened and then raised to relieve the stress.

Possible explanations for the improved damage resistance of overcoated mirrors are (1) that the absorption of the titania layer may depend on its exposure to the atmosphere and (2) that the total stress of the coating and its mechanical strength is changed by the presence of an overcoat layer. To study these possibilities, additional coatings were prepared on which overcoats were deposited after various time delays. Control parts were included to separate the effect of thermal and vacuum cycling. Those coatings which received overcoats immediately had the highest damage threshold. However, some improvement was observed for mirrors overcoated after a delay, even of several months.

4.2 Substituted High-Index Layers

Titania (TiO_2) has the highest refractive index of materials which are normally used for visible and near I-R mirrors. Thus, although other high-index materials could be substituted for the titania, they have lower refractive index so, if used in combination with SiO_2, more layers are required to achieve equal reflectivity. The basic objection to increased number of layers is simply the complexity and cost of the coating. However, because the electric field maxima decrease rapidly at interfaces further from the air interface, the possible advantages of alternate high-index materials could be realized without increasing the coating's complexity by depositing additionalhigh/low-index pairs on the basic TiO_2/SiO_2 QWS. To evaluate this prospect, a set of mirrors was coated by OCLI with one and two additional layer pairs. The high-index materials in the study were ZrO_2, Ta_2O_5, Al_2O_3 and an amorphous TiO_2 (an OCLI propriety material). The ZrO_2 and Ta_2O_5 mirrors had thresholds greater than the base TiO_2/SiO_2 mirror, while the amorphous TiO_2 had the same threshold and the Al_2O_3 mirror had lower threshold than the base stack. However the base TiO_2/SiO_2 mirrors themselves had anomalously low threshold making these results

inconclusive. In a repeat experiment, two Ta_2O_5/SiO_2 pairs were added to each of six, eleven-layer TiO_2/SiO_2 mirrors. Three of the six also were overcoated. While the OC mirror thresholds were greater than the NOC threshold, no improvement resulted from the added Ta_2O_5/SiO_2 layers.

4.3 Electric-Field Strength

The facts that (1) damage to HR coatings occurs in the outermost layers where the electric-field strength is greatest and (2) TiO_2 is more strongly absorbing than SiO_2 suggested possible improvement from altering layer thicknesses so as to reduce the average field strength and absorption in the TiO_2 layers. Three TiO_2/SiO_2 mirrors were coated by OCLI for maximum reflectivity at 1.192 μm, and 1.071 μm, 0.915 μm. When irradiated with 1.06 μm pulses, different standing-wave field intensities were generated. Table 3 gives the peak-and-average-field strength in the outermost titania layer, the field strength at the first interface, the total absorption (measured by laser calorimetry at OCLI) and the damage threshold for each coating.

Table 3. Field Strength, Absorption and Damage Threshold for Shifted-Stack HR Coatings

Wavelength of Max. Reflection (m)	Standing-Wave Field in First TiO_2 Layer			Absorption (ppm)	Damage Threshold (J/cm^2)
	Peak	Average	Interface		
1.193	0.92	0.29	0.92	590	8.0
1.071	0.83	0.40	0.83	450	8.9
0.915	1.34	1.14	0.92	2300	9.0

Interestingly, although the three mirrors had large differences in peak-and-average-field strength and in absorption, their thresholds were nearly equal. Because the interface field strengths were also nearly equal, we thought that the interface field might be the important factor. To study that possibility, OCLI coated two sets of OC mirrors with different layer thickness. One set was the normal, QWS design and the other was a nonquarter wave design in which the interface electric field had a value two-thirds that of the normal, QWS interface field. Several runs of each design were coated. Different designs were made in alternate runs to reduce systematic errors. Damage measurements gave the surprising result that those mirrors with lower interface field strength also had lower thresholds. It is possible that the higher, net tensile stress of the nonquarter wave mirror caused its threshold to be lower. We are presently studying the influence of stress on OC mirror damage thresholds.

4.4 Absorption

To determine the correlation between damage threshold and coating absorption, OCLI prepared a series of HR coatings deposited at different oxygen pressures. Coating absorptions of 10^{-5} - 10^{-2} were measured by laser-calorimetry at OCLI. We found that coatings with absorption greater than 10^{-4} had damage thresholds which generally decreased with increasing absorption. Those coatings with absorption less than 10^{-4} had thresholds which were uncorrelated with the absorption. This result however does not imply that the threshold is independent of coating absorption. The important point is that damage results from heat deposition in a small volume localized around a defect or impurity. The absorption coefficient in that small volume can be very much larger than the average absorption. The laser calorimeter, on the other hand, measures the average absorption over the the area of the laser beam and the thickness of the coating. It is this volumed-averaged absorption which we find is not strongly correlated with damage threshold. Further understanding of the connection between absorption and threshold would be greatly aided by the ability to measure absorption in a spatially resolved volume of 1 μm dimensions.

5. AR Coatings

Whereas damage to HR coatings occurs in the outermost layers, AR coating damage usually initiates at the substrate interface. The damage induced by pulses of durations up to several nanoseconds is a collection of small pits with diameters of 1-5 μm which are characteristic of the total thickness of the coating. Viewed collectively by the unaided eye, these pits appear as a haze. Individual pits can be resolved, and the evolution of their morphology with increasing fluence studied by optical or electron microscopy. Figure 3 shows photographs of a surface damage site taken by SEM(5). The photographs strongly suggest an explosive eruption upward and outward from the substrate interface. At the edge of the irradiated area, where the beam fluence is low, the damaged site consists of a raised area with radial cracks in the outer coating layers. At somewhat higher fluence, a 3μm diameter disk is loosened and, at higher fluence, blown away, exposing the substrate surface. Note the evidence of melted material at the bottom of the pit and also some material ejected out on top of the surrounding area.

Two additional facts are consistent with the assumption that the interface region has significantly larger absorption than the surrounding coating and substrate material. First, although the standing-wave electric-field peak intensity in AR coatings is less than in HR coatings, AR damage thresholds are less than HR thresholds. This result suggests that the substrate interface, which is irradiated in AR but not in HR coatings, plays an important role. Second, AR coating damage thresholds do not depend strongly on the absorption average over the coating thickness. That result indicates that absorption is not uniform; rather it is high in some places and low in others. Estimates of the interface absorption coefficient of $10 - 10^3$ cm^{-1} were made at OCLI from the absorption measured for coatings of different thickness.

Damage experiments on AR coatings were designed primarily to study effects of absorption at the substrate interface and in the coating layers. These experiments included variations of substrate materials and surface preparation, coating design and deposition processes and coating materials.

Substrates of BK-7 and fused silica were polished either by conventional or by bowl-feed process and then coated with identical AR coatings. The damage thresholds did not depend on the substrate material, but did improve on the bowl-feed polished surfaces. The distribution of thresholds on conventional and bowl-feed polished surfaces is shown in figure 4. The increase in median threshold for coatings on bowl-feed polished surfaces is interesting in view of the fact that the damage thresholds of bare surfaces polished by conventional or bowl-feed process are equal. Consequently the difference in the coating thresholds is attributable to differences in the chemical state of the surface, which probably changes the coating's absorption.

The effect of undercoat layers of SiO_2 or Al_2O_3 deposited between the substrate and first layer of the AR coating was studied further. The results of this and earlier studies showed that presence of the undercoat increases the median damage threshold 30%. However the variation in thresholds among samples of both undercoated and nonundercoated parts was large. We think the statistical improvement effected by the undercoat is associated with change in the chemical or impurity environment at the substrate interface.

6. Thin Film Materials

A range of oxide and fluoride film materials were deposited in single and multilayer coatings to determine whether these common materials offer improved damage thresholds.

The oxide films studied were SiO_2, TiO_2 and multilayer combinations of the low-index SiO_2 with one of the high-index films TiO_2, Al_2O_3, ZrO_2 and Ta_2O_5. The damage thresholds of all these coatings were nearly equal, although some SiO_2/Ta_2O_5 AR coatings were found with thresholds considerably above average.

We also made a brief survey of fluoride coatings. Single layers of MgF_2, NaF, Na_3AlF_6 and multilayers of MgF_2/ThF_4, MgF_2/PbF_4 and ThF_4/ZnS were tested. The initial results indicated that these materials offer no immediate improvement over the presently used oxide films.

7. Pulsewidth Dependence of Damage Threshold

Laser-induced damage thresholds generally depend on the laser pulsewidth. Bettis et al(6) suggested the empirical scaling law that damage threshold increases as the square root of the pulsewidth, and presented a heuristic argument for such scaling based on the intensity dependence of inverse-Bremsstrahlung plasma absorption. We measured damage thresholds at 0.17 ns, 1.0 ns, 1.6 ns and 3.5 ns. Figure 5 shows the pulsewidth dependence of damage threshold for polished bare surfaces, HR coatings and AR coatings. The solid line corresponds to a square root pulsewidth dependence. We find the square-root increase to be an upper limit which is met only by some bare surfaces. Coating thresholds increase more slowly and some, particularly AR coatings, are nearly independent of pulsewidth between 1 ns and 3.5 ns.

8. Summary

Our measurements can be summarized as follows:

1. Conventional polishing compounds and polished surfaces of BK-7 and fused silica are contaminated with metallic impurities.

2. Pure polishing compounds have been identified, but surfaces fabricated with those compounds have not yet been tested.

3. Removal of the polished layer by CO_2 laser beams increased the damage threshold; surface removal by acid etching, sputter etching, and ion planning was ineffective.

4. Breaking holds promise as a technique for generating clean surfaces, but is troubled by microscopic glass particles generated during breaking.

5. Half-wave SiO_2 overcoats increased the threshold of SiO_2/TiO_2 high reflectors, but overcoated reflectors emit light when irradiated at sub-threshold fluences sufficient to damage non-overcoated reflectors.

6. Substitution of Al_2O_3, Ta_2O_5, or ZrO_2 for TiO_2 in the outer layers of SiO_2/TiO_2 high reflectors produced mixed results - an advantage was not clearly demonstrated.

7. Alteration of film designs to produce lower standing wave intensities at either film interface or in the TiO_2 layers did not increase damage thresholds.

8. Absorptions measured by laser calorimeter correlate with damage thresholds in high reflectors with absorption $> 10^{-4}$, the correlation fails at lower absorption.

9. Thresholds of 4-layer SiO_2/TiO_2 anti-reflective films deposited on super-polished substrates exceeded the thresholds of similiar films deposited on conventionally polished substrates, even though thresholds of the bare substrates were comparable.

10. Fluoride films MgF_2, NaF, Na_3ALF_6, ThF_4, and PbF_4 offered no immediate improvement over presently used oxide films.

11. For pulse durations from 0.1 to 3.5 ns. 1064-nm damage thresholds did not increase, in general, proportional to the square-root of pulsewidth. The square-root scaling was observed on some bare polished surfaces; thresholds of A-R films tested did not vary between 1.0 and 3.5 ns.

9. Conclusions

Defects, not yet identified, dominated all surface and film thresholds. Some techniques for improving thresholds without deliberately attacking the defect problem, such as re-design of the coating or use of alternate materials, were generally ineffective. One method of removing impurities and defects from polished surfaces, laser annealing, was successful; other surface removal techniques failed. Significant improvements in film or surface thresholds will require identification and elimination of the defects causing damage. Occasional films and surfaces with high damage thresholds, and the low value of film and surface thresholds as compared to bulk thresholds, indicate significant improvements are possible.

Acknowledgments

Many persons participated in the experiments we have described. C. K. Carniglia and J. H. Apfel of Optical Coating Laboratories designed and fabricated thin films for measurements reported here. T.A.Tuttle and T. H. Allen, also of OCLI, performed microscopic analysis of damage and measured the film absorption. P. A. Temple of the Naval Weapons Center did the CO_2 laser annealing of bare surfaces. R.L. Landingham of the Chemistry and Materials Science Department at LLL analyzed coating compounds and polished surfaces, andT.M.Quick of the same group developed techniques for breaking glass. G. E. Murphy and S. E. Peluso assisted in the maintenance and operation of the lasers used for damage tests, and A. B. Griffith prepared the manuscript.

We are also grateful to other laboratories and individuals for their assistance to the LLL damage program; reports of several experiments are described elsewhere in these proceedings.

References

1. Milam, D. in Proceedings of the Society of Photo-Optical Instrumentation Engineers, Vol. 140, Optical Coatings II, De Bell, G. W. and Harrison, D. H. eds. 1978.

2. Decker, D. L. and Temple, P. A. in Laser Induced Damage in Optical Materials: 1977 NBS Special Publ. 509, p. 281; Allen, T. H., Apfel, J. H. and Carniglia, C. K. in Laser Induced Damage in Optical Materials: 1978, NBS Special Publ. 541, p. 33.

3. Temple, P. A., Milam, D. and Lowdermilk, W. H., CO_2 Laser Polishing of Fused Silica Surfaces for Increased Laser Damage Resistance at 1.06 μm, elsewhere in the proceedings.

4. Apfel, J. H. Applied Optics, 16, 1880 (1977).

5. The damage sites were photographed using SEM by Carrier, G. F. of Corning Glass Works.

6. Bettis, J.R., House, R. A. and Guenther, A. H. in Laser Induced Damage in Optical Materials: 1976 NBS Special Publ. 462, p. 338.

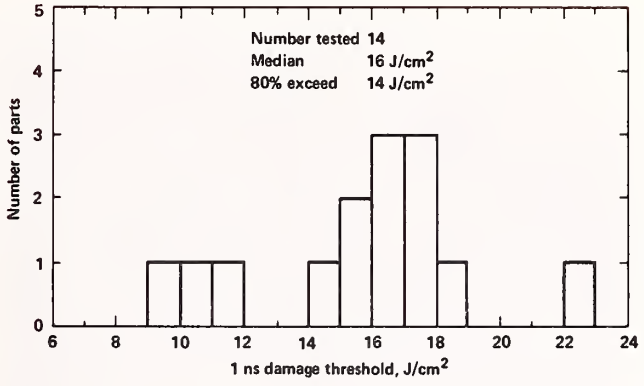

Figure 1. Histogram of damage thresholds of polished, uncoated surfaces of BK-7 and fused silica measured with 1 ns pulses.

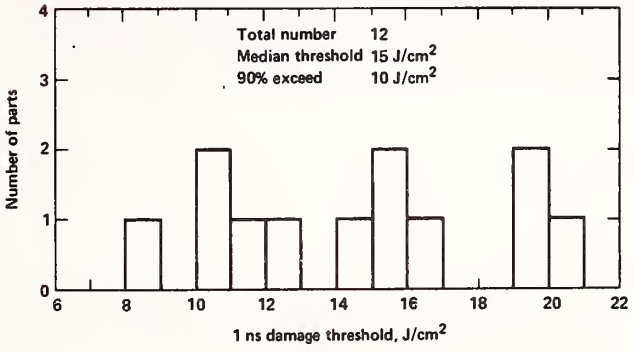

Figure 2. Histogram of damage thresholds of overcoated SiO_2/TiO_2 mirrors measured with 1 ns pulses.

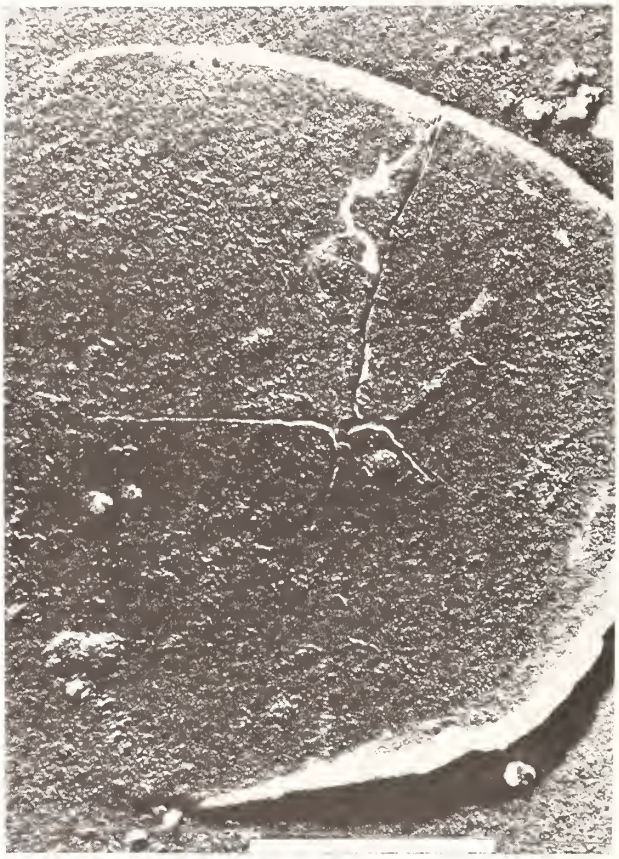

(a)

Figure 3. Damage sites on four-layer SiO_2/TiO_2 AR coating observed by SEM(5). The sites shown in (a), (b), (c) were caused by increasing fluence.

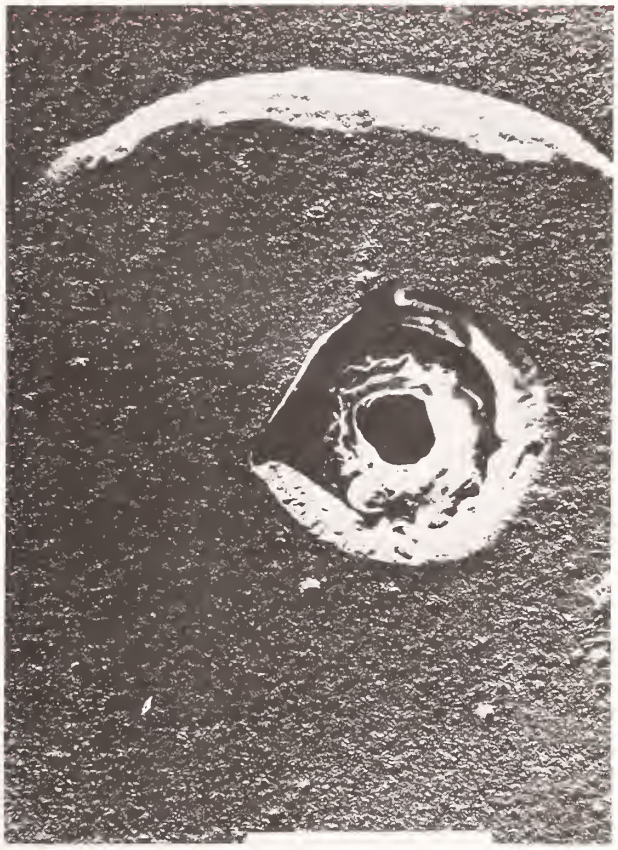

(b)

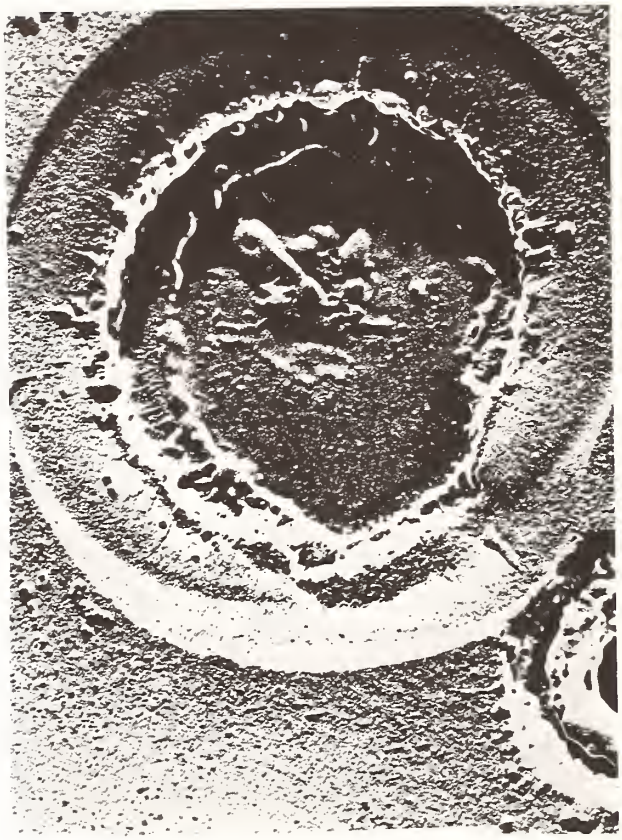

(c)

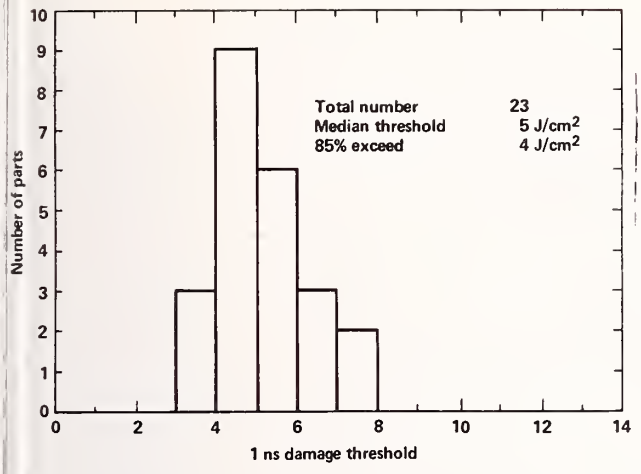

FIGURE 4a

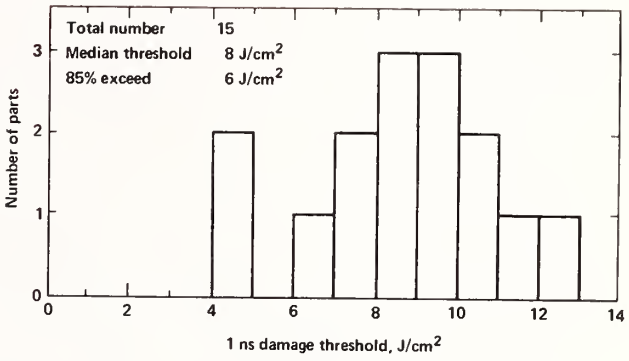

FIGURE 4b

Figure 4. Histogram of damage thresholds of SiO_2/TiO_2 AR coatings on (a) conventionally polished (b) bowl-feed polished surfaces measured with 1 ns pulses.

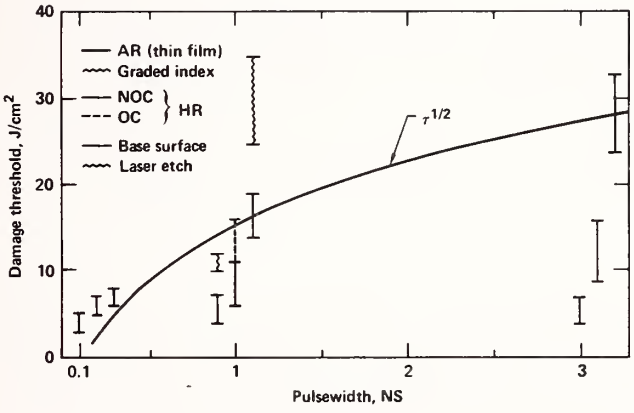

Figure 5. Damage thresholds versus pulse width for bare surface, HR coating and AR coating.

In response to a question on the absence of dependence of the observed damage threshold on the thickness of anti-reflection films, the speaker indicated that film thickness was varied over a factor of two in the course of the investigation, and no detailed calculations of field distribution within the film were carried out. He further indicated that in connection with the studies of phase-separated graded-index surfaces, light scattering was not observed to be a problem.

PULSED DAMAGE THRESHOLDS OF FLOURIDE AND OXIDE THIN FILMS FROM 0.26 μm TO 1.06 μm

T. W. Walker*, A. H. Guenther, and C. G. Fry@
Air Force Weapons Laboratory
Kirtland AFB, New Mexico 87117

and

P. Nielson+
Air Force Institute of Technology
Wright Patterson AFB, Ohio 45433

The pulsed laser-induced damage threshold for CaF_2, MgF_2, ThF_4, MgO, Al_2O_3, TiO_2, SiO_2, HfO_2, and ZrO_2 thin films was measured. The measurements were made at 1.06 μm, 0.53 μm and 0.26 μm with pulse lengths of ~5 and ~15 ns (measured at 1.06 μm). Different film thicknesses of each material were damaged at each wavelength and pulse length. The film thicknesses were 1λ, 1/2 λ, 1/4 λ, 1/6 λ, and 1/8 λ at 1.06 μm.

It was found that the pulse length dependence of breakdown fit with a $[\text{pulse length}]^{\frac{1}{2}}$ curve for most of the materials. Exceptions were found in some oxide coatings at 1.06 μm where the breakdown energy density was essentially independent of the pulse length. The damage threshold of the flouride and SiO_2 films increased with a decrease in film thickness. This did not correlate with changes in the E field inside the thin films. (The oxide films did not exhibit as pronounced a thickness dependence.) The breakdown threshold decreased with decreasing wavelength and correlated inversely with the absorption coefficient, although the correlation was not linear.

There was a marked change in the damage morphonogy of the materials as wavelength was decreased. At 0.26 μm all the oxide material damaged in a uniform region while the flourides damaged as isolated pits. The morphology, pulse length and film thickness trends are discussed in terms of impurity, avalanche ionization, and multiphoton damage models.

Key words: Laser damage, thin films, pulse duration dependence of damage; wavelength dependence of damage; impurity damage; avalanche ionization; multiphoton induced damage; film thickness dependence.

1. Introduction

The damage thresholds of thin films have previously been studied as a function of laser wavelength (1-6) pulse duration (7,8) and film thickness (9). These experiments have generally been uncorrelated since each was performed as a separate study. The interpretation of each uncorrelated result can vary because of variations of absolute results from separate experiments. We report the measurement of the damage threshold of several flouride and oxide thin film coatings as a function of pulse duration, laser wavelength, and film thickness. If a theory of thin film data is to be comprehensive it must explain the correlated variation of the above parameters.

---

* Presented in partial fulfillment of the Ph.D. degree at the Air Force Institute of Technology, Wright Patterson AFB, Ohio

@ Presently at Iowa State University, Ames. Iowa

\+ Presently at Air Command and Staff College, Maxwell AFB, AL

2. Experimental Arrangement

Figure (1) is a schematic diagram of the experimental layout. The beam diagnostic path was maintained to be as close a replica of the high energy damaging path as possible. An optical multichannel analyzer (OMA) was used to assess the beam intensity spatial profile for each laser pulse. Because of the limited spatial resolution of the OMA (100 μm), the focal plane in the diagnostic path, which is equivalent to the high energy damaging focal plane, had to be magnified and reimaged onto the vidicon. This was accomplished by the lens L3 shown in Figure (1).

It was necessary to check the equivalence of the two focal planes and the imaging quality of the lens L3. During damage testing at 2600 Å it was found that HfO_2 films damaged uniformly. These films did not exhibit any isolated pit formation. An obscuration was placed in the near field of the laser beam to produce a distorted far field pattern. The HfO_2 thin film sample was damaged in a nonuniform pattern and the resulting morphological record compared to the OMA output. The result is shown in Figure (2). This procedure was repeated ten times with similar correlation. Calibration of the total system was complicated and will be detailed in a later report.

All damage shots were taken at the focal plane of the lens at L1. Unfortunately, it was not possible to hold the spot size constant over the four laser wavelengths used in the experiment. In order to minimize the spot size change at shorter wavelengths a 1 meter focal length matched set of lenses were used at 0.35 μm and 0.26 μm. The focal spot sizes at 1.06, 0.53, 0.35, and 0.26 μm where 360, 280, 220, and 170 μm respectively. These are given as FWHM points.

The pulse durations were also not constant and were a function of laser wavelength. This was due to the response of the nonlinear frequency connecting crystals. The pulse durations at 1.06, 0.53, 0.35, and 0.26 μm where 15, 14.5, 13.5, and 11.5 ns respectively at the long pulse lengths and 5, 4.8, 4.3, and 3.9 ns at the short pulse lengths. The relative pulse to pulse variation in pulse length was ±5%.

The experimental error was determined to be ±17%, most of which was attributed to the reproducibility energy meter. The maximum variation in vidicon response across the active surface was found to be ±7%. The data shown in Tables 1-5 gives the damage thresholds of the tested thin films in Joules/cm^2. The number following each damage threshold represents the span over which damage and no damage results overlapped. Each threshold is derived from approximately thirty laser shots on the sample.

3. Results

The damage thresholds in Tables 1-5 have been corrected for the standing field pattern inside the thin film by using the equations given by Newnam, et al. (9). The most apparent result is the change in damage threshold with film thickness. This is extraneous to the film thickness dependence reported by Newnam, et al (9), caused by the change in the standing field pattern with film thickness. It should be pointed out that much of the film thickness dependence of damage in TiO_2 was removed by correcting for the standing field inside the film. However, it is clear from the corrected data that this is not the complete explanation.

The data shows a general trend of decreasing thresholds as the laser wavelength decreases. This is in general agreement with the results of Newnam, et. al. (1), and shows a general correlation with the absorptivity measurements. A variation in damage threshold with pulse length is also evident The weakest overall time dependence is shown by ZrO_2. Several of the oxides show a weak dependence at 1.06 μm, but not at shorter wavelengths. The time dependence also increases for many of the thin film materials as the film thickness decreases. Finally, Figure (2) shows the damage morphology as a function of the laser wavelength. It can be seen that there is a consistant decrease in the damage site size as the wavelength is decreased.

4. Conclusions

A theoretical interpretation of this data based on impurity dominated damage will be presented in a later paper. This theoretical model provides an overall interpretation of the pulse length, film thickness and wavelength dependence of the damage threshold. The morphology changes can also be addressed by this model.

5. Summary

In order to understand the damage mechanism in thin films it is extremely beneficial to correlate many of the variables which can occur in the experimental situation. In this experiment the film thickness, laser wavelength and pulse length were all correlated in an attempt to explain the breakdown process. In addition, the morphology was studied as an auxillary source of information. The total integration of these parameters is best explained by an impurity model of the breakdown process.

The authors would like to acknowledge the outstanding technical assistance of Mr. J. Jasso and Mr. M. Morris for their contribution in obtaining the experimental data presented in this paper.

6. References

[1] Newnam, B. E., and Gill, D. H., Special Dependence of Damage Resistance of Refractory Oxide Optical Coatings, Laser Induced Damage in Optical Materials, NBS Special Publication 462, eds. A. J. Glass and A. H. Guenther, US GPO, Washington D.C., (1976)

[2] Porteus, J. O., et al., Multithreshold Evaluation of 175-nanosecond Pulsed Laser Damage to Coating Materials at 2.7 and 3.8 m Wavelengths, Laser Induced Damage in Optical Materials, NBS Special Publication 541, eds. A. J. Glass and A. H. Guenther, US GPO Washington D.C., (1978).

[3] Newnam, B.E., and Gill, D. H., Ultraviolet Damage Resistance of Laser Coatings, NBS Special Publication 541, eds. A. J. Glass and A. H. Guenther, US GPO Washington D. C., (1978).

[4] Fradin, D. W. et al., Comparison of Laser Induced Bulk Damage in Alkali-Halides at 10.6, 1.06, and 0.69 Microns, Laser Induced Damage in Optical Materials, NBS Special Publication 372, eds. A. J. Glass, and A. H. Guenther, US GPO, Washington D.C., (1972).

[5] Smith, W. L., et al., Picosecond Laser-Induced Breakdown at 5321 and 3547 A: Observation of Frequency Dependent Behavior, Phys. Rev. B 15, No. 8, 4039, (1976).

[6] Soileau, M.J., et al., Frequency and Spot-Size Dependence of Laser Damage in the Mid-IR Region, Laser-Induced Damage in Optical Materials, NBS Special Publication 541, eds. A. J. Glass and A. H. Guenther, US GPO, Washington D.C., (1978).

[7] Wang, V., et al., Single and Multilongitudinal Mode Damage in Multilayer Reflectors at 1.06 m as a Function of Spot Size and Pulse Duration, Laser Induced Damage in Optical Materials, NBS Special Publication 435, eds. A. J. Glass and A. H. Guenther, US GPO, Washington D.C. (1975)

[8] Bettis, J.R., et al., Spot Size and Pulse Dependence of Laser Induced Damage, Laser Induced Damage in Optical Materials, NBS Special Publication 462, US GPO Washington, D.C. (1976)

[9] Newnam, B. E., et al., Influence of Standing-Wave Fields on the Laser Damage Resistance of Dielectric Films, Laser Induced Damage in Optical Materials, NBS Special Publication 435, eds. A. J. Glass and A. H. Guenther, US GPO, Washington D.C. (1975).

	Thickness λ (at 1.06 μm)	1.06 μm		0.53 μm		0.353 μm		0.265 μm	
		5 ns	15 ns	5 ns	15 ns	5 ns	15 ns	5 ns	15 ns
MgF_2	1	10.74±11	15.53±7%	4.09±10%	8.75±10%	4.10±11%	4.78±7%	3.21±8%	2.68±15%
	1/2	_____	18.35±5%	7.73±14%	13.43±10%	_____	_____	_____	2.23±9%
	1/4	13.37±17%	19.57±7%	7.99±12%	15.99±3%	3.09±14%	5.37±3%	2.13±16%	3.25±10%
	1/6	_____	_____	9.04±10%	16.04±8%	3.24±8%	6.56±10%	2.00±5%	3.36±5%
	1/8	23.61±21%	38.95±16%	9.83±5%	15.34±13%	2.70±8%	6.25±10%	1.52±16%	3.34±2%
ThF_4	1	7.07±1%	12.85±10%	3.60±10%	9.15±8%	4.24±1%	5.55±2%	1.96±9%	2.80±1%
	1/2	_____	13.00±14%	6.13±10%	12.66±28%	_____	_____	_____	2.71±15%
	1/4	_____	40.92±9%	7.66±10%	16.50±12%	3.90±6%	9.12±3%	1.32±1%	4.39±2%
	1/6	_____	_____	25.44±29%	44.47±9%	4.66±13%	8.67±3%	1.65±7%	4.18±0%
	1/8	30.52±8%	55.77±11%	29.26±8%	51.96±9%	7.89±6%	10.88±15%	1.87±14%	5.31±3%

VALUES ARE IN : J/CM^2

Table 1. M_gF_2 and ThF_4 damage thresholds.

	Thickness λ (at 1.06 μm)	1.06 μm 5 ns	1.06 μm 15 ns	0.53 μm 5 ns	0.53 μm 15 ns	0.353 μm 5 ns	0.353 μm 15 ns	0.265 μm 5 ns	0.265 μm 15 ns
CaF_2	1	15.63±5%	20.28±8%	5.53±20%	11.48±7%	3.47±5%	4.45±3%	2.84±5%	4.73±18%
	1/2	_____	23.48±4%	7.05±1%	13.01±9%	_____	_____	1.40±36%	_____
	1/4	20.00±9%	33.23±26%	13.28±8%	19.70±2%	2.76±41%	5.22±10%	2.29±1%	3.55±0%
	1/6	_____	_____	10.56±13%	21.20±3%	6.30±15%	10.54±2%	2.44±19%	4.91±13%
	1/8	21.94±14%	34.39±4%	15.46±4%	24.83±3%	9173±7%	19.01±10%	2.64±1%	5.98±3%
Al_2O_3	1	11.40±9%	15.17±15%	_____	13.20±10%	3.29±10%	6.69±23%	1.56±7%	2.31±6%
	1/2	_____	17.92±12%	6.59±1%	11.71±11%	_____	_____	_____	_____
	1/4	13.15±1%	20.14±9%	7.33±5%	13.39±6%	2.79±10%	6.07±10%	2.21±6%	2.02±12%
	1/6	_____	_____	7.13±13%	13.81±8%	3.24±16%	5.12±9%	_____	2.51±16%
	1/8	20.02±15%	21.55±1%	8.51±4%	14.09±20%	2.92±10%	5.98±10%	1.74±17%	2.23±15%

VALUES ARE IN : J/CM^2

Table 2. CaF_2 and Al_2O_3 damage thresholds.

Table 2. CaF_2 and Al_2O_3 damage thresholds.

	Thickness λ (at 1.06 μm)	1.06 μm 5 ns	1.06 μm 15 ns	0.53 μm 5 ns	0.53 μm 15 ns	0.353 μm 5 ns	0.353 μm 15 ns	0.265 μm 5 ns	0.265 μm 15 ns
HfO_2	1	4.61±10%	_____	3.99±20%	_____	0.93±5%	_____	1.20±6%	1.19±8%
	1/2	_____	_____	5.04±10%	_____	_____	_____	_____	_____
	1/4	8.52±1%	13.16±2%	5.08±4%	9.20±14%	3.47±7%	4.32±22%	0.77±10%	1.42±6%
	1/6	_____	_____	0.39±10%	0.73±10%	0.71±12%	_____	0.32±1%	0.24±0%
	1/8	5.4±4%	7.94±7%	3.47±3%	5.44±7%	1.64±2%	2.73±9%	0.43±6%	0.73±2%
TiO_2	1	8.88±12%	_____	4.38±29%	_____	0.15±8%	_____	_____	_____
	1/2	11.42±9%	_____	4.82±8%	_____	_____	_____	_____	_____
	1/4	14.91±3%	13.86±14%	6.64±4%	11.82±3%	0.16±10%	_____	_____	_____
	1/6	_____	_____	5.28±9%	8.88±3%	0.06±0%	_____	_____	_____
	1/8	10.07±10%	9.88±7%	6.44±14%	10.82±1%	0.12±0%	_____	_____	_____

VALUES ARE IN : J/CM^2

Table 3. HfO_2 and TiO_2 damage thresholds.

	Thickness λ (at 1.06 μm)	1.06 μm		0.53 μm		0.353 μm		0.265 μm	
		5 ns	15 ns	5 ns	15 ns	5 ns	15 ns	5 ns	15 ns
ZrO_2	1	8.37±10%	———	4.46±14%	———	1.17±3%	———	0.82±4%	0.76±8%
	1/2	10.02±5%	———	———	———	1.50±30%	———	———	0.59±25%
	1/4	10.08±12%	9.53±1%	6.78±2%	6.23±13%	1.89±6%	2.27±1%	0.54±32%	———
	1/6	———	———	4.25±5%	4.97±13%	1.46±5%	———	0.95±18%	1.14±18%
	1/8	10.61±6%	10.90±16%	6.01±7%	6.93±3%	2.79±8%	2.64±3%	0.70±1%	1.07±5%
MgO	1	———	———	———	11.47±20%	———	———	———	———
	1/2	10.27±1%	9.86±4%	6.19±15%	10.03±12%	———	———	———	———
	1/4	14.95±6%	15.01±7%	8.87±7%	16.25±3%	2.86±9%	3.91±1%	1.31±5%	2.34±6%
	1/6	———	———	7.87±11%	14.35±7%	3.15±14%	5.53±14%	2.18±3%	2.99±5%
	1/8	12.21±4%	12.83±4%	10.66±17%	14.27±5%	2.87±14%	4.30±10%	1.66±32%	2.61±16%

VALUES ARE IN : J/CM^2

Table 4. ZrO_2 and MgO damage thresholds.

Table 4. ZrO_2 and MgO damage thresholds.

	Thickness λ (at 1.06 μm)	1.06 μm 5 ns	1.06 μm 15 ns	0.53 μm 5 ns	0.53 μm 15 ns	0.353 μm 5 ns	0.353 μm 15 ns	0.265 μm 5 ns	0.265 μm 15 ns
SiO_2	1	———	———	———	———	———	———	———	———
	1/2	———	———	7.96±6%	———	———	———	———	———
	1/4	23.62±1%	47.36±12%	9.54±15%	19.88±6%	6.06±9%	11.76±2%	1.10±10%	1.94±11%
	1/6	———	———	———	———	———	———	1.56±35%	———
	1/8	42.64±1%	48.69±11%	21.45±13%	49.14±4%	———	14.70±10%	2.58±9%	2.92±12%

VALUES ARE IN : J/CM^2

Table 5. SiO_2 damage thresholds.

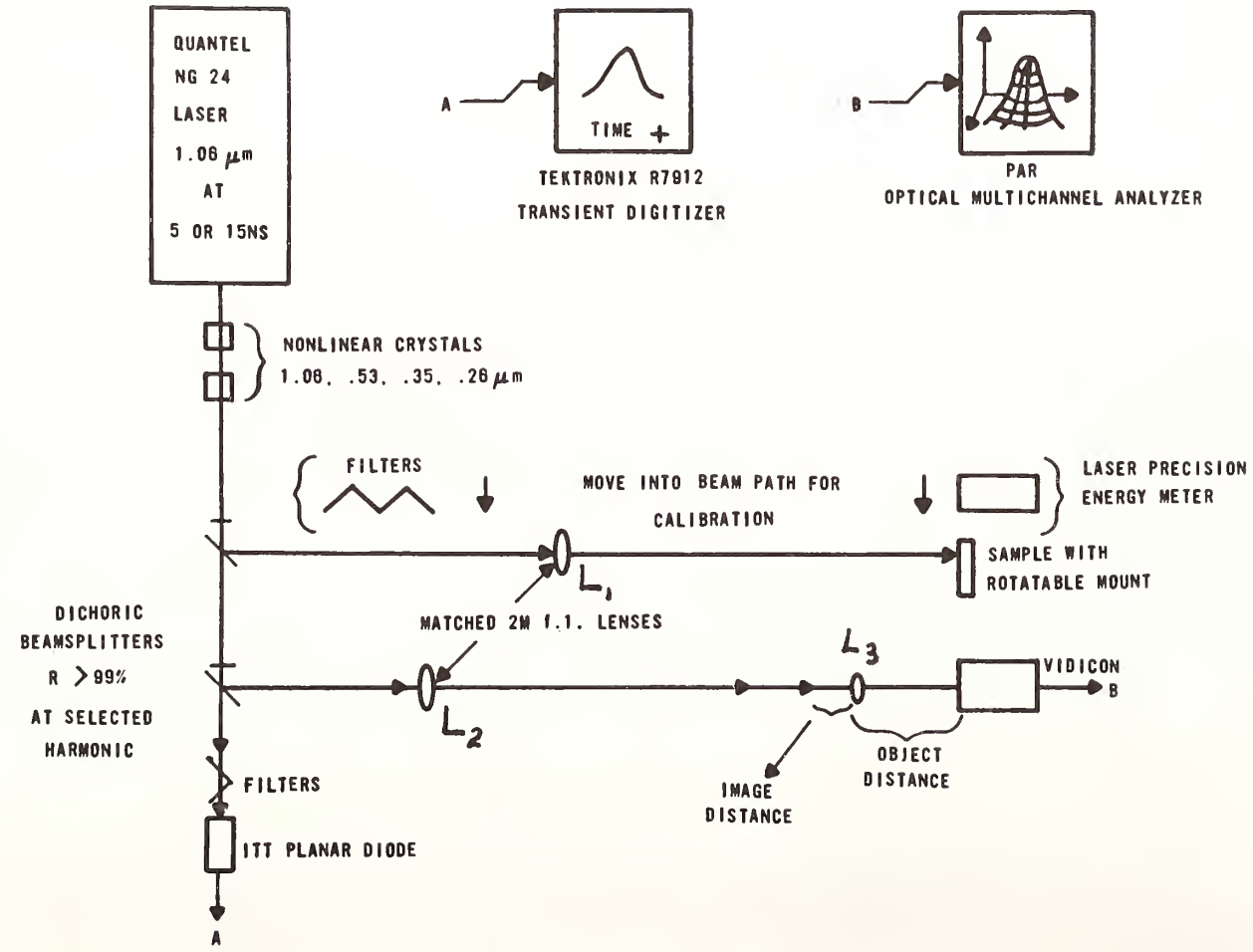

Figure 1. Experimental layout.

Figure 1. Experimental layout.

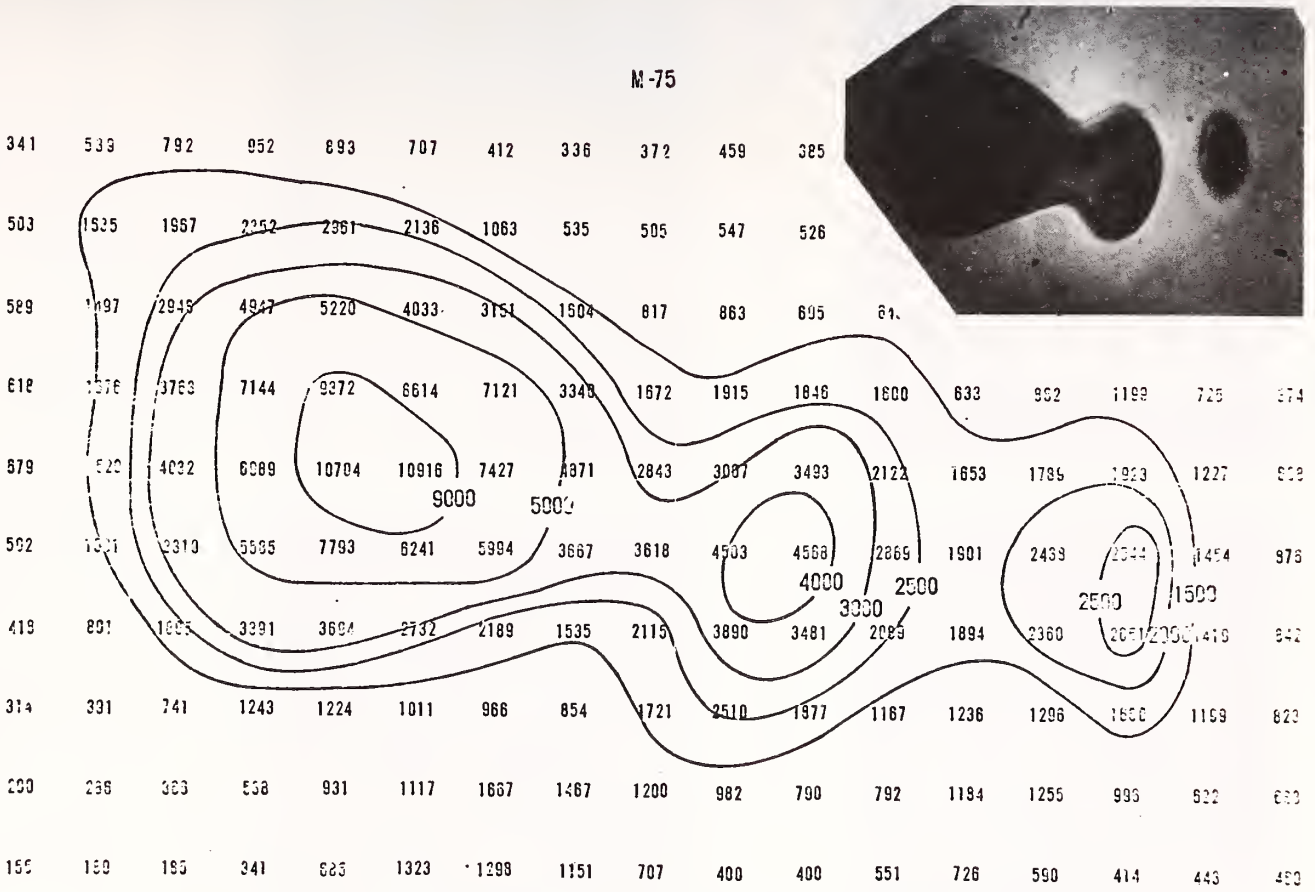

Figure 2: Vidicon Output Laser Profile And Damage Site Morphology

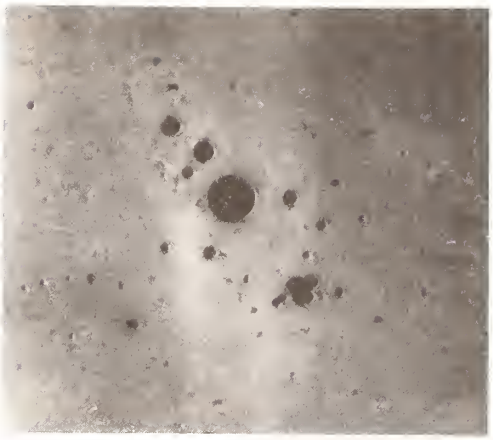

1.06 m

0.53 m

0.35 m

0.26 m

Figure (3): MgO Damage Morphology vs Wavelength

LASER-INDUCED DAMAGE MEASUREMENTS WITH 266-nm PULSES†

T. F. Deaton* and W. L. Smith
University of California
Lawrence Livermore Laboratory
P. O. Box 5508
Livermore, CA 94550

The results of a survey of laser-induced damage thresholds for optical components at 266 nm are reported. The thresholds were measured at two pulse durations--0.150 ns and 1.0 ns. The 30 samples tested include four commercial dielectric reflectors, three metallic reflectors, two anti-reflection films, a series of eight half-wave oxide and fluoride films, and twelve bare surfaces (fluoride crystals, silica, sapphire, BK-7 glass, CD*A and KDP). The 266-nm pulses were obtained by frequency-quadrupling a Nd:YAG, glass laser. Equivalent plane imagery and calorimetry were used to measure the peak fluence of each of the UV pulses with an accuracy of ± 15%; the uncertainty in the threshold determinations is typically ±30%.

Key words: Damage thresholds; laser damage; pulsewidth dependence, picosecond pulses; UV lasers.

1. Introduction

There is currently an increasing interest in the application of visible and ultraviolet lasers to inertial confinement fusion research. Fusion target experiments utilizing the second- and third-harmonic wavelengths of the Argus Laser are currently underway or in planning at Lawrence Livermore Laboratory. Fusion experiments at 266 nm on Argus are probable. A prototype KrF-CH_4 Raman-compressed laser system is also being developed which will involve two UV wavelengths - 268 and 248 nm. There is a clear need for a broad data base of the optical properties of materials that are useful near 266 nm.

In response to this need we have performed a survey of damage thresholds at 266 nm at pulse durations of about 100 psec and about 700 psec of some thirty samples comprising a representative set of the materials and coatings currently available. This subnanosecond data complements the 22 nsec data made available last year [1][1]. The thin films tested include four total reflector films, three metallic reflectors, two anti-reflection films, and a series of eight half-wave fluoride and oxide films. The twelve tested bare surfaces include many important UV window materials -alkali-fluoride and alkaline earth-fluoride single crystals, hot-forged lithium fluoride, fused silica, sapphire - and also BK-7 glass, potassium dihydrogen phosphate (KDP) and cesium dideuterium arsenate (CD*A). It must be noted that the samples tested in this survey have not been specifically developed to have high damage thresholds at 266 nm. They are instead representative of current off-the-shelf components.

†Work performed under the auspices of the U.S. Department of Energy under contract W-7405-eng-48.

*United States Air Force Research Associate.

[1]Figures in brackets indicate the literature references at the end of this paper.

2. Experimental

The laser used for the 100 psec pulse duration measurements consisted of a dye mode-locked Nd:YAG oscillator, two Nd:YAG and two Nd:glass amplifiers. It has been used in the past for short-pulse 1064-nm damage studies [2]. The 700 psec data were obtained after the installation of an actively mode-locked and Q-switched oscillator which provides pulses with durations ranging from 100 psec to 1.2 nsec [3]. The average pulse duration for the dye mode-locked oscillator was 150 psec, as determined by streak camera photography. There were of course significant fluctuations in the pulse duration, on the order of ± 30 psec, due to the statistical nature of the dye. In this experiment we do not at present have the capability to measure a subnanosecond pulse duration in the UV, so the figure 100 psec is simply our best estimate of the average fourth harmonic pulse length, which we believe to be accurate to within ± 20 psec. The longer UV pulses were obtained from 1064 nm pulses of 1.02 nsec duration from the actively mode-locked oscillator. The accuracy of the 1064 nm pulse duration figure is better than 5%, but again the UV pulse duration of 700 psec is estimated, and has an uncertainty of ~ ±50 psec.

The energy of the 1064 nm, linearly polarized laser pulse is determined by a calorimeter sampling the beam via an uncoated BK-7 beamsplitter (fig.1). Second harmonic generation is done by an angle-tuned KD*P crystal (Type I) with conversion efficiency as high as 80% for 100 psec pulses. For some of the work we used a temperature-tuned CD*A crystal with which we obtained similarly high conversion efficiency. The remaining 1064 nm light after the SHG cell is spatially separated from the second harmonic by a prism set approximately at minimum deviation. The 532 nm beam is similarly sampled for energy content via a BK-7 beamsplitter; it then enters an angle-tuned KDP or temperature-tuned ADP crystal for fourth harmonic generation. The maximum conversion efficiency at this stage was on the order of 30%. The 532 nm light remaining after the cell is spatially separated by a quartz prism.

The 266 nm optical circuit is shown in figure 2. The beam is focused by a 2 meter focal length lens; the focal plane occurs at approximately 40 cm beyond the front surface of the sample. After the lens, the beam is split into two parts by a partially reflecting mirror, with 48% of the energy going to an absorbing glass calorimeter (GG19 glass). A second bare beam-splitter directs energy to a vidicon camera and to a multiple-exposure mirror. The off-set angle of the beamsplitters was 3 degrees. A multiple-exposure photograph of each shot is taken with Plus-X film in a plane optically-equivalent to the plane of the front surface of the sample. The laser spot size at the sample plane was approximately 1.0 mm in diameter.

All the samples were irradiated at about 5° from normal incidence, one shot per site. The damage used was the existence of front surface alteration as determined by visual inspection immediately after the shot or by Nomarski microscopy afterward.

Our standard procedure was to fire enough shots to reduce the threshold uncertainty to ± 10% in 266 nm pulse energy. When the beam profile data were analyzed, there was found to be a significant variation in the beam shape, and particularly in the effective area of the beam, from shot to shot. In some cases this variation produced a narrowing of the uncertainty of the peak fluence value at threshold, but in others it increased the uncertainty. Generally the fluence uncertainties are greater for the short pulses, since these were obtained from a dye mode-locked laser instead of the very amplitude-stable AMQO.

The multiple-exposure images of the beam were analyzed by the same techniques used for the 1064 nm laser damage experiments at their laboratory [4]. Experience has shown that the combination of the very stable absorbing glass calorimeter and our photocalibration codes yield peak fluence values accurate to within $\pm$ 10%.

3. Results and Discussion

The damage thresholds for the bare surfaces tested are shown in table 1. There is variation of about one order of magnitude for the group. The first eight samples listed are a series prepared in 1976 similarly and for intended damage testing at 1.06 microns. There is relatively little variation in thresholds for the series, the average being about 1 J/cm^2 at 100 psec and 2-3 J/cm^2 at 700 psec. We hypothesize that the general clustering of these thresholds may be due more to the surface finishing techniques than to any intrinsic behavior.

The remaining samples on the table are from various sources. The silica and BK-7 in particular are substrates intended for coating damage studies at 1.06 microns. The silica sample was particularly damage resistant, at least in a relative sense. The polishing techniques used for this sample, although developed for 1.06 micron, are somewhat more advanced than the simple hand polishing used for our fluoride samples. It is thus conceivable that with improved surface preparation the flouride damage thresholds might be considerably higher.

In light of the widespread application of silica optics in UV laser systems, it is encouraging to note that the silica threshold is as high as it is.

An unexpected result is that, at least for the short pulses, the BK-7 threshold was almost as high as the silica and higher than the fluorides, in spite of its high bulk absorption coefficient of about 6 per cm at 266 nm. We interpret this result as further evidence that surface properties are to a large extent masking the bulk properties of these samples.

The KDP sample threshold of about 6.5 J/cm^2 at 700 psec is a relatively high threshold and is encouraging given the application of KDP in second harmonic generation from 532 nm to 266 nm.

The bottom two LiF samples in table 1 were also damage tested at 1.06 microns by Dave Milam *et. al.* at Lawrence Livermore Laboratory. We found essentially no difference between the single-crystal and hot-forged LiF; the same was found at 1.06 microns. Although 1.06 micron damage thresholds for these samples were rather disappointingly low, at 266 nm they were the highest thresholds measured.

We tested eight half-wave layers of fluorides and oxides on silica substrates, as shown in table 2. With the exception of the yttrium oxide, the thresholds are clustered very closely together and are essentially the same at both pulse durations, and are lower than either the AR films or the high reflector films on dielectric substrates. Given the clustering and the error bars of the measurements, it is tenuous to assign any systematic correlation between the thresholds and bulk material properties such as band gap or index of refraction.

The relative magnitudes of the damage thresholds within the set correlate in a qualitative way with the thresholds for quarter-wave layers of the same materials for 22 nsec pulses reported at this conference last year by Newnam and Gill [1].

We also tested several total reflector and anti-reflective films. The thresholds are listed in table 3. We identify the samples only by a letter because in most cases the coating designs are proprietary, and we consider it to be ill-advised to try to distinguish between designs based only on this limited sampling. The dielectric reflectors average about 1.0 J/cm^2 at 100 psec and 1.8 J/cm^2 at 700 psec.

The AR film thresholds were slightly higher than the reflectors at 100 psec, in contrast to the situation at one micron, in which AR films are typically a factor two weaker than high reflectors. For the 700 psec duration, the AR's were on the average about as strong as the HR's. The metallic reflectors exhibited much lower thresholds than the dielectric reflectors. Finally, we turn to the pulse duration dependence.

The bare surface data are shown plotted versus pulse length in figure 3. The clustering of the fluoride samples is evident. The average pulse length is about $\tau^{0.5}$. The pulse length dependence of the single-layer films is shown in figure 4. The exponential factor of the pulse length dependence averages out to nearly zero. The pulse length dependence of the dielectric reflectors is shown in figure 5. The dependence is between about τ^0 and $\tau^{0.5}$.

4. Conclusions

Because only one sample of each specific type was tested, minor distinctions between materials should not be made on the basis of this data. Our conclusions are that 100 psec the current generally available threshold is about 1 J/cm^2 with a few important exceptions (silica and KDP). At 700 psec, 2-3 J/cm^2 damage thresholds are to be expected at this time, again with the exceptions of silica, KDP, and lithium fluoride.

5. Acknowledgements

We gratefully acknowledge the collaboration of B. Flint and L. Stelmac of Acton Research Corporation, J. Stanford of the Naval Weapons Center, W. Hargreave of Optovac, and J. Ready of Honeywell, in the supply of samples, and the capable assistance of M. Taylor in making the measurements.

References

[1] Newnam, B. E. and Gill, D. H., Laser Induced Damage in Optical Materials: 1978 (NBS Special Publication No. 541, US GPO, Washington, D. C.), p. 190.

[2] Milam, D. Applied Optics 16, 1204 (1977).

[3] Kuizenga, D. J., and Martin, W. E., Performance of Short-Pulse Oscillators for Argus and Shiva, presented at Electro-Optics/Laser 1977 Conference in Anaheim, Ca. (October 25-27, 1977).

[4] Milam, D. Measurement and Identification of Laser Damage Thresholds in Thin Films, presented at S.P.I.E. Technical Symposium East, Washington, D.C. (March 28-30, 1978).

Table 1. Bare surface damage thresholds (J/cm^2) for 266 nm.

Material	Fluence (J/cm^2) 100 psec	700 psec
LiF	0.60 ± 0.39	
BaF_2	0.50 ± 0.13	2.06 ± 0.72
SrF_2	0.47 ± 0.12	1.54 ± 0.51
CaF_2	0.65 ± 0.15	2.37 ± 0.83
MgF_2	1.32 ± 0.32	2.69 ± 0.41
LaF_3	1.80 ± 0.80	3.10 ± 0.70
Al_2O_3	0.75 ± 0.26	
Silica	3.00 ± 0.96	10.00 ± 3.00
BK-7	2.90 ± 0.84	1.94 ± 0.71
CD*A	1.10 ± 0.27	
KDP	>(1.70 ± 0.25)	6.48 ± 1.40
LiF		14.30 ± 2.50
LiF (hot forged)		14.40 ± 2.50

Table 2. Damage thresholds (J/cm^2) for single-layer films ($\lambda/2$ at 266 nm) at 266 nm.

	100 psec	700 psec
Y_2O_3	0.10 ± 0.035	0.26 ± 0.04
ZrO_2	0.51 ± 0.26	0.62 ± 0.14
SiO_2	0.72 ± 0.26	0.44 ± 0.13
AlF_3	0.65 ± 0.15	0.50 ± 0.07
LaF_3	0.70 ± 0.21	0.74 ± 0.20
MgF_2	0.80 ± 0.32	1.24 ± 0.33
P1	0.95 ± 0.25	0.66 ± 0.10
P2	0.85 ± 0.23	---

Table 3. Film damage thresholds (J/cm^2) for 266 nm pulses.

	100 psec	700 psec
Dielectric reflectors		
a	1.30 ± 0.25	3.85 ± 1.1
b	0.50 ± 0.12	0.405 ± 0.085
c	0.92 ± 0.20	1.86 ± 0.55
d	0.85 ± 0.23	1.54 ± 0.26
e	---	1.43 ± 0.26
Metallic reflectors		
a	0.23 ± 0.06	0.60 ± 0.21
b	0.10 ± 0.04	0.066 ± 0.013
c	0.13 ± 0.05	0.045 ± 0.017
AR films		
a	1.10 ± 0.27	1.20 ± 0.12
b	1.60 ± 0.54	0.72 ± 0.16

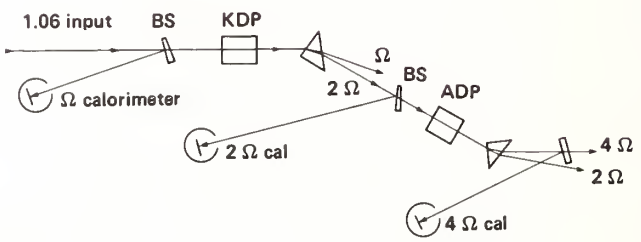

Figure 1. Fourth-harmonic generation optics.

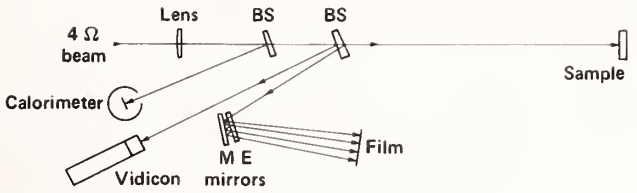

Figure 2. 266 nm damage experimental apparatus.

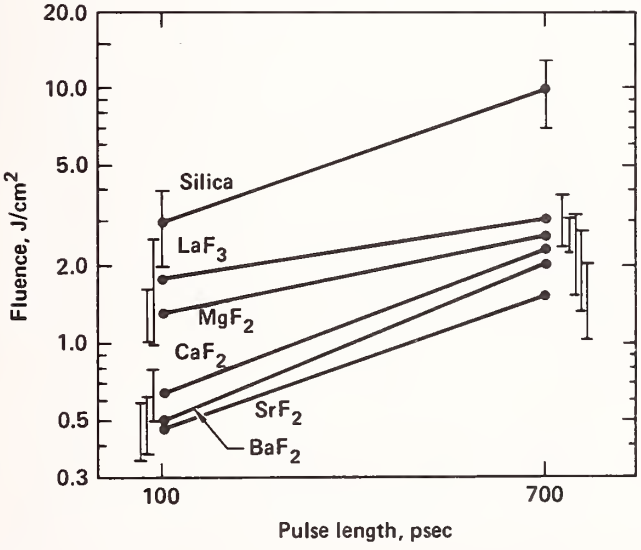

Figure 3. Pulse-length dependence of damage threshold for bare surfaces.

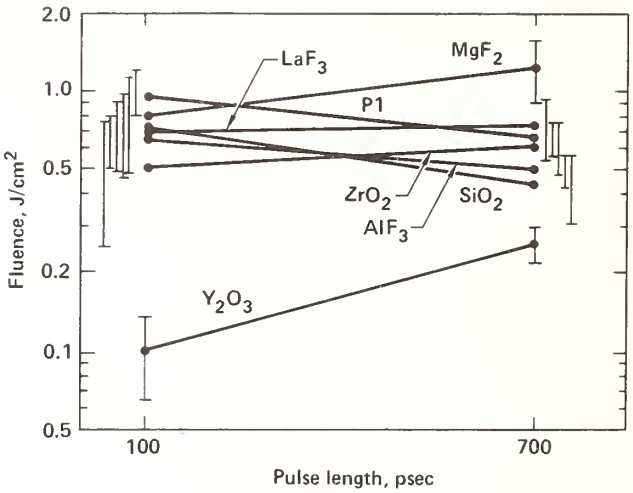

Figure 4. Pulse-length dependence of damage thresholds for single-layer films.

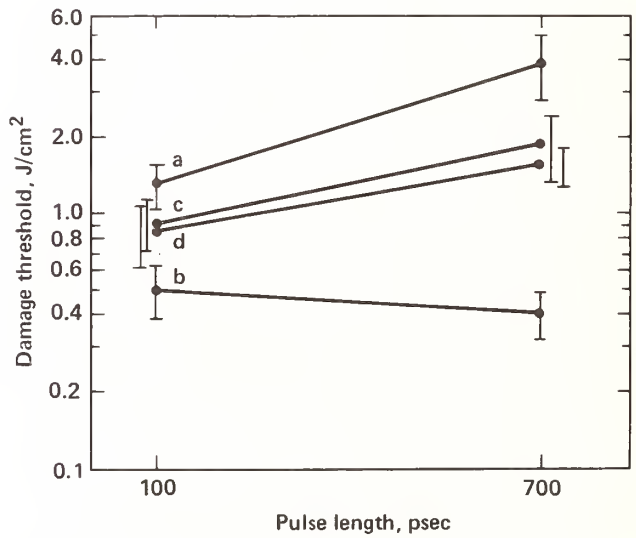

Figure 5. Pulse-length dependence of damage thresholds for dielectric reflectors.

Of all the samples tested, the largest variation in damage threshold at the two different pulse lengths was observed in sodium fluoride. When questioned about this large variation, the speaker indicated that approximately six months elapsed between those two measurements of the same sample, and that the sample was questionable because it had a fogged surface. It was pointed out in discussion that during the six months delay, significant surface contamination could have been present.

HIGH ENERGY LASER OPTICAL TRAIN PERFORMANCE
A REASSESSMENT

Claude A. Klein
Research Division, Raytheon Company
Waltham, Massachusetts 02154

This paper addresses problems relating to thermally induced phase aberrations experienced in a power-optics environment. Specifically, it addresses issues of concern in assessing the performance of High-Energy Laser (HEL) systems with regard to focal intensities and on-target fluences, when thermal lensing phenomena do occur in the optical train. Following Holmes and Avizonis [Appl. Optics 15, 1075 (1976)], a model has been developed that should allow HEL-system designers to complete an evaluation of the degradation in light intensity, which is caused by irradiance-mapping aberrations in the near-field. Perhaps the most important conclusion that was reached is that theories, calculations, and experiments conducted on a "single-component" basis provide highly unreliable guidelines for passing judgement on the merits of mirror/window material candidates, or their projected performance in an optical train.

Key words: Focal intensity; high-energy laser; irradiance mapping; mirror/window materials; on-target fluence; optical train; phase aberration; power optics; thermal lensing.

1. Introduction

High-energy laser (HEL) systems include an optical train consisting of mirrors and windows, which may compromise the system's operation because of unavoidable heating resulting from the absorption of some fraction of the incident laser-beam energy. Available experience [1][1] indicates that catastrophic failure modes associated with thermally induced stresses or temperature excursions are not a major threat. The performance of the optical train, as measured in terms of achievable target irradiances, first degrades on account of "thermal lensing," that is, the process of beam defocusing and beam distorting caused by thermally generated phase aberrations. Since HEL operation usually requires close-to-diffraction-limited characteristics at the far-field focus, this lensing phenomenon must be carefully assessed and evaluated in relation to specific features of the optical train. In this paper, we propose to conduct an analytical investigation of relevant processes and discuss how laser-driven mirror/window distortions may affect the performance of HEL systems with regard to both focal intensities and on-target fluences. Specifically, it will be our goal to derive an approximate expression for the far-field on-axis irradiance, patterned upon the model of Holmes and Avizonis [2], but simple enough to allow HEL system designers to assess the capability of a contemplated optical train, and to evaluate its behavior as a function of key system parameters such as beam-power level and laser run-time.

For this purpose, we have chosen to consider the system illustrated in figure 1, which should be representative of the type of optical trains encountered in HEL technology [3], and to formulate a treatment that is as general and relevant as possible. The laser device will be assumed to generate a collimated circular beam of diameter $\underline{d}$ and power P at the system's entrance aperture. This input gives rise to a near-field irradiance distribution I_{SI}, which can be fairly arbitrary, whereas the phase profile is postulated to be uniform. The beam is transported and processed by means of an optical train, which has all the elements one might normally encounter in an actual system, including the beam-focusing mechanism after expansion to diameter D. We note that, in this configuration, the output window represents the only transmissive component we will be concerned with. Furthermore, any propagation effect such as "thermal blooming" that may take place in the beam-relay tube, will be assumed to generate insignificant aberrations compared to mirror expansion and window distortion.

[1] Figures in brackets indicate the literature references at the end of this paper.

2. Some Key Equations

In the absence of birefringence, the far-field intensity derives from the Huygens-Fresnel integral [4] and amounts to

$$I_{GF} = (k/R_o)^2 \left| \int_0^{D/2} E(\rho) \exp\left[i\delta\phi(\rho,t) \right] \rho \, d\rho \right|^2 \qquad (1)$$

at the Gaussian focus.[2] The "phase-aberration function" $\delta\phi$ maps the cumulative aberrations impressed on the beam while propagating through the optical system and relates to the "wavefront-error function" Δ simply by means of the propagation constant, i.e., $\delta\phi = (2\pi/\lambda)\Delta$. The non-aberrated focal intensity, therefore, is

$$I_{GF}^{(o)} = (k/R_o)^2 \left[\int_0^{D/2} E(\rho) \, \rho \, d\rho \right]^2 , \qquad (2a)$$

which yields [5]:

$$I_{GF}^{(o)} = \kappa_o \frac{\pi (D/2)^2 P}{(\lambda R_o)^2} , \qquad (2b)$$

where κ_o represents a beam-profile factor ($\kappa_o \lesssim 1$) and accounts for the possibility that non-uniform beam intensities may cause some reduction in far-field irradiance, even in the absence of near-field phase distortions.

For weak distortions, we may proceed by expanding $\exp(i\delta\phi)$ to second order, in the manner originally suggested by Born and Wolf [4], which leads to a highly compact expression,

$$I_{GF} = I_{GF}^{(o)} \{ 1 - k^2 \, \text{var}[\Delta] \} , \qquad (3a)$$

if the variance is defined in accord with $\text{var}[\Delta] = \langle \Delta^2 \rangle - \langle \Delta \rangle^2$, the brackets symbolizing amplitude-weighted averages. We note that the reduction in far-field intensity exhibits a familiar "Strehl-ratio" appearance, which says that the performance of the optical train should remain nearly diffraction-limited as long as the variance of the wavefront error does not exceed $(\lambda/14)^2$. If the square root of the variance becomes larger than one tenth of a wave, Eq. (3a) may no longer be valid, the correlation length of the phase aberration then becoming an essential parameter [6]. For instance, in the case of random aberrations whose correlation length is much smaller than the limiting aperture diameter, it can be shown that the loss of intensity in the far field obeys a generalized Strehl relation such as

$$I_{GF} = I_{GF}^{(o)} \cdot \exp\{ -k^2 \, \text{var}[\Delta] \} . \qquad (3b)$$

In this context, Holmes and Avizonis [2] have demonstrated that the degradation factor $\exp\{-k^2 \, \text{var}[\Delta]\}$ provides a convenient tool for optical system analysis irrespective of the nature or origin of the phase aberrations, so long as the wavelength distortion does not exceed a certain threshold corresponding to, say, $\sqrt{\text{var}[\Delta]} = \lambda/5$. Throughout the rest of this paper, we will rely on eq. (3b) for approximating the loss in far-field on-axis brightness owing to the emergence of phase aberrations in the near field.

Some drastic simplifications are called for if the calculation is supposed to focus on those sources of optical distortion directly related to the HEL environment. First, it is postulated that, in a plane located at the entrance of the optical train and perpendicular to the beam axis, there are no phase aberrations. Second, we take it that beam-induced distortions are coherently additive, whereas all other sources of optical distortion are uncorrelated with themselves, with each other, or with thermal distortions [1]. Furthermore, it is assumed

[2] For a listing of the symbols, see table 1.

that uncorrelated path fluctuations, which normally originate from component imperfections, are Gaussian and random in amplitude, with zero mean. On this basis, the variance becomes simply

$$\text{var}\,[\Delta] = \Delta_{I,RMS}^2 + \text{var}\,[\Delta_T] \tag{4}$$

because uncorrelated random wavefront errors enter the far-field irradiance equation in the form of a sum of the squares of the rms contributions from each individual component:

$$\Delta_{I,RMS}^2 = \sum_{i=1}^{N} \sigma_{I,RM_i}^2 + \sigma_{I,PM}^2 + \sigma_{I,OW}^2 \quad . \tag{5}$$

Table 1. Glossary of symbols.

a:	truncation parameter	Y:	Young's modulus
C_p':	volume specific heat	z:	axial coordinate
d:	beam diameter	α:	expansion coefficient
D:	exit aperture diameter	β_S:	surface absorptance
E:	beam amplitude	β_V:	volume absorption coefficient
h:	heat-transfer coefficient	γ:	sensitivity parameter
I:	intensity/irradiance	$\delta\phi$:	phase aberration
I_{GF}:	irradiance at Gaussian focus	δn:	index inhomogeneity
I_{SI}:	intensity at system input	δT:	temperature increase
I_{SO}:	intensity at system output	Δ:	total wavefront error
k:	propagation constant	Δ_I:	wavefront error, imperfections
K:	thermal conductivity	Δ_T:	wavefront error, distortions
ℓ:	face-plate thickness	ε:	differential strain
L:	window thickness	θ_i:	angle of incidence
n:	index of refraction	κ:	beam-profile parameter
N:	number of relay mirrors	λ:	laser wavelength
Nu:	Nusselt number	ν:	Poisson's ratio
P:	beam power	$\pi_{\parallel,\perp}$:	stress-optics coefficients
r:	reduced radial coordinate	ρ:	radial coordinate
R_o:	focal length	σ_I:	rms wavefront error
R:	mirror reflectance	$\sigma_{\rho,\theta}$:	planar stress components
t:	dwell time	σ_z:	axial stress component
t_c:	critical time	τ_f:	figuring error
t_p:	pulse duration	ξ:	mirror distortion coefficient
W_{GF}:	fluence at Gaussian focus	χ:	window distortion coefficient

Similarly, wavefront errors originating from thermally induced distortions are made up of contributions from the relay mirrors,[3] the primary mirror, and the output window, but since the profile of the incident beam is not expected to change significantly, they are deterministic in nature and tend to contribute to the variance in accord with

[3]Note that N is defined here as the number of mirrors that handle the unexpanded beam, hence includes the secondary telescope mirror in addition to the relay mirrors (see fig. 1).

$$\text{var}\,[\Delta_T] = \text{var}\left[\sum_{i=1}^{N} \Delta_{T,RM_i} + \Delta_{T,PM} + \Delta_{T,OW}\right] \quad . \tag{6}$$

3. Laser-Driven Aberrations

In this section, two figures of merit are introduced for the purpose of characterizing the response of mirrors and windows in power optics, from the point of view of thermally induced wavefront errors.

3.1 Mirror Distortion

Currently contemplated power-optics mirror designs consist of a thin, highly reflecting face plate, which transfers the deposited radiation energy to a coolant fluid, through the rear surface, and is stiffly held to a stable, insulated back-up structure that minimizes mechanical (or thermo-mechanical) modes of deformation. The face plate is typically 1-mm thick and is subjected to a heat load owing to the small but unavoidable absorption of laser radiation at the mirror surface. Here, it will be assumed that the face plate reaches a steady-state temperature in a time frame very short compared to the laser-pulse duration.

If bowing and/or related deformations can be effectively suppressed, mirror-induced optical aberrations originate from displacements of the front surface, which are caused by thermal bulging of the face plate. The change in thickness is given by

$$\delta \ell = \int_0^{\ell} \varepsilon_z (z)\, dz \quad , \tag{7a}$$

where the differential strain $\varepsilon_z(z)$ must be evaluated in accord with Hooke's law, including thermal expansion, or

$$\varepsilon_z(z) = \alpha \delta T(z) + (1/Y)\,[\sigma_z - \nu\,(\sigma_\rho + \sigma_\theta)] \tag{8}$$

in the case of axisymmetric loadings. With commonly achieved heat-transfer coefficients, say 1 $W/(cm^2K)$, the face plate should be subjected to minimal axial stresses, which would indicate that, in a first-approximation, we have

$$\delta \ell = (1-R)(\ell^2/2K + \ell/h)\,[\alpha\,(1+\nu)\,\bar{I} - \alpha\nu\bar{I}] \tag{7b}$$

considering that the axial temperature distribution $\delta T(z)$ consists of two terms: (a) the linear temperature drop across the face plate, which reflects the thermal conductivity of the substrate, and (b) the temperature difference between the back and the coolant, which is controlled by the heat-transfer coefficient.

We now assume, with Sparks [7], that the support structure is capable of holding the face-plate rear surface in its original plane. Optical distortions, therefore, are caused by spatially dependent variations of $\delta \ell$, keeping in mind that a factor of two must be applied when evaluating optical path differences impressed upon reflection from a mirror face plate that experiences out-of-plane growth. Since angle-dependent terms always cancel, we conclude that the local wavefront error is best expressed as in (9a), or (9b),

$$\Delta_{T,RM} = -\frac{I_{SI}}{(FoM)_{RM}} \quad , \tag{9a}$$

$$\Delta_{T,PM} = - \frac{I_{SO}}{(FoM)_{PM}} \quad , \tag{9b}$$

the minus sign reminding us that mirror expansion tends to shorten the optical path length. Equation (9) introduces the concept of a figure of merit for cooled, high-average-power laser mirrors, i.e.,

$$FoM_M = \frac{K_{eff}}{(1- R)\ \ell^2 \xi} \quad , \tag{10}$$

where

$$K_{eff} = \frac{K}{1 + (2/Nu)} \tag{11}$$

represents the effective thermal conductivity of the cooled face-plate and, thus, characterizes the heat-removal process, whereas ξ refers to the mirror distortion coefficient, or modified expansion coefficient,

$$\xi = \alpha(1 + \nu) \quad . \tag{12}$$

We note that this figure of merit is in units of watts per square centimeter per centimeter, which points to a straightforward interpretation in the sense that $1/FoM_M$ measures the "optical growth" of the mirror surface per unit incident power density. In table 2, the reader will find a listing of relevant properties of key mirror-material candidates (SiC, Mo, and Cu) with figures of merit for reflectances of 99.8% and heat-transfer coefficients ranging from 0.1 to 10 W $cm^{-2}K^{-1}$.

Table 2. Figures of merit for key mirror-material candidates.

Item	Symbol (unit)	SiC	Mo	Cu
Expansion coefficient	α ($10^{-6}K^{-1}$)	3.5	5.0	16.7
Poisson's ratio	ν (1)	0.3	0.28	0.42
Thermal conductivity	K (W $cm^{-1}K^{-1}$)	4	1.34	3.99
IR reflectance	R (1)	0.998	0.998	0.998
Figure of merit* 1	FoM_M (W cm^{-3})	5.49×10^7	3.89×10^7	1.05×10^7
Figure of merit* 2	FoM_M (W cm^{-3})	4.88×10^9	2.84×10^9	9.37×10^8

*Assumes a 1-mm thick face plate and a heat-transfer coefficient of 0.1 W $cm^{-2}K^{-1}$ (case 1) or 10 W $cm^{-2}K^{-1}$ (case 2).

3.2 Window Distortion

Optical distortion experienced by laser beams in passing through a solid window results from the absorption of laser energy at both surfaces as well as within the pane itself. The phenomena involved are fairly complex and have been the subject of numerous investigations beginning in 1971 [8]; the reader may consult reference 9 for a comprehensive discussion. Specifically, if the windows are disk-shaped and subjected to axially symmetric loadings,

thermally induced optical path differences (OPD) for unpolarized light can be expressed in terms of an average OPD for radial and azimuthal polarizations, which yields:

$$OPD = L\ \{(n-1)[\alpha\delta T - (\nu/Y)(\sigma_\rho + \sigma_\theta)] + (\partial n/\partial T)\delta T - (n^3/4)[\pi_{\parallel} + \pi_{\perp})(\sigma_\rho + \sigma_\theta)]\} \cdot \quad (13)$$

Here, it is implicity assumed that (a) stress-birefringence plays a relatively minor role, (b) suitable window material exhibits isotropic features in the plane of the window, and (c) the stress distribution obeys classical thin-plate theory. In that case, and since wavefront distortions of interest only concern path-length changes stemming from non-uniform contributions, we may simply write:

$$\Delta_{T,W} = L\chi\delta T \quad , \quad (14)$$

where χ represents the window distortion coefficient, which includes not only the contribution arising from surface bulging through constrained expansion, but also the temperature-induced isotropic change in index of refraction, and the photo-elastic effect averaged over the two principal stress directions:

$$\chi = (n-1)\alpha(1+\nu) + (\partial n/\partial T)_{\sigma=0} + (n^3\alpha Y/4)(\pi_{\parallel} + \pi_{\perp}) \quad . \quad (15)$$

As mentioned earlier, birefringence effects are ignored in this model but we may emphasize that, from the point of view of degradation in light intensity at the Gaussian focus, highly promising window materials such as CaF_2 can be "configured" in a manner that eliminates stress-birefringence, independently of the polarization of the incident beam [10].

We now consider a pulsed mode of HEL operation for which time scales are such that lateral heat-conduction and surface-cooling effects can be ignored. In the case of output windows, this "short-time model" implies that local window temperatures image or map the beam fluence at the primary mirror, i.e.,

$$\delta T = \frac{(2\beta_S/L + \beta_V)\ I_{SO} \cdot t}{C'_p} \quad , \quad (16)$$

which takes into account both surface and bulk absorption processes. In essence, this implies that the window generates a local wavefront deformation equal to

$$\Delta_{T,W} = \frac{I_{SO} \cdot t}{FoM_W} \quad , \quad (17)$$

where the figure of merit FoM_W regroups all window-related features that affect thermal lensing:

$$FoM_W = \frac{C'_p}{(2\beta_S + \beta_V L)\chi} \quad . \quad (18)$$

Conceptually, this figure of merit characterizes the susceptibility to thermal distortion in the same manner as the mirror FoM but relates the optical path change to a unit amount of incident fluence instead of intensity. In table 3, the figure of merit of key window-material candidates (CaF_2, KCl, and ZnSe) is listed in conjunction with relevant material properties. Calcium fluoride appears to be, by far, the most promising candidate on the basis of this figure-of-merit assessment, which disregards the potential impact of other system components on the overall aberration picture (see sec. 4).

Table 3. Figure of merit for key window-material candidates.

Item	Symbol (unit)	CaF_2*	KCl**	ZnSe†
Fracture strength	σ_f (kpsi)	12.5	4.5	7.5
Heat capacity	C'_p (J $cm^{-3}K^{-1}$)	2.72	1.35	1.80
Distortion coefficient	χ ($10^{-6}K^{-1}$)	1	-8.5	73
Bulk absorption	β_V(10^{-3} cm^{-1})	0.05	0.5	0.5
Coating absorptance	β_S (10^{-3})	0.15	0.5	1.0
Figure of merit	FoM_W (J cm^{-3})	77.7×10^9	-1.05×10^8	9.86×10^6

* For <111>-oriented, 1-cm thick windows operating at 3.8 μm (DF laser).
** For <111>-oriented, 1-cm thick windows operating at 10.6 μm (CO_2 laser).
† For chemically vapor-deposited, 1-cm thick windows operating at 10.6 μm.

4. Irradiance on Target

According to the model in section 2, the focal irradiance can be approximated as follows:

$$I_{GF} = I_{GF}^{(o)} \cdot \exp\ \{-k^2 \Delta_{I,RMS}^2 - k^2\ \mathrm{var}\ [\Delta_T]\} \qquad (19)$$

if the wavefront error resulting from thermal lensing of imperfect components is handled as in eq. (4). Since the departure from an ideal optical finish is usually specified in terms of rms figuring errors τ_f measured in "waves," and since the window can exhibit spatially dependent index inhomogeneities, we may rewrite eq. (5) in a more explicit manner, or

$$\Delta_{I,RMS}^2 = 4\tau_{f,RM}^2 \sum_{i=1}^{N} 1/\cos^2(\theta_1) + 4\tau_{f,PM}^2 + 2(n-1)^2 \tau_{f,OW}^2 + L^2 \delta n_{RMS}^2 \ . \qquad (20)$$

According to Bennett [1], optical figures of 1/4 wave in the visible can be attained with large-diameter windows, while 1/8-wave surface figures are readily achievable for metallic reflectors; it is thus a straightforward task to verify that, in the absence of thermally induced aberrations, HEL optical trains as described in reference 3 easily meet the requirements of the Maréchal criterion at 10.6 μm.

Returning now to our previous discussion of thermal distortion effects, and making use of the results expressed in eqs. (6, 9, 17), the variance of the beam-induced wavefront error becomes

$$\mathrm{var}\ [\Delta_T] = \mathrm{var} \left[\frac{I_{SO}\, t}{FoM_W} - \frac{NI_{SI} + I_{SO}}{FoM_M} \right] \ , \qquad (21a)$$

where I_{SI} and I_{SO} refer to the beam intensity and its spatial distribution before and after expansion. Since the near-field irradiance distribution is expected to preserve its original profile, and keeping in mind that the variance must be evaluated over the exit-aperture area, we have:

$$\text{var}\,[\Delta_T] = \left[\frac{t}{\text{FoM}_W} - \frac{N(D/d)^2+1}{\text{FoM}_M}\right]^2 \cdot \text{var}\,[I_{SO}] \quad . \tag{21b}$$

At this point, if use is made of a beam-profile factor κ_1 for expressing the variance in terms of the average beam-power density, eq. (21b) can be thrown into a more convenient form,

$$\text{var}\,[\Delta_T] = \frac{\kappa_1^2 P^2}{\pi^2}\left[\frac{t}{(D/2)^2\,\text{FoM}_W} - \frac{N}{(d/2)^2\,\text{FoM}_M}\right]^2 \quad , \tag{21c}$$

because the primary mirror contribution should be negligible. Three comments are in order:

1) Computer modeling indicates that, for realistic laser beams, the profile factor κ_1 will be close to 0.5, even in dealing with the "sugar scoops" of gas-dynamic lasers (GDL) [11]; in this connection, we emphasize that radial heat flow tends to flatten the temperature distribution and wash out the ripples, which means that thermal diffusion always improves (reduces)the profile factor.

2) The bracket in eq. (21c) regroups the system parameters in two terms: a window term, which is time dependent, and a mirror term that sums the wavefront error arising prior to beam expansion; if the figures of merit are both positive, there will be some partial (or total) cancellation depending upon the pulse history, which may result in a dramatic reduction of the net wavefront error originating from thermal lensing of optical system components.

3) Thermally induced wavefront errors, $\sqrt{\text{var}\,[\Delta_T]}$, are power dependent and increase linearly with P; in terms of the far-field performance, this implies that, inevitably, there will be a point of diminishing returns in pushing the laser output beyond some sensible limit.

For ease of manipulation, we now define two "sensitivity parameters," first

$$\gamma_M = \frac{N}{(d/2)^2 \text{FoM}_M} \quad , \tag{22a}$$

which characterizes the impact of N relay mirrors, and

$$\gamma_W = \frac{1}{(D/2)^2 \text{FoM}_W} \quad , \tag{22b}$$

which refers to the output window. The light intensity at the Gaussian focus can thus be expressed in an explicit but still manageable manner:

$$I_{GF} = \kappa_o \frac{\pi(D/2)^2 P}{(\lambda R_o)^2} \cdot \exp[-(2\pi/\lambda)^2 \Delta_{I,RMS}^2] \cdot \exp[-(2\kappa_1)^2 (P/\lambda)^2 (\gamma_W t - \gamma_M)^2] \quad , \tag{23}$$

which clearly shows how beam characteristics and system parameters combine to control the irradiance on target. Upon examining eq. (23), it is immediately seen that, if the window possesses a positive distortion coefficient, there exists a time t_c, which may occur during the pulse, when window lensing exactly cancels the steady-state mirror distortion and, thus, suppresses all thermally induced aberrations; this critical time t_c is given by the ratio γ_M/γ_W, or

$$t_c = N(D/d)^2 \text{FoM}_W/\text{FoM}_M \quad , \tag{24}$$

and involves the number of relay mirrors, the magnification factor, and most importantly, the ratio of the two figures of merit.

We now apply this formalism to the model system specified in reference 3 (d = 6 cm, D = 36 cm, λ = 10.6 μm) on assuming cooled molybdenum mirrors with FoM's as in table 2, and a CVD-ZnSe output window as described in table 3. Figure 2 depicts how the focal intensity, at a distance of 1 km, varies as a function of exposure time, for laser beams that range in power from 1 MW up to a maximum tolerable level of 8 MW. The sequence demonstrates that, indeed, ZnSe windows can have a highly beneficial effect on the performance of HEL systems operating in a long-pulse regime; the critical time t_c occurs at 0.73 sec into the pulse, as signaled by a turnover point, which emphasizes the enhancement of the far-field on-axis intensity throughout the early part of the pulse, at power levels for which mirror distortion becomes a significant factor.

5. Fluence on Target

Some applications of HEL systems require an evaluation of the energy fluence deposited on target in a single pulse of duration t_p:

$$W_{GF} = I_{GF}^{(o)} \exp\left[-(2\pi/\lambda)^2 \Delta_{I,RMS}^2\right] \cdot \int_o^{t_p} \exp[-(2\kappa_1)^2 (P/\lambda)^2 (\gamma_W t - \gamma_M)^2]\,dt \ . \qquad (25a)$$

The integration is fairly straightforward and yields

$$\int_o^{t_p} \exp[\,\cdot\,]\,dt = \frac{\sqrt{\pi}\,(\lambda/P)}{4\,\kappa_1\,\gamma_W} \left\{ \mathrm{erf}[2\kappa_1 (P/\lambda)\,\gamma_M] + \mathrm{erf}[2\kappa_1 (P/\lambda)(\gamma_W t_P - \gamma_M)] \right\} , \qquad (26)$$

which leads to

$$W_{GF} \simeq 0.8 \ \frac{\pi^{3/2} (D/2)^4 \mathrm{FoM}_W}{2\lambda R_o^2} \left\{ \mathrm{erf}\,[(P/\lambda)\gamma_M] + \mathrm{erf}[(P/\lambda)(\gamma_W t_P - \gamma_M)] \right\} \qquad (25b)$$

for a system that verifies the Maréchal criterion in the absence of power-driven aberrations and exhibits beam-intensity profiles typical of GDL's. Note that the fluence increases very rapidly (fourth power!) with the size of the output-aperture and depends explicitly on the figure of merit of the window, independently of the bracketed expression, which cannot exceed a maximum value of two.

In discussing eq. (25b), we may consider three distinct possibilities, on assuming positive mirror/window sensitivity parameters:

1) Short-duration pulses ($t_p < \gamma_M / \gamma_W$). It is seen in figure 3, which applies to our model system (sec. 4), that the fluence initially increases linearly with beam power, goes through an optimum power regime in the 4 to 6 MW range, then falls off as partly compensated mirror aberrations become quite large and dominate the far-field intensity pattern.

2) Critical-duration pulse ($t_p = \gamma_M / \gamma_W$). The bracket in eq. (25b) reduces to the first error-function term, thus indicating that the fluence grows steadily with beam power as window aberrations now provide adequate compensation to preserve the quality of the beam.

3) Long-duration pulses ($t_p > \gamma_M / \gamma_W$). As depicted in figure 3 for pulses of 1 and 2 sec, the situation shows strong evidence of saturation in terms of both input power and pulse length. In effect, the fluence on target tends to reach a plateau of

$$W_{GF}^{(max)} = \frac{\kappa_o}{\kappa_1} \cdot \frac{\pi^{3/2}(D/2)^4 FoM_W}{2\lambda R_o^2} \cdot \exp[-(2\pi/\lambda)^2 \Delta_{I,RMS}^2] \quad , \tag{27}$$

which is independent of the near-field power level but depends on the beam profile in accord with

$$\frac{\kappa_o}{\kappa_1} = \frac{(1-e^{-a})^2}{a^2 \sqrt{\text{var } [\exp(-2ar^2)]}} \tag{28}$$

in the case of truncated Gaussians. Within a factor of two, this is precisely the result of Klein and Pappis [12] for the energy-deposition capability of HEL output windows, as obtained in the context of a single-component type investigation; this factor thus measures the "gain" that can be achieved with an optical train that affords compensation, as can be easily verified by setting $\gamma_M = 0$ in eq. (25b).

Finally, and for the sake of comparison, we may consider the hypothetical case of an optical train whose components are invulnerable to laser-driven aberrations; the fluence on target then is simply

$$W'_{GF} \simeq 0.8 \frac{\pi(D/2)^2 P}{(\lambda R_o)^2} \cdot t_p \tag{29}$$

and increases linearly with beam power and pulse duration, as predicted by elementary diffraction theory (see fig. 3). More relevant is the case of no window-induced aberrations, for which we have

$$W''_{GF} \simeq 0.8 \frac{\pi(D/2)^2 P}{(\lambda R_o)^2} \cdot t_p \exp [-(P/\lambda)^2 \gamma_M^2] \quad , \tag{30}$$

the exponential term reflecting the impact of mirror expansion. The on-target fluence always peaks at the power level that optimizes the far-field brightness (see sec. 4) and shows strong non-linear features beyond that point; this is depicted in figure 3 for short-duration pulses and demonstrates that the presence of the selenide window leads to a substantial enhancement of the energy-delivery capability of our model system.

6. Conclusions

- Equation (23) expresses the focal intensity of thermally aberrated HEL beams in a simple manner, which clearly shows how beam characteristics and system parameters combine to control the irradiance on target. In this context, an important result emerges: If the window has a positive distortion coefficient, window lensing suppresses the steady-state mirror distortion at a time t_c given by $t_c = N(D/d)^2 FoM_W/FoM_M$, where N counts the number of relay mirrors, D/d is the telescope magnification, and the figures of merit are as defined in section 3.

- At all other times, the behavior can be strongly non-linear, depending on the beam-profile factor, but ultimately window distortion dominates and renders the beam unfocusable. In terms of energy fluences deposited on target, this leads to radically differing beam-power dependence patterns for "short" pulses compared to "long" pulses; the presence of a positively lensing window, however, always results in a substantial enhancement of the energy-delivery capability of HEL systems.

• In applying these considerations to a model system representative of the type of optical trains used for projecting HEL beams at a distant target, we find that CVD-ZnSe windows can have a highly beneficial impact on the far-field performance of systems operating in a "long-pulse" mode. In the absence of a material window, laser-driven mirror aberrations always degrade the focusing ability of the optical train, which results in on-target irradiance levels much below those achievable if there is a selenide window at the exit aperture.

References

[1] Bennett, H. E., in Laser-Induced Damage in Optical Materials: 1976 (NBS special publication 462, Washington, 1976), p. 11.

[2] Holmes, D.A., and Avizonis, P.V., Applied Optics 15, 1075 (1976).

[3] Accetta, J. S., and Shea, R.F., Proc. SPIE 121, 132 (1977).

[4] Born, M., and Wolf, E., Principles of Optics (Pergamon Press, New York, 1975), Chap. 5.

[5] Klein, C. A., in Proc. First Int. Conf. Lasers (STS Press, McLean/Virginia, 1978), p. 283.

[6] Hogge, C., Butts, R., and Burlakoff, M., Applied Optics 13, 1065 (1974).

[7] Sparks, M., in Proc. High Power Laser Optical Components and Component Materials Meeting (DARPA, Washington, 1977), p. 66.

[8] Sparks, M., J. Applied Physics 42, 5029 (1971).

[9] Klein, C. A., Infrared Physics 17, 343 (1977).

[10] Klein, C. A., Applied Phys. Letters 35, 52 (1979).

[11] Petri, F., Levine, A., and Burns, J., in Proc. Fifth Conf. Infrared Laser Window Materials (AFML, Dayton/Ohio, 1975), p. 488.

[12] Klein, C., and Pappis, J.,in Proc. Infrared Laser Window Materials Meeting (DARPA, Washington, 1976), p. 39.

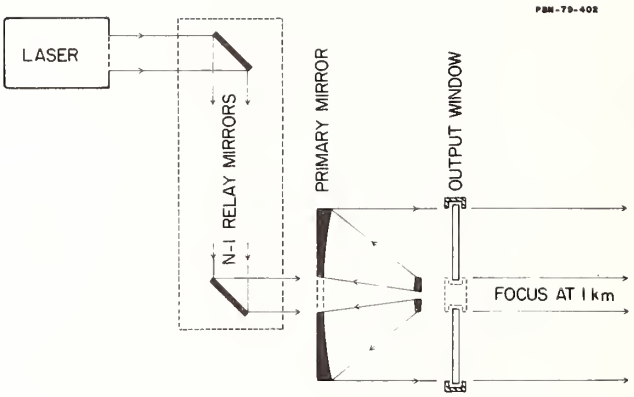

Figure 1. Schematics of a high-energy laser optical train.

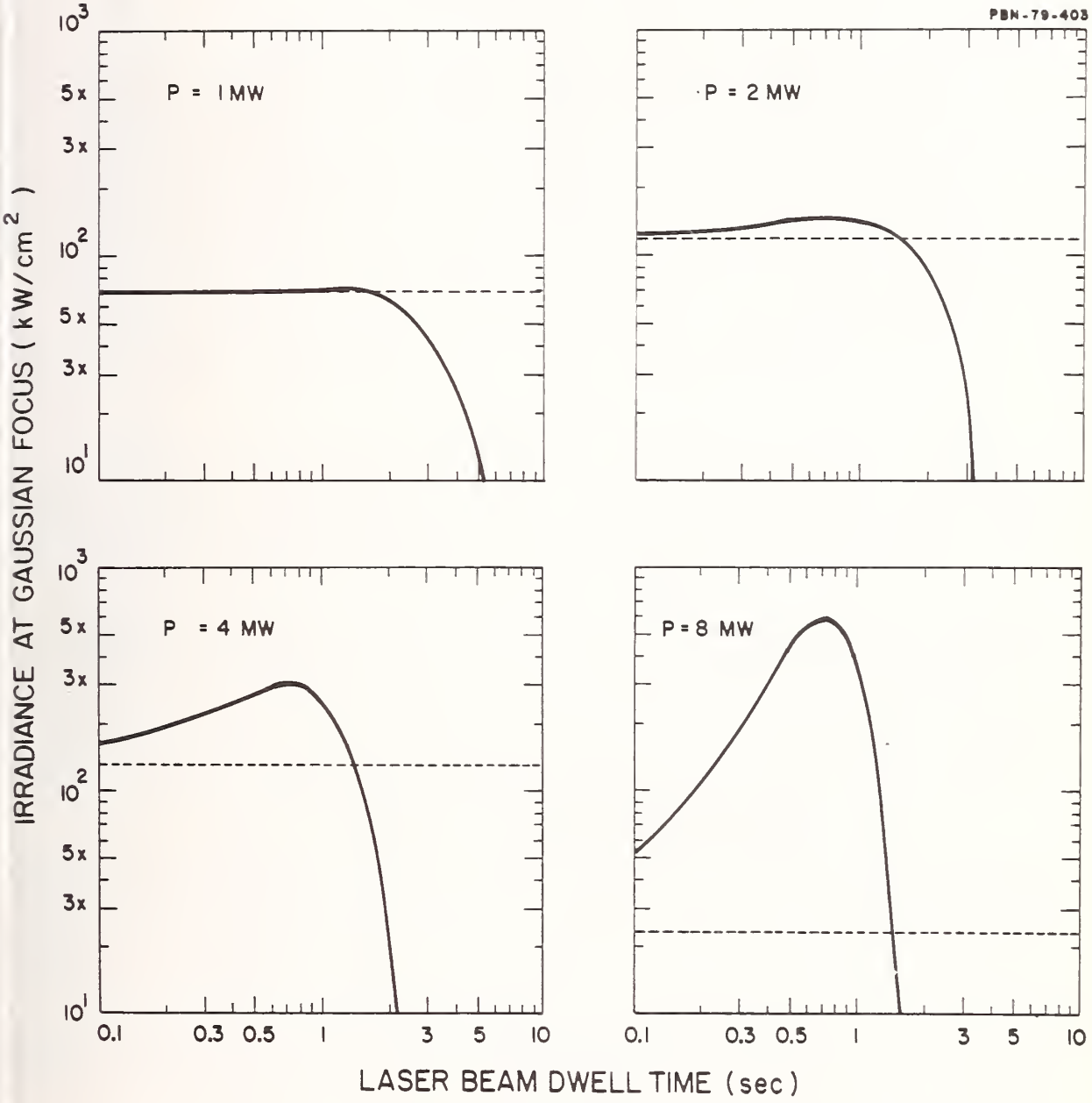

Figure 2. Time dependence of the light intensity at the Gaussian focus of the model system described in section 4. The solid curves assume the presence of a CVD-ZnSe window at the system's exit aperture. The broken lines refer to the predicted steady-state irradiance if there are no thermally induced window aberrations.

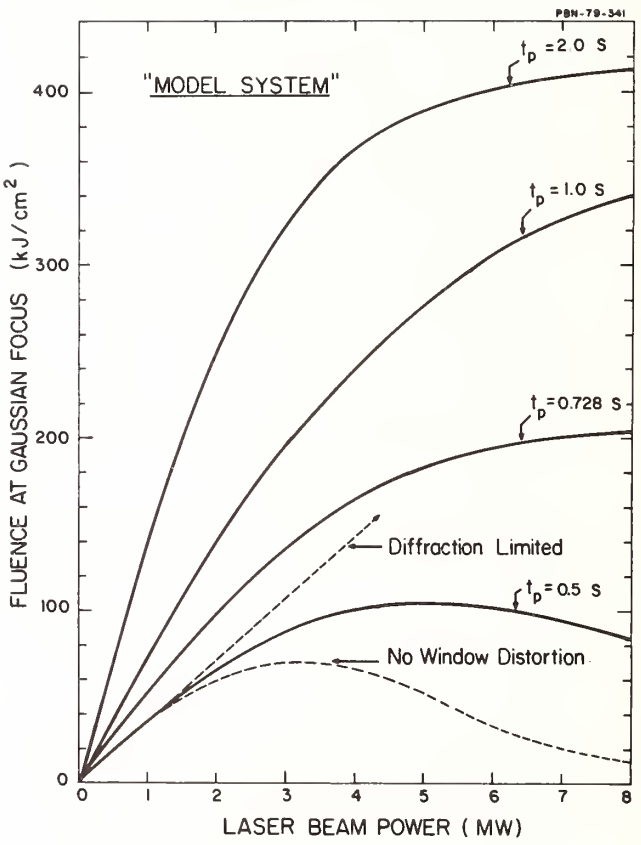

Figure 3. Beam-power dependence of the energy fluence at the Gaussian focus of the model system described in section 4. Laser pulse durations range from 0.5 to 2 sec.

ANALYSIS OF AN IMPERFECTLY COATED CONICAL ELEMENT FOR HIGH ENERGY LASER RESONATORS

W. P. Latham, Jr.
Air Force Weapons Laboratory
Kirtland AFB, NM 87117

The scalar field approximation is normally used in the analysis of eigenmodes and eigenvalues for high energy laser resonators. Recently, Dr. D. Fink demonstrated the need to account for the vector nature of the electromagnetic field when conical elements are used in resonators. Dr. G. C. Dente at the AFWL has developed a theory for the analysis of such polarization effects. When polarization effects are included, an unacceptable mode has been shown to exist in a conical-element, annular-gain laser which is currently being studied at the AFWL. A special optical coating placed on a conical resonator mirror would make the resonator mode acceptable by introducing a 90° phase shift between polarization states which are parallel and perpendicular to the plane of incidence upon reflection at a 45° angle of incidence. The study presented here gives the analysis for a related resonator within Dente's theory. The results indicate the tolerance limits of such a coating for a conical element in a high energy device.

Key words: Coatings design; polarization effects; resonator analysis.

1. Introduction

The solutions for unstable resonator modes are traditionally determined using the Fox and Li [1][1] iterative approach after assuming a linearly polarized scalar field. For simple unstable resonators, this approximation is valid because the polarization state is unchanged on a round trip through the resonator. That is, the linear polarization state is an eigen-polarization state for a simple unstable resonator, so that scalar field theory is valid.

Fink [2] initially showed that for some conical elements, the linear polarization state is changed on a round trip through the element. One such conical element, which scrambles a linear polarization state, is the retroreflecting cone. The eigen-polarizations of a cone are radial and azimuthal polarization but not linear polarization. However, a cone would preserve a linear polarization state upon reflection, if it were coated with a 90° phase shift coating. If the coating introduces a 90° phase shift between the radial and azimuthal components, there is a 180° phase shift for a round trip through the cone, and it acts like a plane mirror. That is, for a perfect 90° phase shift, the cone no longer effects the polarization state of the field, and the traditional scalar field approach can be used.

The polarization effect introduced by conical elements is an important effect in the annular gain high energy laser resonators currently being studied at the Air Force Weapons Laboratory (AFWL). The half-symmetric unstable resonator (HSUR) with a coated rear cone is a simple example of an unstable resonator with a conical element. In the HSUR, the polarization effect is removed by a perfect 90° phase shift. However, for an imperfectly coated cone, the polarization effect must be included by using both components of the electromagnetic field.

The need to correct the polarization effect defines the requirements on a new high energy laser material. A broad wavelength band 90° phase shift coating which can withstand high intensities and can be uniformly deposited on a conical mirror is required.

Recently, the general theory of resonators with polarizing elements has been presented by Dente [3]. The purpose of this paper is to demonstrate that the general form of the eigen-equations for a HSUR can be solved using standard resonator techniques. Furthermore, the polarization effects due to variations in the phase shift introduced by imperfectly

[1] Figures in brackets indicate the literature references at the end of this paper.

coating a conical element within the HSUR are presented. The imperfect coating analysis for the HSUR with rear cone defines the tolerance requirements on the coating. Coating designs have been developed by Southwell [4] and Scott [5], and these are discussed.

2. Resonator Analysis of a Half-Symmetric Unstable Resonator with a Coated Rear Cone.

The general theory for resonators with elements that mix Fourier components of the field through polarization effects was presented by Dr. G. C. Dente [3]. For the HSUR, only the mixing of the ℓ=0 and ℓ=2 states is considered, that is in Dente's notation L=1. For L=1, the x- and y-components of the field are

$$E_x = f_1(r)e^{i\phi}\cos\phi + g_1(r)e^{i\phi}\sin\phi \quad , \tag{1}$$

and

$$E_y = f_1(r)e^{i\phi}\sin\phi - g_1(r)e^{i\phi}\cos\phi \quad . \tag{2}$$

The general form is obtained by using the sum and difference functions S_1 and D_1, which are

$$S_1(r) = f_1(r) + ig_1(r) \quad , \tag{3}$$

and

$$D_1(r) = f_1(r) - ig_1(r) \quad . \tag{4}$$

Substituting eqs (3) and (4) into eqs (1) and (2) gives

$$E_x = \frac{1}{2}\left[S_1(r) + e^{i2\phi}D_1(r)\right] \quad , \tag{5}$$

and

$$E_y = \frac{1}{2}\left[S_1(r) - e^{i2\phi}D_1(r)\right] \quad . \tag{6}$$

Note that the form of the field is a linear superposition of an ℓ=0 and ℓ=2 Fourier component. For a simple unstable resonator, each Fourier component is a mode of the aligned resonator. Thus Fourier components are sometimes called ℓ modes. The resonator mode for the case studied here is a superposition of two simple resonator ℓ modes.

For a half-symmetric unstable resonator with a coated rear cone, the eigen-equations are given in matrix form by

$$\lambda \begin{pmatrix} D_1 \\ S_1 \end{pmatrix} = \begin{pmatrix} K_2 & 0 \\ 0 & K_0 \end{pmatrix} \begin{pmatrix} \frac{1-R}{2} & \frac{1+R}{2} \\ \frac{1+R}{2} & \frac{1-R}{2} \end{pmatrix} \begin{pmatrix} D_1 \\ S_1 \end{pmatrix} , \tag{7}$$

where R is the negative of the ratio of the radial and azimuthal reflectivities. For this case, K_0 and K_2 are the ℓ=0 and ℓ=2 round trip propagators. The reference plane for a round trip is taken to be the plane of the rear cone. A round trip is defined by the propagation from the rear plane to the feedback mirror, the application of the feedback mirror phase sheet, and the propagation from the feedback mirror to the rear plane. Note that eq (7) can be generalized to a more complicated resonator by including more matrices to describe the resonator and more ℓ components for the field.

The complex reflectivity ratio, R, in eq. (7) determines the strength of the mixing due to the polarization effect. The 90° phase shift case, which corresponds to the plane mirror, is given by R = -1. For R = -1, the top half and bottom half of the matrix equation in eq. (7) decouple, so that there are two independent equations for S_1 and D_1. That is, there is no mixing. The uncoated rear cone is given by R=1. In this case, the two equations for S_1 and D_1 can be solved by substituting one equation into the other. The result is a

quadratic eigen-equation involving λ^2 and two propagation operators. For complex values of R between +1 and -1, the rear element corresponds to an imperfectly coated rear cone. That is, the rear element is not a plane mirror nor is it an uncoated cone.

The eigen-equations in eq (7) were solved using the power method [1]. For the perfectly coated rear cone (R = -1), the eigenvalues for a normal half-symmetric resonator agree to three places with eigenvalues published in the literature [6].

After the solution has converged, the rear cone polarization operator was applied, and the power in the S_1 and D_1 terms was determined by

$$P_{S_1} = 2\pi \int_0^b dr\, r\, |S_1(r)|^2 \quad , \tag{8}$$

where b is the radius of the integration region at the rear plane. The radius b is set to be sufficiently larger than the geometric beam size to include all of the diffracted light. The power expression for D_1 is identical to eq (8) with S_1 replaced by D_1. The power integrals were calculated using a simple numerical integration technique. Results of the power method calculations for two equivalent Fresnel number resonators for various phase shifts and wavelengths are presented in the next section.

3. Results and Discussion

The results of power method calculations for two equivalent Fresnel numbers for various phase shifts are listed in Table I. Since D_1 is the ℓ=2 mode, the right-hand column gives the percentage of power in the ℓ=2 mode. The rest of the power is in the ℓ=0 mode for this simple case. Table I indicates that the percentage power in the ℓ=2 mode scales with the equivalent Fresnel number. The percentage power in D_1 for the Neq=8.5 case is about twice the percentage power in D_1 for the Neq=4.25 case for all values of phase shift.

The results of the power method calculation for two phase shifts for various wavelengths are listed in Table II. As the wavelength is varied without changing the other parameters of the resonator, the equivalent Fresnel number varies. For a wavelength of 3.6μm, the equivalent Fresnel number of the resonator is nearly Neq ≃ 9.0, and the power method does not converge.

Table II indicates that, if the coating can be applied to the rear cone within a ±5° tolerance of 90°, the mode of the resonator will be very nearly an ℓ=0 mode. However, the existing coating design [4] is within this tolerance between wavelengths 3.6μm to 4.0μm only. If there is appreciable power for smaller or larger wavelengths, there can still be a substantial percentage of the power in the ℓ=2 mode.

Southwell [4] initially showed that a 90° phase shift coating could be designed for a single wavelength by using quarterwave pairs of high and low refractive index thin films. Scott [5] and Southwell [7] have refined the design using 20-layer ZnS and ThF_4 dielectric stacks to obtain a near 90° phase shift over a broad wavelength band. For these designs, the variation in phase shift about 90° is less than ±3°. Thus, the proposed design satisfies the requirement of ±5° about 90° phase shift which was determined by the resonator analysis. However, there may still be deposition and damage problems with the proposed coating design. Currently, AFWL is studying the problems of layer thickness deposition on conical elements and multilayer dielectric stack damage.

Table I. Percentage power in D_1 vs. rear cone phase shift.

	Phase Shift (degrees)	Eigenvalue Magnitude	Eigenvalue Phase (degrees)	Percent Power in D_1
Neq = 4.25				
	90	0.6484	8.67	0.0
	88.75	0.6480	7.41	0.137
	87.5	0.6471	6.10	0.545
	86.25	0.6455	4.77	1.215
	85	0.6432	3.41	2.136
	83.75	0.6403	2.00	3.278
	82.5	0.6367	0.56	4.629
Neq = 8.5				
	90	0.6224	-0.40	0.0
	88.75	0.6221	-1.67	0.255
	87.5	0.6212	-2.99	1.015
	86.25	0.6198	-4.35	2.258
	85	0.6178	-5.75	3.957
	83.75	0.6153	-7.20	6.061
	82.5	0.6123	-8.70	8.527

Table II. Percentage power in D_1 vs. wavelength.

	Wavelength (μm)	Neq	Eigenvalue Magnitude	Eigenvalue Phase (degrees)	Percent Power in D_1
$\Delta\phi$= 90°					
	3.55	9.099	0.5970	14.72	0.0
	3.7	8.730	0.6099	-7.70	0.0
	3.8	8.500	0.6224	-0.40	0.0
	3.9	8.282	0.6210	6.76	0.0
	4.0	8.075	0.5964	15.44	0.0
	4.1	7.878	0.5900	-14.47	0.0
$\Delta\phi$= 85°					
	3.55	9.099	0.5928	9.37	4.242
	3.7	8.730	0.6044	-13.17	4.933
	3.8	8.500	0.6178	-5.75	3.957
	3.9	8.282	0.6166	1.47	3.353
	4.0	8.075	0.5915	10.17	3.709
	4.1	7.878	0.5839	-20.02	6.554

References

[1] Fox, A.G., and Li, T., Resonator modes in a maser interferometer, Bell Syst Tech J. 40, 453 (1961).

[2] Fink, D., Polarization effects in axicons, Applied Optics 18, 581 (1979).

[3] Dente, G.C., Polarization effects in resonators, Applied Optics 18, 2911 (1979).

[4] Southwell, W.H., Multilayer coatings producing 90° phase change, Applied Optics 18, 1875 (1975).

[5] Scott, M.L., Analysis of LS-14 phase coatings, Sixth Annual Tri-Service Chemical Laser Symposium, KAFB, 28-30 Aug 79, p. TH3-3.

[6] Butts, R.R., and Avizonis, P.V., Asymptotic analysis of unstable laser resonators with circular mirrors, JOSA 68, 1072 (1978).

[7] Southwell, W.H., Multilayer coating design achieving broad band 90° phase shift, Applied Optics, to be published.

NONLINEAR ABSORPTION IN DIRECT-GAP CRYSTALS

A. Vaidyanathan*, T. W. Walker and A. H. Guenther
Air Force Weapons Laboratory
Kirtland AFB, NM 87117

and

S. S. Mitra
Department of Electrical Engineering
University of Rhode Island
Kingston, RI 02881

and

L. M. Narducci
Physics Department
Drexel University
Philadelphia, PA 19104

A critical review of the Keldysh, Braunstein and Basov formulations of the nonlinear absorption process in direct-gap crystalline solids is presented. The two-photon absorption coefficients in several alkali halides and semiconductors are calculated by means of the above three models and compared with available experimental data. It is concluded that the Keldysh formula offers a sufficiently accurate description of the multiphoton absorption process, even when the photon multiplicity is small. This is in contrast to the frequently expressed view that the Keldysh formula is incorrect for small photon multiplicities. It is found that the Keldysh formula is closely related to Braunstein's formula for allowed-allowed transitions, while Basov's formula corresponds to the allowed-forbidden case. It is also shown that the predictive accuracy of the Braunstein formulas can be increased by the use of nonparabolic energy bands and excitonic intermediate states. Finally, the Basov formula, which until now was considered to be the most accurate description of the two-photon absorption process, is shown to contain several errors.

Key words: Multiphoton absorption; nonlinear absorption; two-photon absorption coefficients.

1. Introduction

Nonlinear absorption in crystalline solids has been a subject of great interest during the past fifteen years [1]. This interest has been stimulated in part by the role of nonlinear absorption in laser-induced damage of optical components, as well as by its many fundamental applications in solid state physics. In spite of an abundance of published literature, quantitative understanding of nonlinear absorption is far from satisfactory. Specifically, the two-photon absorption coefficients predicted by different theoretical methods differ from each other and from the experimental data by as much as three orders of magnitude [2]. Furthermore, there are important discrepancies regrading the multiphoton formulas due to Keldysh [3] and Basov[4]. In this contribution we attempt to resolve some of these controversies and propose two modifications to the Braunstein model which bring its predictions closer to the experimental data.

*This work was supported in part by an AFSC/NRC Postdoctoral Resident Research Associateship.

2. Comparison of the Keldysh , Braunstein and Basov models

The general theory of multiphoton absorption in atoms was outlined by M. Goppert-Mayer [5] in the early days of quantum mechanics. When this early theory is applied to the electronic transitions from the valence band v to the conduction band c of a direct-gap crystalline solid by the simultaneous absorption of two photons of frequency ω, one obtains the following expression for the transition rate per unit volume:

$$W = \frac{2\pi}{\hbar} \int d^3 \vec{k} \sum_n \left| \frac{H_{vn} H_{nc}}{E_{vn}(\vec{k}) - \hbar\omega} \right|^2 \delta(E_{vc}(\vec{k}) - 2\hbar\omega) . \qquad (1)$$

In eq. (1) H_{ij}'s are the interaction Hamiltonian matrix elements between bands i and j, whose energy separation at wavelength $\vec{k}$ is E_{ij}, the $\vec{k}$ integral extends over the entire first Brillouin zone , the index n extends over all possible intermediate states, and the delta function expresses the energy conservation requirement.

Braunstein and Ockman [6] simplified eq. (1) by assuming that there was only one intermediate state, which was above the final conduction band, and that all the three energy bands were parabolic and isotropic (see fig. 1). Depending on the symmetries of the bands, three types of two-photon transitions were possible: allowed-allowed (a-a), allowed-forbidden (a-f) and forbidden-forbidden (f-f). Basov et al. [4] simplified eq. (1) by assuming that the intermediate states were in the initial valence and final conduction bands themselves. They also assumed the energy bands to be isotropic and quadratic functions of k and they included the two highest valance bands in their calculation. Keldysh [3] approached the problem of multiphoton transitions differently. He assumed the electronic wave functions in the presence of the strong radiation to be described not by the ordinary Bloch functions, but by the Houston functions of the form given below:

$$\Psi_{\vec{p}}(\vec{r}, t) = U_{\vec{p}}(\vec{r}) \exp\left\{\frac{i}{\hbar}\left[\vec{p}(t)\cdot\vec{r} - \int_0^t E\left(\vec{p}(\tau)\right) d\tau\right]\right\}. \qquad (2)$$

In eq. (2) E and $\vec{p}$ are the electronic energy and momentum respectively, while U is the periodic part of its wave function Ψ. The electronic momentum in the presence of the electromagnetic radiation is given by

$$\vec{p}(t) = \vec{p} - e\vec{A}_o \sin\omega t/\omega . \qquad (3)$$

As a result of this, Keldysh's final result contained multiphoton transitions of all order, even though he used only first order perturbation theory to evaluate the transition probabilities. It is also worth pointing out that Keldysh assumed a nonparabolic dependence of the energy bands on the wave vector:

$$E_{vc}(\vec{k}) = E_g\left(1 + \frac{\hbar^2 k^2}{m^*_{vc} E_g}\right)^{1/2} . \qquad (4)$$

In eq. (4) E_{vc} is the energy separation between bands v and c whose reduced effective mass is m^*_{vc} and minimum energy gap is E_g. All of the above three models assumed the interaction Hamiltonian to be of the form $H = \frac{e}{mc}\vec{A}\cdot\vec{p}$, where $\vec{A}$ is the vector potential.

The two-photon absorption coefficient β is obtained from the two-photon transition rate per unit volume W with the aid of the equation

$$\beta = 4\,\hbar\omega W/I^2 \,; \tag{5}$$

We list below the final formulas for the two-photon absorption coefficients obtained within the context of the Braunstein, Basov and Keldysh models

$$\beta_{Br}^{a-a} = \frac{2^{5/2}\,\pi e^4 \left(m^*_{vc}\right)^{3/2} \Delta E \left(\Delta E - E_g\right) f_{vn} f_{nc} \left(2\hbar\omega - E_g\right)^{1/2}}{\varepsilon_\infty c^2 m^2 (\hbar\omega)^3 \left[\Delta E - \hbar\omega + \frac{m^*_{vc}}{m^*_{vn}}\left(2\hbar\omega - E_g\right)\right]^2} \,, \tag{6}$$

$$\beta_{Br}^{a-f} = \frac{2^{9/2}\pi e^4 \left(m^*_{vc}\right)^{5/2} \Delta E\, f_{vn} \left(2\hbar\omega - E_g\right)^{3/2}}{3\,\varepsilon_\infty\, c^2 m^3\, (\hbar\omega)^3 \left[\Delta E - \hbar\omega + \frac{m^*_{vc}}{m^*_{vn}}\left(2\hbar\omega - E_g\right)\right]^2} \,, \tag{7}$$

$$\beta_{Basov} = \frac{2^{21/2}\,\pi e^4 \left(m^*_{vc}\right)^{1/2} \left|p_{vc}\right|^2 \left(2\hbar\omega - E_g\right)^{3/2}}{\varepsilon_\infty c^2 (\hbar\omega)^5\, m^2} \,, \tag{8}$$

$$\beta_{Keldysh} = \left(\frac{2\,\pi e^4}{9\varepsilon_\infty c^2 \sqrt{\hbar\omega\, m^*_{vc}}\; E_g^{\,2}}\right) \exp\left(4\left(2 - \tilde{E}_g/E_g\right)\right)$$

$$\times \exp\left(-4 + \frac{2\,E_g}{\hbar\omega}\right) \int_0^{\sqrt{4 - 2\,E_g/\hbar\omega}} e^{y^2}\, dy \,. \tag{9}$$

In eq. (6) - (9) ΔE is the minimum energy separation between bands v and n whose reduced effective mass is m^*_{vn}, f_{ij}'s are the oscillator strengths, ε_∞ is the high frequency dielectric constant of the crystalline material, E_g is the minimum energy gap between bands v and c, while $\tilde{E}_g$ is the effective energy gap [3] in the radiation field:

$$\tilde{E}_g = E_g + \frac{e^2 E_o^2}{4 m^*_{vc} \omega^2} \,,$$

where E_o is the amplitude of the electric field of the radiation. Eqs. (6) and (7) have taken into account the correction factor $\frac{1}{\varepsilon_\infty^2}$ pointed out by Mitra et al. [2].

As one can see there is very little resemblance between the above formulas, and their interrelationship is unclear. More importantly it has long been stated that the Keldysh formula is either incorrect or invalid for small photon multiplicity [4, 7-10], and that the Braunstein and Basov formulas are more accurate. However very little evidence has been advanced to support these statements. On the contrary the recent calculations of Mitra et al.[2] reveal that of the three models described above, the Keldysh formulation gives two-photon absorption coefficients in closest agreement with the experimental results. Mitra et al. also noted that the predictions of the Basov formula are much larger than the other two theoretical estimates, as well as the experimental data. This result is also disturbing since the Basov formulation is a description of the allowed-forbidden transition, and one would expect the allowed-forbidden transitions to be much weaker than the allowed-allowed transitions. In the following sections we attempt to resolve some of these contradictions, and propose two modifications to the Braunstein model which result in increased accuracy.

2.1. Keldysh Formula

We followed the derivation of the Keldysh formula closely and could not find any reason to think this formula is less accurate than Braunstein's and Basov's formulas for two-photon absorption. In fact we found that the two-photon absorption edge resulting from the Keldysh formula agrees very well with that predicted by Braunstein's formula for allowed-allowed transitions, as shown below. Close to the two-photon absorption edge $2\hbar\omega \simeq E_g$, the Keldysh formula described by eq. (9) reduces to the following form.

$$\beta_k \simeq \frac{\pi e^4 \exp(4)(2\hbar\omega - E_g)^{1/2}}{9\varepsilon_\infty c^2 (2m^*_{cv})^{1/2} (\hbar\omega)^3} \quad . \tag{10}$$

In deriving eq. (10) we have made use of the fact that the effective gap $\tilde{E}_g$ is very close to E_g, which is a necessary condition for the applicability of the Keldysh formula.

The two-photon absorption edge ($2\hbar\omega \simeq E_g$) resulting from the Braunstein's formula for allowed-allowed transitions is

$$\beta_{Br}^{a-a}\ (2\hbar\omega \simeq E_g) \simeq \frac{2^{9/2}\ \pi e^4 (m^*_{vc})^{1/2} (m/m_c - 1)\ (2\hbar\omega - E_g)^{1/2}}{9\varepsilon_\infty c^2\ (\hbar\omega)^3 m} \quad , \tag{11}$$

where m_c is the conduction electron effective mass. Eq. (11) is obtained from eq. (6) if one uses the following sum rules [11, 12]

$$f_{vn} = m/(2m^*_{vc}) \quad , \tag{12}$$

$$f_{nc} = \frac{m}{m_c} - 1 \quad , \tag{13}$$

and assumes $\Delta E = 2E_g$. This latter assumption is justified since the Braunstein two-photon absorption coefficient is not sensitive [6] to ΔE as long as $\Delta E > E_g$. From eqs. (10) and (11), again for $2\hbar\omega \simeq E_g$

$$\frac{\beta_k}{\beta_B^{a-a}} \simeq \frac{\exp(4)}{32} \quad \frac{m}{m^*_{vc}} \quad \frac{1}{\left(\frac{m}{m_c} - 1\right)} \quad . \tag{14}$$

For semiconductors $m_c << m$ and $m^*_{vc} \simeq m_c$. Under these conditions eq. (14) gives

$$\beta_k \simeq 1.7\ \beta_{Br}^{a-a} \ ; \text{ while}$$

for alkali halides $m_c \simeq 0.5m$ and $m^*_{vc} \simeq m_c$, and $\beta_k \simeq 3.4\ \beta_{Br}^{a-a}$.

2.2. Basov Formula

The rather large two-photon absorption coefficients predicted by the Basov formula in the past evidently arise from several errors in the Basov formula. We will now discuss these errors and offer corrections.

Basov et al. [4] used the following relations for the interaction Hamiltonian and vector potential:

$$H = \frac{e}{mc} \vec{A} \cdot \vec{p} \quad , \tag{15}$$

$$A_o^2 = \frac{8\pi c\ I}{\varepsilon_\infty^{1/2}\ \omega^2} \, . \tag{16}$$

The proper expression for A^2 consistent with eq. (15) is [13]

$$A_o^2 = \frac{2\pi c\ I}{\varepsilon_\infty^{1/2}\ \omega^2} \, . \tag{17}$$

Basov et al. also assumed the intra-conduction-band Hamiltonian matrix elements to be

$$H_{cc} = \frac{eA}{m_c c} \hbar k \quad , \tag{18}$$

with a similar expression for the valence-band matrix elements. The appropriate quantum mechanical expression for these forbidden transitions is [11, 14]

$$H_{vv} = H_{cc} = \frac{eA}{mc} \hbar k \quad , \tag{19}$$

where m is the free electron mass. Finally, a correction factor of 1/3 should be introduced in the Basov formula due to the averaging of the matrix elements, over all directions in $\vec{k}$ space. (Lee and Fan [15] earlier stated without explanation that a correction factor of 1/48 should be applied to the Basov formula. Their factor obviously arises from the averaging of the matrix elements and the correction of the vector potential.) When all the corrections are made, Basov's expression for the two-photon absorption coefficient takes the form

$$\beta_{Basov}(\omega) = \frac{2^{13/2}\pi e^4 \left(m^*_{cv}\right)^{5/2} E_g f_{vc}}{3\,\varepsilon_\infty c^2 m^3 (\hbar\omega)^5} \left(2\hbar\omega - E_g\right)^{3/2}, \qquad (20)$$

with f_{vc} as given by eq. (12).

This final corrected Basov formula eq.(20) coincides with the result obtained from Braunstein's formula for allowed-forbidden transitions, eq. (7) if the intermediate states are taken to be in the initial and final bands themselves, and the two topmost valence bands are considered for the initial state. Further, when eq. (20) is applied to several semiconductors and alkali halides, the resulting two-photon absorption coefficients are found to be much smaller than those predicted by the Keldysh and Braunstein formulas for allowed-allowed transitions (see Tables II and III).

2.3. Braunstein Formula

In an attempt to reduce the magnitude of the disagreement between the experimental nonlinear absorption coefficients and the predictions of the Braunstein formula for allowed-allowed transitions, we introduced two modifications in the Braunstein model. First, the parabolic energy bands in the Braunstein formula are replaced by nonparabolic energy bands of the form described by eq. (4). The resulting two-photon absorption coefficient for allowed-allowed transitions is

$$\beta^{a\text{-}a} = \frac{8\pi e^4 (m^*_{cv})^{3/2} \Delta E (\Delta E - E_g) f_{vn} f_{nc}}{\varepsilon_\infty c^2 m^2 \left(E_g\right)^{1/2} \left(\hbar\omega\right)^2} \left[\left(\frac{2\hbar\omega}{E_g}\right)^2 - 1\right]^{1/2}$$

$$\times \left[\Delta E \left\{1 + \frac{E_g}{\Delta E} \frac{m^*_{vc}}{m^*_{vn}} \left(\left(\frac{2\hbar\omega}{E_g}\right)^2 - 1\right)\right\}^{1/2} - \hbar\omega\right]^{-2}. \qquad (21)$$

In the case of alkali halides, the intermediate state is assumed to be an excitonic level in the forbidden-gap, instead of a higher conduction band. Tables II and III show that these modifications do bring the results of the Braunstein formula for allowed-allowed transitions closer to the experimental values.

3. Conclusion

The Keldysh formula is shown to be closely related to Braunstein's formula for allowed-allowed transitions. The Basov formula on the other hand is shown to be a special case of Braunstein's formula for allowed-forbidden transitions. Several errors in the original Basov formula are indicated and corrected. The predictive accuracy of the Braunstein formula is increased by including nonparabolic energy bands and excitonic intermediate states.

On comparing the experimental values of the two-photon absorption coefficients with those predicted by the above three models, after including the indicated corrections and modifications, we note the following. The allowed-forbidden formulas grossly underestimate the two-photon absorption coefficient. The Keldysh and modified Braunstein formulas for allowed-allowed transitions give more reasonable results. However, in many cases only an order of magnitude agreeement is obtained between theory and experiment. This points to the need for further refinement of the theoretical models.

Table I. Value of parameters used for alkali halides.

The effecitve masses appropriate for the valence bands are not available in the literature and were taken to be infinitely large.

Crystal	ε_∞ at 0.266 μm (Ref. 17)	E_g(eV)	ΔE(eV) for excition (Ref. 17)	ΔE(eV) for higher conduction band	Conduction band effective mass (in units of free electron mass) (Ref. 18)	Reduced Effective mass(in units of free electron mass) (Ref. 18)
NaCl	2.68	8.97 (Ref. 16)	6.36	12.7 (Ref. 16)	0.6	--
KCl	2.468	8.9 (Ref. 18)	6.52	11.6 (Ref. 16)	0.496	--
RbCl	2.484	8.5 (Ref. 18)	7.29	9.9 (Ref. 18)	0.66	--
KBr	3.1	7.3 (Ref. 19)	6.0	9.5 (Ref. 18)	0.48	--
KI	3.756 (3.11 at 0.355 μm)	6.3 (Ref. 19)	5.06	7.2 (Ref. 18)	--	0.21
RbI	3.675 (2.99 at 0.355 μm)	6.37 (Ref. 19)	5.04	6.9 (Ref. 18)	--	0.32

Table II. Comparison of theoretical and experimental two-photon absorption coefficients (in units of 10^{-3}cm/MW) in several direct-gap semiconductors

Crystal	Wavelength (μm)	Calculated					Published experimental results (Ref. 2)
		Allowed-Allowed			Allowed-Forbidden		
		Keldysh	Braunstein	Modified Braunstein	Braunstein	Basov	
CdS	0.694	6.1	2.19	3.26	0.04	0.608	30, 70, 660
ZnSe	0.694	6.4	2.03	2.96	0.018	0.297	40
GaAs	1.064	18.7	6.65	11.56	0.014	0.214	200,300,800,5600,9000
	1.318	22.6	10.08	13.99	0.01	0.221	33
InP	1.064	25.8	7.63	14.77	0.018	0.267	260, 180-260
CdTe	1.064*	23	7.37	12.21	0.023	0.459	200-300
InSb	10.64	2100	1185	1223	0.0006	0.127	256, 15000, 16000

*This wavelength was incorrectly reported as 1.318 μm in Ref. 2.

Table III. Comparison of theoretical and experimental two-photon absorption coefficients (in units of 10^{-3}cm/MW) in several direct-gap alkali halides

Crystal	Wavelength (μm)	Calculated					Published experimental results (Ref. 17)
		Allowed-Allowed			Allowed-Forbidden		
		Keldysh	Braunstein	Modified Braunstein	Braunstein	Basov	
NaCl	0.266	0.226	0.0365	0.227	0.004	0.038	3.5 ±25%
KCl	0.266	0.291	0.052	0.286	0.005	0.04	1.7 ±20% 2.7 ±30%
RbCl	0.266	0.344	0.028	0.061	0.028	0.16	1.02 ±15% 1.26 ±30%
KBr	0.266	0.502	0.073	0.160	0.04	0.265	2.0 ±30%
KI	0.266	0.802	0.080	0.362	0.02	0.1	3.75 ±20%
	0.355	1.02	0.176	0.744	0.01	0.055	7.29 ±20%
RbI	0.266	0.655	0.037	0.284	0.041	0.187	2.49 ±20%
	0.355	0.848	0.081	0.582	0.019	0.092	5.08 ±15%

4. REFERENCES.

[1] J. M. Worlock in Laser Handbook, ed. F. T. Arecchi and E. O. Schultz-DuBois (North Holland, Amsterdam, 1972), vol 2.

[2] S. S. Mitra, L. M. Narducci, R. A. Shatas, Y. F. Tsay, and A. Vaidyanathan, App. Opt. 14, 3038 (1975).

[3] L. V. Keldysh, Sov. Phys. JETP 20, 1307 (1965).

[4] N. G. Basov, A. Z. Grasyuk, I. G. Zubarev, V. A. Katulin, and O.N. Krokhin, Sov. Phys. JETP 23, 366 (1966).

[5] M. Göppert-Mayer, Ann. Phys. (Leipzig) 9, 273 (1931).

[6] R. Braunstein, Phys. Rev. 125, 475 (1962); R. Braunstein and N. Ockman, Phys. Rev. 134, A499 (1964).

[7] J. H. Yee, Phys. Rev. 3, 355 (1971).

[8] H. D. Jones, and H. R. Reiss, Phys. Rev. B 16, 2466 (1977).

[9] F. Adduci, I. M. Catalano, A. Cingolani, and A. Minafra, Phys. Rev. B 15, 926 (1977)

[10] M. H. Weiler, Phys. Rev. B7, 5403 (73).

[11] R. A. Smith, Wave Mechanics of Crystalline Solids, (Chapman and Hall, London, 1969), Second ed., p. 457.

[12] J. Callaway, Quantum Theory of the Solid State, (Academic, New York, 1974), part A, p. 248.

[13] L. I. Schiff, Quantum Mechanics, (McGraw Hill, New York, 1955), Second ed., p. 250.

[14] J. Bardeen, F. J. Blatt, and L. H. Hall in Proceedings of the Conference on Photoconductivity, Atlantic City, 1954, ed. G. H. Breckenridge, B. R. Russell, and E. E. Hahn (Wiley, New York, 1956), p. 146.

[15] C. C. Lee and H. Y. Fan, Appl. Phys. Lett. 20, 18 (1972).

[16] M. L. Cohen and V. Heine in Solid State Physics, ed. H. Ehrenreich, F. Seitz and D. Turnbull (Academic, New York, 1970) vol 24, p. 37.

[17] P. Liu, W. L. Smith, H. Lotem, J. H. Bechtel, and N. Bloembergen, Phys. Rev. B 17, 4620 (1978).

[18] R. S. Knox and K. J. Teegarden in Physics of Color Centers, ed. W. B. Fowler (Academic, New York, 1968).

[19] R. T. Poole, J. G. Jenkin, J. Liesegang, R. C. G. Leckey, Phys. Rev. 11, 5179 (1975).

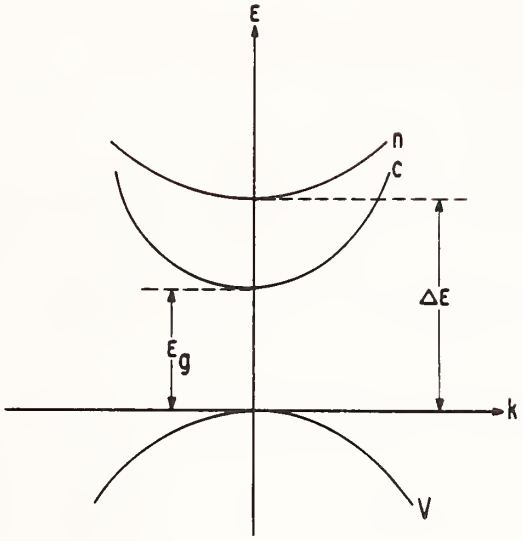

Fig. 1.

The energy band model used in Braunstein's formulation. v, c, and n refer to the initial valence, final conduction, and intermediate conduction bands, respectively. All the three energy bands are assumed to be parabolic.

The speaker indicated that deposition rates of 50-200 angstroms per minute were used in this work, but he expressed confidence that these deposition rates could be increased by a factor of two or more if that were important for commercial production.

COMPETING MECHANISMS IN LASER-INDUCED DAMAGE

A. Vaidyanathan*, T. W. Walker, and A. H. Guenther
Air Force Weapons Laboratory
Kirtland AFB, NM 87117

The thresholds for laser-induced intrinsic damage in several alkali halide crystals are calculated by means of separate avalanche and multiphoton ionization models, as well as by a combination of the two. The appearance of 10^{18} electrons/cm^3 in the conduction band is taken as the criterion for damage. Numerical calculations are performed for nanosecond and picosecond pulse durations, with wavelengths ranging from 1.064 to 0.355 μm. Upon comparing these theoretical predictions with available experimental results, it is found that, in general, the avalanche mechanism yields damaging optoelectric field strengths in good agreement with the experimentally measured values. The field strengths required for damage solely due to multiphoton ionization are substantially higher. However, when the photon multiplicity is less than or equal to four, the damage fields predicted by the multiphoton model are often smaller than those calculated for catastrophic avalanche multiplication, and are in better agreement with the experimentally measured damage thresholds. Furthermore, It is noted that neither the avalanche nor the multiphoton ionization model, when considered alone, can satisfactorily explain the experimentally observed frequency and pulse length dependence of the damage fields over the entire reported range of these parameters. It is thus suggested that it is more appropriate to combine these two mechanisms.

Key Words: Avalanche ionization; laser-induced damage; multiphoton ionization.

1. Introduction

The avalanche multiplication [1] and multiphoton ionization [2] processes are two competing mechanisms by which a pulse of high power laser can cause irreversible damage to optical materials. In an attempt to understand the relative importance of these two mechanisms in causing damage to the dielectrics, we have calculated the damage electric field strengths in several alkali halide crystals within the frameworks of a classical avalanche model [1] and the Keldysh multiphoton ionization formula [2]. The theoretical predictions are compared with the published experimental results regarding the optoelectric field strengths at damage as well as their variations with the laser frequency and pulse width. From this comparison it is concluded that in order to better explain all of the experimental observations, the above two processes must be combined into a single formulation, with due attention paid to their interdependency.

---

*AFSC/NRC Postdoctoral Resident Research Associate

2. Theory

2.1. Avalanche model

Within the framework of the classical avalanche model [1] the rate of energy gain of a conduction electron from an alternating electric field $\vec{F} = \vec{F}_o \cos \omega t$ is given by

$$\left(\frac{d\varepsilon}{dt}\right)_F = \frac{e^2 F_o^2 \tau_k}{m^*(1+\omega^2 \tau_k^2)} \quad , \tag{1}$$

where τ_k is the electron phonon relaxation time for large angle scattering, and m* is the conduction electron effective mass. The rate of energy loss to the lattice phonons is

$$\left(\frac{d\varepsilon}{dt}\right)_L = \frac{\hbar\omega_p}{\tau_L} \quad , \tag{2}$$

where τ_L is the relaxation time when both large- and small-angle scatterings are considered and ω_p is the average phonon frequency. If there are n_{co} conduction electrons per unit volume when the laser irradiation is initiated, the conduction electron density at the end of the pulse t_p seconds will be

$$n_c = n_{co} 2^{(t_p/t_i)} \quad , \tag{3}$$

where t_i is the time interval during which a conduction electron starting with zero energy attains an energy equal to the band-gap energy. It is well known that [3] when the conduction electron density reaches a value of the order of $10^{18}/cm^3$, the absorption of the residual laser becomes appreciable, leading to localized heating and subsequent irreversible damage to the optical material. For this reason the appearance of 10^{18} conduction electrons/cm^3 is taken as the criterion for laser-induced damage in these calculations.

A more stringent criterion for damage would be the proximity of the plasma frequency to the laser frequency. However, we did not use this criterion in our calculations, since the multiphoton model (to be described below) becomes invalid due to the large Stark shifts in the energy bands at the field strengths needed to satisfy the above condition. We further assume that the ionization of weakly bound sites such as F-centers, impurities, etc., give rise to an initial conduction electron density of $10^9/cm^3$. With these assumptions, we obtain from eqs. (1) - (3) the expression for the damaging electric field amplitude in mks units:

$$F_{damage} \simeq \left[\frac{m^*(1+\omega^2\tau_k^2)}{e^2\tau_k} \left(\frac{\Delta \ell n 10^9}{0.693 t_p} + \frac{\hbar\omega_p}{\tau_L} \right) \right]^{1/2} \quad , \tag{4}$$

where Δ is the band gap energy of the crystal. Eq. (4) is an expression for the electric field amplitude in pure dielectric materials at the onset of damage.

We will later use this equation to calculate the numerical values of the damage field strengths in several crystalline dielectrics.

2.2. Multiphoton absorption

Keldysh [2] has theoretically derived an expression for the probability of electronic transitions from the highest valence band to the lowest conduction band of a direct-gap crystalline solid when intense electromagnetic radiation is incident on the crystal. In his analysis the energy of the photon is assumed to be smaller than that of the band-gap, and transitions are presumed to take place between Stark-shifted energy bands. Keldysh presented the following expression for the transition rate per unit volume:

$$W = \frac{2\omega}{9\pi}\left(\frac{\sqrt{1+\gamma^2}}{\gamma}\,\frac{\mu^*\omega}{\hbar}\right)^{3/2} Q\left(\gamma, \frac{\chi}{\hbar\omega}\right) \times \exp\left\{\frac{-\pi < \frac{\chi}{\hbar\omega} + 1 > \left[K\left(\frac{\gamma}{\sqrt{1+\gamma^2}}\right) - E\left(\frac{\gamma}{\sqrt{1+\gamma^2}}\right)\right]}{E\left(\frac{1}{\sqrt{1+\gamma^2}}\right)}\right\} . \tag{5}$$

In eq. (5) μ^* is the reduced effective mass of the conduction electron and valance hole, χ is the effective band-gap in the radiation field given by

$$\chi = \frac{2\Delta}{\pi}\,\frac{\sqrt{1+\gamma^2}}{\gamma}\,E\left(\frac{1}{\sqrt{1+\gamma^2}}\right) , \tag{6}$$

the functions E and K are complete elliptic integrals of the first and second kind, while γ is the ratio of the radiation frequency to the tunneling frequency given by

$$\gamma = \frac{\omega\sqrt{\mu^*\Delta}}{eF_0} . \tag{7}$$

The symbol $<\cdots>$ in eq. (5) denotes the integer part of the argument, and the function Q is given by

$$Q(\gamma, y) = \left[\frac{\pi}{2K\left(\frac{1}{\sqrt{1+\gamma^2}}\right)}\right]^{1/2} \sum_{n=0}^{\infty} \left(\Phi\left\{\left[\frac{\pi^2\,(2 < y + 1 > - 2y + n)}{2K\left(\frac{1}{\sqrt{1+\gamma^2}}\right) E\left(\frac{1}{\sqrt{1+\gamma^2}}\right)}\right]^{1/2}\right\} \times \exp\left\{\frac{-n\pi\left[K\left(\frac{\gamma}{\sqrt{1+\gamma^2}}\right) - E\left(\frac{\gamma}{\sqrt{1+\gamma^2}}\right)\right]}{E\left(\frac{1}{\sqrt{1+\gamma^2}}\right)}\right\}\right), \tag{8}$$

where Φ is the Dawson integral. The laser electric field strengths necessary to damage the dielectrics solely by multiphoton absorption will be later calculated with the aid of eqs. (5) - (8), for the condition

$$Wt_p \simeq 10^{18} \text{electrons/cm}^3. \tag{9}$$

2.3. Combination of avalanche and multiphoton models

Vinogradov and Faizullov [4] combined the effects of multiphoton and avalanche mechanisms by assuming that the two processes were independent of each other. They obtained the following expression for the conduction electron density:

$$n_c = \left(n_{c0} + \frac{W}{\omega_i} \right) \exp(\omega_i t_p) - \frac{W}{\omega_i} \ , \tag{10}$$

where W and ω_i are the multiphoton and avalanche ionization frequencies respectively.

3. Results and discussion

Eqs. (4) - (10) were used to calculate the damage optoelectirc field strengths in NaCl, KCl, KBr, NaF, LiF, and CaF_2 for typical laser wavelengths and pulse durations (see Table 1). The following values of the parameters were used in our calculation [1]:

$$\tau_k = 1.36 \times 10^{-15} \text{sec}, \ \tau_L = 8.77 \times 10^{-16} \text{ sec, and } \hbar\omega_p = \frac{1}{40} \text{ eV}$$

In addition the values of the band structure parameters used in these computations are listed in Table II. The elliptic integrals and Dawson integrals encountered in the Keldysh formula were evaluated numerically. We included a sufficient number of terms in the infinite sum in eq. (8) to obtain convergency of the order of 0.01.

3.1. Damage threshold

The damaging field strengths predicted by the avalanche model scatter around the experimentally measured values within a factor of approximately four. The electric field strength needed for dielectric breakdown caused solely by the absorption of four or more photons are much larger, and thus this mechanism plays a secondary role when $\Delta >> h\omega$. However, in many cases (e.g., NaCl, KCl, KBr, etc.) when $\Delta \leq 4\ h\omega$, the damage field in the multiphoton model is smaller than that due to the avalanche mechanism, and in closer agreement with the experimental results. When the multiphoton and avalanche mechanisms are combined as in eq. (10), the resulting damage thresholds are closer to the smaller of the above two estimates. This result apparently arises from treating the two processes as independent of each other, while in fact they are interdependent.

From Table I we also note that most of the experimental damage thresholds are smaller than the predictions of either theory. The reason for this is probably that the theoretical calculations are for intrinsic breakdown in pure crystalline materials, while the experimental values are largely governed by impurities and defects.

3.2. Dependence of damage field on frequency and pulse duration

In fig. 1 we have plotted the variation of the optoelectric field strength at damage threshold in NaCl as a function of the laser frequency. According to the avalanche model the damage field should increase with increasing frequency approximately as $(1 + \omega^2\tau_k^2)^{1/2}$ (see also eq. 4). The multiphoton model on the other hand predicts a sharp decrease in the damage threshold with increasing frequency. The experimental data [6] show that the damaging optoelectric field strength increases with increasing frequency up to that of ruby laser, and decreases on further increase in frequency. Furthermore, the experimentally observed dependence of the damage field on laser frequency is much weaker than the predictions of either of the above two theories. From the comparison of the theoretical predictions with the experimental data we conclude that a combination of the multiphoton and avalanche mechanisms is closer to the real situation than either of the two mechanisms considered alone. We also believe that including the effect of multiphoton transitions on the avalanche ionization frequency will bring the theoretical predictions closer to the experimental results.

In fig. 2 we have plotted the pulse width dependence of the damage fields in NaCl at 1.06 μm. It is noted that the avalanche model predicts a weak inverse dependence of the approximate form $F_o \sim t_p^{-0.035}$, while the multiphoton model predicts a somewhat stronger variation of the form $F_o \sim t_p^{-0.155}$. The experimental dependence is stronger than either of these two predictions, being of the approximate form $F_o \sim t_p^{-0.25}$ [14]. This once again points to the need for further refinement of the theoretical models.

4. Conclusion

It is shown that neither the avalanche nor the multiphoton model alone can explain all of the experimentally observed features of laser-induced damage. It is suggested that it is more appropriate to combine these two mechanisms into a single formulation. This should be done in a more detailed and appropriate manner through treatment of their interdependency. Specifically the effect of multiphoton transitions on the avalanche growth rate constant should be included. The energy dependence of the collision frequencies as well as the effects of surface states,impurities, color centers, etc., should also be considered. Calculations incorporating the above are currently under active pursuit.

5. References

[1] M. Sparks and C. J. Duthler, Theoretical Studies of High-Power Ultraviolet and Infrared Materials, Fifth Technical Report, Xonics Inc., Van Nuys, CA, June 1975; M. Sparks, Current status of electron-avalanche breakdown theories, Laser-Induced Damage in Optical Materials: 1975, A. J. Glass and A. H. Guenther, Eds. NBS Special Publication 435, 1975, pp. 331-346.

[2] L. V. Keldysh, Ionization in the field of a strong electromagnetic wave, Sov. Phys. JETP, Vol 20, pp. 1307-1314, 1965.

[3] N. Bloembergen, Laser-induced electric breakdown in solids, IEEE J. Quantum Electron., Vol QE-10, pp. 375-386, 1974.

[4] An. V. Vinogradov and F. S. Faizullov, Role of many-photon and impact ionization in the breakdown of dielectrics by picosecond laser pulses, Sov. J. Quantum Electron., Vol 7, pp. 650-652, 1977.

[5] D. W. Fradin, N. Bloembergen, and J.P. Lettelier, Dependence of laser-induced breakdown field strength on pulse duration, Appl. Phys. Lett., Vol 22, pp. 635-637, 1973.

[6] A. A. Manenkov, New results on avalanche ionization as a laser damage mechanism in transparent dielectrics, Laser-Induced Damage in Optical Materials: 1977, A. J. Glass and A. H. Guenther, Eds, NBS Special Publication 509, 1977, pp 455-464.

[7] D. W. Fradin, E. Yablonovitch, and M. Bass, Confirmation of an electron avalanche causing laser-induced bulk damage at 1.06 μm, Appl. Opt., Vol 12, pp. 700-709, 1973.

[8] W. L. Smith, J. H. Bechtel, and N. Bloembergen, Dielectric-breakdown threshold and nonlinear-refractive-index measurements with picosecond laser pulses, Phys. Rev B, Vol 12, pp. 706-714, 1975.

[9] D. W. Fradin and M. Bass, Electron avalanche breakdown induced by ruby laser light, App. Phys. Lett., Vol 22, pp. 206-208, 1973.

[10] W. L. Smith, J. H. Bechtel, and N. Bloembergen, Picosecond laser-induced breakdown at 5321 and 3547 A: Observation of frequency-dependent behavior, Phys. Rev. B, Vol 15, pp. 4039-4055, 1977.

[11] R. T. Poole, J.G. Jenkin, J. Liesegang, and R. C. G. Leckey, Electronic band structure of the alkali halides. I. experimental parameters, Phys Rev. B, Vol 11, pp. 5179-5189, 1975.

[12] R. S. Knox and K. J. Teegarden, Alkali halide crystal excitation, Physics of Color Centers, W. B. Fowler, Ed. New York: Academic, 1968, p. 34.

[13] G. W. Ruboff, Far-ultraviolet reflectance spectra and the electronic structure of ionic crystals, Phys. Rev. B, Vol 5, pp. 662-684, 1972.

[14] J. R. Bettis, R. A. House, and A. H. Guenther, Spot size and pulse duration dependence of laser-induced damage, Laser-Induced Damage in Optical Materials: 1976, A. J. Glass and A. H. Guenther, Eds. NBS Special Publication 462, 1976, pp. 338-345.

6. Figures

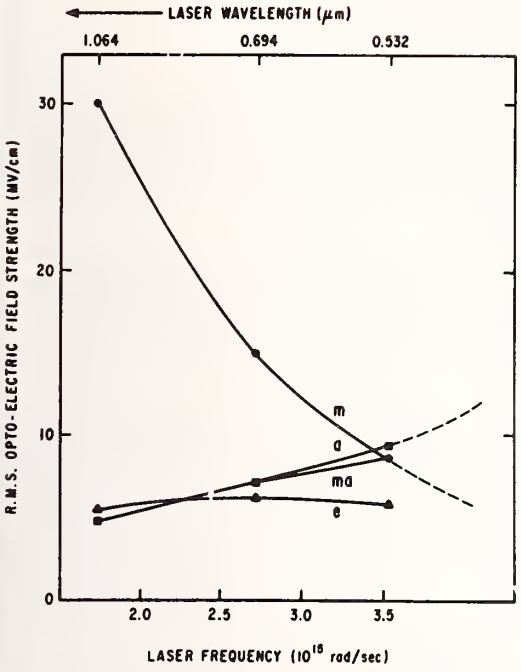

Fig. 1 - Variation of the optoelectric field strength at the onset of intrinsic damage in crystalline NaCl, with laser frequency. (The appearance of 10^{18} electrons/cm^3 in the conduction band was taken to the damage criterion.) m - multiphoton model, a - avalanche model, ma - multiphoton assisted avalanche, and e - experimental.[6] The --- curves represent the extensions of the theoretical predictions to higher frequencies, where multiphoton effects should dominate.

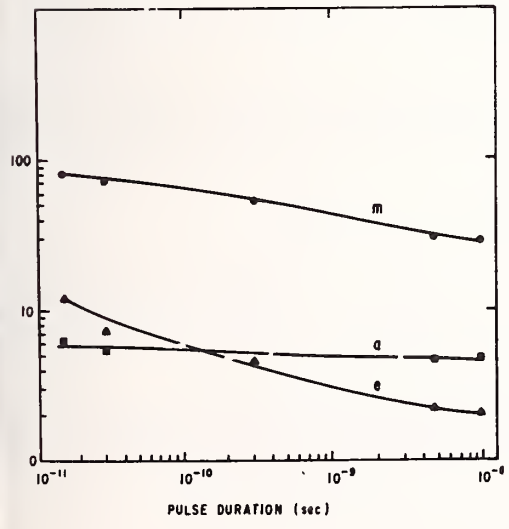

Fig. 2 - Variation of the optoelectric field strength at damage with pulse duration in NaCl crystal for 1.06μm radiation. (The appearance of 10^{18} electrons/cm^3 in the conduction band was taken to be the damage criterion.) m - multiphoton model, a - avalanche model, and e - experimental.

Table I. Comparison of calculated and experimental r.m.s. electric field strengths at damage

Crystal	Wavelength (μm)	Pulse duration (10^{-9} secs)	r.m.s. electric field (Mv/cm) in the crystal at damage				Reference to experiments	Photon energy / Gap Energy
			Avalanche model	Multiphoton model	Multiphoton Assisted avalanche	Experimental		
NaCl	1.064	10.3	4.94	29	4.94	2.1	5	0.135
	1.064	10.0	4.94	30	4.94	5.49	6	0.135
	1.064	4.7	4.94	31	4.94	2.3 ± 0.46	7	0.135
	1.064	0.3	5.01	53	5.01	4.7	5	0.135
	1.064	0.03	5.63	74	5.63	7.34 ± 15%	8	0.135
	1.064	0.015	6.24	77	6.24	12.4 ± 3.7	5	0.135
	0.694	14	7.28	14	7.24	2.2 ± 0.44	9	0.208
	0.694	10	7.28	15	7.24	6.14	6	0.208
	0.532	8	9.31	8.7	8.7	5.72	6	0.272
KCl	1.064	10	4.50	27.3	4.49	4.25	6	0.134
	1.064	4.7	4.94	29	4.49	1.14	7	0.134
	1.064	0.03	5.63	69	5.12	5.86 ± 15%	8	0.134
	0.694	10	6.61	13.5	6.58	4.55	6	0.206
	0.532	8	8.50	8.2	8.20	2.54	6	0.269
KBr	1.064	10	4.42	19.2	4.41	3.51	6	0.16
	1.064	4.7	4.42	21	4.42	0.76	7	0.16
	1.064	0.03	4.94	44	4.94	5.33 ± 15%	8	0.16
	0.694	10	6.51	8.67	6.47	3.78	6	0.246
	0.532	8	8.36	7.6	7.5	3.85	6	0.321
NaF	1.064	4.7	4.51	92	4.57	3.28	7	0.101
	1.064	0.03	5.35	>200	5.34	10.77 ± 15%	8	0.101
	0.532	0.021	10.70	38	10.10	19.4	10	0.203
	0.355	0.021	15.79	29	13.78	40-99	10	0.308
LiF	1.064	0.03	5.47	>200	5.47	12.24 ± 15%	8	0.086
	9.532	0.021	11.01	58.5	10.94	26.5	10	0.171
	0.355	0.021	16.31	31.5	14.20	35-70	10	0.257
CaF_2	1.064	0.03	5.39	>200	5.37	14.44 ± 15%	8	0.09
	0.532	0.021	10.80	56	10.70	25.2	10	0.19
	0.355	0.021	16.16	29.5	13.90	18-33	10	0.289

Table II. Values of band structure parameters used

Crystal	Energy Gap (eV) (Ref. 11)	Conduction electron effective mass / Free electron mass (Ref. 12)
NaCl	8.6	0.6
KCl	8.7	0.496
KBr	7.3	0.48
NaF	11.5	-
LiF	13.6	-
CaF_2	12.1 (Ref. 13)	-

The conduction electron effective masses for the flourides are not available in the literature. 0.5 was assumed as a reasonable value for these compounds. All the valence electron effective masses were assumed to be infinitely large.

THEORY OF ELECTRON-AVALANCHE BREAKDOWN IN SOLIDS*

M. Sparks, T. Holstein, R. Warren, D. L. Mills,
A. A. Maradudin, L. J. Sham, E. Loh Jr., F. King
Pacific-Sierra Research Corporation
Santa Monica, California 90404

Electron-avalanche breakdown in solids is explained by a theory that is predictive and agrees with experimental results for the magnitude of the breakdown field and its temperature dependence, pulse-duration dependence, material-to-material variation, and wavelength dependence for $\lambda \geq 1$ μm. The good agreement between experiment and theory with no parameters adjusted is obtained by using improved magnitudes and energy dependences of the electron-phonon relaxation frequencies. The contributions of both optical and acoustical phonons to electron loss and diffusion must be included. The breakdown field E_B is calculated by solving an eigenvalue equation obtained from the diffusion transport equation. Simple models and interpretations of the diffusion equation afford physical insight into breakdown and render the breakdown conditions predictable. Preliminary results indicate that the diffusion approximation fails for wavelengths considerably shorter than 1 μm, but that E_B decreases with decreasing λ as a result of multiphoton absorption before the diffusion approximation fails.

Key words: Alkali halides; electron-avalanche breakdown; electron-phonon scattering; Fokker-Planck equation; laser damage; multiphoton absorption; theory

1. Introduction

In spite of many previous attempts to develop a viable model of laser-induced damage to alkali halides, there has yet to appear a theory capable of simultaneously explaining the magnitude of the breakdown field as a function of temperature, wavelength, pulse duration, and its variation from material to material. A re-examination of the model assumptions of the electron-avalanche theory, with particular attention to the magnitude and energy dependence of the electron scattering rates, shows that the transport-equation approach explains available data without the need to introduct new mechanisms. In particular, the predictions of the theory agree well with the new Lebedev data [1][1] for wavelengths $\lambda \geq 1.06$ μm. A cardinal reason for the good agreement, contrasted to poor agreement of previous similar theories, is the use of more realistic electron-phonon scattering rates. Umklapp processes, which were neglected in previous treatments [2,3], are essential. The resulting electron-phonon scattering rates increase with increasing electron energy $\mathcal{E}$ at large $\mathcal{E}$. It is also necessary to include both optical and acoustical phonons.

2. The Model

In the electron-avalanche picture of dielectric breakdown, a small number of "seed" electrons drift upward in energy in the conduction band through interaction with the laser field, retarded by scattering from phonons. The electron undergoes a random walk of progressively increasing kinetic energy until it achieves a threshold energy $\mathcal{E}_i$. The electron then drops to the bottom to the conduction band after creating an exciton. The rapid photoionization of the exciton injects a second electron into the bottom of the conduction band. Eventually, in sufficiently high fields, enough electrons ($\approx 10^{18}$ cm^{-3}) are created to disrupt the lattice through Joule heating.

*Supported by the Air Force Office of Scientific Research. Background investigations were supported by the Defense Advanced Research Projects Agency.

[1] Figures in brackets indicate the literature references at the end of this paper.

ing to the largest β. Dual-space eigenfunctions must be used in the scalar-product expansion coefficients because the system operator is nonHermitian.

3. Solutions of the Diffusion Equation

An extensive series of studies of the eigenvalue problem outlined above was carried out for detailed models of acoustical- and optical-phonon contributions to $\gamma_k(\mathcal{E})$ and $\gamma_L(\mathcal{E})$. The energy variations of these quantities resulting from proper incorporation of Umklapp scattering (through a simple model) is an essential feature of the problem. This analysis will be described in a full-length publication to appear elsewhere. With the detailed results in hand, it is possible to mimic the results surprisingly well through use of the Fokker-Planck equation with $D(\mathcal{E})$ and $V(\mathcal{E})$ chosen as constants (independent of energy). The solutions to the eigenvalue equation, obtained from eqs. (1) and (7), which are easily attained analytically, are sufficiently simple to afford insight into the avalanche process and to allow scaling without numerical computation. The solutions are even sufficiently accurate for use as first-order approximations to the exact numerical results.

From the above breakdown criterion that the avalanche process creates a sufficient electron density to cause excessive Joule heating, Sparks [4] obtained the result $\beta\, t_p^{(eff)} \approx 17$, where $t_p^{(eff)}$ is an effective pulse length, chosen as 1/3 the actual pulse duration for Gaussian pulses. This is done because the avalanche rate β has a very strong variation with E, and only the center of the pulse is effective in triggering the breakdown. In any case, the breakdown field is insensitive to the value of βt_p in the nanosecond region. From the analytic solution and this criterion, the breakdown field may be written

$$E_B = E_d\, E_{VO} \quad , \tag{8}$$

where

$$E_{VO} = (3\mathcal{E}_{ph}\, \gamma_L/\sigma)^{1/2} \cong \omega\left[\frac{3\mathcal{E}_{ph}m}{e^2}\right]^{1/2}\left[\frac{\gamma_L}{\gamma_K}\left(1 + \frac{\gamma_k^2}{\omega^2}\right)\right]^{1/2} \tag{9}$$

is the value of E at which V vanishes, and

$$E_d \cong [1 + \ell ng + \ell n(1 + \ell ng)]^{-1/2}$$

for nanosecond pulses, where

$$g = k_B\, \mathcal{E}_{ph}\, \gamma_L\, t_p/51\mathcal{E}_i \quad . \tag{10}$$

The significance of this decomposition of E_B lies first in the weak dependence of E_d (and hence E_B) on the parameters $\mathcal{E}_i$ and t_p for nanosecond pulses, while E_{VO} depends strongly on $\mathcal{E}_{ph}$, γ_k, γ_L, and ω. The weak dependence of the breakdown field on the band gap (or, to be precise, on $\mathcal{E}_i$) and on the laser-pulse duration t_p for nanosecond pulses was at first surprising. However, the previously used, average-electron criterion for breakdown, $E_B = E_{VO}$, also gave E_B independent of $\mathcal{E}_i$ and t_p.

At 1.06 μm, the inequality $\gamma_k << \omega$ is valid; while at 10.6 μm, the inequality $\omega << \gamma_k$ is valid. Thus, eq. (9) gives

$$E_{VO} \cong \omega(3\mathcal{E}_{ph}m/e^2)^{1/2}\,(\gamma_L/\gamma_k)^{1/2} \quad , \qquad \text{at 1.06 μm} \quad , \tag{11}$$

and

Although the laser energy is absorbed in finite quanta, a Fokker-Planck equation is used to describe the absorption process and the energy losses suffered from collisions with phonons. Preliminary results indicate that the Fokker-Planck diffusion equation fails for wavelengths considerably shorter than 1 μm for sodium chloride. The large-quantum energy gains then have to be considered as difference processes, rather than being approximated by differential processes. However, the preliminary results also indicate that multiphoton processes cause the breakdown field to decrease with decreasing wavelength before the large-quantum effects become important. Thus, the Fokker-Planck diffusion equation and multiphoton absorption will be sufficient to explain breakdown if the preliminary results are verified.

The Fokker-Planck equation can be written as a diffusion equation in energy space

$$\partial n(\mathscr{E},t)/\partial t + \partial J/\partial \mathscr{E} = 0 \quad , \tag{1}$$

where $n(\mathscr{E},t)d$ is the number of electrons with energy between $\mathscr{E}$ and $\mathscr{E} + d\mathscr{E}$, and

$$J(\mathscr{E},t) = V(\mathscr{E})\, n(\mathscr{E},t) - D(\mathscr{E})\, \partial n(\mathscr{E},t)/\partial \mathscr{E} \, , \tag{2}$$

Here $V(\mathscr{E})$ and $D(\mathscr{E})$ are the effective velocity and diffusion coefficient in energy space. Both depend on energy, temperature, and laser frequency. For fields comparable to the breakdown field, ignoring small field independent contributions to D, we obtain

$$V(\mathscr{E}) = \frac{1}{3}\sigma(\mathscr{E})\, E^2 - \mathscr{E}_{ph}\, \gamma_L(\mathscr{E}) \, , \qquad D(\mathscr{E}) = \frac{1}{6}\sigma(\mathscr{E})E^2 \tag{3}$$

Here E is the root-mean-square electric field and the electrical conductivity is defined as

$$\sigma(\mathscr{E}) = \frac{e^2\, \gamma_k(\mathscr{E})}{m[\omega^2 + \gamma_k^2(\mathscr{E})]} \, , \tag{4}$$

where $\gamma_k(\mathscr{E})$ is the rate at which *current* carried by electrons of energy $\mathscr{E}$ is relaxed, $\gamma_L(\mathscr{E})$ is the rate at which the electron loses *energy* to the phonons, e and m are the electron charge and effective mass, ω is laser frequency, and $\mathscr{E}_{ph}$ is an average phonon energy. The boundary conditions are

$$n(\mathscr{E}_i,t) = 0 \, , \tag{5}$$

corresponding to no electrons accelerated past the exciton threshold, and

$$J(0,t) = 2\, J(\mathscr{E}_i,t) \, , \tag{6}$$

corresponding to the "flux doubling" feature of exciton creation followed by photoionization.

The partial-differential transport equation (1) is converted to an ordinary-differential eigenvalue equation by using the approximation

$$n(\mathscr{E},t) = n(\mathscr{E}) \exp(\beta t) \tag{7}$$

and by assuming that the avalanche phenomenon is dominated by the eigenvalue β having the greatest real part. All of the numerical work locates this largest eigenvalue. In fact, only a single positive real eigenvalue was obtained in simple models for $V(\mathscr{E})$ and $D(\mathscr{E})$ (for example, V and D constant, or V constant and $D \sim \mathscr{E}$) that render the Fokker-Planck equation analytically soluble. The approximation in eq. (7) can be justified by general considerations of the diffusion equation (1) (the time constant $\tau_{dif} = \mathscr{E}_i^2/D$ for attaining the eigenfunction form of eq. (7) is short with respect to the pulse duration), by explicit solution of the complete partial differential equation (1), or by expanding the initial electron distribution in eigenfunctions and neglecting all terms except the one correspond-

$$E_{VO} \cong (3\mathscr{E}_{ph} m/e^2)^{1/2} (\gamma_L \gamma_k)^{1/2} \quad , \qquad \text{at } 10.6 \ \mu m \ . \tag{12}$$

The electron-phonon relaxation frequencies γ_k and γ_L are sketched as functions of $\mathscr{E}$ in fig. 1. From eq. (11) it is seen that at 1.06 μm, the breakdown field is controlled by the ratio γ_L/γ_k, which is greatest at low electron energies, as illustrated in fig. 1. By contrast, at 10.6 μm, E_B is controlled by the product $\gamma_L \gamma_k$, which is greatest at the highest electron energies. The values of γ_k and γ_L used in the constant-D-and-V model must be chosen according--as the low-$\mathscr{E}$ values at 1.06 μm and as the high-$\mathscr{E}$ values at 10.6 μm. This necessity to use different γ's at different frequencies explains the previous failure of constant-γ models that was pointed out by Sparks [4].

The result in eq. (8) also explains why the average-electron result $E_B = E_{VO}$ is too large. The value of E_d in eq. (8) is less than unity. Furthermore, since E_d is nearly constant (for nanosecond pulses) the scaling obtained from the average-electron result $E_B = E_{VO}$ is rather accurate, provided that the appropriate frequency-dependent values of γ_k and γ_L are chosen, as discussed above. This scaling with temperature, wavelength, pulse duration, and material parameters obtained from eq. (8) or from $E_B = E_{VO}$ explains the experimental scaling well.

4. Numerical Results

To obtain quantitative values for the breakdown field, the eigenvalue equation was integrated numerically with a predictor-corrector algorithm using eqs. (2) through (5) together with the boundary conditions. Figure 2 is the resulting plot of the multiplication exponent β as a function of E for sodium chloride at room temperature and 1.06 μm. For low fields--which are attained for nanosecond pulses--it can be shown by analytic methods that

$$\beta = (51/t_p)\ g\ (E^2/E_{VO}^2)\ \exp[-E_{VO}^2/E^2] \quad . \tag{13}$$

This result in eq. (13) verifies the result above that the breakdown field is sensitive to changes in the value of E_{VO} (shifting the $\beta(E)$ curve in fig. 2 from left to right according to the scaling $\beta \sim \exp(E_{VO}^2/E^2)$ in eq. (13)) but is insensitive to changes in the value of g (shifting the steep $\beta(E)$ curve up and down), the dramatic rise of β with increasing E predicted by eq. (13) is seen in fig. 2. By contrast, for high fields the figure shows the behavior $\beta \sim E^2$, which is necessary because the electron energy gain is dominated by the σE^2 term. For picosecond pulses--for which β is typically in the high-field region--the breakdown field is more sensitive to values of $\mathscr{E}_i$ and t_p than it is in the nanosecond region. For example, using the breakdown criterion $\beta t_p \cong 51$, the breakdown field can be read off the curve in fig. 2. Changing the value of t_p and the corresponding breakdown value of $\beta_B = 51/t_p$ gives small changes in E_B in the steep, low-field region appropriate to nanosecond pulses, but gives larger changes in E_B in the relatively flatter high-field region of $\beta \sim E^2$ appropriate to picosecond pulses.

Figure 3 shows the relatively good agreement between theory (solid curve) and experiment [1,5,6,7] points). A major difficulty in comparing theory with experiment is that there is no way at present to determine whether experimental values are intrinsic or extrinsic. Indeed the recent Lebedev [1] values of E_B are greater than previous experimental values. Although it is not certain that the intrinsic values have ever been attained, even in the Lebedev experiments, the good agreement between the theoretical

results with no parameters adjusted and the Lebedev experimental results for the magnitude, temperature dependence, pulse-duration dependence, material-to-material dependence, and wavelength dependence of E_B suggests that the Lebedev breakdown thresholds are intrinsic and that the previous lower values of E_B were extrinsic.

Soileau and coworkers [8] suggested that spot-size scaling possibly could reconcile the results of various workers. They suggested that the value of E_B should be a function of the focal-volume size because the probability of having a starting seed electron in the volume decreases as the volume decreases. Experiments with seed electrons supplied by a separate source, examination of the probabilistic character of breakdown for small focal volumes and the deterministic character for large focal volumes, or other verification of the spot-size scaling law is needed because it is currently thought that the seed electrons are easily generated from impurities, dislocations, or grain boundaries, for example. The breakdown is thought to be controlled by the avalanche process, rather than by the generation of the seed electrons. However, there have been no experiments or convincing theories to support these beliefs, and verification of the suggested mechanism giving the spot-size scaling would be useful.

In order to demonstrate the sensitivity of the value of E_B to values of the parameters in the theory, a different value of the electron-chlorine-ion scattering cross section σ_{Cl} (which appears in γ_k and γ_L) was chosen. All results were recalculated for this single new value and are shown as dotted curves in figs. 3 through 5. The improved agreement between theory and experiment for the adjusted value of σ_{Cl} has no important significance other than illustrating the sensitivity of E_B to the value of the parameter σ_{Cl} because adjusting parameters to obtain agreement between theory and experiment is unwise and almost always misleading. Nevertheless, improved experimental values of σ_{Cl} would be welcomed because the unadjusted value used was the value for chlorine gas taken from the atomic-physics literature.

The agreement in fig. 4 between theory and experiment [1] for the temperature dependence of E_B for sodium chloride at room temperature and 1.06 μm is good. Lower theoretical values than the experimental values of E_B, as in fig. 4 for 10.6 μm, are quite surprising because previous theories have universally suffered by predicting values of E_B greater than the experimental values and because intrinsic processes lower the experimental value of E_B. The simplicity of the constant-D-and-V model affords the explanation of the low theoretical 10.6 μm values. At 10.6 μm, very-high-frequency (i.e., high-energy) phonons control the values of γ_k and γ_L because high-energy electrons determine the value of E_B, as discussed above. Since the reduction in σ_{Cl} with increasing energy is not known experimentally, the energy dependence of σ_{Cl} was neglected. In order to partially compensate for this neglected energy dependence, the phonon dispersion relations outside the first Brillouin zone were approximated by constants (equal to the zone-boundary values). This constant high-energy-phonon frequency approximation overestimates the value of E_B. The overestimate does not occur at 10.6 μm because the low-energy electrons that control E_B at 10.6 μm interact with low-frequency phonons in the first Brillouin zone. Improved estimates of the 10.6 μm breakdown field, using more realistic dispersion relations for the high-frequency phonons, will be made.

The good agreement between theory and experiment [1] for the material-to-material variation of E_B at room temperature and 1.06 μm is seen in fig. 5.

5. Summary

Numerical studies of the Fokker-Planck form of the kinetic equation using models of electron-phonon scattering with Umklapp processes included produce good agreement with

experiments [1,5] for the magnitude of the breakdown field and its temperature dependence, pulse-duration dependence, material-to-material variation, and wavelength dependence for $\gamma \geq 1.06$ μm with no parameters adjusted. Simple results of the constant-D-and-V model are invaluable in understanding the results, scaling to different conditions, relating the present and previous theoretical results, and in showing that the breakdown at 1.06 μm and 10.6 μm involve different physics.

REFERENCES

[1] Gorshkov, B. G., Danileiko, Yu. K., Epifanov, A. F., Lobachev, V. A., Manenkov, A. A., Sidorin, A. V., Soviet Physics (JETP) 45, 612 (1977); Manenkov, A. A., in Laser induced damage in optical materials: 1977, Glass, A. J., and Guenther, A. H., eds, National Bureau of Standards, Washington, D.C. (NBS Spec. Publ. 509) p. 455.

[2] Holway, L. H. and Fradin, D. W., J. Appl. Phys., 46, 279 (1975).

[3] Fröhlich, H., Proc. R. Soc. A, 160, 230 (1937); Fröhlich, H., Adv. Phys. 3, 325 (1954).

[4] Sparks, M., in Laser induced damage in optical materials: 1975, Glass, A. J., and Guenther, A. H., eds, National Bureau of Standards, Washington, D.C. (NBS Spec. Publ. 435), p. 331; Sparks, M., in Theoretical studies of high power ultraviolet and infrared materials, section C and section B, Xonics 5th technical report, 30 June 1975.

[5] Fradin, D. W., Bloembergen, N., Lettlier, J. P., Appl. Phys. Lett. 22, 635 (1973).

[6] Fradin, D. W., Yablonovitch, E., and Bass, M., Appl. Opt., 12, (700), 1973.

[7] Smith, W. L., Bechtel, J. H., and Bloembergen, N., Phys. Rev., 15, (4039), 1977.

[8] Soileau, M. J., Bass, M., and van Stryland, E. W., in Laser induced damage in optical materials: 1978, Glass, A. J., and Guenther, A. H., eds, National Bureau of Standards, Washington, D.C. (NBS Spec. Publ. 541), p. 309.

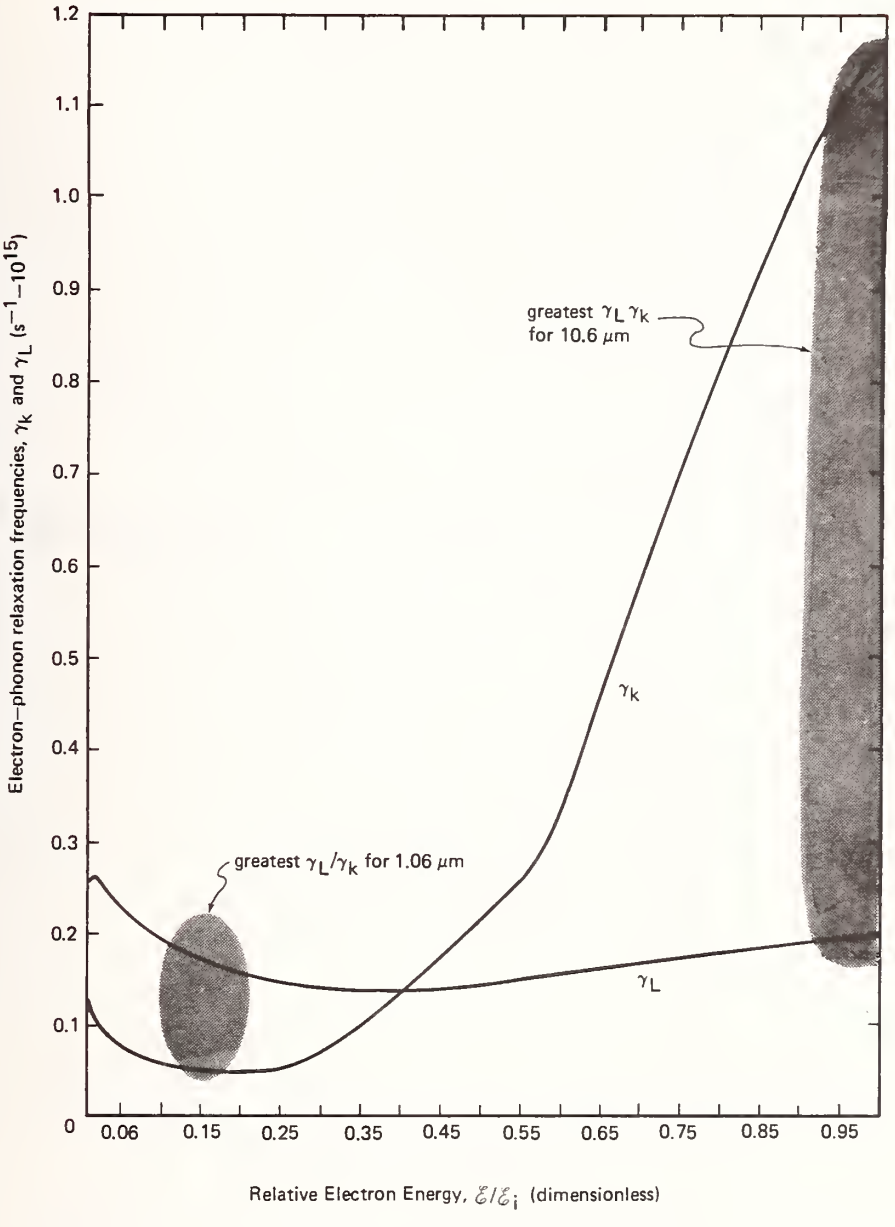

Figure 1. Energy variation and magnitude of the energy-loss rate γ_L and energy-transport rate γ_k for sodium chloride at room temperature.

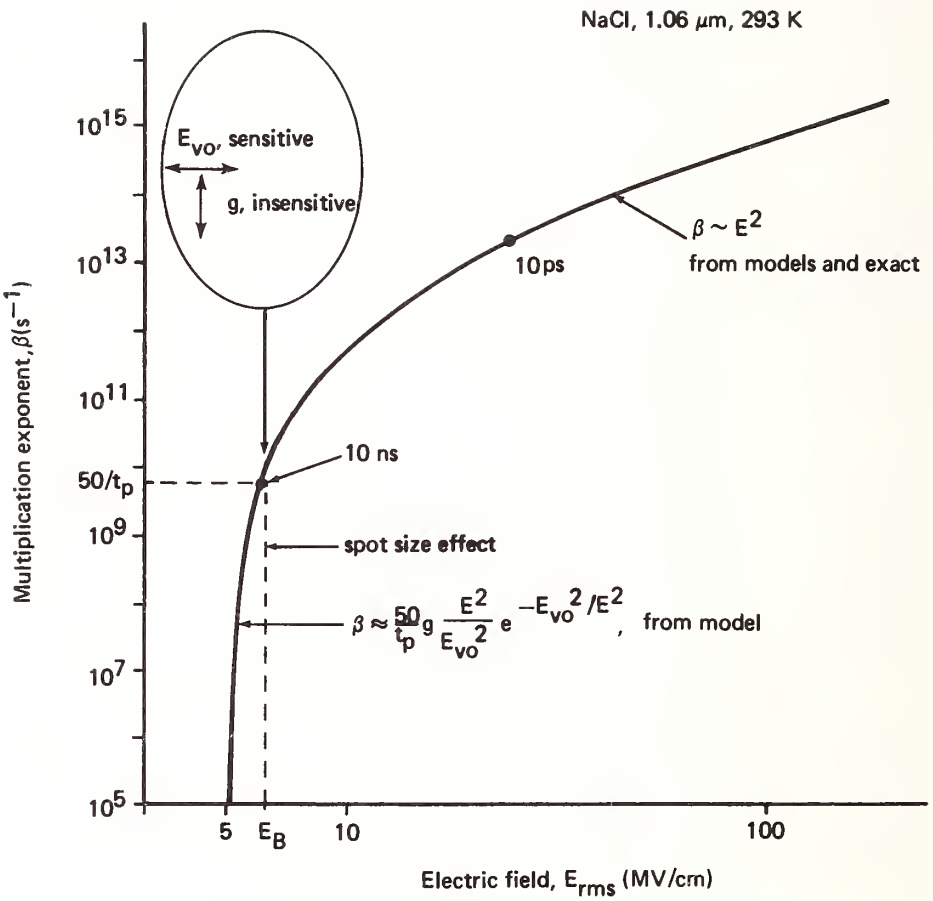

Figure 2. Numerical solution of the Fokker-Planck equation for sodium chloride at room temperature and 1.06 μm.

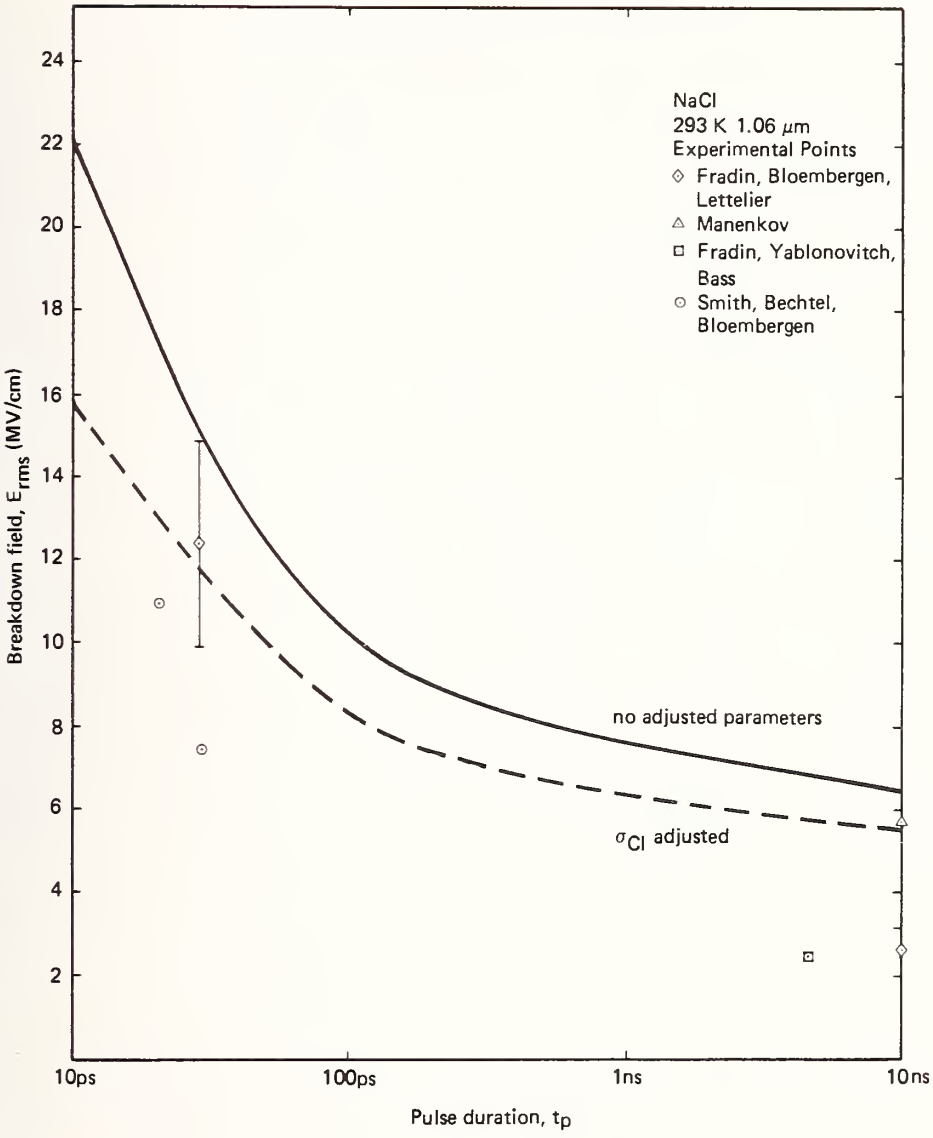

Figure 3. Comparison of experimental [1,5,6,7] pulse-duration dependence of the breakdown field E_B (points) with the theoretical result (solid curve) for sodium chloride at room temperature and 1.06 μm. The dashed curve illustrates the sensitivity of E_B to the parameter change discussed in the text.

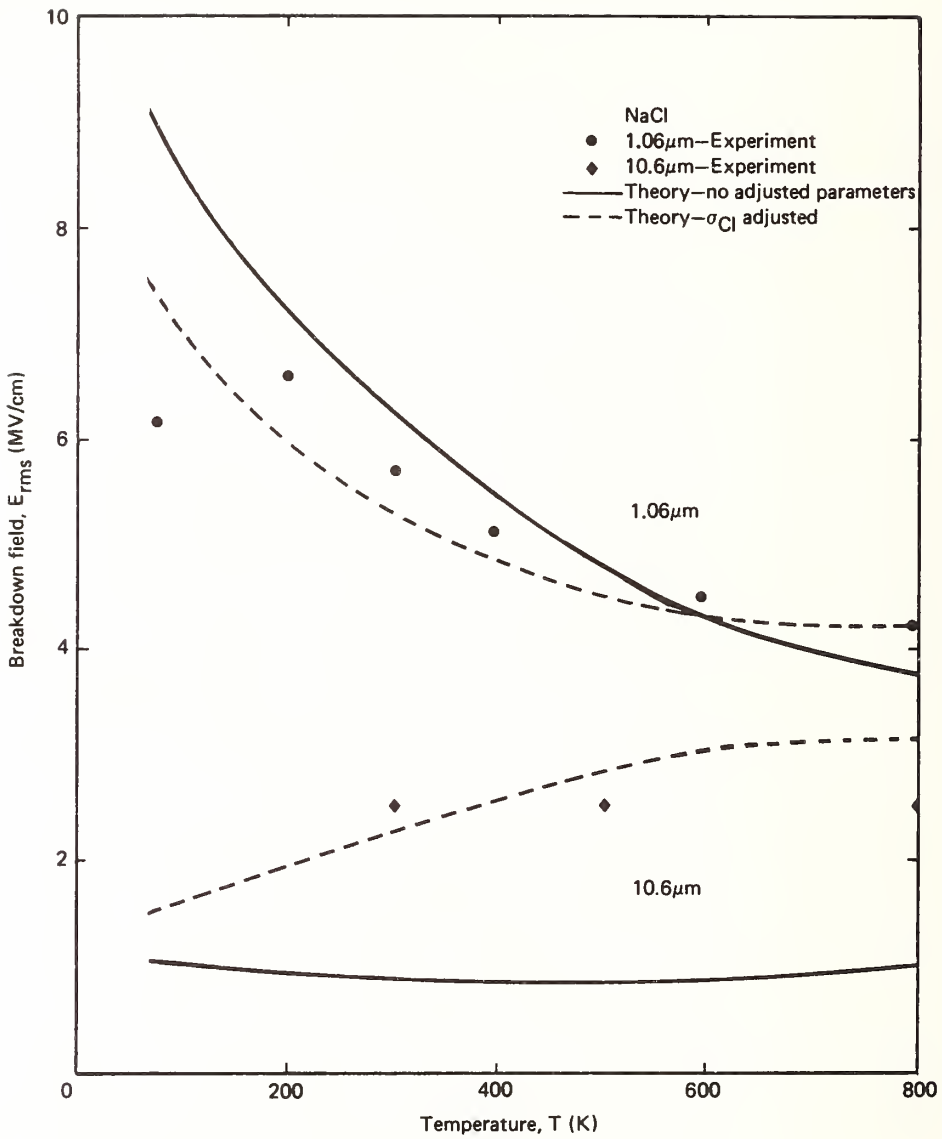

Figure 4. Comparison of experimental [1] temperature dependence of the breakdown field (points) with the theoretical result (solid curve) for sodium chloride at 1.06 μm and 10.6 μm. The dashed curve illustrates the sensitivity of E_B to the parameter change discussed in the text.

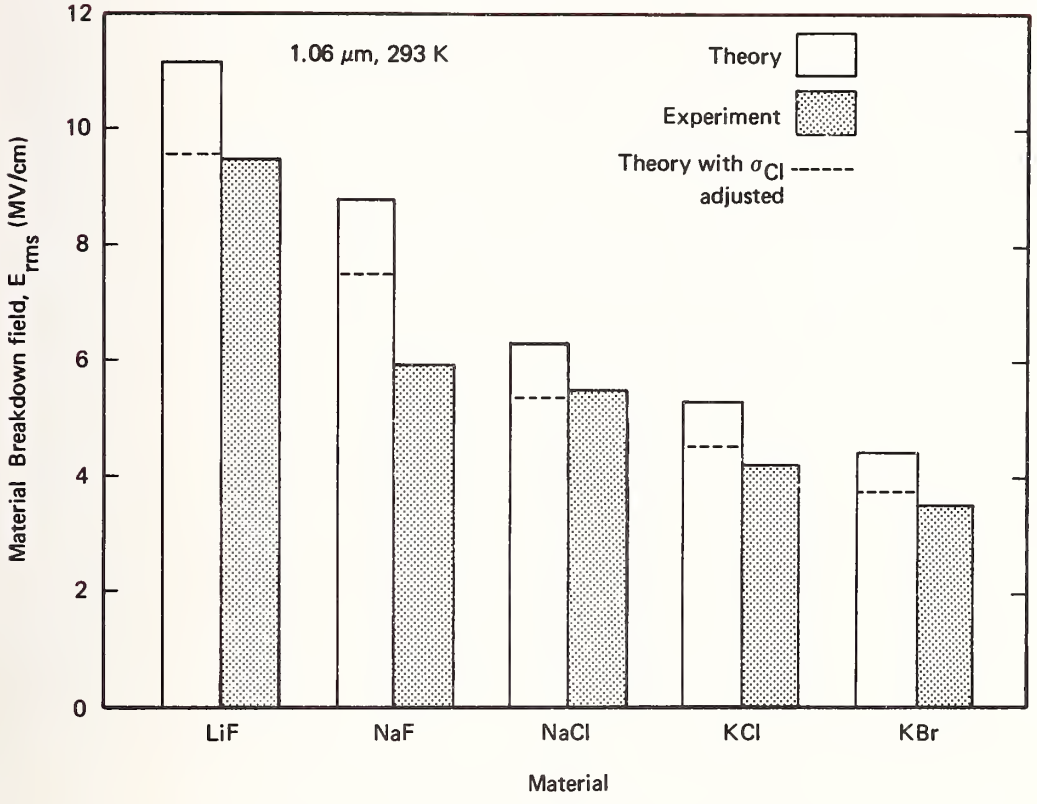

Figure 5. Comparison of the experimental [1] material-dependence of the breakdown field (cross-hatched bars) with the theoretical results (solid-line bars) at room temperature and 1.06 μm. The dashed bars illustrate the sensitivity of E_B to the parameter change discussed in the text.

In response to a question concerning the differences between the theory presented here and the theory presented by Manenkov a year ago, the speaker indicated that the main difference was in the detail of the treatment of the electron-phonon processes. In this treatment, the electron-phonon collision frequency was taken to be quite different than in Manenkov's treatment. Furthermore, in this treatment, a number of parameters of the theory were taken to depend on temperature, including band gap, occupation number, etc., whereas in Manenkov's treatment the only explicit temperature dependence was in the phonon occupation number. The speaker was asked why Manenkov's data could be treated as intrinsic. He indicated that it might not be intrinsic but that the good agreement with the predictions of the theory regarding the dependennce of the breakdown threshold on wavelength, temperature and choice of material was very encouraging, and that Manenkov's data appeared to be as close to intrinsic data as one could obtain. A number of questions came up in the discussion regarding particular approximations in the theory. Finally, the point was raised concerning how intrinsic avalanche breakdown could exhibit a pulse length dependence when in itself it was a very rapidly occurring, strongly non-linear process. The point was not satisfactorily resolved in the course of the discussion.

IMPURITY BREAKDOWN MODEL IN THIN FILMS

T. W. Walker[@], A. Vaidyanathan[*], A. H. Guenther
Air Force Weapons Laboratory
Kirtland AFB, New Mexico 87117

and

P.Nielsen[+]
Air Force Institute of Technology
Wright Patterson AFB, Ohio 45433

The impurity model for breakdown given by Hopper and Uhlmann was examined. The case for nonmetallic impurities was derived from the thermal equations and affords the results of Hopper and Uhlmann when the correct limits are taken. These equations were then compared to an exact solution given by Goldenberg and Tranter, in which it is not assumed that the radial temperature distribution within the particle is a constant. It was found that the exact solution does not agree with the approximate solutions when the thermal conductivity of the impurity is small. In this case, the temperature in the particle is not uniform and the damage threshold can be substantially lower.

The Mie absorption coefficient was then combined with the exact solution. For nonmetallic impurities the results predict a damage threshold which depends on the film thickness. The experimental results for CaF_2, ThF_4, and MgF_2 were found to agree very well with these theoretical predictions. This agreement was found to hold at both the 5 ns and 15 ns pulse lengths and at 1.06 μm, 0.53 μm, and 0.26 μm wavelengths.

Further theoretical calculations show that different size impurities are the most damage sensitive at different pulse lengths (and wavelengths). The calculation of breakdown threshold as a function of pulse length for fused silica surfaces fit very accurately to a $\sqrt{t}$ curve, in agreement with the results of D. Milam.

Key Words: Laser damage; impurity-induced damage; pulse duration dependence of damage; Mie absorption coefficient.

1. Introduction

There has been a great deal of theoretical work on laser-induced damage produced by impurities in bulk optical material (1-5). At the present it is uncertain whether damage in even very pure bulk materials is produced by avalanche or multiphoton ionization of by isolated impurity sites (6). Experimental data (7, 8, 9, 10) indicates a spot size dependence of the breakdown level that is difficult to explain by either multiphoton or avalanche ionization. In thin films the role of impurities in the damage process is expected to be even greater. For example, the absorption coefficient of most thin films is between 10 cm^{-1} to 1000 cm^{-1}, where in bulk form the range is several orders of magnitude smaller. Surfaces fall in between these two extremes of absorption. This high absorptivity of thin films is generally believed to be due to impurities in the film which are included during the deposition process. Experimental data also indicates that the breakdown threshold is more than an order of magnitude lower for thin films that for the bulk form of the same materials (8).

@ Submitted in partial fulfillment of the Ph.D. degree at the Air Force Institute of Technology, Wright Patterson AFB, Ohio
* N.R.C. Postdoctoral Resident Research Associate
+ Presently at Air Command Staff College, Maxwell AFB, AL

2. Theory

The model which will be used in this work for impurity damage is that of spherical absorbing particles embedded in a uniform host material. The impurity is assumed to absorb the incident radiation and increase in temperature relative to the surrounding host material. A straightforward solution to the thermal equations can be obtained if it is assumed that the heat flow out of the particle is determined solely by the thermal conductivity of the host material. This is true if the thermal conductivity of the impurity is infinite, in which case the temperature within the impurity is uniform. The solution is straightforward and the result is the same as given by Hopper and Uhlman (2). The temperature in the host is

$$T = \frac{3QI}{2\Pi\,\bar{C}_p D_h m r}\left\{\frac{1}{q-m}\,\mathrm{erfc}\,\frac{r-a}{2(D_h t_p)^{\frac{1}{2}}} - \frac{1}{q+m}\,\mathrm{erfc}\,\frac{r-a}{2(D_h t_p)^{\frac{1}{2}}}\right.$$
$$- \frac{1}{q-m}\exp\left[\frac{(q-m)(r-a)}{2a} + \frac{(q-m)^2 D_h t_p}{4a^2}\right]\mathrm{erfc}\left[\frac{r-a}{2(D_h t_p)^{\frac{1}{2}}} + \frac{(q-m)(D_h t_p)^{\frac{1}{2}}}{2a}\right] \qquad (1a)$$
$$\left. + \frac{1}{q+m}\exp\left[\frac{(q+m)(r-a)}{2a} + \frac{(q+m)^2 D_h t_p}{4a^2}\right]\mathrm{erfc}\left[\frac{r-a}{2(D_h t_p)^{\frac{1}{2}}} + \frac{(q+m)(D_h t_p)^{\frac{1}{2}}}{2a}\right]\right\}$$

Inside the impurity we have

$$T_p = \frac{3QI}{2\Pi\,\bar{C}_p D_h m a}\left\{\frac{1}{q-m}\left[1 - \exp\left(\frac{D_h t_p (q-m)^2}{4a^2}\right)\mathrm{erfc}\left(\frac{(q-m)(D_h t_p)^{\frac{1}{2}}}{2a}\right)\right]\right. \qquad (1b)$$
$$\left. - \frac{1}{q+m}\left[1 - \exp\left(\frac{D_h t_p (q+m)^2}{4a^2}\right)\mathrm{erfc}\left(\frac{(q+m)(D_h t_p)^{\frac{1}{2}}}{2a}\right)\right]\right\}$$

where $\bar{C}_p$ is the volume specific heat of the impurity; $\bar{C}_h$ is the volume specific heat of the host material; $q = 3\bar{C}_h/\bar{C}_p$ and $m = (q(q-4))^{\frac{1}{2}}$; D_h is the thermal diffusivity of the host material. Equation (1) is the result that is frequently used in impurity damage work (1, 3, 11). It is important to note that equations (1a) and (1b) are not valid for q less than or equal to 4. For q greater than 4 we must have $\bar{C}_h$ greater than $(4/3)\bar{C}_p$ (usually the case for metallic impurities in glass). If q is less than 4, the case for dielectric impurities, the correct solution is

$$T_p = \frac{3QI}{\Pi a \bar{C}_p D_h (q^2+m^2)}\left\{1 + \exp\left(\frac{D_h(q^2-m^2)t_p}{4a^2}\right)\mathrm{erfc}\left(\frac{q\sqrt{D_h t_p}}{2a}\right)\left[\frac{q}{m}\sin\left(\frac{2qm\,D_h t_p}{4a^2}\right)\right.\right.$$
$$\left. - \cos\left(\frac{2qmD_h t_p}{4a^2}\right)\right] + \frac{2}{\sqrt{\Pi}}\exp\left[\frac{D_h(q^2-m^2)t_p}{4a^2} - \left(q\sqrt{\frac{D_h t_p}{2a}}\right)^2\right] X \qquad (2)$$
$$\left.\left[\int_0^{m\sqrt{\frac{D_h t_p}{2a}}} e^{-y^2}\left[\sin\left(\frac{2yq\,D_h t_p}{2a} - \frac{2mqD_h t_p}{4a^2}\right) - \frac{q}{m}\cos\left(\frac{2yq\,D_h t_p}{2a} - \frac{2mqD_h t_p}{4a^2}\right)\right] dy\right]\right\}$$

It can be shown that under the proper limiting conditioning that both equation (1) and the correct equation for q = 4 are obtained from equation (2). In equation (2) $m = (q\,q-4\,)^{\frac{1}{2}}$.

Recent research (12, 13) indicates that the impurities in flouride films are oxides. For example, thorium flouride (ThF_4) contains ThO_2 and/or $ThOF_2$. Oxides and other dielectric materials typically have a very small coefficient of thermal diffisivity (14), which violates the basic assumption made in obtaining equations (1) and (2). This means that these equations cannot be used in treating dielectric impurities in dielectric host materials.

In light of the above, an exact solution is required to the thermal equations of spherical impurities. The exact thermal equations are given in equations (3) and (4).

$$\left.\begin{aligned} \frac{d^2(r\bar{T}')}{dr^2} - \frac{sr\bar{T}'}{D_p} &= -\frac{rQI}{K_p s} \quad 0 \le r < a \\ \frac{d^2(r\bar{T})}{dr^2} - \frac{sr\bar{T}}{D_h} &= 0 \qquad\qquad r > a \end{aligned}\right\} \tag{3}$$

$$\left.\begin{aligned} \bar{T} &= \bar{T}' \qquad\qquad r=a \\ K_p \frac{d\bar{T}'}{dr} &= K_h \frac{d\bar{T}}{dr} \end{aligned}\right\} \tag{4}$$

The solution to these equations was obtained by Goldenberg and Tranter (13). The result is

$$T_p = \frac{a^2 QI}{K_p}\left[\frac{1}{3}\frac{K_p}{K_h} + \frac{1}{6}\left(1-\frac{r^2}{a^2}\right) - \frac{2ab}{r\Pi}\int_0^{\infty} \frac{e^{\frac{-y^2 t_p}{\gamma_1}}}{y^2} \frac{(\text{siny-ycosy})(\sin(ry/a)\,dy}{(\text{csiny-ycosy})^2 + b^2y^2\sin^2 y}\right] \tag{5}$$

where $\gamma_1 = a^2/D_p$; $c = 1-(K_h/K_p)$; $b = (K_h/K_p)(D_p/D_h)^{\frac{1}{2}}$; K_h and K_p are the host and impurity thermal conductivities, respectfully; D_p is the impurity thermal diffusivity; t_p is the laser pulse length. The exponential in equation (5) involves the constant $D_p t_p/a$, where equations (1) and (2) contain $D_h t_p/a$. Since the integration in equation (5) is from zero to infinity, it is easy to make a change of variable and cast (5) into the same form. Figure (1) shows a plot of the incident energy per unit area required to heat a particle at its boundry (r = a) to a temperature of 2000°K as a function of the particle size. Curves (1) and (2) are equations (1) and (5) respectively. The material parameters are for a metallic impurity in a silicate host material. As expected the agreement is excellent in this case over the range of impurity sizes that were used. Figure (2) shows another comparison of equation (5) (curve 1) and equation (2) (curve 2). The material parameters are for dielectric impurities and q less than 4. In this case very poor agreement is obtained between the two equations. This is a result of the uniform temperature assumption made in obtaining equation (2).

The integral in equation (5) converges rapidly and there are no practical reasons for using equations (1) or (2) instead of (5). It is clear that the Goldenberg and Tranter solution to the thermal equations is not known to many researchers working in the field of laser-induced damage. This is pointed out by the fact that in most of the work on impurity dominated damage (4-6, 9-11, 15-31), there is no reference to this solution. However, in the research cited there are many references to the solution of Hopper and Uhlmann (1), given by equation (1). In all fairness to these latter researchers, their prime concern was platinum inclusions in silicate laser glasses, for which case their approach is quite acceptable.

The breakdown criteria which will be used in this model will be one of achievement of a specific temperature. A fixed critical temperature is set, for example the melting temperature of the host material, and the incident energy density is plotted against the impurity size. The minimum energy per unit area required to heat an impurity to the critical temperature is taken as defining the damage threshold. Calculations of impurity damage involving stresses (2), shock waves (16, 23, 28), and even avalanche ionization (11) have been carried out in an attempt to study the final stages of damage. It is assumed in this work that once the critical temperature is reached the damage proceeds instantaneously and catastrophically. This assumption is supported by the fact that as the temperature approaches the melting point of the host of impurity, the absorption increases dramatically (11, 15, 23, 31). At this point the breakdown then evolves nonlinearly and rapidly. The slower process by which the critical temperature is reached determines most the physical nature of the breakdown event. Therefore, the critical temperature criteria for breakdown should predict the parametric trends in the experimental data.

There has not been a treatment of impurity dominated breakdown which has used the Mie absorption cross-section for the impurities. It can be seen from the previous figures that the size of impurity which is easiest to damage is of the same order of magnitude as the wavelength of the laser pulse. If impurities are of this size then their energy absorption is best described by Mie absorption.

As equation (5) stands there is no frequency dependence. However, if we introduce an asymptotic analytic expression for the Mie absorption cross-section in place of Q in equation (5), this is no longer the case. Such an expression can be obtained for the Mie cross-section if the real index (n) of refraction is between 1 and 2, and the imaginary index (n') is much less than one. We then have (32, 33)

$$Q = 2\Pi a^2 \left(1 + \frac{e^{\frac{-8\Pi n' a}{\lambda}}}{8\Pi n' a/\lambda} + \frac{\left(e^{\frac{-8 n' a}{\lambda}} - 1\right)}{\left(\frac{8\Pi a n'}{\lambda}\right)^2} \right) \qquad (6)$$

where a is the radius of the impurity and λ is the wavelength of radiation. This cross-section is valid for a dielectric impurity and gives a wavelength dependence.

The range of n and n' over which equation (6) is valid would not include metallic impurities. The Mie absorption for metallic impurities can be approximated by

$$Q = \Pi a^2 \left(\frac{A\lambda}{n' a} + B \right) \qquad (7)$$

where A and B are empirical constants which depend on the particular metal.

The greatest difficulty in applying a Mie coefficient in the theory is that the composition of the impurities is not known for most films. Also, the imaginary index of refraction n' is a function of frequency. As a result of the above points, comparison between experiment and theory must be relative and not absolute. That is, the impurity model can only predict trends in the breakdown field and not absolute damage thresholds.

It has been pointed out that resonances can exist in the absorption cross-section (34, 35) which are not predicted by equations (6) and (7). These resonances can be shown to be of no importance for the cases treated here (36).

3. Comparison of Theory with Experimental Data

The impurity model can be examined in terms of the trends in the experimental data. Figures (3) to (6) provide a comparison of the ThF_4 data to theoretical calculations based on equations (5) and (6). In each figure the damage threshold is plotted as a function of the film thickness. The solid curves are the theoretical calculations. In the case of ThF_4 the impurity was modeled as ThO_2. There is evidence to support the existance of this impurity or $ThOF_2$ in the ThF_4 films (13). Fortunately, thermal constants for ThO_2 were available.

The most obvious feature of this impurity model is the prediction of an increase in damage threshold with a decrease in film thickness. This occurs because it is assumed in the model that the maximum size an impurity can have is limited by the film thickness. That is, as the film thickness increases so do the impurity sizes. This situation has been well supported by work at Perkin-Elmer (12) in which this phenomenon has been observed for many types of films. The theoretical curves in the figures are adjusted to the data at each wavelength. This is done by selecting one data point for either the 5ns or 15ns data and normalizing the appropriate theoretical curve at that point. The other theoretical curve for the remaining pulse width is then normalized by the same factor so that the relative position between the two curves is not changed. Therefore, the theoretical curves in each figure have been normalized to a single data point.

It is apparent from the figures that this model gives a good prediction of both the film thickness and the pulse width dependence of the damage threshold in ThF_4. The theoretical curves also track well with the data as the wavelength is changed and predict the observed decrease in film thickness dependence of damage at shorter wavelengths. The greatest point of disagreement is at 15ns and 1.06 μm for the 1/8 μm thick film. The measured damage threshold is close to that of the bare fused silica surface threshold. It is at this point that we would expect the greatest departure from theory due to the very high energy densities involved. Many more effects can become important at these high field strengths which could reduce the measured from the predicted threshold. The theoretical curves show a flattening over more of the film thickness at 0.35 and 0.26 μm as opposed to 1.06 and 0.53 m. It is not evident in the Mie cross-section given in equation (6) and the thermal equation (5), but this theory predicts that when the laser wavelength is reduced the size of the impurity that is most sensitive to damage is also reduced. The flattening of the theoretical curves at the shorter wavelengths occurs because the size of the impurity which is easiest to damage is included by more of the thin films. The particular value of film thickness at which the damage thresholds begin to rise is also shifted to thinner films at shorter wavelengths for the same reason. Both of these trends are observed in the data.

It can alse be noted that at the shorter wavelengths there is an increase in the damage threshold of the 4 μm thick films above the theoretical curves. This trend has been discussed in another work (36).

Although ThF_4 theoretical curves indicate that the pulse width dependence is properly described at all wavelengths the data is only for two pulse widths. It is interesting to compare the laser pulse width dependence predicted by the impurity model with data taken over a greater pulse width range. Figure (7) shows how this can be accomplished. The two curves represent 5 and 15ns damage curves as a function of particle size. It is clear that as the pulse width is decreased the threshold decreases and smaller sized particles are damaged. If a series of these curves are plotted for different laser pulse widths, then the minimum thresholds can be plotted as a function of pulse width. The resulting graph gives the desired predicted behavior. The procedure was used to obtain the theoretical curve for fused silica that is shown in Figure (8). The data was taken from Milam, et al. (37) and is for fused silica surfaces. The agreement between the theory and the data is excellent. Milan (37) made a best fit of a $(t_p)^{\frac{1}{2}}$ and found that this curve also gave a good fit to the data. However, this fit is not as good as that shown in Figure (8).

Since the comparison between theory and experiment in Figures (6) through (9) was made by normalizing the curves at each wavelength, they do not provide a reasonable picture of the predicted wavelength dependence. Figure (9) compares the theoretical and experimental values of the damage threshold of M_gF_2 films as a function of wavelength. The theoretical predictions and experimental data are given for both 1/8 and 1μm thick films. The theory and experiment both show a faster drop in the damage threshold for the 1/8 μm film that for the 1μm thick film as the wavelength decreases. The theoretical curve for the 1/8 μm film has been normalized to the 0.26 μm data point. The theoretical curve for the 1μm film is normalized so that the relative positions of the two theoretical curves do not change. The experimental data shows a faster decrease in damage threshold at 0.53 μm than the theoretical curves. A possible explanation for this can be found in the imaginary index of refraction used in the Mie absorption cross-section. The index was picked to fit with a transparent dielectric impurity (n' less than 0.01) at 1.06 μm. For this case the imaginary index of refraction increases with decreasing wavelength. This feature was not included in the theory because of the

lack of knowledge of the impurity composition and concentration. Based on absorption curves for dielectric materials this increase could be expected to be more pronounced at wavelengths shorter than 0.53μm. Without a detailed knowledge of the impurities it is not possible to bound the magnitude of this effect. What can be said is that if the wavelength dependence of the index could have been included in the theory, the curves would also have exhibited a faster drop in the damage threshold at shorter wavelengths.

4. Conclusion

The impurity model, with the Mie absorption cross-section, gives excellent agreement with experimental data. The theory predicts the correct trends of damage threshold with laser pulse length, wavelength, and film thickness. The complete experimental data is presented elsewhere (38). In that paper it was pointed out that the morphology of the damage sites changed with decreasing laser wavelength. In general the site size decreased and the number density of sites increased. In the impurity model this can be attributed to the increase in the Mie absorption of the smaller impurities as the wavelength is decreased. That is, smaller impurites become more likely to damage at shorter wavelengths. Recent research (25, 30) has shown that the number density of impurities increases as the impurity size decreases. This would explain the increase in damage site density. Thus, the impurity model also predicts the correct morphology trends.

5. References

[1] Hopper, R.W. and Ulhmann, D.R., Mechanism of Inclusion Damage in Laser Glass, Appl. Phys. 41, No. 10, 4023,(1970).

[2] Danileiko, Y.K., et al., The Role of Absorbing Inclusions in Laser-Induced Damage of Transparent Dielectrics, Sov. Phys. JETP 36, No. 3, 541,(1973).

[3] Anisimov, S.I. and Makshantsev, B. I., Role of Absorbing Inclusions in the Optical Breakdown of Transparent Media, Sov. Phys. -Solid State 15, No. 4, 743, (1973).

[4] Milam, D., et al.,Laser Damage Threshold for Dielectric Coatings as Determined by Inclusions, Appl. Phys. Lett. 23, No. 12, 654, (1973).

[5] Danileiko, Y. K., et al., Role of Absorbing Defects in the Mechanism of Laser Danage of Real Transparent Dielectrics, Sov. J. Quant. Elect. 4, No. 8, 1005, (1975).

[6] Danileiko, Y. K., et al., Surface Damage of Ruby Crystals by Laser Radiation, Sov. Phys. JETP 31, No. 1, 18, (1970).

[7] Wang, V., et al., Single and Multi-longitudinal Mode Damage in Multilayer Reflectors at 10.6 m as a Function of Spot Size Pulse Duration, Laser Induced Damage in Optical Materials, NBS Special Publication 435, eds. A. J. Glass and A. H. Guenther, US GPO Washington D.C., (1975).

[8] Bettis, J. R., et al., Spot Size and Pulse Dependence of Laser Induced Damage, Laser Induced Damage in Optical Materials, NBS Special Publication 462, US GPO Washington D.C. (1976).

[9] Kovalev, A. A., et al., Dependence of the Damage Threshold of Polymethylmeta-crylate on the Duration of Laser Pulses and Dimensions of Irradiated Region, Sov. Phys. JETP 43, No. 1, 69, (1976)

[10] Sparks, M. and Duthler, C. J., Theory of Infrared Absorption and Material Failure in Crystals Containing Inclusions, J. Appl. Phys. 44, No. 7, 3038, (1973).

[11] Makshantsev, B. I., et al., Effect of Absorbing . Development of Avalanche Ionization, Sov. Phys.-Solid State 16, No. 1, 103, (1974).

[12] R. Austin and A. H. Ledger, Perkin-Elmer, private communications.

[13] Humphreys, T. W., et al., Surface Micro-analysis Technicques for Characterization of Thin Films, to be published in Laser Induced Damage in Optical Materials, (1979).

[14] Sparks, M. and Duthler, C. J. , Theoretical Studies of High-Power Ultraviolet and Infrared Materials, p. 11, Eight Technical Report, (1976).

[15] Zakharov, S. I., et al., Phenomenology of Formation of Shock Waves in the Volume of a Dielectric by a Focused Monopulse, Sov. Phys. Dakl. 19 No. 11, 779, (1975).

[16] Danileiko, Y. K., et al., Prethreshold Phenomena in Laser Damage of Optical Materials, Sov. J. Quant. Elect. 6. No. 2, 236, (1976).

[17] Aleshin, I.V., et al., Optical Breakdown of Transparent Media Containing Micro-inhomogeneities, Sov. Phys. JETP 43, No. 4, 631, (1976).

[18] Libenson, M. N., Plasma-chemical Model for Optical Breakdown of Transparent Dielectrics, Sov. Tech. Phys Lett. 3, No. 5, 180, (1977).

[19] Artem'ev, V.V., et al., Statistics of Micro-scopic Inhomogeneities and Optical Breakdown of Transparent Media, Sov. Phys. Tech. Phys. 22, No. 1, 106, (1977).

[20] Picard, R. H., et al., Statistical Analysis of Defect Caused Laser Damage in Thin Films, Appl. Opts. 16, No. 6, 1563, (1977).

[21] Karpov, O.V., et al., Interaction of Laser Radiation with a Heterogeneous Medium, Zhurnal Prikladnoi Spektroskopii 29, No. 3, 415, (1978).

[22] Lysikov, Y. I., Calculation of the Kinetics of Propagation of a Powerful Light Beam in a Transparent Dielectric with Impurities, Zhurnal Prikladnoi Mekhanikii Tekhnicheskoi Fiziki, No. 5, 60, (1978).

[23] Kosolobov, S. N. , et al., Shock Mechanism for Dissipation of Laser Energy in a Transparent Dielectric with Microscopic Inclusions and Impurities, Sov. Phys. Tech. Phys. 23, No. 9, 1133, (1978).

[24] Kovalev, A. A. and Makshantsev, B. I., Surface Damage Caused by Laser Radiation to Solid Transparent Dielectrics, Sov. J. Quant. Elect. 8, No. 5, 659, (1978).

[25] Artem'ev, V. V., et al., Correlation Between the Radiation Breakdown and Microscopic Inhmogeneities of a Dielectric Coating, Sov. Phys. Tech. Phys. 26, No. 12, 1467, (1978).

[26] Kosolobov, S. N., et al., An Impact Mechanism in Diverting Energy From Absorbing Inclusions at Laser Destruction of Transparent Dielectrics, Opt. Commun. 24, No. 3, 355, (1978).

[27] Morichev, I.E., et al., Laser Breakdown and Temperature Dependence of Absorption in Quartz, Sov. Phys. Tech. Phys. 23, No. 10, 1254, (1978).

[28] Ivanov, L. I., et al., Laws Governing the Formation of Shock Waves Under the Influence of Laser Emission of the Absorbing Solids, Problemy Prochnosti, No. 6, 99, (1978).

[29] Sokolovskiy, R. I., and Tyurin, Y. L., Absorption of Intense Radiation in a Transparent Dielectric Which Contains Microcontaminants, Izvestiya Vysshikh Uchebynkh Zavedeniy Fizika, No. 6(193), 90, (1978).

[30] Leonov, R. K., et al., Methods of Invesitgating the Role of Absorbing Microinclusions in Damage to Transparent Dielectrics by Laser Radiation; I. Passive Methods, Sov. J. Quant. Elect. 8, No. 6, 729, (1978).

[31] Danilieko, Y. K., et al., The Mechanism of Laser-Induced Damage in Transparent Materials Caused by Thermal Explosion of Absorping Inhomogeneities, Sov. J. Quant. Elect. 8, No. 1, 116, (1978).

[32] Van de Hulst, H. C., Light Scattering by Small Particles, John Wiley & Sons, Inc., New York, (1957).

[33] Cook, R. J., and Butts, R. R., Aerosol Induced Thermo-Optical Degredation of a High Intensity Laser Beam, Laser Digest, AFWL-TR-73-273, p. 69, (1973).

[34] Bennett, H. S., and Rosasco, G. J., Resonances in the Efficiency Factors for Absorption: Mie Scattering Theory, Appl. Opts. 17., No. 4, 491, (1978).

[35] Rosasco, C. J., and Bennet, H. S., Internal Field Resonance Structure: Implications for Optical Absorption and Scattering by Microscopic Particles, J. Opt. Soc. Am 68, No. 9, 1242, (1978).

[36] Walker, T. W., Laser Induced Damage to Optical Thin Film Coatings, Ph.D. Thesis, Air Force Institute of Technology, Wight Patterson AFB OH.

[37] Milam, D., 1064-nm Laser Damage Threshold of Polished Glass Surfaces as a Function of the Pulse Duration and Surface Roughness, Laser Induced Damage in Optical Materials, NBS Special Publication 541, US GPO Washington, D. C. (1978).

[38] Walker, T. W., et al., Pulsed Damage Thresholds of Flouride and Oxide Thin Films from 0.26 μm to 1.06 μm, NBS Special Publication 568, US GPO, Washington D. C. (1979).

Figure 1. Comparison of the exact solution of thermal equation No. 5, with approximate solution when q > 4, equation No. 1.

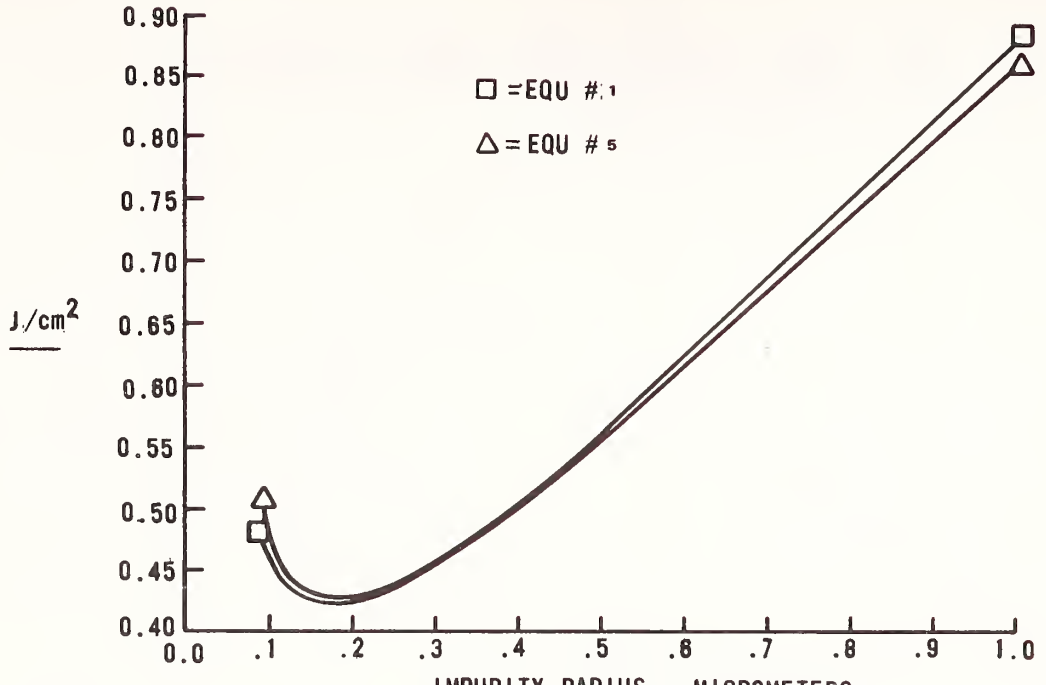

KH - 0.020 TEMP IN K DEG - 2000.0 CP - 2.430 EL - 1.000
KP - 2.380 WL IN UM . 1.06 C- 10.000 D - 0.006 DP- 0.960 Q - 4.198
TIME PULSE- 15 ns

Figure 2. Comparison of the exact solution of thermal equation No. 5, with approximate solution when q > 4, equation No. 2.

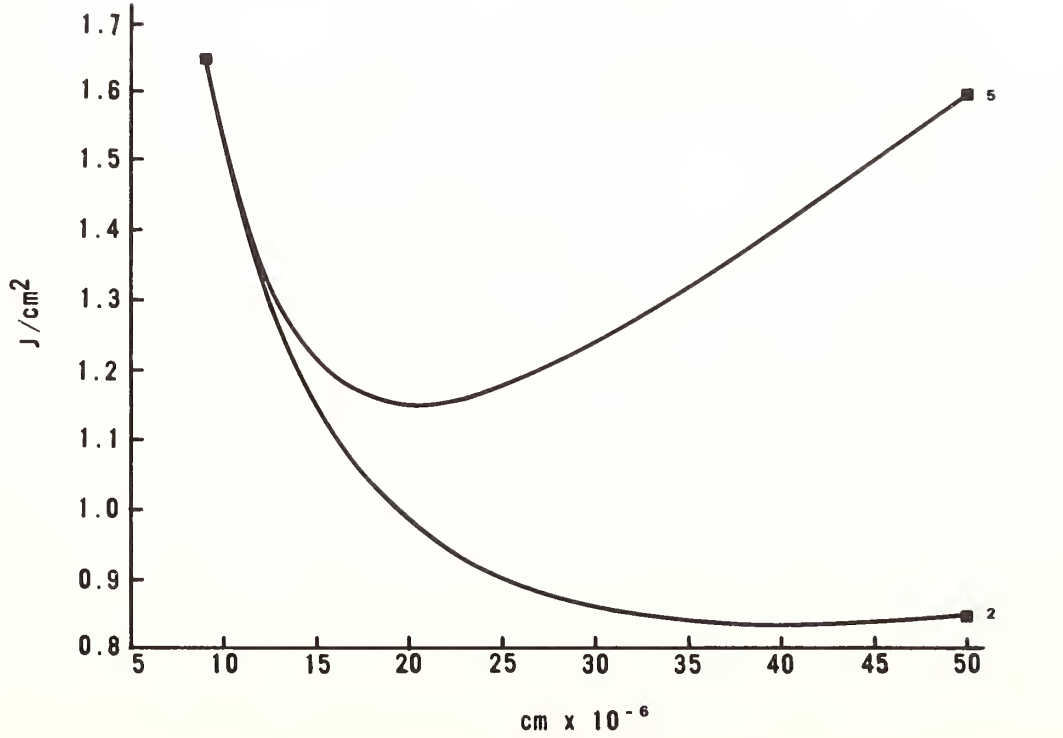

Figure 3. Damage threshold versus film thickness at 1.06 μm laser wavelength

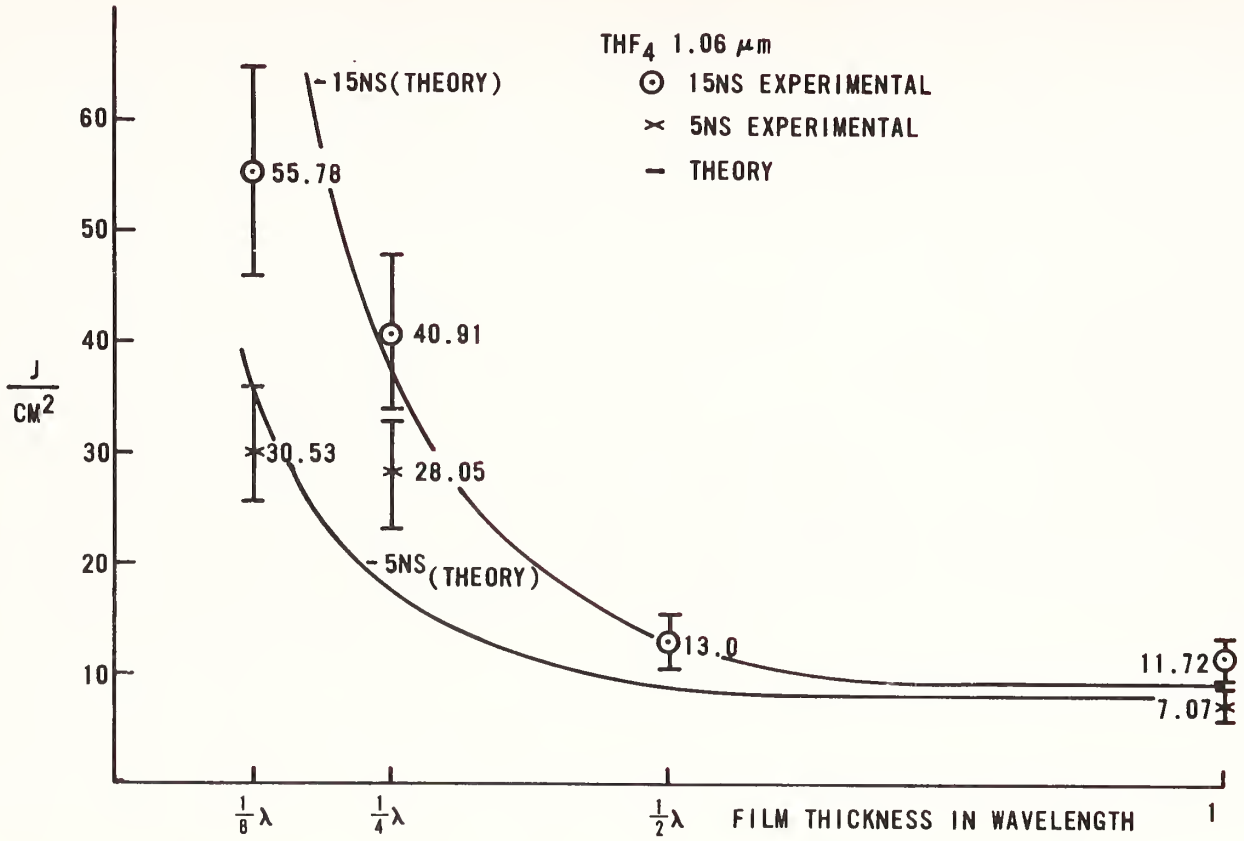

Figure 4. Damage threshold versus film thickness at 0.53 μm laser wavelength

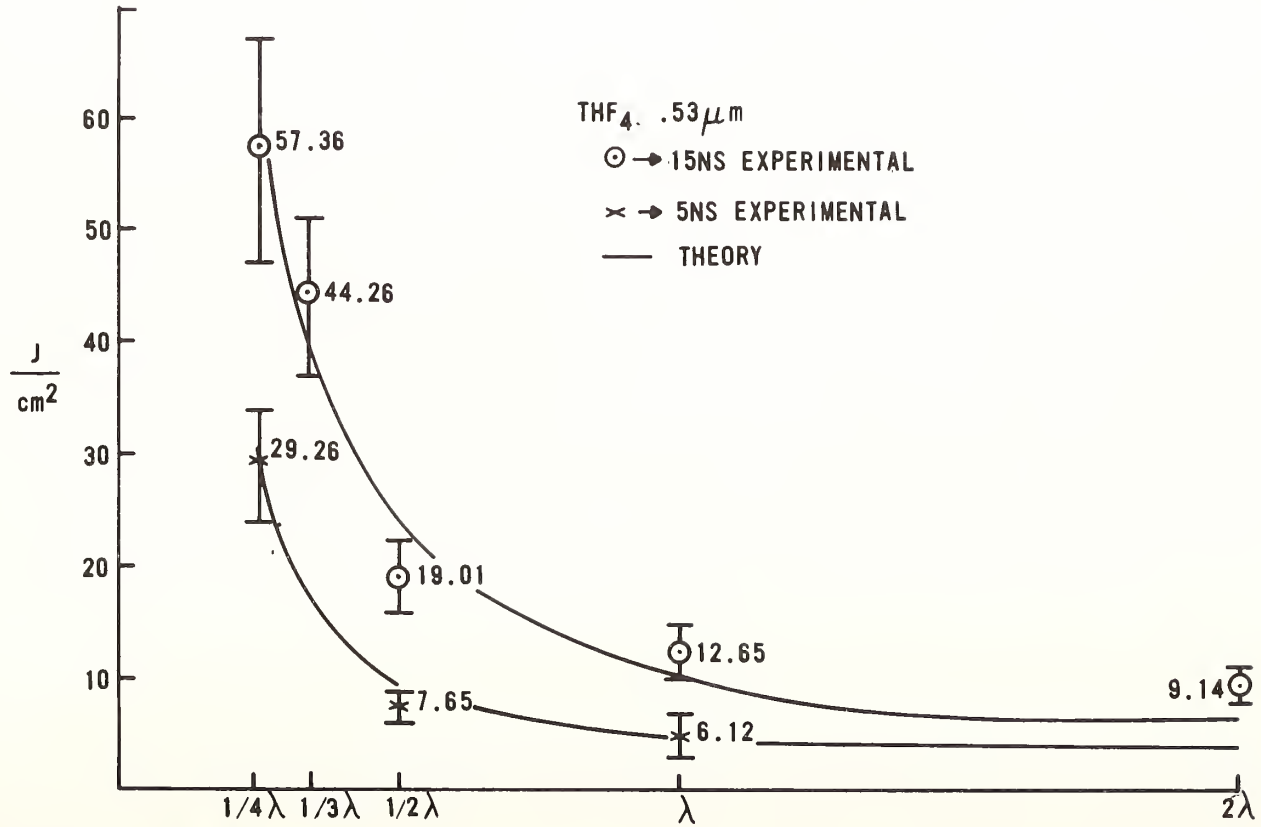

Figure 5. Damage threshold versus film thickness at 0.35 μm laser wavelength

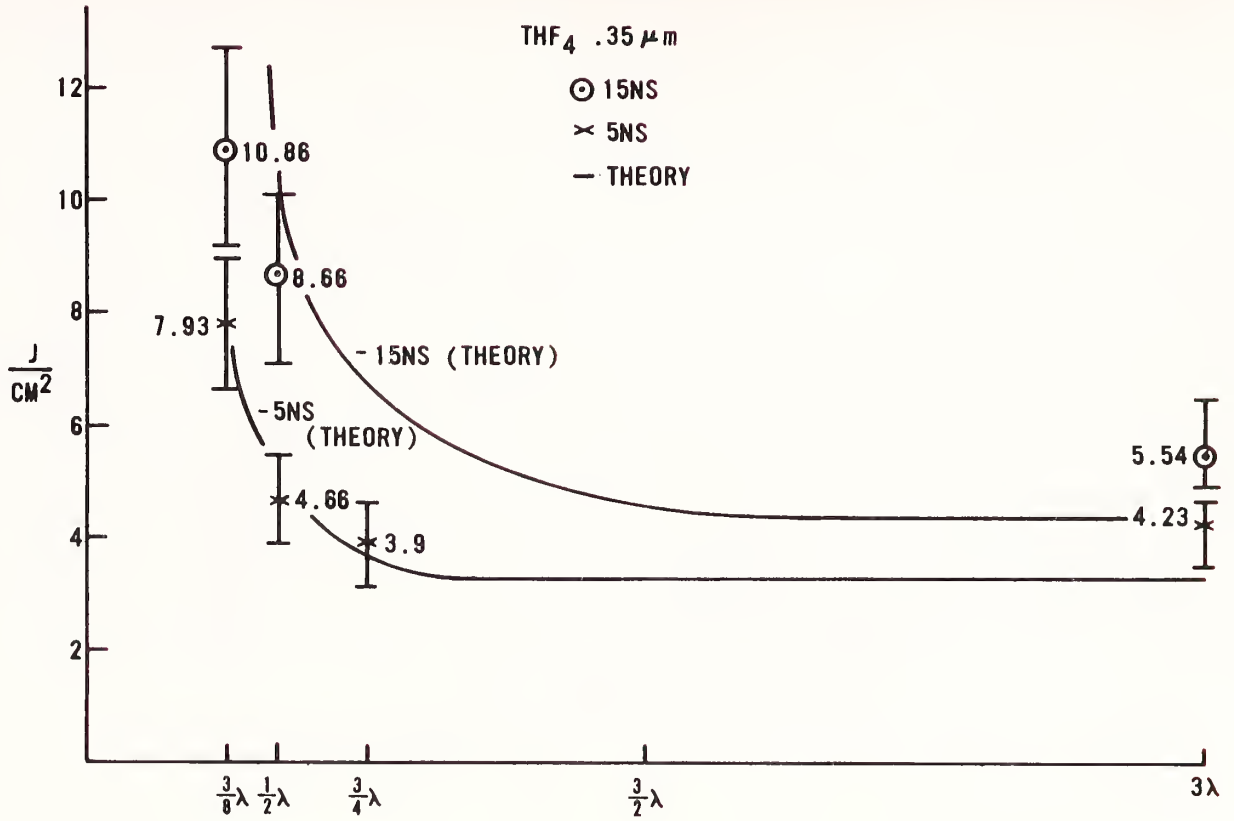

Figure 6. Damage threshold versus film thickness at 0.26 μm laser wavelength

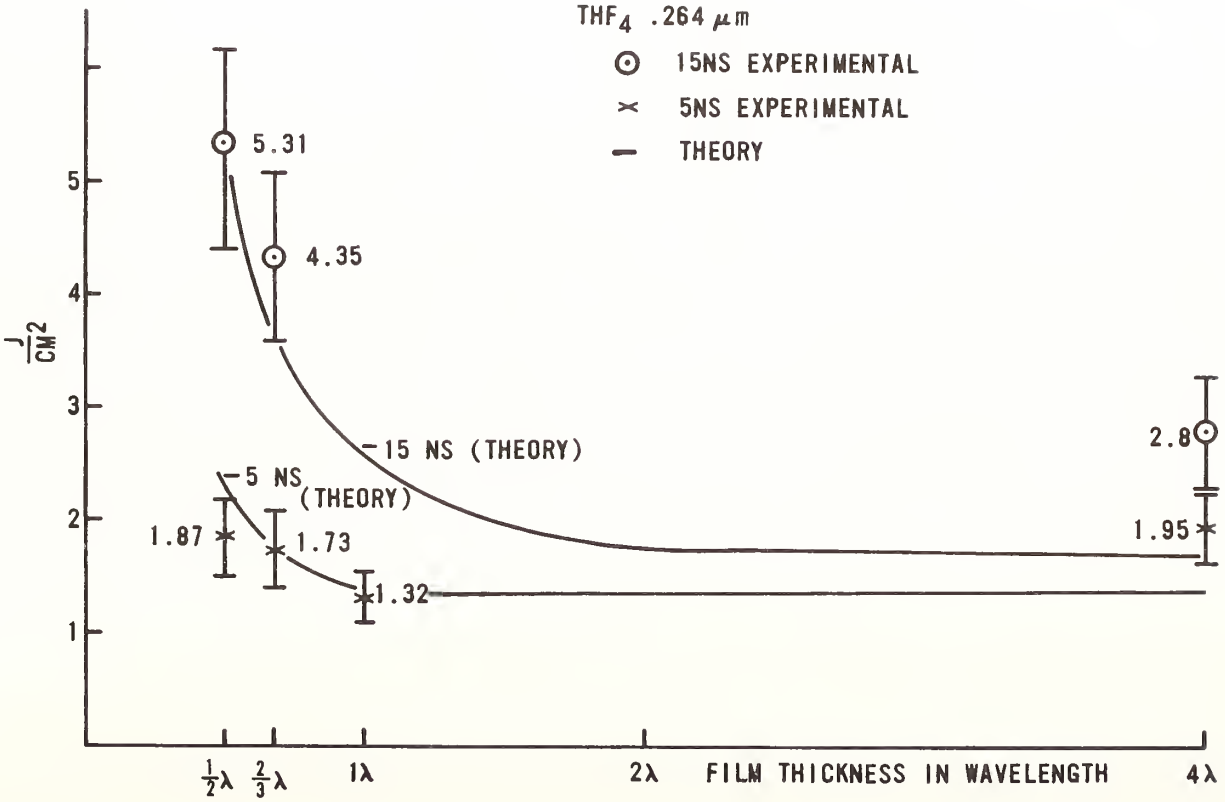

Figure 7. Variation of damage threshold with impurity size for 15ns and 5 ns laser pulses

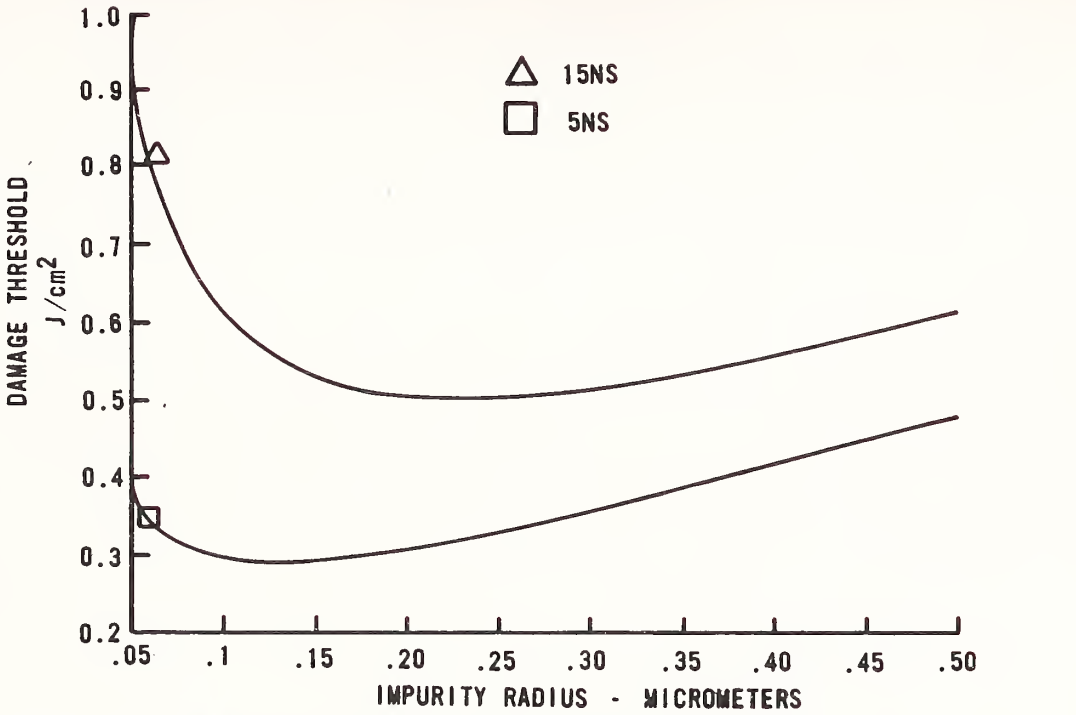

KH - P.PEP TEMP IN K DEG - 2000.0 CP - 2.430 EL - 1.000
KP - 2.360 2.380 WL IN UM - 1.06 C- 3.000 D- 0.010 DP - 0.960 Q - 4.100

Figure 8. Damage threshold of fused silica surfaces as a function of laser pulse length. The solid curve is theory based on equation 5. The data points are taken from Milam, et al. (37).

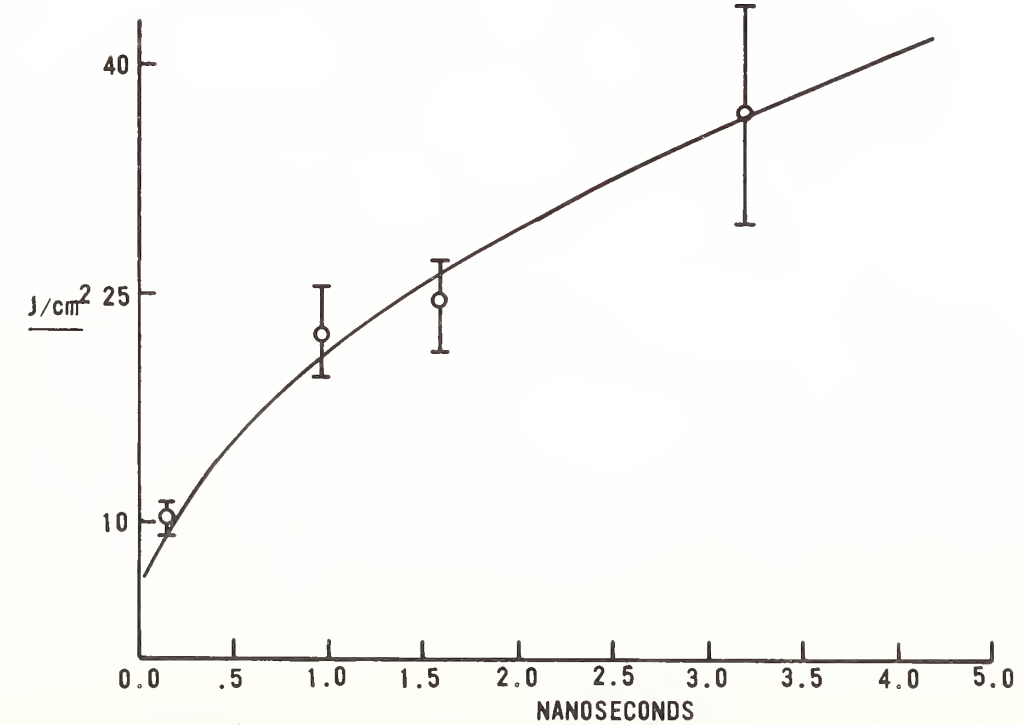

Figure 9. MgF_2 Damage Threshold versus Laser Wavelength.

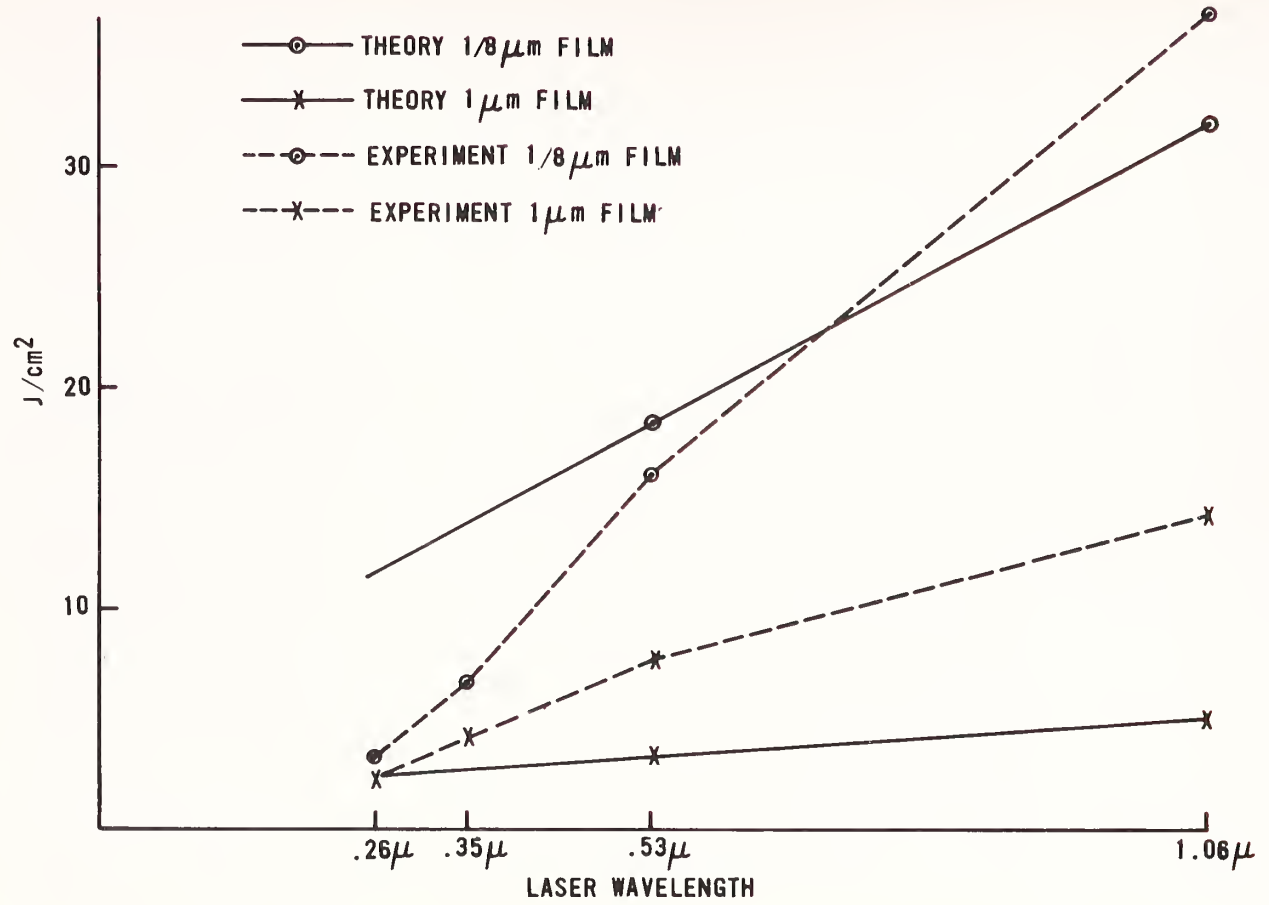

The question was raised about the importance of including the temperature dependence of the thermal diffusivity. It was pointed out that the thermal diffusivity can change by an order of magnitude as a function of temperature in going from room temperature to the damage temperature for thermal damage in the material and that the change can be of either sign. The speaker pointed out that this variation has been included, for example, in the work of Manenkov and his collaborators and that it adds significant complexity to the calculation. The expected spot size dependence of the damage threshold was discussed at length. The speaker indicated that on the basis of the model advanced in this paper, the spot size dependence would be expected to be much weaker in thin films than in bulk materials. He further pointed out that one would not expect to see an absolute correlation between the absorption in the thin film and the observed propensity for damage, because the absorption damage threshold corresponds to the number of particles available at that size most easily damaged, at the pulse duration used in the particular experiment.

FREQUENCY AND FOCAL VOLUME DEPENDENCE OF LASER-INDUCED BREAKDOWN IN WIDE BAND GAP INSULATORS*

M. J. Soileau
Michelson Laboratory, Physics Division
Naval Weapons Center, China Lake, California 93555

M. Bass
Center for Laser Studies
University of Southern California, Los Angeles, California 90007

and

P. H. Klein
Naval Research Laboratory
Code 5222, Washington, DC 20375

The frequency and focal volume dependence of the laser-induced breakdown fields of selected wide band gap insulators were investigated. The breakdown phenomenon that is reported in this work is the same process that has been called "intrinsic" damage by other workers. Measurements were conducted with pulsed (31 to 140 nsec), simple spatial mode lasers at wavelengths of 10.6, 3.8, 2.7, and 1.06 μm. The results indicate that multiphoton-assisted electron avalanche breakdown is a likely mechanism for laser-induced failure in these materials over the wavelength range studied. For small focal volumes, volumes smaller than the inverse of the free electron density, the frequency dependence of breakdown is determined by multiphoton ionization of impurity levels. This initiates an avalanche and leads to the observation that breakdown fields decrease with increased laser frequency. For large focal volumes, the free electrons initially present in the crystal initiate the breakdown, and the frequency dependence is determined by the electron-phonon relaxation time. Thus, for large focal volumes, the laser-induced breakdown fields increase with increasing laser frequency. From these results it is clear that crystal defects and impurities play an important role in what has been called "intrinsic" damage. As this is the case, breakdown experiments cannot be relied upon for accurate measurements of the nonlinear index of refraction, n_2.

Key words: Alkali halides; intrinsic damage; IR windows; laser damage; self-focusing; spot size dependence.

Introduction

The objectives of this work were to examine (a) the frequency dependence of laser-induced breakdown thresholds in alkali halides in a manner that is independent of focal-spot radius, (b) the dependence of the breakdown threshold on focal-spot radius in regions where self-focusing can be discounted, and (c) the potential of improved material processing techniques for increasing the laser damage resistance of highly transparent materials. Threshold measurements were made on specimens from three different classes of material purity at four laser wavelengths (10.6, 3.8, 2.7, and 1.06 μm) and three to seven different focal-spot radii. The measurements obtained from selected alkali halide crystals at different focal volumes were used to establish empirical scaling laws for the breakdown fields of these materials. These scaling laws were then applied to determine the damage threshold as a function of frequency for a common focal volume and to extrapolate the results of small focal volume measurements to the limit of large focal volumes. The results indicate that the dispersion in damage thresholds over the wavelength range of 10.6 to 1.06 μm is a

*Work supported by the Office of Naval Research.

function of the focal volume. At small focal volumes (on the order of 3 to 5 x 10^{-9} cm^3), the laser damage thresholds decrease with decreasing wavelength, while in the limit of large focal volumes (volumes greater than 10^{-4} cm^{-3}), the laser damage thresholds increase with decreasing wavelengths.

The problem of laser-induced breakdown of highly transparent materials has been studied by many workers [1][1] and has been the subject of at least three review papers [2-4]. Electron avalanche breakdown has been suggested as the mechanism of failure for the alkali halides in the 10.6- to 1.06-μm region [5,6]. However, there has been considerable controversy as to the frequency dependence of the laser-induced damage fields in these materials [7]. In experiments where the laser light is focused into the material, a pronounced dependence of the breakdown field on the focal-spot radius has been observed by some workers, while other workers claim no dependence of breakdown field on focal-spot radius. There exist discrepancies in the experimentally determined breakdown thresholds and disagreement as to whether or not the measured breakdown thresholds are intrinsic properties of the materials. These discrepancies and disagreements are discussed in detail in reference [8].

In the present work, the laser-induced breakdown thresholds of alkali halide crystals were measured. The type of damage studied was that which previously had been called intrinsic damage [2-6]. The single-mode output of the irradiation source was focused into the bulk to a very small focal spot so that inclusions and other gross defects in the material could be avoided. Near threshold this type of damage was characterized by (a) a bright flash and fracture at the beam focus and (b) an abrupt truncation of the beam transmitted through the material at or near the peak of the pulse. One conclusion of this work is that this type of failure is dependent upon the defects present in a material. There is some disagreement as to whether or not a property of a material that is related to defects is properly called intrinsic. Therefore, in this work, such failure is referred to as breakdown or laser-induced breakdown.

Specially prepared high-purity specimens were found to have significantly higher damage thresholds than commercially available specimens of the same material when irradiated with small focal volumes. However, in the limit of large focal volume, the damage thresholds for high-purity specimens and the commercially available specimens of a given material tended to converge to a common value. Within a given group of specimens of a specific material from any one vendor, the variation in damage threshold was greatest at longer wavelengths and smaller focal volumes.

In the discussion that follows, we will show that these properties of the damage process are consistent with a mechanism in which the electron avalanche breakdown is initiated by multiphoton ionization of defects. The different wavelength dependences are attributed to the requirement that for small focal volumes the "starter" electrons in the avalanche process must be produced by multiphoton excitation of defect states; whereas, for large volumes, there are generally enough conduction band electrons present to initiate the avalanche process.

Experimental

The basic experimental arrangement used in this work is shown in figure 1. A detailed description of the experimental procedures and lasers used in this work are given in references [7] and [8]. The occurrence of laser-induced breakdown was determined by (a) viewing a change in scattering of a coaxial HeNe beam in a 20-power microscope, (b) observing a visible flash and/or fracture in the sample, and (c) monitoring the transmitted waveform distortion (see fig. 2). In this work it was found that all three of these effects occurred simultaneously, i.e., when damage occurred, the HeNe laser scatter increased, a visible flash and fracture was observed, and the transmitted waveform was abruptly truncated. The threshold for failure was defined as that flux which produced damage in 50% of the sites when each site was irradiated only once. Each site was irradiated only once, and only bulk damage thresholds were measured.

[1] Figures in brackets indicate the literature references at the end of this paper.

At 10.6, 3.8, and 2.7 μm, the focal-spot radius was varied by focusing with three different focal length lenses. The lenses used and the resultant measured focal-spot radii ($1/e^2$ intensity points) are summarized in table 1. The same single-element ZnSe miniscus lenses (which were designed for minimum spherical aberrations) were used at the three wavelengths.

Table 1. Measured focal-spot radii for 10.6-, 3.8-, and 2.7-μm experiments.

Lens No.	Focal length at 10.6 μm (cm)	Lens diameter (cm)	Focal spot radius ($1/e^2$ in intensity)(μm)		
			HF (2.8 μm)	DF (3.8 μm)	CO_2 (10.6 μm)
1	2.54	2.54	9.55	10.60	20.50
2	6.35	2.54	12.55	13.55	45.00
3	12.70	5.08	26.50	28.50	85.00

The focal-spot radius was varied at 1.06 μm by varying the distance between the focusing lens and the cavity waist (this quantity is designated Z_3) and by using lenses of different focal lengths. The 1.06-μm laser was operated in the TEM_{00} mode (Gaussian intensity distribution), and the focused spot was diffraction limited. As a result, the focal-spot radius could be varied in a linear fashion by varying Z_3. All the alkali halide specimens were tested at three different spot sizes. Selected specimens were tested at four additional spot sizes. The focal-spot radii used and the relevant beam parameters are summarized in table 2. A detailed description of the techniques used to measure the focal-spot radii is given in reference [8].

Table 2. Focal-spot radii for the 1.06-μm experiments.

Lens No.	Focal length at 1.06 μm (cm)	Lens diameter (cm)	Focal-spot radius ($1/e^2$ in intensity) (μm)
1	5.0	1.0	5.00 5.33 5.64 6.15[a,b] 10.29[a]
2	8.0	1.5	19.29[a] 22.83[b]

[a] Indicates focal radius at which all specimens were measured.
[b] Indicates measured values of focal radius. These were found to be equal to the values calculated from Gaussian optics.

The average pulse widths used in these experiments were 90, 80, 120, and 31 nsec for the 10.6-, 3.8-, 2.7-, and 1.06-μm lasers, respectively [8]. Since the pulse widths are not the same for all the data points, one might question whether the data are pulse-width dependent for this pulse-width region. There is some dispute about the pulse-width dependence for pulse widths of the order of several to hundreds of nanoseconds. Some workers claim there is a dependence [9], and others claim no dependence on pulse width [10,11]. We tested specimen 78-NC-6 at 10.6 μm with t_p = 60 nsec and t_p = 107 nsec. The resulting thresholds were the same to within ±3.5%, which was well within experimental error. Thus, we found no pulse-width dependence for these experimental conditions.

Three classes of alkali halide crystals were examined in this work: (1) spectroscopic-grade material from the Harshaw Chemical Company[2], (2) laser-grade material from the Harshaw Chemical Company, and (3) reactive-atmosphere-processed (RAP) [12] material from the Naval Research Laboratory[3]. The RAP crystals were grown by the Bridgeman method. Gettered argon was the cover gas, and carbon tetrachloride vapor was used for reaction with oxygen-containing anions. The OH^- content was approximately 40 to 65 parts per billion, as determined by vacuum ultraviolet spectroscopy[3]. Several single-crystal specimens of NaCl, KCl, and KBr from each group were tested.

Manenkov [13] has reported that in testing 100 randomly selected NaCl specimens, approximately 20% had significantly higher damage thresholds. He suggested that these exceptional specimens were displaying failure due to an intrinsic process. The specimens used in this work were carefully screened prior to damage testing in order to maximize the chances of seeing exceptional specimens of the type measured by Manenkov. Only specimens satisfying the following criteria were used as specimens for this work: (1) No observable absorption bands in the 0.5- to 10.6-μm range, (2) residual absorption of the order of 10^{-3} cm^{-1} or less measured by laser calorimetry [8], and (3) no visible scattering centers when viewed with a 20-power microscope with HeNe laser illumination (0.6328 μm).

Data

The frequency and focal-spot radius dependence of the laser-induced breakdown intensity thresholds of RAP-grown NaCl are given in figure 3. The trends in frequency and focal radius dependence shown in figure 3 are the same for the Harshaw spectroscopic and laser-grade NaCl and for the three classes of KCl and KBr tested. The peak on-axis intensity (I_B), the rms electric field (E_B), and the peak power at the damage threshold for all the specimens tested are tabulated in the Appendix. The quantity w_o given in figure 3 and the Appendix is the radius of the focused beam corresponding to the $1/e^2$ points of the intensity. The values given for the quantities w_o, I_B, and E_B do not include any corrections for the effects of self-focusing. Self-focusing does not enter in these experiments for the reasons discussed in reference [8].

Inspection of figure 3 reveals that there is a distinct dependence of laser damage threshold on the radius of the focal spot (w_o) used to irradiate the specimens. As is shown in figure 3, the measured intensity thresholds can be fit by a linear dependence on the effective focal volume (V),

$$I(\lambda, w_o) = a[V(\lambda, w_o)]^{-1} + b \qquad (1)$$

In the above equation, the effective focal volume (which is porportional to w_o^4/λ) is chosen to be the volume for which the intensity drops to 0.80 of the peak on-axis intensity. The "effective" focal volume is then computed using the method derived by Fradin et al. [14].

Note that the focal volume dependence was strongest at longer wavelengths (see fig. 3 and the Appendix). This type of behavior is consistent with the model discussed in the following section, which assumes that damage is initiated by the most easily ionized defect within the focal volume. The defect is thought to initiate an avalanche by providing a conduction band electron through multiphoton ionization. As the focal volume gets larger, the probability of finding a defect which can be ionized by a lower order multiphoton process, and thus lower intensity, increases. At shorter wavelengths, the probability for ionization of a defect can be much higher for a given order multiphoton process. If one assumes that the density of defects is proportional to the ionization potential, then one would expect a focal volume dependence until a volume is reached that gives high probability of finding a defect that can be ionized by a low order process. The volume at which this occurs would be smaller at higher photon energies, as is observed in this work.

---

[2] Harshaw Chemical Co., 6801 Cochran Rd., Solon, OH 44139.

[3] The RAP-grown materials were supplied by Dr. P. H. Klein, who performed the vacuum ultraviolet characterization of the OH^- concentration in the crystals.

Discussion of Results

The frequency dependence of the laser-induced breakdown thresholds at constant focal volume was analyzed in the context of the avalanche breakdown model[4]. In the electron avalanche model the number of conduction band (or nearly free) electrons increases with time as [2-4]

$$N(t) = N_o \exp \int_o^t \alpha(E(t'))dt' \quad , \tag{2}$$

where N_o is the density of electrons present at the start of the avalanche, $\alpha(E(t'))$ is the ionization rate, and $E(t')$ is the rms electric field. The rate of energy absorbed by the plasma is given by

$$W(t) = \frac{e^2\tau_c}{m^*} \frac{|E(t)|^2 N(t)}{1 + \omega^2\tau_c^2} \quad , \tag{3}$$

where m^* and e are the electron effective mass and charge, ω is the laser angular frequency, and τ_c is the electron relaxation time.

Yablonovitch [5,6] initially proposed that N_o was the density of free electrons present in the material prior to laser illumination, and that the frequency dependence was due to the $1/(1 + \omega^2\tau_c^2)$ term in eq. (3). Sparks [20] pointed out that the value of N_o estimated by Yablonovitch was much too large, and that for more realistic values of N_o the probability of finding an initially free electron in small focal volumes used in experiments by Yablonovitch [5,6], Fradin [21,11], and other workers was essentially zero. Thus, one must generate the starting electrons which lead to electron avalanche breakdown.

Multiphoton ionization of defects within the gap has been suggested by several workers as the source of the starting electrons (N_o) in the electron avalanche. It will be demonstrated in the derivation which follows that this mechanism gives a frequency dependence of the breakdown field consistent with the experimental results of this work.

Consider focal volumes which are small relative to the inverse density of free electrons naturally present in the lattice. Suppose, as was suggested by Milam [22], that for "intrinsic-like" damage there is a crystal defect of ionization energy ε_D such that

$$\varepsilon_L < \varepsilon_D < \varepsilon_G \quad , \tag{4}$$

where ε_L is the laser photon energy, and ε_G is the band gap energy. The defect is assumed to be uniformly distributed throughout the material with density η. The number of free electrons generated by n-photon absorption from these defects is

$$N_o = \eta\gamma^n E^{2n} \quad , \tag{5}$$

where $n = \langle \varepsilon_D/\varepsilon_L \rangle$ is the integer part of $\varepsilon_D/\varepsilon_L$, and γ is a numerical constant proportional to the matrix elements of the intermediate states. It should be emphasized that eq. (5) is a simplification, but the key functional dependence on E of the n-photon absorption is correct. The quantity $\gamma^n E^{2n}$ is the probability that a single electron will be raised above the band gap and is, therefore, always ≤ 1, as is $\sqrt{\gamma}\,E$.

---

[4] The electron avalanche models used to analyze the laser-induced breakdown experiments all have as their origin the dc breakdown experiments of Von Hipple [15] in 1937 and subsequent analysis prior to 1950 of this work by Frölich [16], Seitz [17], and Callen [18]. O'Dwyer [19] has compiled a monograph which summarizes the "pre-laser" work on dielectric breakdown in solids.

We define $\phi(E)$ as

$$\phi(E) = \int_0^{t'} \alpha(E(t))dt \quad . \tag{6}$$

Substitution of eqs. (5) and (6) into eq. (3) gives

$$W(t) = \frac{e\tau_c}{m^*} \frac{|E(t)|^2 \eta_\gamma n_E 2n_e \phi(E)}{(1 + \omega^2\tau_c^2)} \quad . \tag{7}$$

If we assume that $\varepsilon_L << \varepsilon_D$, then $n = \langle \varepsilon_D/\varepsilon_L \rangle$ is much larger than one. For large n, the absorbed energy and thus the laser damage threshold dependence on laser frequency will be dominated by the quantities containing exponential and power dependence of ε_L and E. This means that for defects with relatively high ionization energy, the frequency dependence of the breakdown field is just the frequency dependence of the free electron density.

The temporal dependence of the electron density enters through the exponential dependence of the ionization rate. The breakdown process is known to occur very rapidly, within the 1 nsec response time of the detectors used in this work and within 5 psec for laser pulse widths of the order of 25 psec [23]. Thus, one can assume E = constant; hence, $\alpha(E)$ is constant over the breakdown time, t_B. This permits ϕ to be simplified as

$$\phi = \int_0^t \alpha(E(t))dt' \doteq \alpha(E)t_B \quad . \tag{8}$$

Careful analysis of the pulses transmitted through the specimens indicates that little attenuation of the laser beam occurs until the rapid breakdown process produces a critical density, N_c. The critical density occurs when the plasma frequency equals the laser frequency. The frequency dependence of N_c must be included in the analysis of the frequency dependence of the breakdown process.

The critical density is related to the laser frequency by

$$N_c = \frac{\omega_p^2 m^* \varepsilon_o}{e^2} = \frac{(\hbar\omega_2)^2 m^* \varepsilon_o}{\hbar^2 e^2} = \varepsilon_L^2 B \quad , \tag{9}$$

where $B = (m^*\varepsilon_o)/(\hbar^2 e^2)$ is a constant for each material.

Equating eq. (9) with the right-hand side of eq. (2), taking the natural log of both sides, and rearranging terms gives

$$\phi = 2 \ln \left[\varepsilon_L \frac{\sqrt{B}}{\eta} \right] - 2n \ln(\sqrt{\gamma}E) \quad . \tag{10}$$

Recall that $\sqrt{\gamma}E$ is less than one, and thus the $\ln(\sqrt{\gamma}E)$ is negative. As a result, the above equation can be rewritten as

$$\phi = 2 \ln \left[\varepsilon_L \frac{\sqrt{B}}{\eta} \right] + 2 \frac{\varepsilon_D}{\varepsilon_L} |\ln(\sqrt{\gamma}E)| \quad . \tag{11}$$

The exact form of the ionization rate, $\alpha(E)$, is not known. It will be shown that the exact form of $\alpha(E)$ is not important to this analysis as long as $\partial\alpha/\partial E > 0$. A fit to the experimental data of Fradin et al. [24] gives

$$\alpha(E) = A_o E^{3.133} \quad , \tag{12}$$

where A_o = a constant over the range of laser fields of interest (1 to 10 MV/cm). Fradin's expression in eq. (11) gives

$$E^{3.133} = A \ln\left[\varepsilon_L \frac{\sqrt{B}}{\eta}\right] + 2\left\langle\frac{\varepsilon_D}{\varepsilon_L}\right\rangle |\ln(\sqrt{\gamma}E)| \quad , \tag{13}$$

where $A = 2/(t_B A_0)$ = a constant.

Note that eq. (13) contains terms in E and ε_L raised to powers, as well as natural log terms in the same quantities. The $\ln(\sqrt{\gamma}E)$ term varies slowly with E relative to $E^{3.133}$. Similarly, the $\ln[\varepsilon_L(\sqrt{B}/\eta)]$ term varies slowly relative to the $1/\varepsilon_L$ term. A common approximation in such situations is to set the natural log terms equal to constants [25]. In the approximation that the natural log terms are constant relative to $E^{3.133}$ and $1/\varepsilon_L$, eq. (13) gives

$$E^{3.133} = a + \frac{b}{\varepsilon_L} \quad , \tag{14}$$

where a and b are constants.

The important feature of eq. (14) is that the breakdown field decreases as laser frequency (photon energy) increases, and the frequency dependence is not very strong. This behavior is consistent with the results of laser breakdown measurements in this work for small focal volumes. The laser breakdown fields for RAP-grown NaCl are plotted in figure 4, as is the least squares fit of the data to eq. (14). Similar results were obtained for other materials studied in this work [8].

We have just shown that for small focal volumes the breakdown field decreases with increasing laser frequency. We now consider the limit of large focal volume. For this case, there are a large number of free electrons present within the focal volume. The measured breakdown fields are considerably lower than for the case of small focal volume. The low thresholds at larger volumes mean that the probability of high-order multiphoton effects is diminished. The rate of energy absorption by the specimen is given by

$$W(t) = \frac{e^2\tau_c}{m^*} \frac{|E(t)|^2 N_o e^{\int^t \alpha(E(t))dt'}}{(1 + \omega^2\tau_c^2)} \quad . \tag{15}$$

If we assume, as before, that the breakdown occurs as N_c is approached and occurs very rapidly (so that E(t) = E, a constant), then eq. (9) gives

$$N_c = B\varepsilon_L^2 = N_o e^{\alpha(E)t_B}$$

or

$$\alpha(E) = \frac{2}{t_B}\ln \varepsilon_L + \frac{2}{t_B}\ln B - \frac{1}{t_B}\ln N_o \quad . \tag{16}$$

The above analysis indicates that the field needed to produce the critical density for this situation is only weakly dependent on the laser frequency, and the frequency dependence of the breakdown field will be determined by the $\omega^2\tau_c^2$ term in eq. (15). This equation can be recast in the form

$$E_B = E_o(1 + \omega^2\tau_c^2)^{1/2} \tag{17}$$

or

$$\frac{1}{E_B^2} = \frac{1}{E_o^2} - \left(\frac{\omega^2}{E_B^2}\right)\tau_c^2 \quad , \tag{18}$$

where E_o = dc breakdown field.

The data from this work for the limit of large focal volumes can be fit to eq. (18) to obtain an estimate of E_o and τ_c. The results are given in table 3. The frequency dependences of the breakdown fields in RAP-grown NaCl for the large focal volume limit are plotted in figure 5.

Table 3. Estimates of relaxation time and dc. Breakdown fields for RAP-grown NaCl, KCl, and KBr.

Material	Relaxation time ($\times 10^{-15}$ sec)	Estimated dc breakdown field (MV/cm)	Measured dc [15] breakdown field (MV/cm)
RAP:NaCl	1.15	1.69	1.50
RAP:KCl	1.56	1.20	1.01
RAP:KBr	1.22	0.82	0.69

The value of τ_c given in table 3 for NaCl is in fair agreement with the calculations by Sparks [20] ($\tau_c \sim 1.4 \times 10^{-15}$ sec) and with the values suggested by Manenkov [13] ($\tau_c \sim 1.67 \times 10^{-15}$ sec). The extrapolated dc breakdown fields are in reasonable agreement with those measured by Von Hipple [15]. However, one should not put much emphasis on this agreement since the materials used in the dc measurements were different as were the sources of systematic error (e.g., space charge effects in the dc measurements).

Conclusions

Measurements were made of the wavelength and focal volume dependence of laser-induced breakdown thresholds in selected wide band gap materials. The damage irradiations were performed at 10.6, 3.8, 2.7, and 1.06 μm over a factor of 10^4 range in focal volumes. The results indicate that the dispersion in damage thresholds over the 10.6- to 1.06-μm wavelength range is a function of focal volume. At small focal volumes (3 to 5 $\times 10^{-9}$ cm^3), the laser damage thresholds decrease with decreasing laser wavelengths, while in the limit of large focal volumes ($> 10^{-4}$ cm^3) the laser damage thresholds increase with decreasing laser wavelengths. Variations in damage thresholds among specimens of a specific material were found to be greatest at longer wavelengths and smaller focal volumes. High-purity RAP materials were found to have substantially higher breakdown thresholds for small focal volumes than commercially available specimens of the same materials but had essentially the same breakdown thresholds as the commercially available materials in the limit of large focal volumes.

This type of behavior is consistent with a multiphoton-assisted electron avalanche breakdown model. The different wavelength dependences are due to the requirement that for small focal volumes the "starter" electrons in the avalanche process must be produced by multiphoton excitation of defect states; whereas, for large focal volumes, conduction band electrons initially present initiate the avalanche process.

All the results reported in this work are for what has been called "intrinsic" damage, i.e., damage that occurs at or near the peak of the laser pulse (near threshold), abruptly truncates the beam transmitted through the specimen, and produces a bright flash and fracture at the focal point of the laser. These results indicate that such events are not intrinsic properties of the materials. We found substantial variations in the laser breakdown thresholds among samples of a given material from a given supplier. Even larger variations were found among specimens of a given material from different suppliers. Factors of two variations in breakdown threshold were sometimes found in measurements made in different positions in a given specimen. These results are consistent with what has been reported by Olness [26,27], Leung et al. [28], Allen et al. [29], Yasojima et al. [30,31], Manenkov [13], and Soileau et al. [32]. Such variations in breakdown thresholds are inconsistent with the results of Bloembergen [2], Fradin [3], Smith [4], and Yablonovitch [5]. However, careful reading of Yablonovitch's thesis [5] indicates that he too found variations of as much as a factor of two in the breakdown threshold in some materials tested at 10.6 μm. Comparison of the results of this work for Harshaw laser-grade NaCl with that reported in references [5] - [7] and [10] for similar focal volumes reveals that breakdown thresholds agree to within experimental error. Thus, one may conclude that most of the discrepancies in laser breakdown thresholds found in the literature are due to real variations in laser damage thresholds among specimens of a given material and the dependence of the breakdown threshold on focal volume. The laser breakdown thresholds among the RAP-grown alkali halides tested were systematically higher for the higher band gap materials. However, this

correlation of damage thresholds with band gap was not maintained for all specimens tested. For example, the Harshaw laser-grade NaCl laser-induced breakdown threshold at 1.06 μm was 15% lower than that for Harshaw laser-grade KCl.

The technique used by Zverev [33], Fradin [34], and Smith et al. [35] (ZFS) to measure n_2 and the laser-induced breakdown intensity, I_m, is inconsistent with the results of this work. This inconsistency is due to the focal volume dependence of I_m (assumed to be constant in the ZFS procedure). The results of this work indicate that self-focusing does not play a role in damage experiments performed with tightly focused beams. A possible explanation for the lack of observed self-focusing effects is that negative changes in refractive index due to the prebreakdown free electron plasma cancel the positive change in refractive index due to electrostriction and bound electronic effects (see references [8], [36], and [37]).

The focal radius dependences determined in this work are believed to be associated with the densities of defects in the materials having different ionization potentials. Thus, the dependences are not expected to be universally true. Recent results by Gomelauri et al. [38] indicate that there is no focal radius dependence for the alkali halides at 2.7 μm for focal radii from 14 to 24 μm, while in this work a factor of two variation of breakdown intensity was found over this focal radius range.

APPENDIX

Summary of Damage Measurements

Single-pulse laser damage measurements were made on selected specimens of single-crystal NaCl, KCl, and KBr. Specimens included two classes of commercially available material and RAP materials. Damage thresholds were measured as a function of the irradiated volume at 10.6, 3.8, 2.7, and 1.06 μm. The results of these measurements are summarized in tables 1 - 7. Listed in these tables are the average values (denoted by $\langle\ \rangle$) of the peak on-axis intensity breakdown thresholds, $\langle I_B \rangle$, the rms electric fields, $\langle E_B \rangle$, corresponding to $\langle I_B \rangle$, and the peak power (P_B) of the breakdown thresholds. The quantity w_o is the radius of the focused beam corresponding to the $1/e^2$ points of the intensity. The quantities w_o, $\langle I_B \rangle$, and $\langle E_B \rangle$ listed in tables 1 - 7 do not include any effects of self-focusing.

Table 1. Average breakdown thresholds for RAP-grown NaCl.

λ(μm)	w_o(μm)	$\langle I_B \rangle$ (GW/cm^2)	$\langle E_B \rangle$ (MV/cm)	P_B(MW)
10.6	20.5	95.70	4.92	1.26
	45.0	10.86	1.66	0.69
	90.0	$\geqslant$ 6.67	$\geqslant$ 1.30	2.23
3.8	10.6	97.43	4.95	0.34
	13.55	65.11	4.04	0.38
	28.5	31.03	2.79	0.79
2.7	9.55	66.08	4.07	0.19
	12.55	36.58	3.03	0.18
	26.5	28.33	2.67	0.63
1.06	6.15	101.0	4.99	0.12
	10.29	60.20	3.85	0.20
	19.29	54.22	3.69	0.64
	22.83	54.79	3.70	0.90
	5.0	175.0	6.57	0.14
	5.33	126.0	5.57	0.13
	5.64	125.0	5.56	0.12

Inspection of tables 1 - 7 reveals that there is a distinct dependence of laser damage threshold on the radius of the focal spot used to irradiate the specimens. The size dependence is seen in all specimens tested, whether they failed by breakdown processes or thermal processes. Since the object of this work was to study breakdown processes, we will concentrate on the size dependence of breakdown-like events.

There is no question that there exists a size dependence for breakdown-like events. The evidence for such effects is overwhelming. In this work over an order of magnitude of photon energies for air breakdown, high threshold, and low threshold materials has been observed. Breakdown-like events are those events characterized by (at threshold) (a) always occurring at the focal point, (b) truncation of the transmitted pulse within the detector response time ($\sim$ 1 nsec), and (c) a bright visible flash. There are several plausible physical arguments that could explain observed size dependence, and these are examined in turn in the discussions that follow.

Since much of the data can be fit to a quadratic dependence on focal-spot radius, one concludes that the threshold was peak power dependent, thus indicating that self-focusing was dominating the results. This is fairly easy to discount by several arguments. First, the size dependence levels off or disappears entirely as one goes to larger spot sizes.

Table 2. Average breakdown thresholds for RAP-grown KCl.

$\lambda(\mu m)$	$w_o(\mu m)$	$\langle I_B \rangle$ (GW/cm^2)	$\langle E_B \rangle$ (MV/cm)	P_B(MW)
10.6	20.5	74.73	4.41	.99
	45.0	6.36	1.29	.41
	90.0	$\geqslant$ 5.0	$\geqslant$ 1.14	1.45
3.8	10.6	103.0	5.17	.36
	13.55	45.0	3.42	.26
	28.5	20.13	2.29	.51
2.7	9.55	45.5	3.44	.13
	12.55	29.5	2.77	.15
	26.5	15.83	2.03	.35
1.06	6.15	66.78	4.17	0.079
	10.29	51.32	3.65	0.17
	19.29	38.13	3.15	0.45
	5.0	124.0	5.68	0.097
	5.33	109.0	5.31	0.11
	5.64	97.0	5.02	0.097

Table 3. Average breakdown thresholds for RAP-grown KBr.

$\lambda(\mu m)$	$w_o(\mu m)$	$\langle I_B \rangle$ (GW/cm^2)	$\langle E_B \rangle$ (MV/cm)	P_B(MW)
10.6	20.5	29.9	2.64	0.40
	45.0	4.12	0.98	0.26
	90.0	$\geqslant$ 2.82	$\geqslant$ 0.81	0.88
3.8	10.6	69.6	4.15	0.25
	13.55	35.8	2.96	0.21
	28.5	6.33	1.25	....
2.7	9.55	41.5	3.19	0.12
	12.55	15.7	1.96	0.78
	26.5	5.01	1.11	0.11
1.06	6.15	47.1	3.33	0.056
	10.29	25.2	2.40	0.084
	19.29	15.8	1.91	0.185

Self-focusing would have given the opposite type behavior, i.e., there would have been little or no spot size dependence for small spots where low total power was required for damage. For large spots requiring high total power, the spot size dependence would have saturated at a quadratic dependence. Higher threshold specimens would have shown this quadratic dependence for the smallest spot sizes. Exactly the opposite type behavior was observed in these experiments. As the focal spot sizes were increased, the dependence of threshold intensity on the focal-spot radius decreased and in some cases disappeared. Specimens with the highest threshold at 1.06 μm had the smallest size dependence, e.g., the RAP NaCl samples. These discussions of the role of self-focusing in these experiments are made more quantitative in reference [8], where self-focusing is discussed in detail.

The influence of thermal diffusion can be ruled out. First, even for the smallest spots, the thermal diffusion distance (the distance heat deposited in the center of the beam diffuses during the laser pulse) is 1/10 the focal radius and would contribute, at

Table 4. Average breakdown thresholds for Harshaw spectroscopic-grade NaCl.

$\lambda(\mu m)$	$w_o(\mu m)$	$\langle I_B \rangle$ (GW/cm^2)	$\langle E_B \rangle$ (MV/cm)	P_B(MW)
10.6	20.5	73.4	4.31	0.97
	45.0	11.17	1.68	0.71
	90.0	> 4.11	> 1.02	> 1.05
3.8	10.6	94.6	4.87	0.34
	13.55	72.9	4.27	0.42
	28.5	24.7	2.49	0.63
2.7	9.55	58.0	3.81	0.17
	12.55	50.8	3.57	0.25
	26.5	24.7	2.49	0.55
1.06	6.15	66.7	4.05	0.079
	10.29	43.5	3.27	0.15
	19.29	33.1	2.85	0.39

Table 5. Average breakdown thresholds for Harshaw laser-grade NaCl.

$\lambda(\mu m)$	$w_o(\mu m)$	$\langle I_B \rangle$ (GW/cm^2)	$\langle E_B \rangle$ (MV/cm)	P_B(MW)
10.6	20.5	39.7	3.17	0.52
	45.0	9.06	1.51	0.58
	90.0	> 4.11	> 1.02	1.68
3.8	10.6	65.59	4.06	0.23
	13.55	45.33	3.37	0.26
	28.5	17.7	2.11	0.45
2.7	9.55	61.03	3.92	0.18
	12.55	35.60	2.99	0.18
	26.5	16.83	2.06	0.37
1.06	6.15	27.65	2.61	0.033
	10.29	14.93	1.92	0.050
	19.29	12.04	1.72	0.151

most, a 20% variation in threshold with spot size. Second, most of the specimens tested failed at the peak of the pulse near threshold. Thermal failure would have occurred at the end of the pulse near threshold.

Diffusion of hot electrons (nonthermal electrons) out of the focal volume, size-dependent electron energy loss mechanisms such as self-trapping, and different densities of defects with various thresholds are other possible mechanisms for spot size dependence. These three possible mechanisms are not easily dismissed and must be analyzed in detail. One thing that all of these three size-dependent effects have in common is that they depend on focal volume. Thus, the experimental data should be analyzed for focal volume dependence, and when making size-independent comparisons, all data should be scaled to a common focal volume.

Since the 1.06-μm focal spots were diffraction limited and the 10.6-μm focal spots were nearly diffraction limited, one can compute the focal volumes for these wavelengths. The focal spots at 2.7 and 3.8 μm were not diffraction limited, and thus the focal volumes at these wavelengths were computed from the measured focal-spot radii and depths of focus.

Table 6. Average breakdown thresholds for Harshaw spectroscopic-grade KCl.

$\lambda(\mu m)$	$w_o(\mu m)$	$\langle I_B \rangle$ (GW/cm^2)	$\langle E_B \rangle$ (MV/cm)	$P_B(MW)$
10.6	20.5	19.2	2.23	0.25
	45.0	5.97	1.25	0.38
	90.0	> 4.02	> 1.02	1.27
3.8	10.6	43.30	3.35	0.15
	13.55	22.23	2.40	0.13
	28.5	14.17	1.92	0.36
2.7	9.55	32.9	2.92	0.094
	12.55	20.5	2.31	0.102
	26.5	14.7	1.95	0.324
1.06	6.15	52.1	3.68	0.062
	10.29	38.8	3.18	0.129
	19.29	32.6	2.91	0.381

Table 7. Average thresholds of Harshaw laser-grade KCl.

$\lambda(\mu m)$	$w_o(\mu m)$	$\langle I_B \rangle$ (GW/cm^2)	$\langle E_B \rangle$ (MV/cm)	$P_B(MW)$
10.6	20.5	17.65	2.14	0.23
	45.0	5.22	1.17	0.33
	90.0	> 3.2	> 0.92	1.07
3.8	10.6	44.53	3.40	0.16
	13.55	19.87	2.27	0.12
	28.5	15.30	1.99	0.39
2.7	9.55	35.87	3.05	0.10
	12.55	21.40	2.36	0.16
	26.5	13.87	1.90	0.31
1.06	6.15	59.50	3.93	0.071
	10.29	32.57	2.91	0.11
	19.29	39.77	3.21	0.47

The smallest focal volume used in measuring the breakdown thresholds of all the specimens was $V_{6.15} = 0.36 \times 10^{-9}$ cm^3, the focal volume corresponding to $w_o = 6.15$ μm at 1.06 μm. $V_{6.15}$ was chosen as unit of focal volume, and all other focal volumes were normalized using $V_{6.15} = 1$. The data at each wavelength were then fit to a linear dependence on focal volume,

$$I(\lambda, w_o) = a[V(\lambda, w_o)]^{-1} + b \quad . \tag{1}$$

In the above discussions, the focal volume is chosen to be the volume for which the intensity drops to 0.80 of the peak intensity.

Tables 8 - 10 summarize the focal volume dependence of the damage thresholds measured in this work. Note that in all cases the focal volume dependence was strongest at longer wavelengths. This type behavior is consistent with the model which assumes that damage is initiated by the most easily ionized defect within the focal volume. The defect is thought to initiate an avalanche by providing a conduction band electron through multiphoton ionization. As the focal volume gets larger, chances of finding a defect which can be ionized by

Table 8. Focal volume dependence of threshold intensity for RAP-grown material. V is expressed in units of 0.36 x 10^{-9} cm^3, intensity in units of GW/cm^2.

Material	λ(μm)	Best fit (least squares)	Correlation (r^2)
NaCl	10.6	$I_V = 1085\ V^{-1} + 8.83$	.9986
		$I_V = 1099\ V^{-1} + 7.74$	.9997
		$I_V = 1114\ V^{-1} + 6.63$	.9999
	3.8	$I_V = 548\ V^{-1} + 28.21$	.9988
	2.7	$I_V = 290\ V^{-1} + 29.93$	.9934
	1.06	$I_V = 47.07\ V^{-1} + 53.97$	.9999
KCl	10.6	$I_V = 874\ V^{-1} + 4.73$	.9986
		$I_V = 879\ V^{-1} + 4.37$	.9992
		$I_V = 883\ V^{-1} + 4.05$	.9995
	3.8	$I_V = 675\ V^{-1} + 11.28$	.9252
	2.7	$I_V = 214\ V^{-1} + 17.20$	.9653
	1.06	$I_V = 24.72\ V^{-1} + 2.82$	1.000
KBr	10.6	$I_V = 330\ V^{-1} + 3.50$	.9986
		$I_V = 334\ V^{-1} + 3.16$	.9997
		$I_V = 339\ V^{-1} + 2.82$	1.000
	3.8	$I_V = 521\ V^{-1} + 2.74$	.9920
	2.7	$I_V = 275\ V^{-1} + 3.92$	1.000
	1.06	$I_V = 29.16\ V^{-1} + 18.30$	.9647

a lower order multiphoton process and thus lower intensity increase. At shorter wavelength ionization potential of a defect can be much higher for a given order multiphoton process. If one assumes that the density of defects is porportional to the ionization potential, then one would expect a focal volume dependence until a volume is reached that gives high probability of finding a defect that can be ionized at a low order process. The volume at which this occurs would be smaller at higher photon energies, as is observed in this work.

The focal volume dependence at 10.6 μm was not precisely determined since damage to the surface prevented a determination of the bulk threshold for large spot sizes. The numbers given for the largest focal volume at this wavelength is that intensity which would

Table 9. Focal volume dependence of the breakdown thresholds of commercially available NaCl. V is in units of 0.36 x 10^{-9} cm^3, I_V in units of GW/cm^2.

Material	λ(μm)	Best fit (least squares)	Correlation (r^2)
NaCl (spectroscopic grade)	10.6	$I_V = 795\ V^{-1} + 9.68$	.9986
		$\bar{I}_V = 821\ V^{-1} + 7.76$	.9999
		$I_V = 844\ V^{-1} + 5.99$	.9970
	3.8	$I_V = 583\ V^{-1} + 25.45$	.9729
	2.7	$I_V = 219\ V^{-1} + 31.11$	.7273
	1.06	$I_V = 31.21\ V^{-1} + 35.91$	.9600
NaCl (laser grade)	10.6	$I_V = 392\ V^{-1} + 8.33$	.9986
		$\bar{I}_V = 409\ V^{-1} + 7.04$	.9991
		$I_V = 426\ V^{-1} + 5.74$	.9917
	3.8	$I_V = 396\ V^{-1} + 16.65$	.9986
	2.7	$I_V = 322\ V^{-1} + 18.15$	.9788
	1.06	$I_V = 15.32\ V^{-1} + 12.40$	.9955

damage only the rear surface when focused in the bulk. Higher intensities would damage the front surface and thus prevent propagation into the bulk. Thus, the numbers given are a lower limit for the bulk thresholds. These lower limits were used to obtain the top entry in tables 8 - 10 for the focal volume dependence. The lower entry assumes that the threshold was the same as that of the previous focal volume. The actual value of the breakdown threshold for this focal radius was within these two limits.

The pulse widths were not the same for the different wavelengths used in this work. The pulse widths were approximately 90, 85, 120, and 31 nsec for the 10.6-, 3.8-, 2.7-, and 1.06-μm lasers, respectively. There is some dispute about the pulse width dependence of breakdown thresholds for pulse widths of the order of several to hundreds of nanoseconds. Some workers claim there is a dependence, and others claim no dependence. Specimen 78-NC-6, a Harshaw laser-grade NaCl crystal, was tested with pulse widths of 70 and 107 nsec at 10.6 μm. The resulting intensity thresholds were the same to within ±3.5%, which is within experimental error. Thus, no pulse-width scaling was applied to the results of this work.

Table 10. Focal volume dependence of the breakdown thresholds of commercially available KCl. V is in units of 0.36×10^{-9} cm^3, I_V in units of GW/cm^2.

Material	λ(μm)	Best fit (least squares)	Correlation (r^2)
KCl (spectroscopic grade)	10.6	$I_V = 169\ V^{-1} + 5.65$	.9986
		$\bar{I}_V = 176\ V^{-1} + 5.15$	.9994
		$I_V = 182\ V^{-1} + 4.63$	.9935
	3.8	$I_V = 243\ V^{-1} + 12.66$	.9973
	2.7	$I_V = 137\ V^{-1} + 14.35$	.9982
	1.06	$I_V = 18.04\ V^{-1} + 34.31$	.9562
KCl (laser grade)	10.6	$I_V = 159\ V^{-1} + 4.92$	.9986
		$\bar{I}_V = 166\ V^{-1} + 4.39$	.9991
		$I_V = 173\ V^{-1} + 3.87$	.9916
	3.8	$I_V = 236\ V^{-1} + 10.96$	.8271
	2.7	$I_V = 164\ V^{-1} + 13.71$	.9972
	1.06	$I_V = 24.04\ V^{-1} + 34.83$	.8698

References

[1] The National Bureau of Standards series of publications on Laser Induced Damage to Optical Materials, edited by A. J. Glass and A. H. Guenther, deals with this subject extensively, and the references contained within these publications are further guides to the literature on the subject of laser damage to optical materials. These reports are available from the U.S. Government Printing Office, Washington, D.C. The report numbers and dates of publications are:

	NBS Spec. Publ.	Year
a.	341	1970
b.	356	1971
c.	372	1972
d.	387	1973
e.	414	1974
f.	435	1975
g.	462	1976
h.	509	1977
i.	541	1978

[2] Bloembergen, N., IEEE J. Quantum Electron. QE-10, 375 (1974).

[3] Fradin, D. W., Laser Focus, 41 (Feb. 1974).

[4] Smith, W. Lee, Opt. Engr. 17, 489 (1978).

[5] Yablonovitch, E., Ph.D. Thesis, Harvard University, 1972, unpublished.

[6] Yablonovitch, E., Appl. Phys. Lett. 19, 495 (1971).

[7] Soileau, M. J., Bass, M., and Van Stryland, E. W., in reference [1-i], p. 309.

[8] Soileau, M. J., Ph.D. Thesis, University of Southern California, Aug. 1979.

[9] Bettis, J. R., House II, R. A., and Guenther, A. H., in reference [1-g], p. 338.

[10] Manenkov, A. A., private communication, Sept. 1978.

[11] Fradin, D. W., Yablonovitch, E., and Bass, M., Appl. Opt. 12, 700 (1973).

[12] Pastor, R. C., and Pastor, A. C., in Crystal Growth in a Reactive Atmosphere, (Pergamon Press, New York, 1975), pp. 117-124. Materials Res. Bull. 10.

[13] Manenkov, A. A., in reference [1-h], p. 455.

[14] Fradin, D. W., Bass, M., Bua, D. B., and Holway, Jr., L. H., Visible and Infrared Laser-Induced Damage to Transparent Materials, AFCRL-TR-0082, Air Force Systems Command, Bedford, Mass., 1974.

[15] Von Hipple, A., J. Appl. Phys. 8, 815 (1937); Phys. Rev. 54, 1096 (1938).

[16] Frölich, H., Proc. Roy. Soc. A160, 230 (1937).

[17] Seitz, F., Phys. Rev. 76, 1375 (1949).

[18] Callen, H. B., Phys. Rev. 76, 1394 (1949).

[19] O'Dwyer, J. J., The Theory of Dielectric Breakdown of Solids (Oxford University Press, London, 1964).

[20] Sparks, M., in reference [1-f], p. 331.

[21] Fradin, D. W., Ph.D. Thesis, Harvard University, 1973.

[22] Milam, D., in reference [1-g], p. 350.

[23] Anther, J. P., and Bass, M., Appl. Phys. Lett. 31, 412 (1977).

[24] Fradin, D. W., Bloembergen, N., and Letellier, J. P., Appl. Phys. Lett. 22, 635 (1973).

[25] Powers, Prof. E. A., University of Southern California, Los Angeles, private communication, 1979.

[26] Olness, D., Appl. Phys. Lett. 8, 283 (1966).

[27] Olness, D., J. Appl. Phys. 39, 6 (1968).

[28] Leung, K. M., Bass, M., and Balbin-Villaverde, A.G.J., in reference [1-f], p. 107.

[29] Allen, S. D., Braunstein, M., Giuliano, C. R., and Wang, V., in reference [1-e], p. 66.

[30] Yasojima, Y., Takeda, M., and Onnishi, Y., Jpn. J. Appl. Phys. 7, 552 (1968).

[31] Yasojima, Y., Ohmari, Y., Okumura, N., and Inuishi, Y., Jpn. J. Appl. Phys. 14, 815 (1975).

[32] Soileau, M. J., Bennett, H. E., Porteus, J. O., Temple, P. A., and Bass, M., in Proc. 5th Annual Conf. on Infrared Laser Window Materials, 1-4 Dec. 1975, Las Vegas, Nev., compiled by C. R. Andrews and C. L. Strecker (Arlington, Va., DARPA, 1976), p. 391.

[33] Zverev, G. M., and Poshkov, V. A., Sov. Phys.-JETP 30, 616 (1970).

[34] Fradin, D. W., IEEE J. Quantum Electron. QE-9, 954 (1972).

[35] Smith, W. L., Bechtel, J. H., and Bloembergen, N., Phys. Rev. B12, 706 (1975).

[36] Kelley, P., Schmid, A., and Bräunlich, Phys. Rev. B 20, 815 (1979).

[37] Schmid, A., Kelly, P., and Bräunlich, P., Phys. Rev. B 16, 1569 (1977).

[38] Gomelauri, G. V., and Manenkov, A. A., Kvant. Elektron. 6, 45 (1979).

Figures

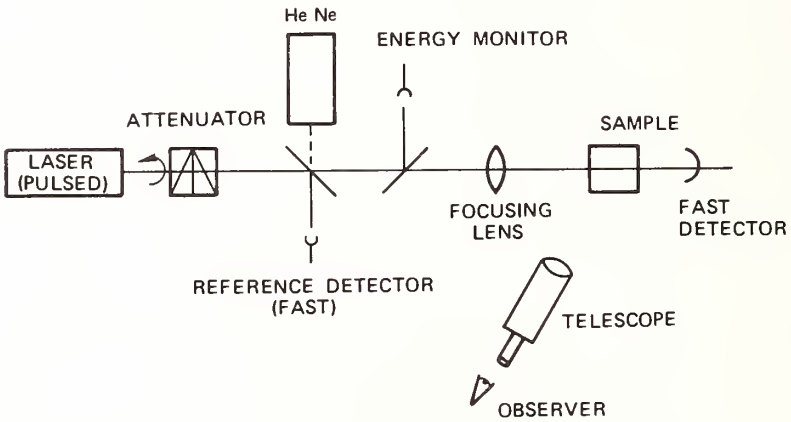

Figure 1. Typical setup for laser-induced breakdown experiments. The linearly polarized, single-mode output of a pulsed laser operating at 10.6, 3.8, 2.7, and 1.06 μm was focused into the bulk of a highly transparent specimen. Fast detectors (1-nsec response time) were used to monitor the shape before entering and after transmission through the specimen (see fig. 2). A coaxial HeNe beam was used for alignment and to monitor the occurrence of damage. Polarizer-analyzer combinations were used to attenuate the beam. The analyzer was fixed to insure constant polarization of the beam reaching the specimen.

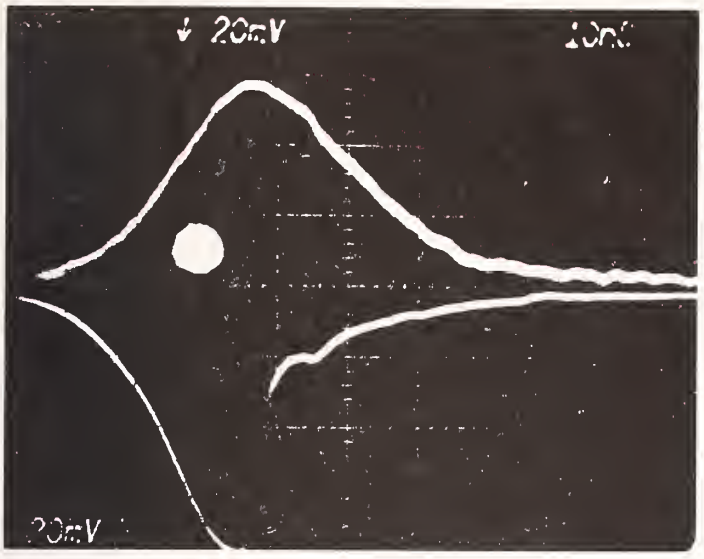

Figure 2. Laser waveform related to the occurrence of bulk damage in KCl at 1.06 μm. The top trace is the reference pulse, and the bottom trace is the transmitted pulse showing the abrupt truncation of the pulse for damage near threshold. The laser burn profile is also shown (slightly left of center).

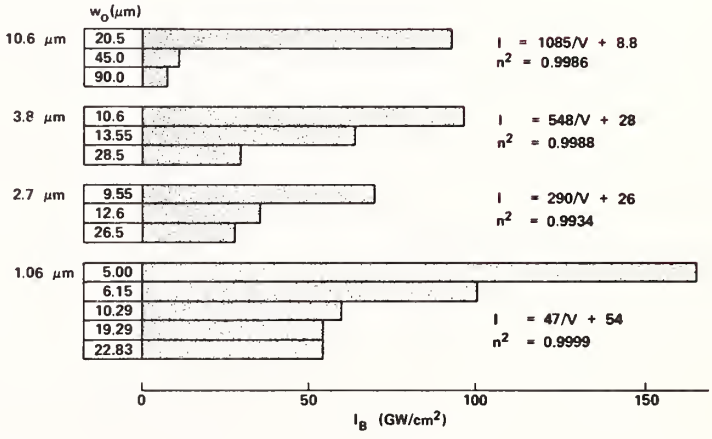

Figure 3. Breakdown intensity for RAP-grown NaCl. The breakdown thresholds given above are the average values for four separate specimens. Each specimen was tested at every spot size and wavelength. The equations at the right of the figure are the least squares fit of the data to an inverse volume dependence. Volume, V, is in units of 0.36×10^{-9} cm^3, and the intensity is in units of GW/cm^2.

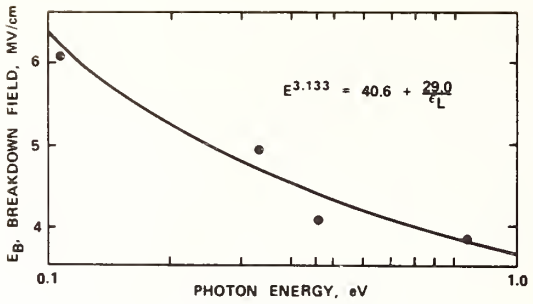

Figure 4. Breakdown fields for RAP-grown NaCl. In these plots the average breakdown fields for five NaCl RAP-grown crystals are given. The thresholds have been reduced to a common focal volume using the relations given in the Appendix. The 1.06-, 2.7-, and 3.8-μm measurements were all done at V_{eff} = 7.88 units (one volume unit is 0.36 x 10^{-9} cm^3) and are not scaled in this figure.

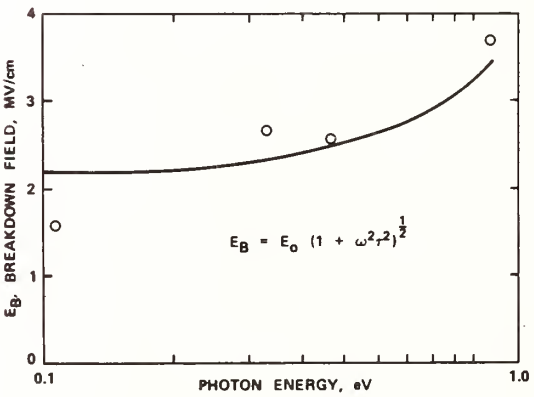

Figure 5. Breakdown fields for RAP-grown NaCl in the limit of large focal volumes, V > 10^{-4} cm^3. Note that the frequency dependence for this case is characteristic of electron avalanche breakdown.

A question was raised concerning the test of this theory by damage measurements made in materials in which an excess of readily ionized electrons was created by one means or another. The speaker pointed out that work had been done by Yashima and co-workers using color-centered alkali halides (Japanese J. Appl. Phys. 14, 815, 1975). In material which was free of color centers, the breakdown field was seen to increase as the wavelength shifted from 1 micrometer to 0.69 micrometers, while in color-centered materials, although the absolute breakdown field was lower, the frequency dependence was just the opposite, with the breakdown field decreasing as the wavelength was decreased. This is consistent with a multiphoton process for the color centers, and would seem to support the predictions of the theory presented in this paper. The question was raised concerning the extension of this theory to surface damage. The speaker indicated that he would expect a different spot size dependence because in surface damage it is only the area of the focal spot rather than the three-dimensional volume which is of importance. However, it was pointed out that in surface damage it is often the presence of a uniform contaminant layer which determines the damage threshold, in which case no spot size dependence would be expected.

SBS INFLUENCE ON LASER DAMAGE OF OPTICAL MATERIALS

P. Balkevičius, E. Kosenko, J. Lukošius, E. Maldutis
Institute of Physics of Academy of
Science of Lithuanian SSR, Vilnius

The influence of the stimulated Brilloin scattering (SBS) on the damage of optical materials has been experimentaly investigated. It is shown that depending on the experimental conditions, the SBS changes the threshold and the bulk damage character. It can decrease or increase the magnitude of the threshold power of the laser beam, which damages the surface of the optical systems. The SBS increases (the increase of more than 100 times has been registred), but not decreases the threshold power of the bulk damage, as it was thought ealier.

It is shown, that the reason of the decrease of the bulk damage threshold and the changes of the damage thresholds of the surface of the optical system is a redistribution of the laser beam intensity caused by the SBS, which decreases the intensity in the focal region of lens.

The influence of the laser beam redistribution on the damage thresholds and self-focusing is also discussed.

Key words: Damage morphology; damage thresholds; laser bulk damage; laser surface damage; optical materials; stimulated Brilloin scattering (SBS); self-focusing.

1. Introduction

The problem of the SBS influence on laser damage of optical materials has been investigated for 15 years. In most cases the works dealing with this problem are experimental because a complete solution of the SBS of focusing laser beam equation can not be obtained even by modern computers. In the previous work on this problem the generation of intense coherent acoustical oscillations in the SBS process was regarded as one of the possible mechanisms of the damage. In later papers the opinion was expressed that the SBS doesn't play the main role in the damage. A sufficiently extensive bibliography on this problem and the role of the SBS in the damage is presented in /1-5/[1].

In the present paper the role of the SBS in optical damage is investigated experimentaly and the changes of the damage thresholds are measured. The main material of the investigation was optical glass K-8 and fused silica.

2. Experimental Methods and Techniques

In the experiment of the SBS influence on the optical damage, it is necessary to control the SBS power, leaving other conditions unchanged.

[1] Figures in brackets indicate the literature references at the end of this paper.

It is known, that the intensity of the SBS is $I_{SBS} \sim \exp gI_L l$, where I_L - laser beam intensity, l - length of the active material. The amplification coefficient g depends on the spectral width of the laser radiation. If it is sufficiently wide, then g decreases. In order to monitor the SBS power the spectrum of the laser radiation was changed.

In the experiments the radiation of the second harmonic of Nd glass laser has been used. The intensity distribution over the incident beam cross section was approximately Gaussian. The beam divergence was close to the difraction. The main parameters of the radiations are given in the table.

Table 1. Main parameters of radiations

Laser number	λ, μm	τ, ns	D, mm	$\delta\nu$, cm^{-1}	Spectral characteristics	Q-switching
1a	0,53	10	4	$\leqslant$0.2	several (up to five) frequences	passive
1b	0,53	10	4	$\leqslant$0.02	single-frequency	passive
2a	0,53	20	4	2	multi-frequency	active
2b	0,53	20	4	$\leqslant$0.02	single-frequency	passive

where τ - pulse duration, D - diameter of the beam on a lens.

The use of the second harmonic of the radiation provided the lack of the feed-back coupling between the laser and the SBS radiation. The main scheme of the experiment is shown in fig. 1. The time characteristics of the laser and the scattered pulses were registred by the same fast photocell and the oscilloscope. The SBS pulse was detained with respect to the laser. The spectrum characteristics of the pulses were measured by Fabry-Perot interferometer. The energetical characteristics of the pulses were measured by the calorimeters. The damage threshold for certain focal length of the lens is considered to be the minimal power of the incident laser pulse upon the sample causing the damage which is visualy noticed in the beam of the He-Ne laser or in the appearance of the spark at the moment of the damage. Both methods equaly determine the damage threshold.

3. Measurements and Results

Investigations of the bulk damage threshold of the glass K-8, placed in the focal region of spherical lens (f = 33 cm), caused by the radiation of 1a or 2a laser, showed that the damage threshold in the case of the equal radiation power changes several times. It was found, that the SBS power changes simultaneously. Several conclusions can be made:

1) In the case of sufficiently large transformation of laser radiation in the SBS, the damage does not take place. This contradicts to the damage mechanism due to stress, formed by the coherent acoustic phonons, generated in the process of the SBS.

2) The SBS influences the damage threshold. A narrow spectrum radiation (large SBS) does not cause the damage when the laser power is more then 0.6 MW. On the other hand a wide spectrum radiation (without SBS) causes the damage when the laser power is 0.3 MW.

For a more through study of the SBS influence on the optical damage of optical system the damage of the back surface of sample 1 has been investigated (fig. 1b, the widest line) by two contrary correlating beams controlled by the spectrum and the intensity. The first was the laser beam, and the second beam was generated in the process of the SBS of focused (f = 15 cm) 1b laser beam in sample 2, which was placed 1.5÷2 mm from the back surface of sample 1. In this way an exact coincidence of opposed beams has been automatically reached.

Having changed the material of the second sample the spectrum of the second beam also been changed. The energy of the second beam, measured at the front surface of sample 1, reached 0,8 of the first. When the laser 1a was used the second beam (SBS) was absent.

It was established:

1) In the absence of the second sample (there is no SBS for both radiations) the damage threshold does not depend on the width of the beam spectrum.

2) The damage of the surface of the system, consisting of 2 equal samples (e.g. optical glass K-8) caused by the narrow spectrum radiation and acomponied by strong SBS, does not take place when the power of the first beam is 5 times larger than the damage threshold of a separate sample. When the spectrum is wide, the damage threshold of the system remains the same as for a separate sample.

3) The damage threshold of the system, consisting of two samples of different materials (e.g. glass K-8 and fused silica) caused by the narrow spectrum radiation decreases 1.7 times as compared with the threshold of the separate sample. In the case of the wide spectrum radiation the threshold remains the same.

The increase of the damage threshold can be accaunted by the interaction of the incident and scattering radiations, which cause a hard exitation of the SBS generation in the first sample. That is why the intensitv of the incident radiation upon the back surface decreases considerably.

The decrease of the threshold can be explained by summing up the actions of the opposed beams. In the first sample the generation of the SBS in this case is absent due to the violation of synchronism.

In order to understand the mechanism of the SBS influence on damage deeper, both samples of the previous experiment were "connected", and the character of the bulk damage of the glass K-8 was investigated. The radiation of lasers 1a and 1b was focused (f = 15 cm) in the bulk of the sample. The radiation of laser 1a (with several frequences) up to 5 MW was lower than the SBS threshold. In single-frequency regime (laser 1b) the same power was higer than the SBS threshold (0.44 MW). The damages, obtained without the SBS are ($\sim$ 20 mm) thin ($\lesssim 2\,\mu m$) tracks, beginning in the focus of the lens (fig. 3).

When the power is increased, the length of the tracks also increases. The character of the damages caused by a single-frequency laser (with SBS),

is essiantially different: the length of the tracks is not longer than 6 mm. A comparatively large damage in the form of a star (fig. 3), depending upon the power, in the end of the track directed to the end of the lens can be seen.

In fig. 4 is the dependence of the tracks length on the radiation power of laser given. The experimental results, introdusing the investigations without the SBS, are described well by the formula /6/:

$$L = 2\sqrt{2}\,(n_2/cn_o)^{1/2}\,(R/a)^2\,(P_L - P_t)^{1/2},$$

where L - the lengths of the track; P_t - the damage threshold (in our case $P_t = 0.33$ MW); n_o and n_2 - linear and non-linear refractive indexes; R and a - curvature radius and beam radius on the surface of the sample.

The length of the track caused by the radiation with the SBS weekly depends on the laser power.

The obtained results can be explained by the following physical model. The track is formed as the result of a focus movement opposite the laser beam. The shortening of the track is due to the fact that the focal region is covered by the zone in which the process of parametrical interaction of incident and scattered radiations and transformation of laser radiation to SBS takes place. The zone moves more rapidly than the focus of the selffocusing beam. The laser radiation intensity in the focal region decreases, and the growth of the track stops.

In order to observe directly the redistribution of the laser radiation and the SBS along the beam the intensity of the luminescense of rhodamine 6 G solution in heavy water with the angle of 90° towards the direction of the beam has been investigated.

The radiation of the main harmonic of the two Nd glass lasers 2a and 2b was focussed into the volume of the solution by spherical lens (f = 15 cm). The chosen focus length of the lens exhibited strong SBS when the radiation with the narrow spectrum was used, and the SBS was absent when the radiation with the wide spectrum was employed. The zone of luminescence was photographed and photometered.

It has been established, that the zones of the luminescence are strongly different, the radiation of both lasers being equal in power (fig. 5). In the first case ($\delta\nu \lesssim 0.02$ cm^{-1}, $P_{SBS} \approx 0{,}8\,P_L$) the increase of the intensity has been observed ($I_{SBS} + I_L$) at the front surface of the cell; it was practically constant up to the focal region of the lens and it increased slightly in the focal region of the lens. In the second case ($\delta\nu = 2$ cm^{-1}; without the SBS), the intensity increases constantly up to the focal region of the lense. It should be noted, that in the first case the intensity at the first surface of the cell is almost two times larger, and in the focal region it is considerably lower than in the second case.

In this way it was prowed that the SBS, redistributing the laser radiation intensity, limits it in the focal region and therefore plays an important role in the damage process.

Taking into consideration that the SBS threshold is determined not only by the radiation parameters, but also by the properties of the

material, it should be reasonable to expect changes in the relative damage thresholds for different materials in which the SBS thresholds (quantity of acoustooptical relation) are different.

The SBS power can be varified by changing not only the laser radiation spectrum, but also by varying the length of the interaction of the laser radiation with the material, i.e. the lens focal length. In this way the special conditions were chosen, where for the radiation with the narrow spectrum, the SBS threshold was higer then the damage threshold ($f \leqslant 15$ cm for K-8 and $f \doteq 3$ cm for fused silica) and it was lower ($f > 15$ cm for K-8 and $f \geqslant 7.5$ cm for fused silica) than the damage threshold.

For the radiation with the wide spectrum (laser 2a) the SBS threshold was higer then the damage threshold in the whole interval of the investigated focal length of the lenses. Fig. 6 shows the dependence of bulk damage thresholds by laser radiation with narrow (□ ; △) and wide (○ ; ◇) spectrum as a function of focal length of lens for glass K-8 (□ ; ○) and fused silica (△ ; ◇). It is clear that in the case of the radiation with the wide spectrum (without the SBS), the relation of the bulk damage thresholds of glass K-8 and fused silica is constant in the investigated interval of the focal length of the lenses. In the same interval of the focal length of the lenses the thresholds differ strongly when the laser radiation spectrum is narrow: the damage threshold of fused silica is about 4 times greater than the damage threshold of glass K-8 for lens $f = 3$ cm and more than 100 times greater for the lens $f = 10$ cm. There is no damage at points marked by arrows.

The increase of the observed effect of the damage threshold in fused silica can be explained by stronger transformation of the main radiation into the SBS. This is in good agreement with greater acousto-optical relation of fused silica.

4. Discussion

It was proved experimentaly, that SBS, redistributing laser radiation, changed the damage thresholds. Under the same conditions, when the narrow spectrum laser radiation generates intensive SBS, the wide spectrum laser radiation having the same power always produces long thin tracks. The appearance of long tracks points to the self-focusing. Due to the fact that there are no absorbtion lines near the laser wave length, the self-focusing doesn't depend strongly[2] on the width of the radiation spectrum. Consequently, self-compression of laser beam must also influence the redistribution of the narrow spectrum laser radiation. It is not dificult to estimate this roughly:

$$I_{SBS} = I_o \exp I_L g l, \qquad \text{when } I_{SBS} \ll I_L$$

$$I_L = P_L/S = 4P_L/\pi\, d_o^2\, (1 - P_L/P_{cr});$$

[2] When there are some frequences (modes) of radiation, the time modulation of laser pulse changes nonlinear refractive index and can change the process of self-focusing. This problem in the theory of self-focusing is not discussed. But it is easy to estimate that this process is not effective and it does not change the damage threshold sufficiently.

where d_o - the diameter of the beam in the focus of a lens; P_{cr} - critical power of self-focusing of laser radiation. The comparison of the intensities of the SBS and the laser radiation, taking into consideration the self-compression of the laser beam when $P_L \rightarrow P_{cr}$, shows that the SBS intensity increases faster than the laser one. Consequently, the SBS is much more dependent on the laser intensity change caused by the self-focusing, than the intensity of the laser radiation itself. The decrease of the beam diameter caused by its self-compression preceeds the self-focusing and forms the conditions for the SBS appearance. But the SBS, carring out the energy from the sample, limits and even suppresses its further self-focusing.

The relations between the self-focusing and the SBS can be different depending on the length of the coherence of radiation. When the length of the coherence is small, self-focusing suppresses the SBS. When the coherence length is rather large, self-compression causes the SBS, which then carries out the radiation, and does not allow the beam to self-focus.

5. Conclusions

1. The SBS increases the bulk damage threshold of optical materials. It was established that under special conditions the threshold with the SBS exceeds more than 100 times the damage threshold without the SBS.

2. The SBS changes the damage threshold of the surface of the optical systems. It was established that depending on the experimental conditions, the threshold can be increased more than 5 times and decreased up to 1.7 time.

3. The reason of the increase of the bulk damage threshold and the changes of the damage thresholds of the surface of the optical system is considered to be the redistribution of the incident energy caused by the SBS along the beam.

4. The transformation of the incident energy into the scattered one occurs in the very front zone of the sample, where the intensity of both radiations is comparatively low. In the same zone the main part of the coherent acoustic oscillations energy is localised. These oscillations, due to a large cross-section of the zone, are not sufficiently intensive to create any damages.

5. The increase of the damage threshold has been observed in optical glases, in the crystals of quartz and TGS, in the water, heavy water, benzene and, apparently, takes place in all materials, the damage of which is accompanied by a strong SBS.

6. The intensity of the laser radiation in the focal region is determined not only by the power of the incident radiation, the diameter of the focal region and self-focusing but also by the power of the scattering radiation. That is why for the comparisson of optical resistance of various materials it is necessary to take into consideration the amount of the SBS on the damage threshold.

7. Strong stimulated scattering for 180° of another type, will, apparently, influence the damage as in the case of the SBS.

6. References

1. Laser handbook, ed. by Arecchi F.T. and Schulz O - Du Bois. North-Holland Publ. Co., 1972.
2. Shen Y.R., Prog. Quant. Electr., 4, 1 (1975).
3. Vlasov D.V., Kasjanov J.S., Korobkin V.V., Fabelinski I.L., Fiz. Tverd. Tela, 17, 3574 (1975).
4. Balkevičius P., Lukošius J., Maldutis E., Zh. Tekh. Fiz. Pisma, 3, 542 (1977).
5. Balkevičius P., Kosenko E., Lukošius J., Maldutis E., Kvantovaja Elektronika, 5, 2032 (1978).
6. Zverev G.M. and Pashkov V.A., Zh. Eksp. Teor. Fiz, 57, 1128 (1969).

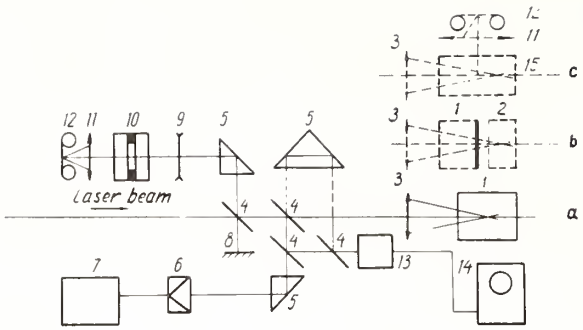

Fig. 1. Scheme of the experiment. 1 - samples, 2 - SBS generator, 3 - spherical lens, 4 - glass plates, 5 - prisms, 6 - callorimeter, 7 - microvoltmeter, 8 - metallic mirror, 9 - diversing lens, 10 - interferometer Fabry-Perot, 11, 12 - photocamera with objective, 13 - photocell, 14 - oscillograph, 15 - cell.

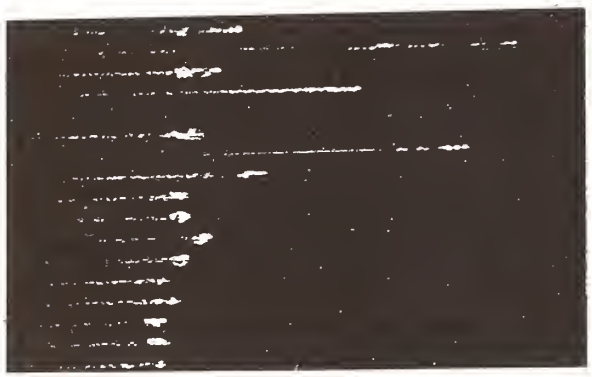

Fig. 2. Typical bulk damage morphology of glass K-8. Long tracks - without SBS, short tracks-with SBS. The distance between tracks - 0.5 mm.

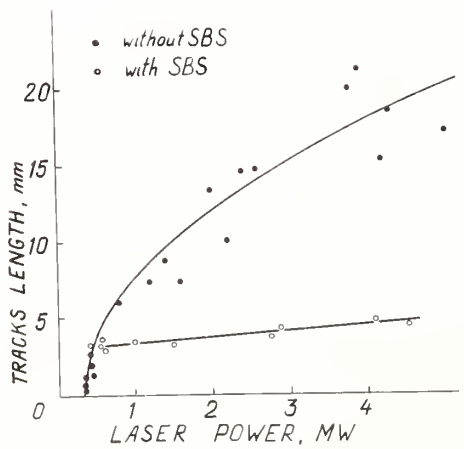

Fig. 3. Tracks length as a function of the laser beam power.

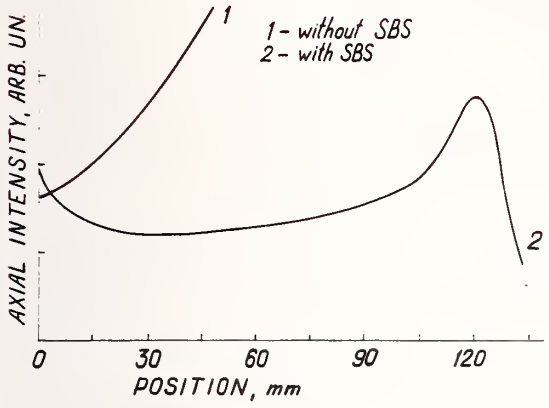

Fig. 4. Distribution of laser axial intensity along the beam in rhodamine 6G solution.

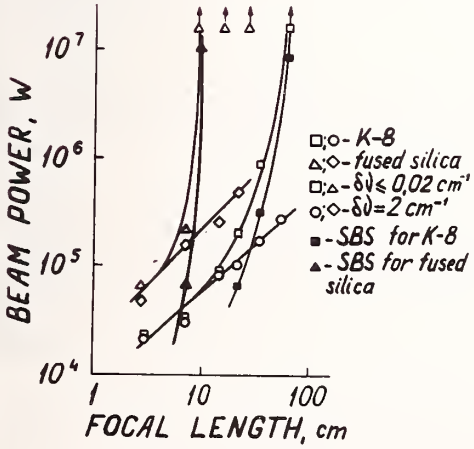

Fig. 5. The damage thresholds as a function of the lens focal length.

COMPUTER SIMULATION OF DAMAGE MORPHOLOGY

by

P. Kelly and D. Ritchie
Physics Division
National Research Council of Canada

and

A. Schmid and P. Bräunlich
Physics Department
Washington State University

Our progress to-date on the computer simulation of the spatio-temporal behavior of a fast, just damaging pulse focused into an optical material is illustrated in the form of a 16 mm movie. The time and space dependent intensity is shown in profile by the assignment of different colours and allows one to follow beam deformation as the pulse propagates through the medium.

Our present code PULSE is a major modification of the work we first reported at last year's damage conference. It is intended to be sufficiently flexible to accommodate any flux, wavelength, material or temperature dependence of the dielectric function and any possible mechanism of electronic excitation of the solid (avalanche, multiphoton generation, etc.), as well as various conceivable mechanisms for converting the energy of the photon field to excited electron and phonon distributions with an ultimate increase in lattice temperature.

In particular, we illustrate the simulation of the experimental arrangement of W. L. Smith et al [1] who reported the damage morphology of NaCl using 21 psec pulses at 0.5321 μ, where we have included the nonlinear interaction of the polaron model by A. Schmid et al [2].

At last year's symposium [3] we presented an adaption of the computer code RAMSES to the problem of damage in solids. We now consider a significant modification of that work: namely, the grid is now placed on the solid (over the interaction volume) and the pulse propagates through it. Our new code PULSE is illustrated in the following 16 mm movie. Denoting the total energy for intrisic damage, ξ, as that obtained by W. L. Smith et al. [1] we illustrate the effect of varying the energy content of a clipped gaussian pulse. Our first runs used a coarse grid of 41 μ (Δx) by 4μ (Δr) so that $\Delta t \sim 0.2$ psec for $10\times\xi$, $\sqrt{10}\times\xi$, $2\times\xi$ and finally ξ.

In the last "coarse" run there appears to be little non-linear interaction, but by blowing-up the interaction volume, that is using a grid of 7μ (Δx) by 0.9μ (Δr) so that $\Delta t \sim 1.04$ psec one can see in fine detail the beam break-up close to the optic axis near the focal point.

And finally we illustrate the history of the ionization fraction, in this case, the number of polarons created. Close to the center of the interaction volume this fraction reaches 5×10^{-3}, or $1.2\ 10^{20}$ polarons per cm^3. The computer code and some of the results will be presented for publication elsewhere.

SUMMARY OF MOVIE

The 16 mm colour film of the above runs was shown twice. In summary, we note that for high energies, $\sim 10\ \xi$ very little of the pulse propagates throgh the "focal point" before there is significant non-linear interaction of the remainder of the pulse is "deflected" from the hot spot created. As the energy is decreased, more and more of the pulse is required to create the equivalent hot spot and the extent of the spot and the break-up effects are measurably different. The coarse run with the just damaging energy content ξ shows almost no interaction, yet after the pulse has traversed the crystal (we run it

through 4000 μ of NaCl) the ionization fraction is still high but located in a few microns around a "focal spot." The last run showed in fine detail the extent of the spot created and indeed the beam breaks up close to the optic axis. It was pointed out that more work is required to attach any significance to the present analysis in terms of elucidating on the damage observed by Smith et al. [1]. However, it could be concluded that we have shown that any theory of intrinsic damage must include the spatial as well as the temporal behavior of a pulse as it propagates through non-linear medium.

REFERENCES

[1] W. L. Smith et al, Harvard University Technical Report No. 665, 1976 (unpublished).

[2] A Schmid et al, Phys. Rev. B 20, 815, 1979.

[3] NBS Special Publication 541, Glass & Guenther, p. 296, 1978.

[4] H. D. Dudder and D. B. Henderson, Comp. Phys. Comm. 10, 155, 1975.

The discussion centered on the difficulty of observing breakdown at threshold. Since the highly localized breakdown site is very small when the plasma is first created the amount of the beam obscured by the plasma is not very great and as a result any attempt to see a sudden sharp climb in the transmitted beam intensity may prove very difficult. If the pulse is long enough or if the pulse is well above threshold the initial plasma will grow very quickly, obscuring a large fraction of the beam, and the well known pulse cut-off will be observed.

APPENDIX I -- PARTICIPANTS

J. Abate
Laboratory for Laser Energetics
250 East River Road
Rochester, New York 14623
716-275-5181

Wayne Anderson
USAF Academy
ASAFA/DFP
USAF Academy, Colorado 80840
303-472-2394

Joseph H. Apfel
Optical Coating Laboratory, Inc.
2789 Giffen Avenue
Santa Rosa, CA 95402
707-545-6440

Philip C. Archibald
Naval Weapons Center, Code 3818
China Lake, California 93555
714-939-2869

William P. Barnes
ITEK Corporation
10 Maguire Road
Lexington, MA 02173
617-276-2246

Michael Bartowewcz
Lockheed R&D, Dept. 52-54
3251 Hanover Street, Bldg. 201
Palo Alto, CA 94034
415-493-4411, ext. 45051

Michael Bass
Center for Laser Studies
University of Southern California
University Park
Los Angeles, CA 90007
213-741-7994

Harold E. Bennett
Naval Weapons Center, Code 38101
Michelson Laboratory
China Lake, California 93555
714-939-2869 or 939-3832

Jean M. Bennett
Naval Weapons Center, Code 38103
Michelson Laboratory
China Lake, California 93555

Arnold Bloom
Coherent, Inc.
3210 Porter Drive
Palo Alto, California 94304
415-493-2111

Norman Boling
Optical Coating Laboratory
2789 Giffen Avenue
Santa Rosa, CA 95403
707-545-6440

E. C. Borsare
W.J. Schafer Associates
10 Lakeside Office Park
Wakefield, MA 01880
617-246-0450

Gordon Boultbee
Optical Coating Lab., Inc.
P.O. Box 1599
Santa Rosa, CA 95402
707-545-6440, ext. 202

Professor Rubin Braunstein
Physics Department
University of California
Los Angeles, California 90024

Charles K. Carniglia
Optical Coating Lab., Inc.
2789 Giffen Avenue
Santa Rosa, CA 95402
707-545-6440

Gary E. Carver
Optical Sciences Center
University of Arizona
Tucson, Arizona 85721
602-626-1493, ext. 4754

George E. Chamberlain
Electromagnetic Technology Division
National Bureau of Standards
Boulder, Colorado 80303
303-499-1000, ext. 3706

Chang H. Chi
Hughes Aircraft Co., M/S 6-D137
Centinella & Teale
Culver City, CA 90230
213-391-0711, ext. 7121

Evan Chicklls
Sanders Associates
MER12-1220
95 Canal Street
Nashua, NH 03061
603-885-3010

Peter P. Chow
Honeywell, Inc.
System & Research Center
2600 Ridgway Parkway, MN 17-2329
Minneapolis, MN 55413
612-378-5471

Terrance F. Deaton
University of California
Lawrence Livermore Laboratory
L-465
Box 5508
Livermore, CA 94550
415-422-6059

Donald L. Decker
Naval Weapons Center
Code 3816
China Lake, CA 93555
714-939-3247

John A. Detrio
University of Dayton
Research Institute
300 College Park
Dayton, Ohio 45469
513-229-3527

Joseph J. Devaney
Los Alamos Scientific Laboratory
55, MS 529
Box 1663
Los Alamos, NM 87544
505-667-6904

Dr. B. Dischler
Fraunhofer Institut
fur Angewandte Festkorperphysik
Eckerstrasse 4
D-7800 Freiburg
West Germany

T.M. Donovan
Naval Weapons Center, Code 3812
China Lake, CA 93555
714-446-2115

Terry A. Dorschner
Raytheon Company, Research Division
28 Seyon Street
Waltham, MA 02154

Major Glenn R. Doughty
AFIT/ENP
Wright Patterson AFB, Ohio 45433
513-255-2012

Richard W. Dyer
W.J. Schafer Associates
10 Lakeside Office Park
Wakefield, MA 01880
617-246-0450

Johannes Ebert
Universitat Hannover
Angewanote Physik
Welfengarten 1
3000 Hannover
West Germany
GER 0511 7624894

David F. Edwards
Los Alamos Scientific Laboratory
MS-564
Los Alamos, NM 87545
505-667-7102

Ed Enemark
Optical Coating Laboratory, Inc.
P.O. Box 1599
Santa Rosa, CA 95402
707-545-6440, ext. 113

Albert Feldman
Materials Building, A259
National Bureau of Standards
Washington, D.C. 20234
301-921-2840

Nils C. Fernelius
University of Dayton
Research Institute
300 College Park Avenue
Dayton, Ohio 45469
513-254-2641

Dennis Fischer
Thin Film Dept. Manager
Coherent Inc.
3210 Porter Drive
Palo Alto, CA 94043
415-493-2111

Lawrence B. Fogdall, Research Engineer
Boeing Company
Physics Technology
P.O. Box 3707
Seattle, Washington 98124
206-655-6711

Robert P. Freese
Institute of Optics
University of Rochester
Rochester, New York 14627
716-275-5632

Wesley D. Gerber
Ford Aerospace & Communications Corp.
Aeronutronic Division
Ford Road
Newport Beach, California 92663
714-759-6545

Joe Giove
ILC Technology
399 Java Drive
Sunnyvale, CA 94086
408-745-7900

Ann Toby Glassman
University of Dayton
Research Institute
300 College Park
Dayton, Ohio 45469
513-229-3724

Ron Goe
Rockwell International
Rocketdyne Division
D/588, BA30
6633 Canoga Avenue
Canoga Park, CA 91304
213-882-3310

William T. Goosey
Eastman Kodak Co.
Department 144
20 Avenue E
Rochester, New York 14650
716-726-6442

Alex Glass
Lawrence Livermore Labs
Box 808
Livermore, CA 94550
415-422-5354

Art Guenther
AFWL/CA
Kirtland AFB, NM 87115
505-264-9856

George Graves
University of Dayton
Research Institute
300 College Park
Dayton, Ohio 45305
513-229-2517

Marc von Gunten
Spectra-Physics
1250 W. Middlefield Road
Mountain View, CA 94042
415-961-2550, ext. 310

Wilford N. Hansen
Physics Department
Utah State University
Logan, Utah 84322

Douglas H. Harrison
Spectra-Physics
1250 West Middlefield Road
Mountain View, CA 94042
415-961-2550, ext. 466

James E. Harvey
University of Dayton
Research Institute
AFWL/ALR, Bldg. 401
Kirtland AFB, NM 87117
505-247-0512

Bill Herrmann, Jr.
Optic Electronic Corp.
11477 Pagemill Road
Dallas, Texas 75243
214-349-0190

Robert Hinebaugh
AGMC/MLLS
Newark AFS
Newark, Ohio 43055
614-522-7695

R.B. Hemphill
Vought Corporation
Advanced Technology Center
P.O. Box 226144
Dallas Texas 75266

Samuel J. Holmes
Northrop Research & Technology
1 Research Park
Palos Verdes Peninsula, CA 90274
213-377-4811

Alan K. Hopkins
Air Force Materials Laboratory
AFML/LPO
Wright Patterson AFB, Ohio 45433
513-255-4474/4098

Thomas W. Humpherys
AFWL/ALR
Kirtland AFB, NM 87117
505-264-1776

Stephen D. Jacobs
Laboratory for Laser Energetics
University of Rochester
250 East River Road
Rochester, NY 14623
716-275-4837

Carl R. Jacobson
Raytheon Service Co.
Missile Systems Division, M22-2
Hartwell Road
Bedford, MA 01730
617-274-7100, ext. 3156

G.T. Johnston
University of Dayton
Research Institute
AFWL/ALR, Bldg. 401
Kirtland AFB, NM 87117
505-247-0512

Eric G. Johnson, Jr.
Optical Electronic Metrology Group
Electromagnetic Technology Division
National Bureau of Standards
Boulder, Colorado 80303
303-499-1000, ext. 3234

Kenneth Jungling
AFWL/ALR
Kirtland AFB, NM 87117
505-264-1776

Thomas Kardos
Broomer Labs, Inc.
23 Sheer Plaza
Plainview, New York 11803
516-249-1544

Paul Kelly
Physics Division
National Research Council
Ottawa, Ontario
Canada

Major Charles D. Kennedy
USAF-AFIT
AFIT-EN Box 4031
Wright-Patterson AFB, Ohio 45433

William E. Kienzle
Science Applications, Inc.
Suite 310
101 Continental Blvd.
El Segundo, CA 90245

Philipp H. Klein
U.S. Naval Research Laboratory
Code 5222
Washington, D.C. 20390
202-767-3671

Claude A. Klein
Raytheon Company
28 Seyon Street
Waltham, MA 02173
617-899-8400

Robert A. Lawton
Electromagnetic Technology Division
National Bureau of Standards
Boulder, Colorado 80303
303-499-1000, ext. 3806

Harald Küster
Institut fur Angewandte Physik
Welfengarten 1
3000 Hannover 1
0511-762-4894
West Germany

David J. Krus
Harshaw Chemical Co.
Crystal & Electronic Products Dept.
6801 Cochran Road
Solon, Ohio 44139
216-248-7400

Nils Laegreid
Battelle Northwest Labs
Materials Dept.
231-Z-200 West Area
Richland, WA 99352
509-942-2417

William P. Latham
AFWL/ALR
Kirtland AFB, NM 87117
505-264-0721

Hubert P. Le Bodo
Chief, Laser Division
Laboratoire National d'Essair
1 Rue Gaston Boissier
Paris
France 75015

Kenneth Leibold
Eastman Kodak Co.
Research & Engineering Dept. 339
901 Elmgrove Road
Rochester, NY 14650
716-724-5578

Steven R. Lindle
AFWL/ALR
Kirtland AFB, NM 87117
505-264-1776

W. Howard Lowdermilk
Lawrence Livermore Laboratory
P.O. Box 5508, L-465
Livermore, CA 94550
415-422-5498

Mike Lunt
Director, Technical Optics, Ltd.
Second Avenue, Onchan
Isle of Man
Great Britain
0624 4443 (UK)

Ronald L. Lusk
AFWL/ALR
Kirtland AFB, NM 87117
505-264-1776

Fred McClung
Hughes Aircraft, Bldg. 6
M.S. E-125
Culver City, CA 90230
213-391-0711, ext. 4715

Ron W. MacPherson
Electro Optics Division
Centre de Recherches pour
la Defense Valcartier
P.O. Box 880, Courcelette, Quebec
Canada G0A 1R0
418-844-4645

Mark Madigan
Optical Coating Lab., Inc.
Technical Products Division
P.O. Box 1599
Santa Rosa, CA 95402
707-545-6440

John R. McNeil
New Mexico State University
Box 3-PSL
Las Cruces, NM 88003
505-522-9467

David Milam
Lawrence Livermore Labs
7000 E. Ave.
Livermore, CA 94550
415-422-5499

P.A. Miles
Raytheon Missile Systems Division
Hartwell Road
Bedford, MA 01730
617-274-7100, ext. 4515

Charles W. Mitchell
University of Dayton
Research Institute
AFWL/ALR, Bldg. 401
Kirtland AFB, NM 87117
505-247-0512

Dennis Morelli
Optical Coating Lab., Inc.
Technical Products Division
P.O. Box 1599
Santa Rosa, CA 95402
707-545-6440

Jacques Mouchart
Laboratoires de Marcoussis, CR-CGE
Route de Nozay
Marcoussis
France 91460

Henry M. Musal, Jr.
Lockheed Research Laboratory
D5256, B201
3251 Hanover Drive
Palo Alto, CA 94304
415-493-4411

C. Taylor Myers
Northrop Corporation
Electro-Mechanical Division
500 E. Orangethorpe Avenue
Anaheim, CA 92801

Brian E. Newnam
Los Alamos Scientific Laboratory
P.O. Box 1663, MS 564
Los Alamos, NM 87545
505-667-3519

Davis B. Nichols
Boeing Aerospace Co.
M.S. 88-46
P.O. Box 3999
Seattle, WA 98124
206-773-8938

Marc Novaro
Centre d'Etude de Limeil
BP 27, Villeneuve
St. Georges
France 94190

J.M. O'Hare
Professor of Physics
University of Dayton
300 College Park
Dayton, Ohio 45469
513-229-2331

Russell Ono
TRW Corporation (DSSG), 01/1261
1 Space Park
Redondo Beach, CA 90278
213-535-1792

Roger A. Paquin
Perkin Elmer Corporation
Main Ave., M.S. 278
Norwalk, CT 06856
203-762-4085

Alex Parker
MIT Lincoln Laboratories
P.O. Box 73
Lexington, MA 02173
617-862-5500

Walter T. Pawlewicz
Battelle - Pacific Northwest Lab.
P.O. Box 999
Richland, WA 99352
509-942-2537

Bruce J. Pierce
University of Dayton
Research Institute
UDRI (AFWL/ALR)
Kirtland AFb, NM 87117
505-264-3013

Ben C. Platt
R. & D. Associates
ATO 9377
Albuquerque, NM 87119
505-264-3013

Robert D. Poirier
Perkin Elmer Corp.
77 Danbury Road, MS 420
Wilton, CT 06897
203-762-4947

Thomas M. Pollak
Sanders Associates
MER 12-1214
95 Canal Street
Nashua, NH 03060
603-885-4405

James O. Porteus
Naval Weapons Center
Code 3817
China Lake, CA 93555
714-939-3827

Frank Rainer
Lawrence Livermore Laboratory
P.O. Box 5508, L-465
Livermore, CA 94550
415-422-4376

John F. Ready
Honeywell, Inc.
Material Sciences Center
10701 Lyndale Ave., S
Bloomington, MN 55420
612-887-4430

John Reeves
Hughes, 77 45 24
Centinella & Teale Streets
Culver City, CA 90230
213-391-0711, ext. 3159

Jim Rinefierd
Laboratory for Laser Energetics
250 East River Road
Rochester, NY 14623
716-275-3418

Doug Ritchie
Physics Division
National Research Council
Montreal Road, Bldg. M-36, R-1211
Ottawa, Kiaosi, Ontario
Canada
613-993-9334

Herbert B. Rosenstock
Code 5504
Naval Research Laboratory
Washington, D.C. 20375
202-767-2225

Werner Ryseck
Siemens AG
8 Munchen 70
Hofmanstrasse 51
Germany
72263297

Ansgar Schmid
Physics Department
Washington State University
Pullman, WA 99164

Marion L. Scott
University of Dayton
Research Institute
AFWL/ALR
Kirtland AFB, NM 87117
505-822-0436

Steven C. Seitel
Naval Weapons Center
China Lake, CA 93555
714-939-2470

Robert R. Shannon
Optical Sciences Center
University of Arizona
Tucson, Arizona 85721
602-626-3345

David Shemwell
Perkin Elmer Corporation
M/S 240, Optical Systems
Main Avenue
Norwalk, CT 06856
203-762-4871

Glenn Sherman
Laser Power Optics Corp.
9062 Willoughby Road
Pittsburgh, PA 15237
412-366-7478

Philip A. Simpson
Electromagnetic Technology Division
National Bureau of Standards
Boulder, Colorado 80303
303-499-1000, ext. 3789

Aaron A. Sanders, Chief
Optical Electronic Metrology Group
Electromagnetic Technology Division
National Bureau of Standards
Boulder, Colorado 80303
303-499-1000, ext. 4341

W. Lee Smith
Lawrence Livermore Labs
Box 5508, L-465
Livermore, CA 94550
415-422-8209

Marion F. Soileau, Jr.
Naval Weapons Center
Code 3817
China Lake, CA 93555
714-939-3049

Gunnar Sorensen
Institute of Physics
University of Aarhus
8000 Aarhus C
Denmark

Marshall S. Sparks
Scientific Research Center
1640 Fifth Street, Suite 216
Santa Monica, CA 90401
213-394-0210

Charles L. Strecker
AFML/LPO
Wright-Patterson AFB, Ohio 45433
513-255-4474

Virgil Strahan
Rockwell International
031-278-063
3370 Miraloma Ave.
Anaheim, CA 92803
714-632-6547

Paul M. Sutton
Ford Aerospace & Communication Corp.
Ford Road
Newport Beach, CA 92663
714-759-5852

Paul Temple
Naval Weapons Center
China Lake, CA 93555
714-939-3247

Y.S. Touloukian
CINDAS/Purdue University
2595 Yeager Road
W. Lafayette, IN 47906
317-463-1581

Norman L. Thomas
University of California
Lawrence Livermore Laboratory
L-461
P.O. Box 808
Livermore, CA 94550
415-422-0486

James H. Tillotson
Rocketdyne
Advanced Laser Concepts
6633 Canoga Avenue
Canoga Park, CA 91304
213-884-2762

A. Vaidyanathan
AFWL/CA
Kirtland AFB, NM 87117
505-264-3982

Harshadrai Vora
Honeywell Corporate Material
Sciences Center
10701 Lyndale Ave., S
Bloomington, MN 55420
612-887-4412

Thomas Walker
AFWL/ALR
Kirtland AFB, NM 87117
505-264-8212

Nelson W. Wallace
Rockwell International
Rocketdyne Division 055-BA/30
6633 Canoga Avenue
Canoga Park, CA 91304
213-884-3854

David A. Walsh
University of Dayton
Research Institute
300 College Park Avenue
Dayton, Ohio 45469
513-254-2641

Paul E. Werner
Electromagnetic Technology Division
National Bureau of Standards
Boulder, Colorado 80303
303-499-1000, ext. 3439

Kurt Wiedemann
Siemens AG
Hofmannstrasse 51
West Germany
08977226892

Thomas Wiggins
AFWL/ALR
Kirtland AFB, NM 87117
505-264-1776

Richard T. Williams
Naval Research Laboratory
Code 5581
Washington, D.C. 20375
202-767-2768

Harry V. Winsor
DARPA/MSO
1400 Wilson Blvd.
Arlington, VA 22209
202-694-3031

G. Richard Wirtenson
University of California
Lawrence Livermore Laboratory
L-465
P.O. Box 5508
Livermore, CA 94550
415-422-1332

Shew M. Wong
Rockwell International
Rocky Flats, B/779
P.O. Box 464
Golden, Colorado 80020
303-497-2080

R.M. Wood
General Electric Co., Ltd.
Hirst Research Centre
East Lane, Wembley
Middlesex
United Kingdom
01-904-1262

Matt Young
Electromagnetic Technology Division
National Bureau of Standards
Boulder, Colorado 80303
303-499-1000, ext. 3223

Robert Zimmerer
Scientech, Inc.
5649 Arapahoe Ave.
Boulder, Colorado 80303
303-444-1361

 ☆ U. S. GOVERNMENT PRINTING OFFICE : 1980 311-046/162

NBS-114A (REV. 9-78)

U.S. DEPT. OF COMM. BIBLIOGRAPHIC DATA SHEET	1. PUBLICATION OR REPORT NO. NBS SP 568	2. Gov't. Accession No.	3. Recipient's Accession No.

4. TITLE AND SUBTITLE

Laser Induced Damage in Optical Materials: 1979

5. Publication Date: July 1980

6. Performing Organization Code

7. ~~AUTHOR(S)~~ (Editors)
Harold E. Bennett (NWC), Alexander J. Glass (LLL), Arthur H. Guenther (AFWL) & Brian E. Newnam (LASL)

8. Performing Organ. Report No.

9. PERFORMING ORGANIZATION NAME AND ADDRESS

NATIONAL BUREAU OF STANDARDS
DEPARTMENT OF COMMERCE
WASHINGTON, DC 20234

10. Project/Task/Work Unit No.

11. Contract/Grant No.

12. SPONSORING ORGANIZATION NAME AND COMPLETE ADDRESS *(Street, City, State, ZIP)*
American Society for Testing and Materials
Office of Naval Research
Department of Energy
Defense Advanced Research Project Agency

13. Type of Report & Period Covered

14. Sponsoring Agency Code

15. SUPPLEMENTARY NOTES

Library of Congress Catalog Card Number: 80-600100

☐ Document describes a computer program; SF-185, FIPS Software Summary, is attached.

16. ABSTRACT *(A 200-word or less factual summary of most significant information. If document includes a significant bibliography or literature survey, mention it here.)*

The Tenth Anniversary Symposium on Optical Materials for High Power Lasers (Boulder Damage Symposium) was held at the National Bureau of Standards in Boulder, Colorado, 30-31 October 1979. The Symposium was held under the auspices of ASTM Committee F-1, Subcommittee on Laser Standards, with the joint sponsorship of NBS, the Defense Advanced Research Project Agency, the Department of Energy, and the Office of Naval Research. About 150 Scientists attended the Symposium, including representatives of the United Kingdom, France, Canada, Japan, West Germany, and Denmark. The Symposium was divided into sessions concerning Transparent Optical Materials and the Measurement of Their Properties, Mirrors and Surfaces, Thin Film Characteristics, Thin Film Damage, Considerations for High Power Systems, and finally Theory and Breakdown. As in previous years, the emphasis of the papers presented at the Symposium was directed toward new frontiers and new developments. Particular emphasis was given to materials for high power apparatus. The wavelength range of prime interest was from 10.6 μm to the uv region. Highlights included surface characterization, thin film substrate boundaries, and advances in fundamental laser-matter threshold interactions and mechanisms. The scaling of damage thresholds with pulse duration, focal area, and wavelength was discussed in detail. Harold E. Bennett of the Naval Weapons Center, Alexander J. Glass of the Lawrence Livermore Laboratory, Arthur H. Guenther of the Air Force Weapons Laboratory, and Brian E. Newnam of the Los Alamos Scientific Laboratory were co-chairmen of the Symposium. The Twelfth Annual Symposium is scheduled for 30 September - 1 October 1980 at the National Bureau of Standards, Boulder, Colorado.

17. KEY WORDS *(six to twelve entries; alphabetical order; capitalize only the first letter of the first key word unless a proper name; separated by semicolons)* Laser damage, laser interaction; optical components; optical fabrication; optical materials and properties; thin film coatings.

18. AVAILABILITY ☒ Unlimited

☐ For Official Distribution. Do Not Release to NTIS

☒ Order From Sup. of Doc., U.S. Government Printing Office, Washington, DC 20402

☐ Order From National Technical Information Service (NTIS), Springfield, VA. 22161

19. SECURITY CLASS (THIS REPORT)	21. NO. OF PRINTED PAGES
UNCLASSIFIED	530
20. SECURITY CLASS (THIS PAGE)	**22. Price**
UNCLASSIFIED	$9.50

USCOMM-DC

NBS TECHNICAL PUBLICATIONS

PERIODICALS

JOURNAL OF RESEARCH—The Journal of Research of the National Bureau of Standards reports NBS research and development in those disciplines of the physical and engineering sciences in which the Bureau is active. These include physics, chemistry, engineering, mathematics, and computer sciences. Papers cover a broad range of subjects, with major emphasis on measurement methodology and the basic technology underlying standardization. Also included from time to time are survey articles on topics closely related to the Bureau's technical and scientific programs. As a special service to subscribers each issue contains complete citations to all recent Bureau publications in both NBS and non-NBS media. Issued six times a year. Annual subscription: domestic $13; foreign $16.25. Single copy, $3 domestic; $3.75 foreign.

NOTE: The Journal was formerly published in two sections: Section A "Physics and Chemistry" and Section B "Mathematical Sciences."

DIMENSIONS/NBS—This monthly magazine is published to inform scientists, engineers, business and industry leaders, teachers, students, and consumers of the latest advances in science and technology, with primary emphasis on work at NBS. The magazine highlights and reviews such issues as energy research, fire protection, building technology, metric conversion, pollution abatement, health and safety, and consumer product performance. In addition, it reports the results of Bureau programs in measurement standards and techniques, properties of matter and materials, engineering standards and services, instrumentation, and automatic data processing. Annual subscription: domestic $11; foreign $13.75.

NONPERIODICALS

Monographs—Major contributions to the technical literature on various subjects related to the Bureau's scientific and technical activities.

Handbooks—Recommended codes of engineering and industrial practice (including safety codes) developed in cooperation with interested industries, professional organizations, and regulatory bodies.

Special Publications—Include proceedings of conferences sponsored by NBS, NBS annual reports, and other special publications appropriate to this grouping such as wall charts, pocket cards, and bibliographies.

Applied Mathematics Series—Mathematical tables, manuals, and studies of special interest to physicists, engineers, chemists, biologists, mathematicians, computer programmers, and others engaged in scientific and technical work.

National Standard Reference Data Series—Provides quantitative data on the physical and chemical properties of materials, compiled from the world's literature and critically evaluated. Developed under a worldwide program coordinated by NBS under the authority of the National Standard Data Act (Public Law 90-396).

NOTE: The principal publication outlet for the foregoing data is the Journal of Physical and Chemical Reference Data (JPCRD) published quarterly for NBS by the American Chemical Society (ACS) and the American Institute of Physics (AIP). Subscriptions, reprints, and supplements available from ACS, 1155 Sixteenth St., NW, Washington, DC 20056.

Building Science Series—Disseminates technical information developed at the Bureau on building materials, components, systems, and whole structures. The series presents research results, test methods, and performance criteria related to the structural and environmental functions and the durability and safety characteristics of building elements and systems.

Technical Notes—Studies or reports which are complete in themselves but restrictive in their treatment of a subject. Analogous to monographs but not so comprehensive in scope or definitive in treatment of the subject area. Often serve as a vehicle for final reports of work performed at NBS under the sponsorship of other government agencies.

Voluntary Product Standards—Developed under procedures published by the Department of Commerce in Part 10, Title 15, of the Code of Federal Regulations. The standards establish nationally recognized requirements for products, and provide all concerned interests with a basis for common understanding of the characteristics of the products. NBS administers this program as a supplement to the activities of the private sector standardizing organizations.

Consumer Information Series—Practical information, based on NBS research and experience, covering areas of interest to the consumer. Easily understandable language and illustrations provide useful background knowledge for shopping in today's technological marketplace.

Order the **above** *NBS publications from: Superintendent of Documents, Government Printing Office, Washington, DC 20402.*

Order the **following** *NBS publications—FIPS and NBSIR's—from the National Technical Information Services, Springfield, VA 22161.*

Federal Information Processing Standards Publications (FIPS PUB)—Publications in this series collectively constitute the Federal Information Processing Standards Register. The Register serves as the official source of information in the Federal Government regarding standards issued by NBS pursuant to the Federal Property and Administrative Services Act of 1949 as amended, Public Law 89-306 (79 Stat. 1127), and as implemented by Executive Order 11717 (38 FR 12315, dated May 11, 1973) and Part 6 of Title 15 CFR (Code of Federal Regulations).

NBS Interagency Reports (NBSIR)—A special series of interim or final reports on work performed by NBS for outside sponsors (both government and non-government). In general, initial distribution is handled by the sponsor; public distribution is by the National Technical Information Services, Springfield, VA 22161, in paper copy or microfiche form.

BIBLIOGRAPHIC SUBSCRIPTION SERVICES

The following current-awareness and literature-survey bibliographies are issued periodically by the Bureau:

Cryogenic Data Center Current Awareness Service. A literature survey issued biweekly. Annual subscription: domestic $25; foreign $30.

Liquefied Natural Gas. A literature survey issued quarterly. Annual subscription: $20.

Superconducting Devices and Materials. A literature survey issued quarterly. Annual subscription: $30. Please send subscription orders and remittances for the preceding bibliographic services to the National Bureau of Standards, Cryogenic Data Center (736) Boulder, CO 80303.

U.S. DEPARTMENT OF COMMERCE
National Bureau of Standards
Washington, D.C. 20234

OFFICIAL BUSINESS

Penalty for Private Use, $300

POSTAGE AND FEES PAID
U.S. DEPARTMENT OF COMMERCE
COM-215

U.S.MAIL

SPECIAL FOURTH-CLASS RATE
BOOK